The Faint and the Furious: Probing the Low-Mass End of Core-Collapse Supernovae with the Zwicky Transient Facility

Thesis by
Kaustav Kashyap Das

In Partial Fulfillment of the Requirements for the
Degree of
Doctor of Philosophy

CALIFORNIA INSTITUTE OF TECHNOLOGY
Pasadena, California

2026
Defended April 24, 2026

© 2026

Kaustav Kashyap Das
ORCID: 0000-0001-8372-997X

All rights reserved

ACKNOWLEDGEMENTS

This thesis was possible only because of the time, patience, kindness, critique, and love of many people. I have been extremely fortunate to learn and do science in the company of wonderful mentors, collaborators, friends, and family. I am deeply grateful to everyone who shaped this journey, supported me through its difficult parts, and made the good parts so much more meaningful. Whatever I have learned, and whatever I become next, will always carry a part of each of you.

First, I want to thank my advisor and mentor, Mansi. It has been a privilege to learn from you and to have your guidance throughout my PhD. It meant a lot to know that I could come to you with any question, half-formed idea, or worry, and that you would always respond thoughtfully and have my back. Thank you for teaching me scientific rigor, for the many rounds of feedback on my writing, especially on proposals (and abstracts!), and for pushing me to make my arguments clearer and sharper. Through your direct mentorship, and by watching you up close, I learned how to do time-domain astronomy, work within large collaborations, build scientific programs, care deeply for the people who make the science possible, and keep a genuine joy for astronomy at the center of the work. I hope to carry these qualities with me as I continue my journey in science.

I am grateful to my thesis committee members, Jim, Shri, Vikram, and Dimitri, for their guidance, feedback, and support at different stages of my PhD.

Shri, thank you for your honest feedback and the many backyard conversations. Some of those conversations left me sleepless for a few nights, but they also pushed me to become a better scientist. I am also grateful for the Young UVEX Club, the binary-star sessions, and the thinkshops you organised, which gave me the opportunity to tinker with astronomy beyond my immediate field.

I am also very grateful to Lynne Hillenbrand, our option representative, for her support during my first year at Caltech. Beginning graduate school during COVID came with many uncertainties, and I am thankful for her help and advice as I navigated the transition into PhD life during that confusing time.

This thesis was made possible by the Zwicky Transient Facility collaboration, which taught me how large-scale time-domain astronomy works in practice.

Jesper, thank you for your careful reading and detailed feedback on all my manuscripts, for the literature and technical expertise you shared, for the questions you raised dur-

ing talks and draft reviews, and for the excitement you bring to supernova science. Your love for supernovae has been deeply inspiring, and I have learned so much from our conversations. I hope you continue to beat all the AI bots and remain the number one supernova scanner!

Christoffer, I have probably spent more hours discussing science with you than with almost anyone else. I benefited so much from being able to bounce ideas off you, whether I was asking silly questions, working through rough ideas, or debugging code. Thank you for always listening patiently, helping me think more clearly, and making the science better at many stages.

I have also benefited greatly from conversations with theorists, both in interpreting the results of this thesis and in shaping the motivation for several of the projects.

I am grateful to Jim Fuller for all the conversations about massive binaries and progenitor channels that lead to the explosions discussed in this thesis.

I am also grateful to Anders Jerkstrand for hosting me at Stockholm University and for teaching me the complex details of nebular spectroscopy.

Thanks also to Tony Piro for welcoming me to group meetings at Carnegie and for the lessons I learned there, from shock-cooling emissions to many other theoretical aspects of transients.

I was very fortunate to be part of the NGPS commissioning team. Until then, I had mostly used instruments that were already well-oiled machines; being part of the behind-the-scenes effort to bring a new instrument to life on a large telescope was both exciting and eye-opening. It taught me how much careful work, patience, and problem-solving go into making smooth science possible. Thank you to Rob, Christoffer, Matt, Dave, Chaz, Mansi and everyone at Palomar who made this such a valuable experience.

I am very thankful to the current and past members of Mansi's group and the Caltech Time-Domain group: Christoffer, Robert, Tomás, Sam, Viraj, Yuhan, Shreya, Yashvi, Yu-Jing, Maggie, Nicholas, Wynn, Theo, and others. You taught me the ABCs of the field, quite literally in the case of supernovae, and created an environment where it was easy to ask naive questions and learn from one another. Thank you for the group meetings, office conversations, and shared observing nights. You are the best scientists, and more importantly, the bestest human beings!

This thesis uses hundreds of spectra, and I have been fortunate to be part of more

than 90 observing runs at Palomar and Keck. It has been a privilege to spend so much time at some of the best facilities in the world. I am grateful to the staff and support astronomers, especially Shelly, Josh, and Michael at Keck, and Kathleen, Isaac, Paul, and the telescope operators, who made much of this science possible. A special shout-out to the photons that traveled millions of light-years from exploding stars, landed on our telescope detectors, and ended up in this thesis. I hope the long journey was worth it!

I want to thank the people who introduced me to astronomy and helped me fall in love with it during my undergraduate years. I am grateful to Pankaj sir, Yogesh sir, Alyssa, Omkar, and Catherine for giving me early opportunities and guiding me through my first astronomy projects. I am thankful for the NIUS camp at HBCSE and for the astronomy schools at IUCAA and NCRA. They opened a door I had barely known existed coming from a part of India with little exposure to science, and even less to astronomy.

The Caltech Astro graduate community made this journey much more joyful. I am especially grateful to my batchmates. We had a strange beginning to graduate school, with COVID, remote classes, and me joining lectures at 3 a.m. from India. Your support made that first year smoother, warmer, and much easier to get through. Later, moving to a new country and a new continent was not easy, and I am especially thankful to Tony and Nik for showing me around and making California feel a little more like home. Thank you also to my officemates over the years, Tony, Delina, Hazel, and Yashvi, for conversations that ranged from science to life to complete nonsense.

I am also thankful to the Indian cohort: Himanshu, Mrunmay, Divesh, Kartik, and Aakila. I am especially grateful to Himanshu for listening to my many rants, for being my travel companion on many fun trips exploring LA and California, and many Annapurna dinners together!

To my roommates over the years, Divesh, Simon, Yashvi, Jean, Viraj, Sitanshu, Sameer, and others, thank you for making home feel like home. And of course, Yashvi's cats, Merry and Pippin, deserve their own special mention for being the purrfect companions after long days at the office.

I am grateful to the chess communities that helped keep me sane: the Caltech collegiate chess team, the Caltech Chess Club, and the many people I met through chess. I am also thankful to Sagar, Amruta, Samay, and everyone at ChessBase

India for the stories, commentary, and joy that gave me a much-needed escape at times.

I strongly believe that it is a privilege to pursue astronomy, trying in some small way to understand the Universe. I am grateful to the Indian and U.S. taxpayers whose support made my education and this research possible.

I am also thankful for the opportunities I have had to give back by sharing the excitement of science with broader communities. Thanks to the West Karbi Anglong District Government, the Titabor District Government, and the Adarsha Vidyalaya organization for enabling me to give science talks in remote parts of Assam, India. It was a delight to speak with students from rural and underprivileged backgrounds, and to find joy in their wonder and curiosity. I am also grateful for the outreach opportunities at Caltech, especially through the Astro Outreach events organized by the amazing Cameron Hummels.

I am grateful to all my teachers, from my school days onward, for encouraging my never-ending list of questions and for believing in a young boy who dreamed of a world much larger than the one he knew.

To my partner, Nishi, thank you for being my constant pole star through all the highs and lows since high school. Thank you for being there through every joy and sorrow, every moment of doubt and every small victory. Thank you for believing in me through every uncertain step, and for making even the hardest days feel lighter. “Skystars!”

I am also grateful to my friends from school and undergrad: Ajay, Nachiket, Wrishik, Kishan, Mitul, Chiranjib, Priyambada, Wasif, Purbarag, Shilpismita, Nilotpal, Merlyn, and many others. Thank you for the years of friendship, laughter, support, and memories. I am blessed to have you in my life.

To my brother, thank you for your love, endless support, and for always cheering me on.

Finally, to my mother, my first teacher: thank you for every sacrifice you made, and for everything you carried quietly so that this journey could be possible. Thank you for building a home where curiosity was encouraged and learning was treated as something joyful. I owe my love for learning to you.

Whatever I have learned, and whatever I become next, will always carry a part of each of you.

ABSTRACT

The final fates of massive stars shape the chemical enrichment of galaxies, the formation of compact remnants, and the birth environments of new generations of stars. These fates depend sensitively on initial mass, mass loss, binary interaction, and late-stage stellar structure. At the low-mass boundary of core collapse, stars with initial masses of $\approx$ 8–12 $M_\odot$ occupy a critical transition region: below this range, stars are expected to end as white dwarfs, while above it, they undergo core collapse to form neutron stars or black holes. Yet the location and outcome of this boundary remain uncertain. For a typical initial mass function, around 50% of potential core-collapse supernova (CCSN) progenitors lie in this mass range, but their explosions are rarely identified. This deficit likely reflects the connection between these low-mass progenitors and low-luminosity SNe that are difficult to detect at larger distances.

In this thesis, I address these observational challenges by leveraging the depth and cadence of the Zwicky Transient Facility (ZTF). I led the largest volume-limited supernova surveys to date: the ZTF Census of the Local Universe (CLU) survey and the Complete Astronomical Transient Survey within 150 Mpc (CATS150). I also contributed to the commissioning and science validation of the Next Generation Palomar Spectrograph, enabling efficient and systematic spectroscopic studies of faint and nearby transients. Together, these efforts provide a robust observational foundation for probing the low-mass end of core collapse.

This thesis systematically searches for low-mass CCSNe across the full sequence of envelope stripping, beginning with hydrogen-rich Type II explosions and extending to partially and fully stripped systems. Using the CLU survey, I construct the largest systematic sample of Type IIP SNe to date and show that low-luminosity Type IIP events account for only a small fraction, 8^{+1}_{-2}%, of the core-collapse population. Lightcurve modeling places these events at the low-^{56}Ni, low-energy, low-ejecta-mass end of the hydrogen-rich population. Nebular spectroscopy identifies at most two plausible electron-capture SN candidates, indicating that this channel occupies a very narrow super-asymptotic giant branch (sAGB) progenitor mass window, $\Delta M \lesssim$ 0.02–0.06 $M_\odot$.

I then show that binary-stripped explosions also populate the low-mass regime, arising from low-mass helium stars with inflated radii during the final stages of stellar evolution. This population includes Ca-rich Type IIb and double-peaked

Type Ibc SNe, and extends to ultra-stripped and interaction-powered extremes such as SNe 2023zaw and 2018erx. These events demonstrate that stripped-envelope explosions can reach extremely low radioactive yields and may be underrepresented in current samples unless their emission is boosted by shock cooling or circumstellar interaction.

Taken together, these results show that neither hydrogen-rich nor stripped low-mass channels alone can account for all explosions expected from 8–12 $M_{\odot}$ progenitors. This discrepancy suggests that the effective lower-mass boundary for successful core collapse may be higher than commonly assumed, that some events remain undetected due to dust obscuration, or that a fraction of progenitors collapse directly to form black holes.

PUBLISHED CONTENT AND CONTRIBUTIONS

Das, K. K., A. Gangopadhyay, et al. (2026). "SN 2018erx: A fast-evolving, dust-reddened Type Icn supernova with broad C II emission lines". In: Submitted to *Publications of the Astronomical Society of the Pacific*. arXiv: 2605.24811.
K. K. D. led the analysis, modeling, interpretation, and manuscript preparation.

Das, K. K., A. Jerkstrand, et al. (2026). "Low-Luminosity Type IIP Supernovae from the Zwicky Transient Facility Census of the Local Universe. III: Hunting for electron-capture supernovae using nebular spectroscopy". In: Submitted to *Publications of the Astronomical Society of the Pacific*. arXiv: 2605.18960.
K. K. D. led the sample construction, analysis, modeling, interpretation, and manuscript preparation.

Das, K. K., M. M. Kasliwal, et al. (2026). "Low-luminosity Type IIP Supernovae from the Zwicky Transient Facility Census of the Local Universe. II. Lightcurve Analysis". In: *Publications of the Astronomical Society of the Pacific* 138.2, article 024204. doi: 10.1088/1538-3873/ae33f5.
K. K. D. led the sample construction, analysis, modeling, interpretation, and manuscript preparation.

Das, K. K., M. M. Kasliwal, et al. (2025). "Low-luminosity Type IIP Supernovae from the Zwicky Transient Facility Census of the Local Universe. I. Luminosity Function, Volumetric Rate". In: *Publications of the Astronomical Society of the Pacific* 137.4, article 044203. doi: 10.1088/1538-3873/adcaeb.
K. K. D. led the sample construction, analysis, modeling, interpretation, and manuscript preparation.

Das, K. K., C. Fremling, et al. (2024). "SN 2023zaw: An Ultrastripped, Nickel-poor Supernova from a Low-mass Progenitor". In: *The Astrophysical Journal Letters* 969.1, article L11. doi: 10.3847/2041-8213/ad527a.
K. K. D. led the sample construction, analysis, modeling, interpretation, and manuscript preparation.

Das, K. K., M. M. Kasliwal, et al. (2024). "Probing Presupernova Mass Loss in Double-peaked Type Ibc Supernovae from the Zwicky Transient Facility". In: *The Astrophysical Journal* 972.1, article 91. doi: 10.3847/1538-4357/ad595f.
K. K. D. led the sample construction, analysis, modeling, interpretation, and manuscript preparation.

Das, K. K., M. M. Kasliwal, et al. (2023). "Probing the Low-mass End of Core-collapse Supernovae Using a Sample of Strongly-stripped Calcium-rich Type IIb Supernovae from the Zwicky Transient Facility". In: *The Astrophysical Journal* 959.1, article 12. doi: 10.3847/1538-4357/acfeeb.

K. K. D. led the sample construction, analysis, modeling, interpretation, and manuscript preparation.

TABLE OF CONTENTS

Acknowledgements . . . iii
Abstract . . . vii
Published Content and Contributions . . . ix
Table of Contents . . . x
List of Illustrations . . . xiv
List of Tables . . . xxxvii
Chapter I: Introduction . . . 1
1.1 Core-collapse supernovae and the low-mass boundary of stellar death 1
1.2 Uncertain mass boundaries and fates in the 8–12 $M_\odot$ regime . . . 3
1.3 The importance of the 8–12 $M_\odot$ regime . . . 5
1.4 Systematic volume-limited supernova surveys . . . 7
1.5 Hydrogen-rich channels at the low-mass boundary of core collapse . 10
1.6 H-poor/binary channels at the low-mass boundary of core collapse . . 13
Chapter II: Commissioning and Science-Validation of the Next Generation Palomar Spectrograph . . . 18
2.1 Introduction . . . 18
2.2 First science observations . . . 18
2.3 Throughput measurements from commissioning standard-star observations . . . 19
2.4 Science-validation observations and observer-facing tools . . . 21
2.5 Enabling high spectroscopic completeness . . . 22
2.6 Summary . . . 24
Chapter III: The Complete Astronomical Transient Survey within 150 Mpc (CATS150) . . . 25
3.1 Survey design . . . 25
3.2 Alert filtering . . . 27
3.3 Survey completeness . . . 28
3.4 Transient demographics and subtype mix . . . 28
3.5 Preliminary luminosity function . . . 30
3.6 Summary . . . 31
Chapter IV: Low-Luminosity Type IIP Supernovae from the Zwicky Transient Facility Census of the Local Universe. I: Luminosity Function, Volumetric Rate . . . 33
4.1 Introduction . . . 35
4.2 Sample Selection . . . 37
4.3 Data . . . 45
4.4 Extinction Correction . . . 46
4.5 Luminosity function . . . 47
4.6 The Volumetric rate of Type IIP SNe using skysurvey . . . 51

4.7 Discussion . . . 54
4.8 Summary . . . 59
4.9 Data Availability . . . 60
4.10 Acknowldegement . . . 61
4.11 Appendix: Progenitor Mass from pre-explosion images Vs SN peak magnitude . . . 62
4.12 Appendix: Distance correction for nearby galaxies . . . 62
4.13 Appendix: ZTF Pipeline Recovery Efficiency Fits . . . 62
4.14 Appendix: Sample of CLU Type II SNe . . . 64
Chapter V: Low-Luminosity Type IIP Supernovae from the Zwicky Transient Facility Census of the Local Universe. II: Lightcurve Analysis . . . 84
5.1 Introduction . . . 85
5.2 Sample Selection . . . 88
5.3 Data . . . 88
5.4 Extinction Correction . . . 89
5.5 Analysis . . . 91
5.6 Results . . . 99
5.7 Discussion . . . 107
5.8 Conclusion . . . 120
Chapter VI: Low-Luminosity Type IIP Supernovae from the Zwicky Transient Facility Census of the Local Universe. III: Hunting for electron-capture supernovae using nebular spectroscopy . . . 151
6.1 Introduction . . . 152
6.2 Sample . . . 156
6.3 Spectroscopy Data . . . 158
6.4 Spectra processing and analysis . . . 159
6.5 Estimating ZAMS mass . . . 167
6.6 Electron-capture SN diagnostics . . . 171
6.7 Conclusion . . . 179
Chapter VII: Probing the low-mass end of core-collapse supernovae using a sample of strongly-stripped Calcium-rich Type IIb Supernovae from the Zwicky Transient Facility . . . 216
7.1 Introduction . . . 218
7.2 Data . . . 220
7.3 Methods and Analysis . . . 226
7.4 Discussion . . . 235
7.5 Conclusion . . . 246
7.6 Data availability . . . 248
Chapter VIII: Probing pre-supernova mass loss in double-peaked Type Ibc SNe from the Zwicky Transient Facility . . . 256
8.1 Introduction . . . 258
8.2 Sample Selection . . . 260
8.3 Data . . . 261
8.4 Methods and Analysis . . . 265
8.5 Constraining progenitor mass . . . 272

8.6 Mass-loss scenarios . . . 278
8.7 Summary and Future Goals . . . 285
8.8 Data availability . . . 287
8.9 Acknowldegement . . . 287
8.10 Appendix . . . 296
Chapter IX: SN 2023zaw: an ultra-stripped, nickel-poor supernova from a low-mass progenitor . . . 302
9.1 Introduction . . . 304
9.2 Discovery and follow-up observations . . . 305
9.3 Methods and analysis . . . 308
9.4 Discussion: Progenitor and evolutionary pathway . . . 318
9.5 Conclusion . . . 321
9.6 Data availability . . . 324
9.7 Acknowldegement . . . 324
9.8 Appendix . . . 326
Chapter X: SN 2018erx: A Fast-Evolving, Dust-Reddened Type Icn Supernova with Broad C II Emission Lines . . . 335
10.1 Introduction . . . 336
10.2 Discovery and follow-up observations . . . 339
10.3 Extinction correction . . . 342
10.4 Observed properties . . . 346
10.5 Analysis and Results . . . 353
10.6 Discussion . . . 370
10.7 Conclusion . . . 376
10.8 Data availability . . . 379
10.9 Acknowledgements . . . 379
Chapter XI: Conclusion . . . 386
11.1 Summary . . . 386
11.2 Missing supernovae from 8–12 $M_\odot$ progenitors: tension with a Salpeter-like IMF . . . 388
11.3 Future . . . 391
Bibliography . . . 397

LIST OF ILLUSTRATIONS

Number *Page*

1.1 Schematic illustration of the possible evolutionary pathways and final fates of intermediate-mass (8–12 $M_\odot$) stars. In this critical transition regime between white dwarf formation and core collapse, small differences in core growth, mass loss, and binary interaction can lead to a diverse range of outcomes, including ONe white dwarfs, electron-capture supernovae, and iron core-collapse supernovae. The shaded purple arrows indicate the full set of viable evolutionary channels available to stars in this mass range. 2

1.2 The black line shows the luminosity function for core-collapse SNe calculated from the ZTF BTS sample (Perley et al. 2020). Current constraints at the faintest end of the BTS CCSN luminosity function are poor because of the small number of SNe. A central goal of this thesis is to determine where the falloff occurs and where the luminosity function peaks at the faintest end. 8

1.3 Summary schematic of the binary channels emphasized in this thesis. Left to right, the retained envelope mass decreases from hydrogen-rich single-star explosions to progressively stripped binary outcomes. 14

2.1 First science spectrum obtained with NGPS, corresponding to ZTF24abrfcqd / SN 2024aaqp. The spectrum was classified during commissioning as a Type Ia supernova at redshift $z = 0.045$ and reported in TNS AstroNote 2024-340 (Transient Name Server 2024). 20

2.2 Total system throughput of NGPS as a function of wavelength for the four channels (C. Fremling et al., in prep). The shaded regions indicate the measured throughput variations across repeated observations, while the dashed gray curves show the expected throughput from the instrument model. Prominent dips correspond to atmospheric absorption features and instrumental transitions between channels. We also show the DBSP throughput (dashed line) for comparison. 22

2.3 Diagnostic breakdown of unclassified transients in the CLU experiment. A large majority of unclassified sources had poor-S/N spectra, nearly half were affected by bright host backgrounds, and slightly more than half never obtained even a single spectrum. 23
3.1 Spectroscopic completeness as a function of peak apparent magnitude for CATS150 and CLU (Das et al. 2025b). The CATS150 curve includes the gain enabled by NGPS at the faint end, maintaining substantially higher completeness than CLU toward $m_{peak} \approx 18.5$–20 mag. 26
3.2 Demographic summary of the classified CATS150 science sample to $m_{peak} \leq 20$. The sample was dominated by Type II and Type Ia events, but it also contained a substantial stripped-envelope component together with a clear low-luminosity thermonuclear tail. 31
3.3 Observed peak r-band absolute-magnitude distributions for the three main supernova families in the classified CATS150 science sample to $m_{\rm peak} \leq 20$. The horizontal axis is reversed so that the faint end lies to the left. These distributions are not corrected for host extinction or Malmquist bias, and should therefore be interpreted as preliminary observed luminosity functions rather than intrinsic ones. 32
4.1 Example of SN light curves and the GP interpolations. The apparent magnitudes have been corrected for Galactic and host extinction. The lower panels show the slope of the light curves, i.e., the derivative of the GP fits, in units of mag per day. The vertical dashed red line shows the epoch of the first detection. The vertical dashed grey line shows the epoch of last non-detection. The vertical solid red and blue lines show the epochs of peak r- and g-band magnitudes, respectively. 39
4.2 The distribution of the number of SNe in the final ZTF CLU Type IIP sample, consisting of 330 SNe, as a function of peak r-band absolute magnitude, with and without host-extinction correction 41
4.3 *Left:* The $g - r$ colors of the ZTF CLU Type II SN sample are shown in colored circles. The average color and standard deviation (1σ range) of the distribution, after filtering out SNe with Na I D EW > 1 Å, are shown by the black solid line and blue shaded region, respectively. *Right:* The sample $g - r$ color distribution after host-extinction correction. The color template is available in DOI:10.5281/zenodo.14538857. 46

4.4 The cumulative distribution of the spectroscopic completeness of the ZTF CLU survey (with 2064 saved transients) as a function of peak r-band apparent magnitude. The dashed line accounts for the entire sample, whereas the solid black line omits 79 transients that are probably spurious. As a conservative lower limit, we consider the completeness depicted by the solid dashed line. 47

4.5 The ZTF pipeline recovery efficiency as a function of apparent magnitude (*upper*) and as a function of the ratio of local surface brightness and target flux (*lower*). The best-fit parameters of the logistic function is listed in Appendix 4.13. The data required to reproduce the plot is available in DOI:10.5281/zenodo.14538857. 48

4.6 The peak r-band absolute magnitude distribution of the sample of 330 Type IIP SNe in CLU with Poisson errorbars before host-extinction correction (left) and after host-extinction correction (right). The volume-corrected luminosity function is shown in solid blue, while the raw distribution is shown in dashed green. GP fit is shown in blue. The luminosity function data is available in DOI:10.5281/zenodo.14538857. 49

4.7 The r-band lightcurve template for Type IIP SNe. The solid points depict the mean lightcurve magnitudes of the ZTF CLU Type IIP sample. The line and shaded regions show the 1σ uncertainties derived from the GP fit. 52

4.8 *Left:* The plot shows the number of LLIIP SNe that satisfy the filtering criteria as a function of the volumetric rate. The data points and the shaded region indicate the mean and standard deviation of detected transients, derived from 30 iterations of the simulated survey for each input volumetric rate. The dashed black line represents the observed number of Type IIP SNe in the ZTF CLU sample. *Right:* The fraction of simulations yielding the observed number of transients (within a 10% margin) is plotted against the volumetric rate. 52

4.9 The cumulative distribution of the luminosity function of the ZTF CLU Type IIP sample. The IIP and LLIIP volumetric rates are shown by the horizontal dashed lines. 53

4.10 The redshift completeness factor of the galaxy catalogs as a function of the host redshift and $W1$-band magnitude, measured in Fremling et al. (2020). The red stars depict the hosts of the SNe of the CLU Type IIP sample. 55

4.11 Comparison of the ZTF CLU Type II SNe luminosity function in r-band with the LOSS (r-band), PS1 (r-band), CCCP (r-band), SDSS (I-band), BTS (r-band) surveys (in shaded orange or green). The blue, green, and purple line depicts the volume and host-extinction corrected, only host-extinction corrected and only volume corrected distribution of the CLU Type IIP SNe sample, respectively. 56
4.12 The distribution of the Zero-Age Main-Sequence (ZAMS) mass estimated for Type II SNe from pre-explosion images as a function of the peak r-band magnitude. 63
4.13 Corner plots for the logistic function fit to the pipeline efficiency as a function of apparent magnitude (*left*) and the ratio of the alert apparent magnitude to the local surface brightness (*right*). 64
5.1 The upper panels show Gaussian Process fits to the lightcurves (shaded regions). Vertical dashed red lines indicate the epochs of first detection; vertical dashed grey lines mark the estimated explosion epochs. Vertical solid red and blue lines show the epochs of peak r- and g-band magnitudes, respectively. Vertical solid violet lines denote the start and end of the r-band plateau phase. Green dashed lines mark the epoch when the flux reaches 50% of the peak, used to compute the rise time. The lower panels show the light curve slope in units of mag day^{-1} and the change in slope (Δ slope) in units of mag day^{-2}. 90
5.2 Distribution of observable properties of the r-band light curves for the SN sample. From left to right and top to bottom, the panels show the distributions of: (1) plateau duration, (2) optically thick phase duration (OPTd), (3) plateau slope, (4) rise time to peak, and (5) magnitude drop between the plateau and the tail phase. These observables are measured from the Gaussian Process fits described in Section 5.5. LLIIP SNe with $M_r \geq -16$ are shown in hatched red, those with $M_r < -16$ in blue, and the full sample is shown in black. The median (50th percentile) and the 16th and 84th percentiles of the distributions are indicated as median$^{+84\text{th}-50\text{th}}_{-50\text{th}-16\text{th}}$ in the legend. 91

5.3 Observable light curve parameters as a function of r-band peak absolute magnitude (M_r). From left to right and top to bottom, the panels show: (1) plateau duration vs. M_r, (2) optically thick phase duration (OPTd) vs. M_r, (3) plateau slope vs. M_r, (4) rise time vs. M_r, and (5) the magnitude drop between the plateau and tail vs. M_r. In the last panel, upper limits are indicated by V-shaped triangles for SNe without a detected tail phase. LLIIP SNe with $M_r \geq -16$ are shown in red, while SNe with $M_r < -16$ are shown in blue. See details in Section 5.6. 92

5.4 Left: Expansion velocities measured from the absorption minima of the H I λ6563 P-Cygni line for all SNe in our sample. Each marker and color represents a unique SN. Right: Mean H I λ6563 velocities with standard deviation for the full sample (black), LLIIP SNe with $M_r \geq -16$ (red), and brighter SNe with $M_r < -16$ (blue). 92

5.5 Left: Fractional distribution of bolometric luminosity at the mid-plateau phase. LLIIP SNe with $M_r \geq -16$ are shown in hatched red, those with $M_r < -16$ in blue, and the full sample is shown in black. Right: Correlation between mid-plateau bolometric luminosity and nickel mass inferred from the bolometric lightcurve tail. LLIIP SNe with $M_r \geq -16$ are shown in red, and SNe with $M_r < -16$ are shown in blue. 93

5.6 Bolometric light curve fits using semi-analytical models from Nagy and Vinkó (2016). Red dots show the observed bolometric luminosities, while black lines represent the best-fit model lightcurves. The panels show (left to right, top to bottom): ZTF20aapchqy (SN 2020cxd), ZTF21abouuat (SN 2021ucg), ZTF24aarvbxj (SN 2024lby), ZTF23abnogui (SN 2023wcr), ZTF24aabppgn (SN 2024wp), and ZTF22aarycqo (SN 2022ojo). 101

5.7 Radiation-hydrodynamical model fits to the r- and g-band light curves using the model grid from Moriya et al. (2023). The model grid in Moriya et al. (2023) has been extended to include 9 $M_\odot$ and 10 $M_\odot$ progenitors with explosion energies in the range (1–5) $\times$ 10^{50} erg. The panels show (left to right, top to bottom): ZTF24aaemydm (SN 2024chx), ZTF22abyivoq (SN 2022acko), ZTF22aativsd (SN 2022ovb), ZTF23aackjhs (SN 2023bvj), ZTF21aaobkmg (SN 2021eui) and ZTF19acytcsg (SN 2019wvz). 102

5.8 Distributions of ejecta mass, nickel mass, explosion energy, and radius using semi-analytical models from Nagy and Vinkó (2016). LLIIP SNe with $M_r \geq -16$ are shown in hatched red, SNe IIP with $M_r < -16$ in blue, and the full sample is shown in black. 102

5.9 Distributions of the ZAMS mass, explosion energy, CSM radius, nickel mass, CSM structure parameter, and mass loss rates using radiation-hydrodynamical models from Moriya et al. (2023). LLIIP SNe with $M_r \geq -16$ are shown in hatched red, those with $M_r < -16$ in blue, and the full sample is shown in black. 103

5.10 The r- and g-band lightcurve of ZTF22abtspsw/SN 2022aagp with GP fits (shaded regions). Vertical lines mark key epochs: first detection (dashed red), explosion epoch (dashed grey), r- and g-band peaks (solid red and blue), plateau start and end (solid violet), and 50% peak flux (dashed green). The lower panels show the light curve slope (mag day^{-1}) and its change (Δ slope, mag day^{-2}). The steepest observed drop of > 3.5 mag was seen in this SN, consistent with predictions for ECSN and failed SNe with little or no nickel mass. . 104

5.11 Ejecta mass (top) and explosion energy (bottom) versus progenitor radius, derived using the scaling relations from Goldberg et al. (2019). Red lines denote SNe with $M_r > -16$ 108

5.12 Left: Radial density profile of the $8-10$ M$_\odot$ stellar progenitor models used in Utrobin et al. (2017), Kozyreva et al. (2021), Sato et al. (2024) Center: Density profile as a function of mass coordinate of the $8-10$ M$_\odot$ stellar progenitor models used in Utrobin et al. (2017), Kozyreva et al. (2021) Right: Density profile of FeCCSN and ECSN models used in Sato et al. (2024). The radii of the photosphere (r_{ph}) and the recombination front (r_{rec}) at 40 days after explosion are indicated by vertical lines. 110

5.13 Correlations between peak r-band magnitude and physical parameters (nickel mass, explosion energy, energy per unit mass, radius, ejecta mass), and among the physical parameters themselves, based on semi-analytical models from Nagy and Vinkó (2016). LLIIP SNe with $M_r \geq -16$ are shown in red, SNe IIP with $M_r < -16$ in blue. . . 113

5.14 Correlations between peak r-band magnitude and physical parameters (nickel mass, explosion energy, energy per unit mass, radius, ejecta mass), and among the physical parameters themselves, based on radiation-hydrodynamical model fits from Moriya et al. (2023). LLIIP SNe with $M_r \geq -16$ are shown in red, those with $M_r < -16$ in blue. 114
5.15 Correlation matrices of physical parameters derived from semi-analytical model fits (left) and radiation-hydrodynamical model fits (right). . . 114
5.16 Nickel mass versus explosion energy for a range of core-collapse SN models, compared to our observations. Theoretical models include 1D, 2D and 3D simulations (Ebinger et al. 2019, Sukhbold et al. 2016, Bruenn et al. 2016, 2023, Sandoval et al. 2021, Bollig et al. 2021, Burrows et al. 2024). The observational sample includes semi-analytical fits (green open circles) and radiation-hydrodynamical model fits (black) from this work. 115
5.17 Left: Comparison of explosion energies from our SN sample with predictions from recent 3D core-collapse simulations by Burrows et al. (2020). Right: Comparison of mid-plateau bolometric luminosities for our SN sample (horizontal lines) with theoretical predictions from Barker et al. (2022a) (black points), which relate luminosity to iron core mass. 117
5.18 Left: Mid-plateau $(g-r)$ colors compared to the ECSN color criterion from Sato et al. (2024), distinguishing explosions of sAGB stars from RSGs, shown in dashed black. Light curves of the SNe with the bluest (SN 2021tyw, mid-plateau $(g-r) = 0.2$ mag; center) and reddest (SN 2022jzc, mid-plateau $(g-r) = 1.4$ mag; right) mid-plateau colors. 119
5.19 All correlations between peak r-band magnitude and physical parameters (nickel mass, explosion energy, energy per unit mass, radius, ejecta mass), and among the physical parameters themselves, based on semi-analytical models from Nagy and Vinkó (2016). LLIIP SNe with $M_r \geq -16$ are shown in red, SNe IIP with $M_r < -16$ in blue. . . 148

5.20 Correlations between peak r-band magnitude and physical parameters (nickel mass, explosion energy, energy per unit mass, radius, ejecta mass), and among the physical parameters themselves, based on radiation-hydrodynamical model fits from Moriya et al. (2023). LLIIP SNe with $M_r \geq -16$ are shown in red, those with $M_r < -16$ in blue. 149

5.21 Comparison of physical parameters derived from semi-analytical light curve fits (y-axis) and radiation-hydrodynamical model fits (x-axis). Panels show nickel mass (left), ejecta mass versus ZAMS mass (center), and kinetic energy (right). Dashed lines indicate the one-to-one relation. Error bars reflect the 16th–84th percentile uncertainties from each method. 150

6.1 Keck/LRIS nebular spectra of ZTF24abtczty/SN 2024abfl at 149 d, 334 d and 393 d after explosion. The black curve shows the spectrum smoothed with a Savitzky–Golay filter, while the faint gray curve indicates the raw data. Colored vertical dashed lines mark the rest wavelengths of prominent nebular features, as labeled at the top (e.g. Mg I] λ4571, [O I] $\lambda\lambda$6300, 6364, H I λ6563, [Ca II] $\lambda\lambda$7291, 7323, and [C I] λ8727). The right-hand panels zoom in on the 7000–7500 Å region around the [Ca II] $\lambda\lambda$7291, 7323 complex, highlighting the narrow [Ca II] emission and the neighboring Fe- and Ni-peak features. . 160

6.2 Left: H I λ6563 FWHM for all objects in our sample as a function of phase. The colored points represent the ZTF CLU LLIIP sample, the literature comparison sample is shown in gray, and low-luminosity literature events are highlighted in yellow. Right: Same objects but showing the fractional [O I] luminosity $f_{[\mathrm{O\,I}]}$, as defined in Section 6.4. Dashed lines connect measurements of the same SN across different epochs. Throughout this paper, all quoted phases are measured relative to the estimated explosion epoch of each SN. . . . 161

6.3 Nebular H I λ6563 FWHM as a function of phase and peak absolute magnitude for our sample. Points are color-coded by M_{peak}, and the best-fit weighted plane is shown in gray. The trend indicates that fainter SNe exhibit systematically narrower nebular H I lines. A two-dimensional projection of this relation is shown in the top-left panel of Figure 6.4. 163

6.4 Correlation of nebular observables with r-band light-curve properties. Each column shows a different nebular diagnostic as a function of phase: H I λ6563 FWHM (left), the [Ca II]/[O I] ratio (middle), and the fractional [O I] luminosity $f_{[\mathrm{O\,I}]}$ (right). The three rows use different photometric quantities for the color coding: peak absolute magnitude (top), plateau slope (middle), and plateau duration (bottom). SNe with steeper plateau slopes, which are associated with higher luminosity (Das et al. 2025e), tend to have broader nebular H I emission. In contrast, we do not see any clear dependence of the nebular line widths or flux ratios on the plateau duration. A positive correlation between $f_{[\mathrm{O\,I}]}$ and phase is also visible, as discussed in Section 6.4. 165

6.5 Comparison of the ZTF LLIIP sample with literature LLIIP SNe and published nebular models. The colored points show the ZTF+CLU LLIIP SNe, and the yellow points show low-luminosity LLIIP events from the literature. Model tracks from Dessart et al. 2021b (D21), Dessart et al. 2025 (D25), Jerkstrand et al. 2014a (J14), and Jerkstrand et al. 2018 (J18) are shown for reference. The three panels present the evolution of the fractional [O I] luminosity (left), the [O I]/[Ca II] flux ratio (middle), and the H I λ6563 FWHM (right) as functions of phase. 169

6.6 Fractional [O I] flux as a function of phase for the ZTF LLIIP sample (colored symbols) and for literature comparison SNe (gray points). The background color shows the ZAMS mass predicted by our Gaussian Process regression model, which maps phase and fractional [O I] flux to M_{ZAMS} as described in Section 6.5. 170

6.7 Top left: distribution of ZAMS masses inferred for the ZTF LLIIP sample. Top right: cumulative distribution of the inferred masses, with Monte Carlo realizations shown in blue and the best-fit power-law slope α indicated. Bottom left: correlation between the fractional [O I] luminosity and the r-band peak magnitude. Bottom right: weak correlation between the inferred ZAMS mass and the r-band peak magnitude. Pearson coefficients for the two relations are shown in each panel. 172

6.8 Required width of the sAGB ECSN window $\Delta M_{\rm sAGB}$ as a function of the CCSN threshold mass $M_{CC,min}$. The blue shaded region indicates the range of $\Delta M_{\rm sAGB}$ values consistent with the empirical constraints. 180
6.9 Example of the nebular spectral analysis procedure for ZTF22abtjefa/SN 2022aaad at phase 332 d. Top panels show the original rest-frame, extinction-corrected spectrum with the fitted host-galaxy continuum (left) and the continuum-subtracted spectrum (right), with shaded regions indicating the line-poor windows used to define the continuum. Bottom left panels show the isolation of the [O I] $\lambda\lambda$6300, 6363 feature using a local pseudo-continuum defined by minima in the smoothed spectrum, followed by Gaussian fitting to measure the line flux and width. Bottom right panels show the multi-component Gaussian fit to the 7000–7500 Å region and the resulting isolated [Ca II] $\lambda\lambda$7291, 7323 profile after subtracting all other fitted lines. 203
6.10 Nebular spectra of ZTF22abtjefa/SN 2022aaad. 204
6.11 Nebular spectra of ZTF22abtjefa/SN 2022aaad. 205
6.12 Nebular spectra of ZTF24abtczty/SN 2024abfl. 206
6.13 Nebular spectra of ZTF23aackjhs/SN 2023bvj. 206
6.14 Nebular spectra of ZTF24aaejecr/SN 2024btj. 207
6.15 Nebular spectra of ZTF23aanxrjm/SN 2023kmk. 208
6.16 Nebular spectra of ZTF23aaquhaz/SN 2023mpz. 208
6.17 Nebular spectra of ZTF22aakdbia/SN 2022jzc. 209
6.18 Nebular spectra of ZTF22abssiet/SN 2022zmb. 209
6.19 Nebular spectra of ZTF22abvaetz/SN 2022aang. 209
6.20 Nebular spectra of ZTF23aabksje/SN 2023azx. 210
6.21 Nebular spectra of ZTF23abgmhgw/SN 2023vci. 210
6.22 Nebular spectra of ZTF22abyivoq/SN 2022acko. 211
6.23 Nebular spectra of ZTF23abnogui/SN 2023wcr. 212
6.24 Nebular spectra of ZTF23abpbuha/SN 2023usp. 212
6.25 Nebular spectra of ZTF23absscow/SN 2023ywa. 213
6.26 Nebular spectra of ZTF23abvgvab/SN 2023abim. 213
6.27 Nebular spectra of ZTF24aaasazz/SN 2024ov. 214
6.28 Nebular spectra of ZTF24aabppgn/SN 2024wp. 214
6.29 Nebular spectra of ZTF24aaezido/SN 2024cro. 214
6.30 Nebular spectra of ZTF24aaplfjd/SN 2024jxm. 215

7.1 Lightcurves for our sample of nine Ca-rich Type IIb SNe. This has forced-photometry from ZTF, ATLAS and follow-up observations from various instruments. See Section 7.2 for further description on the photometry. The left y-axis shows the apparent magnitude (mag) and the right y-axis shows the absolute magnitude (mag), without host extinction correction. The x-axis shows the number of rest-frame days since the second peak. 221
7.2 Collage of few spectra for the SNe in our sample showing H and He emission lines. The phase of the spectra is measured as the number of rest-frame days since the second peak. 223
7.3 Nebular spectra showing the [Ca II] $\lambda\lambda$7291, 7324 and [O I] $\lambda\lambda$6300, 6364 lines. The phase of the spectra is measured as the number of rest-frame days since the second peak. 224
7.4 The expansion velocity of the He I line for each SN of our sample represented by the filled dots. The blue shaded region shows the 1σ region of the ejecta velocity calculated for a sample of usual Type IIb SNe in Fremling et al. (2018) 227
7.5 ^{56}Ni-mass distribution for our sample of SNe IIb compared to the SN IIb population presented in Taddia et al. (2018). 233
7.6 Ejecta mass distribution for our sample of SNe IIb compared to the SN IIb population presented in Taddia et al. (2018). 234
7.7 Comparison of the lightcurves of the Ca-rich Type IIb SNe in our sample (in filled shapes of different types) with canonical Type IIb SNe lightcurves from Taddia et al. (2018) (in blue circles). The y-axis shows the absolute magnitude (mag), with galactic extinction correction. The x-axis shows the number of rest-frame days since the second peak. 235
7.8 Comparison of the ^{56}Ni-mass and the ejecta mass based on the Arnett fit for our sample and usual stripped-envelope Type IIb SNe from Taddia et al. (2018) and USSNe from De et al. (2018a), Yao et al. (2020). We find that the SSSNe in our sample is a transient class between the USSNe and the usual stripped-envelope SNe (SESNe) (rough boundaries indicated by the vertical dashed lined). We also note that there is a region in the parameter-space which is unoccupied by the SESN population. 236

7.9 The absolute B-band magnitude of CCSN host galaxies as a function of redshift. Our hosts are found in the least-luminous (10^{-3} $L^{\star}$) to the most luminous star-forming galaxies ($\lesssim 5$ $L^{\star}$) ($L^{\star}$ is the characteristic luminosity of the B-band luminosity function of star-forming galaxies). Most Ca-rich IIb hosts have luminosities of 10^{-2} to a few $L^{\star}$, similar to regular CCSNe (indicated by the contours encircling 68, 90 and 95% of the PTF+iPTF CCSN sample Schulze et al. 2020). We also indicate the $L^{\star}$ presented in Faber et al. (2007) and multiples of it with gray. 237

7.10 The host population in the mass-SFR plane. All sources exploded in star-forming galaxies. This is illustrated by their location with respect to the main sequence of star-forming galaxies (grey-shaded region). The majority of hosts also have properties consistent with those of CCSNe from the PTF+iPTF surveys (grey contours indicate the region encircling 68, 90 and 95% of the sample Schulze et al. 2020) 238

7.11 The projected physical offset distribution of all the SNe in our sample compared with the distribution for other types of SNe measured in De et al. (2020b). We note that there is a distinct offset from the Gap Ca-rich Type I SNe, known to occur in quenched environments. . . . 239

7.12 The red crosses shows the [O I] luminosities calculated from the nebular spectra for the Ca-rich Type IIb sample. The luminosity is normalized to the ^{56}Co decay energy. We compare these to models of stripped envelope core-collapse SNe from Jerkstrand et al. (2015a). We also show the measured normalized [O I] luminosities from the nucleosynthesis calculations of Yoshida et al. (2017) and the Ca-rich IIb iPTF 15eqv. 240

7.13 The measured O mass lower limits are shown with the horizontal dashed lines. The O yield for the ejecta arising from the He-star progenitor models, which assume an evolution in a binary system (Dessart et al. 2021a) are shown in solid blue dots and those arising from the single-star models (Sukhbold et al. 2016) are shown in filled orange stars. We also plot the O mass for nucleosynthetic models of higher ZAMS stars (Nomoto et al. 1997, Rauscher et al. 2002, Limongi and Chieffi 2003) and for lower ZAMS stars from USSNe models of Yoshida et al. (2017) and Moriya et al. (2017). 241

7.14 Comparison of the ejecta properties we observe (horizontal dashed lines) for our sample with that for the explosion models based on He stars evolved with the nominal mass-loss rate from Dessart et al. (2021a) (solid dots). From top to bottom, we show the ejecta mass $M_{\rm ej}$, ejecta kinetic energy $E_{\rm kin}$, the ^{56}Ni-mass, and the oxygen yield. . 247
7.15 The $g-r$ color evolution of the SNe in our sample represented by red crosses compared to the Type IIb SNe sample of Taddia et al. (2018) in gray diamonds. 250
7.16 The full-wavelength range of the nebular spectra shown in Figure 7.3. The phase of the spectra is measured as the number of rest-frame days since the second peak. 251
7.17 Shock cooling model (Piro et al. 2021) fits to multi-band data. 252
7.18 Radioactive (Arnett et al. 1989) fits to bolometric luminosity data excluding the data points fit by shock-cooling. 255
8.1 *Left:* Parameter space of peak magnitude of the first peak versus time above half maximum of the first peak $t_{1/2}^{\rm first}$ for all double-peaked SNe observed by ZTF as part of the BTS and CLU surveys. The Type Ibc(BL) SNe in the figure are part of the sample in this work. *Right:* We see a correlation in the peak magnitude of the first and second peaks of the SNe following $M_2 = 0.8 \times M_1 - 4.7$. M_1 and M_2 are the peak magnitudes of the first and second peak respectively. The solid line shows the best-fit linear relation. We can infer from the $y = x$ dashed line that the second peak is brighter than the first peak for most sources. The correlation could imply that the SNe that show double-peaked lightcurves have He-star progenitors that shed their envelope in binary interactions. 262
8.2 The interaction timescale for various SNe in the literature (from data compiled in Brethauer et al. 2022) showing signatures of CSM interaction including SNe Ibc, Ibn, Icn are shown by the colored lines. The blue-shaded region shows the range of timescale of the first peak for our sample consistent with shock-cooling ($t_{1/2}^{\rm first} < 8$ days). 263
8.3 Lightcurve of SN 2021gno ($E(B-V)_{\rm MW} = 0.01$). The lightcurves of the other SNe can be found in Appendix 8.10. 269
8.4 Comparison of the r-band absolute magnitude light curve of SN 2021gno to the other sources in the sample. The comparison for the other sources can be found in Appendix 8.10. 270

8.5 *Top:* Lightcurves of double-peaked Type Ibc SNe in our sample, obtained through forced-photometry from ZTF, ATLAS, and follow-up observations from various instruments. Further details on the photometry can be found in Section 9.2. The left y-axis represents the apparent magnitude (mag), while the right y-axis shows the absolute magnitude (mag). The absolute magnitude measurements assume Milky Way and host extinction values from Table B. The x-axis shows the number of rest-frame days since the epoch of the second peak. *Bottom:* The three SNe in the bottom panel have an unusually long first peak with $t_{1/2}^{\rm first} > 15$ days. We leave the detailed lightcurve analysis of these SNe for future work. 273

8.6 Spectral sequence for SN 2021gno (Type Ib) taken as part of the ZTF and CLU surveys. See Section 8.4 for details on the spectra obtained. Spectral sequence for the other sources can be found in Appendix 8.10. 274

8.7 *Left:* The filled shapes represent the expansion velocity of the He I λ5876 line for each SN in our sample. The blue-shaded region indicates the 1σ range of the ejecta velocities calculated for a sample of canonical Type IIb and Type Ibc SNe from Fremling et al. (2018). *Right:* The filled shapes represent the expansion velocity of the O I λ7774 line for each SN in our sample. Again, the blue-shaded region represents the 1σ range of the ejecta velocities calculated for a sample of normal Type IIb and Type Ibc SNe from Fremling et al. (2018). 274

8.8 Comparison of the CSM parameters of the sample in this paper with CSM properties of other SNe in the literature (from Brethauer et al. 2022). We note that the physical parameters have been estimated with a variety of observational “tracers" and hence probe different regions of the CSM. 275

8.9 The distribution of measured ^{56}Ni mass vs ejecta mass for SNe in this sample compared to normal Type Ibc, IIb SNe from Taddia et al. (2018). 276

8.10 The O mass measurements are depicted by horizontal dashed lines. The O yields from the He-star progenitor models, assuming binary evolution (Dessart et al. 2021a), are represented by solid blue dots. The O yields from the single-star models (Sukhbold et al. 2016) are indicated by filled orange stars. Additionally, we show the O mass predictions from nucleosynthetic models of lower ZAMS stars from USSNe models by Yoshida et al. (2017) and Moriya et al. (2017). . . 276
8.11 Comparison of the envelope parameters derived using analytical shock-cooling model as described in Section 8.4 (in red cross) with *bound* envelope properties from various binary and single star models (WF22; Wu and Fuller 2022a), (L20; Laplace et al. 2020) and (T15; Tauris et al. 2015). The SNe with low progenitor masses ($\lesssim 12\ M_{\odot}$) and higher progenitor masses are shown in red and blue respectively. 277
8.12 Comparison of the envelope parameters derived using analytical shock-cooling model as described in Section 8.4 (in red cross) with *unbound* CSM predictions from various pre-SN mass-loss models: late-time stable binary mass transfer (BMT; Wu and Fuller 2022a), late-time unstable binary mass transfer via common envelope (BMT CE; Wu and Fuller 2022a), late-time binary mass transfer with shock breakout at optical depth ~ 30 (BMT 30; Wu and Fuller 2022a), wave-driven mass loss (WD; Leung et al. 2021a, Shiode and Quataert 2014), pulsation-pair instability driven mass loss (PPI; Renzo et al. 2020, Leung et al. 2019). The SNe with low progenitor masses ($\lesssim 12\ M_{\odot}$) and higher progenitor masses are shown in red and blue respectively. 278
8.13 Shock cooling model (Piro et al. 2021) fits to multi-band data. 299
8.14 Radioactive (Arnett et al. 1989) fits to bolometric luminosity data. . . 300
8.15 Density profile of the single He-stars of different masses before late-time mass transfer used in Section 8.6. 301
9.1 *Left:* Pan-STARRS image of the host-galaxy of SN 2023zaw, UGC 03048 in the $grizy$ filters. The location of the transient is indicated by the white cross at the center. *Right:* Star-formation rate (SFR) map of the environment around SN 2023zaw (see Section 9.3). SN 2023zaw (position marked by the red circle) exploded in a star-forming region of the host galaxy close to regions of more vigorously star-forming regions. The image has a size of 4.1×6.7 kpc. The SFR scale is not corrected for attenuation. 306

9.2 *Left:* The multiband lightcurve collage of SN 2023zaw. The x-axis shows rest-frame days since the r-band peak (MJD = 60287.7). The photometry data has been corrected for Milky Way ($A_{V,MW}$ = 0.77 mag) and host extinction ($A_{V,host}$ = 1.12 mag) as described in Section 10.3. The vertical magenta lines represent epochs of spectral observations. *Right:* The g-band lightcurve of SN 2023zaw compared with other fast-evolving transients in the literature – fast-declining Type I SNe – SN 2010X (Kasliwal et al. 2010), SN 2019bkc (Prentice et al. 2020, Chen et al. 2020), the kilonova AT 2017gfo (Abbott et al. 2017), ultra-stripped SN candidates – SN 2019dge (Yao et al. 2020), iPTF14gqr (De et al. 2018c), SN 2019wxt (Shivkumar et al. 2023, Agudo et al. 2023), SN 2022agco (Yan et al. 2023). We also compare with Type Ibc and Type Ibn SN lightcurve templates from Taddia et al. (2015) and Hosseinzadeh et al. (2017a), respectively. 307

9.3 The spectra of SN 2023zaw (in black) compared with other fast-evolving transients in the literature – fast-declining Type I SNe – SN 2010X (Kasliwal et al. 2010), ultra-stripped SNe candidates – SN 2019dge (Yao et al. 2020), iPTF14gqr (De et al. 2018c), SN 2019wxt (Shivkumar et al. 2023, Agudo et al. 2023), SN 2022agco (Yan et al. 2023), canonical Type Ib SN – iPTF14bvn (Fremling et al. 2018), Type Ibn – SN 2006jc (Foley et al. 2007). We also compare with theoretical predictions for '.Ia' SNe (Shen et al. 2010) and nickel-free SN models (Kleiser and Kasen 2014). The spectra are corrected for Milky Way and host extinction. The x-axis represents the rest wavelength. The He I and Ca II emission lines are shown in dashed vertical lines. The telluric absorption features are indicated by the $\oplus$ symbol. 311

9.4 *Top:* Comparison of the bolometric luminosity, best-fit radius, and temperature evolution of SN 2023zaw from the blackbody fits described in Section 9.3 with ultra-stripped SN candidates: SN 2019dge (Yao et al. 2020), iPTF14gqr (De et al. 2018c), SN 2019wxt (Shivkumar et al. 2023, Agudo et al. 2023), and SN 2022agco (Yan et al. 2023). *Bottom left:* Shock-cooling emission model fit to the early-phase multiband light curve as described in Section 9.3. *Bottom right:* Best fits for bolometric luminosity with radiation-hydrodynamics and analytical models as described in Section 9.3. 313

9.5 We compare the estimated ejecta mass and nickel mass with Type Ibc SNe from Taddia et al. (2018), double-peaked Type Ibc SNe from Das et al. (2023b) and other ultra-stripped SN candidates – SN 2019dge (Yao et al. 2020), iPTF14gqr (De et al. 2018c), SN 2019wxt (Shivkumar et al. 2023, Agudo et al. 2023), SN 2022agco (Yan et al. 2023). The red plus sign denotes the best-fit parameters by fitting shock cooling emission + nickel decay to the lightcurve after host-extinction correction. 315

9.6 Comparison of the $r-$band and bolometric luminosity of SN 2023zaw with theoretical models for '.Ia' SNe (Shen et al. 2010), nickel-free SNe (Kleiser et al. 2018), electron-capture SN (Moriya and Eldridge 2016), and accretion-induced collapse of white dwarf (Darbha et al. 2010). The bold blue and green lines indicate the best-fit '.Ia' and nickel-free SN models, respectively. 322

9.7 We compare the time above half maximum and peak luminosity of SN 2023zaw with stripped-envelope supernovae from the BTS experiment (Perley et al. 2020). For sources with two peaks in the $r-$band lightcurve, the second peak is used. We also compare with other fast-evolving transients – SN 2019dge (Yao et al. 2020), SN 2019bkc (Prentice et al. 2020, Chen et al. 2020), iPTF14gqr (De et al. 2018c), iPTF16hgs (De et al. 2018b), AT 2018cow (Perley et al. 2019), ZTF18abvkwla or AT2023abbd (Ho et al. 2020). 326

9.8 Spectral sequence for SN 2023zaw. The phases are in rest-frame days since the r-band peak (MJD = 60287.7). See Section 9.2 for details on the obtained spectra. 329

9.9 The $g - r$ (*left*) and $r - i$ (*right*) color evolution of SN 2023zaw compared to other fast transients – SN 2005ek (Drout et al. 2013), SN 2019dge (Yao et al. 2020), iPTF14gqr (De et al. 2018c), iPTF14hgs (De et al. 2018b). The gray line shows the intrinsic color template for Type Ib SNe from Stritzinger et al. (2018). 330

9.10 The $r-$band lightcurve of SN 2023zaw compared with other fast-evolving transients in the literature – fast-declining Type I SNe – SN 2010X (Kasliwal et al. 2010), SN 2019bkc (Prentice et al. 2020, Chen et al. 2020), the kilonova AT 2017gfo (Abbott et al. 2017), ultra-stripped SN candidates – SN 2019dge (Yao et al. 2020), iPTF14gqr (De et al. 2018c), SN 2019wxt (Shivkumar et al. 2023, Agudo et al. 2023), SN 2022agco (Yan et al. 2023). 331

9.11 The envelope properties of SN 2023zaw (red cross) compared with double-peaked Type Ibc SNe (black squares) from Das et al. (2023b), USSN candidates (circles) – iPTF14gqr, SN 2019dge, SN 2019wxt, SN 2022agco (De et al. 2018c, Yao et al. 2020, Shivkumar et al. 2023, Agudo et al. 2023, Yan et al. 2023), and Type Ibn SNe (purple diamonds) – SN 2006jc, SN 2019wep, SN 2019up, SN 2012jpk, SN 2019deh, LSQ13ddu (Anupama et al. 2009, Pellegrino et al. 2022b, Clark et al. 2020). 332

9.12 *Left:* Comparison of the envelope properties of SN 2023zaw with theoretical models for *bound* stellar material – binary and single star models from Wu and Fuller (2022a) (WF22), Laplace et al. (2020) (L20) and Tauris et al. (2015) (T15). *Right:* Comparison of the the envelope properties of SN 2023zaw with theoretical models for *unbound* stellar material – late-time binary mass transfer (BMT; Wu and Fuller 2022a), wave-driven mass loss (Leung et al. 2021a, Shiode and Quataert 2014), pulsation-pair instability driven mass loss (PPI; Renzo et al. 2020, Leung et al. 2019). 333

9.13 Corner plots showing the posterior constraints of the model parameters in the shock-cooling emission (left) and radioactive decay (right) models described in Section 9.3. 334

10.1 Multi-band optical and near-infrared lightcurves of SN 2018erx. The left axis shows the observed apparent magnitudes, while the right axis indicates the corresponding absolute magnitudes. Both axes are corrected for Milky Way extinction, but no correction for host or circumstellar dust extinction has been applied. The phase is given in rest-frame days relative to the epoch of r-band maximum. Downward triangles denote nondetections. The epochs of spectroscopic observations are indicated by vertical purple lines. 340

10.2 Keck/LRIS spectrum of SN 2018erx obtained at a phase of +2.4 days (rest-frame) relative to r-band maximum. The grey line shows the original spectrum, while the black curve indicates a smoothed version. The purple shaded regions mark the wavelengths of prominent C II $\lambda\lambda$4267, 5145, 5890, 6578, and 7236 emission lines. 341
10.3 Cumulative distribution functions (CDFs) of rise time (left) and decline time (right) for stripped-envelope SN subclasses from the ZTF Bright Transient Survey (BTS) sample, while the SNe Icn sample combines the BTS SNe Icn with SN 2019jc, SN 2021ckj, SN 2023qre, and SN 2023rau. The vertical dashed line indicates the measured values for SN 2018erx, showing that it lies among the most rapidly evolving events relative to the broader populations of SNe Ib, Ic, Ic-BL, and IIb. 347
10.4 r-band absolute-magnitude lightcurve of SN 2018erx compared with rapidly evolving transients and SESNe from the literature. Red symbols show SN 2018erx assuming no host extinction ($A_V = 0$), while purple symbols show the extinction-corrected lightcurve adopting $A_V = 3.3$ mag. For comparison, lightcurves of several fast transients and interacting SESNe (colored markers) and a broader sample of stripped-envelope SNe (gray markers) are shown. The shaded regions indicate template lightcurves for SNe Ibn (G17; Hosseinzadeh et al. 2017a) and SNe Ibc (T15; Taddia et al. 2015). SN 2018erx evolves on a significantly faster timescale than typical SESNe. 348
10.5 Spectral evolution of SN 2018erx from −1.6 to +16.4 days relative to r-band maximum. The spectra are shown in the host-galaxy rest frame and have been vertically offset for clarity. The gray lines show the original spectra, while the black curves indicate smoothed versions. Indentifications of prominent lines are marked with dashed vertical lines, including C II, He I, N II, N III, O I, and Ca II. 350
10.6 Comparison of the +2.4 day Keck/LRIS spectrum of SN 2018erx (black) with representative spectra of Type Ibn (blue) and Type Icn (red) supernovae at phases of $\sim$ 3–10 days relative to peak. The spectra are shown in the rest frame and vertically offset for clarity. Dashed vertical lines mark the wavelengths of prominent spectral features, including C II, He I, He II, N II, N III, and Ca II. 352

10.7 Velocity profiles of prominent C II emission lines in SN 2018erx compared with representative Type Icn supernovae. The panels show the regions around C II λ7236, λ6587, and λ5890. Spectra are plotted in velocity space relative to the rest wavelength of each transition. The spectrum of SN 2018erx (black) is compared with those of the Type Icn events SN 2022ann (red) and SN 2019hgp (blue). The similar line widths and profiles highlight the strong C II emission characteristic of carbon-rich interacting SESNe. 353

10.8 Evolution of the blackbody parameters derived from multi-band photometry of SN 2018erx. Top: bolometric luminosity ($L_{\rm bb}$); middle: blackbody temperature ($T_{\rm bb}$); bottom: blackbody radius ($R_{\rm bb}$) as a function of rest-frame phase relative to r-band maximum. Black symbols show results obtained assuming no host extinction ($A_V = 0$), while brown symbols correspond to extinction-corrected values adopting $A_V = 3.3$ mag. Correcting for the inferred host attenuation significantly increases the inferred temperature and luminosity while reducing the emitting radius near peak. 354

10.9 Multi-band light-curve fit of SN 2018erx using the CSM-interaction model implemented in `redback`. The observed photometry in the g, r, and i bands is shown as colored points, while the solid curves represent the best-fitting model. 360

10.10 Corner plot showing the posterior distributions of the CSM-interaction model parameters obtained from the `redback` fit to the multi-band lightcurve of SN 2018erx. The diagonal panels show the marginalized posterior distributions, while the off-diagonal panels show the parameter covariances. The dashed lines indicate the median values and 1σ credible intervals. 361

10.11 Comparison of the circumstellar interaction parameters inferred for SN 2018erx with literature samples of Type Ibn/Icn SNe. Left: Inner CSM radius R_0 versus CSM mass $M_{\rm CSM}$. The black star marks the values inferred for SN 2018erx from the `redback` interaction modeling, while blue and red symbols show literature estimates for SNe Ibn and SNe Icn, respectively. Right: Cumulative distribution functions (CDFs) of the inferred interaction parameters ($M_{\rm ej}$, $M_{\rm CSM}$, R_0, $v_{\rm ej}$, and $\rho_{\rm CSM}$) for literature samples of SNe Ibn (blue) and SNe Icn (green). The dashed vertical line indicates the corresponding value for SN 2018erx. 362

10.12 Comparison of the ^{56}Ni mass ($M_{\rm Ni}$) and ejecta mass ($M_{\rm ej}$) of SN 2018erx with SESNe from the literature. The red symbol marks SN 2018erx, while blue triangles denote Type Icn events (Pellegrino et al. 2022b). The arrow indicates that the inferred ^{56}Ni mass is an upper limit. Gray symbols show literature measurements for other SESN subclasses from D24 (Das et al. 2023b), D23 (Das et al. 2023a), and T18 (Taddia et al. 2018), as well as ultra-stripped SN candidates (USSN) from Das et al. (2024a). SN 2018erx occupies the regime of both low ejecta mass and low ^{56}Ni mass. 366

10.13 Schematic illustration of the CSM environment inferred for SN 2018erx from the lightcurve and spectral modeling. The figure summarizes the compact C-rich inner CSM responsible for the rapid interaction, together with the more extended dusty component inferred from the strong extinction and late-time near-infrared excess. 377

A1 Measurement of the Balmer decrement in the host-galaxy spectrum at the position of SN 2018erx using a late-time Keck/LRIS observation. The continuum-subtracted host spectrum used to measure the line fluxes. The shaded regions mark the wavelength windows used to integrate the Hβ and Hγ emission lines. 382

A2 Evolution of the optical color $(g - r)$ for SN 2018erx compared with Type Ibn (blue symbols) and Type Icn (pink symbols) supernovae from the literature. Filled black circles show the observed colors of SN 2018erx assuming no host extinction ($A_V = 0$), while open black circles show the extinction-corrected values adopting $A_V = 3.3$ mag. Phases are given relative to r-band maximum. Compared to the comparison samples, SN 2018erx exhibits unusually red colors if no host extinction is applied, while the extinction-corrected colors are broadly consistent with the color evolution of other interacting SESNe. 384

A3 Comparison of the envelope properties of SN 2018erx with theoretical models for *bound* stellar material – binary and single star models from Wu and Fuller (2022a) (WF22), Laplace et al. (2020) (L20) and Tauris et al. (2015) (T15). *Right:* Comparison of the the envelope properties of SN 2023zaw with theoretical models for *unbound* stellar material – late-time binary mass transfer (BMT; Wu and Fuller 2022a), wave-driven mass loss (Leung et al. 2021a, Shiode and Quataert 2014), pulsation-pair instability driven mass loss (PPI; Renzo et al. 2020, Leung et al. 2019). 385

11.1 This thesis progressively fills the ejecta-mass/56Ni-mass phase space toward the low-mass, low-nickel end for stripped-envelope SNe. The gray symbols represent literature measurements for Type Ib/Ic supernovae from the Carnegie Supernova Project (Taddia et al. 2018), together with candidate ultra-stripped supernovae (USSNe) from the literature, including iPTF14gqr (De et al. 2018c), SN 2019dge (Yao et al. 2020), SN 2019wxt (Shivkumar et al. 2023, Agudo et al. 2023), and SN 2022agco (Yan et al. 2023). Type Icn SNe are taken from Pellegrino et al. (2022a). The colored symbols highlight objects analyzed in this thesis. Taken together, these objects extend the observed distribution into the previously sparsely populated regime of low ejecta mass and low ^{56}Ni mass. 389

11.2 Missing supernovae from 8–12 $M_\odot$ progenitors. The observed fractions of low-luminosity and stripped-envelope channels (colored wedges) fall short of expectations from a Salpeter initial mass function combined with the cosmic star-formation rate, indicating that a significant fraction of low-mass core-collapse events remain unaccounted for. . . 390

11.3 LSST will probe the faint end of the core-collapse supernova luminosity function to significantly larger distances, increasing the accessible volume by a factor of ~ 250 and enabling a systematic census of the faintest explosion channels. The shaded region indicates the predicted luminosity range of failed supernova "precursors" and "postcursors," which remain largely unexplored with current surveys. The vertical dashed line marks the approximate sensitivity limit of ZTF within 100 Mpc. The blue histogram shows the ZTF CLU volume-limited sample (Das et al. 2025b). 391

11.4 Three future directions that build directly on this thesis: identifying precursor activity before explosion, mapping the full power budget of stripped-envelope supernovae, and constraining which explosions form black holes. Horizontal dashed lines indicate approximate ZTF and Rubin/LSST single-epoch depth limits at 100 Mpc. 393

11.5 Schematic illustration of the discovery space for faint and fallback-powered core-collapse supernovae. The left panel shows the early-time lightcurve evolution, where higher-cadence surveys such as LS4 and ZTF are well suited to capture the rise and peak of low-luminosity events. The right panel highlights the late-time regime, where LSST can probe the declining lightcurves and constrain fallback onto compact remnants, including black hole formation. The dashed lines mark representative detection limits at 50 Mpc, demonstrating that LSST will uniquely access the regime of extremely low-luminosity, fallback-powered events that are largely inaccessible to current surveys. 395

LIST OF TABLES

Number *Page*

3.1 Summary of the real-time CATS150 alert filter. The table lists the implemented numerical criteria used to define the nearby-transient stream. 29

3.2 Cumulative CATS150 completeness as a function of limiting peak apparent magnitude for the completed survey accounting. 29

3.3 Monthly CATS150 completeness to $m_{peak} \leq 20$ for the completed survey accounting. 30

4.1 Sample selection summary 41

4.2 Summary table of the CLU Type II SN sample. Only the first 45 rows are shown here. The full table is shown in the Appendix 4.14. The peak absolute magnitudes have been measured by assuming Milky Way extinction ($A_{V,MW}$) and host galaxy extinction ($A_{V,host}$) as described in Section 10.3. The t_{expl} column shows the explosion epoch. The Peak mag_r shows the peak r-band absolute magnitude. A machine-readable version of the full sample table is available in DOI:10.5281/zenodo.14538857. 42

A Distance measurements used for galaxies < 25 Mpc. 63

B Summary table of the CLU Type II SN sample. The peak absolute magnitudes have been measured by assuming Milky Way extinction ($A_{V,MW}$) and host galaxy extinction ($A_{V,host}$) as described in Section 10.3. The t_{expl} column shows the explosion epoch. The Peak mag_r shows the peak r-band absolute magnitude. A machine-readable version of the full sample table is available in DOI:10.5281/zenodo.14538857. 65

A Definition of light-curve shape parameters based on light-curve phase, slope (mag day^{-1}), and rate of change of slope Δ_{slope} (mag day^{-2}). . . 93

B Summary of r-band lightcurve observables, divided into faint ($M_r \geq -16$), bright ($M_r < -16$), and the full sample. Median values with uncertainties and full observed ranges are shown. Plateau slopes are scaled by a factor of 10^{-2} mag day^{-1}. 100

C Best-fit physical parameters derived from semi-analytical model fits (Nagy and Vinkó 2016) for faint ($M_r \geq -16$), bright ($M_r < -16$), and all Type IIP SNe. Reported values include the median and 16th/84th percentile uncertainties, along with the full observed range. Nickel masses are scaled by a factor of 10^{-2} $M_\odot$. 106
D Best-fit physical parameters derived from radiation-hydrodynamical model fits (Moriya et al. 2023) for faint ($M_r \geq -16$), bright ($M_r < -16$), and all Type IIP SNe. Reported values include the median and 16th/84th percentile uncertainties, along with the full observed range. 107
A Light-curve parameters for SN II, sorted by faintest peak r-band absolute magnitude (M_r). ZTF and IAU names are shown in separate columns. The table includes rise time, plateau duration (Plat. dur.), optically thick duration (OPTd), decline rate during the plateau (Slope, in $\times 0.01$ mag day^{-1}), and the plateau-to-tail drop (Δmag). The full machine-readable table is available on Zenodo. 125
B Priors used in the MCMC fitting with the semi-analytical models from Nagy and Vinkó (2016). 128
C Priors used in the MCMC fitting with the radiation-hydrodynamical models from Moriya et al. (2023). 128
F Spectral log and H I λ6563 velocity measurements. 128
D Posterior estimates of explosion and progenitor properties based on fits to the semi-analytical models from Nagy and Vinkó (2016). We list the median values of ^{56}Ni mass ($M_{\rm Ni}$), ejecta mass ($M_{\rm ej}$), progenitor radius (R_0), and kinetic energy ($E_{\rm kin}$). The 16th and 84th percentiles are used to quantify the lower and upper uncertainties around the median. A full machine-readable version of this table is available on Zenodo. 143
D Continued. 144
D Continued. 145
E Posterior estimates of explosion and progenitor properties based on fits to the radiation-hydrodynamical models from (Moriya et al. 2023). A machine-readable version of this table is available on Zenodo. 146
E Continued. 147
E Continued. 150
A ZTF CLU LLIIP Sample Summary 156

B Spectral log of nebular spectra of LLIIP SNe. Throughout this paper, all quoted phases are measured relative to the estimated explosion epoch of each SN. 158
C Nebular spectral diagnostics for ZTF and selected comparison SNe, ordered from highest to lowest ECSN score. For each feature, the presence of an emission line is quantified using both the line SNR and peak ratio, with detection thresholds calibrated on the Jerkstrand et al. (2018) 9 $M_{\odot}$ nebular models (see Table H). Cells marked in green ('yes') indicate measurements consistent with ECSN expectations, red ('no') indicate measurements that contradict ECSN expectations, and grey ('maybe') indicate ambiguous cases. 174
D Spectral log of nebular spectra of brighter ZTF Type IIP SNe. 185
E Spectral Log for 120 nebular spectra of 54 non–ZTF Type II SNe . . 185
F Nebular measurements, plateau properties, peak absolute magnitudes, and ZAMS estimates for the LLIIP sample. 189
G Per-spectrum ZAMS mass estimates from the GP inversion. Uncertainties include a 10% systematic added in quadrature. 197
H ECSN diagnostic weights and thresholds. 202
A Summary of the sample of SNe presented in this work. Subscripts 1 and 2 refer to the peak parameters of the first and second peaks, respectively. The absolute magnitudes are corrected for Milky Way and host-galaxy extinction (see Section 7.3). 222
B Summary of the host extinction parameters for our sample. 229
C Log of the spectral observations and expansion velocity for few spectral lines in km/s. The phases are measured as the number of rest-frame days since the second peak. 230
D Summary of the nebular properties. The phases are measured as the number of rest-frame days since the second peak. We note that the oxygen mass measured here is a lower limit on the oxygen mass in the ejecta. The lower and upper limits of the O mass provided in the 'O mass' column correspond to 4000 K and 3400 K, respectively. . . 231
E Summary of the best-fit parameters obtained from shock cooling modeling of the first peak. 231

F Summary of the best-fit physical parameters obtained by radioactive decay modeling of the second peak of the SNe in our sample. The 'Ar' subscript refers to the Arnett et al. (1989) model while the 'KK' subscript refers to the Khatami and Kasen (2019) model. 232
G Summary of the blackbody properties for SN 2021sjt (Truncated). All the best-fit parameters including bolometric luminosity, radius and temperature for each object will be provided as machine-readable tables after publication here. 253
H Summary of the photometry data used for SN 2021sjt (Truncated). The photometry and spectroscopy data for each object will be provided as machine-readable tables after publication here. 253
I The models and fitting parameters used for CIGALE 254
J Summary of the host-galaxy best-fit parameters 254
A Steps for selecting our sample. See Section 8.2 for details regarding each step. 261
B Summary of the sample of 17 SNe used in this paper. The sources which have been mentioned previously in the literature are labeled with a superscript with a footnote of the list of papers where they were discussed. The absolute magnitudes have been measured by assuming Milky Way extinction ($A_{V,MW}$) and host galaxy extinction ($A_{V,host}$) as described in Section 10.3. Subscripts 1 and 2 refer to the peak parameters of the first peak and second peak respectively. 264
C Summary of the nebular properties. 288
D Shock cooling modeling 289
E Order of magnitude shock-cooling CSM estimates 290
F Order of magnitude shock-breakout CSM estimates 291
G Summary of the best-fit physical parameters obtained from radioactive-decay modeling of the second peak of the SNe in our sample. The 'Ar' subscript refers to the Arnett et al. (1989) model, while the 'KK' subscript refers to the Khatami and Kasen (2019) model. The photospheric velocity is estimated as described in Section 8.4. 292
H Bound stellar material properties of single star. 293
I Bound stellar material properties after binary mass transfer 294
I Continued... 295
J Summary of the photometry data used for SN 2018lqo (Truncated). . 297
K Summary of the blackbody properties for SN 2018lqo (Truncated). . 298

L Spectral log and ejecta velocity measurements. 300
A Comparison of explosion properties of SN 2023zaw with ultra-stripped SN candidates – SN 2019dge (Yao et al. 2020), iPTF14gqr (De et al. 2018c), iPTF16hgs (De et al. 2018b), SN 2019wxt (Shivkumar et al. 2023, Agudo et al. 2023), SN 2022agco (Yan et al. 2023). 316
B Emission line flux measurements of the star-forming region at the SN site. 327
C Truncated photometry data for SN 2023zaw. The full machine-readable version will be made available on GitHub after publication. The photometry data has been corrected for Milky Way extinction. . . 328
D Spectroscopy log. 328
E Summary of the blackbody properties for SN 2023zaw. A machine-readable version of this table will be made available on GitHub after publication. 331
F Priors used for shock-cooling emission model fitting described in Section 9.3. 332
G Priors used for nickel decay model fitting described in Section 9.3. . . 332
A Priors and constraints adopted for the `redback` CSM interaction fit. . 359
B Posterior median values and 68% credible intervals (16th and 84th percentiles) for the CSM interaction model parameters. 359
A1 Photometry after MW extinction correction. 382
A2 Spectroscopy log 383
A3 Blackbody evolution of SN 2018erx before and after extinction correction. Blank entries did not pass the quality cut $\sigma_{L_{\rm bb}}/L_{\rm bb} < 1$ because their best-fit luminosity uncertainties are too large. 383

Chapter 1

INTRODUCTION

1.1 Core-collapse supernovae and the low-mass boundary of stellar death

Core-collapse supernovae (CCSNe) mark the explosive endpoints of massive stars and are among the most important feedback channels in astrophysics (e.g., Janka 2012, Burrows and Vartanyan 2021). They inject kinetic energy, momentum, and newly synthesized elements produced both during stellar evolution and in the explosion itself into the interstellar medium, regulate subsequent star formation, and drive the chemical and dust evolution of galaxies (Nomoto et al. 2013, Colling et al. 2018, Sarangi et al. 2018). CCSNe also leave behind neutron stars and black holes, linking stellar evolution to high-energy phenomena across cosmic time (Woosley and Bloom 2006, Abbott et al. 2017, Kasliwal et al. 2017). Because massive stars evolve on short timescales, the CCSN rate broadly traces recent star formation and connects transient demographics directly to stellar evolution and the initial mass function (Horiuchi et al. 2011).

A massive star's initial mass largely determines its final outcome: low-mass stars ($\lesssim 8$ $M_\odot$) end as white dwarfs, while more massive stars ($\gtrsim 12$ $M_\odot$) undergo core collapse, leaving neutron stars or black holes. The transition between these channels occurs in the intermediate range of ~8–12 $M_\odot$, making this one of the most important and uncertain boundaries in stellar evolution (e.g., Janka 2012). The ~8–12 $M_\odot$ regime is uniquely sensitive to the details of late-stage stellar evolution. Stars in this range develop partially degenerate cores whose composition and structure ultimately set their final fate, with some evolving toward classical Fe-core collapse and others instead undergoing collapse triggered by electron captures in ONeMg cores. This sensitivity arises because these progenitors have lower pre-SN compactness and are particularly affected by uncertain processes such as thermal pulses, convective boundary mixing, and final-stage mass loss (e.g., Miyaji et al. 1980, Woosley and Heger 2015, Sukhbold et al. 2016). As a result, relatively small differences in core growth and envelope evolution can redirect otherwise similar progenitors toward qualitatively different outcomes, including heavy white-dwarf formation, electron-capture supernovae, or low-mass Fe-core-collapse explosions. We discuss these evolutionary pathways in more detail in Section 1.2.

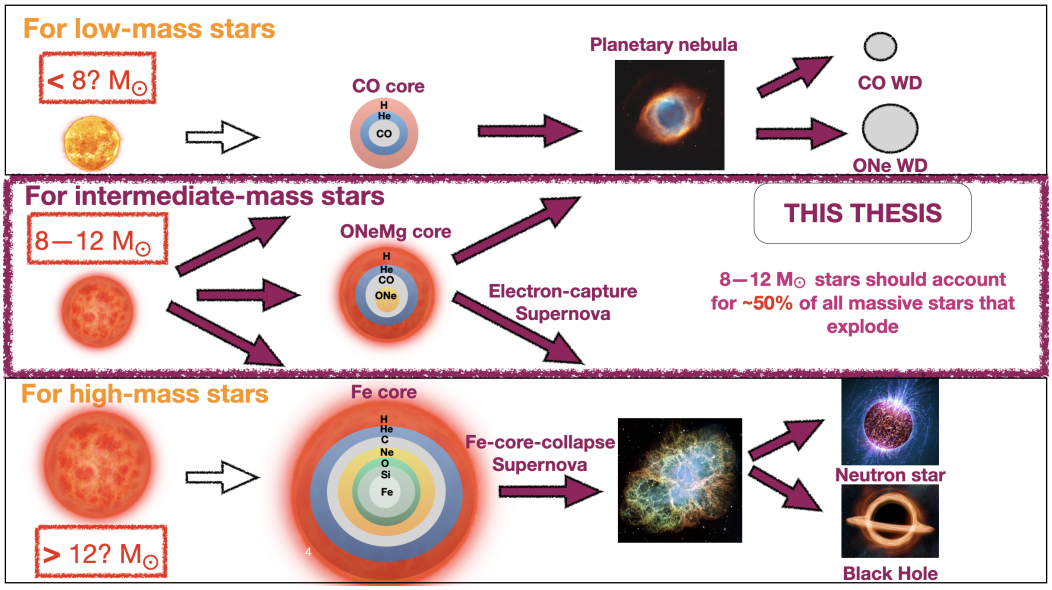

Figure 1.1: Schematic illustration of the possible evolutionary pathways and final fates of intermediate-mass (8–12 $M_{\odot}$) stars. In this critical transition regime between white dwarf formation and core collapse, small differences in core growth, mass loss, and binary interaction can lead to a diverse range of outcomes, including ONe white dwarfs, electron-capture supernovae, and iron core-collapse supernovae. The shaded purple arrows indicate the full set of viable evolutionary channels available to stars in this mass range.

The intermediate ~8–12 $M_{\odot}$ mass range is also important from a demographic perspective. Because the initial mass function rises steeply toward lower masses, stars near the minimum mass for core collapse, corresponding to this interval, are expected to contribute to around half of the total CCSN population. This makes the low-mass boundary especially important not only for understanding which stars explode, but also for broader questions involving supernova rates, chemical enrichment, stellar evolution, and compact-remnant demographics. We discuss these implications in more detail in Section 1.3.

However, SNe associated with low-mass progenitors remain surprisingly rare in observed samples (e.g., Turatto et al. 1998, Spiro et al. 2014, Jäger et al. 2020, Müller-Bravo et al. 2020, Reguitti et al. 2021, Yang et al. 2021). One likely explanation is that these events are intrinsically faint and therefore difficult to detect beyond the very nearby universe. Theory has long predicted that the lowest-mass core-collapse explosions should be systematically weaker than canonical CCSNe, with lower explosion energies, reduced ^{56}Ni yields, and correspondingly fainter luminosities (Janka 2012, Sukhbold et al. 2016, Melson et al. 2015, Müller 2016, Burrows et al.

2019, Burrows and Vartanyan 2021). Constraining this faint end therefore requires systematic, volume-limited surveys that are sensitive to intrinsically low-luminosity events. The survey strategy adopted in this thesis is motivated by exactly this need, and is discussed in Section 1.4.

A central goal of this thesis is to determine the observable outcomes of stars born near this boundary. I begin by considering the fate of stars in this mass range that evolve effectively as single stars, or at least retain most of their hydrogen envelopes until explosion, and discuss these channels in Section 1.5. I then turn to systems whose evolution is altered by binary interaction, leading to partial or extensive stripping of their hydrogen, and in some cases helium, envelopes before explosion. These stripped and interaction-shaped channels, which may also populate the low-mass end of the core-collapse distribution, are discussed in Section 1.6.

1.2 Uncertain mass boundaries and fates in the 8–12 $M_\odot$ regime

The fate map of the 8–12 $M_\odot$ regime can be organized in two steps: first, whether the star ends its life as a white dwarf or proceeds to core collapse; and second, among stars that do undergo collapse, whether the instability is triggered in an ONeMg core of an sAGB star or an Fe core of a red supergiant (RSG).

The uncertain boundary between white-dwarf and neutron-star formation

A central observational goal of this thesis is to constrain the minimum mass for core collapse by building a systematic census of low-luminosity nearby supernovae. Chapters 4 and 5 are motivated by the idea that a systematic sample of core-collapse SNe can be compared with expectations from the IMF and used to infer where the core-collapse population first turns on. In evolutionary terms, the first question in this mass range is whether the star collapses at all. Below the collapse threshold, stars avoid core collapse and end as white dwarfs; just above it, they continue toward neutron-star-forming collapse. This boundary is especially sensitive to late-stage mass loss and dredge-up, because those processes determine whether core growth can outpace envelope removal.

CO white dwarf. Below $M_{\rm CO}$, the star develops a degenerate CO core but avoids carbon ignition under conditions that would drive the core toward collapse. After envelope loss on the asymptotic giant branch, the remnant is a CO white dwarf. Published estimates of $M_{\rm CO}$ span roughly ~7–9.5 $M_\odot$, depending on the adopted input physics (e.g., Siess 2007, Poelarends et al. 2008). While such stars may later

participate in thermonuclear SN Ia channels in binaries, they do not contribute directly to the core-collapse SN population.

ONe white dwarf. Just above $M_{\rm CO}$, carbon ignition typically occurs off-center in a partially degenerate core, and the star can build an ONe-dominated core. Stars in this regime are commonly referred to as super-asymptotic giant branch (sAGB) stars. If envelope removal outpaces core growth, the star ends as an ONe white dwarf rather than collapsing. A representative value often quoted for this transition is $M_{\rm ONe}$ ~8–10 $M_\odot$(e.g., Jones et al. 2013), though it remains strongly model dependent. This part of the boundary is especially relevant in binaries, where Roche-lobe overflow or common-envelope evolution can efficiently strip the envelope and prevent collapse.

Among collapsing stars: ONeMg-core versus Fe-core fates

Once collapse does occur, the next observational question is whether any of the faintest explosions arise from the electron-capture channel. A systematic search for ECSN-like events, carried out in Chapter 6, can therefore constrain the allowed sAGB window and the narrow initial-mass interval separating ONe white-dwarf formation from neutron-star birth through collapse of an ONeMg core. In evolutionary terms, the question is whether the star collapses as an electron-capture supernova from an ONeMg core, or instead continues through neon, oxygen, and silicon burning to form an iron core.

Electron-capture supernova. If the ONeMg core instead grows to near the Chandrasekhar mass before envelope loss terminates burning, electron captures on Ne and Mg reduce the electron fraction, soften the equation of state, and trigger collapse of the sAGB star (e.g., Miyaji et al. 1980, Nomoto 1984, Kitaura et al. 2006, Janka et al. 2008). These electron-capture supernovae are predicted to produce weak explosions ($\sim 10^{50}$ erg) and very small ^{56}Ni yields ($\sim 10^{-3}$ $M_\odot$) in neutrino-driven models (e.g., Kitaura et al. 2006, Janka et al. 2008, Wanajo et al. 2009). A key subtlety in this regime is the role of off-center burning and mixing: in some models the flame reaches the center and produces a more standard ONeMg core susceptible to collapse, while in others it stalls and may instead leave a hybrid C–O–Ne structure. The initial-mass interval that produces ECSNe may be narrow and highly sensitive to uncertain mass loss and dredge-up physics (Siess 2007, Poelarends et al. 2008, Doherty et al. 2015).

Fe-core-collapse supernova. Above $M_{\rm ECSN}$, the core ignites neon, proceeds through oxygen and silicon burning, and builds an iron core that collapses once it exceeds the effective Chandrasekhar mass. This is the classical Fe-core-collapse pathway. Estimates of $M_{\rm ECSN}$ span a wide range, roughly ~8.8–11 $M_\odot$ in different studies (e.g., Nomoto 1984, Takahashi et al. 2013, Jones et al. 2013, Woosley and Heger 2015, Kirsebom et al. 2019), reflecting the sensitivity of the problem to late burning, mass-loss prescriptions, and convective boundary mixing. At the low-mass end of Fe-core collapse, models predict steep density gradients outside the core, low envelope binding energies, and relatively low neutrino luminosities compared to higher-mass progenitors, tending toward lower explosion energies and smaller ^{56}Ni yields (e.g., Janka 2012, Sukhbold et al. 2016, Müller 2016, Burrows et al. 2019, Burrows and Vartanyan 2021). The lowest-mass progenitors in this channel that retain hydrogen envelopes are expected to end their lives as red supergiants (RSGs) and explode as H-rich SNe.

While the exact transition masses between CO core formation, ONe core formation, and electron-capture supernovae remain uncertain, most stellar evolution models place these boundaries within the intermediate-mass range of ~8–12 $M_\odot$. In this regime, the boundary between white-dwarf and neutron-star formation is itself uncertain: some stars avoid collapse and end as white dwarfs, while others undergo core collapse to form neutron stars, either through electron-capture or Fe-core-collapse.

1.3 The importance of the 8–12 $M_\odot$ regime

Demographic importance

The demographic importance of the low-mass boundary of core collapse follows directly from the steepness of the stellar initial mass function (IMF). For a Salpeter-like IMF (Salpeter 1955),

$$\frac{\mathrm{d}N}{\mathrm{d}M} \propto M^{-\alpha}, \qquad \alpha = 2.35, \tag{1.1}$$

the number of stars decreases rapidly with increasing mass. As a result, stars capable of core collapse are concentrated close to the minimum collapse mass.

For a power-law IMF, the fraction of core-collapse progenitors in an interval $[M_1, M_2]$ is

$$f(M_1, M_2) = \frac{\int_{M_1}^{M_2} M^{-\alpha}\,\mathrm{d}M}{\int_{M_{\rm min}}^{M_{\rm max}} M^{-\alpha}\,\mathrm{d}M} = \frac{M_1^{1-\alpha} - M_2^{1-\alpha}}{M_{\rm min}^{1-\alpha} - M_{\rm max}^{1-\alpha}}, \tag{1.2}$$

for $\alpha \neq 1$.

For a Salpeter slope and $M_{\rm min} = 8\ M_\odot$, the 8–12 $M_\odot$ interval contains

$$f(8, 12) \approx 0.44\text{–}0.48 \tag{1.3}$$

for $M_{\rm max} = 100\text{–}40\ M_\odot$. In other words, roughly ∼45% of all CCSN progenitors are expected to lie in this range. Even the narrower 8–10 $M_\odot$ interval contributes ≈ 27–29%.

If the highest-mass stars contribute less efficiently to the *observed* CCSN population, the relative importance of the low-mass end becomes even larger:

$$f(8, 12) \approx 0.54\text{–}0.59 \tag{1.4}$$

for $M_{\rm max} = 25\text{–}20\ M_\odot$. Thus, depending on the effective upper mass limit for visible explosions, the 8–12 $M_\odot$ regime may account for roughly ∼40–60% of core-collapse events.

Because the IMF is steep, CCSN rates are also sensitive to the minimum collapse mass itself: increasing $M_{\rm min}$ from 8 to 9 $M_\odot$ reduces the expected progenitor count by ∼15–17%, while increasing it to 10 $M_\odot$ reduces it by ∼27–30%. The practical consequence is that uncertainty in the fate of stars near the minimum collapse mass propagates directly into the expected rate and composition of the observed CCSN population.

Broader astrophysical relevance

Beyond the demographic argument above, the importance of the 8–12 $M_\odot$ regime can be summarized in four ways:

1. **IMF weighting and CCSN rates.** Because the IMF places so much weight near the minimum mass for collapse, uncertainty in the fate of 8–12 $M_\odot$ stars maps directly into uncertainty in the normalization of the CCSN rate and in the faint end of the CCSN luminosity function. This is especially relevant in the long-standing discussion of whether faint CCSNe are systematically missed by current surveys (e.g., Horiuchi et al. 2011, Botticella et al. 2012, Horiuchi et al. 2013, Cappellaro et al. 2015, Xiao and Eldridge 2015, Jencson et al. 2019b).

2. **Galactic chemical evolution.** Low-mass Fe-core CCSNe and ECSNe synthesize different mixtures of intermediate-mass, iron-peak, and neutron-rich

trans-iron material, so even a modest ECSN contribution can leave a measurable imprint on galactic abundance patterns (e.g., Wanajo et al. 2009). Chemical-evolution models that include ECSN-like channels can help explain several isotopes that are otherwise difficult to reproduce in the solar inventory, including ^{48}Ca, ^{50}Ti, ^{54}Cr, ^{58}Fe, ^{64}Ni, ^{82}Se, ^{86}Kr, and several isotopes between Zn and Zr (Jones et al. 2019).

3. **Late stellar-evolution tracks.** This regime is where uncertainties in second dredge-up, thermal pulses, convective boundary mixing, mass loss, and binary stripping have some of their largest consequences for final fate. Constraining which stars explode, and through which channel, therefore provides a critical observational test of late-stage evolution in super-AGB stars, low-mass red supergiants, and stripped helium stars (e.g., Miyaji et al. 1980, Woosley and Heger 2015, Siess and Lebreuilly 2018). Because these same physical processes set the mapping between initial mass and final outcome, they also represent one of the dominant sources of uncertainty in stellar population synthesis models, particularly in predicting the relative rates of white-dwarf formation, electron-capture supernovae, and iron core-collapse supernovae.

4. **Compact remnants and gravitational-wave progenitors.** The same mass range sits at the transition between white-dwarf and neutron-star formation and therefore shapes compact-remnant demographics. In binaries, stripped low-mass core-collapse channels are especially relevant for producing compact binaries that later merge as gravitational-wave sources (Podsiadlowski et al. 2004, Tauris et al. 2013, 2015, 2017, Jiang et al. 2021).

1.4 Systematic volume-limited supernova surveys

As discussed above, stars in the ~8–12 $M_\odot$ regime are expected to produce some of the faintest core-collapse explosions. Their low explosion energies and reduced ^{56}Ni yields naturally lead to low peak luminosities, and in cases where the hydrogen envelope is partially or fully stripped, also to more rapidly evolving light curves. These events therefore occupy a region of parameter space characterized by both low luminosity and, in some cases, fast timescales.

If such explosions are common, then incompleteness at the low-luminosity end becomes a central obstacle in connecting stellar-evolution theory to the observed CCSN population. Historically, this part of the luminosity function has been defined by a heterogeneous collection of nearby events, with limited spectroscopic follow-

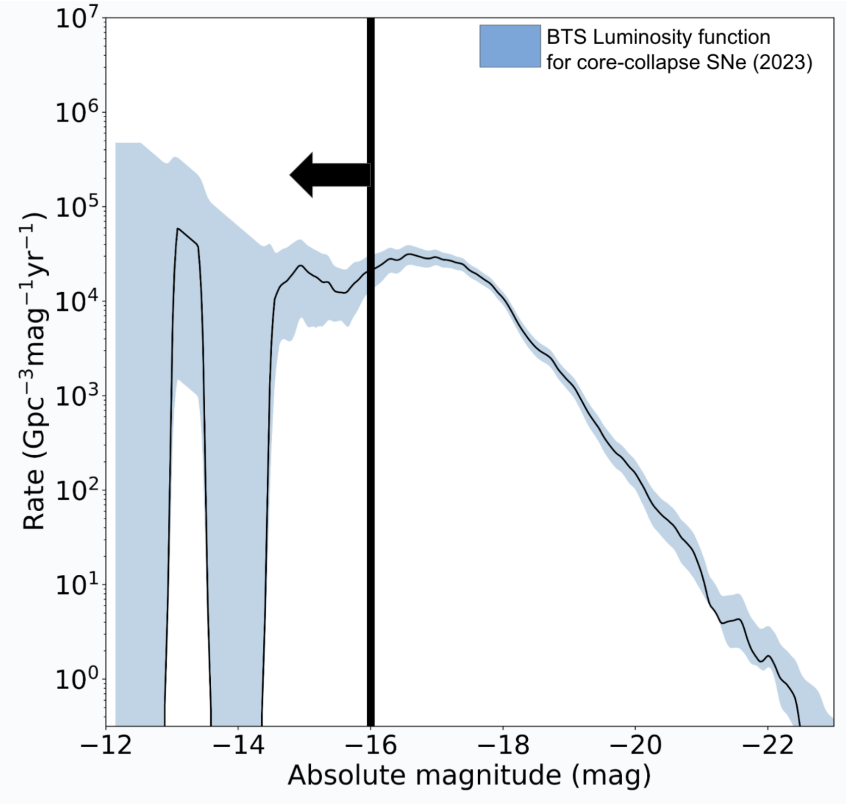

Figure 1.2: The black line shows the luminosity function for core-collapse SNe calculated from the ZTF BTS sample (Perley et al. 2020). Current constraints at the faintest end of the BTS CCSN luminosity function are poor because of the small number of SNe. A central goal of this thesis is to determine where the falloff occurs and where the luminosity function peaks at the faintest end.

up. As a result, although the brighter CCSN population is reasonably well mapped, the true rate and luminosity distribution of the faintest explosions remain much less secure.

This motivates nearby, effectively volume-limited survey strategies with high spectroscopic completeness. Earlier surveys such as Lick Observatory Supernova Search (LOSS; Li et al. 2011), the Panoramic Survey Telescope and Rapid Response System (PS1; Sanders et al. 2015), the Sloan Digital Sky Survey II Supernova Survey (SDSS-II SNS; Taylor et al. 2014), the Caltech Core-collapse SN Project (CCCP; Arcavi et al. 2012) and the Bright Transient Survey (BTS; Perley et al. 2020) established the value of systematic nearby SN searches, but they were less effective at recovering the faintest explosions (Figure 1.2). The survey framework used in this thesis was designed specifically to address that gap.

ZTF-based nearby supernova surveys: CLU and CATS150

The observational framework used throughout this thesis is built on the Zwicky Transient Facility (ZTF), a wide-field optical time-domain survey on the Samuel Oschin 48-inch Schmidt telescope at Palomar Observatory (Bellm et al. 2019b, Graham et al. 2019, Dekany et al. 2020, Masci et al. 2019). With its 47 $\deg^2$ camera, rapid survey speed, and typical single-visit depth of about $r \approx 20.5$ mag in 30 s exposures, ZTF scans the northern sky on timescales of a few days. In its public Northern Sky Survey, it provides g- and r-band coverage every two nights. This combination of wide area, depth, and cadence makes ZTF particularly well suited for discovering nearby supernovae, including intrinsically faint and rapidly evolving transients that would be missed in shallower or lower-cadence surveys.

The first stage relevant here was the Census of the Local Universe (CLU), a ZTF experiment designed to construct a spectroscopically complete sample of transients in the nearby universe by combining the ZTF alert stream with a galaxy catalog of known distances. During ZTF Phase I, CLU operated as a volume-limited nearby supernova survey (De et al. 2020b), targeting transients within 200 Mpc that were spatially coincident with galaxies in the CLU galaxy catalog (Cook et al. 2019). That catalog contains roughly 234,500 galaxies with distance information, assembled from existing spectroscopic surveys together with the CLU-Hα survey (Cook et al. 2019).

Beginning in January 2021, CLU Phase II was redesigned to better target the low-luminosity population that is most relevant for this thesis. The selection was tightened to transients within 150 Mpc, located within 30 kpc of or visibly associated with a CLU galaxy, and with peak absolute magnitudes fainter than -17 mag. This shifted CLU from a purely volume-limited survey toward a volume- and luminosity-limited experiment optimized to recover the faint end of the nearby supernova population. Brighter transients within the same volume were primarily classified as part of a separate ZTF Bright Transient Survey (BTS; Perley et al. 2020), a complementary magnitude-limited program targeting transients brighter than ~ 18.5 mag. I led Phase II of CLU from 2022 onward, during its operation from January 2021 through November 2024. Over the course of the program, we classified more than 1700 transients, making CLU the largest volume-limited supernova survey to date and providing the statistical foundation for the population measurements developed in the chapters that follow.

CLU also exposed the main remaining observational bottleneck. Although the

overall spectroscopic completeness reached about $\sim$ 85%, it dropped in the faint regime, to roughly $\sim$ 70% at magnitudes of $\sim$ 19–20. This is precisely the range in which intrinsically faint and rapidly evolving nearby explosions become hardest to secure. Pushing the census further therefore required more efficient spectroscopy.

That next step was enabled by the Next Generation Palomar Spectrograph (NGPS) on the Hale 200-inch telescope. My role in commissioning focused on the observational work needed to bring the instrument into scientific use, including first-light and science-validation spectra, calibration observations used for throughput characterization, and datasets used to validate spectral resolution and on-sky performance. These efforts were directly tied to the survey goals of this thesis, because the limitations exposed by CLU—low-S/N spectra of faint targets, host-galaxy contamination, and inefficient follow-up—are precisely the areas in which NGPS offers the largest gains (Chapter 2).

Building on CLU and enabled by NGPS, I then served as PI of the Complete Astronomical Transient Survey within 150 Mpc (CATS150), designed to target $>$ 95% spectroscopic completeness for supernovae within 150 Mpc in the ZTF alert stream, including the critical 18–20 mag regime (Das et al. 2025c). Over its first year of operation, from February 2025 to January 2026, CATS150 reached a spectroscopic completeness of 97.2% while classifying 456 extragalactic transients. A more detailed discussion of my role in NGPS commissioning is given in Chapter 2, and the design and overview of CATS150 are given in Chapter 3. That chapter shows that the high-completeness local-survey strategy advocated throughout this thesis is now practical at scale: CLU established the statistical baseline, and CATS150 demonstrated that $>$ 95% spectroscopic completeness is achievable even in the 18–20 mag regime where many of the faint transients of greatest interest reside.

With that survey framework established, I now turn to the physical channels most likely to populate the low-mass end of the CCSN distribution. The physical channels discussed below are arranged broadly in increasing order of envelope stripping: I begin with hydrogen-rich explosions from progenitors that retain most of their envelopes until collapse, and then move to progressively more stripped binary channels.

1.5 Hydrogen-rich channels at the low-mass boundary of core collapse

A central goal of this thesis is to determine how stars near the minimum mass for core collapse manifest observationally. The simplest expectation is that some

progenitors evolve effectively as single stars, without significant binary interaction, and retain most of their hydrogen envelopes until explosion.

Hydrogen-rich low-mass explosions: Red-supergiant Fe-core collapse

Among the channels near the low-mass boundary, the most common outcome is that the star retains most of its hydrogen envelope and ends its life as a red supergiant (RSG). Such stars explode as hydrogen-rich (Type II) supernovae and dominate nearby volume-limited samples, comprising nearly 70% of the population (Li et al. 2011). If stars near the minimum mass for core collapse contribute significantly to the CCSN budget, much of that contribution is therefore expected to appear in hydrogen-rich events. Within this broad class, the clearest candidate channel is low-luminosity Type IIP supernovae (LLIIP SNe).

Here I use "low-luminosity Type IIP" for events with peak magnitudes fainter than roughly $M_r \gtrsim -16$ mag, following the historical definition used in the literature (e.g., Pastorello et al. 2004, Spiro et al. 2014, Reguitti et al. 2021) and based on direct pre-explosion progenitor detections for a small number of nearby LLIIP SNe, which likewise place them in the low-mass RSG or sAGB regime close to the minimum mass for core collapse (Maund et al. 2005, Li et al. 2006, Mattila et al. 2008, O'Neill et al. 2019, Van Dyk et al. 2023b). Observed LLIIP SNe are characterized by low expansion velocities, typically ∼1300–2500 km s^{-1} at ∼50 days after explosion, small ^{56}Ni masses of order $\sim$ 0.005 $M_\odot$, and explosion energies well below the canonical 10^{51} erg scale (e.g., Spiro et al. 2014, Reguitti et al. 2021, Das et al. 2025c, Jerkstrand et al. 2018, Lisakov et al. 2017). Together, these properties are consistent with explosions of ∼8–12 $M_\odot$ progenitors, as supported by light-curve simulations (Fraser et al. 2011, Pumo et al. 2017), evolutionary models of low-mass red supergiants (Lisakov et al. 2017), and nebular spectroscopy (Jerkstrand et al. 2018).

Even so, the observational sample remained small for many years. Before the systematic nearby samples used in this thesis, only about a dozen bona fide LLIIP SNe had been studied in detail in the literature (Turatto et al. 1998, Spiro et al. 2014, Jäger et al. 2020, Müller-Bravo et al. 2020, Reguitti et al. 2021, Yang et al. 2021, Valerin et al. 2022, Kozyreva et al. 2022, Bostroem et al. 2023, Teja et al. 2024, Dastidar et al. 2025). That limited sample made it difficult to determine whether LLIIP SNe truly represent a rare channel, or instead the faint tail of a much more important population that had been missed due to observational biases.

Chapters 4 and 5 address that gap using the ZTF CLU survey, constructing a systematically selected nearby sample of Type IIP supernovae. The final sample includes 330 Type IIP SNe, including 36 low-luminosity events, roughly tripling the literature sample of LLIIP SNe. Chapter 4 shows that the Type IIP luminosity function does not hide a large unseen population of extremely faint events: fewer than 1.5% of Type IIP SNe are fainter than -14.5 mag, and LLIIP SNe account for only 8^{+1}_{-2}% of all core-collapse supernovae. Chapter 5 then shows that LLIIP SNe occupy the low-^{56}Ni, low-explosion-energy, and low-mass end of the H-rich SN distribution, consistent with a ~8–12 $M_\odot$ RSG or sAGB progenitor.

Hydrogen-rich low-mass explosions: sAGB ONeMg-core electron-capture supernovae

The second single-star route at the low-mass boundary is the electron-capture supernova channel, expected to arise from sAGB progenitors. In this channel the star builds an electron-degenerate O+Ne+Mg core. Electron captures on Ne and Mg then reduce the electron fraction and destabilize the core as it approaches the Chandrasekhar mass, triggering collapse (Miyaji et al. 1980, Nomoto 1984, Kitaura et al. 2006, Janka et al. 2008, Takahashi et al. 2013, Jones et al. 2013, Hiramatsu et al. 2021a, Wang et al. 2026).

Neutrino-driven explosion calculations predict low explosion energies of $\sim 10^{50}$ erg and small ^{56}Ni masses of $\sim 10^{-3}$ $M_\odot$ (Kitaura et al. 2006, Janka et al. 2008, Wanajo et al. 2009, Jones et al. 2013, Wang et al. 2026). These predictions overlap strongly with the observed properties of the faintest Type II events, making low-luminosity Type IIP SNe natural candidates for ECSN searches. At the same time, this overlap makes the channel difficult to identify at early times: photospheric light curves and early spectra can be broadly similar for ECSNe and low-mass Fe-core CCSNe because both may retain extended hydrogen envelopes and eject comparable envelope masses. A central question is therefore how many LLIIP SNe arise from low-mass Fe-core collapse and how many instead originate from the sAGB/electron-capture route.

Nebular spectroscopy is especially valuable in this context because, once the ejecta become optically thin, the emission directly traces the composition and structure of the inner burning products rather than the outer hydrogen envelope. ECSNe from single-star progenitors are expected to lack both O- and He-rich shells, resulting in nebular spectra dominated by H/He emission with weak oxygen lines (Jerkstrand

et al. 2018). If the innermost regions are visible, contributions from neutron-rich iron-group elements such as stable Ni may also appear (Wanajo et al. 2009). In contrast, low-mass iron-core-collapse supernovae retain thin Si, O, and He shells that produce distinct nebular features. Nebular spectroscopy can therefore distinguish ECSNe through the absence of these layers and the corresponding suppression of oxygen-rich emission (Jerkstrand et al. 2018).

Yet nebular studies of LLIIP SNe have so far been dominated by individual objects (Turatto et al. 1998, Pastorello et al. 2006b, Van Dyk et al. 2012b, Jäger et al. 2020, Müller-Bravo et al. 2020, Bostroem et al. 2023, Van Dyk et al. 2023b), and even broader nebular compilations of Type II SNe contain very few truly low-luminosity events. Chapter 6 addresses this gap using the first systematic sample of nebular spectra of LLIIP SNe from the ZTF CLU survey. Its most striking result is that at most two objects satisfy the conservative criteria adopted to identify ECSNe from sAGB progenitors, implying that the sAGB progenitor window is narrower than $\Delta M_{\rm sAGB} \sim 0.02$–$0.06$ $M_\odot$, substantially smaller than predictions from stellar-evolution models.

1.6 H-poor/binary channels at the low-mass boundary of core collapse

Not all stars near the minimum mass for core collapse die with intact hydrogen envelopes. Because most massive stars are born in binaries, a substantial fraction undergo interaction through Roche-lobe overflow, common-envelope evolution, or mergers, which can strongly reshape their final structure (e.g., Sana et al. 2012, Moe and Di Stefano 2017). Near the low-mass end of core collapse, such interaction can strip hydrogen from otherwise ordinary progenitors and expose low-mass helium (~ 2.5 $M_\odot$) and CO (~ 1.5 $M_\odot$) cores that, in isolation, might instead have produced faint hydrogen-rich supernovae. These stripped configurations naturally lead to explosions with lower ejecta masses, lower oxygen yields, and often lower ^{56}Ni masses, redistributing the same $\sim$ 8–12 $M_\odot$ ZAMS population into faint and fast stripped transients. Only recently have high-cadence surveys such as PTF, iPTF, ZTF, and ATLAS begun to map this parameter space, from the broader class of rapidly evolving optical transients (Drout et al. 2014) to specific low-ejecta-mass stripped-envelope supernovae (De et al. 2018a, Yao et al. 2020). Yet the most weakly explored region remains the low-ejecta-mass, low-^{56}Ni end of the stripped-envelope population, where some of the clearest signatures of low-mass stripped core collapse may emerge.

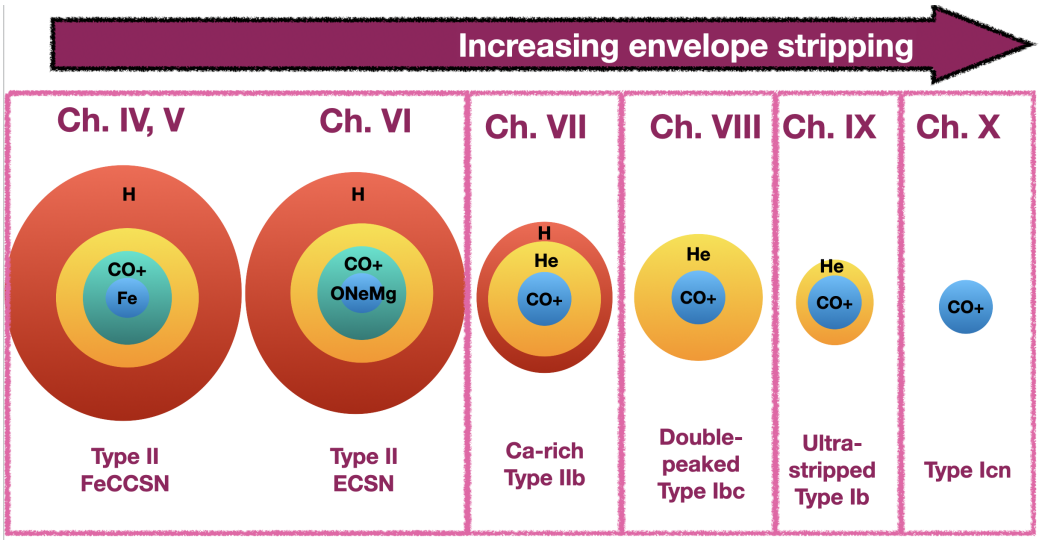

Figure 1.3: Summary schematic of the binary channels emphasized in this thesis. Left to right, the retained envelope mass decreases from hydrogen-rich single-star explosions to progressively stripped binary outcomes.

Binary evolution can also shift the boundary between white-dwarf and neutron-star formation. Early Roche-lobe overflow can prevent the second dredge-up that would otherwise reduce the core mass in single stars, allowing some systems near this transition to continue toward ECSNe or low-mass Fe-core collapse (Podsiadlowski et al. 2004, Tauris et al. 2015, Poelarends et al. 2017, Siess and Lebreuilly 2018). Exactly where that transition lies remains model dependent, since convection, mass-transfer efficiency, and wind mass loss all shift the allowed initial-mass and orbital-period ranges (Poelarends et al. 2017, Siess and Lebreuilly 2018). The minimum mass for core collapse is therefore not fixed, but can be modified by prior binary interaction.

The channels discussed below are arranged in roughly increasing order of stripping: from Ca-rich Type IIb supernovae that retain a small residual hydrogen layer, to double-peaked Type Ibc events that are more completely stripped, to the ultra-stripped channel anchored by SN 2023zaw, and finally to the interaction-powered extreme represented by SN 2018erx.

When hydrogen is not completely stripped: Ca-rich Type IIb SNe

A low-mass stripped channel arises when binary interaction removes most, but not all, of the hydrogen envelope prior to explosion. If a small residual hydrogen layer remains, of order $\sim 0.1\ M_{\odot}$, the SN can appear spectroscopically as a Type IIb

SN. In Chapter 7, I identify a population of 9 fast-evolving Type IIb SNe whose late-time spectra are unusually Ca-rich and O-poor, consistent with explosions of low-mass helium stars that retained a small but detectable hydrogen layer. Nebular spectroscopy provides a particularly powerful diagnostic in this regime. Oxygen is predominantly synthesized during hydrostatic burning and increases strongly with progenitor mass, whereas calcium shows a weaker dependence. The nebular Ca/O ratio therefore traces the core mass of the progenitor (Fransson and Chevalier 1989, Jerkstrand et al. 2014a, 2015a, Fang et al. 2022).

Despite retaining a small amount of hydrogen at the time of collapse, these events evolve faster and have lower ejecta masses than typical H-poor/Type Ibc supernovae, with weak oxygen emission indicating low-mass progenitors. Their properties point to binary progenitor systems with a low-mass He star undergoing strong stripping, potentially producing compact remnants in close orbits that may be detectable with gravitational-wave observatories such as LISA.

When the low-mass helium stars puff up: double-peaked Type Ibc SNe

Stellar-evolution calculations predict that low-mass helium stars can expand substantially during advanced burning stages, as their tenuous helium envelopes respond strongly to late core contraction, reaching radii of tens to hundreds of solar radii (e.g., Laplace et al. 2020, Wu and Fuller 2022a). This expansion can create extended, low-density material around an otherwise compact stripped progenitor, providing a natural route to renewed late-time Roche-lobe overflow.

One observational manifestation of this extended material is the presence of an early, short-lived luminosity excess preceding the main radioactive peak. In double-peaked stripped-envelope supernovae, this first bump is interpreted as shock-cooling emission produced when the SN shock traverses extended material, either a bound envelope or recently ejected CSM (e.g., Rabinak and Waxman 2011a, Nakar and Piro 2014, Piro 2015, Piro et al. 2021). Such early bumps are common in Type IIb SNe with extended H envelopes, but are much less frequent in ordinary Type Ibc SNe, whose progenitors are typically assumed to be compact. Chapter 8 presents the discovery and systematic population study of 17 double-peaked Type Ibc SNe out of 475 Type Ibc events in ZTF. Their lightcurves and nebular spectroscopy point to late-stage expansion or recent mass loss in low-mass helium stars before collapse.

When the low-mass He stars are stripped to the bone: Ultra-stripped SNe

One expected outcome of binary stripping at the low-mass boundary is a population of stripped-envelope supernovae with unusually small ejecta masses and very low ^{56}Ni yields. These events are important because they provide one of the clearest observational channels through which low-mass core collapse may appear once most or all of the hydrogen envelope has been removed. Recent high-cadence surveys have begun to reveal this part of parameter space, but it remains only sparsely populated observationally.

The most extreme versions of this channel are expected in helium-star + compact-object binaries. After a common-envelope phase, a naked helium star orbiting a neutron star can undergo a second, post-helium-burning stripping episode through case BB Roche-lobe overflow, leaving only a very small residual envelope before collapse (Tauris et al. 2013, 2015, Jiang et al. 2021). Helium-star donors with initial masses of ~ 2.5 M$_\odot$ in short-period binaries can then end either as ultra-stripped ECSNe or as weak Fe-core CCSNe, with the outcome set primarily by the final CO-core mass and the degree of stripping (Tauris et al. 2015). In this regime, the explosions eject very little mass and synthesize only modest amounts of ^{56}Ni (Suwa et al. 2015, Müller et al. 2018, Tauris et al. 2017). Radiative-transfer models therefore predict fast, faint stripped transients with rise times of only a few days and peak magnitudes at the low-luminosity end of the stripped-envelope supernova population (Moriya et al. 2017).

Within this broader landscape, Chapter 9 is anchored by SN 2023zaw, an unusually rapid and faint stripped-envelope supernova that provides a direct observational foothold for this low-mass stripped channel. The properties of SN 2023zaw are consistent with a low-mass progenitor in a compact binary system, potentially producing remnants that merge within a Hubble timescale. With an inferred nickel mass of only $M_{\rm Ni} \approx 0.002$ M$_\odot$—the lowest yet measured for a stripped-envelope supernova—it points to a population of similar low-nickel, rapidly evolving stripped-envelope SNe that are likely underrepresented in current samples and may only be recovered through their early shock-cooling emission.

When the circumstellar material is dense: interaction-powered stripped-envelope SNe

A more extreme outcome of binary stripping arises when dense circumstellar material (CSM) is present at the time of explosion. In this case, the observed emission

can be dominated by ejecta–CSM interaction rather than by radioactive decay. The best-known subclass is Type Ibn, defined by narrow helium emission lines and weak or absent hydrogen features, indicating interaction with He-rich CSM (e.g., Pastorello et al. 2008, Hosseinzadeh et al. 2017b). The more recently identified Type Icn class extends this picture to interaction with H/He-poor and likely C/O-rich material, producing narrow or intermediate-width carbon and nitrogen lines (Perley et al. 2022b, Pellegrino et al. 2022a).

These interaction-powered events are relevant to the low-mass problem because several Type Ibn and Icn supernovae show evidence for very low ^{56}Ni masses and nebular spectra dominated by helium emission, with comparatively weak oxygen-rich features. These properties are consistent with explosions of low-mass helium stars, where the small core mass limits oxygen production and radioactive yield. In this picture, the observed emission is powered primarily by ejecta–CSM interaction. In Chapter 10, we present the discovery and analysis of SN 2018erx, a fast-evolving, unusually red interacting stripped-envelope supernova with carbon-rich interaction signatures and very low ejecta and ^{56}Ni masses. Heavily dust-reddened events like SN 2018erx may therefore be missed in optical surveys, and may only be detected or classified when their luminosity is enhanced by CSM interaction.

The goal of this thesis is to construct a systematic view of core-collapse supernovae arising from intermediate-mass stars in the ~8–12 $M_\odot$ range, corresponding to the lowest-mass end of core collapse. This is enabled by systematic, volume-limited supernova surveys with high spectroscopic completeness, which allow a robust characterization of low-luminosity explosions. In essence, the central question running through this thesis is: *what are the observable explosive outcomes of stars at the low-mass end of core-collapse?*

Chapter 2

COMMISSIONING AND SCIENCE-VALIDATION OF THE NEXT GENERATION PALOMAR SPECTROGRAPH

2.1 Introduction

The Next Generation Palomar Spectrograph (NGPS; PI Kasliwal) is a new instrument on the Palomar Hale 200-inch telescope, designed to replace the long-serving Double Spectrograph (DBSP; Oke and Gunn 1982). NGPS is a general-purpose, visible-light, medium-resolution spectrograph with a four-channel design covering approximately 310–1040 nm. Its optical design includes a three-way adjustable slicer at the focal plane, which reduces slit losses while preserving spectral resolution, together with fixed volume phase holographic (VPH) gratings and channel-optimized coatings that emphasize high throughput and efficiency.

NGPS was designed to achieve more than a factor of three improvement in throughput relative to DBSP. For the science program developed in this thesis, this gain directly addresses several key limitations in the study of faint nearby transients, including limited sensitivity at the faint end, strong host-galaxy contamination, and inefficient acquisition. The connection between these capabilities and spectroscopic completeness is discussed in Section 2.5.

This chapter documents the observational commissioning and science-validation program through which NGPS was demonstrated to be ready for scientific use. I participated in 19 commissioning nights with NGPS, including 9 nights on-site at Palomar and 10 nights of remote observing. My principal contribution to this effort included acquiring many of the datasets used in these tests, obtaining the first science spectrum during commissioning, developing observer documentation, debugging and improving automated acquisition, contributing to throughput measurements, and performing empirical workflow checks required for efficient operation. A more detailed analysis of the instrument performance will be presented in Fremling et al., in prep.

2.2 First science observations

An important early part of the commissioning effort was obtaining first-light spectra and confirming end-to-end operation on sky. First light was achieved on 2024

November 13, followed immediately by the acquisition of the first science spectrum on 2024 November 14, marking a rapid transition from initial on-sky testing to scientific use. The first science target, which I observed during commissioning, was the transient ZTF24abrfcqd / SN 2024aaqp, discovered by the Zwicky Transient Facility on 2024 November 8, at a magnitude of $m_g \approx 19.6$ and subsequently brightened to $m_r \approx 17.6$ over the following week.

The resulting NGPS spectrum, reduced using the NGPS quicklook reduction tool (C. Fremling et al., in prep), was of sufficient quality for us to classify the source as a Type Ia supernova at redshift $z = 0.045$ (Transient Name Server 2024). The spectrum shows a prominent Si II λ6355 absorption feature characteristic of Type Ia supernovae, corresponding to an expansion velocity of $\sim 12500\,\mathrm{km\,s^{-1}}$. Comparison with spectral templates indicates a close match to normal Type Ia supernovae such as SN 2011fe and SN 2011by at phases $\sim$ 2–5 days before peak brightness. The redshift was independently constrained using host-galaxy emission lines detected in the NGPS spectrum.

This observation demonstrated that NGPS was capable of producing classification-quality transient spectroscopy at an early stage of commissioning, and it established the full end-to-end observer workflow from acquisition through reduced spectrum on a real transient target. The first science spectrum is shown in Figure 2.1. At that stage, only the r- and i-band channels had been installed and commissioned. These two channels were already sufficient for transient classification and were subsequently used extensively for the volume-limited supernova survey that I led, described in the next chapter.

Beyond first light, the commissioning observations were designed to test NGPS under the range of circumstances expected in routine operations. This included observations of calibration standards, narrow-lined sources for resolution testing, and longer integrations on faint science targets. While the initial 2024 commissioning focused on the installed r- and i-band channels, the instrument reached its full four-channel configuration in June 2025.

2.3 Throughput measurements from commissioning standard-star observations

A key component of NGPS science-validation during commissioning was an empirical measurement of the throughput in each of the four channels. The purpose of this test was to verify that the delivered sensitivity and bandpass shapes were

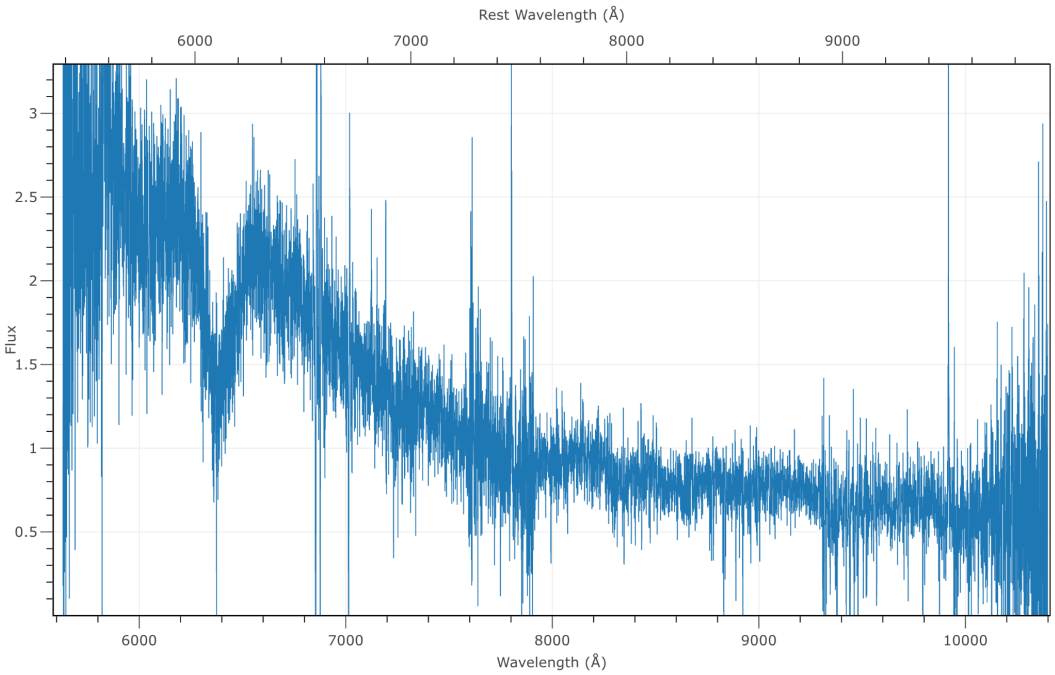

Figure 2.1: First science spectrum obtained with NGPS, corresponding to ZTF24abrfcqd / SN 2024aaqp. The spectrum was classified during commissioning as a Type Ia supernova at redshift $z = 0.045$ and reported in TNS AstroNote 2024-340 (Transient Name Server 2024).

consistent with expectations. The data used for this analysis were obtained from spectrophotometric standard-star observations taken during commissioning, including well-calibrated standards such as Feige 34, BD+28°4211, and G191-B2B. The full throughput-analysis procedure and instrument-level characterization are discussed in detail by C. Fremling et al., in prep.

The throughput calculation was performed by comparing the extracted one-dimensional spectra of the standard stars with tabulated reference spectra for the same objects. For each channel, the measured counts were first converted from ADU to electrons using the appropriate detector gain and then normalized by the exposure time. The observed spectrum was next corrected for wavelength-dependent losses external to the instrument itself. We used a Palomar atmospheric extinction curve as the baseline extinction correction, with empirical adjustments in the strongest telluric absorption regions to better reproduce the deep O_2 and H_2O bands at red wavelengths. In addition, the wavelength-dependent reflectivity of the Hale 200-inch telescope was divided out so that the final product represented the NGPS instrument throughput rather than the combined atmosphere + telescope + instrument response.

The tabulated standard-star spectrum was interpolated onto the NGPS wavelength grid and converted from flux density, F_λ, to photon flux using

$$N_\gamma(\lambda) = \frac{F_\lambda(\lambda)\,\lambda}{hc}.$$

Because the wavelength grid is not perfectly uniform, the extracted counts were also divided by the wavelength-bin width, $\Delta\lambda$, in order to obtain an observed count rate per unit wavelength. The instrumental throughput was then estimated as

$$T_{inst}(\lambda) = \frac{1}{A_{tel}} \frac{C(\lambda)\,g}{t_{exp}\,\Delta\lambda\,R_{tel}(\lambda)} 10^{0.4\,k(\lambda)\,X} \left[N_\gamma^{std}(\lambda)\right]^{-1},$$

where $C(\lambda)$ is the extracted signal in ADU, g is the channel-dependent gain, t_{exp} is the exposure time, $R_{tel}(\lambda)$ is the telescope reflectivity, $k(\lambda)$ is the atmospheric extinction coefficient, X is the airmass, and A_{tel} is the effective collecting area of the telescope.

The resulting throughput curves for the U, G, R, and I channels are shown in Figure 2.2. Overall, the measurements recover the expected bandpass locations and general wavelength dependence in all four channels. The agreement with the reference throughput curve is generally strongest in the central part of each channel, while larger differences appear near channel edges and in regions affected by strong telluric absorption. This is likely because residual uncertainties in extraction, flat-fielding, extinction correction, and detector response are most apparent at the lowest-throughput wavelengths. The shaded regions in the figure represent an approximate 10% systematic uncertainty. These throughput measurements were an important part of NGPS science-validation, both as a direct performance check and as a practical input for early sensitivity estimates and exposure-time planning.

2.4 Science-validation observations and observer-facing tools

Beyond calibration targets, we obtained science-validation observations that provided insight into the effects of slit choice on signal-to-noise ratio, the impact of centering errors on throughput, and the repeatability of acquisition and observing sequences, including the implementation of auto-acquisition for science targets. As part of this effort, I developed an observing cookbook and observer manual for NGPS, documenting the end-to-end process from an observer's perspective, including target setup, acquisition, calibration procedures, observing strategies, and exposure-time estimates. This work translated commissioning experience into a practical framework for routine scientific use.

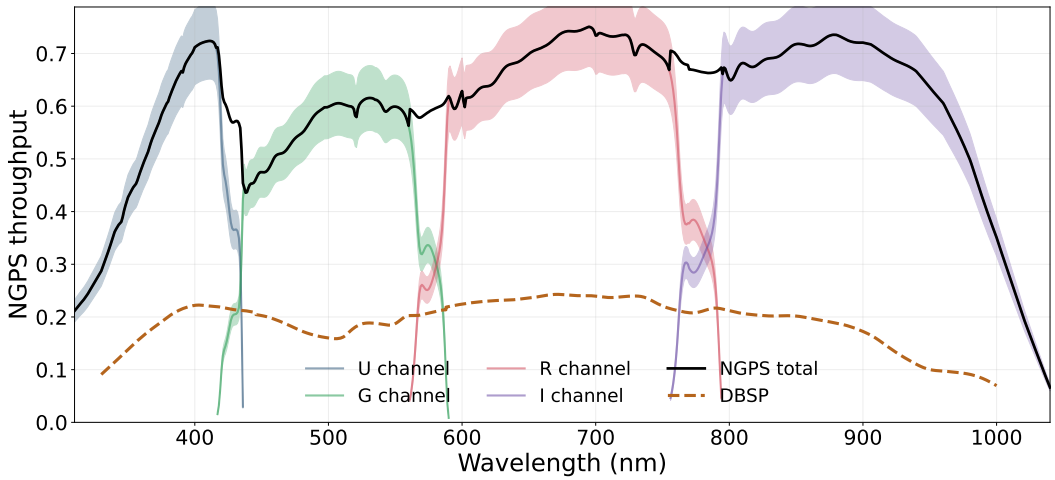

Figure 2.2: Total system throughput of NGPS as a function of wavelength for the four channels (C. Fremling et al., in prep). The shaded regions indicate the measured throughput variations across repeated observations, while the dashed gray curves show the expected throughput from the instrument model. Prominent dips correspond to atmospheric absorption features and instrumental transitions between channels. We also show the DBSP throughput (dashed line) for comparison.

2.5 Enabling high spectroscopic completeness

Earlier local-volume ZTF experiments showed that unclassified transients clustered in a small number of well-defined observational failure modes. Figure 2.3 summarizes this point using the CLU diagnostic sample: about 81% of unclassified sources had poor-S/N spectra, about 46% were projected against bright host-galaxy backgrounds, and about 54% never obtained even a single spectrum. These diagnostics clearly identify the main bottlenecks that any higher-completeness spectroscopic program must overcome.

NGPS addresses these bottlenecks at the level of instrument design and observer workflow. First, the substantially higher throughput measured during commissioning makes it practical to obtain classification-quality spectra for fainter transients within exposure times that are feasible on the Hale telescope. This directly attacks the largest source of incompleteness, namely spectra that exist but remain too low in signal-to-noise ratio for secure classification. Second, the three-slice image slicer reduces slit losses while preserving a narrow effective slice width, which helps suppress host-galaxy background light and improves the separation of transient signal from structured galaxy emission. This is especially important for events located near galaxy nuclei or in high-surface-brightness regions, where conventional long-slit observations can become background dominated.

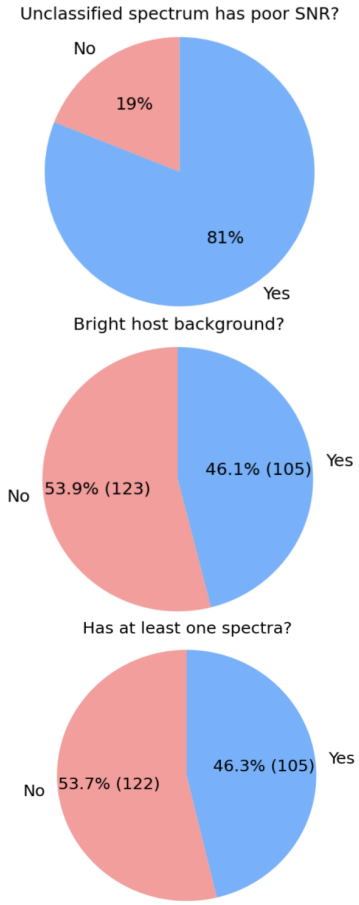

Figure 2.3: Diagnostic breakdown of unclassified transients in the CLU experiment. A large majority of unclassified sources had poor-S/N spectra, nearly half were affected by bright host backgrounds, and slightly more than half never obtained even a single spectrum.

A third failure mode is inefficiency in obtaining any useful spectrum at all. Here, the commissioning work on observer procedures is as important as the raw throughput gain. The efficient automated-acquisition tools, exposure-time calculations, and cookbook instructions make acquisition and setup more repeatable, help select an appropriate observing mode for each target, and ensure that exposure times are matched to the transient brightness and observing conditions.

In practice, this combination of increased throughput, slicer-assisted background suppression, and improved observer-facing tools translates directly into higher spectroscopic efficiency and completeness with NGPS.

2.6 Summary

First-light and first-science spectra established basic on-sky functionality, standard-star observations quantified throughput, narrow-line targets tested spectral resolution, and representative science observations demonstrated that NGPS could be used effectively on real astronomical targets. My principal contributions to this effort included acquiring many of the datasets used in these tests, developing observer documentation, debugging and improving automated acquisition, contributing to throughput measurements, and performing empirical workflow checks required for efficient operation. As a result, my work was closely tied to the transition of NGPS from a newly installed instrument to a scientifically validated spectrograph ready for routine observing.

More broadly, NGPS's performance during commissioning demonstrates why it is especially well suited to the high-completeness classification of faint and difficult nearby transients. The commissioning program described here therefore forms the observational foundation for the Complete Astronomical Transient Survey within 150 Mpc (CATS150; PI Das), which is described in the next chapter.

Chapter 3

THE COMPLETE ASTRONOMICAL TRANSIENT SURVEY WITHIN 150 Mpc (CATS150)

This chapter provides an overview of the Complete Astronomical Transient Survey within 150 Mpc (CATS150; Das et al. (2025d), PI: Das), a ZTF collaboration involving Mansi M. Kasliwal, Theophile Jegou du Laz, Sofia Covarrubias, Christoffer Fremling, Wynn Jacobson-Galan, Sam Rose, and Yu-Jing Qin (Caltech); Dave Cook (Caltech/IPAC); Jesper Sollerman, Anjasha Gangopadhyay, and Avinash Singh (OKC); Igor Andreoni and Jonathan Carney (University of North Carolina at Chapel Hill); Daniel Perley, K-Ryan Hinds, and Jacob Wise (Liverpool John Moores University); and Nabeel Rehemtulla, Adam A. Miller, and Steve Schulze (Northwestern University).

3.1 Survey design

CATS150 was constructed as a volume-limited sample targeting all extragalactic transients at $z < 0.0331$ (~ 150 Mpc) in the ZTF alert stream. Candidates were selected through cross-matching with the NED Local Volume Sample (LVS; Cook et al. 2023), a comprehensive catalog of nearby galaxies. For hosts at $z > 0.01$, candidates were required to lie within a projected physical offset of ≤ 30 kpc from a cataloged galaxy; at lower redshift, where angular sizes are larger and catalog matching is less clean, visually obvious associations were also retained. The survey ran from 2025 January 24 through 2026 January 31.

Earlier ZTF programs such as the Bright Transient Survey (BTS) established 93% completeness for the brightest supernovae (< 18.5 mag) (Perley et al. 2020), but their performance declined in the fainter local regime. CLU extended the focus to the nearby universe while still falling short of the desired completeness at 18–20 mag (Das et al. 2025b) (see Figure 3.1). Across much of the 150 Mpc volume, this apparent-magnitude range corresponds to intrinsically faint explosions, including low-nickel stripped-envelope supernovae, electron-capture candidates, ultra-stripped explosions, and other sub-luminous channels. A highly complete nearby sample in this regime was therefore needed to measure subtype demographics and to constrain the faint end of the SN luminosity function.

CATS150 was designed to close this gap. Its stated goal was to reach better than 95% spectroscopic completeness across the full magnitude range of interest (Das et al. 2025c), and the completed survey showed that this was achievable in practice. The resulting dataset provides a high-completeness local reference sample for faint transients, which will be particularly valuable in the context of next-generation of deep-sky surveys such as the Legacy Survey of Space and Time (LSST; Ivezić et al. 2008) and the Nancy Grace Roman Space Telescope.

NGPS and SEDM on the Palomar 60-inch Telescope formed the backbone of the spectroscopic follow-up, with SEDM efficiently classifying bright targets and NGPS targeting faint, host-contaminated, or otherwise difficult sources that had historically dominated the incompleteness budget. Additional follow-up within the collaboration made use of the GHTS spectrograph on the SOAR Southern Astrophysical Research Telescope (PI: Igor Andreoni), SPRAT on the Liverpool Telescope (PI: Daniel Perley), KAST at Lick Observatory, ALFOSC at the Nordic Optical Telescope (PI: Kaustav Das), and LRIS on the Keck-I telescope (PI: Mansi Kasliwal). Together, this coordinated multi-facility strategy enabled the high level of spectroscopic completeness achieved by CATS150.

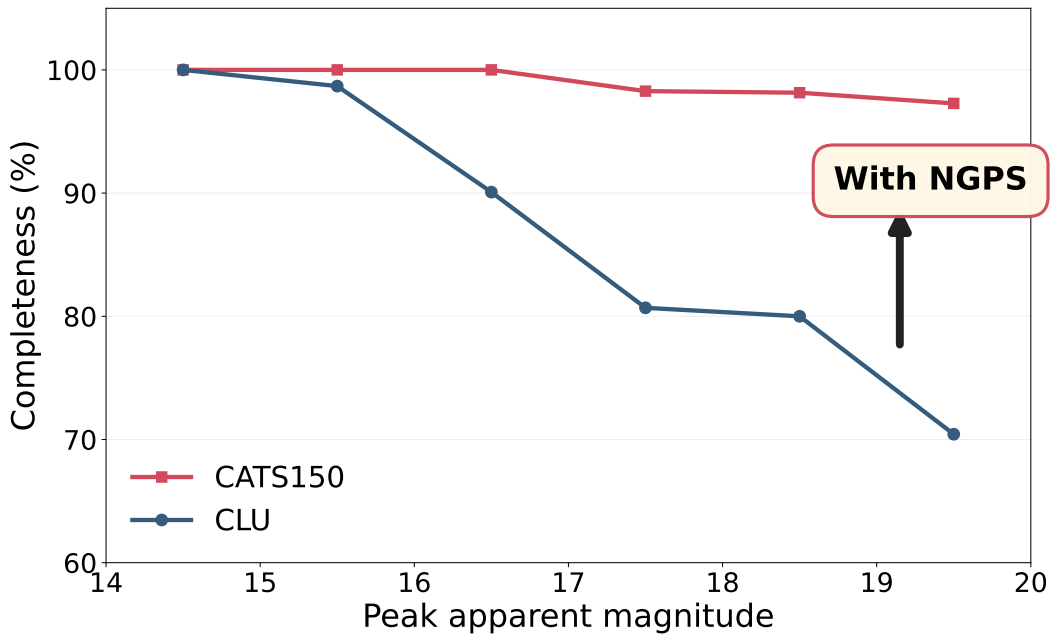

Figure 3.1: Spectroscopic completeness as a function of peak apparent magnitude for CATS150 and CLU (Das et al. 2025b). The CATS150 curve includes the gain enabled by NGPS at the faint end, maintaining substantially higher completeness than CLU toward $m_{peak} \approx 18.5$–20 mag.

3.2 Alert filtering

The real-time CATS150 selection operated on ZTF alert packets generated by the IPAC reduction and alert-production system (Bellm et al. 2019b, Masci et al. 2019). Candidate vetting and follow-up coordination were carried out in Fritz, the ZTF collaboration's SkyPortal instance (Coughlin et al. 2023), while alert queries and catalog cross-matches were handled through Kowalski (Duev et al. 2019). Within this framework, we implemented a custom filter designed to isolate stationary extragalactic transients plausibly associated with nearby galaxies while preserving completeness for faint real events. We applied the following cuts:

- **Alert-quality cuts.** The alert was required to be a positive subtraction residual (isdiffpos > 0) with acceptable machine-learning scores ($rb > 0.3$, $drb > 0.5$), where rb is the real–bogus score and drb is the deep-learning real–bogus score produced by the ZTF alert pipeline (Mahabal et al. 2019), a reasonable PSF width ($0.5 < \mathrm{FWHM} < 8$), fewer than five bad pixels, finite PSF-fit photometry ($m_{\mathrm{PSF}} < 99$), consistency between PSF and aperture magnitudes ($|m_{\mathrm{PSF}} - m_{\mathrm{ap}}| < 0.75$), and no pathological alert history ($n_{\mathrm{det,hist}} \leq 200$).

- **Solar-system rejection.** The current detection was accepted only if it had no nearby cataloged solar-system match, or if the nearest match was sufficiently distant ($d_{\mathrm{SS}} \geq 12''$), lacked a valid catalog magnitude, or was photometrically inconsistent with the alert by at least 2 mag, $|m_{\mathrm{PSF}} - m_{\mathrm{SS}}| \geq 2$.

- **Nearby-host association.** Host association was implemented as a hybrid angular and physical cross-match. Alerts were first matched to NED galaxies within $300''$. For candidate hosts at $z \geq 0.01$, the transient was then projected to the host redshift and the association was retained only if the projected physical offset was sufficiently small (limited to $\lesssim 30\,\mathrm{kpc}$). For the very extended nearby galaxies M31 and M33, a separate geometric check was used instead of the default angular-radius criterion: the transient position was tested against the projected host ellipse defined by the galaxy major axis, minor axis, and position angle. The filter retained the surviving nearby-host metadata, including angular and projected offsets, so that each candidate could be manually vetted in the context of its local environment.

- **Stationarity requirement.** The candidate had to have a corroborating detection at a distinct epoch, $|\Delta t| > 0.007\,\mathrm{d}$. This could be either a prior

positive alert with valid photometry and no close solar-system association, or a forced-photometry point with $S/N \geq 4$ and procstatus = 0.

- **Stellar vetoes.** Obvious PS1 stellar counterparts were rejected if the nearest PS1 source satisfied $\mathrm{sgscore}_1 > 0.76$ and $d_{\mathrm{PS1},1} < 2''$ (Chambers et al. 2016, Tachibana and Miller 2018). Additional bright-star vetoes rejected candidates lying within $20''$ of a PS1 source with $r < 15$ and sgscore > 0.49 for any of the three nearest catalog matches.

- **Gaia parallax veto.** Significant Gaia stellar matches were rejected when $\varpi/\sigma_\varpi \geq 4$, except for candidates effectively nuclear with respect to a nearby host ($d_{\mathrm{host}} \leq 2''$).

- **Brightness requirement.** To remain in the nightly stream, either the current alert or a corroborating prior or forced-photometry detection had to satisfy $m - \sigma_m < 20$.

This filter defined a high-priority nearby-transient stream in which the dominant classes of artifacts, moving objects, and Galactic contaminants had already been removed. The surviving candidates were then manually scanned each night by the CATS150 team on Fritz, where they were vetted in the context of their nearby-host associations and subsequently assigned for spectroscopic follow-up.

3.3 Survey completeness

The completed CATS150 survey ran from 2025 January 24 through 2026 January 31. Table 3.2 gives the cumulative completeness as a function of limiting peak apparent magnitude. Month-to-month performance is summarized in Table 3.3. From February through August 2025 the survey remained between 96.6% and 100% complete, with four consecutive months at 100%. The key result is that we classified 456 transients out of 469 targets with $m_{peak} \leq 20$, corresponding to 97.2% completeness. Performance changed very little at brighter limits: completeness was 97.3% at 19.5 mag and 97.7% at 19.0 mag.

3.4 Transient demographics and subtype mix

Figure 3.2 summarizes the transient demographics of the final CATS150 science sample, which contains 456 classified extragalactic transients. At the broadest level, H-rich core-collapse events form the largest class, with 187 objects (41.0%), followed by thermonuclear supernovae with 164 objects (36.0%) and stripped-envelope

Cut	**criterion**
Alert quality	isdiffpos > 0; $rb > 0.3$; $drb > 0.5$; $0.5 <$ FWHM < 8; $n_{\rm bad} < 5$; $m_{\rm PSF} < 99$; $\lvert m_{\rm PSF} - m_{\rm ap}\rvert < 0.75$; $n_{\rm det,hist} \leq 200$
Solar-system veto	no nearby cataloged SSO, or $d_{\rm SS} \geq 12''$, or no valid $m_{\rm SS}$, or $\lvert m_{\rm PSF} - m_{\rm SS}\rvert \geq 2$ mag
Nearby-host association	Require a NED host association within $300''$; for hosts with $z \geq 0.01$, also require projected offset $\lesssim 30$ kpc; for M31/M33, require that the transient lie within the host ellipse defined by the major axis, minor axis, and position angle.
Stationarity	corroborating prior alert or forced-photometry point at $\lvert\Delta t\rvert > 0.007$ d; forced photometry also required $S/N \geq 4$ and procstatus = 0
PS1 stellar vetoes	reject if sgscore$_1 > 0.76$ and $d_{\rm PS1,1} < 2''$; also reject if any of the three nearest PS1 sources has $d_{\rm PS1} < 20''$, $r < 15$, and sgscore > 0.49
Gaia veto	reject if any Gaia match has $\varpi/\sigma_\varpi \geq 4$, unless $d_{\rm host} \leq 2''$
Brightness cut	require current or corroborating prior or forced-photometry detection with $m - \sigma_m < 20$

Table 3.1: Summary of the real-time CATS150 alert filter. The table lists the implemented numerical criteria used to define the nearby-transient stream.

Peak limit	Classified	Total	Completeness
16.0	39	39	100.0%
16.5	72	72	100.0%
17.0	117	119	98.3%
17.5	171	174	98.3%
18.0	251	254	98.8%
18.5	318	324	98.1%
19.0	387	396	97.7%
19.5	429	441	97.3%
20.0	456	469	97.2%

Table 3.2: Cumulative CATS150 completeness as a function of limiting peak apparent magnitude for the completed survey accounting.

Month	Classified	Total	Completeness
2025 Jan	2	2	100.0%
2025 Feb	51	52	98.1%
2025 Mar	28	29	96.6%
2025 Apr	21	21	100.0%
2025 May	39	39	100.0%
2025 Jun	48	48	100.0%
2025 Jul	36	36	100.0%
2025 Aug	56	57	98.2%
2025 Sep	36	40	90.0%
2025 Oct	40	42	95.2%
2025 Nov	24	25	96.0%
2025 Dec	51	52	98.1%
2026 Jan	24	26	92.3%

Table 3.3: Monthly CATS150 completeness to $m_{peak} \leq 20$ for the completed survey accounting.

supernovae with 95 objects (20.8%). The remaining sample consists of 9 gap transients (2.0%) and 1 tidal disruption event (0.2%). Here "gap transients" refers to classes that occupy the luminosity gap between ordinary novae and supernovae, including eruptive transients, intermediate-luminosity red transients, stellar mergers such as luminous red novae, and Ca-rich transients (e.g., Kasliwal et al. 2012a).

Within the H-rich core-collapse population, the dominant subtype is ordinary Type II, with 171 objects, together with 11 Type IIn events. The thermonuclear sample is dominated by normal Type Ia supernovae, with 142 objects, but also includes a distinct low-luminosity and peculiar tail: 11 91bg-like Type Ia SNe, 5 02cx/Iax-like events, 3 91T-like Type Ia SNe, and 3 additional peculiar Type Ia events. The stripped-envelope sample is likewise substantial, with 30 Type IIb, 28 Type Ib, 27 Type Ic, 5 Ic-BL, 3 Ib/c, 1 Ibn, and 1 additional Type I event. The gap-transient component consists of 4 eruptive transients, 2 ILRTs, 2 luminous red novae, and 1 Ca-rich transient. In addition, the sample contains a single nearby tidal disruption event.

3.5 Preliminary luminosity function

Figure 3.3 shows the observed peak absolute-magnitude distributions in the r-band for the three main supernova families. No host-extinction correction or volume correction has been applied, so these should be read as preliminary observed distri-

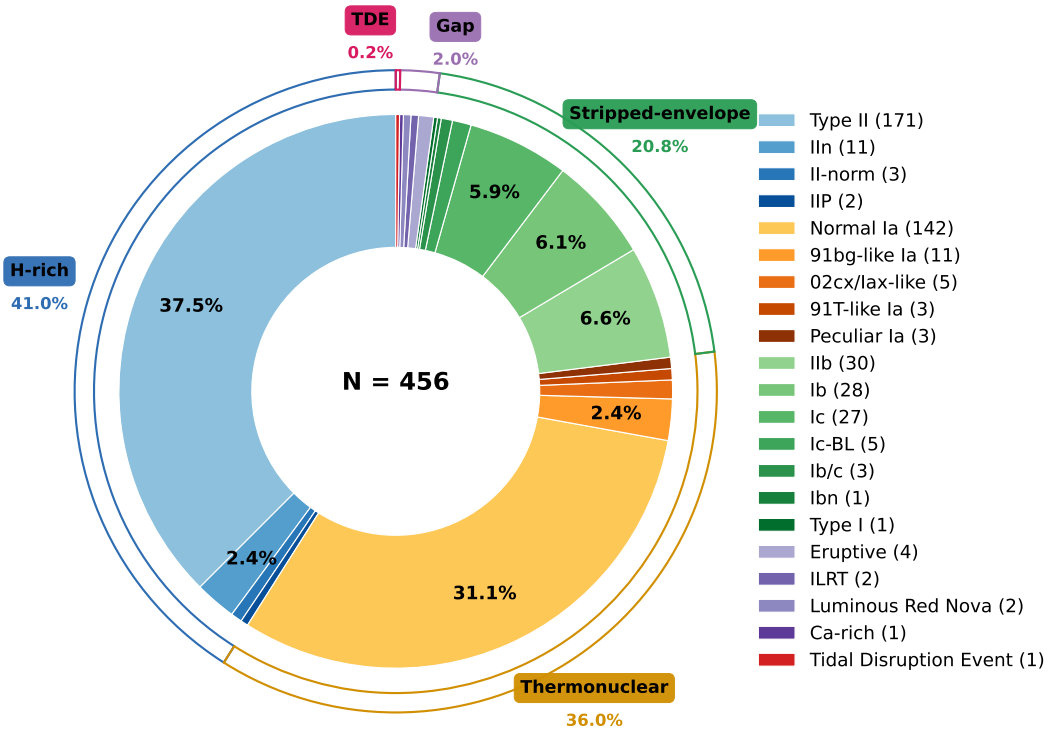

Figure 3.2: Demographic summary of the classified CATS150 science sample to $m_{peak} \leq 20$. The sample was dominated by Type II and Type Ia events, but it also contained a substantial stripped-envelope component together with a clear low-luminosity thermonuclear tail.

butions rather than as a final intrinsic luminosity function.

Thermonuclear events formed the luminous peak, with a median $M_{\mathrm{peak},r} = -18.3$ mag. The H-rich core-collapse and stripped-envelope populations were centered at -16.9 mag and -16.8 mag, respectively. The thermonuclear distribution showed a clear faint tail produced by 91bg-like and 02cx-like events, while the stripped-envelope sample spanned a broad range from low-luminosity IIb/Ib/Ic explosions to a smaller subset of bright Ic-BL component.

3.6 Summary

CATS150 demonstrated that near-complete spectroscopic classification is achievable within 150 Mpc, including the 18–20 mag regime that had previously limited local transient surveys. With this level of completeness, unbiased and systematic statistical studies can be done on SN populations across the full luminosity range, including rare and intrinsically faint channels. In particular, the sample enables population-level studies of low-nickel stripped-envelope supernovae and other sub-luminous

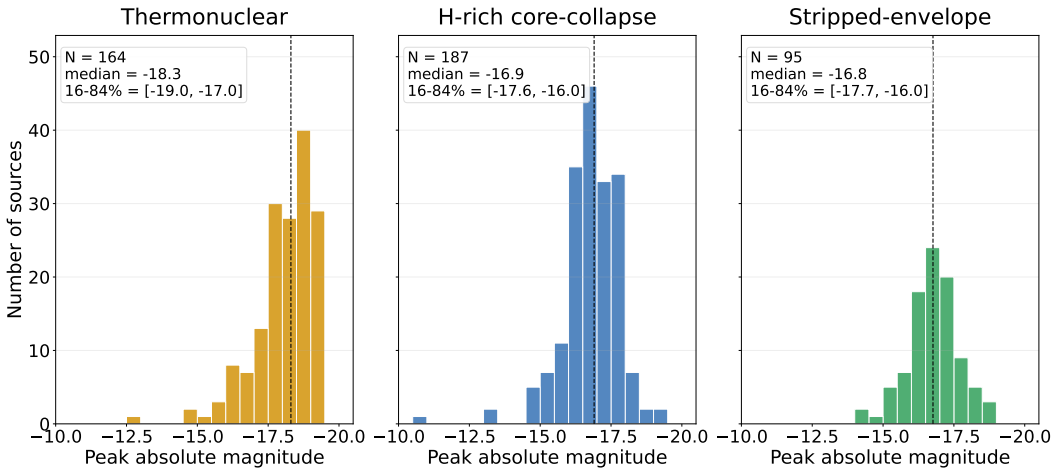

Figure 3.3: Observed peak r-band absolute-magnitude distributions for the three main supernova families in the classified CATS150 science sample to $m_{\rm peak} \leq 20$. The horizontal axis is reversed so that the faint end lies to the left. These distributions are not corrected for host extinction or Malmquist bias, and should therefore be interpreted as preliminary observed luminosity functions rather than intrinsic ones.

explosions, which are the focus of ongoing work. More broadly, CATS150 provides a high-completeness local benchmark that bridges current surveys and the deeper transient discovery space to be explored by Rubin/LSST and Roman, anchoring future studies to a well-characterized nearby reference sample while extending spectroscopic coverage to fainter limits approaching those probed by next-generation wide-field surveys.

Chapter 4

LOW-LUMINOSITY TYPE IIP SUPERNOVAE FROM THE ZWICKY TRANSIENT FACILITY CENSUS OF THE LOCAL UNIVERSE. I: LUMINOSITY FUNCTION, VOLUMETRIC RATE

Das, K. K., M. M. Kasliwal, et al. (2025). "Low-luminosity Type IIP Supernovae from the Zwicky Transient Facility Census of the Local Universe. I. Luminosity Function, Volumetric Rate". In: *Publications of the Astronomical Society of the Pacific* 137.4, article 044203. DOI: 10.1088/1538-3873/adcaeb.

Kaustav K. Das[1], Mansi M. Kasliwal[1], Christoffer Fremling[2], Jesper Sollerman[3], Daniel A. Perley[4], Kishalay De[5], Anastasios Tzanidakis[6], Tawny Sit[7], Scott Adams[1], Shreya Anand[8], Tomas Ahumada[1], Igor Andreoni[9], Seán Brennan[3], Thomas Brink[10], Rachel J. Bruch[11], Ping Chen[11], Matthew R. Chu[10], David O. Cook[12], Sofia Covarrubias[1], Aishwarya Dahiwale[1], Nicholas Earley[1], Anna Y. Q. Ho[13], Avishay Gal-Yam[11], Anjasha Gangopadhyay[3], Erica Hammerstein[14], K-Ryan Hinds[4], Viraj Karambelkar[1], Yihan Kong[15], S. R. Kulkarni[1], Theophile Jegou du Laz[1], Chang Liu[16,17], William Meynardie[1], Adam A. Miller[16,17,18], Guy Nir[10], Kishore C. Patra[10], Priscila J. Pessi[3], R. Michael Rich[19], Nabeel Rehemtulla[16,17,18], Sam Rose[1], Ben Rusholme[12], Steve Schulze[17], Yashvi Sharma[1], Avinash Singh[3], Roger Smith[2], Robert Stein[1], Milan Sharma Mandigo-Stoba[19], Nora L. Strotjohann[11], Yu-Jing Qin[1], Jacob Wise[4], Avery Wold[12], Lin Yan[2], Yi Yang[20], Yuhan Yao[10], Erez Zimmerman[11]

[1] Cahill Center for Astrophysics, California Institute of Technology, Pasadena, CA 91125, USA

[2] Caltech Optical Observatories, California Institute of Technology, Pasadena, CA 91125, USA

[3] The Oskar Klein Centre, Department of Astronomy, Stockholm University, AlbaNova, SE-10691 Stockholm, Sweden

[4] Astrophysics Research Institute, Liverpool John Moores University, IC2, Liverpool L3 5RF, UK

[5] MIT-Kavli Institute for Astrophysics and Space Research, 77 Massachusetts Ave., Cambridge, MA 02139, USA
[6] Department of Astronomy and the DiRAC Institute, University of Washington, Seattle, WA 98195, USA
[7] Department of Astronomy, The Ohio State University, Columbus, OH 43210, USA
[8] Kavli Institute for Particle Astrophysics and Cosmology, Stanford University, Stanford, CA 94305, USA
[9] Department of Physics and Astronomy, University of North Carolina at Chapel Hill, Chapel Hill, NC 27599, USA
[10] Department of Astronomy, University of California, Berkeley, CA 94720, USA
[11] Department of Particle Physics and Astrophysics, Weizmann Institute of Science, Rehovot 76100, Israel
[12] IPAC, California Institute of Technology, Pasadena, CA 91125, USA
[13] Department of Astronomy, Cornell University, Ithaca, NY 14853, USA
[14] Department of Astronomy, University of Maryland, College Park, MD 20742, USA
[15] Institute for Astronomy, University of Hawaii at Manoa, Honolulu, HI, USA
[16] Department of Physics and Astronomy, Northwestern University, Evanston, IL 60208, USA
[17] Center for Interdisciplinary Exploration and Research in Astrophysics (CIERA), Northwestern University, Evanston, IL 60201, USA
[18] NSF-Simons AI Institute for the Sky (SkAI), Chicago, IL 60611, USA
[19] Department of Physics & Astronomy, University of California Los Angeles, Los Angeles, CA 90095, USA
[20] Department of Physics, Tsinghua University, Beijing 100084, China

Abstract

We present the luminosity function and volumetric rate of a sample of Type IIP supernovae (SNe) from the Zwicky Transient Facility Census of the Local Universe survey (CLU). This is the largest sample of Type IIP SNe from a systematic volume-limited survey to-date. The final sample includes 330 Type IIP SNe and 36 low-luminosity Type II (LLIIP) SNe with $M_{\rm r,peak} > -16$ mag, which triples the literature sample of LLIIP SNe. The fraction of LLIIP SNe is 19^{+3}_{-4}% of the total CLU Type IIP SNe population (8^{+1}_{-2}% of all core-collapse SNe). This implies that while LLIIP SNe likely represent the fate of core-collapse SNe of $8-12$ $M_\odot$ progenitors,

they alone cannot account for the fate of all massive stars in this mass range. To derive an absolute rate, we estimate the ZTF pipeline efficiency as a function of the apparent magnitude and the local surface brightness. We derive a volumetric rate of $(3.9^{+0.4}_{-0.4}) \times 10^4$ Gpc^{-3} yr^{-1} for Type IIP SNe and $(7.3^{+0.6}_{-0.6}) \times 10^3$ Gpc^{-3} yr^{-1} for LLIIP SNe. Now that the rate of LLIIP SNe is robustly derived, the unresolved discrepancy between core-collapse SN rates and star-formation rates cannot be explained by LLIIP SNe alone.

4.1 Introduction

Core-collapse supernovae (CCSNe), the explosive endpoints of massive stars, drive chemical evolution in galaxies, provide impetus for the formation of new generations of stars, and leave behind neutron star or black hole remnants. Despite the discovery of over 10,000 SNe, the fate of stars at the low-mass end of CCSNe, with progenitor initial masses of $\approx$ 8–12 $M_\odot$, is not well understood (e.g., see Janka 2012, Sukhbold et al. 2016). Exploring this mass range is important, because it probes the boundary between whether a star has a large enough mass to form a neutron star from its central core or, instead, leaves behind a white dwarf. Also, it is uncertain whether stars in this mass range undergo iron core-collapse from Red Supergiants (RSG) or if electron capture in super-Asymptotic Giant Branch (sAGB) stars drives the SN explosions (Nomoto 1984, Jerkstrand et al. 2018, Leung and Fuller 2020, Kozyreva et al. 2021).

Stars in the 8–12 $M_\odot$ range exhibit a distinctly different core structure compared to those with higher progenitor mass, characterized by significantly lower compactness (Sukhbold et al. 2016). The evolution of such stars is more complex to model than at > 12 $M_\odot$ due to the development of thermal pulses that are numerically challenging to follow, and highly uncertain late-time mass-loss (e.g., Miyaji et al. 1980, Woosley and Heger 2015). The lowest mass CCSNe have steep density gradients outside their degenerate cores, liberate less gravitational binding energy, have lower neutrino luminosities, and ultimately are associated with lower luminosities, explosion energy and nickel yield (Janka 2012, Müller 2016, Burrows et al. 2019, Eldridge et al. 2019, Stockinger et al. 2020, Burrows and Vartanyan 2021, Sandoval et al. 2021, Barker et al. 2022b, Burrows et al. 2024).

It is critical to understand this faint end of the core-collapse luminosity function, constrain their rates and couple the stellar evolution initial mass function (IMF)

to the known SN populations. Determining the SN rate and tying it to the mass boundary between stars that do and do not explode as SNe is vital for determining the number of neutron stars, galactic chemical evolution and dust evolution models, and the total energy released by SNe into the environment. The CCSN distribution traces the formation of massive stars and the CCSN rate should match the massive star formation rate using the known star-formation rate density and IMF, given our current understanding of stellar evolution. However, there is an apparent discrepancy between the two absolute rates with the star-formation implying a much higher CCSN rate than is observed. This ongoing debate has been discussed extensively in the literature (e.g., Horiuchi et al. 2011, Botticella et al. 2012, Horiuchi et al. 2013, Cappellaro et al. 2015, Xiao and Eldridge 2015, Jencson et al. 2019b). One possibility is that this disagreement arises from a missing population of low-luminosity CCSNe.

One such class of faint CCSNe is low-luminosity Type IIP SNe (LLIIP SNe), which likely represent the explosions of $8 - 12$ $M_\odot$ progenitor stars. LLIIP SNe exhibit a faint peak luminosity, defined here as $M_{\rm r,peak} \geq -16$ mag, motivated by prior literature (e.g., Spiro et al. 2014). Recent studies, based on pre-explosion images of SNe 2005cs, 2008bk, 2018aoq, 2022acko (Maund et al. 2005, Li et al. 2006, Mattila et al. 2008, O'Neill et al. 2019, Van Dyk et al. 2023b) also show that SNe with r-band peak > -16 mag have progenitor mass estimates less than 11 $M_\odot$, while those with brighter peak have progenitor masses >12 $M_\odot$(see Figure 4.12 in Appendix 4.11). The nickel mass (~ 0.005 $M_\odot$) of LLIIP SNe is an order of magnitude lower than that typically found in standard Type II SNe (e.g., Rodríguez et al. 2021). Additionally, LLIIP SNe are characterized by slow expansion velocities (approximately $1300 - 2500$ km s^{-1} at 50 days after the explosion), indicating low explosion energies. The low energy and low nickel mass could be explained by the explosion of $8 - 12$ $M_\odot$ progenitors. This is also favored by lightcurve simulations (Pumo et al. 2017, Fraser et al. 2011), evolutionary numerical simulations of low mass RSGs (Lisakov et al. 2017), and nebular spectroscopy (Jerkstrand et al. 2018). A correlation is also observed between the explosion energy, nickel mass and progenitor mass estimates from pre-SN imaging (Eldridge et al. 2019), where lower-mass progenitors (< 12 $M_\odot$) are associated with lower nickel mass (< 0.01 $M_\odot$) and lower explosion energy ($< 2 \times 10^{50}$ erg s^{-1}).

However, there are only about a dozen such objects presented in the literature (Turatto et al. 1998, Spiro et al. 2014, Jäger et al. 2020, Müller-Bravo et al. 2020, Reguitti

et al. 2021, Yang et al. 2021, Valerin et al. 2022, Kozyreva et al. 2022, Bostroem et al. 2023, Teja et al. 2024, Dastidar et al. 2025). For a Salpeter IMF (Salpeter 1955), around 50% of the potential CCSN progenitors reside in the $8 - 12$ $M_{\odot}$ mass range. Given this fact, it is surprising that such SNe are rarely detected. What do half of the stars that undergo core-collapse explode as? It is likely that this deficit of discovery can be explained by the connection between these relatively low-mass progenitors and the occurrence of low-luminosity SNe, which are more difficult to detect and classify.

In this series of three papers, we present the analysis of a sample of 36 LLIIP SNe detected by Zwicky Transient Facility (ZTF) as part of the Census of the Local Universe (CLU) Survey, which roughly triples the number of existing LLIIP SNe in the literature. The focus of the first paper is to estimate their luminosity function and volumetric rates.

To place these results in a broader context, we also present a sample of 330 Type IIP SNe, obtained from the largest systematic volume-limited SN survey to date. The previous Type II SNe sample from a volume-limited sample survey includes 62 Type II SNe from the Lick Observatory Supernova Search (LOSS; Li et al. 2011). Other Type II samples from systematics surveys include 50 Type II SNe from the Panoramic Survey Telescope and Rapid Response System (PS1; Sanders et al. 2015), 34 Type IIP SNe from the Sloan Digital Sky Survey II Supernova Survey (SDSS-II SNS; Taylor et al. 2014) and 21 Type II SNe from the Caltech Core-collapse SN Project (CCCP; Arcavi et al. 2012).

In Section 8.2, we define the sample selection criteria. The data obtained and the extinction correction method are described in Sections 10.2 and 10.3, respectively. In Sections 4.5 and 4.6, we estimate the luminosity function and the volumetric rate of LLIIP SNe and compare with the overall CLU Type IIP SN population. We discuss the implications of the measured LLIIP rates in Section 10.6 and conclude in Section 10.7. In companion Papers II and III, we will present the analysis of their lightcurves and nebular spectra, respectively.

4.2 Sample Selection

Census of the Local Universe

ZTF conducts an optical time-domain survey with the 48-inch Schmidt telescope (P48) situated at Palomar Observatory (Bellm et al. 2019b, Graham et al. 2019, Dekany et al. 2020). The ZTF Census of the Local Universe (CLU) experiment aims

to build a comprehensive spectroscopic sample of transients in the local Universe. To accomplish this, we match the hosts of these transients with the galaxy catalog from the Census of the Local Universe (Cook et al. 2019). This catalog contains around 234,500 galaxies with established distances, compiled from pre-existing spectroscopic galaxy surveys and the CLU-Hα survey (refer to Cook et al. 2019 for further details).

The CLU experiment is designed as a volume-limited SN survey where sources at less than 150 Mpc ($z \leq 0.033$) and spatially coincident with (within 30 kpc) or visibly associated with a galaxy in the CLU catalog were assigned for spectroscopic follow-up for classification. For more detailed discussion of the CLU experiment filtering, see De et al. (2020b). The filter is implemented on the Global Relay of Observatories Watching Transients Happen (`GROWTH`) Marshal (Kasliwal et al. 2019) and the `Fritz` Marshal (van der Walt et al. 2019, Coughlin et al. 2023), both of which are web portals designed for vetting and coordinating transient follow-up observations.

After passing through the CLU filter, the transients are allocated for spectroscopic classification using: the Spectral Energy Distribution Machine (SEDM; Blagorodnova et al. 2018, Kim et al. 2022) at the Palomar 60-inch telescope, the Double-Beam Spectrograph (DBSP; Oke and Gunn 1982) at the Palomar 200-inch Hale telescope, and the Low-Resolution Imaging Spectrometer (LRIS; Oke et al. 1995). In this paper, we consider SNe saved to the CLU experiment starting from 1 October 2018 until 1 April 2024. We exclude the targets saved to ZTF in 2020 as the CLU experiment was inactive during that year. A total of 1745 SNe saved to CLU were classified during this interval.

Sample of LLIIP SNe

We apply the following selection criteria on the ZTF SN sample obtained from the CLU survey:

1. Type II Classification: From the CLU sample, 727 candidates classified as Type II (including subtypes IIP, II, IIL, II-norm, and II-pec) were selected.

2. Peak Magnitude: A Gaussian process fit was applied to the forced photometry light curves, and the sample was restricted to those with a peak magnitude $m_{peak_r} < 20$ mag, resulting in 719 candidates. The peak magnitude and other lightcurve parameters are measured on this GP fit (see Section 9.2 for details.).

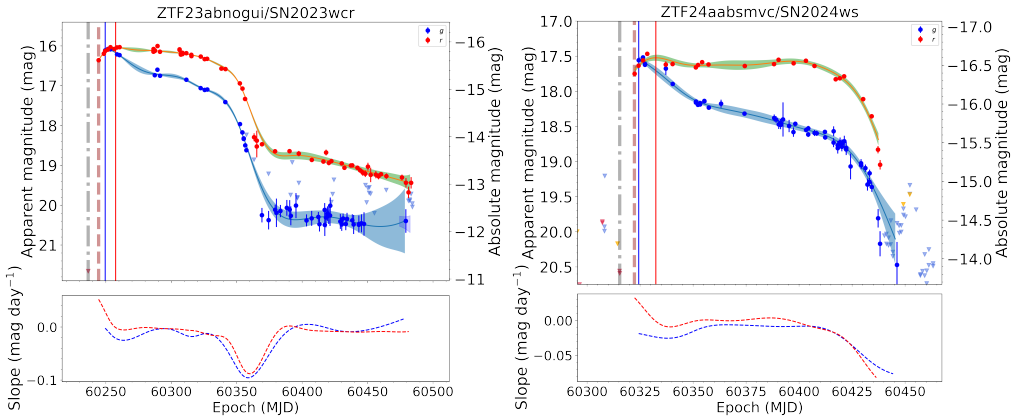

Figure 4.1: Example of SN light curves and the GP interpolations. The apparent magnitudes have been corrected for Galactic and host extinction. The lower panels show the slope of the light curves, i.e., the derivative of the GP fits, in units of mag per day. The vertical dashed red line shows the epoch of the first detection. The vertical dashed grey line shows the epoch of last non-detection. The vertical solid red and blue lines show the epochs of peak r- and g-band magnitudes, respectively.

The 20 mag cut is chosen as the pipeline recovery efficiency and classification completeness drops below 80% for alerts fainter than 20 mag (see Section 4.5).

3. In order to constrain the r-band peak, we first require that the candidates have more than 10 detections, reducing the sample to 626. We also require that the candidates pass any one of the following conditions:

   a) Candidates with at least one detection before the peak and one after the peak, and for which the duration between the last non-detection and the first detection ($t_{firstdet} - t_{lastnon-det}$) was $\leq$ 20 days.

   b) If $t_{firstdet} - t_{lastnon-det} \geq$ 20 days, then candidates with more than 10 pre-peak detections and more than 2 post-peak detections, as well as a magnitude difference $mag_{firstdet} - mag_{peak} > 1$ mag, were considered.

   c) For candidates where the first detection corresponds to the peak, the last non-detection had to occur within 10 days of the first detection.

   394 candidates pass this quality cut.

4. Plateau Criterion: Candidates were required to show a plateau phase, defined as a duration of $\geq$ 40 days with a drop of less than 1 magnitude, resulting in a sample of 330 candidates.

5. Peak Absolute Magnitude: To obtain the absolute magnitudes, we use the distance modulus calculated from the host redshift assuming a cosmological model with $\Omega_M = 0.3$, $\Omega_\Lambda = 0.7$, and $h = 0.7$. For galaxies closer than 25 Mpc, we correct for the Virgo, Great Attractor, and Shapley supercluster infall based on the NASA Extragalactic Database object page (NED[1]; Helou et al. 1991). We ignore corrections due to peculiar motions for galaxies farther than 25 Mpc. If the peculiar motion of the galaxy is $\sim$ 300 km s^{-1}, then the error of the peak magnitude is $\leq$ 0.1 mag. Table A lists the distances used for the nearby galaxies and their references. We apply a K-correction of 2.5$\times$ log(1 + z) for all the SNe in our sample. The LLIIP sample is restricted to those with a peak absolute magnitude less luminous than -16 mag, leaving 48 LLIIP SN candidates.

6. Host Extinction Correction: Finally, after correcting for host galaxy extinction (see Section 10.3 for details), 36 LLIIP SNe remained in the final sample.

The summary of the selection criteria and the sample are provided in Tables A and 4.2 respectively. The distribution of the number of SNe as a function of peak absolute magnitude is shown in Figure 4.2. A complementary ZTF experiment is the magnitude-limited Bright Transient Survey (BTS; Fremling et al. 2020, Perley et al. 2020), aimed at classifying transients brighter than a peak apparent magnitude of 18.5 mag without any redshift cut. 62 SNe in our sample are also part of the Type II SN sample of the BTS survey (Y. Qin et al., in prep.; K. Hinds et al., in prep.)

[1]https://ned.ipac.caltech.edu/

Table 4.1: Sample selection summary

Step	Criteria	# Candidates
1	SNe in CLU classified as Type II (IIP, II, II-norm, II-pec)	727
2	Gaussian process fit to forced photometry lightcurves, $m_{peak_r} < 20$ mag	719
3	Number of detections ($N_{pre-peak} + N_{post-peak}$) > 10	
3A	If first detection is the peak, require that the last non-detection is within 10 days of first detection	
3B	≥1 detection before peak and ≥1 detection after peak and $t_{firstdet} - t_{lastnon-det} \leq 20$ days	394
3C	If $t_{firstdet} - t_{lastnon-det} \geq 20$ days, $N_{pre-peak} > 10$, $N_{post-peak} > 2$, $mag_{firstdet} - mag_{peak} > 1$ mag	
4	Criteria for plateau: There should be a duration of 40 days with a drop of < 1 mag	330
5	LLIIP: Peak absolute magnitude ≥ -16 mag (no host extinction)	48
	LLIIP: Peak absolute magnitude ≥ -16 mag (after host extinction)	36

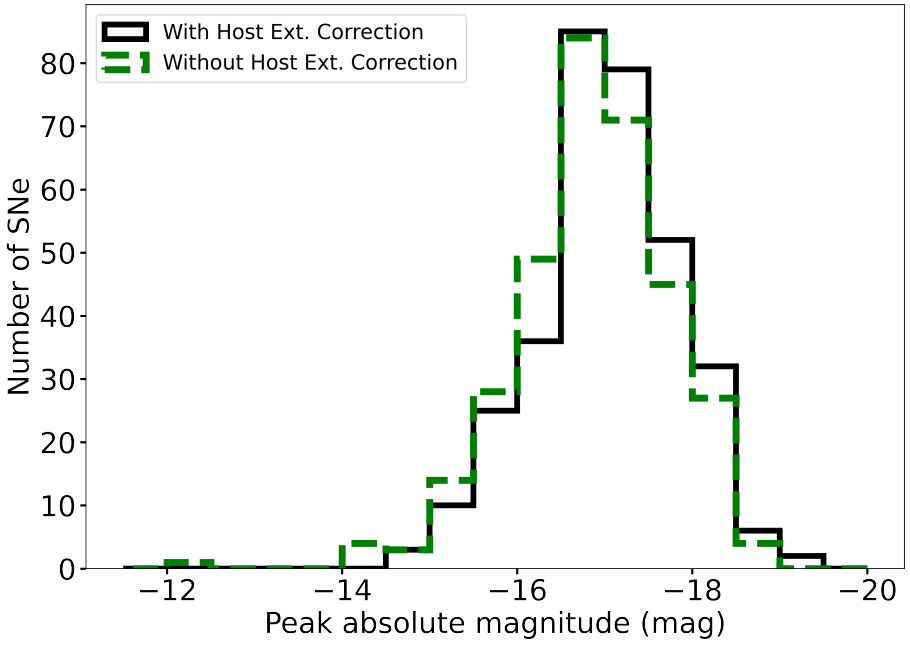

Figure 4.2: The distribution of the number of SNe in the final ZTF CLU Type IIP sample, consisting of 330 SNe, as a function of peak r-band absolute magnitude, with and without host-extinction correction

Table 4.2: Summary table of the CLU Type II SN sample. Only the first 45 rows are shown here. The full table is shown in the Appendix 4.14. The peak absolute magnitudes have been measured by assuming Milky Way extinction ($A_{V,MW}$) and host galaxy extinction ($A_{V,host}$) as described in Section 10.3. The t_{expl} column shows the explosion epoch. The Peak mag_r shows the peak r-band absolute magnitude. A machine-readable version of the full sample table is available in DOI:10.5281/zenodo.14538857.

Name	RA	Dec	Redshift	t_{expl}	1st detection	Peak mag_r	$A_{V,MW}$	$A_{V,host}$
	(hh:mm:ss)	(dd:mm:ss)		(MJD)	(MJD)	(mag)	(mag)	(mag)
ZTF18abnxfve/AT2018lrz	22:29:52.72	+36:43:50.1	0.025	58347.8	58349.3	-15.94	0.30	0.00
ZTF18abrzbtb/SN2018ggu	07:43:04.67	+50:17:22.2	0.019	59120.0	59120.5	-15.66	0.19	0.00
ZTF19aaabzpt/SN2018lab	06:16:26.51	-21:22:32.4	0.009	58479.3	58487.3	-15.81	0.24	0.71
ZTF19aalycsv/AT2019txj	10:48:39.19	+76:48:05.3	0.023	58543.3	58546.2	-15.27	0.07	0.00
ZTF19aamwhat/SN2019bzd	14:47:32.03	-19:45:57.7	0.008	58559.7	58568.4	-15.83	0.24	0.07
ZTF19aatmadu/AT2019esn	14:51:56.11	+51:15:51.2	0.027	58602.4	58605.4	-16.00	0.06	0.00
ZTF19abalqkq/AT2019khq	17:50:41.76	+14:49:26.3	0.014	58645.9	58650.3	-15.76	0.26	1.63
ZTF19abctzkc/AT2019tti	00:18:59.83	+08:46:28.2	0.019	58644.4	58646.4	-15.67	0.55	0.21
ZTF19abejaiy/SN2019krp	14:07:33.70	+14:38:03.3	0.017	58670.2	58671.2	-15.45	0.04	0.00
ZTF19ablfoqa/AT2019tya	02:09:38.03	+01:33:06.7	0.032	58694.0	58694.5	-15.93	0.08	0.00
ZTF19abllxfy/AT2019ttl	21:52:43.47	+38:56:00.8	0.020	58682.9	58690.3	-15.36	0.88	0.00

Table 4.2: Continued.

Name	RA	Dec	Redshift	$t_{\rm expl}$	1st detection	Peak mag$_r$	$A_{V,\rm MW}$	$A_{V,\rm host}$
	(hh:mm:ss)	(dd:mm:ss)		(MJD)	(MJD)	(mag)	(mag)	(mag)
ZTF19acalxgp/AT2019qiq	23:44:56.09	-04:16:33.1	0.029	58735.4	58737.3	-15.86	0.12	0.00
ZTF21aabfwwl/SN2021iy	11:18:31.68	-06:16:40.5	0.014	59217.9	59219.4	-15.55	0.14	0.00
ZTF21aaobkmg/SN2021eui	19:20:55.80	+43:07:14.6	0.015	59273.5	59276.5	-15.34	0.28	0.00
ZTF21aaqgmjt/SN2021gmj	10:38:47.27	+53:30:30.3	0.003	59292.3	59293.2	-15.02	0.06	0.00
ZTF21abbomrf/AT2020ghq	14:45:20.59	+38:44:18.5	0.015	59347.8	59349.2	-15.72	0.03	0.00
ZTF21abglcxm/SN2021qcs	15:29:22.82	-12:14:54.4	0.011	59377.3	59378.2	-15.65	0.43	0.42
ZTF21acdoyqt/SN2021zgm	18:35:48.34	+22:27:45.2	0.013	59479.2	59480.1	-15.51	0.44	0.00
ZTF22aaahubo/AT2022cru	08:23:26.30	-04:55:06.5	0.023	59575.4	59600.3	-15.89	0.12	0.00
ZTF22aakdbia/SN2022jzc	12:05:28.66	+50:31:36.8	0.002	59714.3	59715.2	-14.91	0.05	0.57
ZTF22aanrqje/SN2022mji	09:42:54.06	+31:51:03.6	0.004	59732.7	59741.2	-15.00	0.05	0.85
ZTF22aaywnyg/SN2022pru	11:59:07.65	+52:41:58.5	0.004	59787.7	59797.2	-15.42	0.07	0.00
ZTF22aazmrpx/SN2022raj	02:03:17.52	+29:14:04.9	0.012	59798.4	59800.4	-15.20	0.15	0.00
ZTF22abssiet/SN2022zmb	10:38:43.18	+56:33:14.4	0.014	59885.5	59887.5	-15.72	0.02	0.07
ZTF22abvaetz/SN2022aang	07:59:21.83	+18:06:40.9	0.016	59894.5	59901.5	-15.44	0.08	0.00
ZTF22abyivoq/SN2022acko	03:19:38.98	-19:23:42.8	0.006	59917.8	59922.2	-15.83	0.08	0.00
ZTF23aaarmtb/SN2023qh	09:07:15.44	+37:12:54.8	0.024	59947.4	59957.4	-15.89	0.06	0.00
ZTF23aackjhs/SN1995al	09:50:56.03	+33:33:11.0	0.005	59989.8	59992.3	-14.88	0.04	0.07
ZTF23aagkajy/AT2023gdt	10:30:10.64	+43:21:23.4	0.014	60050.2	60051.2	-15.42	0.03	0.71

Table 4.2: Continued.

Name	RA	Dec	Redshift	$t_{\rm expl}$	1st detection	Peak mag$_r$	$A_{V,\rm MW}$	$A_{V,\rm host}$
	(hh:mm:ss)	(dd:mm:ss)		(MJD)	(MJD)	(mag)	(mag)	(mag)
ZTF23aajrmfh/SN2023ijd	12:36:32.47	+11:13:19.7	0.007	60078.2	60079.0	-15.39	0.09	0.00
ZTF23aamzlzc/AT2023kne	17:25:19.11	+58:49:02.6	0.028	60095.4	60097.3	-15.81	0.10	0.00
ZTF23aaqwpio/AT2023nca	16:39:26.36	+11:12:45.3	0.023	60129.3	60135.2	-15.61	0.14	0.00
ZTF23aasyvbf/SN2023nmh	00:37:38.73	-04:16:53.2	0.020	60142.4	60144.5	-15.93	0.10	0.00
ZTF23abnogui/SN2023wcr	12:23:31.29	+74:57:01.3	0.005	60240.5	60244.5	-15.58	0.09	0.00
ZTF23abvommm/SN2023acbr	02:27:03.18	-09:25:02.3	0.016	60300.7	60305.2	-15.57	0.08	0.00
ZTF24aabppgn/SN2024wp	11:24:39.25	+14:56:52.9	0.014	60320.5	60325.5	-15.52	0.10	0.00
ZTF24aahwfsa/AT2024fas	10:51:55.36	+37:35:23.9	0.026	60393.4	60396.4	-15.80	0.04	0.00
ZTF24aaplfjd/SN2024jxm	0:58:01.36	+30:42:23.84	0.016	60460.0	60460.5	-16.00	0.18	0.00

4.3 Data

In this section, we describe the photometric and spectroscopic data used.

Optical photometry

We perform forced point-spread function photometry on the ZTF difference images at the location of these SNe using the ZTF forced-photometry service developed by Masci et al. (2019, 2023) in g and r bands. For this work, we consider anything less than a 3σ detection an upper limit. We used a Gaussian Process (GP) algorithm[2] (Ambikasaran et al. 2015) to interpolate the photometric measurements and measure the slope. Figure 4.1 shows the lightcurves of SNe 2023wcr and 2024wcs as examples. The vertical dashed red line shows the epoch of first detection, and the vertical dashed grey line shows the epoch of last non-detection. The explosion epoch is defined to be midway between the epoch of first detection and last non-detection. The epochs of peak r- and g-band magnitudes are shown by the vertical solid red and blue lines. The photometry data, lightcurve plots, and spectroscopy of all SNe in the sample will be made available on WISEREP and Zenodo after publication.

Optical spectroscopy

For each transient, at least one spectrum is usually obtained close to the peak luminosity to establish a spectroscopic classification as described in Section 4.2. We employ the `SuperNova Identification` (`SNID`; Blondin and Tonry 2007) code for these classifications. For spectra that show host galaxy contamination, we utilize `superfit` (Howell et al. 2005). The reduction of DBSP spectra follows the procedures outlined in Bellm and Sesar (2016) and Roberson et al. (2022), while the SEDM data reductions are detailed in Rigault et al. (2019). The LRIS spectra were reduced using the automated LPIPE (Perley 2019) pipeline.

We also make use of spectra from the Alhambra Faint Object Spectrograph and Camera at the Nordic Optical Telescope (NOT; Djupvik and Andersen 2010) and from the Spectrograph for the Rapid Acquisition of Transients (SPRAT; Piascik et al. 2014) on the Liverpool Telescope. The NOT data reduction utilized the PyNOT[3] and PypeIt (Prochaska et al. 2020a) pipelines. The SPRAT data is processed using a pipeline based on FrodoSpec (Barnsley et al. 2012).

[2] https://george.readthedocs.io/

[3] https://github.com/jkrogager/PyNOT

4.4 Extinction Correction

Extinction is divided into two components: the first component represents dust extinction from the Milky Way, while the second component accounts for extinction originating from the host galaxies of the SNe. To correct for Galactic extinction, we employ the reddening maps provided by Schlafly and Finkbeiner (2011), the extinction law described by Cardelli et al. (1989) and a value of $R_V = 3.1$.

To estimate the host-galaxy extinction, we use the average $g - r$ color curve of the sample. First, we measure the Na I D absorption lines of the host environment (Poznanski et al. 2012, Stritzinger et al. 2018) when a high SNR SN spectrum is available. To measure the template $g - r$ color, we discard objects with Na I D EW > 1 Å. The 1σ scatter is 0.35 mag. The average color and standard deviation (1σ range) are shown by the black solid line and blue shaded region, respectively, in Figure 4.3. This template is available in DOI:10.5281/zenodo.14538857. We then measure the $A_{\mathrm{V,host}}$ assuming that the SN color exceeding the 1σ $g - r$ template is caused by host extinction. 80 out of the 330 Type IIP SNe has $A_{\mathrm{V,host}} > 0$. The sample color curve after this correction is shown in the right panel of Figure 4.3. The remaining 1σ scatter in the $g - r$ color is likely due to intrinsic properties of the SNe, which could be dominated by photospheric temperature differences (e.g., see de Jaeger et al. 2018). Table 4.2 lists the measured $A_{\mathrm{V,host}}$ values.

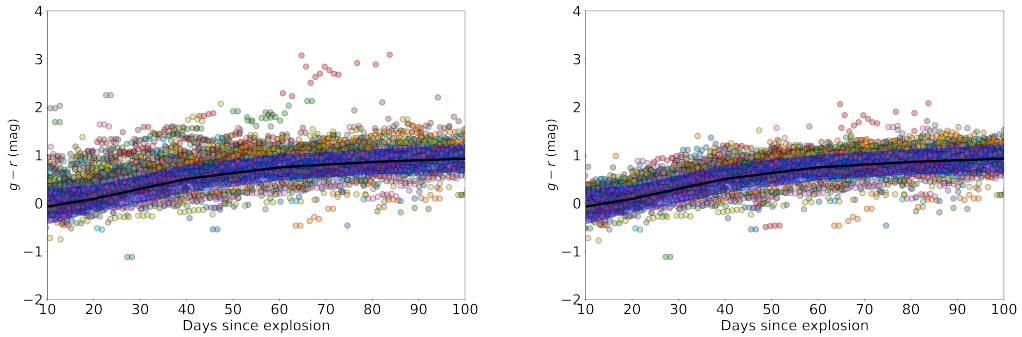

Figure 4.3: *Left:* The $g - r$ colors of the ZTF CLU Type II SN sample are shown in colored circles. The average color and standard deviation (1σ range) of the distribution, after filtering out SNe with Na I D EW > 1 Å, are shown by the black solid line and blue shaded region, respectively. *Right:* The sample $g - r$ color distribution after host-extinction correction. The color template is available in DOI:10.5281/zenodo.14538857.

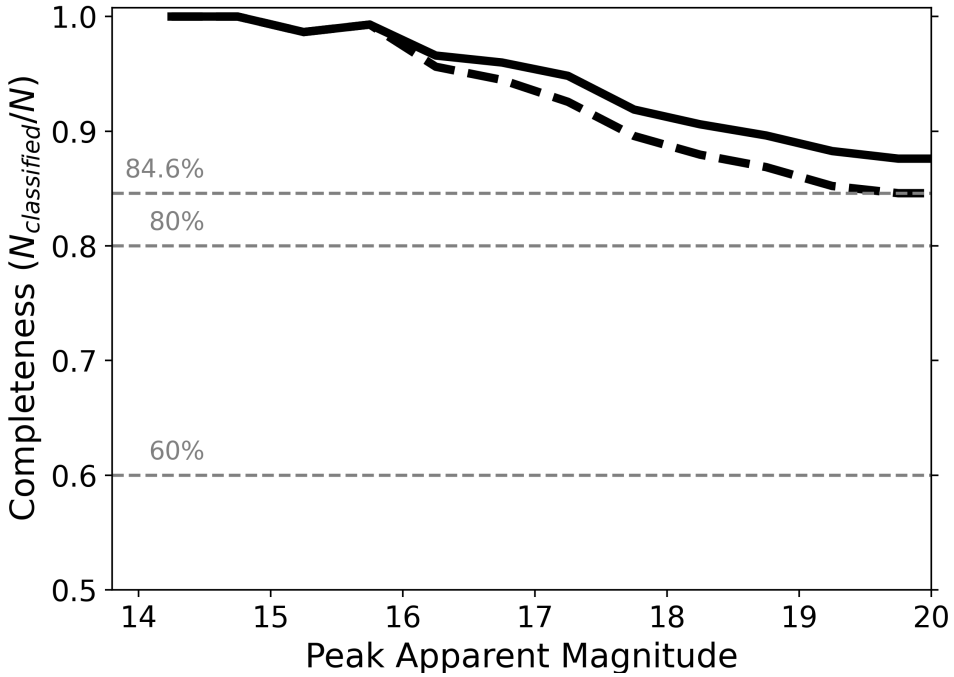

Figure 4.4: The cumulative distribution of the spectroscopic completeness of the ZTF CLU survey (with 2064 saved transients) as a function of peak r-band apparent magnitude. The dashed line accounts for the entire sample, whereas the solid black line omits 79 transients that are probably spurious. As a conservative lower limit, we consider the completeness depicted by the solid dashed line.

4.5 Luminosity function

With the use of our systematic and controlled ZTF CLU event sample, we determine a luminosity function for Type IIP and LLIIP SNe. The CLU LLIIP sample nearly triples the current number of published LLIIP SNe in the literature. Our final sample comprises 330 Type IIP SNe, with 36 ($\approx 11\%$) LLIIP SNe ($M_r > -16$ mag).

We use the r-band photometry to measure the SN II luminosity function and volumetric rate. A volume correction is applied to the luminosity function by weighting each object by $V_{max} = 1/D^3_{max}$, where D_{max} ($\propto 10^{\frac{1}{5}(20-M_r,peak)}$) is the farthest distance at which a transient can be detected given a limiting magnitude of 20 mag. For sources detectable past 150 Mpc, D_{max} was set to the maximum CLU experiment distance of 150 Mpc.

We also correct for the CLU spectroscopic completeness and the ZTF pipeline recovery efficiency factor as they are dependent on the apparent magnitude. Of

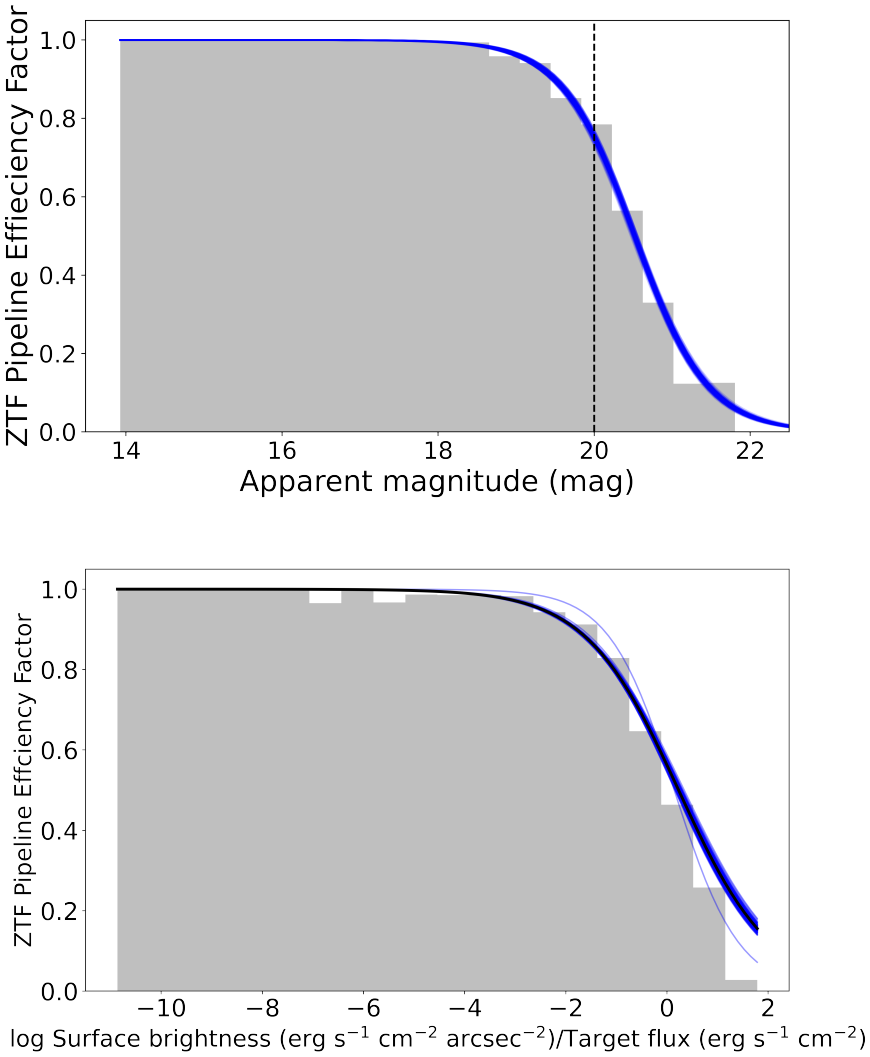

Figure 4.5: The ZTF pipeline recovery efficiency as a function of apparent magnitude (*upper*) and as a function of the ratio of local surface brightness and target flux (*lower*). The best-fit parameters of the logistic function is listed in Appendix 4.13. The data required to reproduce the plot is available in DOI:10.5281/zenodo.14538857.

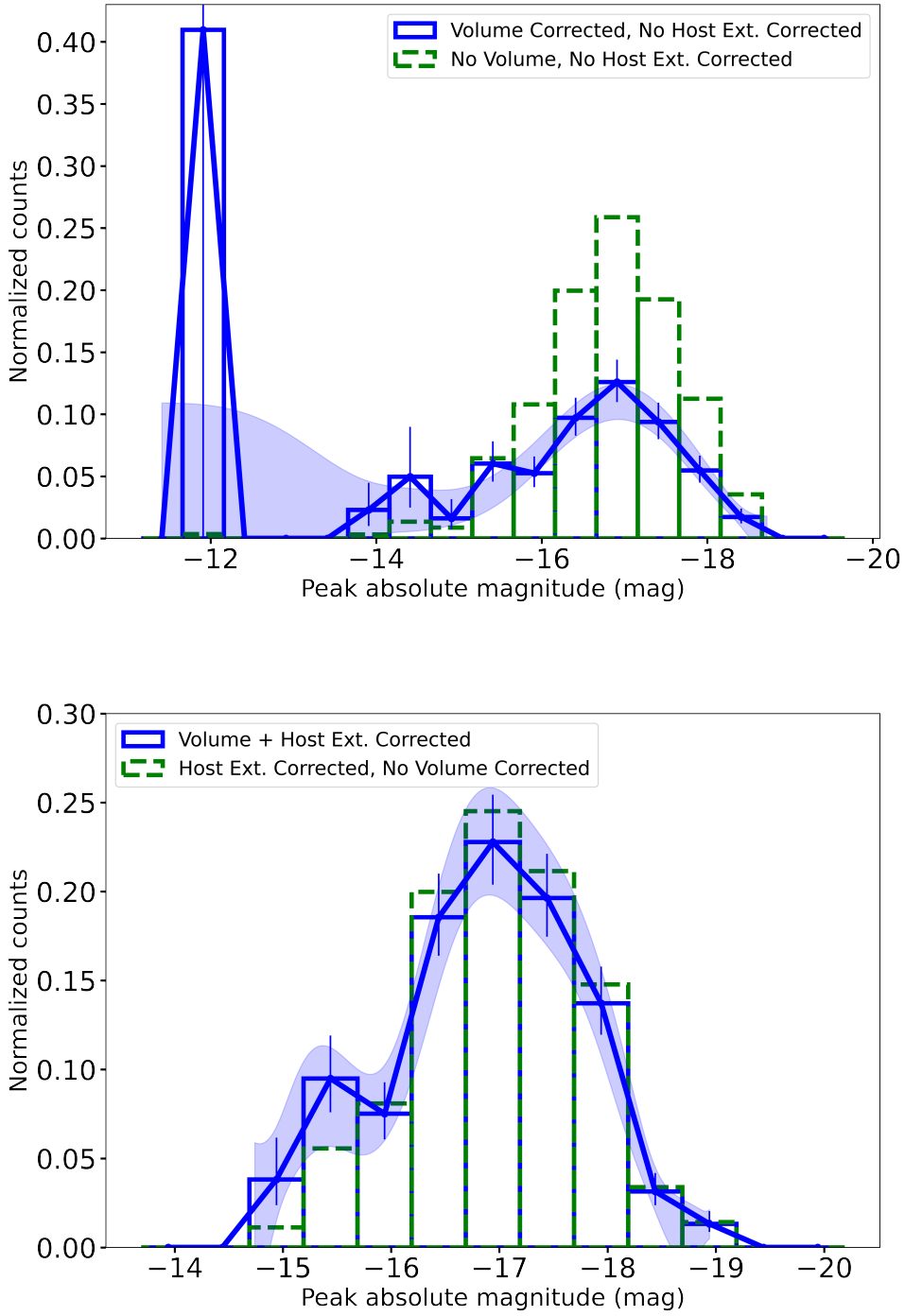

Figure 4.6: The peak r-band absolute magnitude distribution of the sample of 330 Type IIP SNe in CLU with Poisson errorbars before host-extinction correction (left) and after host-extinction correction (right). The volume-corrected luminosity function is shown in solid blue, while the raw distribution is shown in dashed green. GP fit is shown in blue. The luminosity function data is available in DOI:10.5281/zenodo.14538857.

the total of 2064 transients that are saved in CLU, 1745 (84.6%) transients are classified. The overall completeness of the CLU survey as a function of peak apparent magnitude is indicated by the dashed black line in Figure 4.4. There are 79 transients for which we are uncertain whether they are real transients on the basis of their spectroscopic and photometric properties. If we exclude these, the overall completeness is $\sim$ 87% (solid black line). Also, we note that the long-lived nature and relative ease of identifying the Hα P-Cygni feature make Type IIP events easier to classify. So the Type IIP SNe completeness is likely to be higher than the solid black line. As a conservative estimate, for the rest of the paper, we use the spectroscopic completeness depicted by the dashed black line.

The ZTF image subtraction pipeline has two potential sources of inefficiency relevant to this calculation. In each science image, the pipeline actively masks pixels affected by quality criteria, such as saturation from high brightness, cosmic rays, and defective pixels. This dynamic masking does not have a significant effect as Type IIP SNe have long durations ($\sim$100 days) and are eventually detected by the pipeline. A significant issue relates to the decreased efficiency of the image subtraction algorithm for faint alerts and on bright galaxy backgrounds. Here, we model the efficiency of the ZTF pipeline as a function of the alert flux and the ratio of background surface brightness to target flux. To estimate this, we check whether alert photometry exists for a given epoch for which there is a $\geq 5\sigma$ forced photometry detection. The local host surface brightness is extracted using PS1 r-band images with a 3" radius aperture. To estimate the conditional probability of the ZTF pipeline efficiency, we consider the binary data, X, which represents whether the ZTF pipeline successfully recovers a transient in alerts ($X = 1$) or not ($X = 0$). We model X using the Bernoulli distribution:

$$X \sim \mathrm{Bern}(p),$$

where p is parameterized by a logistic function dependent on the ratio (r) of the host surface brightness and the target flux:

$$p(r) = \frac{1}{1 + \exp(a(r - c))},$$

with a and c representing the model parameters that need to be determined. The logistic function was chosen because it smoothly transitions from 1 to 0 and captures the pipeline efficiency behavior as a function of r. We then estimate the model parameters using the `emcee` package (Foreman-Mackey et al. 2013). The best-fit

values of a and c are $a = 1.12^{+0.02}_{-0.02}$ and $c = 0.21^{+0.03}_{-0.03}$ respectively. As expected, the recovery efficiency decreases as this ratio increases. The best-fit efficiency is $\sim 50\%$ when the host surface brightness and target fluxes are comparable.

We also measure the inefficiency as a function of the apparent magnitude alone, using

$$p(m) = \frac{1}{1 + \exp(b(m - d))},$$

where m is the alert apparent magnitude. The best-fit values obtained are $b = 2.28^{+0.03}_{-0.04}$ mag^{-1} and $d = 20.57^{+0.01}_{-0.01}$ mag. The best fits, and corner plots of the MCMC fit are shown in Figure 4.5 and Appendix 4.13, respectively. The best-fit efficiency decreases with an increase in target alert apparent magnitude and is $\approx 80\%$ when the alert magnitude is 20 mag.

We then weight each SN by the corresponding classification completeness factor and the pipeline efficiency factor. The luminosity function thus obtained is shown in Figure 4.6 in blue. The luminosity function without volume correction is shown by the green dashed lines in Figure 4.6. After volume-, incompleteness- and pipeline-efficiency correction, the fraction of LLIIP SNe is $19^{+3}_{-4}\%$ of the entire Type II SN population (see Figure 4.9). The fraction of Type IIP SNe fainter than -15 mag and -14.5 are $< 5\%$ and $< 1.5\%$ respectively.

4.6 The Volumetric rate of Type IIP SNe using skysurvey

First, we create a template r-band lightcurve by compiling the photometry data for all the Type IIP SNe in the sample and apply Gaussian Regression processing (Figure 4.7). We use the `skysurvey` code[4] to estimate the volumetric rate. `skysurvey` simulates light curves as they would be observed based on a light curve template (using `sncosmo`) and survey plan. The survey plan is constructed using the actual pointing schedule of ZTF, detailing observation times, the filters used, and the sky brightness. Additionally, the simulation incorporates data on CCD outlines to account for data losses caused by chip gaps.

For the selection of simulated SNe II from `skysurvey`, we use the forced photometry-based selection criteria outlined in Section 8.2. We require at least two 5σ detections exceeding 20 mag in brightness. These criteria guarantee detection by the ZTF alert system, allowing the transient to pass the CLU filter, with a distance < 150 Mpc to ensure appropriate CLU filter saving and spectroscopic follow-up. Additionally, the

[4]https://github.com/MickaelRigault/skysurvey

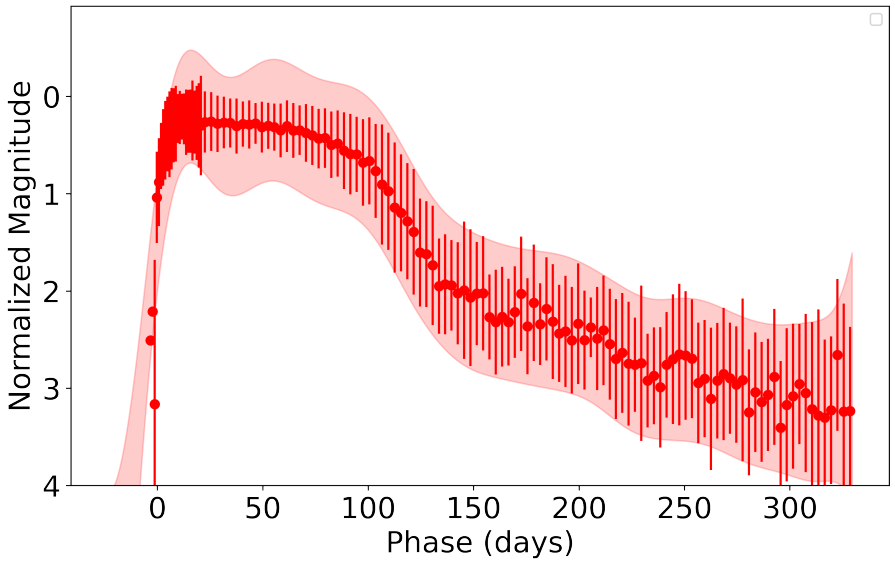

Figure 4.7: The r-band lightcurve template for Type IIP SNe. The solid points depict the mean lightcurve magnitudes of the ZTF CLU Type IIP sample. The line and shaded regions show the 1σ uncertainties derived from the GP fit.

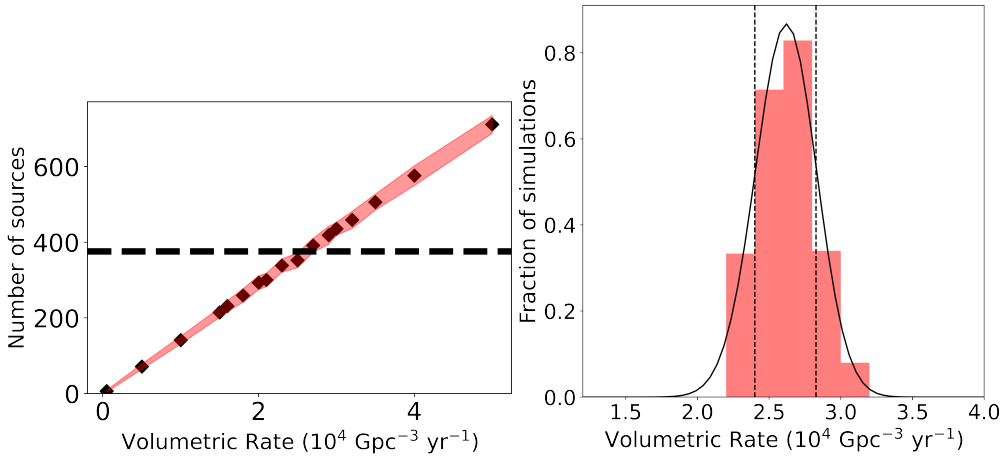

Figure 4.8: *Left:* The plot shows the number of LLIIP SNe that satisfy the filtering criteria as a function of the volumetric rate. The data points and the shaded region indicate the mean and standard deviation of detected transients, derived from 30 iterations of the simulated survey for each input volumetric rate. The dashed black line represents the observed number of Type IIP SNe in the ZTF CLU sample. *Right:* The fraction of simulations yielding the observed number of transients (within a 10% margin) is plotted against the volumetric rate.

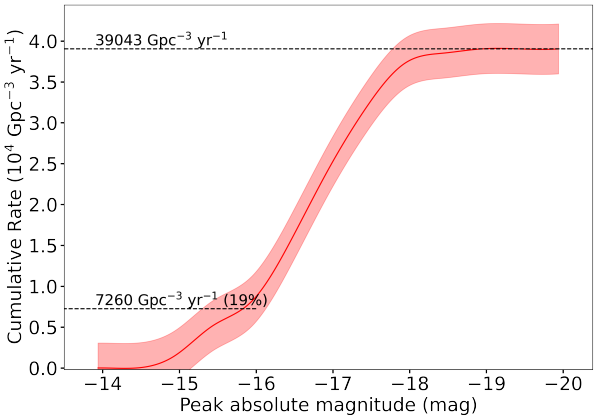

Figure 4.9: The cumulative distribution of the luminosity function of the ZTF CLU Type IIP sample. The IIP and LLIIP volumetric rates are shown by the horizontal dashed lines.

lightcurve quality cuts described in Section 8.2 are employed to consistently filter the `skysurvey` sample.

We generate ZTF lightcurves of Type IIP SNe for a range of input volumetric rates ($0.1–10.0 \times 10^4$ Gpc^{-3} yr^{-1}) for the `skysurvey` simulation up to a distance of 150 Mpc, according to the luminosity function in Figure 4.6. At each rate, 30 survey plan simulations were conducted. For these simulations, we documented the number of transients that successfully passed the filtering process. The detection estimate for each rate was made by computing the mean number of transients detected from the simulations, with the standard deviation serving as the error estimate. Figure 4.8 shows the expected number of detected transients along with the fraction of simulations that yield our observed sample size within an error margin of 10% for a given input volumetric rate.

The fraction of simulations matching our sample size follows a skewed Gaussian distribution, which was used to estimate the rate and its uncertainty based on a 68% confidence interval. This analysis yields a volumetric rate of $(2.6^{+0.3}_{-0.3}) \times 10^4$ Gpc^{-3} yr^{-1}.

This raw `skysurvey` rate already accounts for survey conditions such as weather and cadence as we used the real observing history of ZTF to simulate the light curves as they would have been observed. We now apply corrections for spectroscopic incompleteness, pipeline recovery efficiency and galaxy catalog incompleteness. As shown in Section 4.5, the CLU experiment achieved an overall completeness rate

of $\approx 84\%$.

In the CLU experiment, our methodology restricts the identification of SNe to those in galaxies where a spectroscopic redshift has been established. Therefore, we must correct the `skysurvey` rate of LLIIP events for galaxy catalog incompleteness. To correct for the incompleteness of the galaxy catalog, we used the redshift completeness factor derived from the ZTF Bright Transient Survey (Fremling et al. 2020). We use the redshifts and WISE 3.36 μm absolute magnitudes (MW1) of the host galaxies of our sample and weight each event by 1/RCF(z,MW1) to estimate the effect of galaxy catalog incompleteness (see Figure 4.10). This leads to an underestimate of the volumetric rate by $\approx 19\%$.

Finally, as mentioned earlier, the ZTF image subtraction pipeline has a reduced efficiency of the image subtraction algorithm on bright galaxy backgrounds and fainter targets. We weight each event by the inverse of the Pipeline Efficiency Factor (1/PEF(M, host)). This leads to an underestimate of the rate by $\approx 6\%$.

Applying the corrections described above, we derive a corrected rate of $(3.9^{+0.4}_{-0.4}) \times 10^4$ Gpc^{-3} yr^{-1} for Type IIP SNe and $(7.3^{+0.6}_{-0.6}) \times 10^3$ Gpc^{-3} yr^{-1} for LLIIP SNe.

4.7 Discussion

Comparison to the literature

The ZTF CLU sample of 330 SNe is the largest sample of Type IIP SNe from a systematic volume-limited survey to date. In Figure 4.11, we compare the luminosity function with the r-band Type II Luminosity functions from previous systematic SN surveys – 62 Type II SNe from the Lick Observatory Supernova Survey Search (LOSS; Li et al. 2011), 21 Type II SNe from the Caltech Core-Collapse Project (CCCP; Arcavi et al. 2012), 50 Type II SNe from the Panoramic Survey Telescope and Rapid Response System (PS1; Sanders et al. 2015), 34 Type IIP SNe from the Sloan Digital Sky Survey II Supernova Survey (SDSS-II SNS; D'Andrea et al. 2010, Taylor et al. 2014). We also compare with the sample of 241 Type II SNe from the ZTF BTS used to analyze the rise-time properties of Type II SNe (K. Hinds et al., in prep.). In comparison with the LOSS sample, which is corrected for luminosity bias, we show the volume- and host-extinction corrected distribution in solid black and the volume-corrected but not host-extinction-corrected distribution in dashed violet. Our distribution without host extinction correction matches better with the LOSS luminosity function. In the comparison with the PS1 and CCCP samples, the CLU sample in dashed green is not corrected for luminosity bias. We note that the

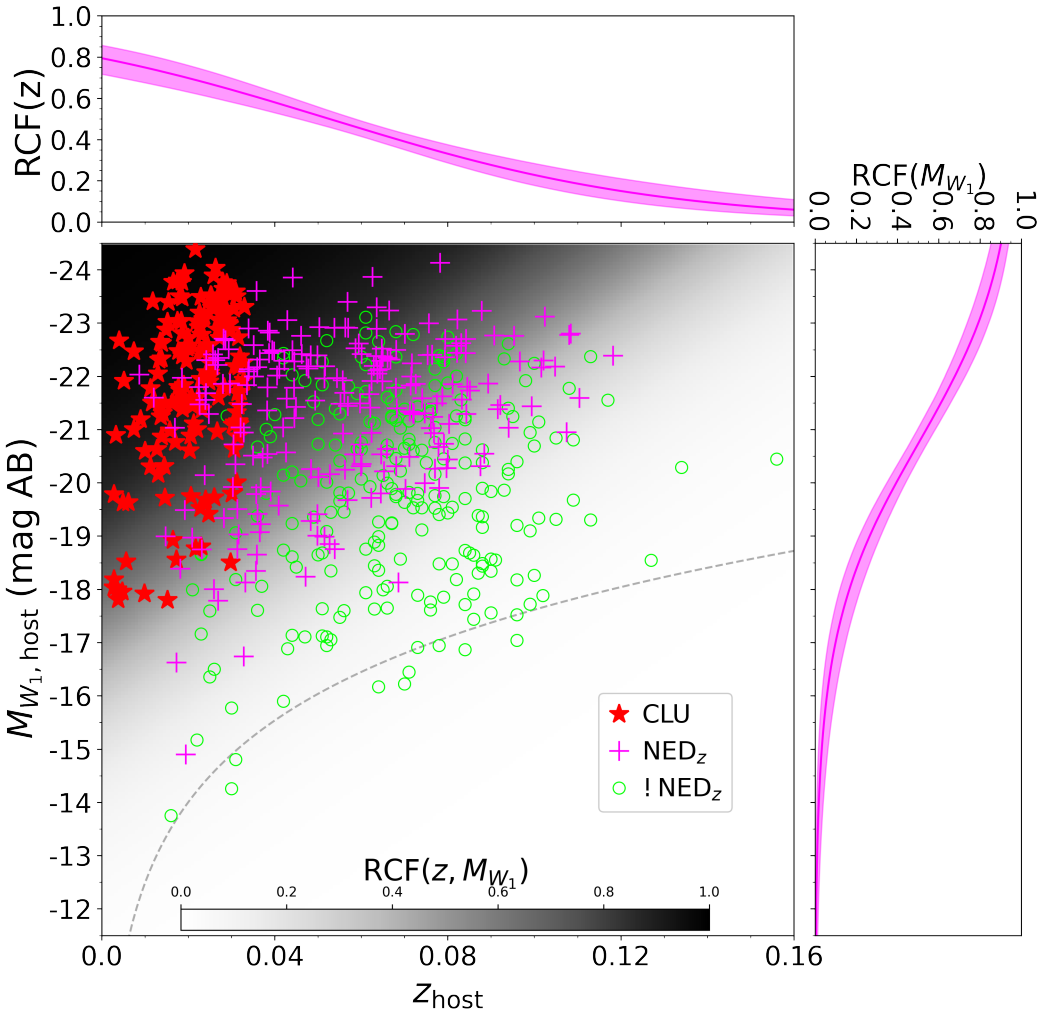

Figure 4.10: The redshift completeness factor of the galaxy catalogs as a function of the host redshift and $W1$-band magnitude, measured in Fremling et al. (2020). The red stars depict the hosts of the SNe of the CLU Type IIP sample.

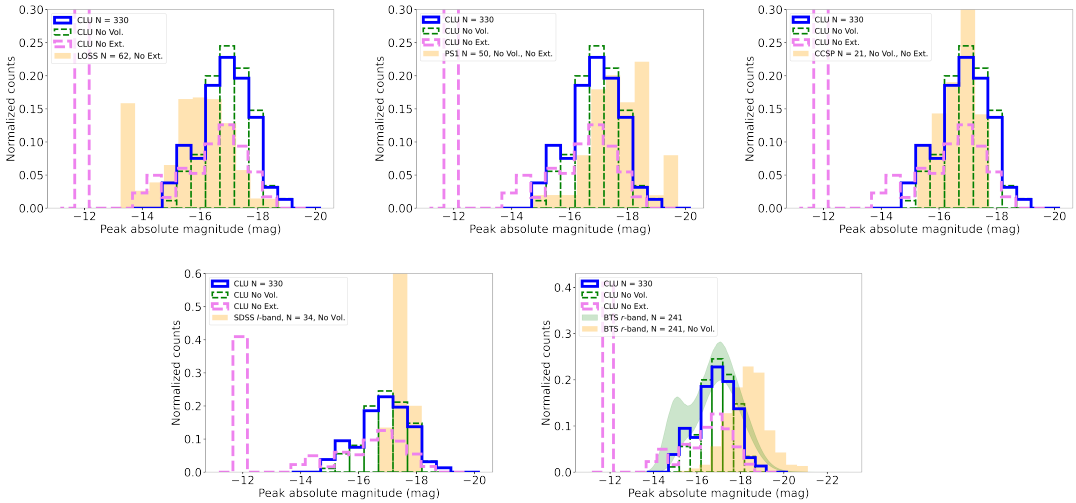

Figure 4.11: Comparison of the ZTF CLU Type II SNe luminosity function in r-band with the LOSS (r-band), PS1 (r-band), CCCP (r-band), SDSS (I-band), BTS (r-band) surveys (in shaded orange or green). The blue, green, and purple line depicts the volume and host-extinction corrected, only host-extinction corrected and only volume corrected distribution of the CLU Type IIP SNe sample, respectively.

PS1 r-band sample was part of a flux-limited survey and the observed distribution follows what one would typically expect without a volume correction. The CCCP experiment was also a flux-limited SN experiment. The observed CCCP distribution falls close to the mean and the fainter end of the dispersion of the ZTF CLU sample without any volume correction. The SDSS Type IIP SN sample from D'Andrea et al. (2010), which shows the I-band magnitude at 50 days post-explosion, does not have any SN fainter than -16 mag. The volume-corrected distribution of the peak r-band magnitude of the BTS Type II SN sample (K. Hinds et al., in prep.) in shaded green closely resembles the ZTF CLU distribution, with a higher fraction of fainter SNe in ZTF CLU sample without any volume correction (in orange), consistent with the experiment design.

We obtained a LLIIP fraction of 19^{+3}_{-4}% of the host-extinction corrected sample of CLU Type II SNe. The fraction of LLII SNe is ~ 45% for the LOSS volume-corrected luminosity function without any host-extinction correction. The fraction of LLIIP in the raw PS1 and CCCP sample distribution is ~ 3% and ~ 9%, respectively.

The volumetric rate for Type II SNe from the LOSS survey was $(4.4^{+1.4}_{-1.4}) \times 10^4$ Gpc^{-3}yr^{-1}. Based on the LOSS survey statistics (Li et al. 2011), Type IIP SNe are 70% of all Type II SNe, thus the Type IIP SN rate is $\sim (3.1^{+1.0}_{-1.0}) \times 10^4$ Gpc^{-3}yr^{-1},

which is consistent with the volumetric rate measured with the CLU sample. The Bright Transient Survey (BTS; Perley et al. 2020) and the Sloan Digital Sky Survey II Supernova Survey (SDSS-II SNS; Taylor et al. 2014) measured an overall core-collapse SN rate. BTS measured a CCSN rate of $(10.1^{+5.3}_{-3.5}) \times 10^4$ Gpc^{-3} yr^{-1}, and SDSS-II SNS measured a CCSN rate of $(10.6^{+1.9}_{-1.9}) \times 10^4$ Gpc^{-3} yr^{-1}. If we assume Type II SNe constitute 57% of all CCSNe and Type IIP SNe are 70% of all Type II SNe (Li et al. 2011), the Type IIP SN rates in BTS and SDSS-II would be $(4.0^{+2.1}_{-1.4}) \times 10^4$ Gpc^{-3} yr^{-1} and $(4.2^{+0.8}_{-0.8}) \times 10^4$ Gpc^{-3} yr^{-1} respectively, which is consistent with the ZTF CLU volumetric rate.

Can LLIIP SNe account for the fate of all $8 - 12$ M$_\odot$stars?

The fraction of massive stars that explode in this mass range is given by:

$$\frac{\int_{M_{\rm min}}^{12} \psi(M)\, dM}{\int_{M_{\rm min}}^{M_{\rm max}} \psi(M)\, dM},$$

where $M_{\rm min}$ is the minimum progenitor mass that explodes, $M_{\rm max}$ is the maximum progenitor mass of stars that explode, and $\psi(M) \propto M^{-2.35}$ for the Salpeter IMF. If we assume $M_{\rm max} = 40\ M_\odot$ and $M_{\rm min} = 8\ M_\odot$, $8 - 12$ M$_\odot$ progenitors should account for 48% of all massive stars that collapse. If we assume $M_{\rm max} = 100\ M_\odot$ and $M_{\rm min} = 8\ M_\odot$, $8 - 12\ M_\odot$ progenitors account for 44% of all massive stars that explode. However, even though LLIIP SNe are the main observational candidates for low-mass CCSNe, we find that LLIIP SNe constitutes only 19^{+3}_{-4}% of all Type IIP SNe. If we assume that 40% of all CCSNe are Type IIP SNe (Li et al. 2011), LLIIP SNe are only 8^{+1}_{-2}% of all CCSNe. The mean local star-formation rate density within ∼150 Mpc is $(17^{+7}_{-5}) \times 10^6$ M$_\odot$ Gpc^{-3} yr^{-1} (Horiuchi et al. 2011). This is also in good agreement with the local cosmic star-formation rate (SFR) of $(18.5 \pm 1.20) \times 10^6$ M$_\odot$ Gpc^{-3} yr^{-1} (Hopkins and Beacom 2006). Assuming a SFR to SN rate conversion factor of 0.0088 (Horiuchi et al. 2011), the local SN rate would be $\approx 14 \times 10^4$ yr^{-1} Gpc^{-3}. Assuming a Salpeter IMF, the expected SN rate for $8 - 12$ M$_\odot$ is $\approx 6.7 \times 10^4$ yr^{-1} Gpc^{-3}, which is more than a factor of $9.2^{+0.8}_{-0.7}$ higher than the ZTF CLU LLIIP SN rate. How can this inconsistency be accounted for?

Observational bias: A possible dominant effect is that many SNe are missed because they are too faint for current optical surveys. We can rule out that faint IIP SN (> -14.5 mag) account for the missing SNe population as they account for < 1.5%

of the entire Type IIP SNe population. However, we note that ZTF CLU is sensitive to only 25 Mpc for potential SNe fainter than −12 mag and up to 40 Mpc for potential SNe fainter than −13 mag. If Type IIP SNe alone were the fate of all progenitors in this mass range, we require that all Type IIP SN fainter than ~ -18 mag originate from this progenitor mass range. The ZAMS mass for the entire sample will be estimated in Papers II and III. The other scenario is that current optical transient surveys like CLU might be missing a significant fraction of low-mass explosions due to extinction (e.g., see Jencson et al. 2019b, Fox et al. 2021). Mattila et al. (2012) estimate that locally $18.9^{+19.2}_{-9.5}$% of the CCSNe are missed by optical surveys. Jencson et al. (2019b) predict an even higher fraction, that $38.5^{+26.0}_{-21.9}$% of the CCSNe are missed by optical surveys. Jencson et al. (2019b) speculate that the objects SPIRITS16ix and SPIRITS16tn may represent a class of low-energy CCSNe arising preferentially in particularly extinguished environments. SPIRITS16tn is consistent with a LLIIP SN, heavily obscured by $A_V = 7 - 9$ mag. Another source of observational bias against LLIIP SNe could be the CLU galaxy catalog, if LLIIP SNe preferentially occurs in small galaxies.

Explode as other classes of transients: We know that the majority (∼70%) of young massive stars live in interacting binary systems and the outer envelopes of ∼33% of massive stars are stripped (e.g., see Sana et al. 2012). Thus, it is possible that a significant fraction of $8 - 12$ $M_\odot$ stars explode as stripped-envelope SNe in binary star systems. These stars with low-mass iron cores produce a low amount of Ni and ejecta mass (Stockinger et al. 2020, Sandoval et al. 2021, Burrows et al. 2024, Moriya et al. 2017, Sawada et al. 2022). Candidates for low nickel mass stripped-envelope SNe include double-peaked Type Ibc SNe such as SN 2021inl (Jacobson-Galán et al. 2022b, Das et al. 2024c), rapidly evolving Type IIb SNe with a half-life of less than 10 days (e.g., Ho et al. 2023, Das et al. 2023a, Fremling et al., in prep), ultra-stripped SNe such as SN 2023zaw (Das et al. 2024b, Moore et al. 2024). Moore et al. (2024) measured a volumetric rate of rapidly-evolving SESNe of $\approx (2.5^{+2.5}_{-1.4} \pm 0.9) \times 10^3$ Gpc^{-3} yr^{-1}, which is only $\approx$ 5% of the Type IIP SN rate. A systematic study of the lowest-nickel mass stripped-envelope SNe in CLU, including their rates and the nickel mass distribution will be explored in a future work. Also, $\sim 7 - 9$ $M_\odot$ sAGB stars are predicted to undergo electron-capture SNe (Nomoto 1984), which could be the origin of the class of Intermediate Luminosity Red Transients (ILRTs) (e.g., AT 2019abn, NGC 300 2008OT-1, SN 2008S; Botticella et al. 2009, Adams et al. 2016, Jencson et al. 2019a, Rose et al. 2024, Valerin et al. 2025). Observations indicate that ILRTs comprise $1 - 10$% of

the overall CCSNe rate (Thompson et al. 2009, Cai et al. 2021, Karambelkar et al. 2023).

Stellar evolution and explosion models: The third explanation could be our limited theoretical understanding regarding the evolution and fate of $8-12$ $M_\odot$ progenitors. Stars in this mass range have a qualitatively different core structure than at >12 $M_\odot$, with significantly lower compactness (Sukhbold et al. 2016). Their evolution is significantly more complex to model due to degeneracy effects. They develop thermal pulses that are numerically challenging to follow. Due to the steeply falling nature of the IMF, the lower mass limit $M_{\rm min}$ strongly affects the fraction of massive stars that explode. For example, if $M_{\rm min} = 9.7$ $M_\odot$, then the fraction of massive stars < 12 $M_\odot$ is $\sim 25\%$. To match the observed rate of LLIIP SNe, we require a minimum progenitor mass of $M_{\rm min} = 11.3^{+0.6}_{-0.7}\,M_\odot$. The low rate of LLIIP SNe can be reasonably explained if a fraction of potential progenitors within this mass range either fail to undergo Fe-core collapse or do not successfully explode. This outcome is plausible if their cores fail to achieve the necessary physical conditions for core collapse. Another possibility in binary stellar evolution is stellar mergers. Sana et al. (2012) predict that more than half of the progenitors of Type II SNe are merged stars or binary mass gainers. Thus, if single stars in the $8-12$ $M_\odot$ merge, then we might instead observe the SN explosions of these progenitors that have a higher mass and undergo more luminous explosions (Zapartas et al. 2019, 2021).

It is likely that one or more of the above factors play a role in explaining the fate of all the lowest-mass stars that undergo core collapse.

4.8 Summary

In summary, we present the largest sample of 330 Type IIP SNe to derive the luminosity function to-date from a spectroscopic complete volume-limited SN survey. The sample is particularly critical to understand the low-luminosity population of CCSNe, with the sample of 36 LLIIP SNe ($M_{\rm r,peak} \geq -16$ mag) tripling the sample of LLIIP SNe in the literature. The key takeaways from the analysis are:

1. The luminosity function peaks at -17 mag and does not show a significant population > -14.5 mag, accounting for < 1.5 % of all Type IIP SNe. The fraction of LLIIP SNe is $19^{+3}_{-4}\%$ of the Type IIP SNe population and $8^{+1}_{-2}\%$ of the CCSN population (see Figure 4.6).

2. We model the efficiency of the ZTF subtraction pipeline as a function of the

alert flux and the ratio of background surface brightness to target flux. As expected, the recovery efficiency decreases as this ratio increases. The best-fit efficiency is $\sim$ 50% when the host surface brightness and target fluxes are comparable. Similarly, the best-fit efficiency decreases with an increase in target alert apparent magnitude and is $\approx$ 80% when the target magnitude is 20 mag (see Figure 4.5).

3. We derive a volumetric rate of $(3.9^{+0.4}_{-0.4}) \times 10^4$ Gpc^{-3} yr^{-1} for Type IIP SNe and $(7.3^{+0.6}_{-0.6}) \times 10^3$ Gpc^{-3} yr^{-1} for LLIIP SNe (see Figures 4.8, 4.9).

4. The expected SN rate for $8 - 12$ M$_\odot$ is $\approx 6.7 \times 10^4$ yr^{-1} Gpc^{-3}, which is more than a factor of $9.2^{+0.8}_{-0.7}$ higher than the ZTF CLU LLIIP SNe rate. While LLIIP SNe represent the explosions of the lowest massive stars that explode, they cannot account for all $8 - 12$ M$_\odot$ progenitors.

The robust LLIIP rate measured in this work shows a significant discrepancy between the calculated and predicted volumetric rates of SNe in the low mass-end ($8 - 12$ M$_\odot$) of core-collapse SNe. Future deep surveys such as the Legacy Survey of Space and Time (LSST; Ivezić et al. 2008) in synergy with high-cadenced surveys of ZTF could reveal a hidden population of ≥ -13 mag CCSNe. To enhance the efficiency of spectroscopic completeness for faint SNe, we will conduct the ZTF Complete Astronomical Transient Survey within 150 Mpc (CATS150; Das et al. 2025c). CATS150 will utilize the high efficiency of the Next Generation Palomar Spectrograph (NGPS) on the Palomar 200-inch Hale Telescope to achieve spectroscopic completeness exceeding 95% for even the faintest SNe. Also, SN survey in the local universe carried out at longer wavelengths by ground-based surveys such as the Wide-field Infrared Transient Explorer (WINTER; Lourie et al. 2020), Dynamic REd All-sky Monitoring Survey (DREAMS; Soon et al. 2020), Prime-focus Infrared Microlensing Experiment (PRIME; Kondo et al. 2023), Cryoscope and space-based telescopes such as the `Nancy Grace Roman Space Telescope` will be critical in constraining the missing SN population due to dust obscuration.

4.9 Data Availability

All the photometric and spectroscopic data of the SNe in the sample will be made available on WISEREP and Zenodo after publication. The meta-data of the sample, extinction template, and pipeline recovery efficiency are available as a machine-readable tables in DOI:10.5281/zenodo.14538857.

4.10 Acknowldegement

We thank the anonymous referee for their constructive feedback, which helped improve the quality of this manuscript.

Based on observations obtained with the Samuel Oschin Telescope 48-inch and the 60-inch Telescope at the Palomar Observatory as part of the Zwicky Transient Facility project. ZTF is supported by the National Science Foundation under Grants No. AST-1440341 and AST-2034437 and a collaboration including current partners Caltech, IPAC, the Oskar Klein Center at Stockholm University, the University of Maryland, University of California, Berkeley , the University of Wisconsin at Milwaukee, University of Warwick, Ruhr University Bochum, Cornell University, Northwestern University and Drexel University. Operations are conducted by COO, IPAC, and UW.

Zwicky Transient Facility access for N.R., A.A.M., S.S., and C.L. was supported by Northwestern University and the Center for Interdisciplinary Exploration and Research in Astrophysics (CIERA). N.R., C.L., and A.A.M. are supported by DoE award #DE-SC0025599.

S. Schulze is partially supported by LBNL Subcontract 7707915.

SED Machine is based upon work supported by the National Science Foundation under Grant No. 1106171.

The ZTF forced-photometry service was funded under the Heising-Simons Foundation grant #12540303 (PI: Graham).

The Gordon and Betty Moore Foundation, through both the Data-Driven Investigator Program and a dedicated grant, provided critical funding for SkyPortal .

This research has made use of the NASA/IPAC Extragalactic Database (NED), which is funded by the National Aeronautics and Space Administration and operated by the California Institute of Technology.

The Liverpool Telescope is operated on the island of La Palma by Liverpool John Moores University in the Spanish Observatorio del Roque de los Muchachos of the Instituto de Astrofisica de Canarias with financial support from the UK Science and Technology Facilities Council.

The W. M. Keck Observatory is operated as a scientific partnership among the California Institute of Technology, the University of California and the National Aeronautics and Space Administration. The Observatory was made possible by the

generous financial support of the W. M. Keck Foundation. The authors wish to recognize and acknowledge the very significant cultural role and reverence that the summit of Maunakea has always had within the indigenous Hawaiian community. We are most fortunate to have the opportunity to conduct observations from this mountain.

4.11 Appendix: Progenitor Mass from pre-explosion images Vs SN peak magnitude

Here, we show the distribution of the Zero-Age Main-Sequence (ZAMS) mass estimated for Type II SNe from pre-explosion images. We can see that all LLIIP SNe have progenitor mass estimates of less than < 11 $M_{\odot}$while SNe brighter than -16 mag have more massive progenitors. The SNe shown here are: SN 2003gd (Maund and Smartt 2009, Smartt 2015), SN 2005cs (Maund et al. 2014, Smartt 2015), SN 2009md (Fraser et al. 2011, Smartt 2015), SN 2006my (Maund et al. 2014, Smartt 2015), SN 2012A (Tomasella et al. 2013b, Smartt 2015), SN 2013ej (Fraser et al. 2014, Smartt 2015), SN 2004et (Crockett et al. 2011, Smartt 2015), SN 2008bk (Maund et al. 2014, Smartt 2015), SN 2004A (Maund et al. 2014, Smartt 2015), SN 2012aw(Kochanek et al. 2012, Smartt 2015), SN 2009hd (Elias-Rosa et al. 2011, Smartt 2015), SN 2009kr (Fraser et al. 2010, Smartt 2015), SN 2012ec (Maund et al. 2013, Smartt 2015), SN 2018aoq (O'Neill et al. 2019), SN 2022acko (Van Dyk et al. 2023a). A positive correlation between progenitor luminosity and $V-$band magnitude at 50 days since explosion is also reported in Rodríguez (2022).

4.12 Appendix: Distance correction for nearby galaxies

Table A lists the distance measurements used for galaxies closer than 25 Mpc. We correct for the Virgo, Great Attractor, and Shapley supercluster infall based on the NASA Extragalactic Database object page (NED[5]; Helou et al. 1991).

4.13 Appendix: ZTF Pipeline Recovery Efficiency Fits

The corner plot for the MCMC fit to

$$p(m) = \frac{1}{1 + \exp(a(m - c))},$$

where m is the alert apparent magnitude is shown in Figure 10.10. The best-fit values are $a = 2.28^{+0.03}_{-0.04}$ and $c = 20.57^{+0.01}_{-0.01}$.

[5]https://ned.ipac.caltech.edu/

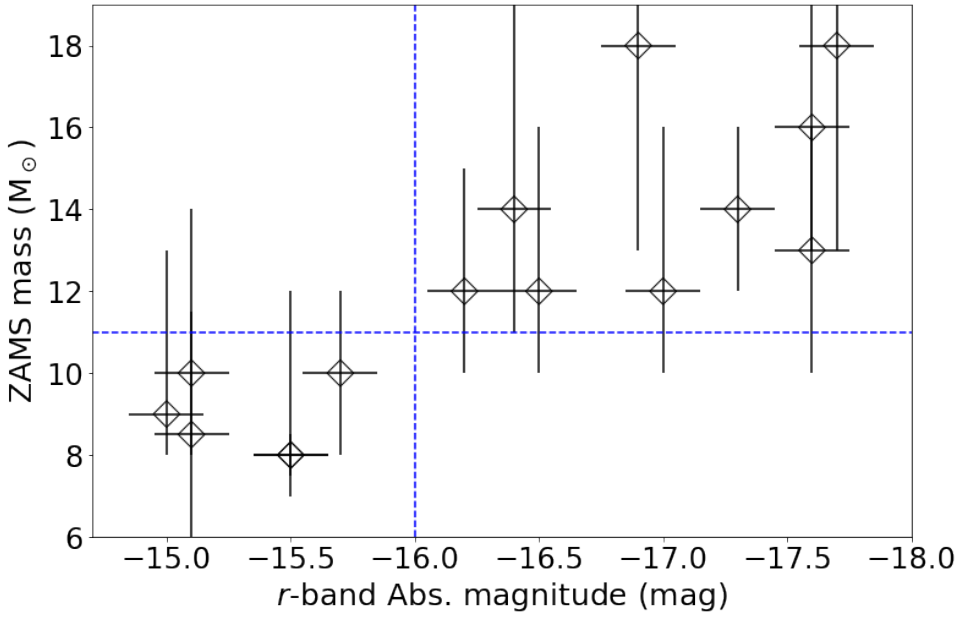

Figure 4.12: The distribution of the Zero-Age Main-Sequence (ZAMS) mass estimated for Type II SNe from pre-explosion images as a function of the peak r-band magnitude.

Table A: Distance measurements used for galaxies < 25 Mpc.

Name	Distance (Mpc)
SN 2021gmj/ZTF21aaqgmjt[a]	13.10
SN 2022acko/ZTF22abyivoq[b]	23.40
SN 2023axu/ZTF23aabngtm[c]	13.68
SN 2023hlf/ZTF23aaitpjv[d]	9.54
SN 2022aagp/ZTF22abtspsw[d]	25.15
SN 2023ijd/ZTF23aajrmfh[d]	14.94
SN 2022jzc/ZTF22aakdbia[d]	19.64

[a]Valerin et al. (2022); [b]Van Dyk et al. (2023a); [c]Shrestha et al. (2024); [d]Helou et al. (1991).

The corner plot for the MCMC fit to

$$p(r) = \frac{1}{1 + \exp(a(r - c))},$$

where r is the ratio of the alert apparent magnitude to the local surface brightness is shown in Figure 10.10. The best-fit values are $a = 1.12^{+0.02}_{-0.02}$ and $c = 0.21^{+0.03}_{-0.03}$.

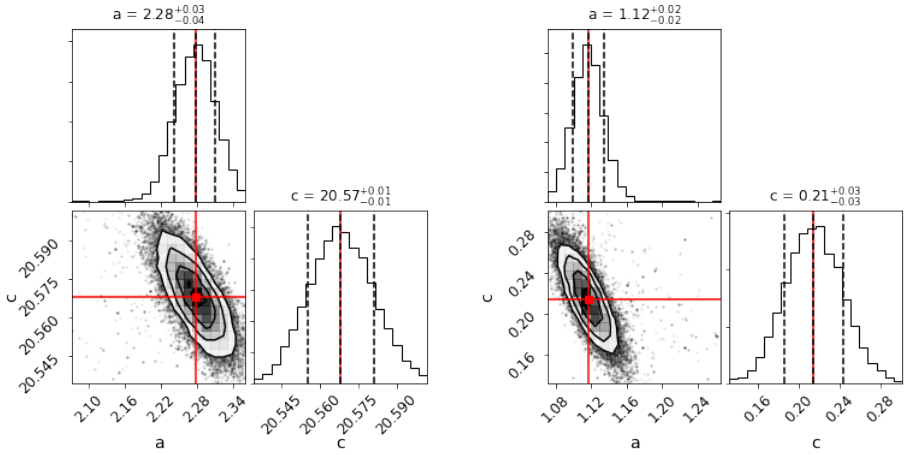

Figure 4.13: Corner plots for the logistic function fit to the pipeline efficiency as a function of apparent magnitude (*left*) and the ratio of the alert apparent magnitude to the local surface brightness (*right*).

4.14 Appendix: Sample of CLU Type II SNe

The full version of the sample summary table is shown in Table B.

Table B: Summary table of the CLU Type II SN sample. The peak absolute magnitudes have been measured by assuming Milky Way extinction ($A_{V,MW}$) and host galaxy extinction ($A_{V,host}$) as described in Section 10.3. The t_{expl} column shows the explosion epoch. The Peak mag_r shows the peak r-band absolute magnitude. A machine-readable version of the full sample table is available in DOI:10.5281/zenodo.14538857.

Name	RA	Dec	Redshift	t_{expl}	1st detection	Peak mag_r	$A_{V,MW}$	$A_{V,host}$
	(hh:mm:ss)	(dd:mm:ss)		(MJD)	(MJD)	(mag)	(mag)	(mag)
ZTF18aaegvyd/SN2019env	09:09:35.63	+29:58:14.4	0.024	58606.7	58608.2	-17.03	0.07	0.00
ZTF18aaqkywr/SN2022giv	12:23:14.92	+51:11:28.3	0.031	59655.9	59670.4	-16.77	0.05	0.00
ZTF18aaqpowv/SN2024iwm	11:28:17.83	+26:58:26.37	0.032	60443.2	60444.2	-17.42	0.05	0.00
ZTF18aaszvfn/SN2021iaw	14:23:07.88	+50:13:14.9	0.027	59306.4	59307.3	-16.77	0.06	0.00
ZTF18aawgrxz/SN2021lmp	15:04:17.64	+48:55:10.7	0.027	59338.9	59339.3	-16.85	0.04	0.42
ZTF18aaxzlmy/SN2018lrq	13:34:51.37	+34:03:20.5	0.025	58218.8	58219.3	-16.62	0.03	0.99
ZTF18abbpxik/SN2018cqp	15:22:50.32	+08:04:49.1	0.032	58282.7	58283.2	-18.08	0.10	0.71
ZTF18abbpyvk/SN2018cqi	13:57:40.91	+17:30:29.1	0.022	58284.7	58286.2	-18.29	0.09	0.07
ZTF18abcpmwh/SN2018cur	12:59:09.12	+37:19:00.1	0.015	58289.7	58291.2	-17.56	0.04	0.00
ZTF18abdbysy/SN2018cyg	15:34:08.48	+56:41:48.6	0.011	58294.8	58295.2	-17.08	0.05	2.05
ZTF18abdfwcy/SN2018cwa	12:42:43.85	+34:06:26.3	0.014	58290.8	58295.2	-17.27	0.05	0.00
ZTF18abdjmfh/SN2018dct	16:15:08.80	+26:33:36.2	0.030	58298.8	58300.3	-18.72	0.12	1.27

Table B: Continued.

Name	RA	Dec	Redshift	$t_{\rm expl}$	1st detection	Peak mag$_r$	$A_{V,\rm MW}$	$A_{V,\rm host}$
	(hh:mm:ss)	(dd:mm:ss)		(MJD)	(MJD)	(mag)	(mag)	(mag)
ZTF18abjkryl/SN2018dzc	18:23:09.26	+21:14:56.4	0.010	58308.4	58308.4	-16.30	0.48	0.49
ZTF18abjndhh/SN2018ecj	11:32:43.02	+62:25:57.9	0.013	58322.2	58324.2	-17.03	0.03	1.34
ZTF18abjovdz/SN2018dht	20:55:19.05	+00:32:18.6	0.024	58309.9	58312.4	-18.36	0.23	1.48
ZTF18abklbam/SN2018elp	14:31:19.10	+21:17:24.7	0.031	58329.2	58331.2	-18.00	0.13	0.00
ZTF18abmdpwe/SN2018evy	18:22:38.17	+15:41:47.6	0.018	58339.2	58340.2	-18.06	0.54	0.00
ZTF18abnxfve/SN2018lrz	22:29:52.72	+36:43:50.1	0.025	58347.8	58349.3	-15.94	0.30	0.00
ZTF18abokyfk/SN2018fif	00:09:26.55	+47:21:14.7	0.017	58350.8	58351.4	-17.12	0.30	0.00
ZTF18abrpkdw/SN2018lsa	21:45:07.20	+15:35:09.0	0.031	58355.8	58357.2	-16.49	0.29	0.00
ZTF18abrzbtb/SN2018ggu	07:43:04.67	+50:17:22.2	0.019	59120.0	59120.5	-15.66	0.19	0.00
ZTF18abvmlow/SN2018lcd	01:51:10.65	-03:29:24.9	0.017	58479.2	58483.2	-18.02	0.08	0.00
ZTF18abvvmdf/SN2018gts	16:36:47.39	+55:44:08.8	0.030	58373.2	58374.2	-18.02	0.05	0.92
ZTF18abwisaz/SN2024kan	22:49:07.02	+32:47:53.12	0.028	60454.5	60456.4	-17.45	0.36	0.00
ZTF18abxbmcl/SN2018hcp	08:22:57.66	+27:42:10.5	0.020	58377.0	58378.5	-19.19	0.10	2.05
ZTF18abzrgim/SN2018gvt	23:07:32.54	+23:00:20.9	0.021	58386.8	58388.3	-17.49	0.63	0.00
ZTF18acbvhit/SN2018hle	03:39:28.11	-13:07:02.4	0.014	58418.7	58422.4	-16.80	0.15	0.21
ZTF18aceqrcy/SN2018joy	10:19:40.32	+12:50:37.7	0.032	58428.0	58429.5	-17.77	0.18	0.99
ZTF18acrflch/SN2018jgy	03:06:59.88	-06:45:14.0	0.029	58445.8	58448.3	-17.38	0.23	0.00
ZTF18acrkaks/SN2018jwq	05:17:54.17	+08:54:51.3	0.030	58438.4	58439.4	-16.51	0.93	0.00

Table B: Continued.

Name	RA	Dec	Redshift	$t_{\rm expl}$	1st detection	Peak mag$_r$	$A_{V,\rm MW}$	$A_{V,\rm host}$
	(hh:mm:ss)	(dd:mm:ss)		(MJD)	(MJD)	(mag)	(mag)	(mag)
ZTF18acrtvmm/SN2018jfp	03:17:56.27	-00:10:10.7	0.023	58448.8	58450.3	-17.55	0.20	0.00
ZTF18acsxkov/SN2018kds	00:10:09.06	-04:42:33.2	0.030	58449.7	58456.2	-16.68	0.09	0.00
ZTF18acurdnh/SN2018jvr	10:07:20.35	+04:04:49.2	0.029	58458.5	58461.5	-16.38	0.05	0.00
ZTF18acurqaw/SN2018hwm	08:21:28.20	+03:09:52.3	0.009	58432.5	58441.4	-17.05	0.07	3.39
ZTF18acyybvg/SN2018kkv	11:34:33.85	+22:31:09.2	0.032	58470.5	58471.5	-16.69	0.06	0.00
ZTF18adachwf/SN2018lev	15:13:08.16	+41:15:49.2	0.029	58472.2	58475.5	-16.94	0.06	0.14
ZTF18adazblo/SN2018ldu	09:09:32.49	+20:24:25.1	0.027	58476.4	58480.4	-16.67	0.11	0.00
ZTF18adbclkd/SN2018kpo	03:40:43.06	-06:25:23.9	0.017	58478.3	58481.3	-17.28	0.15	0.00
ZTF19aaabzpt/SN2018lab	06:16:26.51	-21:22:32.4	0.009	58479.3	58487.3	-15.81	0.24	0.71
ZTF19aadnxnl/SN2019va	13:35:14.68	+44:45:58.6	0.009	58498.5	58502.5	-16.87	0.05	0.00
ZTF19aadnxog/SN2019vb	13:14:23.07	+30:29:06.6	0.020	58498.5	58503.5	-18.04	0.04	0.00
ZTF19aailepg/SN2019amt	11:17:52.25	+30:09:23.5	0.030	58518.4	58522.4	-17.11	0.05	0.00
ZTF19aajwkbb/SN2019bsw	10:05:06.10	-16:24:21.3	0.027	58502.5	58511.4	-16.75	0.14	0.00
ZTF19aaklqoi/SN2021adnr	08:57:54.94	+20:07:12.6	0.031	59514.0	59518.5	-17.27	0.08	1.20
ZTF19aakpxfm/SN2019aor	07:24:57.85	-27:31:53.7	0.025	58476.4	58476.4	-17.94	0.83	0.00
ZTF19aalycsv/SN2019txj	10:48:39.19	+76:48:05.3	0.023	58543.3	58546.2	-15.27	0.07	0.00
ZTF19aamftfu/SN2019cag	02:23:21.52	+53:23:41.3	0.025	58551.6	58556.1	-17.30	0.53	0.00
ZTF19aamwhat/SN2019bzd	14:47:32.03	-19:45:57.7	0.008	58559.7	58568.4	-15.83	0.24	0.07

Table B: Continued.

Name	RA	Dec	Redshift	$t_{\rm expl}$	1st detection	Peak mag$_r$	$A_{V,\rm MW}$	$A_{V,\rm host}$
	(hh:mm:ss)	(dd:mm:ss)		(MJD)	(MJD)	(mag)	(mag)	(mag)
ZTF19aanfnvl/SN2019crk	10:10:31.69	+10:02:37.0	0.032	58561.7	58567.2	-17.77	0.12	0.00
ZTF19aanhhal/SN2019cec	13:41:40.74	+55:40:10.7	0.026	58561.9	58562.3	-17.23	0.03	0.00
ZTF19aaniore/SN2019ceg	16:27:51.64	+62:41:32.5	0.030	58564.5	58567.5	-17.31	0.09	0.00
ZTF19aanqzle/SN2019cmm	11:18:07.29	+75:08:50.8	0.023	58570.2	58572.2	-16.03	0.16	0.00
ZTF19aanrrqu/SN2019clp	12:13:39.83	+16:07:24.4	0.024	58569.8	58572.3	-18.02	0.10	0.00
ZTF19aapafit/SN2019cvz	16:30:54.08	+46:35:18.4	0.019	58576.5	58577.4	-17.05	0.04	0.00
ZTF19aaqxosb/SN2019dok	13:46:51.76	+16:16:53.7	0.019	58588.3	58589.2	-16.64	0.07	0.00
ZTF19aarjfqe/SN2019dvd	12:31:06.89	+00:27:54.6	0.021	58592.8	58596.3	-16.93	0.06	0.00
ZTF19aarykkb/SN2019dzk	17:13:21.95	-09:57:52.1	0.024	58595.4	58598.3	-18.17	1.54	0.00
ZTF19aatmadu/SN2019esn	14:51:56.11	+51:15:51.2	0.027	58602.4	58605.4	-16.00	0.06	0.00
ZTF19aauishy/SN2019evl	13:31:01.26	+34:09:12.5	0.023	58609.3	58612.2	-16.45	0.03	0.00
ZTF19aavrcew/SN2019fyw	13:07:18.44	+02:00:11.5	0.019	58625.2	58633.2	-17.78	0.08	0.00
ZTF19aavtcjs/SN2019gss	15:24:44.44	+68:43:44.3	0.022	58630.3	58633.3	-17.89	0.07	2.19
ZTF19aawgxdn/SN2019gmh	16:31:03.16	+41:09:14.2	0.031	58634.3	58635.2	-17.39	0.03	0.00
ZTF19aaykqsk/SN2019hci	11:16:03.35	-00:31:55.9	0.026	58641.7	58643.2	-17.02	0.17	0.00
ZTF19aayrosj/SN2019hrb	20:54:12.08	+10:33:01.1	0.015	58642.5	58644.5	-17.64	0.26	1.70
ZTF19aazudta/SN2019hqm	17:36:56.18	+21:06:17.1	0.024	58648.8	58650.3	-16.98	0.23	0.00
ZTF19aazyvub/SN2019hnl	23:43:10.25	-02:56:58.6	0.023	58649.5	58651.5	-17.13	0.09	0.00

Table B: Continued.

Name	RA	Dec	Redshift	$t_{\rm expl}$	1st detection	Peak mag$_r$	$A_{V,\rm MW}$	$A_{V,\rm host}$
	(hh:mm:ss)	(dd:mm:ss)		(MJD)	(MJD)	(mag)	(mag)	(mag)
ZTF19abaamsd/SN2019ifm	17:23:41.33	+52:00:36.1	0.024	58652.8	58653.3	-17.33	0.09	0.00
ZTF19abajxet/SN2019hyk	14:17:57.85	+26:25:17.6	0.015	58655.7	58657.2	-17.77	0.06	0.00
ZTF19abalqkq/SN2019khq	17:50:41.76	+14:49:26.3	0.014	58645.9	58650.3	-15.76	0.26	1.63
ZTF19abbnamr/SN2019iex	23:51:03.63	+20:08:43.7	0.014	58659.0	58660.5	-17.40	0.20	0.00
ZTF19abbwfgp/SN2019ikb	17:13:17.71	+43:47:03.5	0.026	58660.8	58661.3	-18.16	0.05	0.00
ZTF19abctzkc/SN2019tti	00:18:59.83	+08:46:28.2	0.019	58644.4	58646.4	-15.67	0.55	0.21
ZTF19abejaiy/SN2019krp	14:07:33.70	+14:38:03.3	0.017	58670.2	58671.2	-15.45	0.04	0.00
ZTF19abjrjdw/SN2019mkr	17:11:05.78	+05:51:07.3	0.022	58687.7	58689.2	-17.56	0.43	0.00
ZTF19abjsmmv/SN2019mor	15:38:38.04	+36:57:31.0	0.019	58693.3	58694.2	-17.13	0.06	0.00
ZTF19ablfoqa/SN2019tya	02:09:38.03	+01:33:06.7	0.032	58694.0	58694.5	-15.93	0.08	0.00
ZTF19abllxfy/SN2019ttl	21:52:43.47	+38:56:00.8	0.020	58682.9	58690.3	-15.36	0.88	0.00
ZTF19abpyqog/SN2019oba	19:57:03.47	+50:11:20.1	0.031	58708.3	58711.2	-17.22	0.40	0.00
ZTF19abqhobb/SN2019nvm	17:25:38.66	+59:26:48.2	0.018	58713.7	58714.2	-17.59	0.08	0.00
ZTF19abqrhvt/SN2019nyk	00:15:15.20	-08:11:21.8	0.021	58713.4	58715.4	-18.09	0.10	0.00
ZTF19abqrhvy/SN2019odf	22:48:44.69	+27:34:18.5	0.032	58714.9	58715.4	-18.18	0.14	0.00
ZTF19abrnjwi/SN2019omb	00:12:39.66	+05:30:32.0	0.028	58717.9	58719.4	-17.20	0.07	0.00
ZTF19abwztsb/SN2019pjs	18:04:40.34	+21:38:04.2	0.007	58731.7	58734.2	-16.23	0.29	0.00
ZTF19abzmoov/SN2019qba	15:37:44.70	+22:25:36.4	0.025	58735.6	58737.1	-16.68	0.12	0.00

Table B: Continued.

Name	RA	Dec	Redshift	$t_{\rm expl}$	1st detection	Peak mag$_r$	$A_{V,\rm MW}$	$A_{V,\rm host}$
	(hh:mm:ss)	(dd:mm:ss)		(MJD)	(MJD)	(mag)	(mag)	(mag)
ZTF19acalxgp/SN2019qiq	23:44:56.09	-04:16:33.1	0.029	58735.4	58737.3	-15.86	0.12	0.00
ZTF19acblhxc/SN2019rho	02:12:49.18	-06:42:05.9	0.017	58753.4	58756.4	-17.21	0.07	0.21
ZTF19acbpqlh/SN2019rpn	21:19:41.19	+37:31:19.3	0.026	58709.8	58711.2	-16.28	0.46	0.00
ZTF19acbwejj/SN2019upq	14:29:08.13	+27:27:00.6	0.014	58754.1	58758.1	-17.80	0.05	0.00
ZTF19acewuwn/SN2019ssl	23:20:17.26	+35:29:35.3	0.027	58771.7	58772.2	-16.96	0.27	0.00
ZTF19acftfav/SN2019ssi	23:30:56.12	+15:29:29.8	0.013	58773.7	58774.2	-16.51	0.19	0.00
ZTF19acgbkzr/SN2019szo	00:19:56.64	+15:05:36.1	0.026	58774.8	58775.3	-16.73	0.13	0.00
ZTF19acgzwbm/SN2019tba	04:55:09.84	-16:09:01.3	0.020	58770.5	58776.5	-16.34	0.18	0.00
ZTF19aclobbu/SN2019twk	02:23:05.28	+46:52:56.7	0.018	58787.3	58788.3	-17.63	0.49	0.00
ZTF19acnphay/SN2019ubr	06:25:52.32	+64:44:38.4	0.014	58769.5	58772.5	-16.57	0.32	2.40
ZTF19acrcxri/SN2019ult	23:58:47.97	+14:44:31.3	0.027	58795.1	58797.1	-18.42	0.11	0.00
ZTF19acryurj/SN2019ust	00:54:22.41	+31:40:12.6	0.022	58798.2	58800.3	-18.10	0.17	0.00
ZTF19actnwtn/SN2019vdl	09:29:31.80	+44:25:20.0	0.025	58803.5	58804.5	-17.35	0.06	0.57
ZTF19actnyae/SN2019vdm	11:26:24.51	+22:37:11.0	0.032	58804.0	58805.5	-16.88	0.04	0.00
ZTF19acvtrxj/SN2019vjl	09:49:23.69	+01:08:46.6	0.025	58808.5	58812.6	-17.58	0.23	0.07
ZTF19acwrrvg/SN2019vsr	02:01:57.73	+44:48:32.1	0.027	58816.7	58819.2	-18.66	0.21	0.00
ZTF19acxgwvo/SN2019wbd	23:20:35.17	-00:52:51.0	0.015	58815.7	58820.2	-17.20	0.10	0.35
ZTF19acyjjni/SN2019xbm	13:07:13.99	+58:08:03.3	0.028	58823.0	58831.6	-16.94	0.04	0.42

Table B: Continued.

Name	RA	Dec	Redshift	$t_{\rm expl}$	1st detection	Peak mag$_r$	$A_{V,\rm MW}$	$A_{V,\rm host}$
	(hh:mm:ss)	(dd:mm:ss)		(MJD)	(MJD)	(mag)	(mag)	(mag)
ZTF19acykzsk/SN2019wqj	02:11:37.09	+34:02:28.7	0.021	58823.2	58827.2	-16.31	0.27	0.07
ZTF19acytcsg/SN2019wvz	10:20:28.67	+50:28:04.5	0.032	58832.5	58833.4	-17.60	0.03	0.00
ZTF19adakmbh/SN2019xgi	21:55:25.49	+34:30:37.8	0.018	58834.1	58837.1	-17.90	0.46	1.63
ZTF20aarenrz/SN2021qyy	11:44:29.64	+69:43:45.4	0.009	59388.8	59390.2	-16.55	0.03	0.00
ZTF21aaabwem/SN2020aeqx	13:13:00.02	+06:10:12.1	0.032	59211.0	59215.5	-16.79	0.10	0.00
ZTF21aaagypx/SN2021V	11:13:07.92	+05:04:19.3	0.027	59213.4	59216.4	-17.43	0.20	0.00
ZTF21aabfwwl/SN2021iy	11:18:31.68	-06:16:40.5	0.014	59217.9	59219.4	-15.55	0.14	0.00
ZTF21aabygea/SN2021os	12:02:54.08	+05:36:53.1	0.019	59219.5	59221.4	-17.28	0.05	0.00
ZTF21aaeoqxf/SN2021aek	11:59:48.02	-21:23:13.0	0.022	59225.5	59227.5	-17.61	0.13	0.00
ZTF21aaeqwov/SN2021htp	07:43:04.75	+50:17:19.4	0.019	59119.0	59119.5	-16.39	0.19	0.00
ZTF21aafepon/SN2021ass	01:50:10.12	+27:38:42.7	0.012	59230.6	59231.1	-16.24	0.23	0.07
ZTF21aafkwtk/SN2021apg	13:41:19.24	+24:29:43.9	0.027	59229.5	59231.4	-16.98	0.03	0.00
ZTF21aagtqna/SN2021brb	18:05:15.31	+46:52:56.0	0.023	59238.5	59248.5	-16.84	0.11	0.00
ZTF21aahgspm/SN2021cah	02:48:30.72	+50:45:36.0	0.016	59250.7	59251.1	-17.43	0.98	0.00
ZTF21aaipypa/SN2021cgu	11:03:03.71	+05:05:53.4	0.025	59252.4	59253.4	-18.34	0.10	0.00
ZTF21aakvroo/SN2021cwe	15:45:31.20	+30:09:43.3	0.032	59257.0	59258.5	-17.11	0.09	0.00
ZTF21aaluqkp/SN2021dhx	11:05:10.37	-15:21:10.1	0.025	59263.3	59264.3	-16.99	0.14	0.00
ZTF21aalxurx/SN2021dqs	13:44:05.74	+43:04:18.0	0.027	59259.9	59264.4	-16.33	0.03	0.00

Table B: Continued.

Name	RA	Dec	Redshift	$t_{\rm expl}$	1st detection	Peak mag$_r$	$A_{V,\rm MW}$	$A_{V,\rm host}$
	(hh:mm:ss)	(dd:mm:ss)		(MJD)	(MJD)	(mag)	(mag)	(mag)
ZTF21aanjvng/SN2021dvk	08:07:38.41	+08:56:24.2	0.030	59269.3	59271.2	-16.65	0.07	0.00
ZTF21aantsla/SN2021ech	12:06:20.42	+37:00:47.1	0.021	59274.3	59275.2	-16.44	0.06	0.00
ZTF21aanzcuj/SN2021enz	12:07:05.23	+42:59:18.3	0.024	59275.9	59276.3	-16.69	0.04	0.00
ZTF21aaobkmg/SN2021eui	19:20:55.80	+43:07:14.6	0.015	59273.5	59276.5	-15.34	0.28	0.00
ZTF21aapkcmr/SN2021fnj	14:23:42.67	+28:20:45.7	0.030	59285.4	59290.4	-17.91	0.05	0.42
ZTF21aapliyn/SN2021foj	13:45:26.60	+47:55:05.3	0.028	59286.3	59291.3	-17.11	0.08	0.00
ZTF21aaqgmjt/SN2021gmj	10:38:47.27	+53:30:30.3	0.003	59292.3	59293.2	-15.02	0.06	0.00
ZTF21aaqjmps/SN2021gvm	13:30:01.22	+13:24:40.2	0.025	59292.8	59294.3	-18.10	0.07	0.00
ZTF21aaqldsj/SN2021hac	14:12:30.45	+34:33:00.3	0.032	59293.3	59294.3	-16.95	0.04	0.00
ZTF21aaqugxm/SN2021hdt	11:34:45.73	+42:57:55.3	0.019	59299.4	59300.3	-18.12	0.07	0.00
ZTF21aaqyifh/SN2021hqe	09:41:30.96	+10:38:22.8	0.019	59297.3	59301.2	-16.86	0.06	0.71
ZTF21aaqyuun/SN2021hkf	11:44:23.27	+08:10:41.4	0.019	59300.3	59302.3	-16.38	0.07	0.00
ZTF21aardvtn/SN2021htp	07:43:04.76	+50:17:19.6	0.019	59119.0	59119.5	-16.42	0.19	0.00
ZTF21aasksnl/SN2021mju	16:41:47.59	+19:21:53.5	0.028	59292.0	59301.4	-16.08	0.21	0.42
ZTF21aavhnpk/SN2021jsf	20:50:21.44	+01:08:29.5	0.028	59313.0	59317.4	-17.33	0.29	0.00
ZTF21aaxtzzj/SN2021kqj	11:04:58.16	+30:01:46.8	0.029	59331.8	59334.3	-17.72	0.07	1.41
ZTF21aazhegf/SN2021llp	09:29:31.17	+25:33:25.0	0.033	59339.2	59340.2	-17.75	0.09	0.00
ZTF21abbomrf/SN2020ghq	14:45:20.59	+38:44:18.5	0.015	59347.8	59349.2	-15.72	0.03	0.00

Table B: Continued.

Name	RA	Dec	Redshift	$t_{\rm expl}$	1st detection	Peak mag$_r$	$A_{V,\rm MW}$	$A_{V,\rm host}$
	(hh:mm:ss)	(dd:mm:ss)		(MJD)	(MJD)	(mag)	(mag)	(mag)
ZTF21abcacpa/SN2021mtb	20:03:44.13	+49:59:34.7	0.027	59350.9	59353.4	-16.45	0.39	0.00
ZTF21abcmzvk/SN2021nli	14:02:12.66	-18:45:16.1	0.030	59354.2	59356.2	-17.62	0.25	0.00
ZTF21abcpbqd/SN2014gz	14:15:50.78	+01:52:57.4	0.026	59359.3	59359.3	-17.72	0.13	0.49
ZTF21abfiuqf/SN2021pla	16:05:38.19	+69:35:41.2	0.024	59375.4	59376.3	-17.00	0.08	0.21
ZTF21abfjaxa/SN2021pkh	12:48:41.97	+26:25:06.7	0.023	59372.2	59373.2	-17.43	0.03	2.05
ZTF21abfjdev/SN2021pqj	11:05:35.47	+19:41:22.2	0.032	59366.2	59367.2	-16.99	0.07	0.00
ZTF21abfoytp/SN2021pnh	15:50:50.63	+22:14:16.1	0.031	59373.8	59376.3	-16.68	0.17	0.49
ZTF21abgilzj/SN2021qcr	17:10:21.60	-03:13:49.7	0.029	59289.0	59295.4	-18.12	1.14	0.00
ZTF21abglcxm/SN2021qcs	15:29:22.82	-12:14:54.4	0.011	59377.3	59378.2	-15.65	0.43	0.42
ZTF21abhhrpj/SN2021qiu	21:45:50.08	+15:11:01.3	0.029	59380.4	59381.4	-17.88	0.24	0.00
ZTF21abiblpl/SN2021qzi	20:45:13.87	-05:37:09.9	0.027	59389.4	59391.3	-17.30	0.17	0.00
ZTF21abioeyq/SN2021rhk	14:03:02.40	+08:45:56.4	0.023	59394.7	59395.2	-17.74	0.07	0.00
ZTF21abjcjmc/SN2021skn	16:24:49.00	+39:44:04.7	0.030	59398.3	59399.2	-18.02	0.03	0.00
ZTF21abjcliz/SN2021skm	16:16:56.05	+21:48:35.8	0.031	59371.8	59372.3	-18.31	0.22	1.34
ZTF21abkajar/SN2021svy	13:09:21.83	+30:55:20.5	0.017	59402.7	59403.2	-17.01	0.03	0.00
ZTF21ablvzhp/SN2021tiq	22:36:54.72	-12:33:41.9	0.024	59409.4	59411.4	-18.12	0.17	0.00
ZTF21abnlhxs/SN2021tyw	23:05:56.45	+14:21:27.8	0.013	59417.9	59419.4	-17.85	0.63	0.00
ZTF21abnudtb/SN2021txr	22:30:50.30	+36:33:48.2	0.026	59416.9	59418.4	-18.10	0.34	0.00

Table B: Continued.

Name	RA	Dec	Redshift	$t_{\rm expl}$	1st detection	Peak mag$_r$	$A_{V,\rm MW}$	$A_{V,\rm host}$
	(hh:mm:ss)	(dd:mm:ss)		(MJD)	(MJD)	(mag)	(mag)	(mag)
ZTF21abouuat/SN2021ucg	22:47:37.67	+39:52:59.4	0.017	59420.4	59422.4	-17.56	0.31	0.00
ZTF21abrluay/SN2021vfh	01:31:38.36	+31:59:23.7	0.025	59432.4	59434.4	-17.01	0.12	0.00
ZTF21abtephz/SN2021wun	15:46:31.98	+25:25:44.6	0.023	59425.7	59427.2	-16.86	0.13	0.14
ZTF21abvcxel/SN2021wvw	03:14:47.39	+40:15:47.7	0.010	59449.4	59449.4	-16.36	0.78	0.00
ZTF21abvcxid/SN2021xat	02:53:03.00	+42:51:07.0	0.032	59449.0	59451.5	-17.11	0.25	0.00
ZTF21acafqtj/SN2021yok	07:28:55.48	+20:35:09.9	0.015	59466.5	59469.5	-17.11	0.14	0.00
ZTF21accdiqz/SN2021ywg	02:58:44.41	+17:15:48.0	0.020	59469.4	59471.4	-17.49	1.08	1.56
ZTF21acceboj/SN2021yyg	05:16:21.03	-13:28:39.9	0.012	59471.0	59471.5	-16.51	0.40	0.00
ZTF21accwcrh/SN2021zco	03:39:13.31	+15:59:04.9	0.032	59472.9	59474.4	-17.50	0.66	0.00
ZTF21acdcxaf/SN2021zex	02:14:05.67	+05:10:35.5	0.031	59475.4	59476.4	-17.09	0.12	0.00
ZTF21acdezwk/SN2021zet	21:52:13.34	-23:22:37.0	0.032	59475.2	59477.2	-18.24	0.10	0.00
ZTF21acdoyqt/SN2021zgm	18:35:48.34	+22:27:45.2	0.013	59479.2	59480.1	-15.51	0.44	0.00
ZTF21acelnth/SN2021zzi	01:34:39.15	+55:25:12.4	0.025	59484.9	59485.3	-17.31	0.87	0.00
ZTF21acfajbc/SN2021aalq	09:50:40.54	+47:57:52.4	0.025	59487.0	59488.5	-18.21	0.02	0.00
ZTF21acgpjbx/SN2021aaqn	02:37:58.18	-01:49:53.2	0.028	59492.8	59494.3	-17.39	0.11	0.00
ZTF21acgqhru/SN2021aatd	00:59:04.17	-00:12:12.0	0.015	59492.8	59494.3	-16.63	0.07	0.00
ZTF21acgrrnl/SN2021aayf	06:22:08.33	+50:25:44.7	0.018	59492.9	59496.4	-16.31	0.39	0.00
ZTF21acgunkr/SN2021aaxs	08:33:35.18	+19:44:30.1	0.026	59490.5	59496.5	-17.77	0.09	0.00

Table B: Continued.

Name	RA	Dec	Redshift	$t_{\rm expl}$	1st detection	Peak mag$_r$	$A_{V,\rm MW}$	$A_{V,\rm host}$
	(hh:mm:ss)	(dd:mm:ss)		(MJD)	(MJD)	(mag)	(mag)	(mag)
ZTF21achkqhi/SN2021abpd	02:28:52.37	-05:29:14.2	0.031	59499.9	59501.4	-17.60	0.07	0.00
ZTF21achpqlr/SN2021abkm	18:22:37.63	+15:42:17.7	0.018	59496.7	59502.2	-16.84	0.54	0.00
ZTF21aciiaio/SN2021abqs	11:21:37.61	+20:09:02.1	0.013	59503.0	59504.5	-16.37	0.07	0.35
ZTF21acissla/SN2021achr	00:22:23.67	-19:47:37.0	0.025	59497.3	59503.3	-17.49	0.05	1.27
ZTF21acjglei/SN2021acma	02:30:33.57	+30:52:17.3	0.018	59514.8	59517.3	-16.61	0.25	0.07
ZTF21ackrkqq/SN2021addc	03:53:38.46	+37:15:47.3	0.019	59519.3	59521.3	-16.38	1.50	0.00
ZTF21aclmgzk/SN2021adxd	00:39:22.90	+02:48:14.5	0.018	59522.3	59524.2	-16.92	0.05	1.06
ZTF21acpqqgu/SN2021aewn	10:04:06.68	+31:11:02.7	0.021	59534.5	59536.5	-16.63	0.07	0.21
ZTF21acqxomi/SN2021afud	09:06:41.11	-10:00:29.0	0.025	59545.4	59550.4	-16.69	0.22	0.00
ZTF22aaacxkp/SN2022abq	13:22:56.82	+28:19:08.9	0.008	59599.2	59600.4	-16.55	0.05	0.00
ZTF22aaahubo/SN2022cru	08:23:26.30	-04:55:06.5	0.023	59575.4	59600.3	-15.89	0.12	0.00
ZTF22aaaowlo/SN2022ces	13:54:14.54	-01:26:34.6	0.024	59614.7	59623.5	-16.80	0.13	0.00
ZTF22aaevwec/SN2022gwg	13:50:25.69	+68:33:18.1	0.031	59675.4	59676.4	-17.67	0.05	0.28
ZTF22aafsqud/SN2022hql	13:48:06.22	+12:04:29.8	0.023	59682.8	59683.2	-17.00	0.09	0.00
ZTF22aagvgwl/SN2022hss	12:25:38.39	+07:11:33.0	0.025	59684.8	59687.4	-17.97	0.07	0.00
ZTF22aahhgjh/SN2022ihb	13:46:13.40	+23:05:10.9	0.030	59691.8	59693.2	-17.59	0.04	0.00
ZTF22aahyqkz/SN2022iob	19:10:37.07	+37:39:18.7	0.028	59684.5	59689.4	-17.62	0.48	0.92
ZTF22aaijrci/SN2022iyl	20:58:08.06	+00:27:10.0	0.030	59694.5	59698.4	-17.04	0.21	0.14

Table B: Continued.

Name	RA	Dec	Redshift	$t_{\rm expl}$	1st detection	Peak mag$_r$	$A_{V,\rm MW}$	$A_{V,\rm host}$
	(hh:mm:ss)	(dd:mm:ss)		(MJD)	(MJD)	(mag)	(mag)	(mag)
ZTF22aajipum/SN2022joe	14:29:20.63	-22:56:09.7	0.026	59704.3	59707.3	-16.54	0.27	0.14
ZTF22aajutqu/SN2022jux	08:07:22.25	+40:23:34.8	0.026	59711.2	59712.2	-17.56	0.16	0.00
ZTF22aajuufc/SN2022juw	08:30:31.46	+18:12:13.7	0.027	59711.7	59712.2	-16.98	0.10	0.00
ZTF22aakdbia/SN2022jzc	12:05:28.66	+50:31:36.8	0.002	59714.3	59715.2	-14.91	0.05	0.57
ZTF22aakdqqg/SN2022kad	14:58:43.33	+11:37:50.8	0.020	59713.4	59714.4	-17.82	0.10	0.00
ZTF22aanrqje/SN2022mji	09:42:54.06	+31:51:03.6	0.004	59732.7	59741.2	-15.00	0.05	0.85
ZTF22aaolwsd/SN2022mxv	23:51:05.12	+20:09:08.9	0.014	59747.4	59751.4	-18.10	0.20	0.00
ZTF22aapargp/SN2022niw	15:57:16.80	+19:28:28.1	0.033	59752.3	59753.3	-17.25	0.10	0.00
ZTF22aarskhm/SN2022ohx	20:46:37.43	-2:21:50.56	0.029	59760.9	59762.4	-17.07	0.18	0.28
ZTF22aarycqo/SN2022ojo	01:44:35.61	+37:41:50.7	0.019	59761.4	59765.4	-19.18	0.15	1.13
ZTF22aaslyzf/SN2022oor	15:04:29.79	+02:20:18.7	0.032	59767.2	59768.2	-17.05	0.14	0.00
ZTF22aasojye/SN2022omr	23:41:41.10	+50:02:58.9	0.023	59766.9	59768.4	-16.89	0.62	0.00
ZTF22aativsd/SN2022ovb	22:22:29.55	+36:00:17.9	0.018	59773.4	59774.4	-18.15	0.37	0.00
ZTF22aatpwfw/SN2022paf	22:05:26.42	-00:31:58.7	0.031	59774.4	59775.4	-16.93	0.28	0.00
ZTF22aattfmb/SN2022oyp	18:05:13.16	+46:52:49.5	0.023	59775.8	59776.3	-16.87	0.11	0.28
ZTF22aaudjgc/SN2022pfx	21:50:50.87	-00:50:48.9	0.027	59775.9	59778.4	-18.03	0.28	0.07
ZTF22aavbfhz/SN2022phi	1:20:15.03	+17:49:56.49	0.029	59779.4	59782.4	-16.60	0.21	0.00
ZTF22aavobvq/SN2022prv	15:40:07.76	+20:40:31.7	0.015	59781.7	59784.3	-18.26	0.17	0.00

Table B: Continued.

Name	RA	Dec	Redshift	$t_{\rm expl}$	1st detection	Peak mag$_r$	$A_{V,\rm MW}$	$A_{V,\rm host}$
	(hh:mm:ss)	(dd:mm:ss)		(MJD)	(MJD)	(mag)	(mag)	(mag)
ZTF22aaxzzoc/SN2022qhc	17:16:35.13	+07:19:44.4	0.022	59789.3	59791.2	-17.28	0.48	0.42
ZTF22aaywnyg/SN2022pru	11:59:07.65	+52:41:58.5	0.004	59787.7	59797.2	-15.42	0.07	0.00
ZTF22aazmrpx/SN2022raj	02:03:17.52	+29:14:04.9	0.012	59798.4	59800.4	-15.20	0.15	0.00
ZTF22abadzpo/SN2022rfz	17:22:20.39	+02:00:58.0	0.030	59799.8	59802.2	-18.65	0.49	0.00
ZTF22abbecow/SN2022rqg	16:56:14.62	+55:01:10.3	0.029	59801.7	59805.2	-16.20	0.07	0.00
ZTF22abfavpu/SN2022tmb	03:20:33.60	+37:29:54.8	0.019	59825.0	59825.5	-17.10	1.04	0.00
ZTF22abfwxtr/SN2022udq	00:05:55.84	+22:29:26.3	0.022	59834.7	59839.2	-16.96	0.20	0.00
ZTF22abfxkdm/SN2022ubb	23:08:58.34	+12:02:39.0	0.016	59834.3	59839.3	-16.57	0.24	0.00
ZTF22abgwgsv/SN2022vpm	17:22:32.88	+26:46:04.2	0.022	59842.7	59843.2	-17.80	0.12	0.00
ZTF22abhsxph/SN2022vyc	04:33:10.32	+76:34:05.3	0.026	59844.9	59846.4	-17.01	0.43	0.00
ZTF22abitour/SN2022wbr	04:29:15.65	+40:14:46.9	0.020	59838.0	59847.5	-16.34	1.67	0.00
ZTF22abkbjsb/SN2022vym	08:54:01.09	+18:41:18.1	0.015	59849.0	59853.5	-16.48	0.06	0.21
ZTF22abkhrkd/SN2022wol	01:51:27.78	+36:03:51.5	0.018	59853.9	59854.3	-16.02	0.21	0.00
ZTF22ablnrcv/SN2022xav	09:39:17.64	+32:18:38.3	0.023	59857.0	59858.5	-16.96	0.05	0.42
ZTF22abmsaxp/SN2022xjk	02:16:32.50	-11:20:59.4	0.013	59860.9	59861.4	-17.15	0.10	0.00
ZTF22abnujbv/SN2022xus	06:54:05.13	+08:34:13.3	0.009	59869.4	59871.4	-16.42	0.60	0.00
ZTF22abpxxil/SN2022yma	03:08:48.32	-07:02:06.5	0.029	59871.9	59873.3	-17.16	0.20	0.49
ZTF22abrexqa/SN2022yyz	19:07:01.55	+28:59:50.0	0.013	59880.1	59881.1	-17.52	0.64	0.00

Table B: Continued.

Name	RA	Dec	Redshift	$t_{\rm expl}$	1st detection	Peak mag$_r$	$A_{V,\rm MW}$	$A_{V,\rm host}$
	(hh:mm:ss)	(dd:mm:ss)		(MJD)	(MJD)	(mag)	(mag)	(mag)
ZTF22absqhkw/SN2022zkc	04:47:58.59	-16:39:37.0	0.032	59885.4	59887.4	-17.40	0.14	0.00
ZTF22abssiet/SN2022zmb	10:38:43.18	+56:33:14.4	0.014	59885.5	59887.5	-15.72	0.02	0.07
ZTF22abtcsyd/SN2022zxt	08:40:16.38	+56:02:36.0	0.026	59891.5	59893.4	-17.25	0.10	0.00
ZTF22abtspsw/SN2022aagp	09:10:41.90	+07:12:20.3	0.005	59895.4	59897.4	-17.09	0.12	0.00
ZTF22abulusd/SN2022aatx	09:15:15.32	+11:53:04.6	0.017	59899.4	59902.5	-17.27	0.08	0.49
ZTF22abvaetz/SN2022aang	07:59:21.83	+18:06:40.9	0.016	59894.5	59901.5	-15.44	0.08	0.00
ZTF22abxomzd/SN2022acbu	02:30:43.15	-02:55:56.9	0.019	59906.8	59910.2	-18.75	0.08	3.11
ZTF22abyivoq/SN2022acko	03:19:38.98	-19:23:42.8	0.006	59917.8	59922.2	-15.83	0.08	0.00
ZTF22abyivxh/SN2022acwe	02:28:07.20	-05:43:37.0	0.030	59917.8	59922.2	-17.22	0.07	0.00
ZTF22abyohff/SN2022acrl	11:34:21.03	+15:39:49.2	0.017	59913.5	59923.5	-16.32	0.12	0.00
ZTF22abyokkf/SN2022acri	14:34:19.17	+25:52:55.4	0.022	59915.0	59923.5	-17.22	0.08	0.00
ZTF22abzdzek/SN2022adtt	01:14:05.28	+38:07:05.2	0.027	59930.2	59932.1	-16.80	0.13	0.00
ZTF22abzqwmp/SN2022adth	10:15:39.94	+45:56:25.2	0.031	59932.8	59933.3	-16.84	0.02	0.00
ZTF22acahbko/SN2022advr	10:22:48.99	+03:45:18.7	0.033	59934.5	59935.4	-16.61	0.10	0.00
ZTF23aaaatjn/SN2023cf	04:26:49.49	+29:56:59.8	0.018	59945.8	59951.2	-18.51	1.26	0.00
ZTF23aaaigqy/SN2023fu	03:06:21.26	+36:01:11.1	0.016	59948.7	59957.1	-17.97	0.66	0.00
ZTF23aaarmtb/SN2023qh	09:07:15.44	+37:12:54.8	0.024	59947.4	59957.4	-15.89	0.06	0.00
ZTF23aaavxye/SN2023abq	15:34:33.34	+41:08:11.6	0.032	59962.7	59967.5	-17.63	0.07	0.00

Table B: Continued.

Name	RA	Dec	Redshift	$t_{\rm expl}$	1st detection	Peak mag$_r$	$A_{V,\rm MW}$	$A_{V,\rm host}$
	(hh:mm:ss)	(dd:mm:ss)		(MJD)	(MJD)	(mag)	(mag)	(mag)
ZTF23aaazdla/SN2023wn	13:36:04.57	-01:35:39.7	0.015	59962.5	59968.5	-16.79	0.09	0.00
ZTF23aabngtm/SN2023axu	06:45:55.32	-18:13:53.5	0.003	59970.3	59972.3	-17.27	1.06	0.00
ZTF23aabtmzm/SN2023blw	07:28:09.44	+52:28:17.5	0.022	59975.7	59979.2	-18.35	0.16	2.97
ZTF23aacdlsh/SN2023bmd	15:10:08.83	+46:06:23.2	0.020	59982.5	59984.5	-16.69	0.07	0.00
ZTF23aacjetk/SN2023buy	08:20:53.69	+39:14:29.7	0.029	59988.3	59991.2	-17.87	0.12	0.00
ZTF23aackdba/SN2023bql	08:11:27.82	+08:56:24.7	0.019	59984.8	59985.3	-16.51	0.07	0.28
ZTF23aackjhs/SN1995al	09:50:56.03	+33:33:11.0	0.005	59989.8	59992.3	-14.88	0.04	0.07
ZTF23aaflnok/SN2023fub	07:40:26.79	+25:08:00.2	0.029	60047.2	60049.2	-17.22	0.12	0.00
ZTF23aafumlg/SN2023fou	12:40:20.46	-10:02:55.1	0.026	60047.8	60050.3	-17.85	0.10	0.00
ZTF23aagkajy/SN2023gdt	10:30:10.64	+43:21:23.4	0.014	60050.2	60051.2	-15.42	0.03	0.71
ZTF23aagkutf/SN2023ghl	11:09:11.73	+53:21:43.9	0.027	60052.2	60053.2	-17.24	0.03	0.00
ZTF23aagqyym/SN2023gjg	09:07:17.96	+37:30:12.6	0.030	60054.2	60055.2	-17.08	0.05	0.00
ZTF23aahqvtz/SN2023gss	14:04:23.54	-27:08:58.1	0.021	60058.8	60059.3	-17.07	0.19	0.00
ZTF23aaiecnn/SN2023gxq	10:18:12.24	+34:40:19.7	0.029	60061.2	60062.2	-16.51	0.04	0.00
ZTF23aailjjs/SN2023hcp	16:48:42.72	+35:56:57.4	0.031	60062.4	60063.4	-17.91	0.05	0.00
ZTF23aaitpjv/SN2023hlf	12:26:26.17	+31:13:32.2	0.002	60053.3	60054.4	-16.53	0.05	5.09
ZTF23aajrmfh/SN2023ijd	12:36:32.47	+11:13:19.7	0.007	60078.2	60079.0	-15.39	0.09	0.00
ZTF23aajsjon/SN2023hzt	13:30:01.55	+75:34:09.0	0.030	60071.9	60076.4	-17.05	0.10	0.00

Table B: Continued.

Name	RA	Dec	Redshift	$t_{\rm expl}$	1st detection	Peak mag$_r$	$A_{V,\rm MW}$	$A_{V,\rm host}$
	(hh:mm:ss)	(dd:mm:ss)		(MJD)	(MJD)	(mag)	(mag)	(mag)
ZTF23aakirso/SN2023jid	22:40:43.23	+36:38:39.5	0.027	59994.8	60054.5	-16.12	0.42	0.00
ZTF23aamfqxc/SN2023jri	23:30:27.09	+30:13:11.2	0.015	60094.2	60097.4	-18.81	0.40	0.28
ZTF23aamqycj/SN2023jvi	13:31:22.27	+25:37:01.0	0.025	60094.8	60097.3	-17.03	0.03	0.00
ZTF23aamzlzc/SN2023kne	17:25:19.11	+58:49:02.6	0.028	60095.4	60097.3	-15.81	0.10	0.00
ZTF23aanymcl/SN2023kzz	17:17:06.29	-14:54:05.1	0.028	60106.8	60110.3	-17.24	1.26	0.00
ZTF23aanzmoz/SN2023kyi	19:16:43.95	-17:30:35.0	0.030	60105.9	60108.4	-17.00	0.33	0.00
ZTF23aaomzth/SN2023rpu	09:23:47.48	+42:11:12.1	0.014	60105.2	60113.2	-16.56	0.05	0.00
ZTF23aaphnyz/SN2023lkw	16:48:36.21	+41:36:02.6	0.031	60117.8	60118.2	-18.07	0.06	0.00
ZTF23aaqknaw/SN2023lzn	00:55:07.58	+31:32:47.6	0.018	60124.4	60128.4	-17.37	0.17	0.85
ZTF23aaqtckr/SN2023mpj	14:34:24.79	+02:53:04.9	0.030	60120.2	60120.3	-16.62	0.10	0.00
ZTF23aaqwpio/SN2023nca	16:39:26.36	+11:12:45.3	0.023	60129.3	60135.2	-15.61	0.14	0.00
ZTF23aasbvab/SN2023ngy	22:18:30.18	+29:14:41.0	0.021	60139.9	60140.3	-16.80	0.22	0.00
ZTF23aasrcyv/SN2023nlu	00:45:09.04	-09:37:38.3	0.020	60142.5	60143.4	-16.78	0.10	0.00
ZTF23aasyvbf/SN2023nmh	00:37:38.73	-04:16:53.2	0.020	60142.4	60144.5	-15.93	0.10	0.00
ZTF23aaxadel/SN2023pbg	00:14:54.90	+26:20:00.4	0.025	60166.9	60168.4	-16.88	0.11	0.00
ZTF23aazprcc/SN2023vhb	12:19:13.19	+22:25:42.4	0.022	60180.1	60181.1	-17.20	0.07	0.21
ZTF23abadrow/SN2023qxp	21:56:14.96	+02:10:27.8	0.028	60175.9	60178.4	-16.65	0.15	0.00
ZTF23abascqa/SN2023rbk	03:15:20.60	+41:36:53.5	0.020	60186.4	60187.4	-17.96	0.38	0.00

Table B: Continued.

Name	RA	Dec	Redshift	$t_{\rm expl}$	1st detection	Peak mag$_r$	$A_{V,\rm MW}$	$A_{V,\rm host}$
	(hh:mm:ss)	(dd:mm:ss)		(MJD)	(MJD)	(mag)	(mag)	(mag)
ZTF23abaxtlq/SN2023rix	02:47:56.84	+41:14:48.3	0.013	60191.9	60192.4	-16.37	0.23	0.00
ZTF23abbsxzs/SN2023rtq	04:51:46.59	+38:56:10.0	0.013	60193.4	60195.4	-17.56	2.68	0.57
ZTF23abbtkrv/SN2023rvo	08:49:16.37	+36:07:14.8	0.025	60193.0	60194.5	-17.05	0.09	0.00
ZTF23aberpzw/SN2023swf	21:05:58.52	-14:50:30.3	0.023	60201.7	60203.2	-16.66	0.17	0.00
ZTF23abhruov/SN2023ucx	03:59:54.88	+32:36:41.1	0.018	60210.4	60215.4	-17.08	0.65	1.91
ZTF23abhyroo/SN2023udb	04:25:05.77	-10:18:51.9	0.033	60219.0	60221.5	-17.25	0.25	0.00
ZTF23abhzfww/SN2023twg	08:45:54.52	+12:47:12.2	0.030	60214.5	60220.5	-17.62	0.09	0.00
ZTF23abiewbt/SN2023ujp	15:57:33.01	+20:02:54.2	0.033	60222.1	60223.1	-17.36	0.12	0.00
ZTF23abjwgre/SN2023vcg	23:56:05.87	+29:22:40.5	0.023	60231.3	60231.3	-16.70	0.17	0.00
ZTF23abkhajf/SN2023vcj	07:55:15.92	+53:44:47.7	0.025	60228.5	60232.5	-17.38	0.09	0.07
ZTF23abmoxlu/SN2023vog	09:45:09.63	+68:35:11.8	0.015	60237.4	60238.4	-17.59	0.28	0.00
ZTF23abndgbw/SN2023way	21:24:11.15	+15:59:22.9	0.018	60240.7	60242.2	-16.68	0.31	0.00
ZTF23abnogui/SN2023wcr	12:23:31.29	+74:57:01.3	0.005	60240.5	60244.5	-15.58	0.09	0.00
ZTF23abonlit/SN2023wuj	08:26:18.36	+02:55:28.6	0.031	60247.0	60248.5	-16.79	0.14	0.00
ZTF23abphqjk/SN2023xgn	03:02:48.82	-15:42:21.6	0.031	60253.9	60254.4	-17.42	0.15	0.00
ZTF23abqwald/SN2023xvo	11:20:24.29	+28:17:55.4	0.033	60234.0	60234.5	-16.90	0.05	0.21
ZTF23absdcgi/SN2023zcu	06:01:06.82	-23:40:29.3	0.006	60288.2	60289.3	-16.73	0.09	0.00
ZTF23abvommm/SN2023acbr	02:27:03.18	-09:25:02.3	0.016	60300.7	60305.2	-15.57	0.08	0.00

Table B: Continued.

Name	RA	Dec	Redshift	$t_{\rm expl}$	1st detection	Peak mag$_r$	$A_{V,\rm MW}$	$A_{V,\rm host}$
	(hh:mm:ss)	(dd:mm:ss)		(MJD)	(MJD)	(mag)	(mag)	(mag)
ZTF24aaabbse/SN2023achj	08:36:07.46	+25:06:47.0	0.023	60303.9	60311.3	-17.79	0.10	0.00
ZTF24aaarlvj/SN2024V	11:52:01.50	+57:41:37.4	0.031	60300.0	60308.5	-16.49	0.04	0.00
ZTF24aaasazz/SN2024ov	11:50:28.79	-18:34:42.8	0.023	60291.0	60291.6	-16.03	0.10	0.00
ZTF24aabppgn/SN2024wp	11:24:39.25	+14:56:52.9	0.014	60320.5	60325.5	-15.52	0.10	0.00
ZTF24aabpzuz/SN2024vs	07:51:07.27	+72:57:57.4	0.010	60317.9	60321.5	-16.70	0.08	0.00
ZTF24aabsmvc/SN2024ws	08:28:46.69	+73:45:08.6	0.012	60318.9	60322.3	-16.15	0.07	0.00
ZTF24aadkwni/SN2024aul	10:21:53.24	+00:17:44.3	0.021	60330.7	60335.4	-17.77	0.13	0.28
ZTF24aaejehf/SN2024bzq	11:44:33.94	+36:26:41.2	0.033	60346.4	60351.4	-17.97	0.05	0.00
ZTF24aaejjps/SN2024btx	11:54:55.45	+29:20:34.5	0.021	60346.4	60351.4	-16.04	0.06	0.00
ZTF24aaejvcx/SN2024atk	13:18:31.13	-14:36:39.1	0.010	60343.2	60351.4	-16.54	0.22	0.00
ZTF24aaemydm/SN2024chx	09:54:28.51	-18:38:10.8	0.013	60352.8	60354.2	-18.01	0.13	0.00
ZTF24aafqzur/SN2024daa	14:25:57.20	-02:23:32.2	0.031	60355.4	60355.5	-16.72	0.15	0.00
ZTF24aagiwoi/SN2024dhi	11:13:08.67	+05:04:28.3	0.027	60360.9	60363.4	-16.65	0.20	0.00
ZTF24aagupsf/SN2024egd	16:30:41.48	+44:30:40.0	0.032	60372.0	60374.5	-17.47	0.04	0.00
ZTF24aahalmb/SN2024ees	12:32:42.19	+14:32:27.4	0.024	60376.8	60379.4	-16.52	0.11	0.00
ZTF24aahewml/SN2024etq	18:13:41.23	+10:56:03.8	0.022	60381.0	60387.5	-16.60	0.51	0.00
ZTF24aahgmyj/SN2024epy	09:46:46.54	+13:31:53.4	0.024	60384.2	60388.2	-16.77	0.12	0.64
ZTF24aahmgck/SN2024faf	11:28:57.38	+73:02:11.9	0.021	60385.8	60388.3	-16.85	0.13	1.27

Table B: Continued.

Name	RA	Dec	Redshift	$t_{\rm expl}$	1st detection	Peak mag$_r$	$A_{V,\rm MW}$	$A_{V,\rm host}$
	(hh:mm:ss)	(dd:mm:ss)		(MJD)	(MJD)	(mag)	(mag)	(mag)
ZTF24aahwfsa/SN2024fas	10:51:55.36	+37:35:23.9	0.026	60393.4	60396.4	-15.80	0.04	0.00
ZTF24aajxppf/SN2024grw	17:58:21.63	+09:40:53.5	0.021	60415.5	60416.5	-18.01	0.48	0.00
ZTF24aakzive/SN2024hpg	21:31:43.20	+0:21:43.71	0.029	60427.7	60430.4	-17.53	0.14	0.00
ZTF24aalceob/SN2024hme	16:05:57.74	+27:11:21.00	0.031	60418.9	60423.4	-16.09	0.10	0.00
ZTF24aamzqsv/SN2024izq	9:24:57.24	+40:23:58.49	0.028	60440.2	60441.2	-16.29	0.04	0.00
ZTF24aaozxhx/SN2024jlf	14:37:42.32	+2:17:04.17	0.006	60457.3	60458.2	-16.99	0.11	0.00
ZTF24aaplfjd/SN2024jxm	0:58:01.36	+30:42:23.84	0.016	60460.0	60460.5	-16.00	0.18	0.00
ZTF24aarajmv/SN2024ldu	19:54:05.17	+49:56:47.25	0.025	60466.4	60469.4	-16.26	0.50	0.00
ZTF24aarvbxj/SN2024lby	20:22:40.78	-8:10:41.95	0.020	60472.4	60473.4	-17.56	0.17	0.00
ZTF24aasktmr/SN2024lss	16:31:22.18	+22:42:08.73	0.024	60479.8	60480.2	-17.19	0.13	0.00
ZTF24aatifzm/SN2024mxq	14:44:05.84	+9:16:47.52	0.031	60480.8	60484.2	-16.83	0.08	0.00

Chapter 5

LOW-LUMINOSITY TYPE IIP SUPERNOVAE FROM THE ZWICKY TRANSIENT FACILITY CENSUS OF THE LOCAL UNIVERSE. II: LIGHTCURVE ANALYSIS

Das, K. K., M. M. Kasliwal, et al. (2026). "Low-luminosity Type IIP Supernovae from the Zwicky Transient Facility Census of the Local Universe. II. Lightcurve Analysis". In: *Publications of the Astronomical Society of the Pacific* 138.2, article 024204. DOI: 10.1088/1538-3873/ae33f5.

Kaustav K. Das[1], Mansi M. Kasliwal[1], Jesper Sollerman[2], Christoffer Fremling[3], Takashi J. Moriya[4,5,6], K-Ryan Hinds[7], Daniel A. Perley[7], Eric C. Bellm[8], Tracy X. Chen[9], Evan P. O'Connor[2], Michael W. Coughlin[10], W. V. Jacobson-Galán[1], Anjasha Gangopadhyay[2], Matthew Graham[1], S. R. Kulkarni[1], Josiah Purdum[3], Nikhil Sarin[2], Steve Schulze[11], Avinash Singh[2], Daichi Tsuna[12], Avery Wold[9]

[1] Cahill Center for Astrophysics, California Institute of Technology, Pasadena, CA 91125, USA

[2] The Oskar Klein Centre, Department of Astronomy, Stockholm University, AlbaNova, SE-10691 Stockholm, Sweden

[3] Caltech Optical Observatories, California Institute of Technology, Pasadena, CA 91125, USA

[4] Astronomical Science Program, Graduate Institute for Advanced Studies, SOKENDAI, 2-21-1 Osawa, Mitaka, Tokyo 181-8588, Japan

[5] National Astronomical Observatory of Japan, National Institutes of Natural Sciences, 2-21-1 Osawa, Mitaka, Tokyo 181-8588, Japan

[6] School of Physics and Astronomy, Monash University, Clayton, VIC 3800, Australia

[7] Astrophysics Research Institute, Liverpool John Moores University, IC2, Liverpool L3 5RF, UK

[8] DIRAC Institute, Department of Astronomy, University of Washington, Seattle, WA 98195, USA

[9] IPAC, California Institute of Technology, Pasadena, CA 91125, USA
[10] School of Physics and Astronomy, University of Minnesota, Minneapolis, MN 55455, USA
[11] Center for Interdisciplinary Exploration and Research in Astrophysics (CIERA), Northwestern University, Evanston, IL 60201, USA
[12] TAPIR, California Institute of Technology, Pasadena, CA 91125, USA

Abstract

The Zwicky Transient Facility Census of the Local Universe survey yielded a sample of 330 Type IIP supernovae (SNe) with well-constrained peak luminosities. In paper I (Das et al. 2025b), we measured their luminosity function and volumetric rate. Here (paper II), we present the largest systematic study of light-curve properties for Type IIP SNe from a volume-limited survey, analyzing a selected subset of 129 events, including 16 low-luminosity Type IIP (LLIIP) SNe with $M_{r,\mathrm{peak}} \geq -16$ mag. We find that plateau slope correlates with peak brightness, with many LLIIP SNe showing positive slopes—suggesting smaller progenitor radii and distinct density profiles compared to brighter Type IIP SNe. The plateau duration shows only a weak dependence on peak brightness, likely suggesting binary interaction. One SN exhibits a plateau-to-tail drop of > 3.5 mag, consistent with an electron-capture or failed SN with very low or zero nickel mass. We derive explosion and progenitor parameters of the entire Type IIP SN sample using semi-analytical and radiation-hydrodynamical models. Based on radiation-hydrodynamical model fitting, LLIIP SNe are characterized by low nickel masses (0.001–0.025 $M_\odot$), low explosion energies (0.1–0.28 $\times 10^{51}$ erg), low ejecta masses ($8.1^{+0.8}_{-1.7}$ $M_\odot$), and ZAMS masses below 11 $M_\odot$. In comparison, the full Type IIP SN sample spans a wider range with nickel masses (0.001–0.222 $M_\odot$), explosion energies (0.10–4.43 $\times 10^{51}$ erg), ejecta masses (5.4–24.8 $M_\odot$), and ZAMS masses (9.3–16.7 $M_\odot$). We find strong correlations between peak brightness, explosion energy, and nickel mass that extend to the low-luminosity end. We conclude that LLIIP SNe represent the faint, low-energy end of the Type IIP population and originate from the lowest-mass core-collapse progenitors.

5.1 Introduction

Core-collapse supernovae (CCSNe) are the explosive deaths of massive stars that play crucial roles in galactic chemical evolution, the formation of new stars, and the creation of compact neutron stars and black holes. Moreover, their luminosi-

ties, rates, and association with massive star formation make them essential tools for probing key astrophysical parameters across vast cosmic volumes. The most common type of core-collapse SNe are Type II SNe (e.g., Li et al. 2011, Shivvers et al. 2017). They arise from the explosions of stars that retain significant portions of their hydrogen envelopes.

Low-luminosity Type IIP supernovae (LLIIP SNe), defined here as those with $M_{\mathrm{r,peak}} \geq -16$ mag, as motivated by prior literature (e.g., Pastorello et al. 2004, Spiro et al. 2014, Reguitti et al. 2021), are particularly intriguing because they are thought to originate from progenitor stars with just enough mass to undergo core collapse. These events likely arise from 8–12 $M_{\odot}$ progenitors, as supported by pre-SN progenitor imaging (Maund et al. 2005, Li et al. 2006, Mattila et al. 2008, O'Neill et al. 2019, Van Dyk et al. 2023b), light curve simulations (Pumo et al. 2017, Fraser et al. 2011), evolutionary models of low-mass red supergiants (RSGs) (Lisakov et al. 2017), and nebular spectroscopy (Jerkstrand et al. 2018). They provide valuable insight into the lower mass threshold for core collapse, which defines the boundary between stars that form white dwarfs and those that form neutron stars or black holes. LLIIP SNe also serve as key candidates for probing the upper mass limit of super-asymptotic giant branch (sAGB) star formation, exploring whether they can explode as electron-capture supernovae (ECSN) (Nomoto 1984, Kitaura et al. 2006, Janka et al. 2008, Takahashi et al. 2013, Jones et al. 2013, Hiramatsu et al. 2021b, Wang et al. 2025), and understanding their role in shaping elemental abundances in subsequent generations of stars (Tsujimoto and Shigeyama 1999, Siess 2006). Furthermore, a typical initial mass function (IMF) predicts that more than 40% of CCSN progenitors fall within the 8–12 $M_{\odot}$ range, with 25% within the 8–10 $M_{\odot}$ subset (Sukhbold et al. 2016). It has also been suggested that LLIIP SNe may instead originate from more massive RSGs with significant fallback (e.g., Woosley and Weaver 1995, Zampieri et al. 2003, Moriya et al. 2010). Thus, systematic studies of LLIIP SNe are essential for improving our understanding of the progenitors, explosion properties, and the dust and chemical enrichment contributed by nearly half of all massive stars that undergo core-collapse.

However, to date, no study of the lightcurve properties of LLIIP SNe has been conducted using data from a systematic SN survey. Due to their low luminosity, they are relatively difficult to detect and classify. There are only about a dozen such objects presented in the literature, focused on single-object studies or small heterogeneous samples. Early examples such as SN 1997D, SN 1999eu and SN 1999br (Turatto

et al. 1998, Pastorello et al. 2004) revealed the defining characteristics of the class: very low plateau luminosities ($M_V \approx -15$ mag), unusually narrow P-Cygni profiles indicating expansion velocities of only ∼1000–2500 km s^{-1}, extremely small ^{56}Ni masses (10^{-3}–10^{-2} M$_\odot$), and low explosion energies. Subsequent studies of nearby events such as SN 2005cs and SN 2008bk (Pastorello et al. 2009a, Mattila et al. 2008, Van Dyk et al. 2012b) connected these faint light curves to low-mass red supergiant progenitors (∼8–12 M$_\odot$) through direct pre-explosion imaging and hydrodynamical modeling. Spiro et al. (2014) modeled a set of underluminous Type IIP SNe and confirmed uniformly low explosion energies; Nakaoka et al. (2018) and Reguitti et al. (2021) found similarly low ^{56}Ni yields and slow expansion velocities for SN 2016bkv and SN 2018hwm, respectively; and studies such as Jäger et al. (2020), Müller-Bravo et al. (2020), Yang et al. (2021), Valerin et al. (2022), Kozyreva et al. (2022), Bostroem et al. (2023), Teja et al. (2024), Dastidar et al. (2025) have recently reported additional LLIIP SN candidates with low luminosities and energetics consistent with either low-mass RSG/sAGB explosions or fallback-suppressed ^{56}Ni production. In contrast to these low-luminosity events, canonical Type II SNe typically reach plateau absolute magnitudes of $M_r \simeq -16$ to -18 mag, have plateau durations of ∼80–120 days, ejecta masses of ∼8–18 M$_\odot$, explosion energies of order $0.3–1 \times 10^{51}$ erg, and ^{56}Ni yields of ∼0.01–0.1 M$_\odot$ (e.g., Hamuy 2003, Anderson et al. 2014b, Sanders et al. 2015, Valenti et al. 2016, Martinez et al. 2022b, Fang et al. 2025). These properties are generally consistent with explosions of RSG progenitors with initial masses ∼12–18 M$_\odot$ (e.g., see Van Dyk 2025).

In Part I of the series of three papers on LLIIP SNe (Das et al. 2025b), we measured the luminosity function and volumetric rate of the largest sample to date of 36 LLIIP SNe (and 330 Type IIP SNe) from the Zwicky Transient Facility Census of the Local Universe (ZTF CLU; Bellm et al. 2019b, Graham et al. 2019, Dekany et al. 2020, Masci et al. 2019, De et al. 2020b) survey. This paper delves into their lightcurve properties. In this paper, we analyze the observed properties of the multi-band lightcurves of a selected subset of 129 Type II SNe and 16 LLIIP SNe. It is well established that the morphology of Type II SN lightcurves depends on key progenitor properties (e.g., final mass, envelope mass, and radius) and on explosion parameters such as the deposited energy and the amount and distribution of synthesized ^{56}Ni (e.g., Kasen and Woosley 2009, Goldberg et al. 2019). Here, we measure observed lightcurve parametrs and infer physical and explosion parameters using semi-analytical and radiation-hydrodynamical models that link SN observables to progenitor properties (e.g., Litvinova and Nadezhin 1983, Hamuy 2003, Kasen and

Woosley 2009, Goldberg et al. 2019, Morozova et al. 2018, Moriya et al. 2023). Such models have been previously applied to both individual events and larger samples of Type II SNe (Hamuy 2003, Arcavi et al. 2011, Anderson et al. 2014b, Spiro et al. 2014, Sanders et al. 2015, Valenti et al. 2016, Gutiérrez et al. 2017a, Morozova et al. 2018, Martinez et al. 2022b,a, Subrayan et al. 2023, Silva-Farfán et al. 2024, Fang et al. 2025). This paper is structured as follows: in Section 8.2, we define the sample selection criteria. The data and extinction correction methods are described in Sections 10.2 and 10.3, respectively. Sections 10.5 and 5.6 detail the fitting methods and results. We discuss the implications of the derived physical properties in Section 10.6 and conclude in Section 10.7.

5.2 Sample Selection

From the ZTF CLU experiment, we selected Type IIP SNe with well-sampled r-band light curves and a clearly defined plateau phase. The selection required (i) a GP-fit peak apparent magnitude of $m_{r,\mathrm{peak}} < 20$ mag, (ii) sufficient temporal coverage around peak and during the plateau (more than ten total detections and at least one detection on both sides of peak, or an equivalent set of conditions ensuring a constrained rise), and (iii) a plateau lasting at least 40 days with < 1 mag decline. We refer to Paper I (Das et al. 2025b) for the complete sample selection criteria to select 330 Type IIP SNe. To select the sample for lightcurve analysis, we require that the end of the plateau phase is observed in the r-band lightcurve. This is to ensure we can extract reliable progenitor and explosion parameters from the lightcurves. The epoch of the end of the plateau ($t_{\mathrm{plateau,end}}$) is determined as the epoch where the derivative of the slope of the r-band lightcurve (Δ_{slope}) reach a local minimum, and its value is < -0.003 mag day^{-2}, indicating a sharp transition (see Section 5.5 and Figure 5.1 for details). This marks the end of the plateau phase in the lightcurve evolution. Using this criterion, we identified 129 candidates that fulfill this selection criterion. Out of these, 68 objects have ≥ 2 r-band data points in the radioactive tail phase, while 61 SNe do not have an observed radioactive tail.

5.3 Data

In this section, we describe the photometric and spectroscopic data used.

Optical photometry

We perform forced photometry on the ZTF difference images using the ZTF forced-photometry service developed by Masci et al. (2019) in g, r and i bands. For this

work, we consider anything less than a 3σ detection an upper limit. In the tail phase, for a few SNe we also took photometry in the g, r, i bands with the Optical Imager (IO:O) at the 2.0 m robotic Liverpool Telescope (Steele et al. 2004) and the Alhambra Faint Object Spectrograph and Camera at the Nordic Optical Telescope (Djupvik and Andersen 2010). The P60 and LT data sets were processed with the FPipe image subtraction pipeline (Fremling et al. 2016), using Sloan Digital Sky Survey (SDSS; Ahn et al. 2012) and PanSTARRS (PS1; Chambers et al. 2016) reference frames. See Das et al. (2025b) for details on photometric observations and reductions. Figure 5.1 shows a few representative lightcurves as examples. The photometry data and lightcurve plots for all the SNe in the sample will be made available on `Zenodo`.

Optical spectroscopy

For each transient, at least one spectrum is usually obtained close to the peak luminosity to establish an initial spectroscopic classification. We primarily utilize the Double Beam Spectrograph (DBSP; Oke and Gunn 1982) on the Palomar 200-inch Hale telescope and the Spectral Energy Distribution Machine (SEDM; Blagorodnova et al. 2018, Rigault et al. 2019, Kim et al. 2022) on the Palomar 60-inch telescope for this purpose. Other instruments used to obtain classification spectra include: the Alhambra Faint Object Spectrograph and Camera at the Nordic Optical Telescope (NOT; Djupvik and Andersen 2010), the Spectrograph for the Rapid Acquisition of Transients (SPRAT; Piascik et al. 2014) on the Liverpool Telescope, the Low-Resolution Imaging Spectrometer (LRIS; Oke et al. 1995) on the Keck I telescope. See Das et al. (2025b) for details on spectral observations and reductions. We employ the `SuperNova Identification` (`SNID`; Blondin and Tonry 2007) and `superfit` (Howell et al. 2005) codes for classifications.

5.4 Extinction Correction

We corrected for Galactic extinction using the maps provided by Schlafly and Finkbeiner (2011). For the corrections, we use the extinction law described by Cardelli et al. (1989) with a value of $R_V = 3.1$.

To estimate host-galaxy extinction, we employ the empirical $g - r$ color template constructed in Paper I (Das et al. 2025b) from a subset of Type IIP SNe with negligible host reddening (identified via weak or absent host Na I D absorption). The intrinsic template has a 1σ scatter of $\sim$0.35 mag. For each SN in our sample, we measure the deviation of its observed $g-r$ color from this template and attribute

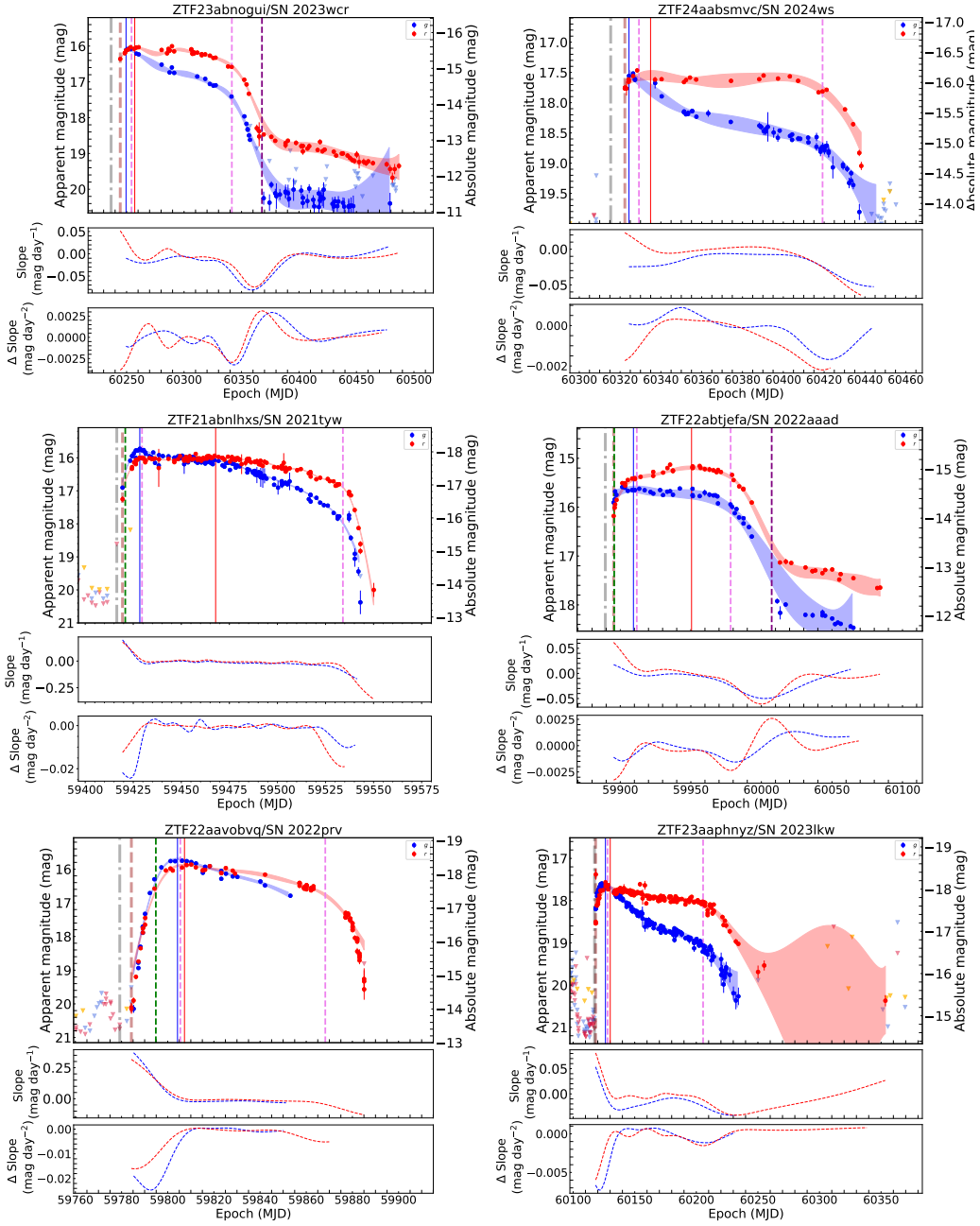

Figure 5.1: The upper panels show Gaussian Process fits to the lightcurves (shaded regions). Vertical dashed red lines indicate the epochs of first detection; vertical dashed grey lines mark the estimated explosion epochs. Vertical solid red and blue lines show the epochs of peak r- and g-band magnitudes, respectively. Vertical solid violet lines denote the start and end of the r-band plateau phase. Green dashed lines mark the epoch when the flux reaches 50% of the peak, used to compute the rise time. The lower panels show the light curve slope in units of mag day^{-1} and the change in slope (Δ slope) in units of mag day^{-2}.

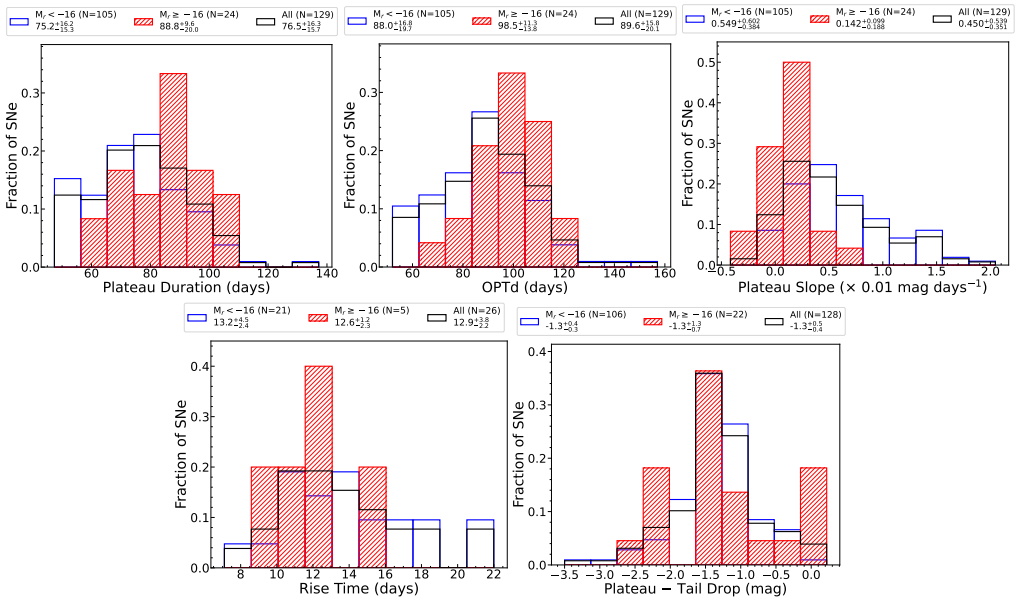

Figure 5.2: Distribution of observable properties of the r-band light curves for the SN sample. From left to right and top to bottom, the panels show the distributions of: (1) plateau duration, (2) optically thick phase duration (OPTd), (3) plateau slope, (4) rise time to peak, and (5) magnitude drop between the plateau and the tail phase. These observables are measured from the Gaussian Process fits described in Section 5.5. LLIIP SNe with $M_r \geq -16$ are shown in hatched red, those with $M_r < -16$ in blue, and the full sample is shown in black. The median (50th percentile) and the 16th and 84th percentiles of the distributions are indicated as $\text{median}^{+84\text{th}-50\text{th}}_{-50\text{th}-16\text{th}}$ in the legend.

any excess beyond the 1σ intrinsic range to host-galaxy reddening, converting it to $A_{V,\text{host}}$ assuming the same extinction law. The template is available on Zenodo. See Das et al. (2025b) for further details.

5.5 Analysis

Observed lightcurve properties

We employed a Gaussian Process (GP) algorithm[1] (Ambikasaran et al. 2015) to fit the r-band and g-band lightcurves. The top panel of Figure 5.1 displays the interpolated r-band lightcurve, the middle panel shows its first derivative with respect to time (i.e., the slope, in mag day^{-1}), and the bottom panel shows the time derivative of the slope, denoted as Δ_{slope} (in mag day^{-2}).

The r-band lightcurve parameters are measured using the following criteria:

[1]https://george.readthedocs.io/

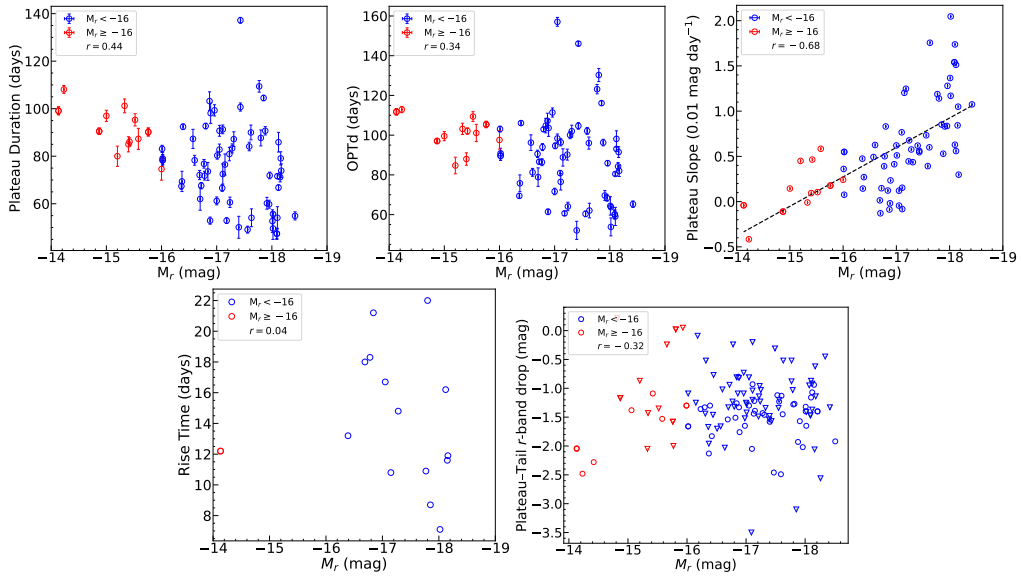

Figure 5.3: Observable light curve parameters as a function of r-band peak absolute magnitude (M_r). From left to right and top to bottom, the panels show: (1) plateau duration vs. M_r, (2) optically thick phase duration (OPTd) vs. M_r, (3) plateau slope vs. M_r, (4) rise time vs. M_r, and (5) the magnitude drop between the plateau and tail vs. M_r. In the last panel, upper limits are indicated by V-shaped triangles for SNe without a detected tail phase. LLIIP SNe with $M_r \geq -16$ are shown in red, while SNe with $M_r < -16$ are shown in blue. See details in Section 5.6.

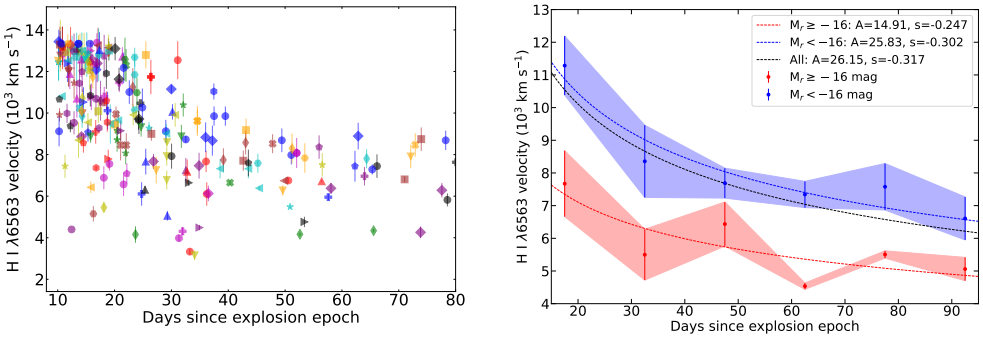

Figure 5.4: Left: Expansion velocities measured from the absorption minima of the H I λ6563 P-Cygni line for all SNe in our sample. Each marker and color represents a unique SN. Right: Mean H I λ6563 velocities with standard deviation for the full sample (black), LLIIP SNe with $M_r \geq -16$ (red), and brighter SNe with $M_r < -16$ (blue).

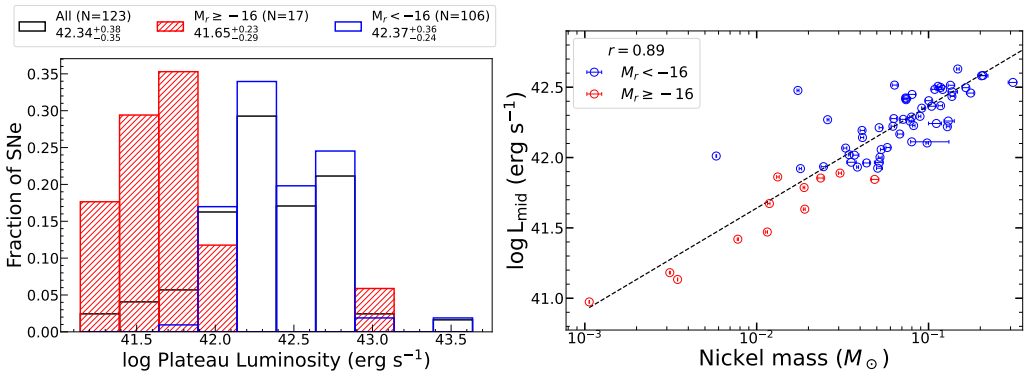

Figure 5.5: Left: Fractional distribution of bolometric luminosity at the mid-plateau phase. LLIIP SNe with $M_r \geq -16$ are shown in hatched red, those with $M_r < -16$ in blue, and the full sample is shown in black. Right: Correlation between mid-plateau bolometric luminosity and nickel mass inferred from the bolometric lightcurve tail. LLIIP SNe with $M_r \geq -16$ are shown in red, and SNe with $M_r < -16$ are shown in blue.

Table A: Definition of light-curve shape parameters based on light-curve phase, slope (mag day^{-1}), and rate of change of slope $\Delta_{\rm slope}$ (mag day^{-2}).

Parameter	Phase / slope condition	$\Delta_{\rm slope}$ condition
$t_{\rm plateau,start}$	Phase < 60 days; earlier of slope < 0.01 mag day^{-1} or maximum $\Delta_{\rm slope}$	Maximum $\Delta_{\rm slope}$
$t_{\rm plateau,end}$	Phase > $t_{\rm plateau,start}$ + 40 days; slope < −0.03 mag day^{-1}	Minimum $\Delta_{\rm slope} < -0.003$ mag day^{-2}
$t_{\rm tail}$	Phase > $t_{\rm plateau,end}$ and < $t_{\rm plateau,end}$ + 50 days; slope < 0	Maximum $\Delta_{\rm slope} \geq 0.002$ mag day^{-2}
$t_{\rm rise}$	Time between half-maximum brightness, (M_r + 0.75) mag, and peak epoch	Not applicable

- Plateau onset ($t_{\rm plateau,start}$): Defined as the earlier of (i) the epoch when the slope becomes shallower than 0.01 mag day^{-1}, or (ii) the epoch when the change in slope with respect to time ($\Delta_{\rm slope}$) reaches its maximum value, measured within 60 days after first detection.

- Plateau end ($t_{\rm plateau,end}$): The epoch of plateau end ($t_{\rm plateau,end}$) is identified after 40 days, when the lightcurve begins to steeply decline. This point is determined as the epoch where $\Delta_{\rm slope}$ reaches a minimum below −0.003 mag day^{-2}, indicating a sharp transition.

- Tail onset ($t_{\rm tail}$): Defined as the epoch post-plateau when $\Delta_{\rm slope}$ reaches a

maximum exceeding 0.002 mag day^{-2}, provided this occurs within 50 days after the plateau ends.

- Rise time ($t_{\rm rise}$): Defined as the time interval between the epoch when the r-band magnitude is 0.75 mag fainter than peak (half-maximum) and the epoch of maximum light.

To estimate uncertainties in these observables, we adopt a Monte Carlo approach. We simulate 50 realizations of each lightcurve based on Gaussian noise scaled to the flux errors. For each realization, we recompute the observables using the same criteria. The standard deviation of the resulting distribution of values is used as the uncertainty on the measurements of these observables. The plateau duration is measured as $t_{\rm plateau,end} - t_{\rm plateau,start}$. The optically thick plateau duration (OPTd) is measured as the duration between the explosion epoch and the midpoint of the plateau end and tail onset epochs. The distributions of these observed parameters are shown in Figure 5.2. A sharp luminosity drop between the plateau and the radioactive tail is a key prediction for both ECSNe and failed SNe with very low or negligible ^{56}Ni production (e.g., Tominaga et al. 2013, Turatto et al. 1998). To identify such ECSN and failed-SN candidates in our sample, we measure the drop in the r-band magnitude from the end of the plateau to the first epoch on the tail, whenever the tail is detected. If a tail does not exist, this is marked as "Limit = yes" in Table A or indicated as a V-shaped triangle in Figure 5.3. These photometric definitions follow the same physical interpretation as those adopted by Anderson et al. (2014b), who also identify the plateau phase through changes in the light-curve slope and characterize the transition to the radioactive tail using the steep post-plateau decline. Our implementation differs in that we use the derivatives of the lightcurve to define these transitions in a fully automated and objective way, whereas Anderson et al. (2014b) relied on parametric spline fits and visually guided measurements for some phases. The data and code used for these measurements will be made publicly available on `Zenodo` and `GitHub` upon publication. The criteria are summarized in Table A.

Measuring H I velocities

We derive expansion velocities of the H I λ6563 line by measuring the minima of the absorption troughs in the P-Cygni profiles. A third-order polynomial is fit to the region surrounding the absorption minimum to estimate the velocity. For spectra with low resolution or strong host-galaxy contamination, we manually inspect and

identify the minimum. Uncertainties are estimated via a Monte Carlo method. We first compute a noise spectrum by subtracting a heavily smoothed version of the original spectrum; the standard deviation of this residual defines the spectral noise. We then generate perturbed realizations by adding Gaussian noise of equal standard deviation to the smoothed spectrum and remeasure the velocity for each realization. The 1σ spread in the resulting velocity distribution is adopted as the measurement uncertainty. Only measurements with a standard deviation less than 50% of their velocity are considered reliable and included. The measured velocities and their errors are documented in Table L.

We find that LLIIP SNe exhibit systematically lower H I λ6563 velocities compared to their higher-luminosity counterparts at all phases Figure 5.4. We fit a power-law of the form $V(t) = A\,t^{-s}$ to the binned velocity measurements. Photospheric velocities in Type II SNe are expected to follow a power-law decline during the plateau phase due to homologous expansion and the recession of the recombination front (e.g., Kasen and Woosley 2009). The best-fit relations are shown in Figure 5.4. For the LLIIP sample, we obtain $V(t) = (14.9 \pm 1.3)\,t^{-0.25\pm0.05}$, and for the full sample $V(t) = (26.2 \pm 2.1)\,t^{-0.32\pm0.05}$, where V is in units of 10^3 km s^{-1} and t is the phase in days since explosion.

In principle, Fe II λ5169 is a better tracer of the photospheric velocity than H I (e.g., Dessart and Hillier 2005). However, most of our spectra were obtained with SEDM at $R \sim 100$, and we do not have sufficient resolution and SNR to robustly measure the Fe II λ5169 absorption profile in most cases. We therefore use the Hα velocity as a practical proxy. When needed for comparison with studies that quote Fe II velocities, we employ the empirical scaling relation between Hα and Fe II derived by Faran et al. (2014a),

$$v_{\mathrm{Fe\,II}} = (0.855 \pm 0.006)\,v_{\mathrm{H}\alpha} - (1499 \pm 87)\ \mathrm{km\ s^{-1}},$$

to estimate the corresponding Fe II velocity. These measured slopes ($s \approx 0.2$–0.4) lie within the range of shallow power-law declines inferred for Type II SN photospheric velocities in previous observational studies (e.g., Faran et al. 2014a, de Jaeger et al. 2019a, Lin et al. 2024). While both LLIIP SNe and brighter IIP SNe show comparable decline rates, LLIIP SNe exhibit lower velocities. At 50 days post-explosion, the average velocity inferred from these fits is approximately 5900 ± 1200 km s^{-1} for LLIIP SNe and 8440 ± 2100 km s^{-1} for SNe with $M_r \geq -16$ mag. These velocities are broadly consistent with those reported for Type II SNe in the literature (Faran et al. 2014a, de Jaeger et al. 2019a, Lin et al. 2024).

Bolometric Luminosity

First, we measure the bolometric luminosity of the SNe in our sample. Since we only have the g- and r-band magnitudes available for most of the SNe in our sample, we estimate the bolometric luminosities using the bolometric correction (BC) approach from Lyman et al. (2014) to estimate the bolometric magnitudes:

$$\mathrm{BC}_g = 0.053 - 0.089 \times (g - r) - 0.736 \times (g - r)^2$$

$M_{bol} = BC_g + M_g$, where M_{bol} is the bolometric magnitude, and M_g is the absolute magnitude of the SN in g-band filter. Jäger et al. (2020) and Yang et al. (2021) showed that the bolometric luminosity of LLIIP SNe measured by bolometric correction approach from Lyman et al. (2014) is similar to that obtained by fitting a blackbody function to multiband photometry, which supports the validity of the empirical correlation for the bolometric correction given by Lyman et al. (2014).

We bin the data into intervals of 2 days and use g- and r-band photometry to get the bolometric luminosity for that epoch. If only one band of photometry is available in a bin, then we use the color from the nearest epoch where photometry data for both bands is available within 10 days to calculate the bolometric luminosity.

The distribution of the plateau bolometric luminosity is shown in the left panel of Figure 5.5. The full sample has a median peak luminosity of $\log(L_{\mathrm{peak}}/\mathrm{erg\ s^{-1}}) = 42.33^{+0.38}_{-0.39}$. LLIIP SNe have lower peak luminosities with a median of $41.65^{+0.24}_{-0.21}$. We find a strong correlation between the mid-plateau bolometric luminosity (L_{mid}) and the nickel mass (Figure 5.5). The nickel mass is measured by fitting the radioactive tail (see Section 5.5). The best-fit relation is

$$\log L_{\mathrm{mid}} = (0.73 \pm 0.05)\ \log M_{\mathrm{Ni}} + (43.09 \pm 0.06),$$

with a Pearson correlation coefficient of $r = 0.89$ and a p-value $< 10^{-5}$. These luminosities are consistent with previous measurements for both normal and low-luminosity Type II SNe. Large-sample studies typically find mid-plateau bolometric luminosities of $\log L_{\mathrm{mid}} \sim 42.3$–$42.7$ erg s^{-1} for ordinary SNe IIP (e.g., Bersten and Hamuy 2009, Pejcha and Prieto 2015, Valenti et al. 2016), whereas underluminous events such as SN 1997D, SN 2005cs, and SN 2008bk exhibit significantly fainter plateaus with $\log L_{\mathrm{mid}} \sim 41.4$–$41.7$ erg s^{-1} (Spiro et al. 2014). The tight correlation we find between L_{mid} and M_{Ni} is also consistent with earlier work showing that fainter plateau luminosities correspond to smaller ^{56}Ni yields (Hamuy 2003, Pejcha and Prieto 2015, Müller et al. 2017, Martinez et al. 2022b).

Estimating physical and explosion parameters

In order to estimate progenitor and explosion parameters of the Type IIP sample, we use semi-analytic models Nagy and Vinkó (2016) and radiation hydrodynamical models from Moriya et al. (2023). We also use scaling relations from Goldberg et al. (2019) to constrain the explosion parameters of LLIIP SNe.

Lightcurve fitting to Semi-analytical models

The model in Nagy and Vinkó (2016) is based on a two-component configuration consisting of a uniform dense stellar core and an extended low-mass envelope where the density decreases as an exponential function. Nagy and Vinkó (2016), Jäger et al. (2020) claim that the results from the two-component semi-analytic LC model are consistent with current state-of-the-art calculations for Type II SNe. They are useful to derive estimates or constraints of basic parameters like the explosion energy, ejected mass, and initial radius of the progenitor as well as the amount of synthesized radioactive nickel. The model assumes spherical symmetry and do not adequately model the initial transient behavior at early stages ($t < 20$ days). Thus, we only fit for lightcurve data 20 days after the explosion. We use the MCMC routine in Jäger et al. (2020) to fit these semi-analytical expressions. The Python code used for these fits will be made available on GitHub after publication. The nickel mass is measured from the lightcurve tail by fitting for both the nickel mass and the gamma-ray trapping efficiency parameter as free parameters. The priors used for the fits are shown in Table B. We fit the semi-analytic models to Type IIP SNe. After marginalization, we have estimates with confidence intervals (1σ) for each of these parameters. The best-fit values for each SN are listed in Table D. The sample statistics are summarized in Table C.

Lightcurve fitting to radiation-hydrodynamical Type II model grids

Moriya et al. (2023) presented a comprehensive model grid containing 228,016 synthetic Type II SN light curves, based on calculations using the radiation-hydrodynamical code STELLA. This set of model grids has previously been used in Subrayan et al. (2023) and Silva-Farfán et al. (2024) to infer explosion parameters for a sample of 45 and 186 Type II SNe, respectively. Here we also include previously unpublished models for lower-mass progenitors ($9, 10$ $M_\odot$) with low explosion energies (1.0, 2.0, 3.0, 4.0, $\times 10^{50}$erg). The overall parameter space covered by the model grid is progenitor masses (9, 10, 12, 14, 16, and 18 $M_\odot$ at the zero-age main sequence

(ZAMS), solar metallicity), explosion energies (0.5, 1.0, 1.5, 2.0, 2.5, 3.0, 3.5, 4.0, 4.5, and 5.0×10^{51} erg), nickel masses (0.001, 0.01, 0.02, 0.04, 0.06, 0.08, 0.1, 0.2, and 0.3 $M_\odot$), mass-loss rates ($10^{-5.0}$, $10^{-4.5}$, $10^{-4.0}$, $10^{-3.5}$, $10^{-3.0}$, $10^{-2.5}$, $10^{-2.0}$, $10^{-1.5}$, and $10^{-1.0}$ $M_\odot$ yr^{-1} with a wind velocity of 10 km s^{-1}), circumstellar matter radii (1, 2, 4, 6, 8, and 10×10^{14}cm), and ten circumstellar structures (β = 0.5, 1.0, 1.5, 2.0, 2.5, 3.0, 3.5, 4.0, 4.5, and 5.0), where β is a wind structure parameter determined by the efficiency of wind acceleration (Moriya et al. 2023). The radioactive nickel is assumed to be uniformly mixed up to half the mass of the hydrogen-rich envelope.

We use this model grid to measure the explosion parameters of the CLU Type IIP SNe. Using Bayesian Inference methods requires the models to be finely sampled within the parameter space. However, because the model grid is discrete and non-uniform, we extrapolate the model parameter by doing a weighted average of the model magnitudes weighted by the separation of the vector space of the nearest-neighbour models from the model vector to be sampled. For a given parameter vector $\vec{\theta}$, the method finds the closest models $\vec{\theta}_{close}$ and weighs them appropriately using

$$m(t, \vec{\theta}) = \sum_{\vec{\theta}_i \in \vec{\theta}_{close}} \hat{w}^{-1}(\vec{\theta}, \vec{\theta}_i) m(t, \vec{\theta}_i), \tag{5.1}$$

where $m(t, t_{\rm exp}, \vec{\theta})$ is the magnitude for a given $\vec{\theta}$ at time t, where

$$w(\vec{\theta}, \vec{\theta}_i) = \left(\prod_j \left| \theta^j - \theta_i^j \right| \right) \left(\left| \theta^j - \theta_i^j \right|_{\rm average} \right)^{-1}. \tag{5.2}$$

The priors used for the fits are shown in Table C. The Python code used for these fits will be made available on GitHub after publication. The best-fit values for each SN are listed in Table E. The sample statistics are summarized in Table D.

The best-fit model lightcurves are shown in Figures 5.6 and 5.7. The distribution of the best-fit parameters are shown in Figures 5.8 and 5.9.

Scaling Relations

Scaling relations have been commonly used to infer explosion parameters from lightcurve observables (Popov 1993, Kasen and Woosley 2009). Ejecta mass ($M_{\rm ej}$), progenitor radius (R), and explosion energy (E) are commonly used as the primary independent variables in scaling relations. In this paper, we use scaling relations derived by Goldberg et al. (2019). We use the following relations to constrain the

ejected mass ($M_{10} \equiv M_{\rm ej}/10\,M_\odot$) and explosion energy ($E_{51} \equiv E_{\rm exp}/10^{51}$ erg) as a function of progenitor radius ($R_{500} \equiv R/500\,R_\odot$), via the following relations:

$$\begin{aligned}\log(E_{51}) = &-0.728 + 2.148\log(L_{42}) - 0.280\log(M_{\rm Ni}) \\ &+ 2.091\log(t_{\rm p,2}) - 1.632\log(R_{500}), \qquad (5.3)\\ \log(M_{10}) = &-0.947 + 1.474\log(L_{42}) - 0.518\log(M_{\rm Ni}) \\ &+ 3.867\log(t_{\rm p,2}) - 1.120\log(R_{500}), \qquad (5.4)\end{aligned}$$

where $M_{\rm Ni}$ is in units of $M_\odot$, $L_{42} = L_{50d}/10^{42}$ erg s^{-1}, L_{50d} is the plateau luminosity 50 days after explosion and $t_{\rm p,2} = t_{\rm p}/100$ days. Here, $t_{\rm p}$ is measured from the parametric fit to the bolometric lightcurve using the following equation used in Goldberg et al. (2019), Valenti et al. (2016):

$$\log(L_{\rm bol}(t)) = \frac{-A_0}{1 + \exp\left(\frac{t-t_{\rm p}}{W_0}\right)} + P_0 t + M_0, \qquad (5.5)$$

where $t_{\rm p}$ represents the inflection point of the lightcurve and corresponds to the midpoint of the plateau-to-tail transition.

The constraints for LLIIP SNe thus obtained are discussed in Section 5.6.

5.6 Results

In this section, we summarize the results obtained using the analysis techniques described above. The best-fit radiation-hydrodynamical values for each SN are listed in Table E, and the sample statistics are summarized in Table D. Similarly, the best-fit values from the semi-analytical modeling are given in Table D, with the corresponding sample statistics summarized in Table C.

Observed Parameters

The observed parameters in the r-band and their errors are shown in Table A. The sample statistics are shown in Table B. The lower and upper uncertainties correspond to the 16th and 84th percentiles, respectively. The distributions of these observed parameters are shown in Figure 5.2.

For LLIIP SNe ($M_r > -16$), the median plateau duration was 89^{+10}_{-20} days, with a range of 64 to 108 days. The median duration of the optically thick phase (OPTd) was 99^{+11}_{-14} days, spanning from 67 to 116 days. The median rise time was 13^{+1}_{-2} days, with a range from 10 to 16 days. The median plateau slope was $0.1^{+0.1}_{-0.2} \times 10^{-2}$ mag day^{-1}, ranging from -0.4 to 0.6×10^{-2} mag day^{-1}. Finally, the change in magnitude

Parameter	Sample	Median	Range
Plateau Duration (days)	$M_r \geq -16$	89^{+10}_{-20}	64–108
	$M_r < -16$	75^{+16}_{-15}	47–137
	All	76^{+16}_{-16}	47–137
OPTd (days)	$M_r \geq -16$	99^{+11}_{-14}	67–116
	$M_r < -16$	88^{+17}_{-20}	52–157
	All	90^{+16}_{-20}	52–157
Rise Time (days)	$M_r \geq -16$	13^{+1}_{-2}	10–16
	$M_r < -16$	13^{+5}_{-2}	7–22
	All	13^{+4}_{-2}	7–22
Plateau Slope ($\times$0.01 mag day^{-1})	$M_r \geq -16$	$0.1^{+0.1}_{-0.2}$	-0.4–0.6
	$M_r < -16$	$0.5^{+0.6}_{-0.4}$	-0.1–2.0
	All	$0.4^{+0.5}_{-0.4}$	-0.4–2.0
Plateau - Tail Drop (mag)	$M_r \geq -16$	$-1.33^{+1.25}_{-0.72}$	-2.48–0.22
	$M_r < -16$	$-1.33^{+0.42}_{-0.35}$	-3.50—0.09
	All	$-1.33^{+0.46}_{-0.41}$	-3.50–0.22

Table B: Summary of r-band lightcurve observables, divided into faint ($M_r \geq -16$), bright ($M_r < -16$), and the full sample. Median values with uncertainties and full observed ranges are shown. Plateau slopes are scaled by a factor of 10^{-2} mag day^{-1}.

between the plateau and the radioactive tail had a median value of $-1.33^{+1.25}_{-0.72}$ mag, with observed values ranging from -2.48 to -0.22 mag. For the full Type IIP SN sample, the median values were 76^{+16}_{-16} days for the plateau duration, 90^{+16}_{-20} days for OPTd, 13^{+4}_{-2} days for the rise time, $0.4^{+0.5}_{-0.4} \times 10^{-2}$ mag day^{-1} for the plateau slope, and $-1.33^{+0.46}_{-0.41}$ mag for the plateau-to-tail drop. The steepest drop of > 3.50 mag was seen in SN 2022aagp, shown in Figure 5.10. A sharp decline from the plateau to the tail is predicted for ECSNe and failed SNe with very low or zero nickel mass (see e.g., Tominaga et al. 2013, Turatto et al. 1998). Other objects with sharp drops include SN 2021tyw (> 3.10 mag), SN 2022prv (2.56 mag), SN 2023vog (2.49 mag) and SN 2020cxd (2.48 mag).

We further investigated how the lightcurve observables correlate with peak magnitude. As shown in Figure 5.3, the plateau slope shows a strong correlation with peak brightness, with a Pearson correlation coefficient of $r = -0.68$ ($p < 10^{-5}$). The best-fit line is given by:

$$\begin{aligned}\text{Plateau slope (0.01 mag day}^{-1}) = (-0.33 \pm 0.04)\, M_r \\ + \ (-4.93 \pm 0.70)\end{aligned}$$

Brighter SNe tend to have steeper plateau slopes, indicating more rapid declines

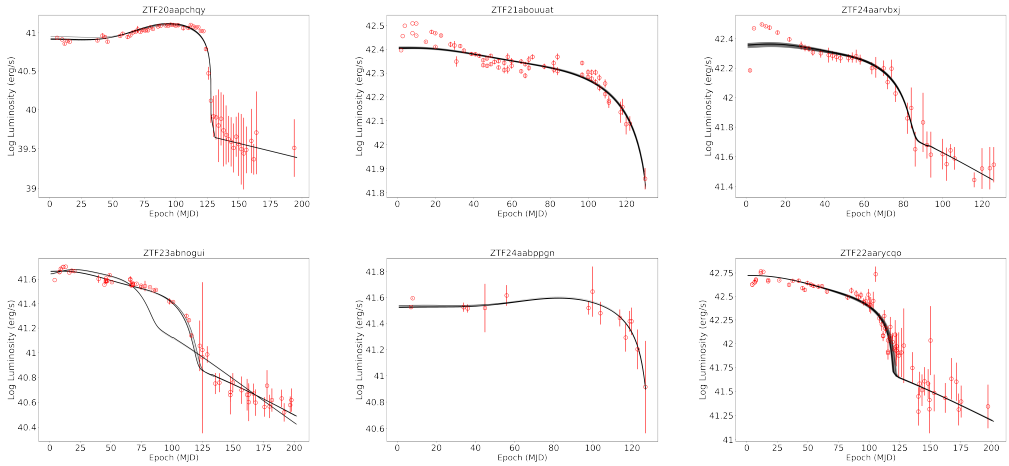

Figure 5.6: Bolometric light curve fits using semi-analytical models from Nagy and Vinkó (2016). Red dots show the observed bolometric luminosities, while black lines represent the best-fit model lightcurves. The panels show (left to right, top to bottom): ZTF20aapchqy (SN 2020cxd), ZTF21abouuat (SN 2021ucg), ZTF24aarvbxj (SN 2024lby), ZTF23abnogui (SN 2023wcr), ZTF24aabppgn (SN 2024wp), and ZTF22aarycqo (SN 2022ojo).

during the plateau phase. We also note that a major fraction of LLIIP SNe have positive slope. The plateau duration shows only a weak correlation with peak magnitude (r = 0.42). The plateau durations for faint and bright SNe span a broad range and overlap significantly. The physical implications for these results are discussed in Section 5.7.

Progenitor and explosion parameters

Nickel mass

For the semi-analytical model fits, the nickel mass is measured only for SNe with a distinct radioactive tail. Within the LLIIP subsample, the median nickel mass is $0.0132^{+0.0089}_{-0.0100}$ $M_\odot$, spanning 0.0009–0.0420 $M_\odot$. The lowest value in our sample is that of SN 2020cxd, with $M_{\rm Ni}$ = 0.0009 $M_\odot$. For the full Type IIP sample, the semi-analytical fits yield a median nickel mass of $0.065^{+0.068}_{-0.047}$ $M_\odot$ (range 0.0009–0.3098 $M_\odot$). The radiation-hydrodynamical fits of Moriya et al. (2023) give broadly consistent values, with a median of $0.038^{+0.059}_{-0.024}$ $M_\odot$ for the full sample and $0.013^{+0.003}_{-0.010}$ $M_\odot$ for the LLIIP subsample. Rodríguez et al. (2021) studied 110 events and found ^{56}Ni masses between 0.005–0.177 $M_\odot$ (average 0.037 ± 0.005 $M_\odot$). Martinez et al. (2022b) reported 0.006–0.069 $M_\odot$ (median $\sim$ 0.036 $M_\odot$) from 17 SNe, while Pejcha and Prieto (2015) and Müller et al. (2017) obtained similar

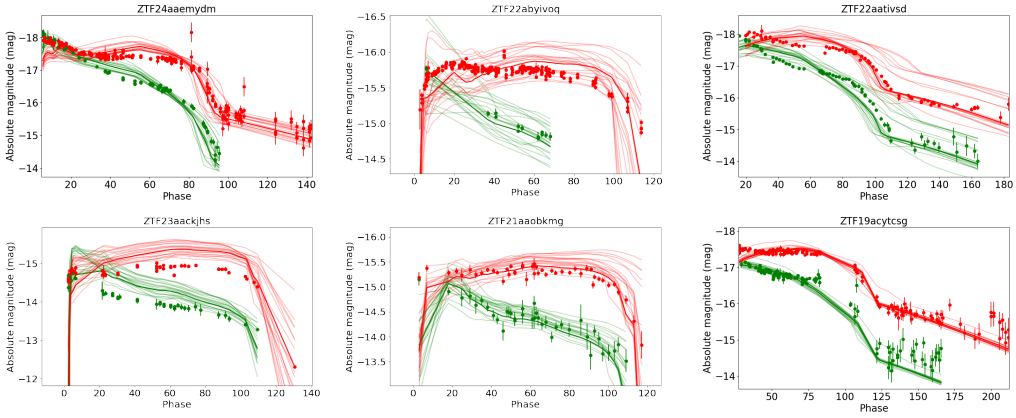

Figure 5.7: Radiation-hydrodynamical model fits to the r- and g-band light curves using the model grid from Moriya et al. (2023). The model grid in Moriya et al. (2023) has been extended to include 9 $M_\odot$ and 10 $M_\odot$ progenitors with explosion energies in the range $(1\text{–}5)\times10^{50}$ erg. The panels show (left to right, top to bottom): ZTF24aaemydm (SN 2024chx), ZTF22abyivoq (SN 2022acko), ZTF22aativsd (SN 2022ovb), ZTF23aackjhs (SN 2023bvj), ZTF21aaobkmg (SN 2021eui) and ZTF19acytcsg (SN 2019wvz).

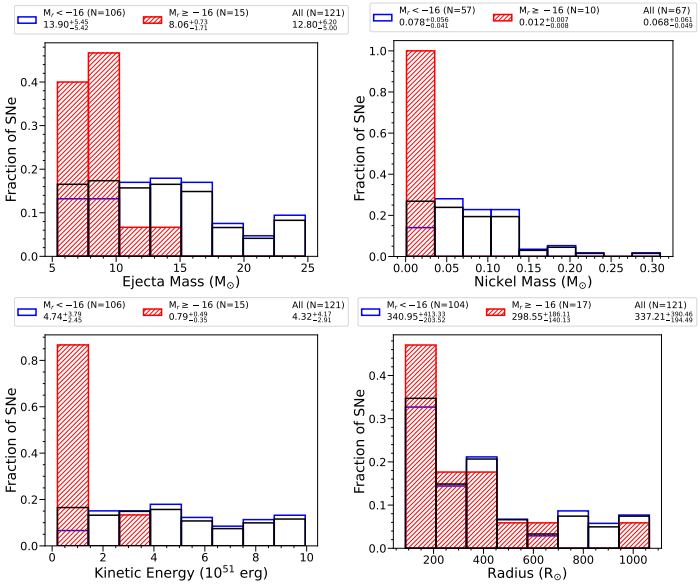

Figure 5.8: Distributions of ejecta mass, nickel mass, explosion energy, and radius using semi-analytical models from Nagy and Vinkó (2016). LLIIP SNe with $M_r \geq -16$ are shown in hatched red, SNe IIP with $M_r < -16$ in blue, and the full sample is shown in black.

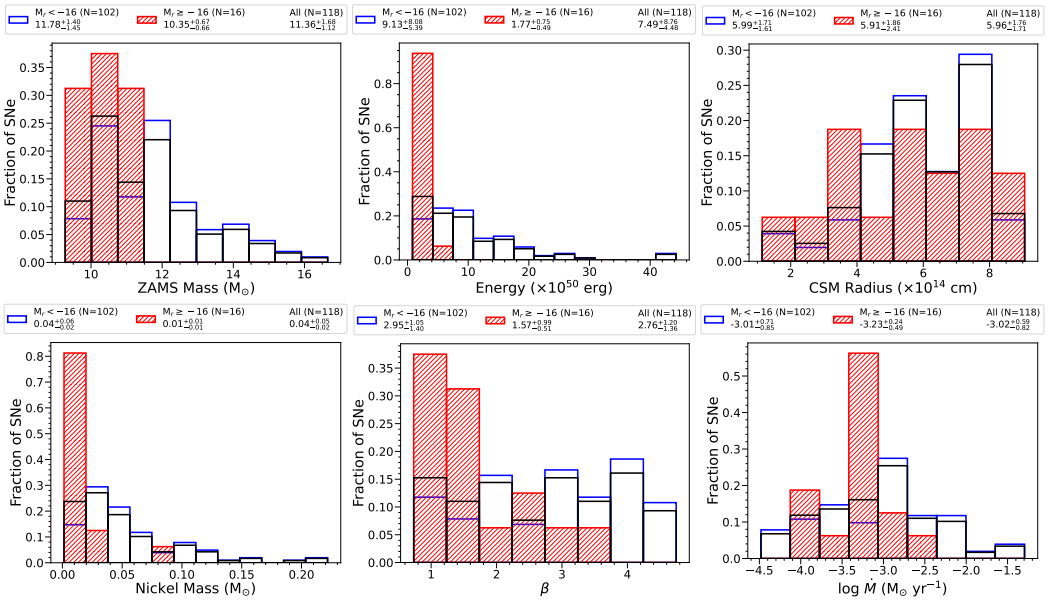

Figure 5.9: Distributions of the ZAMS mass, explosion energy, CSM radius, nickel mass, CSM structure parameter, and mass loss rates using radiation-hydrodynamical models from Moriya et al. (2023). LLIIP SNe with $M_r \geq -16$ are shown in hatched red, those with $M_r < -16$ in blue, and the full sample is shown in black.

medians (~0.03 $M_\odot$) with maxima reaching 0.28 $M_\odot$. Subrayan et al. (2023) measured Ni masses for 45 SNe, with only a single object as low as 0.01 $M_\odot$, while most lie between 0.02 and 0.1 $M_\odot$. Anderson (2019) found a broad distribution (0.001–0.360 $M_\odot$), and Hamuy (2003) reported 0.0016–0.26 $M_\odot$ from 21 SNe. In comparison with these literature samples, the LLIIP SNe in our sample clearly occupy the low end of the nickel-mass distribution. Their very small ^{56}Ni yields are consistent with expectations for explosions of low-mass red supergiant progenitors or events experiencing significant fallback, as discussed in Section 5.7.

Explosion energy

From the Moriya et al. (2023) radiation-hydrodynamical fits, the LLIIP SNe show low explosion energies, with a median of $0.17^{+0.07}_{-0.03} \times 10^{51}$ erg and a range of 0.10–0.28×10^{51} erg. For the full Type IIP sample, the median energy is $0.76^{+0.89}_{-0.44}$×10^{51} erg. In contrast, the semi-analytical Nagy and Vinkó (2016) models yield systematically higher values, with a median of $0.79^{+0.49}_{-0.35} \times 10^{51}$ erg for the LLIIP subsample (range 0.21–3.64×10^{51} erg) and $4.32^{+4.17}_{-2.91} \times 10^{51}$ erg for the full sample (range 0.21–9.94×10^{51} erg). We note that both the ejecta masses and explosion energies from the semi-analytical fits tend to be higher, likely due to the two-component density

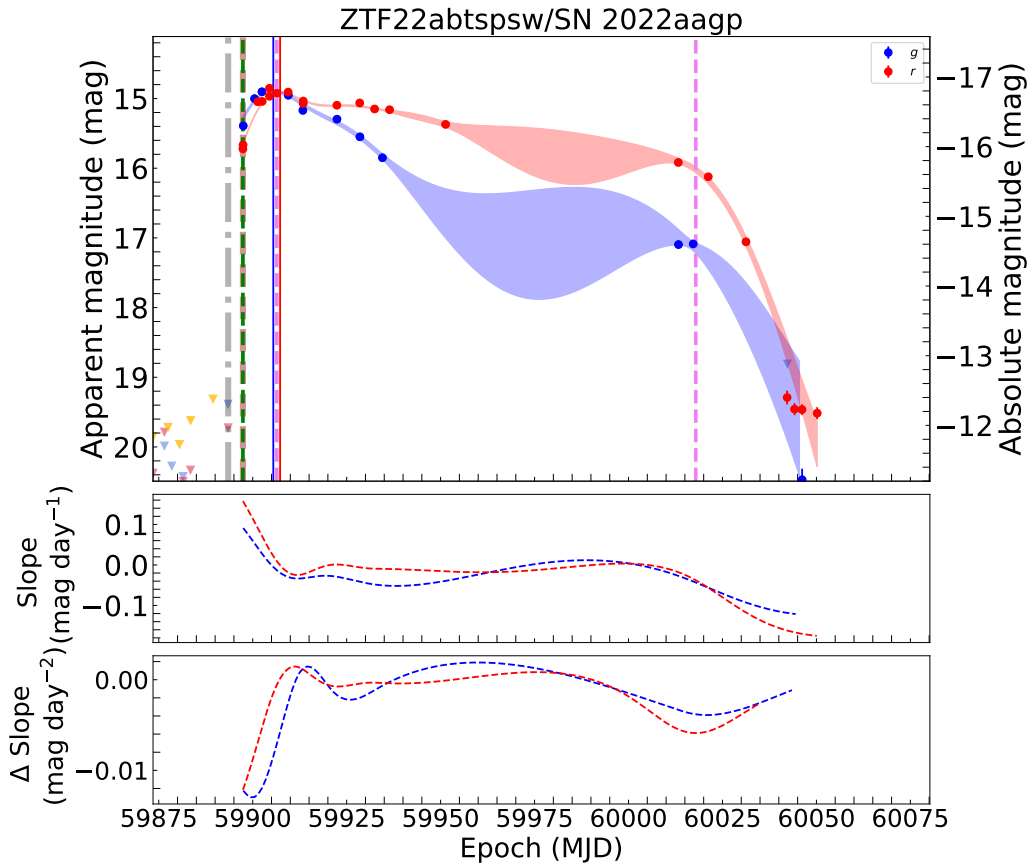

Figure 5.10: The r- and g-band lightcurve of ZTF22abtspsw/SN 2022aagp with GP fits (shaded regions). Vertical lines mark key epochs: first detection (dashed red), explosion epoch (dashed grey), r- and g-band peaks (solid red and blue), plateau start and end (solid violet), and 50% peak flux (dashed green). The lower panels show the light curve slope (mag day^{-1}) and its change (Δ slope, mag day^{-2}). The steepest observed drop of > 3.5 mag was seen in this SN, consistent with predictions for ECSN and failed SNe with little or no nickel mass.

profile assumed in these models; the caveats are discussed further in Section 5.7. In the literature, Hamuy (2003) measured 0.6–5.5×10^{51} erg for 21 Type II SNe, while Utrobin and Chugai (2019) and Pumo et al. (2017) obtained up to 1.4–2.0×10^{51} erg. Martinez et al. (2022b) report a median of 0.61×10^{51} erg (range 0.30–1.01×10^{51} erg). The LLIIP SNe in our sample clearly occupy the low-energy end, clustering just above 10^{50} erg, and may in some cases fall below the model grid minimum of 0.1×10^{51} erg. This supports interpretations in which LLIIP SNe arise from weak explosions of low-mass cores (see Section 5.7).

Ejecta mass/ZAMS mass

The semi-analytical models yield ejecta masses of 5.73–12.89 $M_\odot$ for the LLIIP sample, with a median of $8.06^{+0.73}_{-1.71}$ $M_\odot$. For the full Type IIP sample, the corresponding median ejecta mass is $12.80^{+6.20}_{-5.00}$ $M_\odot$, spanning 5.41–24.79 $M_\odot$. In earlier studies, Martinez et al. (2022b) report a typical ejecta mass of ∼9.2 $M_\odot$ (16–84 percentile range 8.2–12.7 $M_\odot$), while Utrobin and Chugai (2019) infer somewhat higher masses up to ∼14.8 $M_\odot$. Even larger values were found by Hamuy (2003), who estimated ejecta masses in the range 14–56 $M_\odot$ for some Type II SNe. LLIIP SNe lie at the lower end of these distributions, consistent with expectations for low-mass RSG or sAGB progenitors, or for progenitors that have experienced significant envelope stripping prior to core collapse. ZAMS masses inferred in Subrayan et al. (2023) and Silva-Farfán et al. (2024) span 12–16 $M_\odot$, with a steep IMF placing most objects near ∼12 $M_\odot$. From our radiation-hydrodynamical fits, the LLIIP SNe are inferred to arise from relatively low-mass progenitors, with ZAMS masses typically < 12 $M_\odot$ and a median of $10.5^{+0.4}_{-0.7}$ $M_\odot$. For the full Type II sample, the median ZAMS mass is $11.5^{+1.6}_{-1.2}$ $M_\odot$. Thus, the LLIIP subsample lies toward the low-mass end of the progenitor-mass distribution, reinforcing the picture that the faintest events originate from the lowest-mass core-collapse progenitors.

Progenitor radius

The progenitor radii inferred from the semi-analytical fits for the LLIIP SNe span 138–1024 $R_\odot$, with a median of 299^{+219}_{-142} $R_\odot$. For the full Type IIP sample, the corresponding median is 337^{+390}_{-194} $R_\odot$. These radii are smaller than those typically inferred for normal Type II SNe in the literature. For example, Martinez et al. (2022b) report progenitor radii of 460–610 $R_\odot$, with a median of ∼495 $R_\odot$, while Hamuy (2003) found a broad range of 80–600 $R_\odot$ using hydrodynamical modeling. More recently, Irani et al. (2024) identified a bimodal distribution in breakout radii for 34 SNe II, with roughly half of the sample preferring compact radii ($< 10^{14}$ cm) and the other half favoring larger radii ($> 10^{14}$ cm), consistent with substantial diversity in outer-envelope structure among RSG progenitors. For additional context, the radius distribution of 74 Galactic RSGs spans 100–2135 $R_\odot$ with a median of 625^{+393}_{-275} $R_\odot$ (Levesque et al. 2005). Thus, these results suggest that LLIIP progenitors are either intrinsically more compact RSGs, or that their outer hydrogen envelopes have been partially stripped through binary interaction.

Progenitor mass-loss

The radiation-hydrodynamical modeling yields median pre-explosion mass-loss rates of $\log \dot{M} = -3.01^{+0.83}_{-0.60}$ $M_\odot$ yr^{-1} for the full sample, and $\log \dot{M} = -3.32^{+0.37}_{-0.26}$ for the LLIIP subsample. Our results agree well with those of Subrayan et al. (2023) and Silva-Farfán et al. (2024), who report mass-loss rates in the range 10^{-4}–10^{-2} $M_\odot$ yr^{-1} for samples of Type II SNe. The systematically smaller mass-loss rates of the LLIIP subsample may reflect weaker winds or shorter-lived mass-loss episodes prior to explosion. The corresponding CSM radii inferred from the radiation-hydrodynamical fits span 1.1–8.6 $\times 10^{14}$ cm, with a median of $5.8^{+1.9}_{-1.6} \times 10^{14}$ cm for the full sample and $4.3^{+3.0}_{-1.0} \times 10^{14}$ cm for the LLIIP events, indicating an extended circumstellar environment that can influence early-time lightcurve and spectra (e.g., Galbany et al. 2016, Valenti et al. 2016, Förster et al. 2018, Morozova et al. 2018, Bruch et al. 2021, 2023, Jacobson-Galán et al. 2024, Hinds et al. 2025, Jacobson-Galán et al. 2025a).

Parameter	Sample	Median	Range
$M_{\rm Ni}$ (0.01 $M_\odot$)	$M_r \geq -16$	$1.32^{+0.89}_{-1.00}$	0.09–4.20
	$M_r < -16$	$7.36^{+6.36}_{-4.80}$	0.56–30.98
	All	$6.52^{+6.80}_{-4.71}$	0.09–30.98
$M_{\rm ej}$ ($M_\odot$)	$M_r \geq -16$	$8.06^{+0.73}_{-1.71}$	5.73–12.89
	$M_r < -16$	$13.90^{+5.45}_{-5.42}$	5.41–24.79
	All	$12.80^{+6.20}_{-5.00}$	5.41–24.79
$E_{\rm kin}$ (10^{51} erg)	$M_r \geq -16$	$0.79^{+0.49}_{-0.35}$	0.21–3.64
	$M_r < -16$	$4.74^{+3.79}_{-2.45}$	1.04–9.94
	All	$4.32^{+4.17}_{-2.91}$	0.21–9.94
R ($R_\odot$)	$M_r \geq -16$	299^{+219}_{-142}	138–1024
	$M_r < -16$	340^{+407}_{-202}	88–1065
	All	337^{+390}_{-194}	88–1065

Table C: Best-fit physical parameters derived from semi-analytical model fits (Nagy and Vinkó 2016) for faint ($M_r \geq -16$), bright ($M_r < -16$), and all Type IIP SNe. Reported values include the median and 16th/84th percentile uncertainties, along with the full observed range. Nickel masses are scaled by a factor of 10^{-2} $M_\odot$.

Scaling Relations

We investigate the physical properties of the low-luminosity Type IIP (LLIIP) SNe in our sample using scaling relations between plateau luminosity, nickel mass, duration, and progenitor radius. The constraints for LLIIP SNe thus obtained are shown in Figure 5.11. At a representative radius of 500 $R_\odot$, we find that the LLIIP

Parameter	Sample	Median	Range
$E_{\rm exp}$ (10^{51} erg)	$M_r \geq -16$	$0.17^{+0.07}_{-0.03}$	0.10–0.28
	$M_r < -16$	$0.91^{+0.81}_{-0.54}$	0.16–4.43
	All	$0.76^{+0.89}_{-0.44}$	0.10–4.43
$R_{\rm CSM}$ (10^{14} cm)	$M_r \geq -16$	$4.3^{+3.0}_{-1.0}$	1.8–8.6
	$M_r < -16$	$5.8^{+1.9}_{-1.4}$	1.1–8.4
	All	$5.8^{+1.9}_{-1.6}$	1.1–8.6
$M_{\rm Ni}$ (0.01 $M_\odot$)	$M_r \geq -16$	$1.3^{+0.3}_{-1.0}$	0.1–2.5
	$M_r < -16$	$4.1^{+5.9}_{-2.1}$	0.2–22.2
	All	$3.8^{+5.9}_{-2.4}$	0.1–22.2
$M_{\rm ZAMS}$ ($M_\odot$)	$M_r \geq -16$	$10.5^{+0.4}_{-0.7}$	9.4–11.0
	$M_r < -16$	$11.8^{+1.4}_{-1.4}$	9.3–16.7
	All	$11.5^{+1.6}_{-1.2}$	9.3–16.7
$-\log\ \dot{M}$ ($M_\odot$ yr^{-1})	$M_r \geq -16$	$3.32^{+0.37}_{-0.26}$	2.86–4.37
	$M_r < -16$	$3.00^{+0.85}_{-0.72}$	1.29–4.48
	All	$3.01^{+0.83}_{-0.60}$	1.29–4.48

Table D: Best-fit physical parameters derived from radiation-hydrodynamical model fits (Moriya et al. 2023) for faint ($M_r \geq -16$), bright ($M_r < -16$), and all Type IIP SNe. Reported values include the median and 16th/84th percentile uncertainties, along with the full observed range.

SNe are characterized by relatively low ejecta masses ranging from ~ 2.1 to ~ 6.5 $M_\odot$ and low explosion energies between ~ 0.02 and $\sim 0.20 \times 10^{51}$ erg. These results reinforce the picture that LLIIP SNe arise from low-mass progenitors undergoing weak explosions, consistent with those derived from semi-analytical and radiation-hydrodynamical analysis.

5.7 Discussion

LLIIP SNe exhibit less steep gradients, with most displaying upward slopes

We first attempt to explain the positive slope seen in LLIIP SNe through basic order-of-magnitude arguments. In standard Type IIP models such as Popov (1993), the onset of the plateau is set by hydrogen recombination, where the luminosity reaches

$$L_{\rm pl} = 4\pi R_{\rm ej}^2 \sigma T_I^4, \tag{5.6}$$

with $T_I \approx 5000$ K being the hydrogen recombination temperature. For low-luminosity plateaus, this implies a smaller ejecta radius at the onset of the plateau phase, since

$$R_{\rm ej} \propto L_{\rm pl}^{1/2}. \tag{5.7}$$

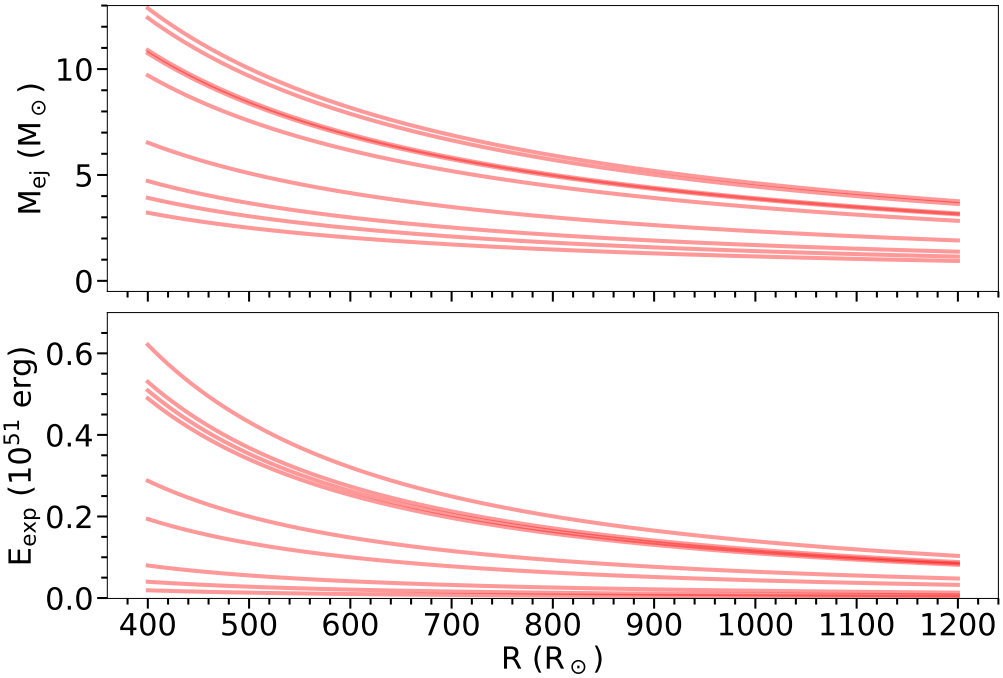

Figure 5.11: Ejecta mass (top) and explosion energy (bottom) versus progenitor radius, derived using the scaling relations from Goldberg et al. (2019). Red lines denote SNe with $M_r > -16$

This is consistent with the lower expansion velocities observed in LLIIP SNe compared to more luminous events, resulting in smaller ejecta radius.

The photon diffusion time at this stage is given by

$$t_{\rm diff,onset} \sim \frac{\kappa M_{\rm ej}}{4\pi R_{\rm ej} c} \propto M_{\rm ej} L_{\rm pl}^{-1/2}, \tag{5.8}$$

and can be estimated as

$$t_{\rm diff,onset} \sim 200 \text{ days} \left(\frac{\kappa}{0.34 \text{ cm}^2 \text{ g}^{-1}}\right) \left(\frac{M_{\rm ej}}{8\ M_\odot}\right) \times \left(\frac{L_{\rm pl}}{3 \times 10^{41} \text{ erg s}^{-1}}\right)^{-1/2}. \tag{5.9}$$

The diffusion time $t_{\rm diff}$ decreases with time as the ejecta expands, owing to both the dilution of density and the recombination-driven reduction in opacity.

Following the explosion, the ejecta cool both adiabatically (on the dynamical timescale $t_{\rm dyn}$) and radiatively (on the diffusion timescale $t_{\rm diff}$). The plateau slope is governed by the ratio of these timescales. When $t_{\rm diff} \gg t_{\rm dyn}$, the internal energy

(dominated by radiation) evolves as

$$\frac{dE_{\rm int}}{dt} = -\frac{E_{\rm int}}{t} \quad \Rightarrow \quad E_{\rm int} \propto t^{-1}. \tag{5.10}$$

As the photosphere recedes, the emergent flux remains approximately blackbody at T_I, with the luminosity given by

$$4\pi R_{\rm ph}^2 \sigma T_I^4 = \frac{E_{\rm int}}{t_{\rm diff}} \approx \frac{E_{\rm int}}{\kappa M_{\rm ej}(r < R_{\rm ph})/(4\pi R_{\rm ph} c)}. \tag{5.11}$$

Assuming a uniform density profile in the inner ejecta, the mass enclosed within radius $R_{\rm ph}$ evolves as

$$M_{\rm ej}(r < R_{\rm ph}) \propto M_{\rm ej} \left(\frac{R_{\rm ph}}{t}\right)^3. \tag{5.12}$$

Combining the above, the photospheric radius evolves as

$$R_{\rm ph}(t) \propto \left(\frac{E_{\rm int}(t)\, t^3}{M_{\rm ej}}\right)^{1/4}. \tag{5.13}$$

Using $E_{\rm int}(t) \propto t^{-1}$, this simplifies to

$$R_{\rm ph}(t) \propto t^{1/2} M_{\rm ej}^{-1/4}, \tag{5.14}$$

and the luminosity becomes

$$L_{\rm pl}(t) = 4\pi R_{\rm ph}^2 \sigma T_I^4 \propto t M_{\rm ej}^{-1/2}. \tag{5.15}$$

Thus, rising plateaus can naturally emerge in the low-luminosity regime.

The notably flatter or slightly rising slopes in LLIIP SNe can also be explained by the contribution of ^{56}Ni decay to the plateau luminosity. In Figure 5.12, we show the radial density and mass profiles of 8–10 $M_\odot$ RSG and sAGB progenitors from the literature. The steeper mass density profiles of low-mass progenitors imply that the photospheric radius remains closer to the core of the star throughout the plateau phase (Sato et al. 2024). As a result, ^{56}Ni decay likely makes a stronger contribution to the overall plateau luminosity. Nakar et al. (2016) demonstrated that ^{56}Ni decay can contribute significantly ($\sim 10\%$) to the total luminosity during the photospheric phase, influencing the plateau slope. Although their models do not explicitly predict rising slopes, a combination of plateau extension and slope flattening could lead to an apparent increase in brightness over time as seen in SN 2016gfy (Singh et al. 2019). Kozyreva et al. (2019) supports this interpretation, showing that both

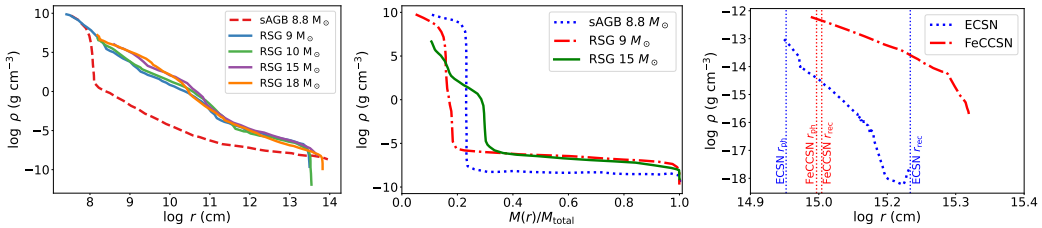

Figure 5.12: Left: Radial density profile of the 8 – 10 $M_\odot$ stellar progenitor models used in Utrobin et al. (2017), Kozyreva et al. (2021), Sato et al. (2024) Center: Density profile as a function of mass coordinate of the 8 – 10 $M_\odot$ stellar progenitor models used in Utrobin et al. (2017), Kozyreva et al. (2021) Right: Density profile of FeCCSN and ECSN models used in Sato et al. (2024). The radii of the photosphere (r_{ph}) and the recombination front (r_{rec}) at 40 days after explosion are indicated by vertical lines.

cooling-envelope emission and nickel distribution shape the late-time behavior of the plateau. However, we note that such ^{56}Ni-driven flattening or rising would not occur unless the progenitor radii were small. For larger progenitors, the recombination-powered luminosity would dominate and naturally decline with time, overpowering the modest nickel contribution. Thus, in the low-luminosity regime, the small radii and low explosion energies of LLIIP progenitors are necessary for ^{56}Ni decay to leave a visible imprint on the plateau slope. Furthermore, Kozyreva et al. (2021) find that ECSNe and low-mass CCSNe from 8–10 $M_\odot$ progenitors exhibit rising light curves in the V and redder bands during the first 50 days, followed by a plateau and a subsequent drop to the radioactive tail. This is consistent with the steadily rising r-band light curves observed in many LLIIP SNe.

Another possible contributor in the rise of the of the lightcurves could be explosion asymmetry. 3D simulations for a 9 $M_\odot$ by Stockinger et al. (2020) show that large nickel-rich plumes can distort the ejecta and drive faster expansion in some directions, which lifts the light curve during the initial decline to the plateau and the early phase of the plateau. However, for a large sample, such viewing-angle-dependent effects are expected to average out.

The plateau duration and peak magnitude are not correlated

Single-star models predict a strong correlation between peak brightness and plateau duration in Type II SNe (e.g., Kasen and Woosley 2009). However, the observed lack of such a correlation suggests that the stars undergo substantial pre-supernova mass loss, likely requiring additional processes such as binary interaction to ex-

plain the observed diversity, especially at the low-mass end. Eldridge et al. (2018), Hiramatsu et al. (2021a), Dessart et al. (2024) also find that binary stripping can explain the duration of plateau seen in Type II SNe lightcurves. This aligns with the increasing observational consensus that a significant number of massive stars are found in binary systems, with many of them undergoing interaction (e.g., Sana et al. 2012, Duchêne and Kraus 2013, Kobulnicky et al. 2014, Sana et al. 2014, GRAVITY Collaboration et al. 2018, Bordier et al. 2022, Guo et al. 2022). Also, Zapartas et al. (2019) estimate that 33–50% of all Type II SN progenitors undergo binary interaction, based on analytical estimates and population-synthesis simulations that track which progenitors exchange mass with a companion prior to explosion. Inferring the explosion and progenitor properties from the lightcurves using models that incorporate self-consistent progenitor evolution with binary effects will constrain the binary fraction and extent of stripping among massive stars that explode as core-collapse SNe.

Correlation of physical parameters

The physical parameters inferred for the sample exhibit a number of clear and physically informative correlations. Figures 5.13 and 5.14 summarize the trends between peak luminosity and the key explosion properties. For the Nagy and Vinkó (2016) semi-analytical fits, nickel mass, kinetic energy, and the energy-to-mass ratio all show strong negative correlations with peak absolute magnitude: fainter SNe systematically eject less ^{56}Ni, have lower kinetic energies, and have smaller specific energies. The trends follow the relations:

$$\log_{10}\left(\frac{M_{\rm Ni}}{M_\odot}\right) = (-0.39 \pm 0.04)M_r + (-7.95 \pm 0.71),$$

$$\log_{10}\left(\frac{E_{\rm kin}}{10^{51}\,{\rm erg}}\right) = (-0.28 \pm 0.03)M_r + (-4.17 \pm 0.46),$$

$$\log_{10}\left(\frac{E_{\rm kin}}{M_{\rm ej}}\right) = (-0.22 \pm 0.02)M_r + (-4.29 \pm 0.29),$$

with Pearson coefficients $|r| \approx 0.7$–0.8. These scalings extend the well-known luminosity–^{56}Ni relation (Hamuy 2003, Pejcha and Prieto 2015, Müller et al. 2017, Martinez et al. 2022b) to the faint end and show that LLIIP SNe occupy the faint, low-energy end of a continuous distribution.

The semi-analytical parameters also correlate with each other. The correlations among physical parameters inferred from the Nagy and Vinkó (2016) models are

shown in Figure 5.15. Nickel mass and kinetic energy are tightly linked ($r = 0.75$), consistent with the idea that more energetic explosions synthesize more ^{56}Ni. The empirical relation,

$$E_{\rm kin}\,[10^{51}\,{\rm erg}] = (22.37 \pm 3.70)\left(\frac{M_{\rm Ni}}{M_\odot}\right)^{0.63\pm0.05},$$

is consistent with predictions in neutrino-driven explosion models (Ebinger et al. 2019, Sukhbold et al. 2016, Bruenn et al. 2016, 2023, Sandoval et al. 2021, Bollig et al. 2021, Burrows et al. 2024), as shown in Figure 5.16. Kinetic energy also correlates strongly with ejecta mass ($r = 0.77$), following

$$E_{\rm kin}\,[10^{51}\,{\rm erg}] = (0.06 \pm 0.02)\left(\frac{M_{\rm ej}}{M_\odot}\right)^{1.63\pm0.13},$$

indicating that explosions with more massive ejecta tend to be more energetic. In contrast, radius and mass-loss rate show only weak or no correlations, implying greater diversity in envelope structure and pre-SN winds.

The correlations inferred from the Moriya et al. (2023) radiation-hydrodynamical models reveal the same trends, but with tighter relationships. Nickel mass and peak magnitude correlate with $r = -0.64$,

$$\log_{10}\left(\frac{M_{\rm Ni}}{M_\odot}\right) = (-0.25 \pm 0.03)\,M_r - (5.64 \pm 0.51),$$

and explosion energy shows an even stronger dependence on luminosity ($r = -0.88$):

$$\log_{10}\left(\frac{E_{\rm exp}}{\rm erg}\right) = (-0.35 \pm 0.02)\,M_r - (6.08 \pm 0.31).$$

The specific energy correlates most strongly with luminosity ($r = -0.91$),

$$\log_{10}\left(\frac{E_{\rm exp}}{M_{\rm ej}}\right) = (-0.38 \pm 0.02)\,M_r - (7.05 \pm 0.29).$$

As in the semi-analytical case, explosion energy and nickel mass are tightly linked ($r = 0.65$),

$$E_{\rm exp} = (5.7 \pm 1.4) \times \left(\frac{M_{\rm Ni}}{M_\odot}\right)^{0.63\pm0.08},$$

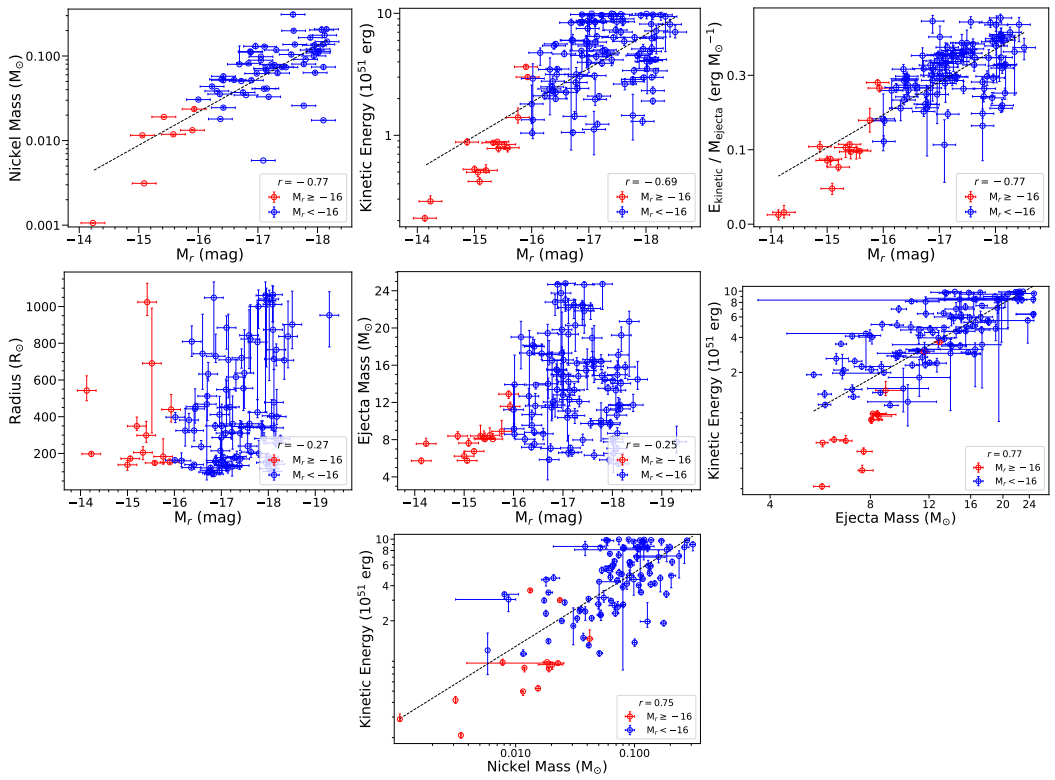

Figure 5.13: Correlations between peak r-band magnitude and physical parameters (nickel mass, explosion energy, energy per unit mass, radius, ejecta mass), and among the physical parameters themselves, based on semi-analytical models from Nagy and Vinkó (2016). LLIIP SNe with $M_r \geq -16$ are shown in red, SNe IIP with $M_r < -16$ in blue.

consistent with neutrino-driven simulations. Mass-loss rate shows no significant correlations ($r < 0.20$), suggesting that pre-SN winds and envelope stripping vary independently of the core properties that set the SN explosion physics. The overall distribution of the physical parameter correlations is summarized in Figures 5.13, 5.14, and the associated correlation matrices.

Caveats of the models

We caution that while the models employed to fit the lightcurves provide useful constraints and correlations, they also introduce several assumptions and systematic effects that may influence the derived parameters. We summarize these below.

A key challenge arises from the degeneracy between key parameters such as ejecta mass, explosion energy, and progenitor radius. Fitting models to photometry in only a couple of passbands allows multiple combinations of physical parameters to produce similar light curves. This degeneracy limits our ability to extract unique

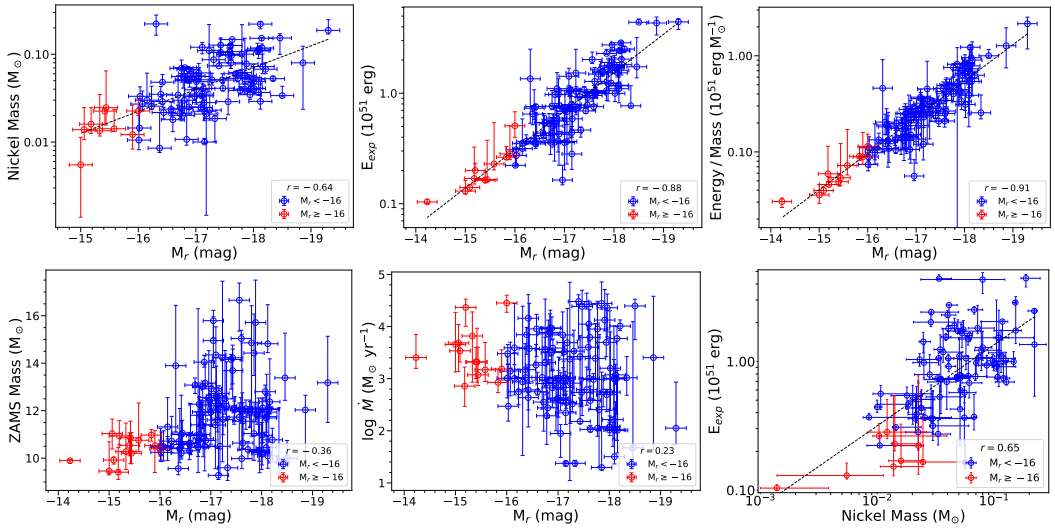

Figure 5.14: Correlations between peak r-band magnitude and physical parameters (nickel mass, explosion energy, energy per unit mass, radius, ejecta mass), and among the physical parameters themselves, based on radiation-hydrodynamical model fits from Moriya et al. (2023). LLIIP SNe with $M_r \geq -16$ are shown in red, those with $M_r < -16$ in blue.

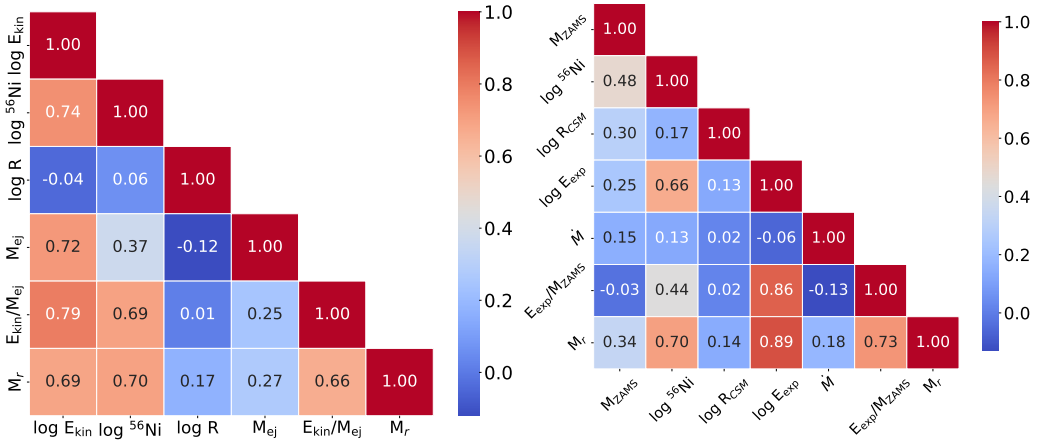

Figure 5.15: Correlation matrices of physical parameters derived from semi-analytical model fits (left) and radiation-hydrodynamical model fits (right).

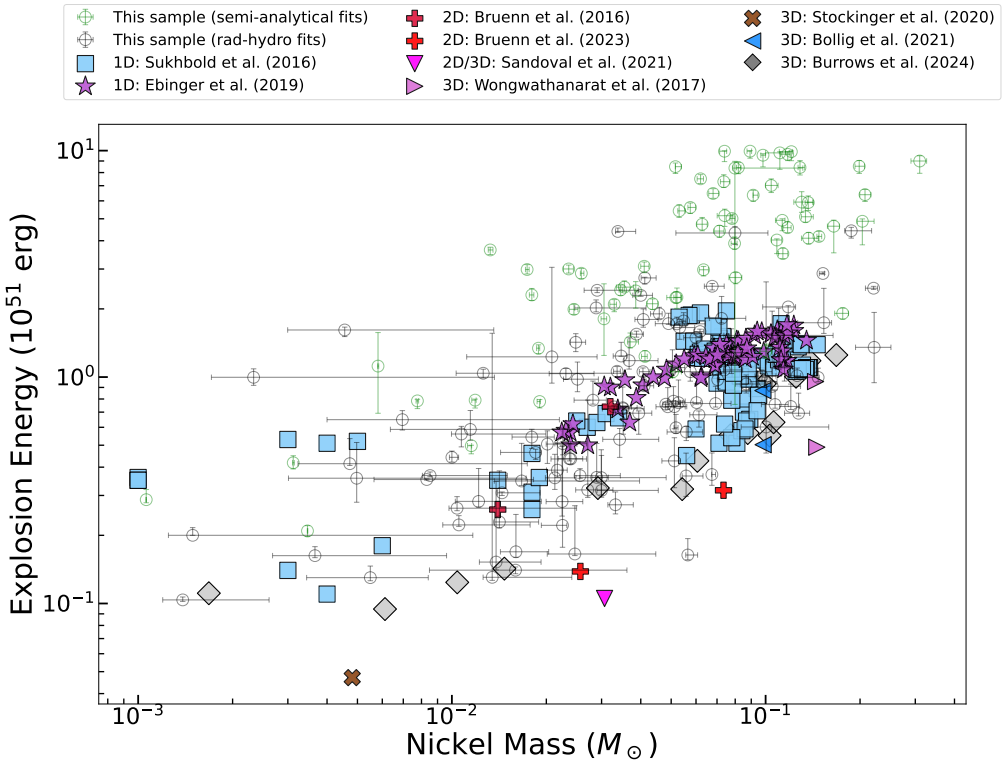

Figure 5.16: Nickel mass versus explosion energy for a range of core-collapse SN models, compared to our observations. Theoretical models include 1D, 2D and 3D simulations (Ebinger et al. 2019, Sukhbold et al. 2016, Bruenn et al. 2016, 2023, Sandoval et al. 2021, Bollig et al. 2021, Burrows et al. 2024). The observational sample includes semi-analytical fits (green open circles) and radiation-hydrodynamical model fits (black) from this work.

solutions from lightcurve fitting alone as discussed in Singh et al. (2024a), Rehemtulla et al. (2025). Goldberg et al. (2019), Goldberg and Bildsten (2020) argue that breaking these degeneracies requires external constraints on at least one physical parameter.

Moriya et al. (2023) attempt to mitigate this degeneracy using the progenitor mass–radius relation embedded in the KEPLER stellar grids. Although their lightcurve model grid spans a wide range of progenitor and explosion properties, it is important to note that there are systematic limitations inherited from the underlying stellar evolution framework. For example, they employ a low mixing-length parameter, leading to progenitor radii that are systematically larger than what is inferred from observational constraints. Additionally, the assumption of continuous wind-driven mass loss throughout stellar evolution results in hydrogen-rich enve-

lope masses that are systematically lower at the time of core collapse. These can influence the lightcurves and the physical parameters derived from fitting them (Hsu et al. 2024). While we incorporate velocity information from photospheric-phase spectroscopy to partially constrain kinetic energy, these measurements are not as constraining as those obtained during the brief shock-cooling phase immediately after explosion, which are more diagnostic (Goldberg et al. 2019). We also note that the lowest explosion energy in the model grid is 10^{50} erg; lower energies are required to better fit the lightcurves of the faintest SNe in our sample.

The semi-analytical two-component lightcurve models developed by Nagy and Vinkó (2016) assume spherical symmetry and do not accurately capture the early shock-cooling behavior at $t < 20$ days. Accordingly, we restrict our fits to data obtained after 20 days post-explosion. Despite their simplicity, Nagy and Vinkó (2016) and Jäger et al. (2020) find that these models yield physical parameters broadly consistent with more sophisticated hydrodynamical simulations for Type IIP SNe. To test this consistency, Yang et al. (2021) compared fitting results to those from hydrodynamical models such as those in Martinez et al. (2020), and found that, in several cases, the inferred ejecta masses are in reasonable agreement. We find that the semi-analytical fits return higher explosion energies and ejecta mass for most SNe. This could be because of the two-component density profile and a simplified method for computing bolometric lightcurves. Prior works have also noted that lightcurve modeling can systematically overestimate ZAMS masses compared to direct progenitor imaging or nebular spectroscopy (e.g., Utrobin and Chugai 2008, 2009b, Maguire et al. 2010, Sanders et al. 2015).

The correlations between physical quantities such as peak luminosity, nickel mass, explosion energy, and ejecta mass are preserved in both approaches. Nevertheless, we also observe that, for individual SN, the absolute values derived from the two methods can differ significantly (Figure 5.21). This highlights the presence of methodological systematics and the need for caution when interpreting parameter estimates from any single modeling framework.

What are the progenitors of LLIIP SNe?

7–12 $M_\odot$ Red Super Giants that undergo core-collapse SNe

We compare our derived explosion parameters to theoretical predictions from neutrino-driven explosion models of core-collapse SNe. Barker et al. (2022a) show that the properties of a progenitor's core can be estimated from optical photometry

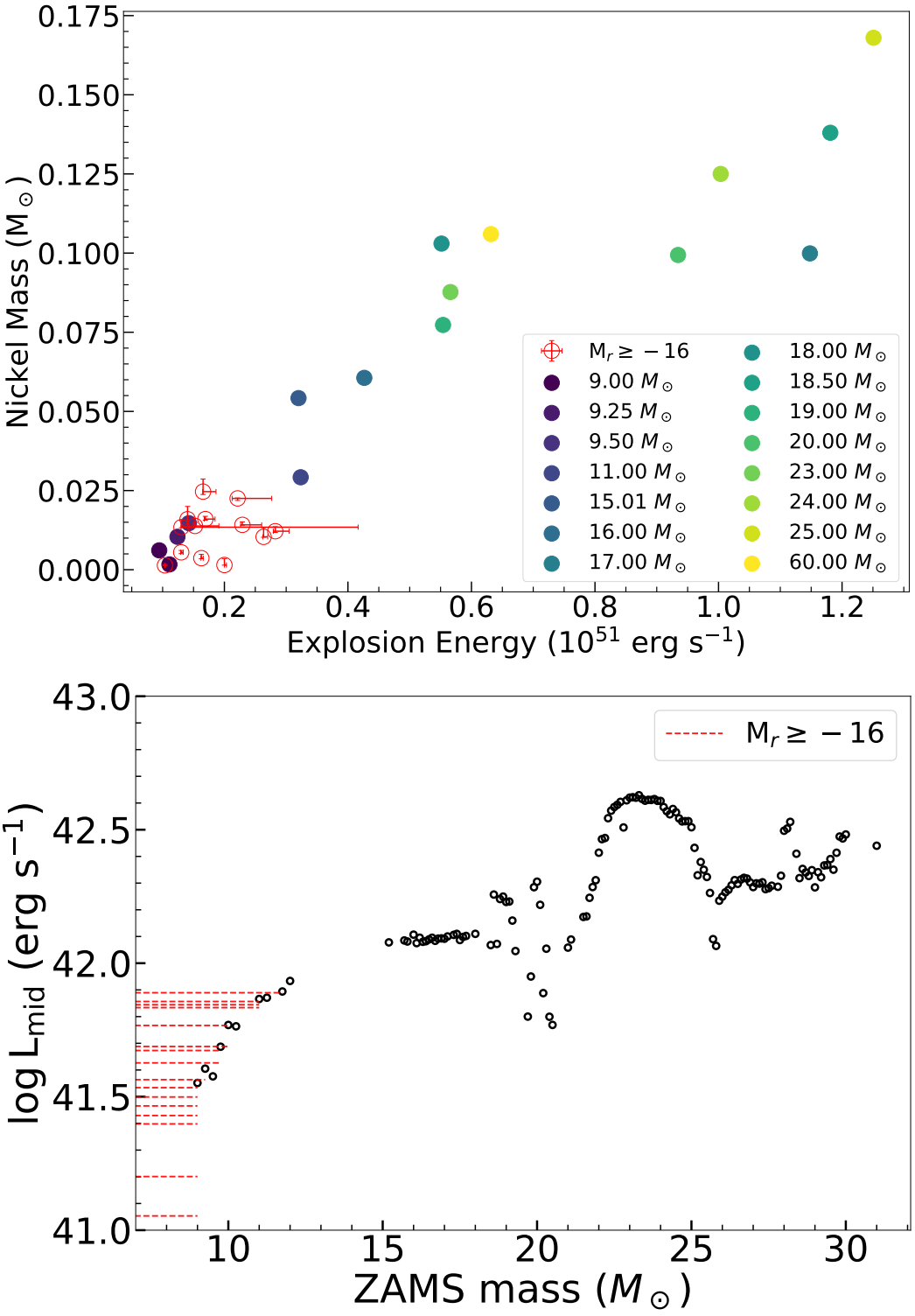

Figure 5.17: Left: Comparison of explosion energies from our SN sample with predictions from recent 3D core-collapse simulations by Burrows et al. (2020). Right: Comparison of mid-plateau bolometric luminosities for our SN sample (horizontal lines) with theoretical predictions from Barker et al. (2022a) (black points), which relate luminosity to iron core mass.

during the plateau phase alone. A linear correlation between iron core mass and L_{50} (luminosity 50 days post-explosion) indicates that optical photometry of Type IIP SNe can effectively probe progenitor cores. They find a robust relationship linking progenitor iron core mass to plateau luminosity (see Figure 5.17). The bolometric luminosities of our LLIIP SN sample align with ZAMS masses below 12 $M_\odot$. However, we note that these models assume that there is no CSM interaction. Additionally, using best-fit ZAMS mass estimates from Moriya et al. (2023) mode fits, the ZAMS mass for LLIIP SNe are lower than 11 $M_\odot$. Furthermore, ejecta masses inferred from semi-analytical model fitting by Nagy and Vinkó (2016) suggest masses ∼8.2 $M_\odot$. Assuming a neutron star mass of 1.4 $M_\odot$, this translates to progenitor masses less than ∼ 11 $M_\odot$.

Also, Recent 3D simulations by Burrows et al. (2020) find explosion energies of approximately 0.1 foe for their lowest ZAMS mass (9 $M_\odot$) progenitor model, compatible with our lowest observed explosion energies from the radiation-hydrodynamical fits (see Figure 5.17). Previous 1D simulations (e.g., Ugliano et al. 2012, Ertl et al. 2016, Sukhbold et al. 2016) yielded explosion energies between 0.1 and 2.0 foe.

Observations and parameterized 1D explosion models suggest typical nickel yields of ∼ 0.05 $M_\odot$ from core-collapse SNe. However, the low nickel masses we measure imply progenitor initial masses toward the low-mass end of the CCSN spectrum. Stars with low-mass iron cores are known to produce significantly reduced nickel yields. For example, Stockinger et al. (2020) and Sandoval et al. (2021) find nickel masses of ∼0.002–0.005 $M_\odot$ for a 9.6 $M_\odot$ progenitor. Recent 3D simulations by Burrows et al. (2024) predict nickel masses in the range 0.002–0.006 $M_\odot$ for a 9 $M_\odot$ progenitor, rising above 0.01 $M_\odot$ for progenitor masses exceeding 9.25 $M_\odot$. These theoretical predictions are consistent with our measured nickel mass for LLIIP SNe.

sAGB stars that undergo Electron-capture SNe

Progenitors in the mass range $8 - 10$ $M_\odot$ may evolve into super-Asymptotic Giant Branch (sAGB) stars and explode as electron-capture supernovae (ECSNe). ECSN simulations consistently produce low explosion energies and nickel yields significantly lower than typical Fe CCSNe but similar to those observed for the lowest-mass Fe CCSNe. According to Sato et al. (2024), ECSNe, without significant circumstellar material (CSM) interaction, exhibit distinctively bluer bolometric lightcurve plateaus compared to Fe CCSNe, characterized by mid-plateau $(g - r)$ colors exceeding the relation $0.008 \times t_{PT} - 0.4$. This difference arises from the lower-density

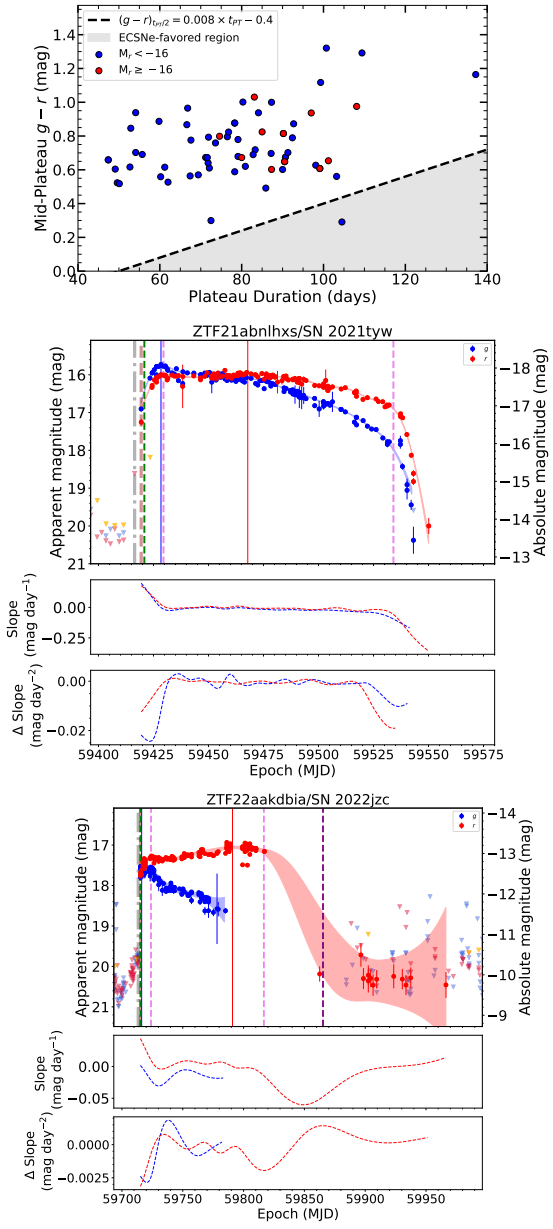

Figure 5.18: Left: Mid-plateau $(g-r)$ colors compared to the ECSN color criterion from Sato et al. (2024), distinguishing explosions of sAGB stars from RSGs, shown in dashed black. Light curves of the SNe with the bluest (SN 2021tyw, mid-plateau $(g-r) = 0.2$ mag; center) and reddest (SN 2022jzc, mid-plateau $(g-r) = 1.4$ mag; right) mid-plateau colors.

envelopes inherent to sAGB progenitors. We plot the mid-plateau colors for our SN sample against the Sato et al. (2024) criterion in Figure 5.18. While SNe 2021tyw, 2022omr, 2021cwe, and 2022prv show bluer mid-plateau colors, their peak luminosities and nickel masses favor an Fe CCSN origin. Among our LLIIP SNe sample, SNe 2023wcr, 2021gmj, 2021zgm, and 2020abcq exhibit notably bluer mid-plateau colors. However, we note that the mid-plateau colors may also be influenced by CSM interaction, as supported by the interaction signatures seen in the spectrum of SN 2021tyw. The lightcurves of the SNe with the bluest (SN 2021tyw, mid-plateau $(g-r) = 0.2$ mag) and reddest (SN 2022jzc, mid-plateau $(g-r) = 1.4$ mag) colors are shown in Figure 5.18.

We also compare the inferred nickel masses and explosion energies of our LLIIP sample to the ECSN models from Kozyreva et al. (2021). The nickel masses ($\sim 10^{-3} - 10^{-4}$ $M_\odot$) and explosion energies ($\sim 0.3 - 1.37 \times 10^{50}$ erg) from our sample closely match those predicted by ECSN simulations for their 8.8 and 9.6 $M_\odot$ progenitor models. Kozyreva et al. (2021) also show that the lightcurves in the U and B bands rises during the first 50 days and then slowly declines, while the light curve in the V and redder bands rises over the same timescale and then settles into a plateau before a steep drop to the radioactive tail. The rising r-band light curves seen in some LLIIP SNe, when coupled with their low nickel masses, are consistent with theoretical expectations for explosions from sAGB stars that undergo ECSNe.

Photospheric properties alone do not reliably distinguish between ECSNe from sAGB stars and Fe-core collapse SNe from red supergiants. Nebular-phase spectroscopy, however, offers definitive diagnostic features due to distinct core compositions and nucleosynthetic pathways (Jerkstrand et al. 2018). A comprehensive analysis of nebular spectra for the LLIIP SN sample will be presented in Paper III.

5.8 Conclusion

We present the largest systematic study of lightcurve properties for Type IIP SNe from the volume-limited ZTF CLU survey, analyzing 129 Type IIP events, including 16 LLIIP SNe. We summarize the key takeaways of the paper here:

1. *Observables:*

    - The median plateau duration for LLIIP SNe is 89^{+10}_{-20} days, compared to 76^{+16}_{-16} days for the full Type IIP sample. The median OPTd is 99^{+11}_{-14} days

for LLIIP SNe and 90^{+16}_{-20} days for the full sample. There is no strong correlation with peak magnitude, likely suggesting binary interaction.

- The plateau slope strongly correlates with peak brightness ($r = -0.68$), with brighter SNe having steeper declines; a significant fraction of LLIIP SNe exhibit positive plateau slopes. This likely implies progenitors for most LLIIP SNe have a smaller radius and different density profile from those of their more luminous counterparts.
- We observe a strong correlation between the mid-plateau luminosity and nickel mass ($r = -0.89$), extending to the low-luminosity end. This can be explained if a strong core explosion leads to both higher explosion energy and greater nickel yield.
- The steepest plateau-to-tail drop of > 3.5 mag was seen in SN 2022aagp. Other objects with sharp drops include SN 2021tyw (> 3.1 mag) and SN 2020cxd (2.5 mag). These are consistent with ECSNe and failed SNe with very low or zero nickel mass.

2. *Explosion and Progenitor Analysis:*

   - Radiation-hydrodynamical modeling: The ZAMS masses for LLIIP SNe are typically below 12 $M_\odot$, with a median of $10.5^{+0.4}_{-0.7}$ $M_\odot$, while that of the overall sample is $11.5^{+1.6}_{-1.2}$ $M_\odot$. The kinetic energies are similarly lower for LLIIP SNe, with a median of $0.17^{+0.07}_{-0.03} \times 10^{51}$ erg, compared to $0.76^{+0.89}_{-0.44} \times 10^{51}$ erg for the overall sample. The inferred mass-loss rates just before explosion are relatively low, with a median $\log \dot{M} = -3.32^{+0.37}_{-0.26}$ for LLIIP SNe, compared to $-3.01^{+0.83}_{-0.60}$ for the overall sample.
   - Semi-analytical modeling: LLIIP SNe have low nickel masses, with a median of $0.013^{+0.089}_{-0.001}$ $M_\odot$ and a range from 0.0009 to 0.0420 $M_\odot$, while that of the overall Type IIP SNe sample is $0.0652^{+0.0680}_{-0.0471}$ $M_\odot$ with a range from 0.0009 to 0.3098 $M_\odot$. The median ejecta mass for LLIIP SNe is $8.06^{+0.73}_{-1.71}$ $M_\odot$ compared to $12.8^{+6.2}_{-5.0}$ $M_\odot$ for the overall sample. Their kinetic energies are also lower, with a median of $0.79^{+0.49}_{-0.35} \times 10^{51}$ erg for LLIIP SNe and $4.32^{+4.17}_{-2.91} \times 10^{51}$ erg for the overall sample.

     Overall, LLIIP SNe occupy the faint, low-energy, low-mass end of the Type IIP population compared to more luminous events.

3. *Correlation of Parameters:*

- Nickel mass, kinetic and explosion energy, and energy-to-mass ratio strongly correlate with peak absolute magnitude, indicating that fainter SNe have systematically lower nickel mass and explosion energies. This is consistent with theoretical core-collapse SN models, which predict a strong correlation between explosion energy and nickel production.
- For the semi-analytical fits, nickel mass and kinetic energy correlates with peak brightness ($r = -0.77$ and $r = -0.69$ respectively). Kinetic energy-to-ejecta mass ratio shows the strongest correlation ($r = -0.77$) with peak brightness. Among physical parameters themselves, kinetic energy correlates strongly with ejecta mass ($r = 0.77$) and with nickel mass ($r = 0.75$).
- For the radiation-hydrodynamical fits, similar trends are observed: peak brightness correlates tightly with explosion energy ($r = -0.88$), nickel mass ($r = -0.64$) and energy-to-ejecta mass ratio ($r = -0.91$). Explosion energy also correlates with nickel mass ($r = 0.65$), while mass-loss rate shows little dependence on other explosion parameters.

The correlations between physical parameters such as peak luminosity, nickel mass, explosion energy, and ejecta mass are preserved across both semi-analytical and radiation-hydrodynamic modeling approaches. Nevertheless, we observe that for individual SNe, the absolute values derived from the two methods can differ significantly. This highlights the presence of methodological systematics and underscores the need for caution when interpreting parameter estimates from any single modeling framework. However, the low explosion energies, nickel masses and progenitor masses inferred for LLIIP SNe are consistent with the explosions of low-mass RSG or sAGB stars with ZAMS masses $\lesssim 12$ $M_\odot$. Distinguishing between these progenitor scenarios will require late-time nebular spectroscopy, which will be pursued in Paper III of this series. The models in this paper assumes single-star evolution. Incorporating progenitor models that account for binary interaction and mass transfer will be crucial for constraining the binary fraction and understanding the diversity of envelope stripping among core-collapse progenitors. We also highlight the need for radiation-hydrodynamic model grids that extend to the lowest progenitor masses in the 8–10 $M_\odot$ range and explore explosion energies below 10^{50} erg to adequately model the faintest Type IIP SNe. The advent of deep, multi-band, high-cadence surveys such as the Legacy Survey of Space and Time (LSST; Ivezić et al. 2008) will enable a more complete census of the faintest slow-evolving core-collapse SNe

and provide critical insights into the lowest-mass stars that explode. It will also offer deep post-plateau limits, facilitating the discovery of more Type IIP SNe with very low or even zero nickel mass, as expected for electron-capture supernovae or failed explosions.

Data Availability

All photometric and spectroscopic data presented in this work will be made publicly available on `Zenodo` and `WISeREP` upon publication. The codes required to reproduce the lightcurve fitting will be uploaded via `GitHub`. Machine-readable versions of all tables, lightcurve plots, and best-fit model plots will also be available on `Zenodo`.

Acknowledgements

We thank the anonymous referee for their constructive feedback, which helped improve the quality of this manuscript.

We thank Jared Goldberg, Daichi Hiramatsu and Kishalay De for valuable discussions.

Based on observations obtained with the Samuel Oschin Telescope 48-inch and the 60-inch Telescope at the Palomar Observatory as part of the Zwicky Transient Facility project. ZTF is supported by the National Science Foundation under Grants No. AST-1440341, AST-2034437, and currently Award 2407588. ZTF receives additional funding from the ZTF partnership. Current members include Caltech, USA; Caltech/IPAC, USA; University of Maryland, USA; University of California, Berkeley, USA; University of Wisconsin at Milwaukee, USA; Cornell University, USA; Drexel University, USA; University of North Carolina at Chapel Hill, USA; Institute of Science and Technology, Austria; National Central University, Taiwan, and OKC, University of Stockholm, Sweden. Operations are conducted by Caltech's Optical Observatory (COO), Caltech/IPAC, and the University of Washington at Seattle, USA.

Zwicky Transient Facility access for S.S. was supported by Northwestern University and the Center for Interdisciplinary Exploration and Research in Astrophysics (CIERA).

M.W.C acknowledges support from the National Science Foundation with grant numbers PHY-2117997, PHY-2308862 and PHY-2409481.

D.T. is supported by the Sherman Fairchild Postdoctoral Fellowship at Caltech.

E.O. is supported by the Swedish Research Council (Project No. 2020-00452).

N.Sarin acknowledges support from the Knut and Alice Wallenberg Foundation through the “Gravity Meets Light" project and by and by the research environment grant “Gravitational Radiation and Electromagnetic Astrophysical Transients” (GREAT) funded by the Swedish Research Council (VR) under Dnr 2016-06012.

SED Machine is based upon work supported by the National Science Foundation under Grant No. 1106171.

The ZTF forced-photometry service was funded under the Heising-Simons Foundation grant #12540303 (PI: Graham).

The Gordon and Betty Moore Foundation, through both the Data-Driven Investigator Program and a dedicated grant, provided critical funding for SkyPortal .

This research has made use of the NASA/IPAC Extragalactic Database (NED), which is funded by the National Aeronautics and Space Administration and operated by the California Institute of Technology.

The Liverpool Telescope is operated on the island of La Palma by Liverpool John Moores University in the Spanish Observatorio del Roque de los Muchachos of the Instituto de Astrofisica de Canarias with financial support from the UK Science and Technology Facilities Council.

The W. M. Keck Observatory is operated as a scientific partnership among the California Institute of Technology, the University of California and the National Aeronautics and Space Administration. The Observatory was made possible by the generous financial support of the W. M. Keck Foundation. The authors wish to recognize and acknowledge the very significant cultural role and reverence that the summit of Maunakea has always had within the indigenous Hawaiian community. We are most fortunate to have the opportunity to conduct observations from this mountain.

Software: Global Relay of Observatories Watching Transients Happen Marshal (GROWTH; Kasliwal et al. 2019) and the Fritz SkyPortal Marshal (Duev et al. 2019, van der Walt et al. 2019, Coughlin et al. 2023). Astropy (Astropy Collaboration et al. 2013), Matplotlib (Hunter 2007), george (Ambikasaran et al. 2015)

Appendix

Table A lists the observable lightcurve parameters such as rise time, plateau duration, and decline rate for the entire sample. Tables B and C summarize the priors used in the semi-analytical and radiation-hydrodynamical model fits, respectively. Tables D and E present the full posterior estimates of explosion and progenitor properties from the two modeling approaches. Table L provides the spectral observation log and Hα velocity measurements. Figure 5.19 shows all the parameter correlations based on semi-analytical fits, while Figure 5.20 shows the same using radiation-hydrodynamical models. Figure 5.21 compares results between the two modeling methods.

Table A: Light-curve parameters for SN II, sorted by faintest peak r-band absolute magnitude (M_r). ZTF and IAU names are shown in separate columns. The table includes rise time, plateau duration (Plat. dur.), optically thick duration (OPTd), decline rate during the plateau (Slope, in $\times 0.01$ mag day^{-1}), and the plateau-to-tail drop (Δmag). The full machine-readable table is available on Zenodo.

ZTF	IAU	M_r (mag)	Rise (days)	Plat. dur. (days)	OPTd (days)	Slope (10^{-2} mag day^{-1})	Δmag (mag)	Limit?
ZTF24abtczty	SN 2024abfl	-14.1	12.2 ± 0.4	99.1 ± 1.5	111.7 ± 1.5	-0.04 ± 0.02	-2.05	no
ZTF20aapchqy	SN 2020cxd	-14.2	–	108.1 ± 1.6	112.9 ± 1.6	-0.42 ± 0.02	-2.48	no
ZTF24abmkros	SN 2024xkd	-14.9	–	90.5 ± 1.3	97.1 ± 1.3	-0.11 ± 0.02	-1.17	yes
ZTF23aackjhs	SN 1995al	-15.0	–	97.0 ± 2.3	99.5 ± 2.3	0.14 ± 0.02	0.22	yes
ZTF22aakdbia	SN 2022jzc	-15.1	9.7 ± 0.3	92.8 ± 5.5	111.0 ± 5.5	-0.18 ± 0.02	-2.28	no
ZTF22abtjefa	SN 2022aaad	-15.1	16.0 ± 0.3	66.5 ± 15.0	85.8 ± 15.0	-0.02 ± 0.03	-1.38	no
ZTF22aazmrpx	SN 2022raj	-15.2	–	80.0 ± 4.2	84.7 ± 4.2	0.45 ± 0.03	-0.87	yes
ZTF20acuhren	SN 2020abcq	-15.3	–	101.2 ± 2.8	103.2 ± 2.8	-0.01 ± 0.02	-2.05	yes
ZTF21aaobkmg	SN 2021eui	-15.4	–	85.0 ± 3.1	88.0 ± 3.1	0.09 ± 0.02	-1.43	yes
ZTF22aaywnyg	SN 2022pru	-15.4	–	86.1 ± 1.6	102.1 ± 1.6	0.46 ± 0.02	-1.09	no
ZTF24aabppgn	SN 2024wp	-15.5	–	95.3 ± 2.5	109.4 ± 2.4	0.1 ± 0.02	-1.35	yes
ZTF23abnogui	SN 2023wcr	-15.6	–	87.3 ± 4.3	101.1 ± 4.3	0.58 ± 0.04	-1.53	no
ZTF24aaucrua	SN 2024nez	-15.8	–	90.2 ± 1.5	105.4 ± 1.5	0.18 ± 0.02	-1.58	yes
ZTF22abyivoq	SN 2022acko	-15.8	–	69.8 ± 6.4	84.7 ± 6.4	0.23 ± 0.04	0.02	yes
ZTF20abeohfn	SN 2020mjm	-15.9	10.7 ± 0.1	64.3 ± 7.6	76.5 ± 7.6	0.05 ± 0.03	0.05	yes
ZTF22abssiet	SN 2022zmb	-15.9	–	66.1 ± 11.3	76.0 ± 11.3	0.18 ± 0.04	-0.24	yes
ZTF19aamwhat	SN 2019bzd	-16.0	–	83.1 ± 1.5	103.1 ± 1.4	0.36 ± 0.02	-2.00	yes
ZTF22abkhrkd	SN 2022wol	-16.0	–	79.1 ± 2.6	90.8 ± 2.6	0.08 ± 0.03	-1.09	yes
ZTF24aaejecr	SN 2024btj	-16.0	–	78.3 ± 2.3	89.6 ± 2.3	0.55 ± 0.03	-1.66	no
ZTF24aaplfjd	SN 2024jxm	-16.0	–	74.6 ± 4.6	97.6 ± 4.6	0.24 ± 0.03	-1.30	no
ZTF19abwztsb	SN 2019pjs	-16.2	–	68.1 ± 37.2	80.0 ± 37.2	0.37 ± 0.2	-1.36	no
ZTF24aabsmvc	SN 2024ws	-16.2	–	90.0 ± 23.0	100.4 ± 23.0	0.26 ± 0.07	-1.25	yes
ZTF22abyohff	SN 2022acrl	-16.3	–	78.7 ± 6.5	88.7 ± 6.4	0.33 ± 0.04	-0.52	yes

Continued on next page

Table A: Continued.

ZTF	IAU	M_r (mag)	Rise (days)	Plat. dur. (days)	OPTd (days)	Slope (10^{-2} mag day^{-1})	Δmag (mag)	Limit?
ZTF21acgrrnl	SN 2021aayf	-16.3	–	77.0 ± 14.8	90.5 ± 14.8	-0.14 ± 0.04	-1.44	yes
ZTF21aaeqwov	AT 2021htp	-16.4	13.2 ± 0.6	92.4 ± 1.1	106.1 ± 1.1	0.27 ± 0.02	-1.30	no
ZTF23abaxtlq	SN 2023rix	-16.4	–	75.2 ± 8.3	87.3 ± 8.3	0.92 ± 0.1	-2.13	no
ZTF21abvcxel	SN 2021wvw	-16.4	–	67.4 ± 1.2	69.4 ± 1.2	0.47 ± 0.03	-1.67	yes
ZTF21aantsla	SN 2021ech	-16.4	–	75.3 ± 8.0	86.5 ± 8.0	0.25 ± 0.04	-1.46	yes
ZTF21aafepon	SN 2021ass	-16.4	–	51.4 ± 9.0	67.9 ± 9.0	0.16 ± 0.05	-0.09	yes
ZTF21acpqqgu	SN 2021aewn	-16.4	–	76.3 ± 9.7	78.3 ± 9.7	0.35 ± 0.05	-0.77	yes
ZTF22abnujbv	SN 2022xus	-16.4	–	53.2 ± 20.7	62.4 ± 20.7	0.58 ± 0.23	-1.83	no
ZTF20acmaaan	SN 2020xyk	-16.4	–	69.4 ± 4.2	75.8 ± 4.2	0.14 ± 0.03	-1.96	yes
ZTF22abfxkdm	SN 2022ubb	-16.6	–	87.3 ± 3.9	96.2 ± 3.9	0.49 ± 0.03	-1.66	yes
ZTF22aavbfhz	AT 2022phi	-16.6	–	78.3 ± 2.0	81.3 ± 2.0	0.63 ± 0.03	-1.02	yes
ZTF22abkbjsb	SN 2022vym	-16.7	–	60.0 ± 9.5	66.5 ± 9.5	0.62 ± 0.1	-1.33	no
ZTF24aabpzuz	SN 2024vs	-16.7	–	62.0 ± 4.7	78.9 ± 4.7	-0.13 ± 0.03	-1.33	yes
ZTF21aanzcuj	SN 2021enz	-16.7	18.0 ± 0.8	72.1 ± 1.9	90.6 ± 1.8	0.01 ± 0.03	-1.54	no
ZTF24aafqzur	SN 2024daa	-16.7	–	67.6 ± 1.2	86.6 ± 1.2	0.15 ± 0.03	-0.94	yes
ZTF21aagtqna	SN 2021brb	-16.8	21.2 ± 1.4	73.6 ± 3.7	104.8 ± 3.7	0.12 ± 0.03	-1.26	no
ZTF18aaszvfn	SN 2021iaw	-16.8	–	76.8 ± 1.7	86.4 ± 1.7	0.39 ± 0.03	-1.23	yes
ZTF19acftfav	SN 2019ssi	-16.8	14.2 ± 0.4	61.7 ± 8.0	76.4 ± 8.0	0.71 ± 0.1	-1.70	yes
ZTF23aasbvab	SN 2023ngy	-16.8	–	92.7 ± 1.1	102.9 ± 1.1	0.83 ± 0.02	-1.32	yes
ZTF23aasrcyv	SN 2023nlu	-16.8	18.3 ± 1.2	71.8 ± 1.8	94.0 ± 1.8	0.5 ± 0.03	-0.24	yes
ZTF22abzqwmp	SN 2022adth	-16.8	–	61.0 ± 11.1	73.6 ± 11.1	0.69 ± 0.13	-0.81	yes
ZTF22aasojye	SN 2022omr	-16.9	–	98.1 ± 4.2	103.6 ± 4.2	0.23 ± 0.02	-1.76	no
ZTF19aadnxnl	SN 2019va	-16.9	–	103.2 ± 3.8	107.2 ± 3.8	-0.09 ± 0.02	-0.80	no
ZTF19actnyae	SN 2019vdm	-16.9	–	52.9 ± 1.4	61.4 ± 1.4	-0.02 ± 0.04	-1.33	no
ZTF23aaxadel	SN 2023pbg	-16.9	–	89.8 ± 6.1	104.6 ± 6.1	0.31 ± 0.03	-0.82	yes
ZTF21abrluay	SN 2021vfh	-17.0	–	75.4 ± 8.8	88.0 ± 8.8	0.08 ± 0.03	-1.28	yes
ZTF22aafsqud	SN 2022hql	-17.0	–	61.2 ± 1.6	71.7 ± 1.6	0.62 ± 0.04	-1.25	yes
ZTF22abhsxph	SN 2022vyc	-17.0	–	80.3 ± 1.4	94.6 ± 1.4	0.51 ± 0.03	-1.42	yes
ZTF19aazudta	SN 2019hqm	-17.0	–	73.7 ± 16.5	90.0 ± 16.5	0.18 ± 0.05	-1.52	yes
ZTF22abfwxtr	SN 2022udq	-17.0	–	99.3 ± 2.3	111.4 ± 2.3	0.41 ± 0.02	-0.73	yes
ZTF21aafkwtk	SN 2021apg	-17.0	–	69.3 ± 6.0	87.0 ± 6.0	0.33 ± 0.04	-1.65	no
ZTF19aapafit	SN 2019cvz	-17.0	–	82.8 ± 2.2	98.3 ± 2.2	0.12 ± 0.02	-1.30	no
ZTF23abbtkrv	SN 2023rvo	-17.0	16.7 ± 1.1	90.7 ± 2.2	157.1 ± 2.2	-0.04 ± 0.02	-0.81	yes
ZTF19acewuwn	SN 2019ssl	-17.0	–	62.8 ± 8.0	83.8 ± 8.0	0.19 ± 0.04	-1.09	yes
ZTF19aailepg	SN 2019amt	-17.1	–	100.9 ± 10.3	109.0 ± 10.3	0.3 ± 0.04	-1.04	yes
ZTF19aazyvub	SN 2019hnl	-17.1	–	74.6 ± 5.1	80.6 ± 5.0	0.39 ± 0.04	-1.44	no
ZTF21aakvroo	SN 2021cwe	-17.1	–	72.5 ± 4.2	76.5 ± 4.2	-0.08 ± 0.03	-0.93	no
ZTF22abtspsw	SN 2022aagp	-17.1	9.0 ± 0.0	111.5 ± 6.3	122.5 ± 6.3	0.99 ± 0.06	-3.50	yes
ZTF18aaxkqgy	SN 2018ccb	-17.1	–	70.0 ± 10.6	74.2 ± 10.6	0.53 ± 0.09	-1.22	no
ZTF22abfavpu	SN 2022tmb	-17.1	–	66.6 ± 1.3	80.9 ± 1.3	0.77 ± 0.03	-2.05	no
ZTF21aapliyn	SN 2021foj	-17.1	–	91.3 ± 1.8	96.4 ± 1.8	0.15 ± 0.02	-1.20	yes
ZTF21acafqtj	SN 2021yok	-17.1	–	59.9 ± 10.6	69.9 ± 10.6	0.37 ± 0.07	-0.20	yes
ZTF21abfiuqf	SN 2021pla	-17.2	–	52.9 ± 1.2	60.6 ± 1.2	1.25 ± 0.05	-1.51	no
ZTF19aanhhal	SN 2019cec	-17.2	–	80.9 ± 2.8	90.2 ± 2.8	0.44 ± 0.03	-0.96	yes
ZTF22abyokkf	SN 2022acri	-17.2	–	91.7 ± 5.2	108.2 ± 5.2	0.08 ± 0.02	-1.14	yes

Continued on next page

Table A: Continued.

ZTF	IAU	M_r (mag)	Rise (days)	Plat. dur. (days)	OPTd (days)	Slope (10^{-2} mag day^{-1})	Δmag (mag)	Limit?
ZTF18aatyqds	SN 2018btl	-17.2	10.8 ± 0.2	76.5 ± 4.4	88.8 ± 4.4	1.2 ± 0.07	-1.39	no
ZTF22aapargp	SN 2022niw	-17.2	–	54.0 ± 9.6	68.7 ± 9.6	0.46 ± 0.09	-1.03	yes
ZTF23aanymcl	SN 2023kzz	-17.2	–	60.6 ± 2.1	64.1 ± 2.1	0.68 ± 0.04	-1.23	yes
ZTF21aavhnpk	SN 2021jsf	-17.3	–	74.3 ± 9.1	78.8 ± 9.0	0.7 ± 0.09	-1.34	yes
ZTF19aaniore	SN 2019ceg	-17.3	–	87.2 ± 3.0	102.0 ± 3.0	0.44 ± 0.03	-1.46	no
ZTF21aabygea	SN 2021os	-17.3	14.8 ± 0.4	83.3 ± 1.8	100.1 ± 1.8	0.58 ± 0.03	-1.43	no
ZTF22absqhkw	SN 2022zkc	-17.4	–	50.1 ± 4.6	52.1 ± 4.6	0.62 ± 0.07	-1.48	yes
ZTF23aaqknaw	SN 2023lzn	-17.4	–	100.7 ± 1.7	104.7 ± 1.6	0.55 ± 0.02	-2.03	yes
ZTF21aaagypx	SN 2021V	-17.4	–	137.2 ± 1.1	146.1 ± 1.1	0.56 ± 0.02	-1.57	yes
ZTF19abbnamr	SN 2019iex	-17.4	–	94.1 ± 10.0	100.6 ± 10.0	0.17 ± 0.03	-1.58	no
ZTF19aawgxdn	SN 2019gmh	-17.4	–	95.9 ± 8.0	105.5 ± 8.0	0.34 ± 0.04	-1.54	yes
ZTF24aagupsf	SN 2024egd	-17.5	–	71.0 ± 7.0	82.4 ± 7.0	0.62 ± 0.07	-2.46	no
ZTF18abzrgim	SN 2018gvt	-17.5	–	73.0 ± 24.1	90.4 ± 24.1	-0.03 ± 0.03	-0.31	yes
ZTF19acytcsg	SN 2019wvz	-17.6	–	77.4 ± 9.2	93.1 ± 9.2	0.25 ± 0.04	-1.13	no
ZTF18aawpwlf	SN 2020hvn	-17.6	–	54.1 ± 3.7	62.1 ± 3.7	1.76 ± 0.13	-1.49	yes
ZTF23abhzfww	SN 2023twg	-17.6	–	90.0 ± 3.0	96.0 ± 3.0	0.6 ± 0.03	-1.45	no
ZTF24aarvbxj	SN 2024lby	-17.6	–	49.1 ± 1.4	60.4 ± 1.4	0.73 ± 0.05	-1.23	no
ZTF19aclobbu	SN 2019twk	-17.6	–	73.7 ± 10.3	84.5 ± 10.3	0.31 ± 0.05	-0.52	yes
ZTF19actnwtn	SN 2019vdl	-17.6	–	84.1 ± 1.7	102.1 ± 1.7	0.39 ± 0.03	-1.09	yes
ZTF21abouuat	SN 2021ucg	-17.6	–	81.3 ± 11.4	98.7 ± 11.4	0.27 ± 0.05	-1.20	yes
ZTF24aaabbse	SN 2023achj	-17.8	–	103.9 ± 9.5	123.8 ± 9.5	0.65 ± 0.06	-1.03	yes
ZTF21acgunkr	SN 2021aaxs	-17.8	–	77.7 ± 16.3	89.5 ± 16.3	0.99 ± 0.21	-0.52	yes
ZTF21abnlhxs	SN 2021tyw	-17.8	8.7 ± 0.2	104.5 ± 1.1	116.1 ± 1.1	0.85 ± 0.02	-3.10	yes
ZTF19abajxet	SN 2019hyk	-17.8	10.9 ± 0.2	67.3 ± 10.9	79.7 ± 10.9	0.95 ± 0.16	-0.88	yes
ZTF19acbwejj	SN 2019upq	-17.8	22.0 ± 7.4	87.7 ± 3.3	130.3 ± 3.3	1.14 ± 0.05	-1.28	no
ZTF23abmoxlu	SN 2023vog	-17.8	10.9 ± 0.2	109.4 ± 2.4	123.2 ± 2.4	1.19 ± 0.03	-2.49	no
ZTF21abhhrpj	SN 2021qiu	-17.9	–	90.7 ± 1.6	96.3 ± 1.6	0.53 ± 0.02	-1.93	no
ZTF22aakdqqg	SN 2022kad	-17.9	15.5 ± 0.6	63.1 ± 12.8	79.6 ± 12.8	1.38 ± 0.28	-1.27	no
ZTF23aailjjs	SN 2023hcp	-17.9	–	60.2 ± 2.5	69.6 ± 2.4	0.83 ± 0.05	-1.57	no
ZTF19aanrrqu	SN 2019clp	-18.0	–	49.6 ± 4.5	53.8 ± 4.5	1.17 ± 0.11	-1.65	no
ZTF24aadkwni	SN 2024aul	-18.0	–	59.8 ± 1.6	68.4 ± 1.6	0.84 ± 0.04	-1.12	no
ZTF21abjcjmc	SN 2021skn	-18.0	7.1 ± 0.0	55.7 ± 0.5	63.7 ± 0.5	2.05 ± 0.04	-1.41	yes
ZTF23abascqa	SN 2023rbk	-18.0	–	71.9 ± 1.3	85.9 ± 1.3	1.28 ± 0.04	-2.02	no
ZTF24aaemydm	SN 2024chx	-18.0	–	64.3 ± 5.6	70.9 ± 5.6	0.92 ± 0.09	-1.40	no
ZTF24aajxppf	SN 2024grw	-18.0	–	52.7 ± 4.6	64.4 ± 4.6	1.37 ± 0.13	-1.32	no
ZTF21aaqugxm	SN 2021hdt	-18.1	–	49.1 ± 8.9	60.9 ± 8.9	1.34 ± 0.25	-1.07	no
ZTF21ablvzhp	SN 2021tiq	-18.1	–	85.9 ± 4.1	98.1 ± 4.1	0.56 ± 0.04	-1.37	yes
ZTF21abgilzj	AT 2021qcr	-18.1	16.2 ± 1.0	66.8 ± 1.1	93.0 ± 1.1	1.51 ± 0.04	-0.92	yes
ZTF21aapkcmr	AT 2021fnj	-18.1	–	54.1 ± 4.6	59.1 ± 4.6	1.74 ± 0.15	-1.34	yes
ZTF19abqrhvt	SN 2019nyk	-18.1	–	47.4 ± 2.0	60.1 ± 2.0	1.54 ± 0.08	-1.47	yes
ZTF21abnudtb	SN 2021txr	-18.1	–	71.6 ± 1.0	80.5 ± 1.0	0.63 ± 0.03	-1.16	no
ZTF23aaphnyz	SN 2023lkw	-18.1	–	77.5 ± 10.7	87.7 ± 10.7	0.46 ± 0.07	-0.95	yes
ZTF22aaolwsd	SN 2022mxv	-18.1	12.6 ± 0.2	104.8 ± 20.0	122.6 ± 20.0	1.35 ± 0.26	-0.87	yes
ZTF19aarykkb	SN 2019dzk	-18.2	–	73.9 ± 2.8	82.0 ± 2.8	0.3 ± 0.03	-0.62	yes
ZTF22aativsd	SN 2022ovb	-18.2	11.6 ± 0.2	71.2 ± 1.9	84.3 ± 1.9	0.84 ± 0.04	-0.94	no

Continued on next page

Table A: Continued.

ZTF	IAU	M_r (mag)	Rise (days)	Plat. dur. (days)	OPTd (days)	Slope (10^{-2} mag day^{-1})	Δmag (mag)	Limit?
ZTF19abqrhvy	SN 2019odf	-18.2	14.0 ± 0.3	93.3 ± 8.4	107.8 ± 8.4	0.71 ± 0.07	-1.14	yes
ZTF19abbwfgp	SN 2019ikb	-18.2	11.9 ± 0.3	79.1 ± 2.7	91.5 ± 2.7	1.05 ± 0.04	-2.06	yes
ZTF22aavobvq	SN 2022prv	-18.3	10.6 ± 0.2	62.8 ± 12.0	86.5 ± 12.0	1.4 ± 0.27	-2.56	yes
ZTF21aaipypa	SN 2021cgu	-18.3	13.2 ± 0.6	90.0 ± 13.1	106.5 ± 13.1	0.98 ± 0.14	-0.45	yes
ZTF19acrcxri	SN 2019ult	-18.4	–	54.9 ± 1.6	65.3 ± 1.6	1.07 ± 0.05	-1.33	yes
ZTF23aaaatjn	SN 2023cf	-18.5	–	84.6 ± 5.7	90.1 ± 5.7	0.89 ± 0.06	-1.92	no
ZTF22aarycqo	SN 2022ojo	-19.3	–	80.8 ± 11.0	96.1 ± 11.0	1.42 ± 0.2	-1.40	no

Table B: Priors used in the MCMC fitting with the semi-analytical models from Nagy and Vinkó (2016).

Parameter	Prior
Initial radius [R (cm)]	$\mathcal{U}[2 \times 10^{12},\ 8 \times 10^{13}]$
Ejected mass [$M_{\rm ej}$ ($M_\odot$)]	$\mathcal{U}[3,\ 25]$
Kinetic energy [$E_{\rm kin}$ (10^{51} erg)]	$\mathcal{U}[0.01,\ 10]$
Thermal energy [$E_{\rm th}$ (10^{51} erg)]	$\mathcal{U}[0.01,\ 10]$
Thomson scattering opacity [κ (cm^2/g)]	$\mathcal{U}[0.1,\ 0.4]$
Density power-law exponent	$\mathcal{U}[0,\ 3]$
Ionization/recombination temperature [$T_{\rm ion}$ (K)]	$\mathcal{U}[0,\ 20000]$
Nickel mass [$M_{\rm Ni}$ ($M_\odot$)]	$\mathcal{U}[5 \times 10^{-4},\ 0.5]$
Gamma-leakage parameter [t_γ^2 (day^2)]	$\mathcal{U}[10^3,\ 10^7]$

Table C: Priors used in the MCMC fitting with the radiation-hydrodynamical models from Moriya et al. (2023).

Parameter	Prior
$M_{\rm ZAMS}$ [M$_\odot$]	$\mathcal{U}(9, 18)$
Explosion Energy [10^{51} erg]	$\mathcal{U}(0.5, 5.0)$
$M_{\rm Ni}$ [M$_\odot$]	$\mathcal{U}(0.001, 0.3)$
Mass-Loss Rate [M$_\odot$ yr^{-1}]	$\mathcal{U}(10^{-5.0}, 10^{-1.0})$
Wind Velocity [km s^{-1}]	Fixed at 10
$R_{\rm CSM}$ [10^{14} cm]	$\mathcal{U}(1, 10)$
Wind Structure Parameter (β)	$\mathcal{U}(0.5, 5.0)$

Table F: Spectral log and H I λ6563 velocity measurements.

Source	Date	Phase (days)	Inst.	H I λ6563 (km s^{-1})
SN 2019env	2019-06-25	51	P60	7980 ± 460
SN 2018bjo	2018-06-12	56	P200	6720 ± 40
SN 2018cbb	2018-05-17	45	P200	6390 ± 110

Table F: Continued.

Source	Date	Phase (days)	Inst.	H I λ6563 (km s^{-1})
SN 2018bdv	2018-05-11	16	P60	10780 ± 640
SN 2024iwm	2024-06-01	18	SEDM	–
SN 2024iwm	2024-06-06	23	Deveny+LMI	–
SN 2024iwm	2024-06-07	24	KAST	–
SN 2021iaw	2021-05-06	33	KAST	–
SN 2018btl	2018-07-16	63	P60	8890 ± 640
SN 2021lmp	2021-05-29	24	SEDM	–
SN 2021lmp	2021-05-31	25	DBSP	–
SN 2020hvn	2020-05-07	17	P60	–
SN 2018lrq	2018-06-21	69	P200	–
SN 2018cqp	2018-07-02	18	P60	–
SN 2018cwa	2018-08-04	43	P200	7710 ± 490
SN 2018dzc	2018-07-30	20	P60	9160 ± 520
SN 2018dzc	2018-07-30	20	P60	8710 ± 570
SN 2018ecj	2018-12-01	129	Keck1	–
SN 2018dht	2018-08-04	24	P60	11840 ± 970
SN 2018dht	2018-08-04	24	P200	10150 ± 50
SN 2018dht	2018-08-04	24	P60	12690 ± 460
AT 2018lrz	2018-09-12	25	P200	10470 ± 20
SN 2018fif	2018-09-04	14	NOT	12930 ± 900
SN 2018fif	2018-09-25	35	P60	9620 ± 560
SN 2018fif	2018-09-25	35	P60	9620 ± 730
SN 2018fif	2018-11-03	73	P60	8470 ± 560
SN 2018fif	2018-11-14	84	P60	–
SN 2018fif	2018-11-19	89	P60	–
SN 2018fif	2018-11-26	96	P60	7320 ± 560
SN 2018fif	2018-12-04	103	P60	8470 ± 460
AT 2018lsa	2018-09-12	17	P200	10690 ± 850
SN 2024kan	2024-06-07	13	SEDM	–
SN 2024kan	2024-06-15	21	DBSP	–
SN 2018gvt	2018-12-05	69	P60	–
SN 2018gvt	2018-12-23	86	P60	–
SN 2018hle	2018-12-24	57	P60	7510 ± 560
AT 2018joy	2018-12-01	24	Keck1	9650 ± 460
AT 2018jwq	2018-12-01	14	Keck1	8870 ± 150
AT 2018kds	2019-01-26	58	P200	5950 ± 160
SN 2018hwm	2018-12-14	33	P200	3330 ± 150
SN 2018hwm	2018-12-17	36	P60	6110 ± 570
SN 2018kkv	2019-01-26	37	P200	–
SN 2018lev	2019-01-03	13	P60	10690 ± 910
SN 2019va	2019-03-13	56	P60	8360 ± 570
SN 2019vb	2019-01-26	10	P200	9920 ± 320
SN 2019amt	2019-03-15	37	P200	11040 ± 390
AT 2019aor	2019-03-19	83	P60	–
AT 2019aor	2019-04-06	100	P60	8420 ± 560

Table F: Continued.

Source	Date	Phase (days)	Inst.	H I λ6563 (km s^{-1})
AT 2019txj	2019-03-15	13	P200	–
AT 2019txj	2019-04-03	32	Keck1	4310 ± 210
SN 2019dvw	2019-04-13	51	P200	5480 ± 70
SN 2019dvw	2019-04-24	62	P200	–
SN 2019dvd	2019-05-02	12	P60	–
AT 2019esn	2019-05-13	13	P200	–
SN 2019gss	2019-06-26	29	P200	9130 ± 550
SN 2019gmh	2019-07-03	32	P60	8880 ± 560
SN 2019gmh	2019-08-15	73	P60	–
SN 2019gmh	2019-09-09	98	P60	6610 ± 450
SN 2019gmh	2019-09-18	106	P60	6610 ± 560
SN 2019gmh	2019-09-18	106	P60	6610 ± 450
SN 2019gmh	2019-09-19	107	P60	–
SN 2019gmh	2019-09-19	107	P60	–
SN 2019gmh	2019-09-24	112	P60	–
SN 2019gmh	2019-09-30	118	P60	–
SN 2019hrb	2019-07-08	29	P60	9010 ± 460
SN 2019hnl	2019-07-03	17	P60	10090 ± 560
AT 2019khq	2019-06-26	14	P200	9520 ± 400
SN 2019iex	2019-07-07	12	P60	12130 ± 860
SN 2019iex	2019-10-21	116	P60	–
SN 2019ikb	2019-07-14	17	P60	12090 ± 560
SN 2019ikb	2019-08-04	37	P60	8670 ± 720
SN 2019ikb	2019-10-08	101	P60	7530 ± 460
SN 2019ikb	2019-10-15	107	P60	10950 ± 1020
SN 2019ikb	2019-10-15	107	P60	7530 ± 460
AT 2019tti	2019-08-31	80	P200	–
SN 2019mkr	2019-08-10	17	P60	13380 ± 460
SN 2019mor	2019-08-19	20	P60	–
SN 2019mor	2019-08-28	29	P60	6780 ± 460
SN 2019mor	2019-08-28	29	P60	7930 ± 460
SN 2019mor	2019-09-02	34	P200	3160 ± 230
AT 2019tya	2019-08-10	11	P200	–
AT 2019ttl	2019-08-04	16	P200	6430 ± 280
SN 2019nvm	2019-09-01	13	UH88	–
SN 2019nvm	2019-09-06	18	NOT	10510 ± 80
SN 2019nvm	2019-11-02	74	P60	8740 ± 560
SN 2019nvm	2019-11-13	85	P60	9890 ± 460
SN 2019nvm	2019-11-14	86	P60	8740 ± 460
SN 2019nvm	2020-01-29	160	NOT	6520 ± 180
SN 2019nyk	2019-09-19	31	P60	–
SN 2019odf	2019-09-22	32	P60	10390 ± 560
SN 2019qba	2019-09-21	11	P60	–
SN 2019qba	2019-09-21	11	P60	12920 ± 460
AT 2019qiq	2019-09-28	18	Keck1	5460 ± 240

Table F: Continued.

Source	Date	Phase (days)	Inst.	H I λ6563 (km s^{-1})
SN 2019rho	2019-10-11	13	P60	13000 ± 460
SN 2019upq	2020-01-05	97	P60	–
SN 2019ssi	2019-11-18	31	P60	–
SN 2019twk	2019-11-13	13	P60	13150 ± 560
SN 2019twk	2019-11-24	23	P60	–
AT 2019ubr	2019-11-05	22	P200	7090 ± 490
SN 2019ult	2019-11-24	16	P200	12430 ± 440
SN 2019ust	2019-11-23	12	P60	–
SN 2019ust	2019-11-24	13	P200	–
SN 2019ust	2019-11-24	13	P200	–
SN 2019ust	2019-11-26	14	P60	–
SN 2019ust	2019-12-10	28	P60	–
SN 2019ust	2020-01-02	51	P60	–
SN 2019vdl	2019-12-16	29	P60	–
SN 2019vdl	2019-12-18	31	P60	–
SN 2019vdm	2019-12-19	31	P60	–
SN 2019vdm	2019-12-23	35	Keck1	7470 ± 620
SN 2019vjl	2019-12-11	19	P60	12970 ± 460
SN 2019vsr	2019-12-18	18	P60	–
SN 2019vsr	2019-12-19	19	P60	10110 ± 910
SN 2019vsr	2019-12-23	23	LT	–
SN 2019vsr	2019-12-23	23	LT	–
SN 2019wbd	2019-12-13	14	P60	–
SN 2019wbd	2019-12-21	22	P200	12290 ± 790
SN 2019wbd	2019-12-27	28	LT	–
SN 2019xbm	2020-01-07	31	P60	12540 ± 910
SN 2019xbm	2020-01-27	51	P200	6750 ± 130
SN 2019wvz	2019-12-28	12	LT	11880 ± 730
SN 2019xgi	2019-12-31	14	P60	8700 ± 860
SN 2019xgi	2019-12-31	14	P60	13290 ± 460
SN 2019xgi	2020-01-01	15	P200	–
SN 2019xgi	2020-01-01	15	P200	12830 ± 1020
SN 2019xvo	2020-01-12	18	P60	–
SN 2019xvo	2020-01-12	18	P60	–
SN 2019xvo	2020-01-27	33	P200	6650 ± 160
AT 2020og	2020-01-27	26	P200	12800 ± 650
AT 2020og	2020-02-14	43	P200	9180 ± 560
SN 2020uu	2020-01-27	18	P200	12740 ± 1030
SN 2020aqb	2020-02-13	24	P60	10980 ± 720
SN 2020aqy	2020-02-02	12	P60	13280 ± 860
SN 2020alg	2020-01-31	11	P60	–
SN 2020alg	2020-02-08	19	LT	–
SN 2020awg	2020-02-07	21	P60	11460 ± 450
AT 2020bow	2020-02-14	79	P200	5820 ± 310
SN 2020cxd	2020-05-22	92	P60	5770 ± 570

Table F: Continued.

Source	Date	Phase (days)	Inst.	H I λ6563 (km s^{-1})
SN 2020cxd	2020-06-25	126	LT	–
SN 2020cxd	2020-06-26	127	P60	–
SN 2020cxd	2020-07-01	132	NOT	–
SN 2020cxd	2020-07-28	159	Gemini	4340 ± 180
SN 2020cxd	2020-10-19	241	Keck1	–
SN 2020edr	2020-03-06	16	P60	12450 ± 560
SN 2020edr	2020-06-12	112	P60	–
SN 2020edr	2020-06-25	125	P200	2920 ± 30
SN 2020edr	2020-06-25	125	P200	3120 ± 100
SN 2020djn	2020-03-04	10	P60	12450 ± 850
SN 2020djn	2020-03-04	10	P60	12450 ± 910
SN 2020drl	2020-03-31	34	P60	–
SN 2020drl	2020-04-15	49	P60	–
SN 2020drl	2020-04-15	49	P60	–
AT 2020dzo	2020-03-22	21	Keck1	11630 ± 540
SN 2020eaf	2021-01-12	311	LRIS	–
SN 2020fqv	2020-04-15	16	P60	12630 ± 870
SN 2020gpe	2020-05-29	48	P60	8520 ± 460
SN 2020ghv	2020-04-23	12	P60	–
SN 2020hyb	2020-05-18	27	LT	–
SN 2020jfo	2020-05-15	11	P60	10810 ± 0
SN 2020jfo	2020-05-25	21	P60	9650 ± 460
SN 2020jfo	2020-05-25	21	KAST	–
SN 2020jfo	2020-05-29	25	KAST	–
SN 2020jfo	2020-06-12	39	P60	7320 ± 460
SN 2020jfo	2020-06-17	44	P60	7320 ± 460
SN 2020jfo	2020-12-04	213	P60	–
SN 2020jfo	2020-12-07	216	ALFOSC	4350 ± 180
SN 2020jfo	2020-12-07	216	NOT	4350 ± 80
SN 2020jfo	2020-12-22	231	SEDM	–
SN 2020jfo	2021-01-16	255	ALFOSC	4170 ± 240
SN 2020jfo	2021-01-16	255	NOT	4170 ± 100
SN 2020jfo	2021-02-04	274	SEDM	–
SN 2020jfo	2021-02-09	279	NOT	4090 ± 100
SN 2020jfo	2021-02-09	279	ALFOSC	4090 ± 120
SN 2020jfo	2021-03-09	307	ALFOSC	4100 ± 180
SN 2020jfo	2021-03-09	307	NOT	4100 ± 230
SN 2020jfo	2021-04-20	349	ALFOSC	3660 ± 260
SN 2020jfo	2021-04-20	349	NOT	–
SN 2020jjj	2020-05-23	17	P60	12360 ± 460
SN 2020kay	2020-05-26	11	P60	12930 ± 450
SN 2020lam	2020-06-04	10	P60	10660 ± 0
SN 2020lam	2020-06-06	12	NOT	9380 ± 300
SN 2020lrr	2020-06-20	17	P60	–
SN 2020lrr	2020-06-23	20	Keck1	–

Table F: Continued.

Source	Date	Phase (days)	Inst.	H I λ6563 (km s^{-1})
SN 2020nif	2020-07-03	10	P60	13440 ± 570
SN 2020nif	2020-07-04	11	P60	–
SN 2020nif	2020-07-23	30	LT	11150 ± 200
SN 2020nny	2020-06-27	20	P60	–
SN 2020noe	2020-07-16	26	P200	11740 ± 250
SN 2020noe	2020-07-16	26	P200	11740 ± 830
SN 2020nyb	2020-07-15	15	P60	12590 ± 560
SN 2020nyb	2020-07-15	15	P60	12590 ± 560
SN 2020oco	2020-07-17	18	P60	–
SN 2020oco	2020-07-21	22	P60	6570 ± 560
SN 2020oco	2020-07-21	22	P60	–
SN 2020oco	2020-07-31	31	NOT	–
SN 2020oco	2020-07-31	31	NOT	3980 ± 160
SN 2020oco	2020-08-10	41	P60	–
SN 2020ofw	2020-08-07	29	NOT	8600 ± 160
SN 2020qmp	2020-12-12	140	DBSP	4560 ± 180
SN 2020qmp	2021-01-08	167	DBSP	4420 ± 90
SN 2020qmp	2021-02-20	210	DBSP	4590 ± 250
AT 2020rid	2020-08-15	24	NOT	–
AT 2020afdi	2020-09-13	35	NOT	4490 ± 130
SN 2020sje	2020-09-20	22	Keck1	8070 ± 540
SN 2020sje	2020-10-11	42	P60	–
SN 2020svn	2020-09-19	12	P60	–
SN 2020svn	2020-09-20	13	P60	–
SN 2020svn	2020-09-21	14	P60	–
SN 2020svn	2020-09-22	15	P60	–
SN 2020szs	2020-10-27	45	P60	7590 ± 460
SN 2020szs	2020-10-27	45	SEDM	–
SN 2020tdm	2020-09-27	15	P60	12460 ± 460
AT 2020ugt	2020-09-28	11	P60	13230 ± 920
AT 2020ugt	2020-10-21	33	P200	–
AT 2020ugt	2020-10-21	33	DBSP	–
SN 2020twk	2020-10-03	13	LT	9530 ± 560
SN 2020twk	2020-10-03	13	P60	12970 ± 850
SN 2020twk	2020-10-04	14	P60	–
SN 2020uim	2020-10-11	14	P60	9990 ± 460
SN 2020uim	2020-10-11	14	P60	–
SN 2020uim	2020-12-12	75	SEDM	–
SN 2020ult	2020-10-21	25	DBSP	–
SN 2020ult	2020-10-21	25	P200	7660 ± 620
AT 2021htp	2020-11-11	44	P60	–
AT 2020thp	2020-10-10	30	P60	–
AT 2020thp	2020-10-21	40	P200	–
AT 2020thp	2020-10-21	40	DBSP	–
SN 2020uqx	2020-10-12	12	P60	–

Table F: Continued.

Source	Date	Phase (days)	Inst.	H I λ6563 (km s^{-1})
SN 2020uqx	2020-10-21	20	DBSP	–
SN 2020uqx	2020-10-21	20	P200	–
SN 2020uqx	2020-10-22	21	P60	–
SN 2020vef	2020-10-15	11	P60	7440 ± 560
SN 2020vef	2020-11-12	39	P60	–
AT 2020wip	2020-10-20	19	Keck1	11900 ± 740
AT 2020wip	2020-12-11	70	SEDM	–
SN 2020wgp	2020-10-23	12	P60	13330 ± 460
SN 2020wgs	2020-10-23	12	P60	–
SN 2020wgs	2020-10-28	17	P60	12390 ± 910
SN 2020wgs	2020-10-30	19	LT	–
SN 2020wgs	2020-10-30	19	LT	–
SN 2020xhs	2020-12-16	58	SEDM	–
SN 2020aasd	2020-12-07	15	LT	12810 ± 1070
SN 2020aaun	2020-12-13	21	SEDM	12710 ± 460
SN 2020abah	2020-12-12	23	LRIS	9920 ± 500
SN 2020aawo	2020-12-04	11	SEDM	–
SN 2020abbl	2020-12-12	20	LRIS	9450 ± 410
SN 2020abbi	2020-12-18	26	SEDM	–
SN 2020abcq	2020-12-10	12	SNIFS	–
SN 2020abcq	2020-12-12	14	SEDM	–
SN 2020absk	2020-12-18	14	LT	9850 ± 560
SN 2020absk	2021-02-07	64	SEDM	7810 ± 460
SN 2020absj	2020-12-12	79	SEDM	–
SN 2020abtf	2020-12-11	12	EFOSC2	–
SN 2020abtf	2020-12-16	17	SEDM	–
SN 2020abtf	8591-12-03	2366876	EFOSC2	–
SN 2020acjg	2021-11-06	140	DBSP	–
SN 2020acjg	2022-02-05	228	LRIS	–
SN 2020acjg	2022-03-04	255	LRIS	–
SN 2020adhh	2021-01-09	21	DIS	–
SN 2020aeqx	2021-01-12	15	LRIS	8560 ± 470
SN 2021V	2021-01-12	12	SEDM	–
SN 2021V	2021-02-08	39	SEDM	–
SN 2021aek	2021-01-26	14	EFOSC2	–
SN 2021aek	2021-02-04	23	EFOSC2	–
AT 2021htp	2021-02-20	143	DBSP	–
SN 2021brb	2021-02-04	10	SEDM	9120 ± 720
SN 2021brb	2021-02-19	25	SEDM	10260 ± 910
SN 2021cgu	2021-03-09	29	SEDM	–
SN 2021cwe	2021-03-07	22	SEDM	–
SN 2021cwe	2021-04-07	52	SEDM	–
SN 2021dvk	2021-04-09	42	DBSP	–
SN 2021enz	2021-03-17	14	SEDM	11430 ± 1020
SN 2021eui	2021-03-17	16	SPRAT	5150 ± 370

Table F: Continued.

Source	Date	Phase (days)	Inst.	H I λ6563 (km s^{-1})
SN 2021eui	2021-05-31	90	SEDM	–
SN 2021gmj	2021-04-05	17	SEDM	9100 ± 570
SN 2021gvm	2021-04-03	14	SPRAT	10240 ± 310
SN 2021hac	2021-04-08	18	SEDM	6880 ± 560
SN 2021hac	2021-05-13	52	NOT	8080 ± 230
SN 2021hac	2021-05-13	52	ALFOSC	8080 ± 720
SN 2021mju	2021-05-31	71	DBSP	6810 ± 150
SN 2021jsf	2021-04-20	11	SEDM	–
SN 2021jsf	2021-04-20	11	SNIFS	–
SN 2021jsf	2021-06-09	59	SEDM	–
SN 2021jsf	2021-06-12	62	DBSP	7440 ± 740
AT 2020ghq	2021-05-24	10	SEDM	–
SN 2021nli	2021-05-31	10	SEDM	13240 ± 1240
SN 2021nli	2021-06-04	14	DBSP	10710 ± 430
AT 2014gz	2021-06-19	24	DIS	–
AT 2021pkh	2021-07-10	32	DBSP	–
SN 2021pqj	2021-06-12	10	DBSP	12770 ± 550
SN 2021pnh	2021-07-09	29	LRIS	5060 ± 230
SN 2021qiu	2021-06-28	12	SPRAT	–
SN 2021qiu	2021-07-05	19	SEDM	13010 ± 450
SN 2021qzi	2021-07-05	10	SEDM	–
SN 2021skm	2021-08-01	53	DBSP	7840 ± 710
SN 2021svy	2021-07-30	22	SEDM	–
SN 2021svy	2021-08-04	27	DBSP	7670 ± 360
SN 2021tyw	2021-08-03	11	EFOSC2	–
SN 2021tyw	2021-08-03	11	EFOSC2	–
SN 2021tyw	2021-08-05	13	EFOSC2	–
SN 2021tyw	2021-08-05	13	EFOSC2	–
SN 2021tyw	2021-08-06	14	EFOSC2	–
SN 2021tyw	2021-08-06	14	EFOSC2	–
SN 2021tyw	2021-08-12	20	EFOSC2	–
SN 2021tyw	2021-08-12	20	KAST	–
SN 2021tyw	2021-08-12	20	SEDM	–
SN 2021tyw	2021-08-12	20	EFOSC2	–
SN 2021tyw	2021-08-17	25	SEDM	6110 ± 570
SN 2021tyw	2021-08-21	29	SEDM	–
SN 2021tyw	2021-08-30	38	SEDM	–
SN 2021tyw	2021-09-13	51	EFOSC2	–
SN 2021tyw	2021-09-13	51	EFOSC2	–
SN 2021tyw	2021-11-09	108	SEDM	–
SN 2021ucg	2022-04-27	271	LRIS	5030 ± 380
SN 2021vfh	2021-08-21	14	SEDM	12970 ± 910
SN 2021vfh	2021-08-22	15	SPRAT	–
SN 2021wun	2021-09-06	36	SEDM	–
SN 2021wun	2022-02-02	182	DBSP	5180 ± 360

Table F: Continued.

Source	Date	Phase (days)	Inst.	H I λ6563 (km s^{-1})
SN 2021wvw	2021-09-25	32	NIRES	–
SN 2021xat	2021-09-08	16	SEDM	–
SN 2021ywg	2021-09-25	12	NIRES	–
SN 2021ywg	2021-09-27	14	DBSP	11990 ± 990
SN 2021yyg	2021-09-27	13	DBSP	11440 ± 750
SN 2021zco	2021-09-27	11	DBSP	–
SN 2021zco	2021-09-29	13	SEDM	–
SN 2021zex	2021-12-19	89	SEDM	6620 ± 450
SN 2021zzi	2021-10-13	15	DBSP	–
SN 2021aatd	2021-10-16	10	SEDM	12510 ± 0
SN 2021aatd	2021-12-06	60	SEDM	–
SN 2021aatd	2021-12-12	66	SEDM	–
SN 2021aatd	2021-12-18	72	SEDM	7910 ± 560
SN 2021aatd	2022-01-12	97	SEDM	–
SN 2021aatd	2022-01-15	100	SEDM	–
SN 2021aatd	2022-01-25	110	SEDM	6760 ± 560
SN 2021aatd	2022-01-25	110	SEDM	7910 ± 560
SN 2021aatd	2022-01-28	112	SEDM	7910 ± 560
SN 2021aatd	2022-01-31	115	LRIS	6320 ± 100
SN 2021aatd	2022-02-08	123	SEDM	–
SN 2021aatd	2022-02-12	127	SEDM	–
SN 2021aatd	2022-08-23	316	LRIS	5290 ± 170
SN 2021aatd	2022-08-23	316	LRIS	–
SN 2021aatd	2022-10-23	376	LRIS	4770 ± 70
SN 2021aatd	2022-10-23	376	LRIS	4390 ± 310
SN 2021aaxs	2021-10-15	11	SEDM	–
SN 2021aaxs	2021-10-21	17	SEDM	13260 ± 850
SN 2021abpd	2021-10-25	12	SEDM	12400 ± 910
SN 2021abqs	2021-10-27	11	SEDM	13130 ± 1030
SN 2021achr	2021-10-31	20	SEDM	–
SN 2021achr	2021-11-06	26	DBSP	9270 ± 300
SN 2021adxd	2021-11-20	15	SEDM	–
SN 2021adxd	2021-11-29	24	SEDM	9710 ± 720
SN 2021adxd	2021-12-01	26	DBSP	–
SN 2021aewn	2021-12-01	14	DBSP	10100 ± 40
SN 2021aewn	2021-12-03	16	SEDM	11740 ± 560
SN 2021aewn	2021-12-12	25	SEDM	–
SN 2021afud	2021-12-08	10	SEDM	–
SN 2021afud	2021-12-11	13	SEDM	–
SN 2021afud	2022-01-12	44	DBSP	–
SN 2022cru	2022-04-27	118	LRIS	4370 ± 60
SN 2022ces	2022-03-02	25	SEDM	9320 ± 460
SN 2022gwg	2022-04-19	12	SEDM	–
SN 2022hql	2022-04-26	12	SEDM	12530 ± 460
SN 2022hss	2022-05-02	16	SEDM	13000 ± 460

Table F: Continued.

Source	Date	Phase (days)	Inst.	H I λ6563 (km s^{-1})
SN 2022iob	2022-05-23	37	DBSP	–
SN 2022iyl	2022-06-08	42	DBSP	–
SN 2022joe	2022-05-23	17	DBSP	9280 ± 60
SN 2022jux	2022-05-23	11	SEDM	–
SN 2022jzc	2022-05-31	16	SEDM	–
SN 2022jzc	2022-06-07	23	SEDM	–
SN 2022jzc	2022-06-08	24	DBSP	4160 ± 400
SN 2022jzc	2022-06-21	37	SEDM	–
SN 2022jzc	2022-06-27	43	SEDM	–
SN 2022jzc	2022-07-01	47	SEDM	–
SN 2022jzc	2022-07-04	50	SEDM	–
SN 2022jzc	2022-07-07	53	ALFOSC	4170 ± 70
SN 2022jzc	2022-07-15	61	SEDM	–
SN 2022jzc	2022-07-20	66	ALFOSC	4340 ± 80
SN 2022mxv	2022-08-21	64	SEDM	–
AT 2022ohx	2022-07-27	25	LRIS	6310 ± 170
SN 2022oor	2022-07-29	21	DBSP	9150 ± 490
SN 2022omr	2022-07-21	14	DBSP	–
SN 2022omr	2022-08-03	26	LRIS	9000 ± 330
SN 2022ovb	2022-07-24	10	SEDM	13370 ± 560
SN 2022paf	2022-07-29	14	DBSP	–
SN 2022oyp	2022-07-29	13	DBSP	–
SN 2022oyp	2022-08-23	37	SEDM	–
AT 2022phi	2022-08-26	37	DBSP	6130 ± 370
SN 2022prv	2022-08-11	20	SEDM	–
SN 2022prv	2022-08-12	21	SPRAT	–
SN 2022prv	2022-08-19	28	SPRAT	–
SN 2022prv	2022-08-24	33	SEDM	–
SN 2022prv	2022-08-25	34	SEDM	–
SN 2022prv	2022-09-01	41	SEDM	–
SN 2022prv	2022-09-07	47	SEDM	–
SN 2022raj	2022-08-20	12	DBSP	–
SN 2022raj	2023-10-07	420	LRIS	2130 ± 90
SN 2022rqg	2022-08-23	12	LRIS	–
SN 2022udq	2022-10-02	19	DBSP	7790 ± 450
SN 2022udq	2022-10-06	23	SEDM	–
SN 2022vyc	2022-10-04	11	SEDM	–
SN 2022wbr	2022-10-02	16	DBSP	10840 ± 530
SN 2022wbr	2022-11-17	61	LRIS	–
SN 2022wbr	2023-01-17	121	LRIS	–
SN 2022wbr	2023-11-20	422	LRIS	–
SN 2022wol	2022-11-26	54	DBSP	–
SN 2022wol	2022-12-16	74	DBSP	4260 ± 280
SN 2022xav	2022-10-21	16	SEDM	–
SN 2022xav	2022-11-14	39	SEDM	7740 ± 560

Table F: Continued.

Source	Date	Phase (days)	Inst.	H I λ6563 (km s^{-1})
SN 2022xav	2022-11-18	43	DBSP	8580 ± 570
SN 2022yma	2022-11-26	36	DBSP	7670 ± 510
SN 2022zkc	2022-11-17	14	SEDM	12570 ± 850
SN 2022zmb	2022-11-18	15	DBSP	9550 ± 460
SN 2022zmb	2023-03-20	136	LRIS	–
SN 2022zmb	2023-04-26	172	LRIS	3090 ± 260
SN 2022zmb	2023-05-24	200	DEIMOS	–
SN 2022zmb	2023-06-11	217	LRIS	–
SN 2022zmb	2023-12-07	394	LRIS	3040 ± 30
SN 2022aaad	2022-11-27	18	SEDM	10020 ± 870
SN 2022aaad	2022-11-29	20	ALFOSC	7490 ± 240
SN 2022aaad	2022-12-04	25	SEDM	8860 ± 570
SN 2022aaad	2022-12-15	36	SEDM	7700 ± 0
SN 2022aaad	2022-12-21	42	SEDM	7700 ± 470
SN 2022aaad	2022-12-22	43	SEDM	7700 ± 0
SN 2022aaad	2022-12-29	50	SEDM	7700 ± 570
SN 2022aaad	2023-01-07	58	SEDM	–
SN 2022aaad	2023-01-15	66	ALFOSC	4730 ± 70
SN 2022aaad	2023-01-23	74	SEDM	–
SN 2022aaad	2023-02-03	85	ALFOSC	4350 ± 60
SN 2022aaad	2023-02-16	98	SEDM	–
SN 2022aaad	2023-02-16	98	SEDM	–
SN 2022aaad	2023-03-09	119	SEDM	–
SN 2022aaad	2023-03-24	134	LRIS	3680 ± 90
SN 2022aaad	2023-03-27	137	SEDM	–
SN 2022aaad	2023-04-02	143	SEDM	–
SN 2022aaad	2023-04-09	150	SEDM	–
SN 2022aaad	2023-04-12	153	SEDM	–
SN 2022aaad	2023-04-16	157	ALFOSC	3640 ± 80
SN 2022aaad	2023-04-20	161	SEDM	–
SN 2022aaad	2023-04-27	168	DBSP	3580 ± 100
SN 2022aaad	2023-04-29	170	NIRES	–
SN 2022aaad	2023-06-11	213	LRIS	3410 ± 80
SN 2022aaad	2023-08-18	281	DBSP	3590 ± 260
SN 2022aaad	2023-09-04	298	SEDM	–
SN 2022aaad	2023-09-07	301	DBSP	–
SN 2022aaad	2023-09-16	310	DBSP	–
SN 2022aaad	2023-09-21	315	SEDM	–
SN 2022aaad	2023-10-07	331	SEDM	7700 ± 570
SN 2022aaad	2023-10-07	331	LRIS	3040 ± 40
SN 2022aaad	2023-11-10	365	DBSP	3150 ± 230
SN 2022aaad	2023-12-07	392	LRIS	2970 ± 90
SN 2022aaad	2024-02-15	461	LRIS	–
SN 2022aaad	2024-03-31	506	LRIS	–
SN 2022aang	2023-03-24	130	LRIS	–

Table F: Continued.

Source	Date	Phase (days)	Inst.	H I λ6563 (km s^{-1})
SN 2022aang	2023-12-07	384	LRIS	–
SN 2022acbu	2022-12-16	22	DBSP	12580 ± 1050
SN 2022acko	2023-02-02	59	SEDM	–
SN 2022acko	2023-08-18	255	DBSP	3950 ± 260
SN 2022acko	2023-09-16	284	DBSP	3570 ± 140
SN 2022acko	2023-09-16	284	DBSP	3840 ± 80
SN 2022acko	2023-11-08	336	LRIS	3730 ± 210
SN 2022acko	2023-12-07	365	LRIS	3580 ± 240
SN 2022acko	2024-02-15	435	LRIS	3700 ± 50
SN 2022acrl	2022-12-19	18	SEDM	10800 ± 460
SN 2022acri	2022-12-18	16	SEDM	12050 ± 910
SN 2022adtt	2023-01-17	30	LRIS	7930 ± 600
SN 2022adth	2023-01-17	27	LRIS	7250 ± 640
SN 2023cf	2023-01-21	19	SEDM	13150 ± 460
SN 2023axu	2023-10-09	255	SEDM	–
SN 2023blw	2023-04-16	73	DBSP	–
SN 2023blw	2023-10-07	243	LRIS	–
SN 2023bmd	2023-03-07	27	SPRAT	–
SN 2023buy	2023-04-07	51	SEDM	8300 ± 720
SN 2023bql	2023-04-16	64	DBSP	6960 ± 440
SN 1995al	2023-03-08	21	SEDM	8460 ± 740
SN 1995al	2023-03-09	22	SEDM	8460 ± 570
SN 1995al	2023-12-07	294	LRIS	2490 ± 100
SN 2023ghl	2023-05-08	19	ALFOSC	9480 ± 940
SN 2023gss	2023-06-10	45	SEDM	–
SN 2023gxq	2023-05-24	26	DEIMOS	–
SN 2023gxq	2023-05-28	30	DBSP	–
SN 2023gxq	2023-06-11	44	LRIS	7600 ± 640
SN 2023gxq	2023-06-12	45	LRIS	–
SN 2023hcp	2023-05-15	16	SEDM	–
SN 2023hlf	2023-05-01	12	SEDM	9980 ± 460
SN 2023ijd	2023-05-28	14	SEDM	–
SN 2023ijd	2023-12-03	201	SEDM	–
SN 2023ijd	2023-12-03	201	SEDM	–
SN 2023ijd	2023-12-06	204	SEDM	–
SN 2023hzt	2023-05-28	20	DBSP	–
SN 2023hzt	2023-06-14	36	SEDM	8830 ± 720
SN 2023jid	2023-05-28	95	DBSP	–
SN 2023kne	2023-06-20	19	DBSP	7560 ± 320
SN 2023kzz	2023-08-18	65	DBSP	–
SN 2023rpu	2023-09-28	108	SEDM	–
SN 2023lzn	2023-07-10	10	SEDM	13290 ± 860
SN 2023mpj	2023-07-11	15	DBSP	9070 ± 440
SN 2023nca	2023-07-18	13	LRIS	–
SN 2023nca	2023-07-23	18	LRIS	–

Table F: Continued.

Source	Date	Phase (days)	Inst.	H I λ6563 (km s^{-1})
SN 2023ngy	2023-07-28	13	SEDM	–
SN 2023ngy	2023-08-01	17	DBSP	7360 ± 90
SN 2023ngy	2023-08-03	19	SEDM	9560 ± 460
SN 2023nlu	2023-08-04	17	SEDM	12800 ± 1250
SN 2023vhb	2023-11-14	80	SEDM	7630 ± 0
SN 2023rix	2023-09-17	12	SEDM	12010 ± 730
SN 2023rtq	2023-09-24	17	SEDM	13030 ± 860
SN 2023rtq	2023-10-07	30	LRIS	10060 ± 370
SN 2023rvo	2023-09-19	13	SEDM	–
SN 2023rvo	2023-10-05	28	DBSP	–
SN 2023ucx	2023-10-07	13	LRIS	12710 ± 1150
SN 2023udb	2023-10-15	13	Deveny+LMI	–
SN 2023udb	2023-10-17	15	LRIS	–
SN 2023twg	2023-10-17	19	SEDM	13220 ± 560
SN 2023vcj	2023-12-09	57	SEDM	–
SN 2023vcj	2023-12-10	58	ALFOSC	6380 ± 260
SN 2023vcj	2023-12-28	76	SEDM	–
SN 2023vcj	2023-12-29	77	SEDM	–
SN 2023vcj	2023-12-30	78	ALFOSC	6280 ± 350
SN 2023vcj	2024-01-06	84	SEDM	7330 ± 560
SN 2023vcj	2024-01-06	84	SEDM	7330 ± 560
SN 2023vcj	2024-01-08	86	KAST	–
SN 2023vcj	2024-01-19	97	ALFOSC	5890 ± 160
SN 2023vcj	2024-01-26	104	SEDM	7330 ± 460
SN 2023vcj	2024-02-11	120	SEDM	–
SN 2023vcj	2024-03-09	146	ALFOSC	4750 ± 190
SN 2023vcj	2024-03-14	151	ALFOSC	4410 ± 120
SN 2023vcj	2024-03-30	166	ALFOSC	4650 ± 330
SN 2023vog	2023-11-01	11	SEDM	–
SN 2023vog	2023-11-13	23	SEDM	11240 ± 920
SN 2023way	2023-11-03	10	SEDM	–
SN 2023way	2023-11-05	12	SEDM	–
SN 2023wcr	2023-12-03	40	DBSP	6650 ± 120
SN 2023wcr	2024-01-13	81	DBSP	5340 ± 210
SN 2023wcr	2024-01-13	81	DBSP	5360 ± 130
SN 2023wcr	2024-02-15	114	LRIS	4480 ± 80
SN 2023wcr	2024-03-15	143	ALFOSC	3980 ± 240
SN 2023wcr	2024-03-19	147	SEDM	–
SN 2023wcr	2024-03-20	148	DBSP	4290 ± 290
SN 2023wcr	2024-04-03	162	SEDM	–
SN 2023wcr	2024-04-12	171	DBSP	4170 ± 150
SN 2023wcr	2024-05-01	190	DBSP	3940 ± 190
SN 2023wcr	2024-07-11	260	DBSP	3600 ± 70
SN 2023xvo	2023-11-21	34	SEDM	–
SN 2023xvo	2023-12-03	45	DBSP	–

Table F: Continued.

Source	Date	Phase (days)	Inst.	H I λ6563 (km s^{-1})
SN 2023zcu	2024-01-10	31	SEDM	9910 ± 570
SN 2023zcu	2024-11-11	335	DBSP	4330 ± 200
SN 2023acbr	2024-02-15	53	LRIS	4760 ± 250
SN 2024V	2024-02-15	53	LRIS	–
SN 2024ov	2024-01-13	30	DBSP	–
SN 2024ov	2024-03-31	107	LRIS	4160 ± 80
SN 2024ov	2024-05-08	144	LRIS	–
SN 2024ov	2024-11-30	345	LRIS	–
SN 2024wp	2024-04-12	90	DBSP	–
SN 2024wp	2024-05-02	110	DBSP	4400 ± 80
SN 2024wp	2024-07-09	177	LRIS	4700 ± 120
SN 2024aul	2024-02-27	36	SPRAT	–
AT 2024bzq	2024-02-23	16	SEDM	–
SN 2024btx	2024-05-08	90	LRIS	4340 ± 160
SN 2024atk	2024-04-10	66	SEDM	7450 ± 560
SN 2024chx	2024-04-03	50	SPRAT	6280 ± 250
SN 2024daa	2024-03-20	33	DBSP	7250 ± 590
SN 2024dhi	2024-04-12	50	DBSP	6740 ± 100
SN 2024egd	2024-03-18	15	ALFOSC	10530 ± 710
SN 2024ees	2024-04-02	25	SPRAT	–
SN 2024etq	2024-03-31	19	LRIS	10590 ± 450
SN 2024epy	2024-03-31	15	LRIS	12880 ± 150
SN 2024faf	2024-04-12	26	DBSP	–
SN 2024grw	2024-04-27	11	SPRAT	–
SN 2024grw	2024-05-06	20	SEDM	13100 ± 560
SN 2024hme	2024-05-07	18	DBSP	10590 ± 960
SN 2024izq	2024-05-31	20	DBSP	9950 ± 360
SN 2024jlf	2024-06-07	11	Binospec	–
SN 2024jlf	2024-06-07	11	SEDM	13340 ± 0
SN 2024jlf	2024-06-10	14	SEDM	13340 ± 0
SN 2024jlf	2024-06-10	14	SEDM	13340 ± 0
SN 2024jlf	2024-06-12	16	SEDM	13340 ± 0
SN 2024jlf	2024-06-18	22	SEDM	12170 ± 740
SN 2024jlf	2024-06-19	23	SEDM	11010 ± 570
SN 2024jlf	2024-06-29	33	LRIS	8730 ± 160
SN 2024jlf	2024-07-04	37	SEDM	9850 ± 460
SN 2024jlf	2024-07-06	39	SEDM	9850 ± 460
SN 2024jlf	2024-07-16	49	SEDM	8690 ± 570
SN 2024jlf	2024-07-27	60	SEDM	–
SN 2024jlf	2024-08-01	65	ALFOSC	7290 ± 240
SN 2024jlf	2024-08-14	78	SEDM	8690 ± 460
SN 2024jlf	2024-08-26	90	SEDM	–
SN 2024jlf	2024-08-30	94	KCWI	–
SN 2024jxm	2024-06-15	16	DBSP	8870 ± 300
SN 2024jxm	2024-08-28	89	DBSP	4980 ± 180

Table F: Continued.

Source	Date	Phase (days)	Inst.	H I λ6563 (km s^{-1})
SN 2024jxm	2024-09-04	96	SEDM	6910 ± 560
SN 2024jxm	2024-09-05	97	SEDM	8060 ± 560
SN 2024jxm	2024-10-09	130	LRIS	5040 ± 200
SN 2024jxm	2024-11-30	181	LRIS	3390 ± 140
SN 2024jxm	2025-01-26	237	LRIS	3220 ± 320
SN 2024ldu	2024-06-18	12	SEDM	–
SN 2024ldu	2024-07-09	33	LRIS	7180 ± 590
SN 2024mxq	2024-07-09	19	DBSP	–

Table D: Posterior estimates of explosion and progenitor properties based on fits to the semi-analytical models from Nagy and Vinkó (2016). We list the median values of ^{56}Ni mass ($M_{\rm Ni}$), ejecta mass ($M_{\rm ej}$), progenitor radius (R_0), and kinetic energy ($E_{\rm kin}$). The 16th and 84th percentiles are used to quantify the lower and upper uncertainties around the median. A full machine-readable version of this table is available on Zenodo.

ZTF name	IAU name	$M_{\rm Ni}$ ($\times 10^{-2}\,{\rm M}_\odot$)	$M_{\rm ej}$ (${\rm M}_\odot$)	R_0 (${\rm R}_\odot$)	$E_{\rm kin}$ ($\times 10^{51}$ erg)
ZTF21abrluay	SN 2021vfh	$11.96^{+1.34}_{-0.84}$	$14.8^{+1.4}_{-2.0}$	350^{+119}_{-185}	$8.49^{+1.03}_{-1.85}$
ZTF22abfxkdm	SN 2022ubb	$2.09^{+0.26}_{-0.29}$	$17.2^{+1.0}_{-0.7}$	237^{+33}_{-17}	$4.64^{+0.33}_{-0.23}$
ZTF23aasrcyv	SN 2023nlu	$0.56^{+5.65}_{-0.42}$	$16.5^{+0.9}_{-6.3}$	419^{+442}_{-189}	$3.16^{+0.44}_{-1.65}$
ZTF22abkhrkd	SN 2022wol	$3.52^{+2.66}_{-1.34}$	$13.9^{+3.2}_{-5.5}$	413^{+326}_{-276}	$2.92^{+0.94}_{-1.98}$
ZTF21aaagypx	SN 2021V	$9.12^{+0.82}_{-0.45}$	$24.7^{+0.3}_{-2.8}$	720^{+49}_{-56}	$6.33^{+0.31}_{-0.45}$
ZTF18aawpwlf	SN 2020hvn	$7.23^{+0.40}_{-0.44}$	$6.3^{+0.6}_{-0.4}$	207^{+45}_{-29}	$2.63^{+0.29}_{-0.27}$
ZTF22aafsqud	SN 2022hql	$2.39^{+1.64}_{-1.34}$	$12.8^{+1.5}_{-1.7}$	286^{+81}_{-105}	$3.97^{+0.63}_{-0.70}$
ZTF21acafqtj	SN 2021yok	$6.52^{+0.25}_{-0.64}$	$14.2^{+0.9}_{-0.6}$	885^{+65}_{-117}	$5.81^{+0.27}_{-0.57}$
ZTF21acpqqgu	SN 2021aewn	$1.89^{+0.16}_{-0.06}$	$13.9^{+0.2}_{-0.5}$	455^{+19}_{-15}	$3.49^{+0.05}_{-0.15}$
ZTF19abqrhvt	SN 2019nyk	$10.79^{+0.40}_{-0.39}$	$10.6^{+0.4}_{-0.4}$	102^{+5}_{-7}	$8.17^{+0.36}_{-0.36}$
ZTF21aaipypa	SN 2021cgu	$7.36^{+6.97}_{-2.09}$	$20.7^{+1.1}_{-5.9}$	707^{+193}_{-104}	$9.41^{+0.58}_{-4.57}$
ZTF20acuhren	SN 2020abcq	$2.27^{+0.27}_{-1.88}$	$8.4^{+1.1}_{-0.3}$	205^{+32}_{-39}	$0.87^{+0.02}_{-0.03}$
ZTF24aaucrua	SN 2024nez	$4.20^{+0.24}_{-0.41}$	$8.9^{+1.2}_{-0.6}$	183^{+97}_{-42}	$1.40^{+0.27}_{-0.14}$
ZTF22aapargp	SN 2022niw	$3.84^{+1.78}_{-1.77}$	$20.3^{+2.7}_{-2.8}$	337^{+278}_{-185}	$8.66^{+0.90}_{-1.44}$
ZTF23aaqknaw	SN 2023lzn	$5.78^{+0.48}_{-0.49}$	$21.8^{+0.3}_{-2.4}$	346^{+28}_{-58}	$9.86^{+0.08}_{-1.51}$
ZTF22abhsxph	SN 2022vyc	$6.11^{+0.33}_{-0.37}$	$16.6^{+1.1}_{-1.3}$	157^{+44}_{-61}	$5.40^{+0.55}_{-0.51}$
ZTF22abzqwmp	SN 2022adth	$0.87^{+0.13}_{-0.56}$	$11.7^{+0.7}_{-1.3}$	1048^{+86}_{-319}	$3.05^{+0.23}_{-0.65}$
ZTF24aabsmvc	SN 2024ws	$1.94^{+1.68}_{-0.84}$	$19.0^{+1.7}_{-3.4}$	160^{+43}_{-33}	$4.75^{+0.45}_{-1.00}$
ZTF21aantsla	SN 2021ech	$5.52^{+0.49}_{-0.69}$	$11.6^{+1.3}_{-0.9}$	443^{+109}_{-77}	$3.16^{+0.47}_{-0.27}$
ZTF19aclobbu	SN 2019twk	$21.80^{+2.30}_{-21.34}$	$16.4^{+3.9}_{-2.2}$	89^{+90}_{-18}	$6.14^{+2.05}_{-6.01}$
ZTF21abnlhxs	SN 2021tyw	$1.80^{+0.13}_{-0.15}$	$14.5^{+0.8}_{-1.1}$	348^{+29}_{-58}	$4.50^{+0.22}_{-0.54}$
ZTF23aanymcl	SN 2023kzz	$9.06^{+0.70}_{-0.53}$	$10.6^{+0.8}_{-0.8}$	361^{+152}_{-137}	$4.91^{+0.52}_{-0.52}$
ZTF21abouuat	SN 2021ucg	$13.76^{+0.75}_{-0.72}$	$22.1^{+0.6}_{-1.2}$	341^{+24}_{-35}	$9.83^{+0.10}_{-0.79}$
ZTF19acrcxri	SN 2019ult	$18.67^{+1.05}_{-15.54}$	$11.7^{+1.1}_{-0.7}$	837^{+192}_{-171}	$8.12^{+0.83}_{-1.71}$
ZTF21aakvroo	SN 2021cwe	$12.83^{+0.71}_{-1.65}$	$6.6^{+1.9}_{-0.4}$	250^{+266}_{-114}	$1.97^{+0.89}_{-0.21}$
ZTF22absqhkw	SN 2022zkc	$8.62^{+0.44}_{-0.36}$	$8.0^{+0.6}_{-0.6}$	310^{+69}_{-95}	$4.16^{+0.49}_{-0.44}$
ZTF18abzrgim	SN 2018gvt	$26.28^{+2.45}_{-1.20}$	$16.3^{+1.4}_{-3.0}$	638^{+235}_{-192}	$8.52^{+1.06}_{-2.32}$
ZTF21aapliyn	SN 2021foj	$10.57^{+1.53}_{-0.42}$	$19.3^{+0.8}_{-3.3}$	129^{+21}_{-29}	$8.53^{+0.50}_{-2.08}$
ZTF21abjcjmc	SN 2021skn	$5.04^{+2.59}_{-0.18}$	$7.8^{+0.3}_{-3.3}$	1041^{+48}_{-444}	$4.32^{+0.18}_{-2.13}$
ZTF22abyohff	SN 2022acrl	$1.08^{+3.73}_{-0.98}$	$17.3^{+2.4}_{-8.0}$	158^{+95}_{-77}	$3.46^{+0.85}_{-1.99}$
ZTF19aazudta	SN 2019hqm	$11.17^{+3.42}_{-1.16}$	$19.8^{+1.9}_{-8.1}$	531^{+274}_{-288}	$8.69^{+0.98}_{-5.05}$
ZTF22aarycqo	SN 2022ojo	$16.51^{+20.29}_{-14.52}$	$7.8^{+1.7}_{-1.2}$	953^{+128}_{-173}	$1.37^{+1.02}_{-0.58}$
ZTF19aamwhat	SN 2019bzd	$1.16^{+0.08}_{-0.04}$	$9.2^{+0.5}_{-0.3}$	163^{+6}_{-15}	$1.04^{+0.09}_{-0.04}$
ZTF22abyokkf	SN 2022acri	$16.85^{+0.86}_{-0.84}$	$22.5^{+0.6}_{-1.5}$	316^{+46}_{-39}	$9.68^{+0.24}_{-0.78}$
ZTF24aaabbse	SN 2023achj	$18.51^{+1.00}_{-0.83}$	$14.9^{+0.7}_{-0.8}$	1000^{+91}_{-120}	$3.39^{+0.21}_{-0.22}$
ZTF19abqrhvy	SN 2019odf	$23.70^{+0.68}_{-13.83}$	$19.2^{+0.9}_{-1.8}$	400^{+148}_{-43}	$7.17^{+0.77}_{-2.52}$
ZTF18aaszvfn	SN 2021iaw	$6.78^{+1.36}_{-0.67}$	$11.5^{+0.4}_{-1.4}$	121^{+14}_{-8}	$2.71^{+0.18}_{-0.19}$
ZTF23aaxadel	SN 2023pbg	$9.87^{+1.26}_{-0.60}$	$15.5^{+1.0}_{-2.4}$	161^{+25}_{-27}	$4.52^{+0.33}_{-1.21}$
ZTF22abfwxtr	SN 2022udq	$1.56^{+4.38}_{-0.23}$	$23.8^{+1.0}_{-6.5}$	412^{+100}_{-66}	$5.59^{+0.32}_{-2.01}$

Table D: Continued.

ZTF	IAU	$M_{\rm Ni}$ ($\times 10^{-2}\,{\rm M}_\odot$)	$M_{\rm ej}$ ($\rm M_\odot$)	R_0 ($\rm R_\odot$)	$E_{\rm kin}$ ($\times 10^{51}$ erg)
ZTF21aaobkmg	SN 2021eui	$1.84^{+0.13}_{-0.13}$	$8.1^{+0.8}_{-0.1}$	299^{+76}_{-38}	$0.89^{+0.01}_{-0.08}$
ZTF24aabpzuz	SN 2024vs	$9.19^{+0.73}_{-0.30}$	$14.0^{+0.6}_{-1.6}$	512^{+98}_{-133}	$6.00^{+0.37}_{-0.98}$
ZTF19aawgxdn	SN 2019gmh	$11.94^{+0.86}_{-0.61}$	$22.5^{+0.5}_{-2.2}$	134^{+18}_{-22}	$9.40^{+0.50}_{-0.90}$
ZTF19aarykkb	SN 2019dzk	$0.80^{+0.25}_{-0.02}$	$14.0^{+0.4}_{-0.9}$	765^{+32}_{-88}	$3.37^{+0.15}_{-0.29}$
ZTF22aazmrpx	SN 2022raj	$0.09^{+0.24}_{-0.01}$	$6.7^{+0.3}_{-0.3}$	349^{+49}_{-24}	$0.52^{+0.06}_{-0.02}$
ZTF21abnudtb	SN 2021txr	$0.74^{+20.24}_{-0.12}$	$15.0^{+0.7}_{-1.5}$	1065^{+45}_{-149}	$6.24^{+3.53}_{-0.71}$
ZTF24aafqzur	SN 2024daa	$6.58^{+0.42}_{-0.35}$	$17.1^{+1.5}_{-1.1}$	98^{+14}_{-15}	$6.00^{+0.72}_{-0.47}$
ZTF22aavobvq	SN 2022prv	$5.91^{+0.77}_{-0.32}$	$15.8^{+0.5}_{-1.2}$	280^{+20}_{-15}	$9.71^{+0.28}_{-0.93}$
ZTF21ablvzhp	SN 2021tiq	$27.63^{+1.35}_{-1.16}$	$17.1^{+0.6}_{-1.1}$	714^{+38}_{-58}	$9.76^{+0.24}_{-0.88}$
ZTF23aaaatjn	SN 2023cf	$15.93^{+2.12}_{-5.28}$	$14.5^{+1.9}_{-1.1}$	902^{+181}_{-132}	$7.02^{+0.95}_{-0.75}$
ZTF21acgunkr	SN 2021aaxs	$2.74^{+3.30}_{-1.43}$	$10.0^{+1.9}_{-2.2}$	806^{+214}_{-312}	$1.46^{+0.72}_{-0.54}$
ZTF21abgilzj	AT 2021qcr	$6.90^{+0.47}_{-0.41}$	$11.7^{+0.8}_{-0.7}$	339^{+26}_{-20}	$2.32^{+0.17}_{-0.14}$
ZTF24aabppgn	SN 2024wp	$2.03^{+0.46}_{-0.48}$	$8.5^{+0.8}_{-0.3}$	691^{+301}_{-379}	$0.84^{+0.04}_{-0.07}$
ZTF20acmaaan	SN 2020xyk	$4.96^{+0.25}_{-0.28}$	$9.5^{+0.7}_{-0.6}$	264^{+225}_{-70}	$2.78^{+0.29}_{-0.25}$
ZTF23aackjhs	SN 1995al	$1.54^{+0.07}_{-0.08}$	$6.2^{+0.5}_{-0.2}$	138^{+23}_{-30}	$0.53^{+0.03}_{-0.02}$
ZTF22abtjefa	SN 2022aaad	$1.15^{+0.00}_{-0.03}$	$5.8^{+0.2}_{-0.2}$	172^{+14}_{-8}	$0.50^{+0.00}_{-0.04}$
ZTF24aaplfjd	SN 2024jxm	$3.05^{+0.06}_{-0.07}$	$11.2^{+2.6}_{-2.2}$	313^{+288}_{-236}	$1.81^{+0.77}_{-0.56}$
ZTF23aaphnyz	SN 2023lkw	$20.34^{+1.83}_{-0.73}$	$13.3^{+0.5}_{-2.2}$	405^{+88}_{-78}	$4.88^{+0.12}_{-1.04}$
ZTF23abnogui	SN 2023wcr	$1.19^{+0.01}_{-0.03}$	$8.1^{+0.6}_{-0.1}$	148^{+8}_{-8}	$0.79^{+0.01}_{-0.06}$
ZTF24aajxppf	SN 2024grw	$10.86^{+0.40}_{-0.42}$	$8.1^{+0.2}_{-0.7}$	180^{+2}_{-44}	$4.03^{+0.05}_{-0.52}$
ZTF24aaejecr	SN 2024btj	$1.89^{+0.02}_{-0.03}$	$8.6^{+0.3}_{-0.4}$	397^{+26}_{-29}	$1.34^{+0.05}_{-0.07}$
ZTF19aailepg	SN 2019amt	$12.87^{+0.45}_{-0.18}$	$22.2^{+1.0}_{-1.7}$	449^{+147}_{-102}	$8.43^{+0.61}_{-0.62}$
ZTF22aaolwsd	SN 2022mxv	$1.74^{+0.03}_{-0.02}$	$15.7^{+0.7}_{-0.7}$	158^{+18}_{-7}	$2.98^{+0.15}_{-0.13}$
ZTF19abqrhvt	SN 2019nyk	$13.71^{+1.02}_{-0.70}$	$7.1^{+0.3}_{-0.3}$	1012^{+102}_{-93}	$4.10^{+0.25}_{-0.23}$
ZTF21aapkcmr	AT 2021fnj	$7.41^{+0.46}_{-0.40}$	$8.7^{+0.6}_{-0.6}$	874^{+153}_{-155}	$5.16^{+0.35}_{-0.53}$
ZTF21aaqugxm	SN 2021hdt	$17.61^{+0.76}_{-1.01}$	$5.4^{+0.3}_{-0.3}$	478^{+180}_{-194}	$1.91^{+0.11}_{-0.11}$
ZTF23abhzfww	SN 2023twg	$13.68^{+0.53}_{-0.31}$	$15.9^{+0.8}_{-0.9}$	823^{+187}_{-184}	$5.90^{+0.41}_{-0.46}$
ZTF22abnujbv	SN 2022xus	$2.45^{+0.07}_{-0.08}$	$8.8^{+0.4}_{-0.4}$	259^{+297}_{-97}	$1.99^{+0.10}_{-0.10}$
ZTF24abtczty	SN 2024abfl	$0.35^{+0.00}_{-0.00}$	$5.7^{+0.3}_{-0.3}$	543^{+80}_{-56}	$0.21^{+0.01}_{-0.01}$
ZTF22aativsd	SN 2022ovb	$20.74^{+0.92}_{-0.78}$	$11.7^{+0.6}_{-0.7}$	141^{+14}_{-8}	$6.39^{+0.35}_{-0.43}$
ZTF19acewuwn	SN 2019ssl	$13.03^{+1.09}_{-0.73}$	$15.0^{+1.2}_{-1.1}$	107^{+33}_{-25}	$5.93^{+0.66}_{-0.59}$
ZTF23aailjjs	SN 2023hcp	$11.76^{+0.22}_{-0.61}$	$13.5^{+0.4}_{-0.6}$	281^{+32}_{-29}	$9.63^{+0.26}_{-0.60}$
ZTF20aapchqy	SN 2020cxd	$0.11^{+0.00}_{-0.00}$	$7.6^{+0.6}_{-0.2}$	197^{+10}_{-14}	$0.29^{+0.03}_{-0.01}$
ZTF24aaemydm	SN 2024chx	$12.08^{+0.11}_{-1.02}$	$14.3^{+0.6}_{-0.6}$	155^{+6}_{-17}	$9.90^{+0.08}_{-0.87}$
ZTF21acgrrnl	SN 2021aayf	$3.85^{+0.06}_{-0.04}$	$12.7^{+0.9}_{-0.9}$	382^{+36}_{-68}	$2.40^{+0.24}_{-0.39}$
ZTF23abaxtlq	SN 2023rix	$1.80^{+0.03}_{-0.03}$	$10.7^{+0.5}_{-0.5}$	809^{+85}_{-81}	$2.31^{+0.16}_{-0.13}$
ZTF21aaeqwov	AT 2021htp	$5.30^{+0.25}_{-0.05}$	$18.1^{+0.9}_{-1.0}$	107^{+98}_{-15}	$5.42^{+0.35}_{-0.34}$
ZTF24aagupsf	SN 2024egd	$7.36^{+0.34}_{-0.18}$	$15.4^{+0.8}_{-0.8}$	555^{+60}_{-121}	$7.29^{+0.53}_{-0.41}$
ZTF22aavbfhz	AT 2022phi	$5.22^{+0.16}_{-0.12}$	$8.6^{+0.6}_{-0.6}$	743^{+215}_{-194}	$2.25^{+0.22}_{-0.24}$
ZTF19acytcsg	SN 2019wvz	$19.88^{+0.78}_{-0.61}$	$16.6^{+0.8}_{-0.9}$	362^{+68}_{-38}	$8.53^{+0.52}_{-0.60}$
ZTF19aazyvub	SN 2019hnl	$7.13^{+0.24}_{-0.28}$	$12.3^{+0.5}_{-0.7}$	136^{+14}_{-19}	$4.41^{+0.26}_{-0.28}$
ZTF19aaniore	SN 2019ceg	$11.75^{+0.31}_{-0.39}$	$14.8^{+0.7}_{-0.6}$	616^{+96}_{-76}	$4.57^{+0.30}_{-0.22}$
ZTF22abkbjsb	SN 2022vym	$5.06^{+0.33}_{-0.08}$	$5.9^{+0.2}_{-0.3}$	632^{+63}_{-37}	$1.06^{+0.04}_{-0.06}$

Table D: Continued.

ZTF	IAU	$M_{\rm Ni}$ ($\times 10^{-2}\,{\rm M}_\odot$)	$M_{\rm ej}$ ($\rm M_\odot$)	R_0 ($\rm R_\odot$)	$E_{\rm kin}$ ($\times 10^{51}$ erg)
ZTF19actnyae	SN 2019vdm	$11.10^{+0.79}_{-1.10}$	$13.4^{+0.9}_{-1.2}$	729^{+120}_{-34}	$9.78^{+0.11}_{-1.51}$
ZTF24aadkwni	SN 2024aul	$13.40^{+0.79}_{-0.40}$	$9.6^{+0.4}_{-0.5}$	150^{+42}_{-21}	$5.10^{+0.46}_{-0.28}$
ZTF19abajxet	SN 2019hyk	$8.02^{+0.38}_{-0.38}$	$9.7^{+0.4}_{-0.4}$	392^{+366}_{-87}	$2.75^{+0.14}_{-0.17}$
ZTF21abfiuqf	SN 2021pla	$3.29^{+0.05}_{-0.10}$	$6.6^{+0.2}_{-0.4}$	453^{+96}_{-99}	$2.10^{+0.10}_{-0.15}$
ZTF24abmkros	SN 2024xkd	$0.78^{+0.01}_{-0.01}$	$8.4^{+0.5}_{-0.4}$	309^{+404}_{-166}	$0.88^{+0.06}_{-0.05}$
ZTF22aakdqqg	SN 2022kad	$10.03^{+0.41}_{-0.46}$	$5.8^{+0.3}_{-0.3}$	1061^{+73}_{-635}	$1.30^{+0.10}_{-0.09}$
ZTF21aafepon	SN 2021ass	$5.17^{+0.20}_{-0.33}$	$7.5^{+0.5}_{-0.4}$	139^{+6}_{-25}	$2.24^{+0.13}_{-0.12}$
ZTF21abvcxel	SN 2021wvw	$3.55^{+0.25}_{-0.20}$	$7.2^{+0.4}_{-0.3}$	123^{+18}_{-7}	$2.50^{+0.16}_{-0.10}$
ZTF23abbtkrv	SN 2023rvo	$9.81^{+0.18}_{-0.15}$	$24.8^{+0.1}_{-3.0}$	178^{+18}_{-12}	$9.54^{+0.14}_{-1.07}$
ZTF19abbnamr	SN 2019iex	$7.40^{+0.12}_{-0.26}$	$22.4^{+0.4}_{-1.5}$	170^{+33}_{-7}	$9.94^{+0.05}_{-1.00}$
ZTF20abeohfn	SN 2020mjm	$2.36^{+0.08}_{-0.09}$	$11.6^{+0.5}_{-0.4}$	439^{+82}_{-68}	$3.00^{+0.12}_{-0.12}$
ZTF19acbwejj	SN 2019upq	$9.13^{+0.33}_{-0.01}$	$24.7^{+0.2}_{-2.7}$	200^{+71}_{-21}	$6.36^{+0.33}_{-0.39}$
ZTF19abbwfgp	SN 2019ikb	$14.79^{+0.30}_{-0.22}$	$11.3^{+0.4}_{-0.3}$	257^{+65}_{-21}	$4.18^{+0.23}_{-0.19}$
ZTF21abhhrpj	SN 2021qiu	$16.49^{+0.70}_{-0.75}$	$11.2^{+0.3}_{-1.3}$	341^{+37}_{-47}	$4.64^{+0.29}_{-1.10}$
ZTF22abssiet	SN 2022zmb	$1.32^{+0.03}_{-0.02}$	$12.9^{+0.3}_{-0.5}$	152^{+18}_{-6}	$3.64^{+0.10}_{-0.17}$
ZTF22abtspsw	SN 2022aagp	$0.58^{+0.00}_{-0.00}$	$10.4^{+2.3}_{-2.5}$	311^{+39}_{-20}	$1.12^{+0.45}_{-0.43}$
ZTF21aavhnpk	SN 2021jsf	$6.28^{+0.24}_{-0.25}$	$12.1^{+0.6}_{-0.6}$	183^{+30}_{-31}	$4.73^{+0.34}_{-0.30}$
ZTF23abascqa	SN 2023rbk	$6.34^{+0.23}_{-0.19}$	$9.8^{+0.4}_{-0.5}$	1033^{+68}_{-362}	$2.98^{+0.10}_{-0.18}$
ZTF19abwztsb	SN 2019pjs	$4.36^{+0.17}_{-0.18}$	$8.1^{+0.4}_{-0.3}$	324^{+121}_{-84}	$2.11^{+0.11}_{-0.12}$
ZTF22aaywnyg	SN 2022pru	$1.90^{+0.01}_{-0.04}$	$8.1^{+0.7}_{-0.0}$	1024^{+102}_{-73}	$0.78^{+0.02}_{-0.05}$
ZTF19actnwtn	SN 2019vdl	$30.98^{+1.62}_{-1.92}$	$18.9^{+1.0}_{-1.5}$	843^{+139}_{-181}	$9.00^{+0.50}_{-1.06}$
ZTF21aabygea	SN 2021os	$7.81^{+0.18}_{-0.12}$	$16.2^{+0.6}_{-0.7}$	175^{+22}_{-9}	$5.01^{+0.20}_{-0.23}$
ZTF23abmoxlu	SN 2023vog	$2.59^{+0.05}_{-0.02}$	$16.4^{+0.7}_{-0.9}$	424^{+68}_{-29}	$2.87^{+0.14}_{-0.16}$
ZTF22aakdbia	SN 2022jzc	$0.31^{+0.00}_{-0.00}$	$7.6^{+0.5}_{-0.3}$	363^{+455}_{-172}	$0.42^{+0.03}_{-0.03}$
ZTF19aadnxnl	SN 2019va	$11.30^{+0.23}_{-0.55}$	$15.6^{+0.6}_{-1.1}$	350^{+19}_{-25}	$4.92^{+0.08}_{-0.49}$
ZTF21aafkwtk	SN 2021apg	$6.20^{+0.14}_{-0.15}$	$17.3^{+0.7}_{-0.7}$	214^{+67}_{-46}	$7.51^{+0.33}_{-0.35}$
ZTF19aanrrqu	SN 2019clp	$11.35^{+0.42}_{-0.36}$	$6.5^{+0.3}_{-0.2}$	118^{+52}_{-35}	$3.51^{+0.21}_{-0.17}$
ZTF23aasbvab	SN 2023ngy	$3.45^{+0.05}_{-0.04}$	$12.0^{+0.5}_{-0.6}$	93^{+32}_{-20}	$2.42^{+0.12}_{-0.13}$
ZTF18aatyqds	SN 2018btl	$4.12^{+0.07}_{-0.10}$	$7.1^{+0.3}_{-0.2}$	710^{+249}_{-207}	$1.23^{+0.08}_{-0.06}$
ZTF21aardvtn	AT 2021htp	$5.75^{+0.23}_{-0.10}$	$18.0^{+0.7}_{-0.9}$	324^{+110}_{-56}	$5.61^{+0.26}_{-0.34}$
ZTF19acftfav	SN 2019ssi	$3.70^{+0.23}_{-0.07}$	$7.1^{+0.5}_{-0.4}$	108^{+8}_{-13}	$1.43^{+0.14}_{-0.08}$
ZTF19aapafit	SN 2019cvz	$8.92^{+0.10}_{-0.20}$	$23.0^{+0.4}_{-1.0}$	135^{+6}_{-9}	$9.94^{+0.05}_{-0.69}$
ZTF24aarvbxj	SN 2024lby	$10.42^{+0.54}_{-0.42}$	$9.7^{+0.5}_{-0.5}$	240^{+73}_{-37}	$7.02^{+0.48}_{-0.49}$
ZTF21aagtqna	SN 2021brb	$8.19^{+0.16}_{-0.11}$	$22.8^{+0.8}_{-1.4}$	88^{+13}_{-10}	$8.42^{+0.47}_{-0.51}$
ZTF22aasojye	SN 2022omr	$5.16^{+0.24}_{-0.00}$	$24.7^{+0.3}_{-2.6}$	150^{+40}_{-12}	$8.50^{+0.32}_{-0.57}$
ZTF21aanzcuj	SN 2021enz	$7.98^{+5.16}_{-0.12}$	$19.4^{+1.0}_{-15.8}$	468^{+54}_{-413}	$8.37^{+0.59}_{-7.62}$
ZTF22abfavpu	SN 2022tmb	$4.10^{+0.14}_{-0.10}$	$11.1^{+0.5}_{-0.6}$	548^{+58}_{-100}	$3.08^{+0.14}_{-0.20}$
ZTF18aaxkqgy	SN 2018ccb	$6.80^{+0.29}_{-0.21}$	$13.3^{+0.7}_{-0.5}$	120^{+10}_{-27}	$6.47^{+0.32}_{-0.31}$
ZTF19aanhhal	SN 2019cec	$7.96^{+0.15}_{-0.20}$	$13.3^{+0.7}_{-0.6}$	129^{+25}_{-52}	$3.89^{+0.26}_{-0.22}$

Table E: Posterior estimates of explosion and progenitor properties based on fits to the radiation-hydrodynamical models from (Moriya et al. 2023). A machine-readable version of this table is available on Zenodo.

ZTF name	IAU name	ZAMS mass ($M_\odot$)	$M_{\rm Ni}$ ($\times10^{-2}$ $M_\odot$)	$R_{\rm CSM}$ ($\times10^{14}$ cm)	β	Energy ($\times10^{51}$ erg)	log $\dot{M}$ ($M_\odot$ yr^{-1})
ZTF22abkhrkd	SN 2022wol	10.2 ± 0.4	$1.44^{+0.93}_{-0.09}$	$7.9^{+1.4}_{-1.0}$	$4.0^{+0.2}_{-0.7}$	$0.31^{+0.01}_{-0.02}$	−0.54
ZTF22abtjefa	SN 2022aaad	11.0 ± 0.6	$1.38^{+1.08}_{-0.32}$	$3.8^{+1.0}_{-0.9}$	$2.5^{+0.2}_{-0.6}$	$0.15^{+0.39}_{-0.02}$	−0.57
ZTF19abqrhvt	SN 2019nyk	11.7 ± 0.9	$3.67^{+1.74}_{-0.27}$	$7.9^{+1.7}_{-3.2}$	$3.7^{+1.1}_{-1.1}$	$1.18^{+0.62}_{-0.20}$	−0.30
ZTF19acewuwn	SN 2019ssl	12.6 ± 1.1	$5.65^{+0.84}_{-0.17}$	$6.5^{+0.7}_{-2.6}$	$0.9^{+0.1}_{-0.2}$	$0.16^{+0.06}_{-0.02}$	−0.47
ZTF21aaqugxm	SN 2021hdt	14.8 ± 1.0	$2.90^{+2.07}_{-0.53}$	$8.2^{+0.9}_{-1.6}$	$0.8^{+1.9}_{-0.1}$	$2.42^{+0.13}_{-0.11}$	−0.49
ZTF24aaasazz	SN 2024ov	10.5 ± 0.5	$3.32^{+0.93}_{-0.36}$	$5.5^{+2.2}_{-0.6}$	$1.1^{+1.6}_{-0.5}$	$0.27^{+0.08}_{-0.05}$	−0.39
ZTF20abyylgi	SN 2020svn	13.4 ± 1.4	$15.33^{+1.80}_{-5.35}$	$8.0^{+0.9}_{-1.9}$	$4.4^{+0.5}_{-0.9}$	$1.74^{+1.45}_{-0.36}$	−0.22
ZTF24aagupsf	SN 2024egd	12.0 ± 0.5	$4.10^{+0.59}_{-0.27}$	$3.4^{+1.6}_{-1.8}$	$4.3^{+0.6}_{-2.2}$	$0.92^{+0.13}_{-0.09}$	−0.64
ZTF21aanzcuj	SN 2021enz	13.1 ± 0.3	$3.43^{+2.28}_{-0.80}$	$4.6^{+1.8}_{-1.5}$	$4.0^{+0.5}_{-0.5}$	$0.53^{+0.12}_{-0.18}$	−0.48
ZTF20acveadu	SN 2020absk	10.3 ± 0.3	$0.47^{+2.53}_{-0.30}$	$5.7^{+2.3}_{-1.5}$	$3.4^{+0.6}_{-0.9}$	$0.41^{+0.24}_{-0.01}$	−0.60
ZTF19aamwhat	SN 2019bzd	10.5 ± 0.7	$1.05^{+1.45}_{-0.23}$	$4.7^{+1.3}_{-1.6}$	$2.4^{+1.0}_{-0.7}$	$0.22^{+0.04}_{-0.01}$	−0.48
ZTF19abbwfgp	SN 2019ikb	12.4 ± 1.2	$7.24^{+2.81}_{-1.22}$	$5.5^{+2.3}_{-1.8}$	$2.9^{+1.4}_{-1.6}$	$1.82^{+0.91}_{-0.16}$	−0.30
ZTF23aanymcl	SN 2023kzz	11.6 ± 0.7	$2.31^{+1.06}_{-0.53}$	$5.3^{+2.3}_{-3.1}$	$3.4^{+0.4}_{-0.8}$	$1.04^{+0.11}_{-0.12}$	−0.46
ZTF18aawpwlf	SN 2020hvn	10.6 ± 0.7	$1.26^{+4.61}_{-0.45}$	$7.8^{+1.0}_{-3.8}$	$3.8^{+0.4}_{-1.3}$	$1.04^{+0.09}_{-0.10}$	−0.41
ZTF18aatyqds	SN 2018btl	12.3 ± 0.5	$2.24^{+0.74}_{-0.50}$	$7.3^{+0.8}_{-3.3}$	$2.8^{+0.5}_{-0.6}$	$0.28^{+0.42}_{-0.08}$	−0.37
ZTF18aaxkqgy	SN 2018ccb	12.1 ± 1.1	$2.82^{+0.58}_{-0.73}$	$6.7^{+1.2}_{-1.3}$	$3.3^{+0.6}_{-0.3}$	$0.79^{+0.34}_{-0.06}$	−0.48
ZTF21acafqtj	SN 2021yok	12.6 ± 0.9	$3.52^{+1.17}_{-1.00}$	$6.0^{+1.7}_{-1.3}$	$4.3^{+0.2}_{-1.7}$	$0.72^{+0.03}_{-0.33}$	−0.45
ZTF20aaiovoy	SN 2020bad	10.5 ± 3.4	$6.93^{+1.67}_{-2.12}$	$6.2^{+1.7}_{-1.1}$	$1.0^{+1.0}_{-0.4}$	$0.76^{+0.29}_{-0.05}$	−0.55
ZTF21aafepon	SN 2021ass	11.0 ± 0.6	$2.89^{+0.52}_{-0.20}$	$7.7^{+1.1}_{-1.0}$	$2.2^{+0.9}_{-1.0}$	$0.36^{+0.30}_{-0.03}$	−0.44
ZTF23abhzfww	SN 2023twg	12.0 ± 0.6	$9.74^{+2.10}_{-0.97}$	$4.4^{+2.3}_{-2.3}$	$3.8^{+1.0}_{-0.9}$	$1.01^{+0.13}_{-0.11}$	−0.58
ZTF20abyzomt	SN 2020szs	12.1 ± 0.6	$6.00^{+0.39}_{-1.03}$	$7.0^{+0.7}_{-1.4}$	$3.8^{+0.4}_{-0.9}$	$1.49^{+0.09}_{-0.15}$	−0.48
ZTF24aaucrua	SN 2024nez	9.9 ± 0.5	$2.96^{+1.50}_{-0.39}$	$3.7^{+1.3}_{-0.8}$	$1.0^{+0.2}_{-0.3}$	$1.16^{+0.18}_{-0.46}$	−0.58
ZTF21aaobkmg	SN 2021eui	10.5 ± 0.5	$0.37^{+1.19}_{-0.20}$	$7.0^{+0.5}_{-1.3}$	$1.7^{+0.5}_{-0.7}$	$0.16^{+0.03}_{-0.01}$	−0.52
ZTF21aagtqna	SN 2021brb	13.0 ± 0.8	$5.18^{+0.16}_{-0.15}$	$6.7^{+0.7}_{-1.2}$	$3.0^{+0.4}_{-0.5}$	$0.60^{+0.17}_{-0.07}$	−0.47
ZTF19aadnxnl	SN 2019va	14.0 ± 0.2	$6.74^{+0.36}_{-0.02}$	$5.8^{+0.1}_{-1.4}$	$4.0^{+0.0}_{-1.2}$	$0.37^{+0.18}_{-0.08}$	−0.54
ZTF19aanrrqu	SN 2019clp	12.1 ± 0.9	$0.23^{+2.27}_{-0.12}$	$5.1^{+1.4}_{-1.8}$	$2.1^{+1.0}_{-1.0}$	$1.00^{+0.18}_{-0.16}$	−0.51
ZTF20aciojzg	AT 2020wip	10.4 ± 0.5	$0.83^{+1.98}_{-0.53}$	$4.4^{+3.4}_{-2.0}$	$1.5^{+1.7}_{-0.7}$	$0.35^{+0.01}_{-0.00}$	−0.56
ZTF22abssiet	SN 2022zmb	10.5 ± 0.9	$1.22^{+1.42}_{-0.38}$	$8.6^{+1.0}_{-2.0}$	$0.8^{+0.8}_{-0.2}$	$0.28^{+0.22}_{-0.03}$	−0.50
ZTF18aaqfqaa	SN 2018bek	10.0 ± 0.5	$3.38^{+0.94}_{-0.12}$	$5.7^{+0.4}_{-1.4}$	$2.0^{+0.2}_{-0.1}$	$4.40^{+0.31}_{-0.08}$	−0.64
ZTF19aailepg	SN 2019amt	12.6 ± 0.5	$12.03^{+1.60}_{-1.90}$	$4.3^{+0.7}_{-0.9}$	$3.0^{+0.7}_{-0.6}$	$0.74^{+0.38}_{-0.04}$	−0.48
ZTF23abaxtlq	SN 2023rix	10.7 ± 0.3	$0.85^{+1.30}_{-0.09}$	$7.4^{+0.7}_{-1.9}$	$3.3^{+0.7}_{-0.3}$	$0.37^{+0.03}_{-0.01}$	−0.48
ZTF21aapkcmr	AT 2021fnj	11.9 ± 1.0	$0.46^{+1.81}_{-0.31}$	$8.4^{+0.7}_{-1.1}$	$4.1^{+0.4}_{-1.4}$	$1.61^{+0.10}_{-0.21}$	−0.48
ZTF18aawgrxz	SN 2021lmp	10.8 ± 0.9	$5.05^{+0.95}_{-0.10}$	$3.3^{+4.7}_{-2.2}$	$1.3^{+0.6}_{-0.2}$	$1.10^{+0.44}_{-0.06}$	−0.60
ZTF21acgrrnl	SN 2021aayf	13.9 ± 2.7	$22.18^{+5.82}_{-5.66}$	$5.8^{+2.8}_{-3.2}$	$3.1^{+1.4}_{-1.6}$	$1.35^{+1.15}_{-0.82}$	−0.47
ZTF22abkbjsb	SN 2022vym	11.0 ± 0.6	$2.13^{+0.72}_{-0.28}$	$5.5^{+2.1}_{-2.8}$	$1.5^{+0.7}_{-0.3}$	$0.36^{+0.19}_{-0.08}$	−0.41
ZTF19aclobbu	SN 2019twk	11.6 ± 1.0	$14.70^{+0.25}_{-4.70}$	$5.7^{+0.5}_{-1.1}$	$4.7^{+0.1}_{-0.9}$	$1.00^{+0.20}_{-0.08}$	−0.31
ZTF22aafsqud	SN 2022hql	11.9 ± 0.9	$0.50^{+2.46}_{-0.39}$	$7.7^{+0.9}_{-4.9}$	$4.0^{+0.8}_{-0.6}$	$0.36^{+0.31}_{-0.15}$	−0.42
ZTF22abfavpu	SN 2022tmb	14.3 ± 2.1	$3.36^{+0.16}_{-0.17}$	$4.9^{+0.9}_{-0.8}$	$1.1^{+0.5}_{-0.5}$	$1.06^{+0.10}_{-0.12}$	−0.47
ZTF21abfiuqf	SN 2021pla	10.5 ± 1.5	$2.08^{+1.64}_{-1.94}$	$4.5^{+4.0}_{-2.0}$	$1.7^{+0.6}_{-0.8}$	$1.23^{+3.65}_{-0.58}$	−0.57
ZTF24aarvbxj	SN 2024lby	11.7 ± 1.0	$2.88^{+2.55}_{-0.84}$	$2.0^{+0.5}_{-0.2}$	$1.6^{+2.1}_{-0.4}$	$2.02^{+0.34}_{-0.16}$	−0.65
ZTF24aaemydm	SN 2024chx	10.2 ± 0.6	$4.90^{+0.13}_{-0.91}$	$5.6^{+0.6}_{-0.4}$	$3.3^{+0.0}_{-0.6}$	$1.72^{+0.38}_{-0.03}$	−0.32
ZTF22abtspsw	SN 2022aagp	11.4 ± 1.6	$2.48^{+0.37}_{-0.20}$	$6.5^{+1.5}_{-1.5}$	$2.4^{+0.6}_{-0.6}$	$1.42^{+0.26}_{-0.26}$	−0.58
ZTF20acfvprb	AT 2020thp	12.1 ± 0.5	$5.09^{+0.91}_{-0.34}$	$7.2^{+1.3}_{-3.1}$	$1.8^{+0.7}_{-0.9}$	$0.78^{+0.25}_{-0.03}$	−0.44
ZTF23aasbvab	SN 2023ngy	11.8 ± 0.8	$2.99^{+3.65}_{-0.88}$	$7.2^{+1.1}_{-3.6}$	$2.5^{+1.1}_{-0.9}$	$0.36^{+0.24}_{-0.12}$	−0.39
ZTF22aaevwec	SN 2022gwg	11.0 ± 1.2	$4.00^{+0.71}_{-0.46}$	$3.7^{+3.6}_{-1.6}$	$1.2^{+1.1}_{-0.3}$	$2.30^{+0.20}_{-0.05}$	−0.65
ZTF21acfajbc	SN 2021aalq	10.8 ± 0.7	$6.76^{+1.24}_{-0.76}$	$4.6^{+1.6}_{-2.6}$	$4.4^{+0.5}_{-0.3}$	$2.52^{+0.14}_{-0.19}$	−0.60
ZTF24aadkwni	SN 2024aul	10.3 ± 1.0	$4.58^{+0.20}_{-0.57}$	$7.4^{+0.6}_{-1.9}$	$2.7^{+0.5}_{-0.4}$	$1.90^{+0.26}_{-0.19}$	−0.43
ZTF21abouuat	SN 2021ucg	16.7 ± 1.0	$9.94^{+1.88}_{-2.02}$	$6.4^{+2.6}_{-5.2}$	$4.7^{+0.2}_{-1.1}$	$0.96^{+0.08}_{-0.11}$	−0.45

Table E: Continued.

ZTF name	IAU name	ZAMS mass ($M_\odot$)	$M_{\rm Ni}$ ($\times10^{-2}$ $M_\odot$)	$R_{\rm CSM}$ ($\times10^{14}$ cm)	β	Energy ($\times10^{51}$ erg)	$\dot{M}$ (log $M_\odot$ yr^{-1})
ZTF18aahfqbc	SN 2018aoq	12.0 ± 0.8	$15.23^{+0.34}_{-0.79}$	$7.7^{+0.2}_{-4.3}$	$4.4^{+0.2}_{-1.3}$	$2.87^{+0.09}_{-0.04}$	−0.48
ZTF21abhhrpj	SN 2021qiu	15.7 ± 3.0	$7.78^{+3.20}_{-0.97}$	$7.8^{+1.0}_{-2.9}$	$2.4^{+0.5}_{-1.0}$	$1.22^{+0.82}_{-0.37}$	−0.44
ZTF20actnuls	SN 2020aawo	12.1 ± 0.6	$3.88^{+0.41}_{-0.34}$	$5.7^{+0.8}_{-1.0}$	$1.8^{+0.5}_{-0.4}$	$1.55^{+0.10}_{-0.09}$	−0.31
ZTF22abnujbv	SN 2022xus	10.6 ± 1.3	$1.67^{+4.59}_{-0.61}$	$2.4^{+1.8}_{-0.9}$	$3.8^{+0.5}_{-0.7}$	$0.35^{+0.32}_{-0.03}$	−0.42
ZTF23abbtkrv	SN 2023rvo	15.8 ± 0.6	$5.58^{+1.47}_{-0.32}$	$5.2^{+2.4}_{-1.2}$	$3.7^{+0.4}_{-0.7}$	$0.37^{+0.19}_{-0.14}$	−0.29
ZTF19aaniore	SN 2019ceg	12.2 ± 1.2	$8.67^{+2.49}_{-1.29}$	$5.8^{+1.7}_{-1.4}$	$2.8^{+2.0}_{-1.5}$	$0.93^{+0.18}_{-0.16}$	−0.55
ZTF22aasojye	SN 2022omr	13.2 ± 0.5	$5.12^{+0.47}_{-0.90}$	$4.2^{+1.7}_{-3.0}$	$4.2^{+0.5}_{-0.6}$	$0.43^{+0.23}_{-0.20}$	−0.45
ZTF20aafckit	SN 2020uu	10.2 ± 1.0	$5.21^{+2.44}_{-0.17}$	$7.9^{+0.9}_{-0.6}$	$3.4^{+0.3}_{-0.5}$	$1.72^{+0.24}_{-0.02}$	−0.32
ZTF21aaagypx	SN 2021V	14.2 ± 1.1	$12.73^{+2.16}_{-2.49}$	$7.7^{+0.7}_{-1.9}$	$3.0^{+0.4}_{-0.2}$	$0.69^{+0.31}_{-0.04}$	−0.34
ZTF19acbwejj	SN 2019upq	14.9 ± 2.7	$10.04^{+11.71}_{-3.36}$	$5.0^{+2.8}_{-2.9}$	$3.3^{+1.1}_{-1.2}$	$0.60^{+4.06}_{-0.28}$	−0.38
ZTF23aackjhs	SN 1995al	9.5 ± 0.7	$0.55^{+0.58}_{-0.41}$	$1.8^{+1.1}_{-0.4}$	$1.2^{+0.8}_{-0.4}$	$0.13^{+0.03}_{-0.01}$	−0.56
ZTF21aaeqwov	AT 2021htp	10.4 ± 1.1	$3.50^{+0.78}_{-0.23}$	$8.3^{+0.8}_{-0.9}$	$1.6^{+0.5}_{-0.6}$	$0.73^{+0.34}_{-0.15}$	−0.58
ZTF19aanhhal	SN 2019cec	14.2 ± 3.8	$11.00^{+10.81}_{-7.29}$	$7.9^{+1.5}_{-1.2}$	$1.8^{+2.6}_{-1.1}$	$1.53^{+0.98}_{-0.89}$	−0.53
ZTF22aanrqje	SN 2022mji	9.4 ± 0.7	$1.60^{+0.87}_{-0.34}$	$4.3^{+1.4}_{-1.0}$	$2.1^{+0.5}_{-0.9}$	$0.17^{+0.16}_{-0.02}$	−0.46
ZTF21aafkwtk	SN 2021apg	12.4 ± 0.4	$3.29^{+0.89}_{-0.31}$	$5.3^{+0.5}_{-1.6}$	$3.5^{+0.2}_{-0.4}$	$0.74^{+0.02}_{-0.04}$	−0.42
ZTF24abmkros	SN 2024xkd	10.8 ± 1.0	$0.39^{+1.84}_{-0.13}$	$6.3^{+2.1}_{-1.2}$	$3.0^{+0.6}_{-0.6}$	$0.11^{+0.01}_{-0.01}$	−0.56
ZTF22aaolwsd	SN 2022mxv	11.7 ± 0.8	$11.49^{+0.96}_{-1.46}$	$6.8^{+2.3}_{-0.8}$	$3.4^{+0.3}_{-0.5}$	$1.10^{+0.65}_{-0.28}$	−0.18
ZTF24abtczty	SN 2024abfl	10.7 ± 0.4	$1.97^{+1.49}_{-1.74}$	$2.6^{+0.4}_{-0.3}$	$1.1^{+0.2}_{-0.2}$	$0.10^{+0.04}_{-0.00}$	−0.45
ZTF19abajxet	SN 2019hyk	11.9 ± 0.5	$6.18^{+0.31}_{-0.54}$	$4.2^{+2.6}_{-2.2}$	$2.5^{+1.2}_{-0.6}$	$1.59^{+0.08}_{-0.16}$	−0.60
ZTF24aaplfjd	SN 2024jxm	10.4 ± 0.3	$2.26^{+0.86}_{-0.26}$	$5.3^{+2.2}_{-1.8}$	$1.6^{+0.3}_{-0.2}$	$0.51^{+0.17}_{-0.11}$	−0.65
ZTF21aantsla	SN 2021ech	11.1 ± 0.6	$2.17^{+0.32}_{-0.33}$	$5.6^{+1.8}_{-1.2}$	$2.4^{+0.4}_{-0.5}$	$0.39^{+0.25}_{-0.05}$	−0.55
ZTF24aajxppf	SN 2024grw	11.0 ± 0.9	$4.07^{+0.94}_{-0.49}$	$5.9^{+2.7}_{-1.8}$	$4.0^{+0.6}_{-0.7}$	$1.80^{+0.41}_{-0.27}$	−0.44
ZTF19acftfav	SN 2019ssi	10.5 ± 0.4	$2.39^{+0.59}_{-0.65}$	$7.0^{+1.8}_{-2.3}$	$3.8^{+0.7}_{-1.7}$	$0.43^{+0.17}_{-0.04}$	−0.52
ZTF20actkmks	SN 2020aaun	10.0 ± 2.8	$8.00^{+1.59}_{-1.11}$	$8.1^{+0.7}_{-2.7}$	$0.7^{+1.2}_{-0.1}$	$1.28^{+0.43}_{-0.26}$	−0.48
ZTF21abnlhxs	SN 2021tyw	14.4 ± 1.3	$5.75^{+9.46}_{-1.21}$	$8.1^{+1.0}_{-2.9}$	$3.1^{+0.7}_{-0.7}$	$1.06^{+0.52}_{-0.19}$	−0.11
ZTF23aaphnyz	SN 2023lkw	12.8 ± 0.3	$10.90^{+2.46}_{-0.93}$	$7.7^{+0.9}_{-3.7}$	$4.4^{+0.4}_{-1.4}$	$1.53^{+0.14}_{-0.12}$	−0.35
ZTF19actnwtn	SN 2019vdl	12.0 ± 0.5	$10.72^{+2.17}_{-2.05}$	$6.2^{+1.3}_{-1.3}$	$3.2^{+1.1}_{-1.2}$	$0.76^{+0.24}_{-0.06}$	−0.56
ZTF18aadsuxd	SN 2020yui	12.0 ± 1.4	$7.99^{+4.37}_{-5.62}$	$5.3^{+3.1}_{-1.5}$	$2.8^{+1.7}_{-0.7}$	$4.33^{+0.58}_{-0.96}$	−0.53
ZTF22aativsd	SN 2022ovb	12.1 ± 0.4	$11.80^{+1.31}_{-4.03}$	$4.5^{+3.4}_{-0.7}$	$4.7^{+0.3}_{-1.5}$	$2.04^{+0.05}_{-0.58}$	−0.58
ZTF23aaqknaw	SN 2023lzn	13.7 ± 0.7	$10.49^{+4.86}_{-0.83}$	$3.8^{+2.5}_{-2.3}$	$2.8^{+0.6}_{-1.0}$	$0.91^{+2.09}_{-0.07}$	−0.53
ZTF24aabsmvc	SN 2024ws	11.3 ± 0.9	$3.00^{+3.10}_{-0.19}$	$4.3^{+1.2}_{-0.8}$	$3.4^{+0.4}_{-1.1}$	$0.32^{+0.27}_{-0.04}$	−0.48
ZTF22abvaetz	SN 2022aang	10.2 ± 0.7	$2.47^{+4.00}_{-0.91}$	$4.1^{+1.6}_{-0.8}$	$3.0^{+0.2}_{-0.6}$	$0.17^{+0.21}_{-0.01}$	−0.49
ZTF22ablnrcv	SN 2022xav	9.3 ± 0.7	$1.00^{+0.10}_{-0.04}$	$1.1^{+0.2}_{-0.1}$	$0.9^{+0.3}_{-0.4}$	$0.44^{+0.06}_{-0.04}$	−0.14
ZTF21aardvtn	AT 2021htp	10.2 ± 0.2	$4.81^{+1.07}_{-0.21}$	$7.8^{+0.7}_{-0.9}$	$1.5^{+0.3}_{-0.4}$	$0.76^{+0.03}_{-0.05}$	−0.62
ZTF22aauurbv	SN 2022pgf	10.4 ± 0.4	$5.32^{+1.24}_{-0.47}$	$7.4^{+0.7}_{-2.1}$	$1.0^{+0.5}_{-0.4}$	$1.65^{+0.28}_{-0.37}$	−0.53
ZTF19aazyvub	SN 2019hnl	11.6 ± 0.5	$4.06^{+0.43}_{-0.21}$	$4.5^{+0.8}_{-0.6}$	$2.0^{+0.2}_{-0.1}$	$1.06^{+0.08}_{-0.10}$	−0.55
ZTF24aaejecr	SN 2024btj	10.5 ± 0.8	$1.26^{+1.82}_{-0.38}$	$7.4^{+0.6}_{-1.7}$	$2.5^{+0.7}_{-1.3}$	$0.43^{+0.16}_{-0.18}$	−0.50
ZTF22aakdqqg	SN 2022kad	12.0 ± 0.8	$3.46^{+0.29}_{-0.39}$	$5.8^{+0.7}_{-1.5}$	$1.7^{+0.7}_{-0.7}$	$1.24^{+0.37}_{-0.01}$	−0.57
ZTF22aarycqo	SN 2022ojo	13.2 ± 1.8	$18.75^{+6.04}_{-1.76}$	$5.3^{+1.5}_{-2.5}$	$4.6^{+0.3}_{-1.3}$	$4.43^{+0.32}_{-0.64}$	−0.31
ZTF23abascqa	SN 2023rbk	10.3 ± 1.0	$4.12^{+0.72}_{-0.21}$	$6.8^{+2.2}_{-2.8}$	$2.1^{+1.7}_{-0.5}$	$2.74^{+0.04}_{-0.33}$	−0.64
ZTF23aasrcyv	SN 2023nlu	11.0 ± 1.2	$5.59^{+1.43}_{-1.47}$	$2.6^{+0.9}_{-0.7}$	$4.6^{+0.3}_{-2.7}$	$0.57^{+0.07}_{-0.10}$	−0.36
ZTF23aailjjs	SN 2023hcp	11.8 ± 0.5	$5.48^{+0.16}_{-0.10}$	$3.9^{+1.4}_{-1.4}$	$3.3^{+1.1}_{-2.4}$	$1.77^{+0.31}_{-0.03}$	−0.62
ZTF21aabygea	SN 2021os	12.5 ± 1.3	$5.12^{+0.97}_{-0.67}$	$7.2^{+0.6}_{-2.4}$	$4.0^{+0.8}_{-1.3}$	$0.74^{+0.02}_{-0.30}$	−0.40
ZTF20acvjagm	SN 2020abtf	12.7 ± 0.4	$1.15^{+2.45}_{-1.02}$	$7.7^{+1.1}_{-1.5}$	$3.9^{+0.3}_{-1.2}$	$0.59^{+0.25}_{-0.12}$	−0.40
ZTF19actnyae	SN 2019vdm	10.5 ± 1.0	$2.51^{+0.83}_{-0.49}$	$6.6^{+1.3}_{-1.0}$	$2.2^{+0.6}_{-1.1}$	$0.98^{+0.37}_{-0.23}$	−0.60
ZTF21ablvzhp	SN 2021tiq	10.1 ± 0.7	$22.09^{+1.30}_{-2.57}$	$2.0^{+0.8}_{-0.0}$	$3.9^{+0.1}_{-0.2}$	$2.47^{+0.09}_{-0.06}$	−0.30
ZTF21aavhnpk	SN 2021jsf	9.6 ± 1.3	$1.85^{+0.15}_{-0.84}$	$1.7^{+0.1}_{-0.2}$	$1.5^{+0.3}_{-0.8}$	$0.46^{+0.03}_{-0.06}$	−0.14
ZTF22aaudjgc	SN 2022pfx	10.4 ± 0.7	$11.09^{+1.04}_{-2.12}$	$3.8^{+1.8}_{-1.2}$	$2.1^{+1.5}_{-1.2}$	$1.17^{+0.32}_{-0.10}$	−0.48

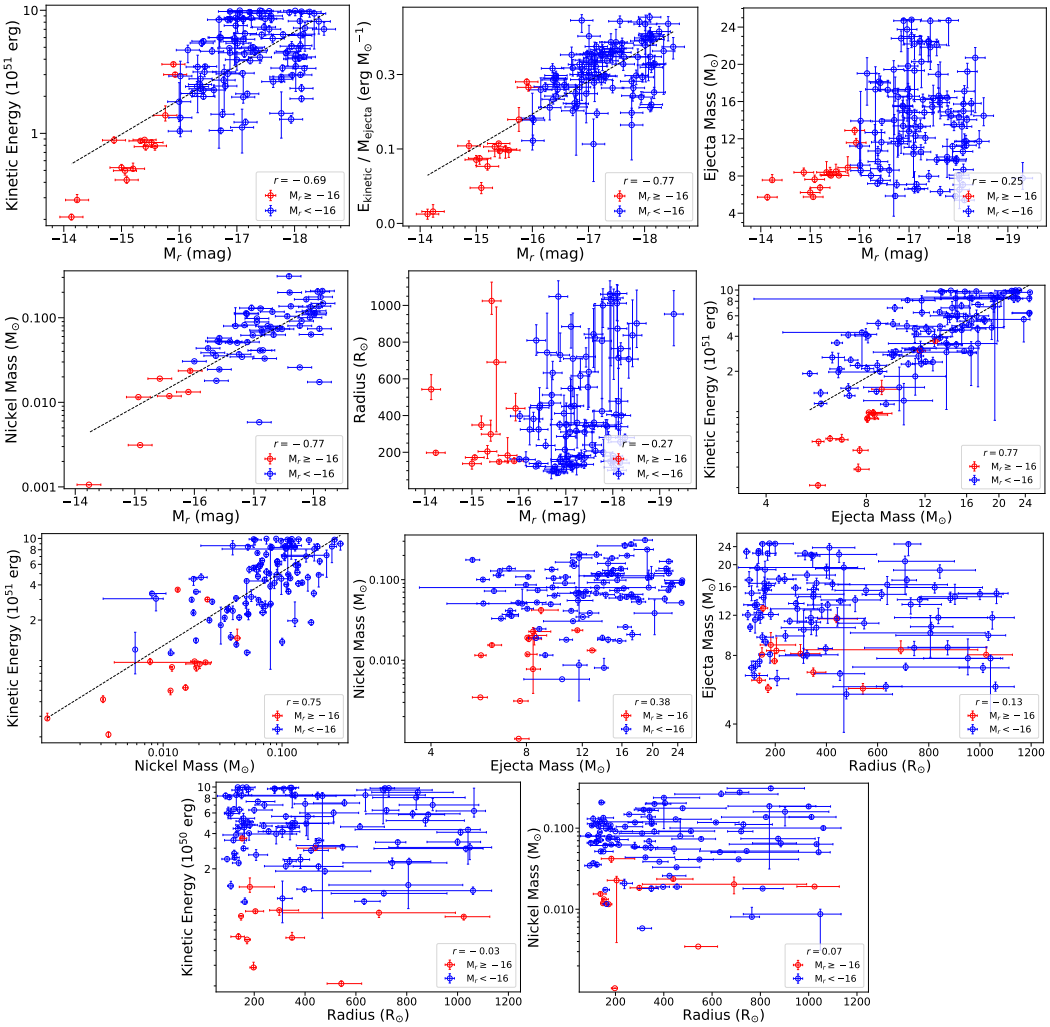

Figure 5.19: All correlations between peak r-band magnitude and physical parameters (nickel mass, explosion energy, energy per unit mass, radius, ejecta mass), and among the physical parameters themselves, based on semi-analytical models from Nagy and Vinkó (2016). LLIIP SNe with $M_r \geq -16$ are shown in red, SNe IIP with $M_r < -16$ in blue.

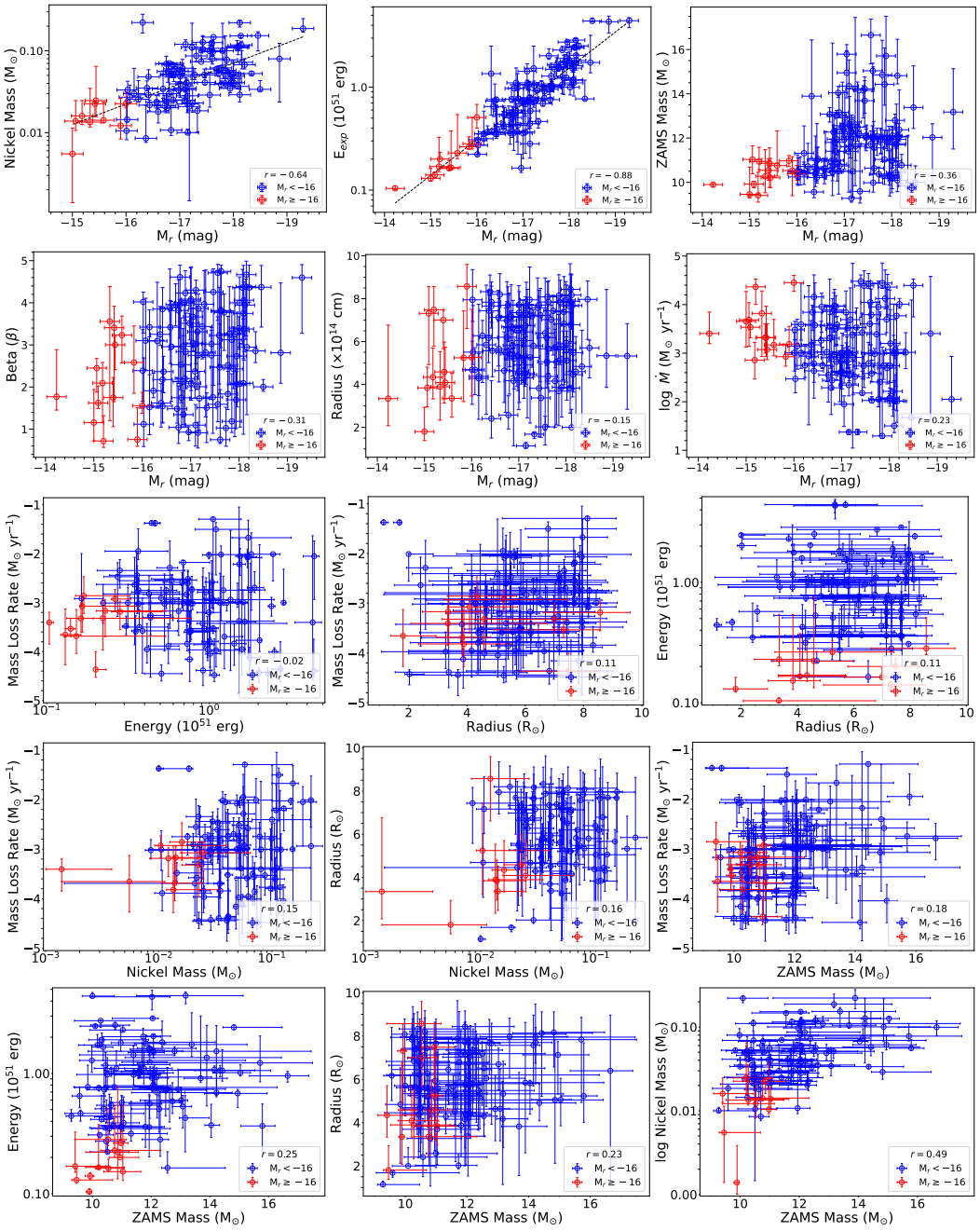

Figure 5.20: Correlations between peak r-band magnitude and physical parameters (nickel mass, explosion energy, energy per unit mass, radius, ejecta mass), and among the physical parameters themselves, based on radiation-hydrodynamical model fits from Moriya et al. (2023). LLIIP SNe with $M_r \geq -16$ are shown in red, those with $M_r < -16$ in blue.

Table E: Continued.

ZTF name	IAU name	ZAMS mass ($M_\odot$)	$M_{\rm Ni}$ ($\times10^{-2}$ $M_\odot$)	$R_{\rm CSM}$ ($\times10^{14}$ cm)	β	Energy ($\times10^{51}$ erg)	$\dot{M}$ (log $M_\odot$ yr^{-1})
ZTF22abfxkdm	SN 2022ubb	10.6 ± 0.4	$2.37^{+0.48}_{-0.38}$	$7.1^{+1.3}_{-2.3}$	$3.9^{+0.9}_{-1.0}$	$0.44^{+0.15}_{-0.02}$	−0.51
ZTF22aavbfhz	AT 2022phi	10.6 ± 1.1	$1.80^{+0.65}_{-0.48}$	$8.2^{+1.0}_{-1.0}$	$3.0^{+1.1}_{-1.3}$	$0.54^{+0.09}_{-0.12}$	−0.44
ZTF22aakdbia	SN 2022jzc	9.9 ± 0.1	$1.60^{+4.04}_{-1.49}$	$7.3^{+1.2}_{-2.4}$	$1.6^{+0.4}_{-0.1}$	$0.14^{+0.01}_{-0.01}$	−0.55
ZTF22aazmrpx	SN 2022raj	10.9 ± 0.5	$0.15^{+2.03}_{-0.05}$	$7.5^{+1.1}_{-1.7}$	$0.7^{+0.6}_{-0.2}$	$0.20^{+0.03}_{-0.00}$	−0.64
ZTF20acfkzcg	AT 2021htp	11.4 ± 0.8	$7.04^{+0.19}_{-0.05}$	$5.4^{+0.2}_{-0.6}$	$1.7^{+0.3}_{-0.7}$	$0.97^{+0.10}_{-0.17}$	−0.59
ZTF21abrluay	SN 2021vfh	12.9 ± 1.4	$4.88^{+1.34}_{-0.81}$	$4.6^{+1.5}_{-1.5}$	$2.1^{+1.6}_{-0.4}$	$0.74^{+0.32}_{-0.04}$	−0.48
ZTF19acytcsg	SN 2019wvz	15.0 ± 0.6	$12.60^{+0.67}_{-1.30}$	$5.1^{+1.0}_{-1.2}$	$2.5^{+1.0}_{-0.6}$	$1.01^{+0.16}_{-0.06}$	−0.61
ZTF19abwztsb	SN 2019pjs	10.7 ± 0.8	$2.56^{+1.76}_{-0.20}$	$6.3^{+0.7}_{-2.2}$	$1.9^{+0.4}_{-0.2}$	$0.37^{+0.05}_{-0.02}$	−0.44
ZTF22aaywnyg	SN 2022pru	10.9 ± 0.9	$2.25^{+0.15}_{-0.65}$	$4.6^{+1.4}_{-1.4}$	$3.4^{+0.5}_{-1.8}$	$0.22^{+0.55}_{-0.09}$	−0.52
ZTF19abbnamr	SN 2019iex	14.2 ± 0.7	$7.38^{+2.14}_{-0.09}$	$7.6^{+1.4}_{-1.9}$	$0.7^{+1.5}_{-0.1}$	$1.07^{+0.08}_{-0.07}$	−0.65
ZTF23abbsxzs	SN 2023rtq	9.8 ± 1.4	$5.27^{+0.34}_{-0.23}$	$4.8^{+1.7}_{-2.7}$	$2.9^{+0.5}_{-0.3}$	$0.77^{+0.40}_{-0.02}$	−0.48
ZTF22abzqwmp	SN 2022adth	11.9 ± 0.6	$1.07^{+1.84}_{-0.15}$	$7.2^{+1.5}_{-1.1}$	$2.1^{+1.1}_{-0.8}$	$0.56^{+0.09}_{-0.14}$	−0.59
ZTF20acitoie	SN 2020wgp	10.7 ± 1.0	$6.02^{+0.39}_{-1.34}$	$5.2^{+0.5}_{-1.4}$	$2.8^{+0.9}_{-0.9}$	$0.77^{+0.32}_{-0.02}$	−0.55
ZTF19aapafit	SN 2019cvz	14.9 ± 1.1	$6.13^{+1.74}_{-0.80}$	$7.1^{+0.6}_{-1.8}$	$3.0^{+0.8}_{-0.2}$	$0.68^{+0.05}_{-0.16}$	−0.41
ZTF20acbjgoa	SN 2020acac	10.5 ± 0.6	$2.71^{+1.10}_{-0.46}$	$4.7^{+1.0}_{-1.2}$	$3.1^{+1.0}_{-0.7}$	$0.32^{+0.95}_{-0.05}$	−0.50
ZTF21abvcxel	SN 2021wvw	9.6 ± 0.6	$0.70^{+3.01}_{-0.59}$	$6.2^{+2.2}_{-1.2}$	$0.9^{+2.1}_{-0.4}$	$0.65^{+0.12}_{-0.13}$	−0.50
ZTF20aapchqy	SN 2020cxd	9.9 ± 0.1	$0.14^{+0.25}_{-0.04}$	$3.3^{+3.4}_{-1.3}$	$1.8^{+1.1}_{-0.3}$	$0.10^{+0.01}_{-0.00}$	−0.53
ZTF18aaszvfn	SN 2021iaw	12.3 ± 0.6	$2.02^{+0.97}_{-0.04}$	$7.7^{+0.9}_{-1.7}$	$3.9^{+0.1}_{-0.8}$	$0.51^{+0.15}_{-0.18}$	−0.46
ZTF20acuhren	SN 2020abcq	10.3 ± 1.0	$1.34^{+2.13}_{-0.17}$	$3.9^{+1.6}_{-1.6}$	$3.6^{+0.8}_{-2.4}$	$0.13^{+2.86}_{-0.01}$	−0.58
ZTF23abnogui	SN 2023wcr	10.8 ± 1.0	$1.42^{+0.95}_{-0.10}$	$3.4^{+1.2}_{-0.9}$	$3.2^{+0.5}_{-0.7}$	$0.23^{+0.31}_{-0.03}$	−0.50
ZTF22abyivoq	SN 2022acko	11.0 ± 0.2	$1.04^{+2.92}_{-0.12}$	$5.2^{+2.2}_{-2.0}$	$2.6^{+0.9}_{-0.7}$	$0.26^{+0.07}_{-0.01}$	−0.47
ZTF22abhsxph	SN 2022vyc	12.2 ± 0.9	$3.94^{+0.79}_{-1.24}$	$7.3^{+1.0}_{-2.4}$	$4.1^{+0.8}_{-2.2}$	$0.69^{+0.03}_{-0.27}$	−0.48

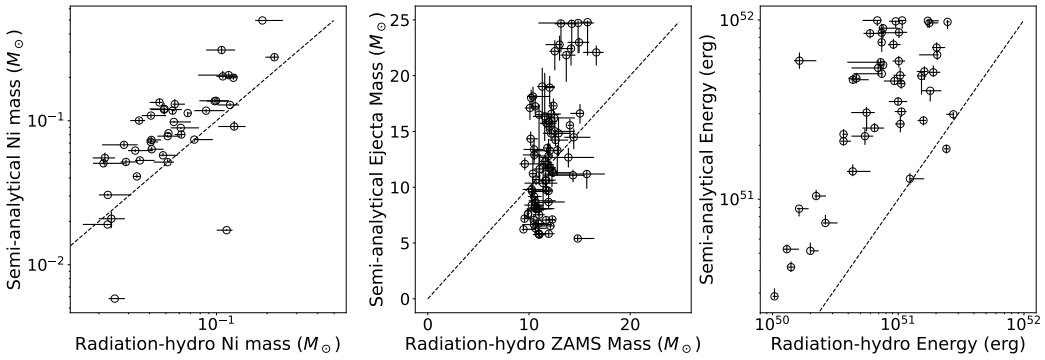

Figure 5.21: Comparison of physical parameters derived from semi-analytical light curve fits (y-axis) and radiation-hydrodynamical model fits (x-axis). Panels show nickel mass (left), ejecta mass versus ZAMS mass (center), and kinetic energy (right). Dashed lines indicate the one-to-one relation. Error bars reflect the 16th–84th percentile uncertainties from each method.

Chapter 6

LOW-LUMINOSITY TYPE IIP SUPERNOVAE FROM THE ZWICKY TRANSIENT FACILITY CENSUS OF THE LOCAL UNIVERSE. III: HUNTING FOR ELECTRON-CAPTURE SUPERNOVAE USING NEBULAR SPECTROSCOPY

Das, K. K., A. Jerkstrand, et al. (2026). "Low-Luminosity Type IIP Supernovae from the Zwicky Transient Facility Census of the Local Universe. III: Hunting for electron-capture supernovae using nebular spectroscopy". In: Submitted to *Publications of the Astronomical Society of the Pacific*. arXiv: 2605.18960.

Kaustav K. Das[1], Anders Jerkstrand[2], Mansi M. Kasliwal[1], Jesper Sollerman[2], Christoffer Fremling[3], Steve Schulze[4], Avishay Gal-Yam[5], Tomas Ahumada[1,6], Shreya Anand[7], Bart van Baal[2], Michael W. Coughlin[8], Sofia Covarrubias[1], Richard Dekany[3], Nicholas Earley[1], W. V. Jacobson-Galán[1], Joahan Castaneda Jaimes[1], Frank J. Masci[9], Yu-Jing Qin[1], Reed Riddle[1], Sam Rose[1], Yashvi Sharma[3]

[1] Cahill Center for Astrophysics, California Institute of Technology, Pasadena, CA 91125, USA

[2] The Oskar Klein Centre, Department of Astronomy, Stockholm University, AlbaNova, SE-10691 Stockholm, Sweden

[3] Caltech Optical Observatories, California Institute of Technology, Pasadena, CA 91125, USA

[4] Center for Interdisciplinary Exploration and Research in Astrophysics (CIERA), Northwestern University, Evanston, IL 60201, USA

[5] Department of Particle Physics and Astrophysics, Weizmann Institute of Science, Rehovot 76100, Israel

[6] Cerro Tololo Inter-American Observatory/NSF NOIRLab, Casilla 603, La Serena, Chile

[7] Kavli Institute for Particle Astrophysics and Cosmology, Stanford University, Stanford, CA 94305, USA

[8] School of Physics and Astronomy, University of Minnesota, Minneapolis, MN 55455, USA
[9] IPAC, California Institute of Technology, Pasadena, CA 91125, USA

Abstract

Electron-capture supernovae (ECSNe) may arise from ONeMg-core collapse in super-asymptotic giant branch (sAGB) stars near the low-mass core-collapse limit (≈ 8–$10\,M_\odot$). At early times, models predict that ECSNe resemble low-mass red supergiant iron-core-collapse SNe (FeCCSNe), making the two channels difficult to distinguish. Nebular spectroscopy, however, can reveal differences in ejecta composition. We present a systematic sample of 19 nebular spectra of low-luminosity Type IIP (LLIIP) SNe from the ZTF CLU survey, obtained 115−450 d after explosion. Their low velocities expose narrow lines blended in brighter SNe, which we identify and model to constrain progenitor properties. We find a strong correlation between the FWHM of H I λ6563 and peak luminosity, showing that LLIIP SNe occupy the low-energy end of the core-collapse population, but no correlation with plateau duration, suggesting that envelope and core properties are not tightly linked. Only one SN reaches the extremely low H I λ6563 widths predicted for the weakest $\sim$9 $M_\odot$ explosion models, implying that such low-energy events are intrinsically rare. Combining our sample with 118 literature nebular spectra of Type II SNe, we infer an IMF slope of 2.1 ± 1.2. We also introduce an 'ECSN score" based on the absence of He- and O-shell emission lines, and identify two plausible ECSN candidates, SN 2023bvj and SN 2024btj. However, neither shows the extremely narrow nebular lines predicted by current ECSN models. If ECSNe arise predominantly through the LLIIP channel, we infer an upper limit on the ECSN rate of $\lesssim$ (5–8) $\times\, 10^2\,\mathrm{Gpc^{-3}\,yr^{-1}}$, corresponding to a narrow sAGB progenitor mass window of $\Delta M_{\mathrm{sAGB}} \lesssim 0.02$–$0.06\,M_\odot$.

6.1 Introduction

The final fate of a star is predominantly determined by its initial mass: stars with lower masses become white dwarfs, while more massive ones undergo core collapse, producing neutron stars or black holes. However, the fate of stars in the intermediate-mass regime, near the threshold between white dwarf and neutron star formation, is not well understood. Stellar-evolution models suggest that stars within the 8–12 $M_\odot$ interval possess distinct core characteristics compared to their more massive counterparts (> 12 $M_\odot$), particularly showing much lower core compactness

(Sukhbold et al. 2016). Modeling their evolution is more challenging than for stars above 12 $M_\odot$ due to complex degeneracy effects (Miyaji et al. 1980, Gutiérrez et al. 2005). Owing to the steep slope of the initial mass function (IMF), a substantial portion, over 40%, of all massive star explosions should occur in the 8–12 $M_\odot$ mass range, with 25% originating from stars between 8–10 $M_\odot$. If many stars above 20 $M_\odot$ collapse into black holes without producing visible supernovae, the 8–12 $M_\odot$ contribution could rise to 50–60% (Sukhbold et al. 2016).

Massive stars with initial masses just below the threshold for forming Fe cores are expected to follow a different evolutionary path: instead of producing Fe cores, they may form electron-degenerate ONeMg cores that collapse through electron-capture reactions. Such events are thought to give rise to electron-capture supernovae (ECSNe) (Miyaji et al. 1980, Nomoto 1984, Kitaura et al. 2006, Janka et al. 2008, Takahashi et al. 2013, Jones et al. 2013, Hiramatsu et al. 2021a, Wang et al. 2026). In the single-star channel, ECSN progenitors are thought to be super-asymptotic giant branch (sAGB) stars by the time collapse occurs. The mass range capable of producing ECSNe is predicted to be narrow ($< 1\ M_\odot$) (Siess 2007, Poelarends et al. 2008, Doherty et al. 2015), and could be even smaller depending on choices for mass-loss rates and third dredge-up efficiency. However, even a 1 $M_\odot$-wide interval would account for ∼15% of CCSNe under a Salpeter IMF, falling to ∼8% for a 0.5 $M_\odot$ range. Whether ECSNe actually occur and what fraction of core-collapse SNe they represent remain key open questions.

While the exact mass range or even the existence of ECSN progenitors remains uncertain, ECSNe are predicted to have low explosion energies ($\sim 10^{50}$ erg) and small ^{56}Ni yields ($\sim 10^{-3}\ M_\odot$) from the neutrino-driven mechanism (Kitaura et al. 2006, Janka et al. 2008, Wanajo et al. 2009, Jones et al. 2013, Wang et al. 2026). However, this holds true also for the lowest-mass Fe CCSNe, and are therefore not sufficient diagnostics. Jerkstrand et al. (2018) showed that nebular spectra can break the degeneracy, concluding that none of the candidates SN 1997D, SN 2005cs or SN 2008bk were ECSNe but rather low-mass Fe CCSNe. With zero of three events confirmed, the ECSN progenitor mass window was preliminarily constrained to $\Delta M_{ZAMS} \lesssim\ 1\ M_\odot$.

The first observational candidate with spectroscopic properties in better agreement with ECSNe than Fe CCSNe was SN 2016bkv (Hosseinzadeh et al. 2018). This supernova also had the very low expansion velocities expected. The main dissonance point lies in the ^{56}Ni mass, estimated at ∼0.02 $M_\odot$, much higher than ECSN

predictions.

An second candidate, SN 2018zd, was proposed by Hiramatsu et al. (2021a). This event had an estimated ^{56}Ni mass (8×10^{-3} $M_{\odot}$) in better agreement with LLIIP SNe, and lacked [C I] lines as predicted for ECSNe. It did however show He lines (weak in ECSNe) and lacked the strong Bowen fluorecence O I 8448 (strong in ECSNe). Later studies questioned this classification, arguing that the extreme properties of SN 2018zd were overestimated due to an incorrect distance, and that the event is consistent with a faint Fe core-collapse SN instead (Zhang et al. 2020, Callis et al. 2021).

Other proposed ECSN-like explosions include the class of Intermediate Luminosity Red Transients, such as, AT 2019abn, NGC 300 2008OT-1, and SN 2008S (Botticella et al. 2009, Adams et al. 2016, Jencson et al. 2019a, Rose et al. 2024, Valerin et al. 2025). They exhibit luminous, dusty progenitors and low-velocity outflows suggestive of sAGB-like systems. Although their physical origins remain debated, ILRTs may represent the non-terminal or weakly-terminal end of the same low-mass core-collapse pathway (Pumo et al. 2009).

The most promising observational analogs of low-mass core-collapse events are low-luminosity Type IIP supernovae (LLIIP SNe), defined here as those with $M_{\rm r,peak} \geq -16$ mag, as motivated by prior literature (e.g., Spiro et al. 2014). Recent studies based on pre-explosion imaging of SNe 2005cs, 2008bk, 2018aoq, and 2022acko (Maund et al. 2005, Li et al. 2006, Mattila et al. 2008, O'Neill et al. 2019, Van Dyk et al. 2023b) show that SNe with r-band peaks fainter than -16 mag have progenitor mass estimates below $\sim$11 $M_{\odot}$, consistent with low-mass red supergiants (RSGs) and sAGB progenitors (see Appendix A in Das et al. 2025c; see also the recent review by Van Dyk 2025). These events exhibit faint plateau luminosities, low expansion velocities, and low explosion energies and nickel masses (e.g., Turatto et al. 1998, Pastorello et al. 2004, Spiro et al. 2014, Jäger et al. 2020, Müller-Bravo et al. 2020, Yang et al. 2021, Valerin et al. 2022, Kozyreva et al. 2022, Bostroem et al. 2023, Teja et al. 2024, Dastidar et al. 2025, Das et al. 2025e), linking their light curves to low-mass progenitors ($\sim$8–12 $M_{\odot}$) through both direct imaging and hydrodynamical modeling. Although these SNe trace the low-mass end of core collapse, photospheric observables cannot distinguish between models with low mass RSG and those with sAGB progenitors. Both retain extended hydrogen envelopes and have similar pre-SN masses, producing photospheric light curves that are nearly indistinguishable despite their different core structures.

The nebular phase offers unique diagnostics to distinguish between these scenarios (Jerkstrand et al. 2018). Once the ejecta become optically thin (∼100 d), the luminosity is powered by ^{56}Co decay and the cooling is dominated by forbidden transitions. As the hydrogen-rich material recombines and becomes transparent, the metal-rich inner layers are exposed, revealing the products of hydrostatic and explosive nucleosynthesis. Nebular spectra therefore provide direct constraints on ejecta composition, nucleosynthetic yields, explosion geometry and the Zero-Age Main Sequence (ZAMS) mass (Fransson and Chevalier 1989, Jerkstrand et al. 2012, 2014a, 2015a, Dessart and Hillier 2020, Dessart et al. 2021a,b, 2025). For ECSNe, progenitor structures at the point of collapse have been calculated by Nomoto (1984), Takahashi et al. (2013), and Jones et al. (2013), while earlier evolutionary models predicted to reach the ECSN stage were developed by Ritossa et al. (1996), Ritossa et al. (1999), Siess (2006), and Woosley and Heger (2015). These studies show that second dredge-up or dredge-out episodes remove nearly the entire helium shell (Nomoto 1987, Ritossa et al. 1996), leaving an ONe core enveloped by a thin O/C shell (a few $\times 10^{-2}\,M_{\odot}$) and a dilute H/He envelope. At collapse, the ONe core and part of the O/C shell undergo explosive burning to iron-group elements (Kitaura et al. 2006, Janka et al. 2008). Longer-term simulations of the neutrino-driven wind show no major modifications to these yields (Wanajo et al. 2009, 2011, Pllumbi et al. 2015). An important consequence is that ECSNe from single-star progenitors lack both an O-rich shell and a He shell in their ejecta. Their nebular spectra should therefore be dominated by lines from the extended H/He envelope, with the possible appearance of neutron-rich iron-group species (e.g., stable Ni and Zn) if the innermost Fe-rich material is visible through the $\sim 8\,M_{\odot}$ envelope (Wanajo et al. 2009). In contrast, low-mass Fe-core CCSNe retain thin Si, O, and He shells, which generate unique signatures. Thus, nebular spectroscopy may distinguish ECSNe primarily through the absence of these layers (Jerkstrand et al. 2018).

There has been no uniform sample of LLIIP SN nebular spectra from a systematic survey. Earlier nebular studies focused on individual objects (Turatto et al. 1998, Pastorello et al. 2006b, Van Dyk et al. 2012b, Müller-Bravo et al. 2020, Jäger et al. 2020, Bostroem et al. 2023, Van Dyk et al. 2023b), and although Fang et al. (2025) collected 50 Type II nebular spectra from the literature, only three were LLIIP SNe. In this work (Paper III), we present a uniform sample of nebular spectra for 19 LLIIP SNe spanning phases from ∼115 to 450 days after explosion, the largest such dataset obtained to date. This work is the third in a series on LLIIP SNe. In Paper I (Das et al. 2025c), we used the Zwicky Transient Facility Census of the Local Universe

(ZTF CLU; Bellm et al. 2019b, Graham et al. 2019, Dekany et al. 2020, Masci et al. 2019, De et al. 2020b) to measure the luminosity function and volumetric rate of Type IIP SNe, using the largest sample of 330 Type IIP SNe to date. In Paper II (Das et al. 2025e), we analyzed 129 Type IIP SNe with semi-analytic and radiation-hydrodynamical modeling to infer explosion and progenitor properties, finding that LLIIP SNe predominantly arise from the low-mass RSG/sAGB population.

Along with our LLIIP sample, we also assemble a comparison set of 120 nebular-phase spectra of canonical Type II SNe from the literature, providing a broader context for interpreting the late-time properties of faint events. The intrinsically narrow nebular emission lines of LLIIP SNe reduce blending and enable secure identification of weak features, allowing us to measure key nebular diagnostics, compare them to theoretical models, assess potential ECSN candidates, and infer ZAMS mass values to constrain the low-mass end of the core-collapse IMF.

The paper is structured as follows. Section 8.2 describes the sample selection, and Section 6.3 summarizes the spectroscopic observations and reduction. Section 6.4 details the spectral processing and analysis methods, and correlations with lightcurve observables. In Section 6.5, we estimate progenitor ZAMS masses and examine the resulting mass distribution and IMF constraints. Section 6.6 introduces nebular diagnostics for identifying ECSN candidates, presents ECSN scores for the LLIIP sample, and estimates the ECSN rate. We summarize our conclusions in Section 10.7.

Table A: ZTF CLU LLIIP Sample Summary

Criteria	Number
LLIIP SNe within 100 Mpc (2022 Nov–2024 Nov) meeting Paper I quality criteria	28
LLIIP SNe with usable nebular spectra (≥ 110 d)	19 (47 spectra)

6.2 Sample

The ZTF CLU experiment aims to build a comprehensive spectroscopic sample of transients in the local Universe within 150 Mpc. The CLU experiment is designed as a volume-limited SN survey where sources at less than 150 Mpc ($z \leq 0.033$) and spatially coincident with (within 30 kpc) or visibly associated with a galaxy in the CLU catalog were assigned for spectroscopic follow-up for classification. In

Paper I, we selected Type IIP SNe from the ZTF CLU experiment with well-sampled r-band light curves and a clearly defined plateau phase. The selection required (i) a Gaussian Process regression–derived peak apparent magnitude of $m_{r,\mathrm{peak}} < 20$ mag, (ii) sufficient temporal coverage around peak and during the plateau (more than ten total detections and at least one detection on both sides of peak, or an equivalent set of conditions ensuring a constrained rise), and (iii) a plateau lasting at least 40 days with < 1 mag decline. We refer to Paper I (Das et al. 2025c) for the complete sample selection criteria.

For this work, we focus on ZTF CLU LLIIP SNe that exploded within a volume of 100 Mpc between 2022 November 1 and 2024 November 1, yielding a sample of 28 events that satisfy the Paper I quality criteria in this period. Among these, we obtained usable late-time spectroscopy for 19 SNe. The remaining events could not be followed spectroscopically at nebular phases either because they were behind the Sun, outside observable windows, or had spectra with too low signal-to-noise ratio to extract robust diagnostics. The final LLIIP spectroscopic sample consists of 19 SNe for which we obtained a total of 47 nebular spectra spanning 115–450 days after explosion. Throughout this paper, all quoted phases are measured relative to the estimated explosion epoch of each SN. This sample provides the first systematic sample of nebular spectra of LLIIP SNe from a volume-limited survey. SN 2022aaad has the most extensive coverage, with eight spectra between 150 d and 450 d. Multi-epoch nebular observations were also secured for SN 2022zmb, SN 2023wcr, SN 2023kmk, SN 2023vci, SN 2024jxm, SN 2024btj, SN 2024cro, and SN 2024abfl, typically with coverage between 150 d and 350 d. Additional LLIIP events observed at nebular phases include SN 2022jzc, SN 2022aang, SN 2022acko, SN 2023mpz, SN 2023ywa, and SN 2024wp, which were generally observed once between 150 d and 350 d. The full spectral log of the LLIIP SN sample is listed in Table 6.2.

For comparison and context, we also include nebular spectra of a small set of more luminous ZTF Type II SNe drawn from the same CLU volume. This bright-ZTF comparison sample consists of 6 SNe with 10 spectra, obtained either as part of routine CLU follow-up or serendipitously during other spectroscopic programs (see Table D for the log.) In addition, we assemble a literature comparison sample of Type II SNe using the dataset summarized in Table E, which contains 54 SNe with a total of 120 nebular spectra. Following the selection criteria of Fang et al. (2025), we require (1) spectral coverage spanning 5000–8500 Å; (2) observations obtained

Table B: Spectral log of nebular spectra of LLIIP SNe. Throughout this paper, all quoted phases are measured relative to the estimated explosion epoch of each SN.

ZTF Name	IAU Name	Date	Phase (d)	Instrument
ZTF22aakdbia	SN2022jzc	2023-04-26	310	Keck/LRIS
ZTF22abssiet	SN2022zmb	2023-04-26	151	Keck/LRIS
ZTF22abssiet	SN2022zmb	2023-06-12	198	Keck/LRIS
ZTF22abtjefa	SN2022aaad	2023-06-12	155	Keck/LRIS
ZTF22abtjefa	SN2022aaad	2023-08-18	222	P200/DBSP
ZTF22abtjefa	SN2022aaad	2023-10-07	272	Keck/LRIS
ZTF22abtjefa	SN2022aaad	2023-11-10	306	P200/DBSP
ZTF22abtjefa	SN2022aaad	2023-12-07	333	Keck/LRIS
ZTF22abtjefa	SN2022aaad	2024-02-15	403	Keck/LRIS
ZTF22abtjefa	SN2022aaad	2024-03-31	448	Keck/LRIS
ZTF22abvaetz	SN2022aang	2023-12-07	312	Keck/LRIS
ZTF22abyivoq	SN2022acko	2023-08-18	241	P200/DBSP
ZTF22abyivoq	SN2022acko	2023-09-16	270	P200/DBSP
ZTF22abyivoq	SN2022acko	2023-11-08	323	Keck/LRIS
ZTF22abyivoq	SN2022acko	2023-12-07	352	Keck/LRIS
ZTF22abyivoq	SN2022acko	2024-02-15	422	Keck/LRIS
ZTF23aabksje	SN2023azx	2024-02-15	387	Keck/LRIS
ZTF23aabksje	SN2023azx	2024-03-31	432	Keck/LRIS
ZTF23aackjhs	SN2023bvj	2023-12-07	220	Keck/LRIS
ZTF23aanxrjm	SN2023kmk	2024-01-13	231	P200/DBSP
ZTF23aanxrjm	SN2023kmk	2024-02-15	264	Keck/LRIS
ZTF23aanxrjm	SN2023kmk	2024-03-31	309	Keck/LRIS
ZTF23aanxrjm	SN2023kmk	2024-05-08	347	Keck/LRIS
ZTF23aaquhaz	SN2023mpz	2023-11-18	138	Keck/LRIS
ZTF23aaquhaz	SN2023mpz	2024-05-08	310	Keck/LRIS
ZTF23abgmhgw	SN2023vci	2024-02-15	165	Keck/LRIS
ZTF23abgmhgw	SN2023vci	2024-03-31	210	Keck/LRIS
ZTF23abnogui	SN2023wcr	2024-03-14	122	Keck/LRIS
ZTF23abnogui	SN2023wcr	2024-03-20	128	P200/DBSP
ZTF23abnogui	SN2023wcr	2024-04-12	151	P200/DBSP
ZTF23abnogui	SN2023wcr	2024-05-01	170	P200/DBSP
ZTF23abnogui	SN2023wcr	2024-07-11	241	P200/DBSP
ZTF23abpbuha	SN2023usp	2024-02-15	115	Keck/LRIS
ZTF23absscow	SN2023ywa	2024-07-09	250	Keck/LRIS
ZTF23absscow	SN2023ywa	2024-10-09	342	Keck/LRIS
ZTF24aaasazz	SN2024ov	2024-11-30	288	Keck/LRIS
ZTF24aabppgn	SN2024wp	2024-07-09	125	Keck/LRIS
ZTF24aaejecr	SN2024btj	2024-07-09	147	Keck/LRIS
ZTF24aaejecr	SN2024btj	2024-11-30	291	Keck/LRIS
ZTF24aaejecr	SN2024btj	2025-01-26	348	Keck/LRIS
ZTF24aaezido	SN2024cro	2024-07-09	180	Keck/LRIS
ZTF24aaplfjd	SN2024jxm	2024-11-30	136	Keck/LRIS
ZTF24aaplfjd	SN2024jxm	2025-01-26	193	Keck/LRIS
ZTF24aaplfjd	SN2024jxm	2025-06-28	346	Keck/LRIS
ZTF24abtczty	SN2024abfl	2025-04-20	149	P200/NGPS
ZTF24abtczty	SN2024abfl	2025-10-22	334	Keck/LRIS

between 110 and 450 d post-explosion to ensure a well-defined nebular phase; and (3) public availability of the spectra through the Open Supernova Catalog (Guillochon et al. 2017) or WISeREP (Yaron and Gal-Yam 2012a).

6.3 Spectroscopy Data

We obtained late-time spectra primarily using the Double Beam Spectrograph (DBSP) on the 5.1 m Hale Telescope at Palomar Observatory and the Low Res-

olution Imaging Spectrometer (LRIS) on the 10 m Keck I Telescope. Additional spectra were acquired with the Alhambra Faint Object Spectrograph and Camera (ALFOSC) on the 2.56 m Nordic Optical Telescope (NOT). DBSP observations used the 600/4000 grating (blue) and the 316/7500 grating (red), providing $R \sim 1000$ over 3200–10000 Å and were reduced following Bellm and Sesar (2016), Roberson et al. (2022). LRIS spectra were taken with the 600/4000 grism (blue) and 400/8500 grating (red), achieving resolutions of ∼5–9 Å and were reduced with the `lpipe` pipeline (Perley 2019). ALFOSC spectra were obtained with a 1.″0 wide slit and grism 4, covering 3500–9000 Å at $R \approx 360$ and were reduced using PyNOT and PypeIt (Prochaska et al. 2020a). We also include one spectrum from the new NGPS spectrograph (Kasliwal et al. 2024) on the Hale Telescope, using 2x3 binning and 1.″5 wide slit ($R \sim 2000$ over 5600–10000 Å), reduced using a tool based on PypeIt. The spectra were gathered on the `Fritz` Marshal (van der Walt et al. 2019, Coughlin et al. 2023), a web portal designed for vetting and coordinating transient follow-up observations. All spectroscopy data will be made public through Zenodo and WISeREP (Yaron and Gal-Yam 2012a).

6.4 Spectra processing and analysis

We measure the nebular emission-line properties for all Type II SNe in our sample using rest-frame, extinction-corrected spectra. Milky Way and host-galaxy extinction values are adopted from Paper I and Paper II. Because our analysis focuses on identifying and quantifying the presence or absence of specific nebular features, comparing fractional line fluxes, and measuring velocity widths, modest uncertainties in extinction do not affect our conclusions. The code and data used in this analysis will be made publicly available on GitHub and Zenodo after publication.

Host-Galaxy Continuum Subtraction

We first subtract the underlying host-galaxy continuum from each spectrum. The reduced blue and red arms of the spectra often have different instrumental responses and can require an artificial splice near the overlap region. To construct a single smooth host continuum, we fit the blue and red sides separately. On the red side we identify five relatively line-poor windows: 5530–5830 Å, 6010–6210 Å, 6750–6950 Å, 7900–8150 Å, and 9000–9450 Å. We compute the mean flux in each available window and fit a piecewise linear curve through at least three such points. On the blue side we select the 4300–5200 Å region, where nebular contamination is minimal, and fit a straight line. The blue and red continuum models are then joined

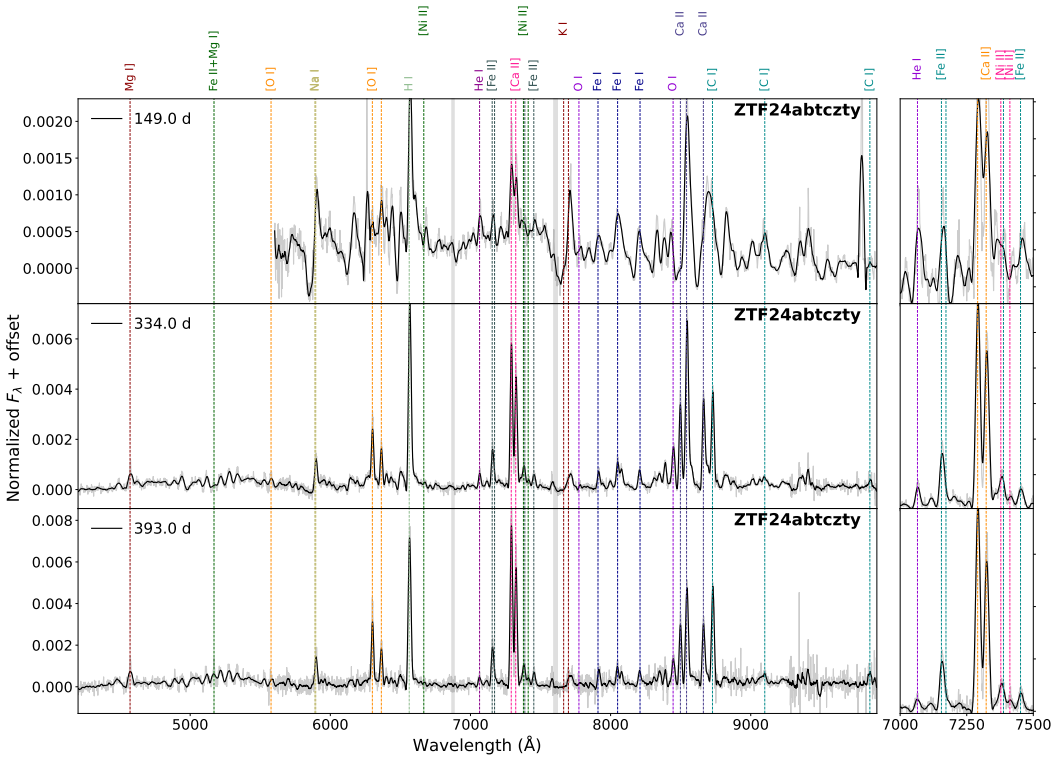

Figure 6.1: Keck/LRIS nebular spectra of ZTF24abtczty/SN 2024abfl at 149 d, 334 d and 393 d after explosion. The black curve shows the spectrum smoothed with a Savitzky–Golay filter, while the faint gray curve indicates the raw data. Colored vertical dashed lines mark the rest wavelengths of prominent nebular features, as labeled at the top (e.g. Mg I] λ4571, [O I] $\lambda\lambda$6300, 6364, H I λ6563, [Ca II] $\lambda\lambda$7291, 7323, and [C I] λ8727). The right-hand panels zoom in on the 7000–7500 Å region around the [Ca II] $\lambda\lambda$7291, 7323 complex, highlighting the narrow [Ca II] emission and the neighboring Fe- and Ni-peak features.

smoothly across the overlap region to form the final continuum, which is subtracted from the observed spectrum. All line measurements below are performed on these host-subtracted data.

Measuring [O I] $\lambda\lambda$6300, 6363 flux

The [O I] $\lambda\lambda$6300, 6363 doublet lies within a broad emission complex that also includes H I λ6563. To isolate the oxygen feature, we first apply slight Savitzky–Golay smoothing to the host-subtracted spectrum and use the smoothed curve only to identify the local minima that bracket the [O I]/Hα blend. A straight line connecting these minima defines the local pseudo-continuum. Subtracting this baseline isolates the emission-line structure. Although the nebular background is not a true continuum but a blend of many faint lines, the same procedure is applied uniformly to

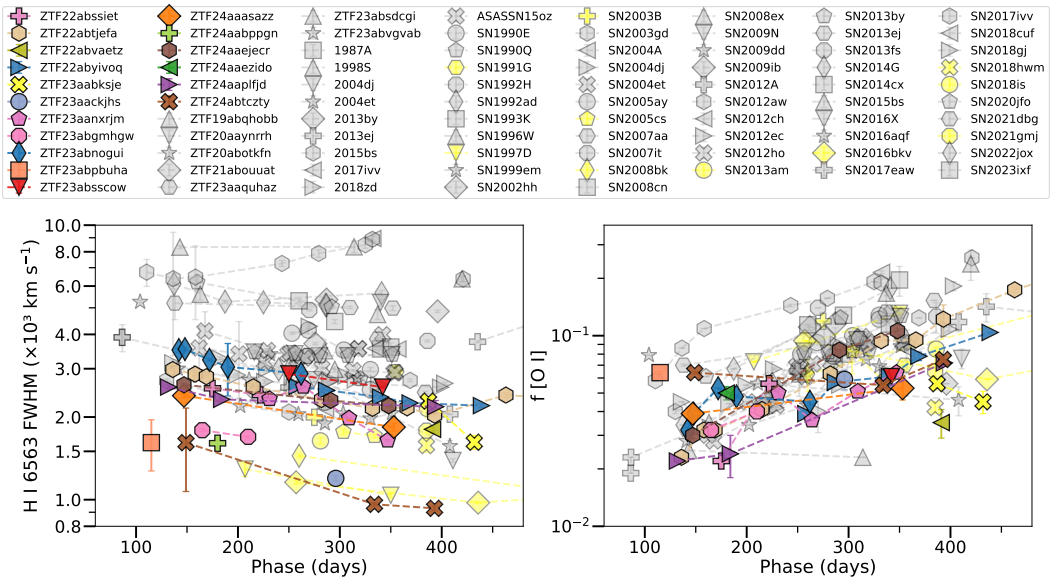

Figure 6.2: Left: H I λ6563 FWHM for all objects in our sample as a function of phase. The colored points represent the ZTF CLU LLIIP sample, the literature comparison sample is shown in gray, and low-luminosity literature events are highlighted in yellow. Right: Same objects but showing the fractional [O I] luminosity $f_{[\mathrm{O\,I}]}$, as defined in Section 6.4. Dashed lines connect measurements of the same SN across different epochs. Throughout this paper, all quoted phases are measured relative to the estimated explosion epoch of each SN.

every SN, ensuring negligible systematic bias for population-level statistics.

We integrate the continuum-subtracted flux across the [O I] feature to obtain the total line flux, and estimate the velocity width by fitting a Gaussian profile (or two components when needed for visibly separated peaks).

Measuring [Ca II] $\lambda\lambda$7291, 7323 flux and the Ni/Fe flux ratio diagnostic

The region around 7000–7500 Å contains several blended nebular lines. We model the spectrum in this range using eight Gaussian components at the rest wavelengths of He I λ7065, [Fe II] λ7155, [Fe II] λ7172, [Ca II] λ7291, [Ca II] λ7323, [Ni II] λ7378, [Fe II] λ7388, and [Ni II] λ7412. All components are fit simultaneously. To extract a clean [Ca II] profile, we subtract the best-fitting contributions of all lines except the two [Ca II] components. The residual yields the [Ca II] flux and FWHM.

The same fit gives fluxes for [Ni II] λ7378 and [Fe II] λ7155. Their ratio serves as a diagnostic of the Ni/Fe mass ratio in the inner ejecta. In ordinary Fe-core CCSNe, [Fe II] dominates, whereas electron-capture SNe are expected to produce a Ni-rich, neutron-rich inner zone, yielding predicted [Ni II]/[Fe II] ratios of $\sim$ 1.3–3.0

(Jerkstrand et al. 2015a).

Fractional [O I] Flux

To enable direct comparison between spectra of different objects and epochs, we also compute the fractional flux of the [O I] line following the prescription in Equation A2 of Barmentloo et al. (2024) and Fang et al. (2025). The total observable flux is defined as

$$\int_{5500\,\text{Å}}^{8000\,\text{Å}} \left(F_\lambda - F_{\text{pseudo}}\right)\, d\lambda, \tag{6.1}$$

where F_λ is the observed spectral flux density and F_{pseudo} is the constant pseudo-continuum level derived from the line-poor windows identified in our host-continuum subtraction procedure (Section 6.4). The fractional [O I] flux is then computed as the ratio of the [O I] line flux to this integrated denominator. Importantly, the fractional [O I] flux has been shown to correlate with ZAMS progenitor mass in nebular-phase models and observations (Fang et al. 2025), making it a powerful diagnostic of progenitor properties. We also find a strong correlation in our sample (see Figures 4 and 5), further supporting the use of fractional [O I] emission as an indicator of progenitor mass of Type IIP SNe. This offers the main advantage that, because both the numerator and denominator are measured from the same extinction-corrected spectrum over a relatively narrow wavelength range, the resulting fractional fluxes are largely insensitive to uncertainties in the extinction correction or absolute flux calibration. In practice, the fractional flux is therefore effectively independent of the photometric calibration, extinction corrections and distance uncertainty, which typically contribute the largest sources of systematic uncertainty in nebular spectral analyses.

Uncertainty Estimation

To estimate uncertainties in fluxes and FWHM, we perform Monte Carlo simulations. After smoothing the host-subtracted spectrum with a Savitzky–Golay filter and subtracting it, we compute the standard deviation of the residuals in the 6000–8000 Å region and adopt this as the noise level. We generate $N = 100$ realizations by adding Gaussian noise of this amplitude.

For each realization, we allow the endpoints of all local continua and the central wavelengths of all fitted components (He I, [Fe II], [Ca II], [Ni II]) to vary within ± 600 km s^{-1} to account for wavelength-calibration uncertainties and finite spectral resolution. We then repeat the full fitting procedure. The standard deviation of

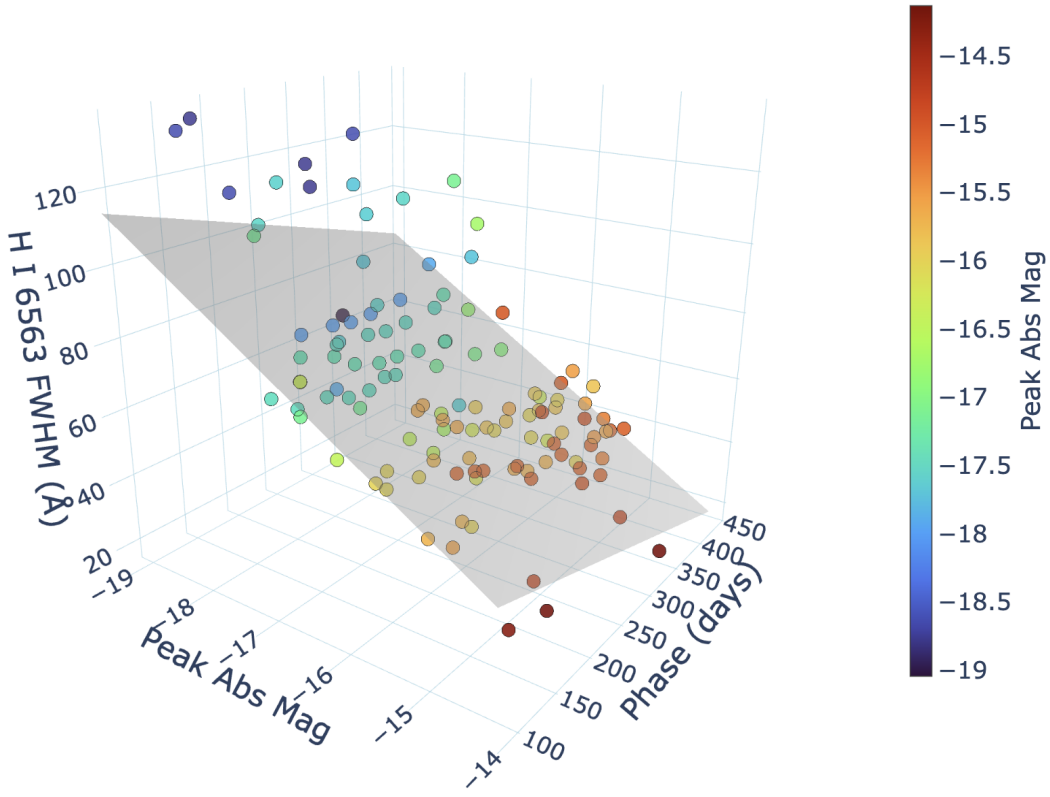

Figure 6.3: Nebular H I λ6563 FWHM as a function of phase and peak absolute magnitude for our sample. Points are color-coded by $M_{\rm peak}$, and the best-fit weighted plane is shown in gray. The trend indicates that fainter SNe exhibit systematically narrower nebular H I lines. A two-dimensional projection of this relation is shown in the top-left panel of Figure 6.4.

the resulting distribution of fluxes, FWHM values, and ratios is adopted as the measurement uncertainty.

Correlation of nebular spectra with lightcurve observables

We measure the key r-band light-curve parameters: peak absolute magnitude, plateau onset, plateau duration, and plateau-end slope, using the same methodology developed in Paper I and Paper II (Das et al. 2025e). Briefly, we determine $t_{\rm peak}$ and $M_{r,\rm peak}$ from a Gaussian Process regression fit to the observed light curve, which provides a smooth, noise-robust representation of the data. The plateau onset ($t_{\rm plateau,\mathit{start}}$) is defined as the earlier of (i) the epoch at which the instantaneous decline rate becomes shallower than 0.01 mag day^{-1}, or (ii) the epoch within 60 d of first detection at which the change in slope ($\Delta_{\rm slope}$) reaches a local maximum. The plateau end ($t_{\rm plateau,\mathit{end}}$) is identified after ~40 d, when the light curve begins its char-

acteristic steep decline, and is measured as the epoch at which $\Delta_{\rm slope}$ first drops below $-0.003\,\mathrm{mag\,day^{-2}}$. The plateau duration is then defined as $t_{\rm plateau,\mathit{end}} - t_{\rm plateau,\mathit{start}}$.

For non-ZTF SNe drawn from the literature, we apply exactly the same GP-based procedure to the published r-band (or R-band) photometry, ensuring uniformity across the combined sample. All light curves are corrected for both Milky Way extinction and host-galaxy extinction using the extinction values reported in the original references. The resulting light-curve parameters, together with the adopted extinction corrections and literature sources, are listed for each of the 54 SNe in Table F.

We now investigate correlations between the nebular spectra properties and the lightcurve observables. As shown in Figure 6.2, the LLIIP SNe in our sample exhibit systematically narrower H I λ6563 emission lines than the brighter comparison SNe from the literature. To quantify this trend, we examine how the nebular H I λ6563 FWHM correlates with the optical peak magnitude and the epoch of the spectrum. We model the observed velocities with a planar relation and the best-fit weighted plane is

$$\begin{aligned}\mathrm{FWHM\ (\AA)} = {} & (-72.76 \pm 1.15) \\ & + (-0.05 \pm 0.01)\ \mathrm{Phase\ (d)} \\ & + (-9.05 \pm 0.07)\ M_{\rm peak}\end{aligned}$$

with a Pearson correlation coefficient $r = 0.65$ and $p < 10^{-3}$ (Figure 6.3). This relation shows that fainter SNe exhibit lower nebular H I velocities at fixed phase, likely because LLIIP events arise from intrinsically low-energy explosions.

When we compare these measurements to nebular spectral models for low-mass progenitors, we find that only a small subset of events reach the very low H I λ6563 widths predicted for extreme low-energy explosions (Figure 6.5). In particular, the Jerkstrand et al. (2018) models for a $9\,\mathrm{M_\odot}$ progenitor with an explosion energy of $E_{\rm exp} \simeq 1.1 \times 10^{50}\,\mathrm{erg}$ produce extremely narrow nebular lines, with H I FWHM values of order $1000\,\mathrm{km\,s^{-1}}$. In our data, only SN 2024abfl in the LLIIP sample, together with SN 1997D and SN 2016bkv from the literature, approach similarly small H I FWHM values. Most of our LLIIP SNe have significantly broader nebular lines at all observed epochs, typically $\gtrsim 2000\,\mathrm{km\,s^{-1}}$, even though they occupy the low-energy, low-^{56}Ni end of the explosion parameter space discussed in Paper II. For a Salpeter IMF, stars in the $\sim$ 8–10 $\mathrm{M_\odot}$ range constitute roughly one quarter of all CCSN progenitors, so the apparent scarcity of events with such narrow nebular

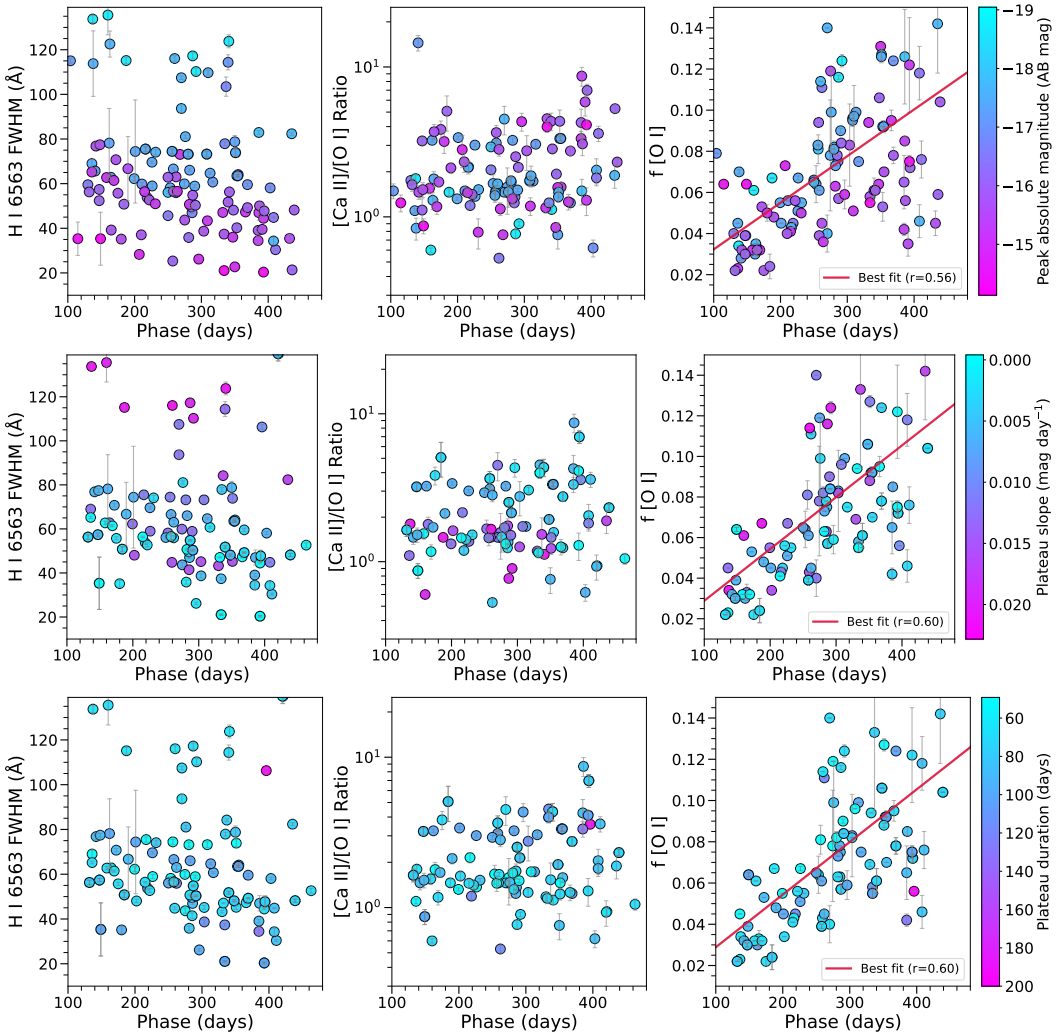

Figure 6.4: Correlation of nebular observables with r-band light-curve properties. Each column shows a different nebular diagnostic as a function of phase: H I λ6563 FWHM (left), the [Ca II]/[O I] ratio (middle), and the fractional [O I] luminosity $f_{[\mathrm{O\,I}]}$ (right). The three rows use different photometric quantities for the color coding: peak absolute magnitude (top), plateau slope (middle), and plateau duration (bottom). SNe with steeper plateau slopes, which are associated with higher luminosity (Das et al. 2025e), tend to have broader nebular H I emission. In contrast, we do not see any clear dependence of the nebular line widths or flux ratios on the plateau duration. A positive correlation between $f_{[\mathrm{O\,I}]}$ and phase is also visible, as discussed in Section 6.4.

lines is somewhat surprising if every star in this mass interval produced a $\sim 10^{50}$ erg explosion.

One possible interpretation is that the effective lower mass limit for successful core collapse is higher than in those calculations, so that only a subset of the nominal 8–9.5 $M_\odot$ population actually reaches core collapse and produces SNe. Alternatively, real explosions at the low-mass end may not be as uniformly weak as seen in some neutrino-driven explosion models (e.g., Burrows et al. 2019, Janka et al. 2008, Burrows et al. 2024). Classic ONeMg and related low-mass neutrino-driven models often yield explosion energies of $\sim 10^{50}$ erg (Janka et al. 2008, Burrows et al. 2019). However, more recent three-dimensional simulations indicate that somewhat higher energies are possible in this regime: for example, Wang & Burrows (2024) obtain $E_{\rm exp} = 1.71 \times 10^{50}$ and 2.07×10^{50} erg for the u8.1 and z9.6 progenitors in 3D, compared with 1.7×10^{49} and 1.29×10^{50} erg for the corresponding one-dimensional models. We note that alternative explosion scenarios, such as the jittering-jet mechanism, also predict somewhat higher explosion energies in this mass regime (e.g., Papish and Soker 2011).

In addition to the comparison with explosion models, we also examined how the nebular observables correlate with photometric properties of the r-band lightcurve (Figure 6.4). We find that SNe with steeper plateau slopes tend to have larger H I λ6563 widths, consistent with the idea that more rapidly declining plateaus correspond to higher luminosities and larger envelope velocities (Paper II). By contrast, we do not observe any significant correlation between nebular-phase line widths or flux ratios and the plateau duration, indicating that the length of the recombination phase is largely decoupled from the core properties such as explosion energy.

We also detect a modest correlation between the fractional [O I] flux and the phase of the nebular spectrum. Across the full sample, the Pearson correlation coefficient between $f_{\rm [OI]}$ and phase is $r \simeq 0.6$ (with $p < 10^{-5}$), and the best-fitting linear relation is

$$f_{\rm [OI]} = (2.0 \pm 0.1) \times 10^{-4}\, t + (0.0112 \pm 0.0003),$$

where t is the phase in days. Although the scatter remains substantial, the values of $f_{\rm [OI]}$ increase slowly over time, as expected once the ejecta become more transparent and the oxygen-rich core contributes a larger fraction of the emergent flux.

We also find a moderate anti-correlation between $f_{\rm [OI]}$ and $M_{r,\rm peak}$, with a Pearson

coefficient $r = -0.50$ (and $p \simeq 8.4 \times 10^{-4}$), following

$$f_{[\mathrm{OI}]} \approx (-0.016 \pm 0.006)\, M_{r,\mathrm{peak}} - (0.18 \pm 0.05),$$

such that fainter SNe exhibit systematically smaller fractional [O I] contributions at fixed phase. This behaviour is consistent with the picture that most LLIIP SNe synthesize smaller oxygen masses and/or have reduced excitation in their oxygen-rich cores.

6.5 Estimating ZAMS mass

We estimated the zero-age main sequence (ZAMS) masses for our sample of LLIIP SNe using the nebular [O I] $\lambda\lambda 6300, 6364$ emission as a proxy for the oxygen core mass and hence the progenitor ZAMS mass. For each SN with nebular spectra, we measured the [O I] doublet flux in spectra obtained at phases ≥ 150 days after explosion, when the ejecta are optically thin and nebular lines directly trace the nucleosynthetic yields. The [O I] flux was normalized by the integrated pseudo-continuum-subtracted flux between 5500 and 8000 Å to form the dimensionless fractional [O I] flux, $f_{[\mathrm{OI}]}$, as defined in Section 6.4. This fractional quantity is closely related to the fractional [O I] flux used in previous work and has been shown to correlate with ZAMS mass in both radiative-transfer models and observed nebular spectra (e.g., Jerkstrand et al. 2014a, 2015a, Fang et al. 2025).

To map the fractional [O I] flux and phase to ZAMS mass, we compared our measurements to the grid of nebular red-supergiant explosion models presented by Jerkstrand et al. (2014a). These models use the `SUMO` spectral synthesis code (Jerkstrand et al. 2011) and span a range of progenitor ZAMS masses for hydrogen-rich core-collapse SNe. We do not combine the Jerkstrand et al. (2018) 9 $M_\odot$ models with the Jerkstrand et al. (2014a) grid because the underlying progenitor and explosion implementations differ substantially. This is also evident in Figure 6.5, where the 9 $M_\odot$ models exhibit non-monotonic behavior in $f_{[\mathrm{OI}]}$ relative to the 12 $M_\odot$ Jerkstrand et al. (2014a) model.

For each model spectrum, we computed $f_{[\mathrm{OI}]}$ in exactly the same way as for the data, and we restricted the training set to model epochs with phases ≥ 150 days in order to minimise systematic biases from residual photospheric contamination. We then trained a Gaussian Process regression (GPR) model on the two-dimensional space of phase and fractional [O I] flux, $(t, f_{[\mathrm{OI}]}) \rightarrow M_{\mathrm{ZAMS}}$. The input training vectors consisted of the model phases and $f_{[\mathrm{OI}]}$ values, and the targets were the corresponding numerical ZAMS masses parsed from the model labels. The GPR

used a squared-exponential kernel of the form

$$k(\mathbf{x}, \mathbf{x}') = C \exp\left[-\frac{(t-t')^2}{2\ell_t^2} - \frac{(f_{[\mathrm{OI}]} - f'_{[\mathrm{OI}]})^2}{2\ell_f^2}\right], \tag{6.2}$$

with characteristic length scales of $\ell_t \approx 50\,\mathrm{d}$ in phase and $\ell_f \approx 0.05$ in fractional [O I] flux. This provides a smooth, non-parametric interpolation between the discrete model points in the $(t, f_{[\mathrm{OI}]})$ plane and yields a continuous mapping to ZAMS mass that is consistent with the radiative-transfer model grid (Figure 6.6).

For each observed spectrum with phase $t \geq 150$ days, we then propagated the measurement uncertainties in $f_{[\mathrm{OI}]}$ into the inferred ZAMS mass using a Monte Carlo procedure. Given the measured fractional [O I] flux $\hat{f}_{[\mathrm{OI}]}$ and its uncertainty σ_f (constructed as described in Section 6.4), we drew $N = 500$ realizations of $f_{[\mathrm{OI}]}$ from a Gaussian distribution $\mathcal{N}(\hat{f}_{[\mathrm{OI}]}, \sigma_f)$ at the observed phase t. For each draw we evaluated the trained GPR at $(t, f_{[\mathrm{OI}]})$ to obtain a sample of M_{ZAMS} values. The 16th, 50th, and 84th percentiles of this Monte Carlo distribution were adopted as the inferred median ZAMS mass and its asymmetric uncertainties for that particular spectrum. We note that we find a moderate correlation between the inferred progenitor masses and the optical peak magnitude. Across the whole sample, the Pearson coefficient between M_{ZAMS} and $M_{r,\mathrm{peak}}$ is $r = -0.58$ (with $p \simeq 6.8 \times 10^{-5}$), and the best-fitting linear relation,

$$M_{\mathrm{ZAMS}} \approx (-1.5 \pm 0.4)\, M_{r,\mathrm{peak}} - (11.7 \pm 1.2)\ \mathrm{M}_\odot,$$

shows that fainter peaks correspond to systematically lower progenitor masses. The resulting ZAMS mass estimates for all SNe are listed in Table F.

We caution that circumstellar interaction or dust formation at late times can suppress or dilute the nebular [O I] emission and alter the observed peak luminosity (e.g., Jacobson-Galán et al. 2025b, Dessart et al. 2025), potentially affecting the inferred M_{ZAMS}–$M_{r,\mathrm{peak}}$ correlation. We also emphasize that the Jerkstrand et al. (2014a) grid extends down only to 12 $M_\odot$. As a result, for SNe with measured $f_{[\mathrm{OI}]}$ values near or below the 12 $M_\odot$ track, the inferred masses rely on extrapolation beyond the lower edge of the model grid and should therefore be interpreted with caution. For SNe in the low-$f_{[\mathrm{OI}]}$ regime associated with progenitors at or below the lowest-mass Jerkstrand et al. (2014a) model, we can robustly conclude that their ZAMS masses are $\lesssim 12\ M_\odot$, even though individual sub-12 $M_\odot$ values are not precisely determined. A more self-consistent determination of ZAMS masses using models spanning the

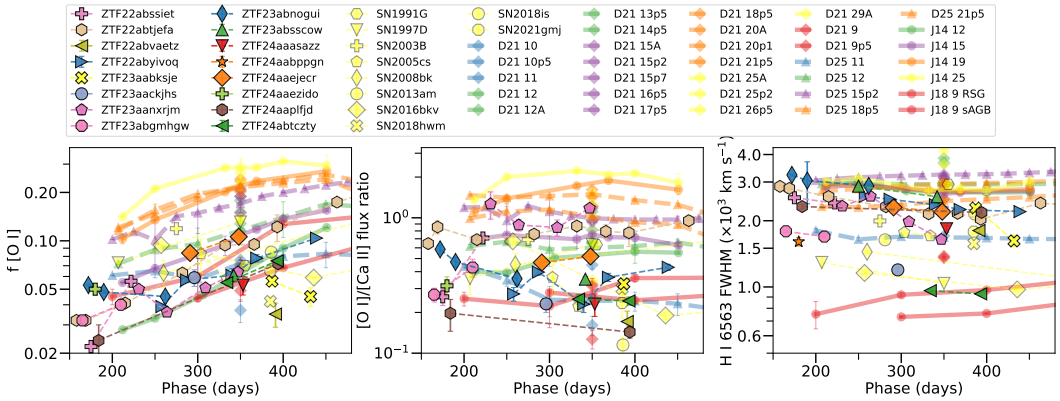

Figure 6.5: Comparison of the ZTF LLIIP sample with literature LLIIP SNe and published nebular models. The colored points show the ZTF+CLU LLIIP SNe, and the yellow points show low-luminosity LLIIP events from the literature. Model tracks from Dessart et al. 2021b (D21), Dessart et al. 2025 (D25), Jerkstrand et al. 2014a (J14), and Jerkstrand et al. 2018 (J18) are shown for reference. The three panels present the evolution of the fractional [O I] luminosity (left), the [O I]/[Ca II] flux ratio (middle), and the H I λ6563 FWHM (right) as functions of phase.

full low- to high-mass range will be presented in future work (A. Bostroem et al., in prep.).

ZAMS mass distribution of LLIIP SNe

To characterise the progenitor population, for every SN we choose the spectrum closest to ~350 d after explosion. This ensures that the fractional [O I] flux is measured during the phase range in which the models show the clearest separation with progenitor mass. We adopt the median ZAMS mass $M_{\mathrm{ZAMS,50}}$ from the GPR-based mapping between phase, fractional [O I] flux, and progenitor mass. The distribution of $M_{\mathrm{ZAMS,50}}$ is strongly weighted toward low progenitor masses: the sample median is $M_{\mathrm{ZAMS}} \simeq 11.2\,\mathrm{M}_{\odot}$, and the 16th and 84th percentiles of the distribution of $M_{\mathrm{ZAMS,50}}$ lies at ≈ 9.9 and $12.7\,\mathrm{M}_{\odot}$ (Figure 6.7). SN 2024btj has a median ZAMS mass above $14\,\mathrm{M}_{\odot}$, however, the 16th–84th percentile range spans ~10-17 $\mathrm{M}_{\odot}$.

IMF constraints from the Type IIP ZAMS mass distribution

We model the underlying progenitor mass distribution of the entire Type IIP sample as a power law

$$\frac{\mathrm{d}N}{\mathrm{d}M} \propto M^{-\alpha},$$

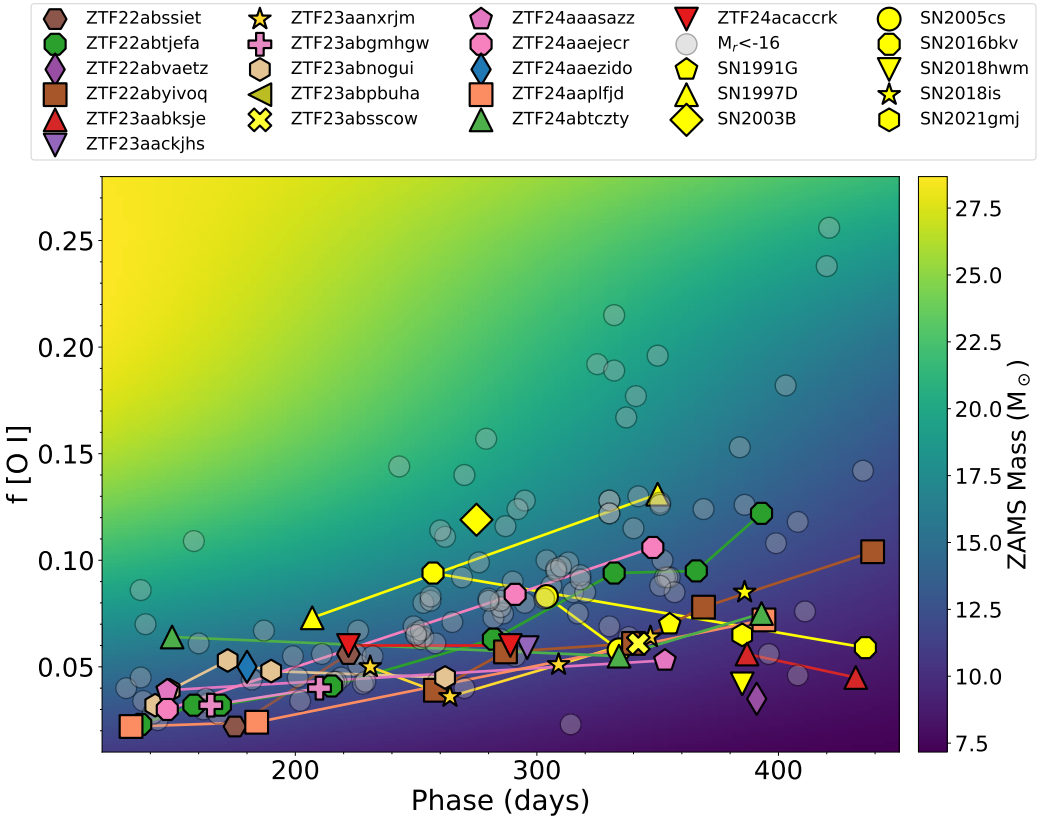

Figure 6.6: Fractional [O I] flux as a function of phase for the ZTF LLIIP sample (colored symbols) and for literature comparison SNe (gray points). The background color shows the ZAMS mass predicted by our Gaussian Process regression model, which maps phase and fractional [O I] flux to $M_{\rm ZAMS}$ as described in Section 6.5.

between a lower cutoff $M_{\rm min}$ and an upper cutoff fixed at $M_{\rm max} = 22\,{\rm M}_\odot$. For each SN, we treat the GP–inferred progenitor mass as a Gaussian with mean $M_{\rm ZAMS,50}$ and dispersion $M_{{\rm ZAMS},std}$; the latter already includes a 10% systematic term added in quadrature to account for modeling uncertainties. To propagate these individual mass uncertainties into the inferred population slope, we perform a Monte Carlo experiment. In each realization, we draw one mass for every SN from its Gaussian distribution, discard values outside the adopted mass range, and then resample the drawn masses with probabilities proportional to the approximate maximum observable volume for each event,

$$w_i \propto V_{{\rm max},i} \propto 10^{0.6\left(20-M_{r,{\rm peak},i}\right)},$$

where $M_{r,{\rm peak}}$ is the peak absolute r-band magnitude. This weighting corrects, in a simple way, for the fact that more luminous SNe are detectable over larger volumes and would otherwise be overrepresented in the raw observed distribution.

To account for the uncertain lower cutoff of the progenitor mass range, we treat $M_{\rm min}$ as a nuisance parameter and allow it to vary between 8 and 12 $M_\odot$ in the Monte Carlo. For each realization, we draw a random $M_{\rm min}$ within this interval, select the resampled masses above this threshold, and fit a truncated power law using a maximum-likelihood estimator to obtain the best-fit slope α_k. Repeating this procedure for 100 realizations yields a distribution of α values that captures both the individual mass uncertainties and the uncertainty in $M_{\rm min}$. From the volume-weighted ensemble we obtain a mean slope of

$$\alpha = 2.1 \pm 1.2,$$

where the quoted uncertainty is the standard deviation of the Monte Carlo ensemble. For comparison, a standard Salpeter-like IMF has $\alpha_{\rm Salpeter} \simeq 2.35$ over the massive-star regime. Within the current uncertainties and the restricted mass range we probe (~8–22 $M_\odot$), our inferred slope is statistically consistent with a Salpeter-like progenitor distribution. However, the slope is only weakly constrained owing to the small sample size and the fact that, while our LLIIP subsample is drawn from a systematic, volume-limited SN survey, the full sample (including more luminous Type II SNe) is heterogeneous and compiled from the literature rather than from a uniform selection. A robust IMF determination for Type IIP progenitors will ultimately require a larger, systematically selected sample of nebular spectra drawn from a volume-limited survey with no intrinsic brightness cut.

6.6 Electron-capture SN diagnostics

ECSN score

An important theoretical motivation for using nebular-line diagnostics comes from the expected ejecta structure of electron-capture supernovae (ECSNe). ECSNe arising from sAGB progenitors lack both an oxygen-rich shell and a helium shell, since their degenerate ONeMg cores collapse before substantial burning can synthesize or expose these layers (e.g., Jerkstrand et al. 2018). As a result, several nebular features that are prominent in Fe-core-collapse SNe are predicted to be absent or strongly suppressed in ECSNe. These include He I λ7065, Mg I] λ4571, and [C I] λ8727, all of which require the presence of He- or O/C-rich zones. Although [C I] λ9850 is also expected to be a useful Fe-core-collapse/ECSN diagnostic, we do not include it in the formal score because the spectra in this wavelength region generally have low SNR across our sample. The absence of an O-rich shell also leads to systematically weak [O I] $\lambda\lambda$6300,6364. In addition, the innermost ejecta

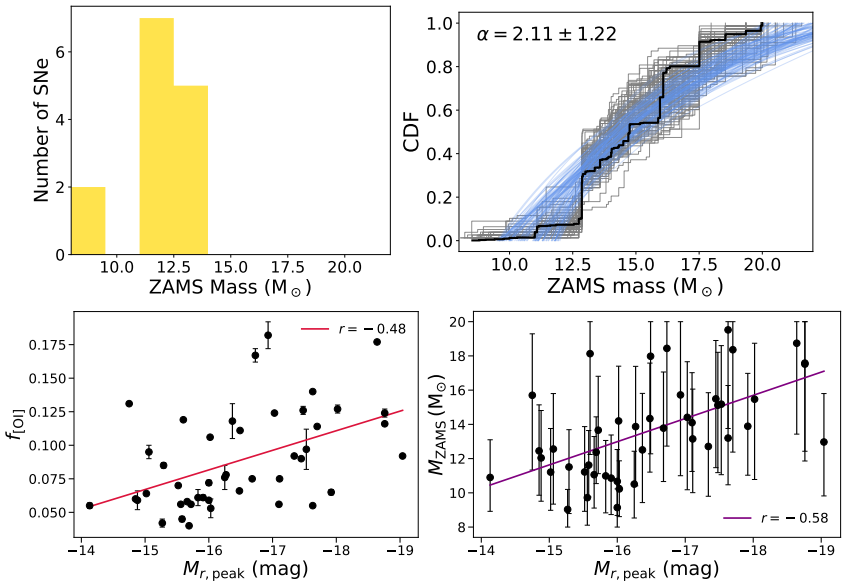

Figure 6.7: Top left: distribution of ZAMS masses inferred for the ZTF LLIIP sample. Top right: cumulative distribution of the inferred masses, with Monte Carlo realizations shown in blue and the best-fit power-law slope α indicated. Bottom left: correlation between the fractional [O I] luminosity and the r-band peak magnitude. Bottom right: weak correlation between the inferred ZAMS mass and the r-band peak magnitude. Pearson coefficients for the two relations are shown in each panel.

of ECSNe are expected to synthesize large amounts of stable ^{58}Ni, giving rise to comparatively strong [Ni II] emission. Although [Fe I] and [Fe II] lines should be intrinsically weak due to the lack of an Fe/Si shell, low-level Fe emission may still arise from explosive burning of the residual envelope, and therefore are not used to distinguish ECSNe from Fe-core-collapse SNe. We note that these qualitative nebular distinctions between ECSNe and Fe-core-collapse SNe predicted by one-dimensional models have also been recently shown to persist in three-dimensional simulations (van Baal et al. 2025).

To ensure uniform classification across the sample, we assess each diagnostic quantitatively. For the line-presence diagnostics He I λ7065, O I λ7774, [C I] λ8727, Mg I] λ4571, and O I λ8447, we extract a 20 Å window centered on the expected wavelength, subtract a local linear continuum, and compute the standard deviation of the residual flux to estimate the noise and line SNR. We also compute a peak ratio, defined as the line peak relative to the peak of [O I] $\lambda\lambda$6300, 6364 in the same spectrum, providing a luminosity-independent scale for comparing weak features across objects. The 'yes' and 'no' thresholds are calibrated using the Jerkstrand et al. (2018) 9 $M_\odot$ nebular models and are listed in Table H; measurements falling between

these thresholds are labeled 'maybe'. For the ratio diagnostics, we use the measured [Ni II]/[Fe II] and [Ca II]/[O I] flux ratios and apply the thresholds in Table H. The observational label is then converted to a numerical score according to whether it supports or contradicts the ECSN expectation. For diagnostics expected to be absent or weak in ECSNe, a 'no' classification is assigned $s_i = +1$, a 'yes' classification is assigned $s_i = -1$, and 'maybe' cases are assigned $s_i = 0$. For [Ni II]/[Fe II], the thresholds in Table H map directly to $s_i = +1$ and -1. For [Ca II]/[O I], we use the ratio only as a one-sided veto: values below the listed 'no' threshold are assigned $s_i = -1$, while all larger values are treated as inconclusive ($s_i = 0$). We also perform a visual inspection to ensure the reliability of each classification, particularly for blended or noisy regions.

Each diagnostic is assigned a weight w_i that reflects its physical robustness and discriminatory power for distinguishing ECSNe from Fe-core-collapse SNe. He I λ7065, O I λ7774, [C I] λ8727, and Mg I] λ4571 are assigned unit weight. O I λ8447 is down-weighted to $w_i = 0.2$ because its formation mechanism is more uncertain and there is tension between models and observations. The [Ni II]/[Fe II] and [Ca II]/[O I] ratios are each assigned $w_i = 0.5$, since they are informative but not uniquely diagnostic and can be sensitive to model details (e.g., Jerkstrand et al. 2015b). Combining the categorical scores s_i with their weights w_i, we compute a normalized ECSN score

$$\text{ECSN score} = \frac{\sum_i w_i s_i}{\sum_i w_i},$$

which lies in the range

$$-1 \leq \text{ECSN score} \leq +1.$$

Scores near +1 indicate that most diagnostics behave as expected for an ECSN, scores near -1 indicate the opposite, and intermediate values represent mixed or inconclusive evidence. To assess the robustness of the ECSN score to the adopted weights and thresholds, we performed 100 Monte Carlo realizations in which both were randomly perturbed by up to ±50% of their nominal values. For every realization we recomputed the full set of ECSN scores. The standard deviation of the ECSN score for each object was below 5% of its nominal value. This shows that the ECSN score is stable against reasonable variations in the adopted weighting scheme and thresholds. All the diagnostics and their color-coded interpretation are listed in Table C.

Table C: Nebular spectral diagnostics for ZTF and selected comparison SNe, ordered from highest to lowest ECSN score. For each feature, the presence of an emission line is quantified using both the line SNR and peak ratio, with detection thresholds calibrated on the Jerkstrand et al. (2018) 9 $M_{\odot}$ nebular models (see Table H). Cells marked in green ('yes') indicate measurements consistent with ECSN expectations, red ('no') indicate measurements that contradict ECSN expectations, and grey ('maybe') indicate ambiguous cases.

SN	Phase (d)	He I 7065	Mg I] 4571	[C I] 8727	O I 7774	O I 8447	[Ca]/[O]	[Ni]/[Fe]	Score
SN 2023bvj	296	no	maybe	maybe	no	yes	maybe	maybe	+0.48
SN 2024btj	291	maybe	no	maybe	no	maybe	maybe	no	+0.22
SN 2024btj	348	no	no	maybe	no	maybe	maybe	no	+0.43
SN 2016bkv	257	maybe	maybe	maybe	maybe	yes	maybe	maybe	+0.04
SN 2016bkv	436	no	yes	maybe	no	yes	maybe	maybe	+0.43
SN 2016bkv	608	no	yes	maybe	no	yes	maybe	maybe	+0.43
SN 2018zd	228	maybe	maybe	maybe	maybe	maybe	maybe	yes	+0.04
SN 2018zd	291	maybe	maybe	maybe	maybe	yes	maybe	yes	+0.09
SN 2018zd	306	no	maybe	maybe	maybe	maybe	maybe	yes	+0.26
SN 2018zd	338	maybe	maybe	maybe	maybe	maybe	maybe	yes	+0.04
SN 2018zd	399	maybe	maybe	no	maybe	maybe	maybe	yes	+0.26
SN 2022zmb	175	no	maybe	maybe	yes	no	maybe	yes	+0.00
SN 2022zmb	222	no	maybe	maybe	maybe	no	maybe	yes	+0.22
SN 2005cs	304	maybe	no	yes	maybe	maybe	maybe	yes	-0.13
SN 2005cs	334	no	maybe	maybe	maybe	maybe	maybe	yes	+0.26
SN 2022jzc	346	maybe	maybe	maybe	maybe	maybe	maybe	yes	+0.04
SN 2023mpz	310	maybe	maybe	maybe	maybe	maybe	maybe	yes	+0.04
SN 2024cro	180	maybe	maybe	maybe	maybe	no	maybe	maybe	-0.04
SN 2024ov	147	maybe	maybe	maybe	maybe	maybe	maybe	no	-0.04
SN 2023wcr	148	maybe	maybe	maybe	maybe	no	maybe	no	-0.09
SN 2023wcr	172	maybe	maybe	maybe	maybe	no	maybe	no	-0.09
SN 2023wcr	190	maybe	maybe	maybe	maybe	no	maybe	no	-0.09

Table C: Continued.

SN	Phase (d)	He I 7065	Mg I] 4571	[C I] 8727	O I 7774	O I 8447	[Ca]/[O]	[Ni]/[Fe]	Score
SN 2023wcr	262	maybe	maybe	maybe	maybe	no	maybe	no	-0.09
SN 2023ywa	250	yes	maybe	maybe	no	maybe	no	no	-0.26
SN 2023ywa	342	yes	maybe	maybe	no	no	maybe	maybe	-0.04
SN 2022aaad	136	yes	maybe	maybe	maybe	maybe	maybe	maybe	-0.22
SN 2022aaad	158	yes	maybe	maybe	maybe	maybe	maybe	maybe	-0.22
SN 2022aaad	169	yes	yes	maybe	maybe	no	maybe	maybe	-0.30
SN 2022aaad	215	yes	maybe	maybe	maybe	yes	maybe	maybe	-0.17
SN 2022aaad	282	yes	yes	maybe	maybe	yes	maybe	yes	-0.17
SN 2022aaad	332	yes	maybe	maybe	maybe	yes	maybe	yes	-0.13
SN 2022aaad	366	yes	yes	maybe	maybe	yes	maybe	maybe	-0.22
SN 2022aaad	393	yes	yes	maybe	maybe	yes	maybe	maybe	-0.22
SN 2022aaad	463	yes	yes	maybe	maybe	yes	maybe	maybe	-0.22
SN 2022aaad	508	maybe	maybe	maybe	maybe	yes	no	maybe	-0.17
SN 2022acko	258	yes	yes	yes	no	no	maybe	maybe	-0.30
SN 2022acko	287	yes	yes	yes	maybe	no	maybe	no	-0.57
SN 2022acko	340	yes	yes	no	maybe	maybe	maybe	maybe	-0.04
SN 2022acko	369	yes	yes	yes	no	no	maybe	maybe	-0.30
SN 2022acko	439	yes	yes	no	no	maybe	maybe	maybe	+0.17
SN 2022aang	391	yes	maybe	maybe	maybe	maybe	maybe	maybe	-0.22
SN 2023azx	387	yes	maybe	maybe	maybe	yes	maybe	no	-0.22
SN 2023azx	432	yes	maybe	maybe	maybe	yes	maybe	no	-0.22
SN 2024wp	180	yes	maybe	maybe	maybe	maybe	maybe	no	-0.26
SN 1997D	207	yes	no	maybe	maybe	no	maybe	no	-0.26
SN 1997D	350	yes	yes	maybe	maybe	maybe	maybe	maybe	-0.26
SN 2008bk	260	yes	yes	yes	maybe	yes	maybe	no	-0.48
SN 2008bk	529	maybe	yes	yes	no	maybe	maybe	maybe	-0.04
SN 2023vci	165	yes	maybe	maybe	maybe	no	maybe	no	-0.30

Table C: Continued.

SN	Phase (d)	He I 7065	Mg I] 4571	[C I] 8727	O I 7774	O I 8447	[Ca]/[O]	[Ni]/[Fe]	Score
SN 2023vci	210	yes	maybe	maybe	maybe	no	maybe	no	-0.30
SN 2023kmk	231	yes	maybe	no	yes	yes	no	no	-0.43
SN 2023kmk	264	yes	maybe	maybe	maybe	yes	maybe	no	-0.22
SN 2023kmk	309	yes	maybe	maybe	maybe	yes	maybe	no	-0.22
SN 2023kmk	347	yes	maybe	maybe	maybe	yes	no	no	-0.43
SN 2024abfl	149	yes	maybe	yes	maybe	yes	no	yes	-0.57
SN 2024abfl	334	yes	yes	yes	no	yes	maybe	maybe	-0.22
SN 2024abfl	393	yes	maybe	yes	no	maybe	maybe	no	-0.26
SN 2023usp	115	yes	maybe	yes	maybe	yes	maybe	yes	-0.35
SN 2024jxm	132	yes	maybe	yes	yes	no	maybe	no	-0.74
SN 2024jxm	241	yes	maybe	maybe	maybe	no	maybe	no	-0.30
SN 2024jxm	394	maybe	maybe	maybe	maybe	maybe	maybe	no	-0.04

ECSN scores of the LLIIP sample

A small subset of objects attain mean ECSN scores higher than that of SN 2016bkv and SN 2018zd. The highest mean ECSN score is found for SN 2023bvj, based on its single available spectrum, followed by SN 2024btj and SN 2016bkv, which also remain positive across multiple epochs. In SN 2023bvj, the high score is driven primarily by the non-detection of He I λ7065 and O I λ7774, together with a detection of O I λ8447; Mg I] λ4571 and [C I] λ8727 remain ambiguous and the ratio diagnostics are inconclusive. We also note that [C I] λ9850 is not detected, further supporting an ECSN interpretation. SN 2024btj shows a robust absence of Mg I] λ4571 and O I λ7774 at both epochs, with [C I] and O I λ8447 either absent or marginal; its [Ni II]/[Fe II] ratio remains consistently low, which limits the overall ECSN score. SN 2016bkv likewise reaches high late-time scores because He I λ7065 and O I λ7774 are absent in the two later spectra while O I λ8447 is present at all epochs, although Mg I] λ4571 is clearly detected at late times. Among the remaining comparison objects, SN 2022zmb shows a modestly positive ECSN score, with non-detections of He I λ7065 and enhanced [Ni II]/[Fe II] partly offset by the absence of O I λ8447 and a detection of O I λ7774 in one spectrum. SN 2005cs has a lower overall score because [C I] λ8727 is clearly present in one spectrum.

At the opposite extreme, SN 2024jxm has the most negative mean ECSN score in the sample, while SN 2024abfl, SN 2023kmk, and SN 2023vci also remain consistently negative at all observed epochs. SN 2024jxm shows He I λ7065 in the early spectra, [C I] emission that is present or at least not clearly absent, and persistently weak [Ni II]/[Fe II]. SN 2023kmk is driven negative by strong He I λ7065 at all epochs, repeated non-detections of [Ni II]/[Fe II], and at some epochs detected O I λ7774 or low [Ca II]/[O I]. SN 2023vci is likewise negative at both epochs because He I λ7065 is present while O I λ8447 and [Ni II]/[Fe II] are both weak. SN 2008bk also disfavors an ECSN interpretation, especially at 260 d where He I λ7065, Mg I] λ4571, [C I] λ8727, and O I λ8447 are all clearly detected.

Taken together, the ECSN scores show that only a handful of LLIIP SNe have nebular spectra that are at least as ECSN-like as SN 2016bkv and SN 2018zd in terms of line ratios and the presence or absence of key features. We regard SN 2023bvj, SN 2024btj, and SN 2016bkv as the strongest ECSN candidates in this diagnostic sense. However, we note that their nebular Hα line widths and fractional [O I] fluxes $f_{[\mathrm{O\,I}]}$ are larger than predicted by the 9 $\mathrm{M}_{\odot}$ low-mass models of Jerkstrand et al. (2018), which favor extremely narrow Balmer lines and very weak [O I]

emission for ECSN-like explosions.

Rate estimate of ECSNe from sAGB stars

Our volume-limited ZTF CLU sample contains 28 LLIIP SNe within 100 Mpc (Paper I), of which 19 have nebular spectra of sufficient quality to measure the diagnostics described above. Among these 19, at most two events, SN 2023bvj and SN 2024btj, have ECSN scores higher than SN 2016bkv and SN 2018zd and therefore qualify as our strongest nebular ECSN candidates within the LLIIP sample. We can therefore use this systematic sample to place an approximate upper limit on the ECSN rate through the LLIIP channel. If both candidates are genuine ECSNe and the nebular subsample is representative of the parent LLIIP population, the implied ECSN fraction within the LLIIP class lies between $2/28 \simeq 0.07$ (normalizing to all 28 LLIIP SNe) and $2/19 \simeq 0.11$ (normalizing only to the nebular subsample). Combined with the volumetric LLIIP rate of $\sim 7.3 \times 10^3\,\mathrm{Gpc^{-3}\,yr^{-1}}$ from Paper I (Das et al. 2025c), this implies an approximate upper limit of $(5\text{–}8)\times 10^2\,\mathrm{Gpc^{-3}\,yr^{-1}}$ on the rate of ECSNe that pass through the LLIIP channel.

In Paper I, we showed that LLIIP SNe constitute $8^{+1}_{-2}\%$ of all CCSNe (Das et al. 2025c). Under the assumption that all ECSNe in the local Universe manifest as LLIIP SNe, the two ECSN candidates identified in our sample therefore imply an ECSN fraction of all CCSNe of approximately f_{ECSN} ~0.004–0.010 after accounting for the uncertainty in the LLIIP-to-CCSN fraction.

To translate this ECSN fraction into a constraint on the progenitor mass range, we adopt the simple picture in which ECSNe arise from sAGB stars at the low-mass end of the CCSN population. We assume that all stars with zero-age main-sequence masses between $M_{\mathrm{CC,min}}$ and $M_{\mathrm{CC,max}} = 120\,M_\odot$ can undergo core collapse, and that the lowest-mass CCSNe are ECSNe produced by sAGB stars. In this picture, the sAGB interval runs from $M_{\mathrm{sAGB,min}}$ to $M_{\mathrm{sAGB,max}}$, and we explicitly set $M_{\mathrm{sAGB,min}} = M_{\mathrm{CC,min}}$. For a Salpeter initial mass function (IMF), $\psi(M) \propto M^{-2.35}$, the fraction of CCSNe that are ECSNe is

$$f_{\mathrm{ECSN}} = \frac{\displaystyle\int_{M_{\mathrm{sAGB,min}}}^{M_{\mathrm{sAGB,max}}} M^{-2.35}\,dM}{\displaystyle\int_{M_{\mathrm{CC,min}}}^{M_{\mathrm{CC,max}}} M^{-2.35}\,dM},$$

where we parameterize the ECSN-producing interval by $\Delta M_{\mathrm{sAGB}} = M_{\mathrm{sAGB,max}} - M_{\mathrm{sAGB,min}}$, and adopt $M_{\mathrm{CC,max}} = 120\,M_\odot$.

For a fiducial choice of $M_{\rm CC,min} = M_{\rm sAGB,min} = 8.5\,M_\odot$, the nominal CCSN fractions above imply $\Delta M_{\rm sAGB} \simeq 0.035\,M_\odot$ to $0.052\,M_\odot$, corresponding to progenitor intervals of approximately 8.50–8.54 $M_\odot$ and 8.50–8.55 $M_\odot$. Varying the CCSN threshold over the plausible range $M_{\rm CC,min} \simeq$ 8–9 $M_\odot$ changes these values only slightly: the corresponding widths are ∼0.033–0.037 $\mathrm{M}_\odot$ for the $2/28$ normalization and ∼0.049–0.055 $\mathrm{M}_\odot$ for the $2/19$ normalization. Even allowing the full 6–9% range for the LLIIP fraction of all CCSNe broadens the inferred window only to about 0.025–0.062 $M_\odot$. These trends are illustrated in Figure 6.8, which shows the required sAGB width $\Delta M_{\rm sAGB}$ as a function of the CCSN threshold mass $M_{\rm CC,min} = M_{\rm sAGB,min}$ for the two empirical ECSN fractions inferred above. The shaded region between the curves marks the range of $\Delta M_{\rm sAGB}$ values consistent with our measurements.

The evolution to sAGB stars is highly sensitive to dredge-up/dredge-out and mass-loss physics, yielding a broad range of predicted ECSN-producing mass windows. However, the progenitor interval inferred here is narrower than most theoretical expectations; for example, $\Delta M_{\rm sAGB} \approx 0.2$–$1.4\,M_\odot$ at solar metallicity (e.g., Poelarends et al. 2008).

We note that the LLIIP channel need not capture the entire ECSN population. Some ECSNe may instead appear as other low-luminosity or interaction-powered transients, such as intermediate-luminosity red transients (e.g., Rose et al. 2024), brighter Type IIP SNe (as proposed for SN 2018zd), or Type IIP-n events with stronger circumstellar interaction (Hiramatsu et al. 2021a, Smith 2013). A systematic, volume-limited survey of late-time nebular spectra across all nearby CCSN subtypes will be required to obtain a more comprehensive measurement of the ECSN rate and the associated sAGB progenitor mass range.

6.7 Conclusion

We obtained usable nebular spectra for 19 (out of 28) LLIIP SNe within 100 Mpc from the ZTF CLU survey discovered between 2022 November 1 and 2024 November 1 that satisfy the Paper I quality criteria, at phases between ∼140 and 450 d after explosion. Their low expansion velocities and explosion energies allow us to resolve narrow nebular emission lines that are typically blended in more energetic Type II SNe. We summarize the key takeaways here:

- The LLIIP SNe in our sample exhibit systematically narrower nebular H I λ6563 emission lines than brighter comparison Type II SNe from the literature. A

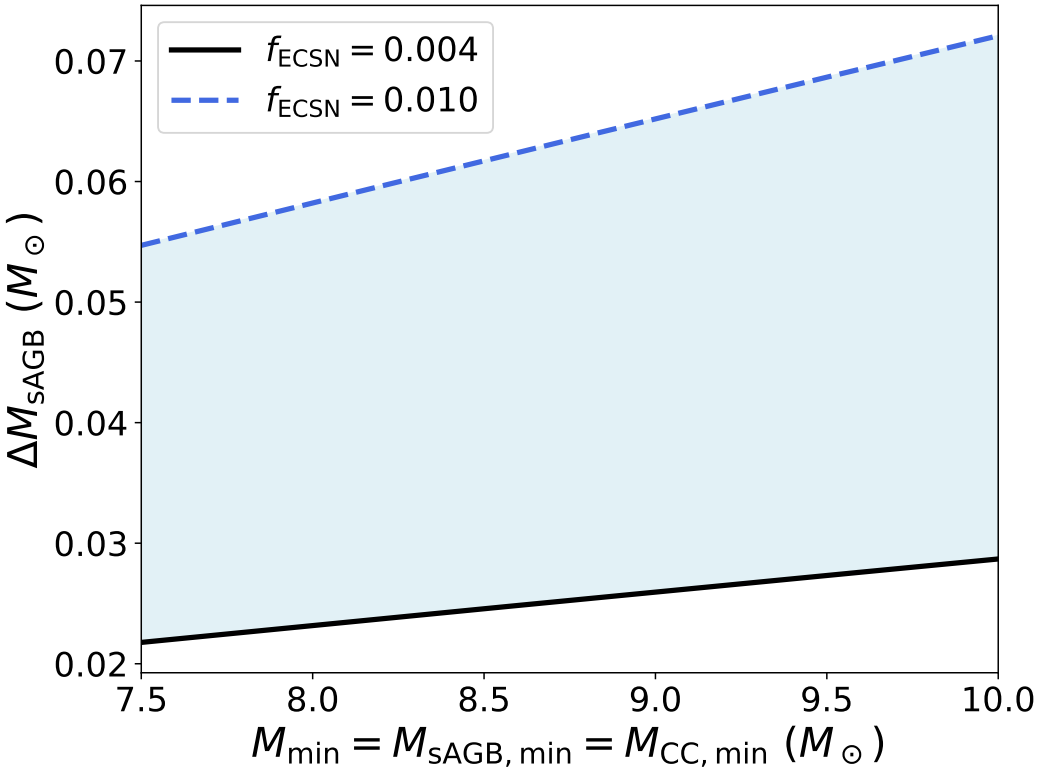

Figure 6.8: Required width of the sAGB ECSN window $\Delta M_{\rm sAGB}$ as a function of the CCSN threshold mass $M_{CC,min}$. The blue shaded region indicates the range of $\Delta M_{\rm sAGB}$ values consistent with the empirical constraints.

planar fit to the H I λ6563 FWHM as a function of phase and peak absolute magnitude,

$$\begin{aligned}\text{FWHM (Å)} = {} & (-72.76 \pm 1.15) \\ & + (-0.05 \pm 0.01)\,\text{Phase (d)} \\ & + (-9.05 \pm 0.07)\,M_{\rm peak}.\end{aligned}$$

with a Pearson correlation coefficient r = 0.65, shows that fainter SNe have lower nebular H I velocities at fixed phase, consistent with intrinsically low-energy explosions.

- When we compare the observed nebular H I widths to models for low-mass progenitors, we find that only SN 2024abfl in our LLIIP sample, together with SN 1997D and SN 2016bkv from the literature, approaches the extremely low H I λ6563 widths predicted for the weakest explosions of $\sim 9\,M_\odot$ RSG or sAGB progenitors (Jerkstrand et al. 2018). Most LLIIP SNe have nebular H I widths of at least $\sim 2000\,\mathrm{km\,s^{-1}}$ despite their low explosion energies and

^{56}Ni masses. Given that 8–10 $M_\odot$ stars represent a substantial fraction of core-collapse progenitors for a Salpeter IMF, this scarcity suggests either that the effective lower mass limit for successful core collapse is higher than in some models or that real explosions near this threshold are not as uniformly weak as core-collapse models predict.

- We do not find any significant correlation between nebular-phase line widths or flux ratios and the lightcurve plateau duration. This indicates that the length of the recombination phase is largely decoupled from the explosion and other core properties probed by the nebular spectra.

- The fractional [O I] flux $f_{[\mathrm{OI}]}$ shows a modest but statistically significant correlation with phase. Across the full sample, the Pearson coefficient between $f_{[\mathrm{OI}]}$ and phase is $r \simeq 0.6$ (with $p < 10^{-5}$), and the best-fitting relation

$$f_{[\mathrm{OI}]} \;=\; (2.0 \pm 0.1)\times 10^{-4}\, t \;+\; (0.0112 \pm 0.0003),$$

  where t is the phase in days, likely shows that $f_{[\mathrm{OI}]}$ increases slowly over time as the ejecta become more transparent and the oxygen-rich core contributes a larger fraction of the emergent flux.

- We estimated zero-age main sequence (ZAMS) progenitor masses using the nebular [O I] $\lambda\lambda 6300, 6364$ emission as a proxy for oxygen-core mass. We find a moderate correlation between the inferred M_{ZAMS} and the optical peak magnitude, with Pearson coefficient $r = -0.58$ (and $p \simeq 6.8 \times 10^{-5}$) and best-fitting relation

$$M_{\mathrm{ZAMS}} \;\approx\; (-1.5 \pm 0.4)\, M_{r,\mathrm{peak}} - (11.7 \pm 1.2)\ \mathrm{M}_\odot,$$

  showing that fainter peaks correspond to systematically lower progenitor masses. We caution that circumstellar interaction or dust formation can modify the observed peak luminosity or suppress nebular [O I] emission, potentially biasing the inferred M_{ZAMS}–$M_{r,\mathrm{peak}}$ relation.

- The distribution of ZAMS mass of LLIIP SNe is strongly weighted towards low-mass progenitors. The median is $M_{\mathrm{ZAMS}} \simeq 11.2\,\mathrm{M}_\odot$ and the 16th to 84th percentiles lie at ≈ 9.9 and $12.7\,\mathrm{M}_\odot$. Twelve out of nineteen SNe have $M_{\mathrm{ZAMS},50} \leq 12\,\mathrm{M}_\odot$, providing robust evidence that the LLIIP progenitor population is dominated by stars in the 8–12 $\mathrm{M}_\odot$ regime. From the volume-weighted ensemble we infer an IMF power-law index of $\alpha = 2.1 \pm 1.2$ over

the $\sim$ 8–22 $M_\odot$ range, which is statistically consistent with a Salpeter-like progenitor distribution.

- To search for electron-capture supernovae, we introduced an "ECSN score" based on the absence of He- and O-shell emission lines and the Ni/Fe diagnostics in the nebular spectra. Only a handful of LLIIP SNe achieve scores that are at least as ECSN-like as SN 2016bkv and SN 2018zd. In our sample, we regard SN 2023bvj and SN 2024btj as the strongest ECSN candidates in this diagnostic sense. However, we note that their nebular Hα line widths are larger than predicted by the 9 $M_\odot$ low-mass models of Jerkstrand et al. (2018), which favor extremely narrow Balmer lines for ECSN-like explosions.

- Within our volume-limited sample of 28 LLIIP SNe, two events out of the full sample and out of the 19 SNe with usable nebular spectra satisfy our ECSN-score criteria. This corresponds to fractions of $2/28 \simeq 0.07$ and $2/19 \simeq 0.11$, which we treat as approximate upper limits on the fraction of LLIIP SNe arising from the ECSN channel. Assuming a volumetric LLIIP rate of $\sim 7.3 \times 10^3\,\mathrm{Gpc^{-3}\,yr^{-1}}$ (Das et al. 2025c), these fractions imply an approximate upper limit on the rate of ECSN candidates passing through the LLIIP channel of $(5\text{–}8) \times 10^2\,\mathrm{Gpc^{-3}\,yr^{-1}}$. If ECSNe predominantly arise through the LLIIP SN channel, and if they originate from sAGB stars at the low-mass end of the CCSN population, then the fact that LLIIP SNe constitute $8^{+1}_{-2}\%$ of all CCSNe (Das et al. 2025c) implies an ECSN fraction of all CCSNe of approximately $\sim$ 0.004–0.010. This corresponds to an sAGB progenitor mass window of order 0.02–0.06 $M_\odot$.

We emphasize that the LLIIP channel need not encompass the full ECSN population. Some ECSNe may instead manifest as other faint or interaction-powered transients, including intermediate-luminosity red transients, relatively brighter Type IIP SNe (as has been proposed for SN 2018zd), or Type IIP-n events with stronger circumstellar interaction. A truly robust measurement of the ECSN rate, and the associated sAGB progenitor mass window, will therefore require a systematic, volume-limited program of late-time nebular spectroscopy spanning all nearby core-collapse supernova subtypes.

We note that none of the nebular spectra match all predicted features of existing low-mass RSG or sAGB models in detail. The 9 $M_\odot$ RSG and sAGB nebular models of Jerkstrand et al. (2018) do not fully explore the effects of multi-dimensional mixing

and core asymmetries, even though recent three-dimensional simulations suggest that the key one-dimensional ECSN versus Fe-core-collapse distinctions remain broadly robust at the lowest masses (van Baal et al. 2025). An additional caveat is that the simplified sAGB nebular model is constructed by replacing the composition with H-zone material throughout, rather than using a fully evolved sAGB progenitor structure. A broader suite of nebular spectral calculations that spans both ONeMg-core and Fe-core explosions at the low-mass end, based on fully evolved sAGB stars, will allow one to establish more reliable and quantitative ECSN diagnostics. It will also be valuable to develop complementary mid-infrared diagnostics, for example with *JWST*, to probe ejecta composition and cooling channels that may be less accessible at optical wavelengths.

Looking ahead, future wide-field time-domain surveys such as LSST will discover large numbers of faint transients. Expanding to a larger, volume-limited sample with uniform late-time spectroscopy across all nearby core-collapse subtypes will enable tighter constraints on the ECSN rate, the sAGB progenitor mass range, and the contribution of ECSNe at the low-mass end of the initial mass function, thereby improving our understanding of how the least massive core-collapse progenitors end their lives.

Acknowledgements

We thank Qiliang Fang, Ryan Chornock, Azalee Bostroem and Luc Dessart for helpful discussions.

W.J.-G. is supported by NASA through Hubble Fellowship grant HSTHF2-51558.001-A awarded by the Space Telescope Science Institute, which is operated for NASA by the Association of Universities for Research in Astronomy, Inc., under contract NAS5-26555.

M.W.C. acknowledges support from the National Science Foundation with grant numbers PHY-2117997, PHY-2308862 and PHY-2409481.

Based on observations obtained with the Samuel Oschin Telescope 48-inch and the 60-inch Telescope at the Palomar Observatory as part of the Zwicky Transient Facility project. ZTF is supported by the National Science Foundation under Grants No. AST-1440341, AST-2034437, and currently Award 2407588. ZTF receives additional funding from the ZTF partnership. Current members include Caltech, USA; Caltech/IPAC, USA; University of Maryland, USA; University of California, Berkeley, USA; University of Wisconsin at Milwaukee, USA; Cornell University,

USA; Drexel University, USA; University of North Carolina at Chapel Hill, USA; Institute of Science and Technology, Austria; National Central University, Taiwan, and OKC, University of Stockholm, Sweden. Operations are conducted by Caltech's Optical Observatory (COO), Caltech/IPAC, and the University of Washington at Seattle, USA.

Zwicky Transient Facility access for S.S. was supported by Northwestern University and the Center for Interdisciplinary Exploration and Research in Astrophysics (CIERA).

The ZTF forced-photometry service was funded under the Heising-Simons Foundation grant #12540303 (PI: Graham).

The Gordon and Betty Moore Foundation, through both the Data-Driven Investigator Program and a dedicated grant, provided critical funding for SkyPortal .

This research has made use of the NASA/IPAC Extragalactic Database (NED), which is funded by the National Aeronautics and Space Administration and operated by the California Institute of Technology.

The Liverpool Telescope is operated on the island of La Palma by Liverpool John Moores University in the Spanish Observatorio del Roque de los Muchachos of the Instituto de Astrofisica de Canarias with financial support from the UK Science and Technology Facilities Council.

The W. M. Keck Observatory is operated as a scientific partnership among the California Institute of Technology, the University of California and the National Aeronautics and Space Administration. The Observatory was made possible by the generous financial support of the W. M. Keck Foundation. The authors wish to recognize and acknowledge the very significant cultural role and reverence that the summit of Maunakea has always had within the indigenous Hawaiian community. We are most fortunate to have the opportunity to conduct observations from this mountain.

Software: Global Relay of Observatories Watching Transients Happen Marshal (GROWTH; Kasliwal et al. 2019) and the Fritz SkyPortal Marshal (Duev et al. 2019, Van der Walt et al. 2019, Coughlin et al. 2023). Astropy (Astropy Collaboration et al. 2013), Matplotlib (Hunter 2007)

Table D: Spectral log of nebular spectra of brighter ZTF Type IIP SNe.

ZTF Name	IAU Name	Date	Phase (d)	Instrument
ZTF19abqhobb	SN 2019nvm	2020-01-29	152	NOT/ALFOSC
ZTF20aaynrrh	SN 2020jfo[a]	2020-12-06	207	NOT/ALFOSC
ZTF20aaynrrh	SN 2020jfo[a]	2021-01-15	247	NOT/ALFOSC
ZTF20aaynrrh	SN 2020jfo[a]	2021-02-08	271	NOT/ALFOSC
ZTF20aaynrrh	SN 2020jfo[a]	2021-03-08	299	NOT/ALFOSC
ZTF20aaynrrh	SN 2020jfo[a]	2021-04-20	342	NOT/ALFOSC
ZTF20abotkfn	SN 2020qmp	2021-02-20	111	P200/DBSP
ZTF21abouuat	SN 2021ucg	2022-04-27	257	Keck/LRIS
ZTF23absdcgi	SN 2023zcu	2024-11-11	329	P200/DBSP
ZTF23abvgvab	SN 2023abim	2024-03-31	104	Keck/LRIS

[a] Nebular spectra of SN 2020jfo are taken from Sollerman et al. (2021).

Appendix

Table D lists the nebular spectral log for the brighter ZTF Type IIP comparison sample. Figure 6.9 illustrates the full nebular spectral analysis workflow on a representative object (ZTF22abtjefa/SN 2022aaad), including host-continuum fitting and subtraction, isolation and Gaussian fitting of the [O I] $\lambda\lambda 6300, 6363$ feature, and multi-component fitting of the 7000–7500 Å region to extract the [Ca II] $\lambda\lambda 7291, 7323$ profile. Table E compiles the spectral log for the literature sample of 120 nebular spectra of non–ZTF Type II SNe used for comparison. Table F summarizes the full set of nebular measurements together with plateau properties, peak absolute magnitudes, and ZAMS mass estimates for the LLIIP sample. Table G reports per-spectrum ZAMS mass estimates from the GP inversion. Table H lists the adopted ECSN diagnostic weights and thresholds. The remainder of the appendix presents the nebular spectra for the LLIIP SNe analyzed in this paper (Figures 6.10–6.30).

Table E: Spectral Log for 120 nebular spectra of 54 non–ZTF Type II SNe

SN	MJD	Phase (d)	Ref.
1990E	48191	253	(1)
1990E	48207	269	(1)
1990E	48242	304	(1)
1990E	48267	330	(1)
1990E	48268	330	(1)
1990Q	48362	320	(1)
1991G	48635	355	(2)(3)
1992H	49042	386	(2)(4)
1992ad	49030	225	(2)(5)
1992ad	49091	286	(2)(5)
1992ad	49092	287	(2)(5)
1993K	49369	295	(2)
1996W	50432	252	(6)
1996W	50475	295	(6)
1997D	50569	207	(64)(65)

Table E: Continued.

SN	MJD	Phase (d)	Ref.
1997D	50712	350	(64)(65)
1998S	51017	143	(66)
1998S	51188	314	(66)
1999em	51793	317	(7)(8)
2002hh	52972	396	(2)(9)
2003B	52897	275	(10)(11)
2003gd	52847	130	(8)(12)
2003gd	52967	250	(8)(12)
2004A	53296	286	(2)(13)(14)
2004dj	53323	136	(2)(15)
2004dj	53351	164	(2)(15)
2004dj	53386	199	(2)(15)
2004dj	53413	226	(2)(15)
2004dj	53440	253	(2)(15)
2004dj	53442	274	(2)(15)
2004dj	53477	290	(2)(15)
2004et	53432	162	(8)(16)(17)
2004et	53471	201	(8)(16)(17)
2004et	53496	226	(8)(16)(17)
2004et	53528	258	(8)(16)(17)
2004et	53552	282	(8)(16)(17)
2004et	53583	313	(8)(16)(17)
2004et	53623	353	(8)(16)(17)
2004et	53624	354	(8)(16)(17)
2005ay	53741	285	(8)(18)(19)
2005cs	53706	157	(8)(20)(21)
2005cs	53852	304	(8)(20)(21)
2005cs	53883	334	(8)(20)(21)
2007aa	54515	384	(22)(23)
2007it	54616	268	(11)(24)
2008bk	54810	260	(11)(25)
2008bk	55079	529	(11)(25)
2008cn	54938	340	(23)(26)
2008ex	54979	285	(2)(27)
2009N	55259	411	(28)
2009dd	55157	232	(6)
2009dd	55333	408	(6)
2009ib	55260	219	(29)
2009ib	55303	262	(29)
2012A	56019	86	(30)
2012A	56341	408	(30)
2012aw	56371	369	(31)(32)
2012ch	56402	357	(2)(33)
2012ec	56546	403	(34)
2012ho	56422	168	(2)(35)
2012ho	56484	229	(2)(35)
2012ho	56504	249	(2)(35)

Table E: Continued.

SN	MJD	Phase (d)	Ref.
2012ho	56506	252	(2)(35)
2012ho	56520	265	(2)(35)
2012ho	56573	318	(2)(35)
2013am	56652	281	(2)(36)
2013by	56564	160	(37)(38)
2013by	56691	287	(37)(38)
2013ej	56932	435	(2)(39)(40)
2013ej	57305	808	(2)(39)(40)
2013ej	56834	337	(2)(39)(40)
2013fs	56841	270	(41)
2014G	56806	137	(42)
2014G	56856	187	(42)
2014G	57010	341	(42)
2014cx	57251	350	(43)
2015bs	57340	420	(44)
2015bs	57341	421	(44)
ASASSN15oz	57604	342	(45)
2016X	57745	340	(46)(47)
2016aqf	57642	202	(48)
2016aqf	57699	259	(48)
2016aqf	57725	285	(48)
2016aqf	57743	303	(48)
2016aqf	57770	330	(48)
2016aqf	57791	351	(48)
2016bkv	57724	257	(67)
2016bkv	57903	436	(67)
2016bkv	58075	608	(67)
2017eaw	58136	250	(49)
2017ivv	58202	110	(50)
2017ivv	58228	136	(50)
2017ivv	58250	158	(50)
2017ivv	58335	243	(50)
2017ivv	58371	279	(50)
2017ivv	58417	325	(50)
2017ivv	58424	332	(50)
2018cuf	58627	335	(52)
2018gj	58397	270	(69)
2018hwm	58810	385	(53)
2018is	58519	386	(51)
2018zd	58360	182	(68)
2018zd	58406	228	(68)
2018zd	58462	284	(68)
2018zd	58469	291	(68)
2018zd	58484	306	(68)
2018zd	58493	315	(68)
2018zd	58516	338	(68)
2018zd	58577	399	(68)

Table E: Continued.

SN	MJD	Phase (d)	Ref.
2020jfo	59190	217	(54)(55)(56)(57)
2020jfo	59230	256	(54)(55)(56)(57)
2020jfo	59254	280	(54)(55)(56)(57)
2020jfo	59281	308	(54)(55)(56)(57)
2020jfo	59324	351	(54)(55)(56)(57)
2021dbg	59610	352	(58)
2021gmj	59678	385	(59)(60)
2022jox	59947	240	(61)
2023ixf	60343	260	(62)(63)

References: (1) Gómez and López (2000); (2) Silverman et al. (2012); (3) Blanton et al. (1995); (4) Clocchiatti et al. (1996); (5) van Dyk et al. (1996); (6) Inserra et al. (2013); (7) Elmhamdi et al. (2003); (8) Faran et al. (2014b); (9) Pozzo et al. (2006); (10) Anderson et al. (2014a); (11) Gutiérrez et al. (2017b); (12) Hendry et al. (2005); (13) Hendry et al. (2006); (14) Gurugubelli et al. (2008); (15) Leonard et al. (2006); (16) Sahu et al. (2006); (17) Utrobin and Chugai (2009a); (18) Tsvetkov et al. (2006); (19) Bufano et al. (2007); (20) Pastorello et al. (2006a); (21) Pastorello et al. (2009b); (22) Chornock et al. (2010); (23) Maguire et al. (2012); (24) Andrews et al. (2011); (25) Van Dyk et al. (2012a); (26) Elias-Rosa et al. (2009); (27) de Jaeger et al. (2019b); (28) Takáts et al. (2014); (29) Takáts et al. (2015); (30) Tomasella et al. (2013a); (31) Bose et al. (2013); (32) Jerkstrand et al. (2014b); (33) Drake et al. (2012); (34) Jerkstrand et al. (2015c); (35) Itagaki et al. (2012); (36) Zhang et al. (2014); (37) Valenti et al. (2015); (38) Black et al. (2017); (39) Bose et al. (2015); (40) Yuan et al. (2016); (41) Yaron et al. (2017); (42) Terreran et al. (2016); (43) Huang et al. (2016); (44) Anderson et al. (2018); (45) Bostroem et al. (2019a); (46) Huang et al. (2018); (47) Ruiz-Carmona et al. (2022); (48) Müller-Bravo et al. (2020); (49) Szalai et al. (2019); (50) Gutiérrez et al. (2020); (51) Dastidar et al. (2025); (52) Dong et al. (2021); (53) Reguitti et al. (2021); (54) Sollerman et al. (2021); (55) Teja et al. (2022); (56) Ailawadhi et al. (2023); (57) Kilpatrick et al. (2023); (58) Zhao et al. (2024); (59) Murai et al. (2024); (60) Meza-Retamal et al. (2024); (61) Andrews et al. (2024); (62) Singh et al. (2024b); (63) Ferrari et al. (2024); (64) Turatto et al. (1998); (65) Benetti et al. (2001); (66) Pozzo et al. (2004); (67) Hosseinzadeh et al. (2018); (68) Hiramatsu et al. (2021a); (69) Teja et al. (2023).

Table F: Nebular measurements, plateau properties, peak absolute magnitudes, and ZAMS estimates for the LLIIP sample.

SN	Phase (d)	$M_{r,\mathrm{peak}}$ (mag)	H I FWHM (Å)	[Ca II]/[O I]	[Ni II]/[Fe II]	$f_{[\mathrm{O\,I}]}$	Plat. (d)	Slope (10^{-2} mag d^{-1})	M_{ZAMS} ($\mathrm{M}_{\odot}$)
ZTF22abssiet	175	-15.72	55.71 ± 0.67	3.83 ± 0.53	1.47	0.022 ± 0.002	66	0.182	$13.62^{+2.84}_{-3.14}$
ZTF22abssiet	222	-15.72	52.70 ± 0.89	1.41 ± 0.09	1.04	0.056 ± 0.001	66	0.182	$13.62^{+2.84}_{-3.14}$
ZTF22abtjefa	136	-15.06	65.21 ± 0.52	$--$	$--$	0.023 ± 0.001	66	-0.015	$12.85^{+2.68}_{-3.05}$
ZTF22abtjefa	158	-15.06	62.72 ± 0.73	1.55 ± 0.13	0.55	0.032 ± 0.001	66	-0.015	$12.85^{+2.68}_{-3.05}$
ZTF22abtjefa	169	-15.06	61.42 ± 0.46	1.17 ± 0.13	0.47	0.032 ± 0.001	66	-0.015	$12.85^{+2.68}_{-3.05}$
ZTF22abtjefa	215	-15.06	56.43 ± 0.30	1.45 ± 0.09	0.52	0.041 ± 0.001	66	-0.015	$12.85^{+2.68}_{-3.05}$
ZTF22abtjefa	282	-15.06	50.70 ± 0.34	1.32 ± 0.10	0.81	0.063 ± 0.001	66	-0.015	$12.85^{+2.68}_{-3.05}$
ZTF22abtjefa	332	-15.06	47.08 ± 0.26	1.15 ± 0.09	0.71	0.094 ± 0.001	66	-0.015	$12.85^{+2.68}_{-3.05}$
ZTF22abtjefa	366	-15.06	47.30 ± 0.48	1.26 ± 0.15	0.53	0.095 ± 0.005	66	-0.015	$12.85^{+2.68}_{-3.05}$
ZTF22abtjefa	393	-15.06	44.48 ± 0.33	1.29 ± 0.27	0.64	0.122 ± 0.023	66	-0.015	$12.85^{+2.68}_{-3.05}$
ZTF22abvaetz	391	-15.44	39.50 ± 1.24	5.84 ± 1.13	0.46	0.035 ± 0.006	–	–	$--$
ZTF22abyivoq	258	-15.83	56.56 ± 1.56	3.65 ± 0.42	0.42	0.039 ± 0.001	70	0.229	$11.19^{+2.02}_{-2.11}$
ZTF22abyivoq	287	-15.83	54.80 ± 0.36	2.52 ± 0.13	0.33	0.057 ± 0.002	70	0.229	$11.19^{+2.02}_{-2.11}$
ZTF22abyivoq	340	-15.83	51.76 ± 0.60	4.34 ± 0.58	0.40	0.061 ± 0.006	70	0.229	$11.19^{+2.02}_{-2.11}$
ZTF22abyivoq	369	-15.83	49.25 ± 0.27	2.75 ± 0.19	0.54	0.078 ± 0.004	70	0.229	$11.19^{+2.02}_{-2.11}$
ZTF22abyivoq	439	-15.83	48.18 ± 0.70	2.32 ± 0.12	0.52	0.104 ± 0.001	70	0.229	$11.19^{+2.02}_{-2.11}$
ZTF23aabksje	387	-15.56	50.05 ± 1.26	3.07 ± 0.51	0.07	0.056 ± 0.001	–	–	$9.85^{+1.81}_{-1.53}$
ZTF23aabksje	432	-15.56	35.45 ± 2.06	2.69 ± 1.19	0.07	0.045 ± 0.006	–	–	$9.85^{+1.81}_{-1.53}$
ZTF23aackjhs	296	-14.88	26.17 ± 0.55	4.32 ± 0.59	0.56	0.059 ± 0.007	97	0.144	$11.89^{+2.77}_{-2.52}$
ZTF23aanxrjm	231	-15.02	50.98 ± 0.81	0.79 ± 0.18	0.18	0.050 ± 0.001	–	–	$11.24^{+2.37}_{-2.23}$
ZTF23aanxrjm	264	-15.02	56.54 ± 0.46	1.13 ± 0.11	0.21	0.036 ± 0.001	–	–	$11.24^{+2.37}_{-2.23}$
ZTF23aanxrjm	309	-15.02	43.36 ± 0.34	1.18 ± 0.16	0.17	0.051 ± 0.001	–	–	$11.24^{+2.37}_{-2.23}$
ZTF23aanxrjm	347	-15.02	36.01 ± 0.23	0.85 ± 0.04	0.19	0.064 ± 0.001	–	–	$11.24^{+2.37}_{-2.23}$
ZTF23abgmhgw	165	-15.69	39.21 ± 0.49	3.70 ± 0.43	0.33	0.032 ± 0.001	–	–	$12.13^{+2.27}_{-1.89}$
ZTF23abgmhgw	210	-15.69	37.07 ± 0.39	2.33 ± 0.35	0.24	0.040 ± 0.001	–	–	$12.13^{+2.27}_{-1.89}$
ZTF23abnogui	142	-15.58	76.82 ± 1.44	1.46 ± 0.15	16.68	0.032 ± 0.001	87	0.584	$11.60^{+2.31}_{-1.75}$

Table F: Continued.

SN	Phase (d)	$M_{r,\mathrm{peak}}$ (mag)	H I FWHM (Å)	[Ca II]/[O I]	[Ni II]/[Fe II]	$f_{[\mathrm{O\,I}]}$	Plat. (d)	Slope (10^{-2} mag d^{-1})	M_{ZAMS} ($\mathrm{M}_{\odot}$)
ZTF23abnogui	148	−15.58	77.43 ± 0.84	1.52 ± 0.17	0.36	0.039 ± 0.001	87	0.584	$11.60^{+2.31}_{-1.75}$
ZTF23abnogui	172	−15.58	70.72 ± 0.73	1.71 ± 0.13	0.33	0.053 ± 0.001	87	0.584	$11.60^{+2.31}_{-1.75}$
ZTF23abnogui	190	−15.58	66.70 ± 14.44	2.12 ± 0.17	0.35	0.048 ± 0.001	87	0.584	$11.60^{+2.31}_{-1.75}$
ZTF23abnogui	262	−15.58	63.03 ± 0.94	2.82 ± 0.28	0.21	0.045 ± 0.002	87	0.584	$11.60^{+2.31}_{-1.75}$
ZTF23abpbuha	115	−14.26	35.32 ± 7.47	1.24 ± 0.16	1.21	0.064 ± 0.001	–	–	−−
ZTF23absscow	342	−15.91	56.28 ± 0.39	2.84 ± 0.14	0.44	0.061 ± 0.002	–	–	$10.88^{+2.39}_{-1.71}$
ZTF24aaasazz	147	−16.03	52.38 ± 0.86	1.11 ± 0.21	0.03	0.039 ± 0.001	–	–	$10.28^{+1.78}_{-1.76}$
ZTF24aaasazz	353	−16.03	40.24 ± 1.38	4.34 ± 0.82	0.14	0.053 ± 0.007	–	–	$10.28^{+1.78}_{-1.76}$
ZTF24aabppgn	180	−15.52	35.14 ± 1.55	4.03 ± 2.10	0.18	0.028 ± 0.014	95	0.105	−−
ZTF24aaejecr	147	−16.02	57.39 ± 0.71	3.21 ± 0.18	0.17	0.030 ± 0.001	78	0.549	$14.05^{+3.15}_{-3.84}$
ZTF24aaejecr	291	−16.02	50.32 ± 0.37	2.14 ± 0.13	0.35	0.084 ± 0.001	78	0.549	$14.05^{+3.15}_{-3.84}$
ZTF24aaejecr	348	−16.02	48.12 ± 0.45	1.93 ± 0.12	0.36	0.106 ± 0.001	78	0.549	$14.05^{+3.15}_{-3.84}$
ZTF24aaezido	180	−14.98	99.98	3.18 ± 0.53	0.47	0.050 ± 0.004	–	–	−−
ZTF24aaplfjd	132	−16.00	56.30 ± 1.02	1.64 ± 0.16	0.05	0.022 ± 0.001	75	0.241	$10.50^{+2.00}_{-1.95}$
ZTF24aaplfjd	184	−16.00	50.79 ± 1.13	5.07 ± 1.34	0.19	0.024 ± 0.006	75	0.241	$10.50^{+2.00}_{-1.95}$
ZTF24aaplfjd	394	−16.00	47.74 ± 2.55	6.98 ± 0.69	0.17	0.072 ± 0.002	75	0.241	$10.50^{+2.00}_{-1.95}$
ZTF24abtczty	149	−14.13	35.33 ± 11.88	0.87 ± 0.10	1.05	0.064 ± 0.001	99	-0.040	$10.91^{+1.94}_{-2.11}$
ZTF24abtczty	334	−14.13	21.06 ± 0.32	3.99 ± 0.33	0.49	0.055 ± 0.002	99	-0.040	$10.91^{+1.94}_{-2.11}$
ZTF24abtczty	393	−14.13	20.36 ± 0.37	4.11 ± 0.28	0.34	0.075 ± 0.003	99	-0.040	$10.91^{+1.94}_{-2.11}$
1987A	198	−−	−−	−−	2.76	−−	–	–	−−
1998S	143	−−	182.06 ± 2.60	1.95 ± 0.11	2.21	0.025 ± 0.001	–	–	$8.92^{+0.78}_{-0.72}$
1998S	314	−−	182.53 ± 8.97	1.28 ± 0.06	0.98	0.023 ± 0.001	–	–	$8.92^{+0.78}_{-0.72}$
2004dj	274	−17.45	59.91 ± 1.24	1.58 ± 0.54	0.24	0.078 ± 0.027	50	1.258	$14.78^{+3.65}_{-3.83}$
2004et	253	−19.04	−−	−−	1.09	−−	100	0.657	$12.95^{+2.90}_{-3.07}$
2004et	253	−19.04	−−	−−	1.09	−−	100	0.657	$13.02^{+2.98}_{-3.20}$
2004et	355	−19.04	63.53 ± 0.52	3.34 ± 0.13	1.02	0.092 ± 0.001	100	0.657	$12.95^{+2.90}_{-3.07}$
2004et	355	−19.04	63.53 ± 0.52	3.34 ± 0.13	1.02	0.092 ± 0.001	100	0.657	$13.02^{+2.98}_{-3.20}$

Table F: Continued.

SN	Phase (d)	$M_{r,\mathrm{peak}}$ (mag)	H I FWHM (Å)	[Ca II]/[O I]	[Ni II]/[Fe II]	$f_{[\mathrm{O\,I}]}$	Plat. (d)	Slope (10^{-2} mag d^{-1})	M_{ZAMS} ($\mathrm{M}_{\odot}$)
2013by	287	−18.76	117.25 ± 1.38	0.77 ± 0.05	0.86	0.116 ± 0.001	67	2.053	$17.86^{+2.14}_{-5.50}$
2013by	287	−18.76	117.25 ± 1.38	0.77 ± 0.05	0.86	0.116 ± 0.001	67	2.053	$17.32^{+2.68}_{-4.97}$
2013ej	435	−17.72	82.36 ± 0.66	1.89 ± 0.34	0.67	0.142 ± 0.024	75	1.742	−−
2015bs	421	−−	139.45 ± 3.26	0.94 ± 0.06	0.82	0.256 ± 0.001	61	0.492	$20.00^{+0.00}_{-6.82}$
2017ivv	332	−−	195.82 ± 4.88	1.05 ± 0.07	3.79	0.215 ± 0.004	–	–	$20.00^{+0.00}_{-5.47}$
2017ivv	332	−−	195.82 ± 4.88	1.05 ± 0.07	3.79	0.215 ± 0.004	–	–	$19.69^{+0.31}_{-5.31}$
2018zd	182	−−	71.66 ± 0.85	1.58 ± 0.18	0.86	0.044 ± 0.001	–	–	$11.47^{+2.47}_{-2.06}$
2018zd	228	−−	65.43 ± 0.68	1.59 ± 0.32	1.31	0.042 ± 0.001	–	–	$11.47^{+2.47}_{-2.06}$
2018zd	291	−−	59.60 ± 0.52	1.18 ± 0.15	1.07	0.055 ± 0.001	–	–	$11.47^{+2.47}_{-2.06}$
2018zd	306	−−	61.82 ± 0.87	1.17 ± 0.29	0.76	0.088 ± 0.015	–	–	$11.47^{+2.47}_{-2.06}$
2018zd	315	−−	59.75 ± 0.73	1.26 ± 0.24	0.59	0.085 ± 0.010	–	–	$11.47^{+2.47}_{-2.06}$
2018zd	338	−−	57.61 ± 0.66	1.32 ± 0.19	0.83	0.064 ± 0.005	–	–	$11.47^{+2.47}_{-2.06}$
2018zd	399	−−	56.21 ± 0.65	1.45 ± 0.23	0.70	0.108 ± 0.003	–	–	$11.47^{+2.47}_{-2.06}$
ASASSN15oz	342	−−	87.36 ± 1.64	0.90 ± 0.03	0.87	0.130 ± 0.001	–	–	$15.74^{+3.34}_{-4.26}$
1990E	253	−−	88.43 ± 0.87	1.80 ± 0.08	0.47	0.080 ± 0.001	–	–	$16.34^{+3.32}_{-5.14}$
1990E	269	−−	90.79 ± 2.90	1.58 ± 0.07	0.27	0.092 ± 0.001	–	–	$16.34^{+3.32}_{-5.14}$
1990E	304	−−	76.83 ± 0.88	1.89 ± 0.07	0.58	0.100 ± 0.001	–	–	$16.34^{+3.32}_{-5.14}$
1990E	330	−−	55.08 ± 3.92	1.38 ± 0.05	0.70	0.128 ± 0.001	–	–	$16.34^{+3.32}_{-5.14}$
1990E	330	−−	65.19 ± 1.16	1.77 ± 0.04	0.36	0.122 ± 0.002	–	–	$16.34^{+3.32}_{-5.14}$
1990Q	320	−−	60.32 ± 3.50	2.98 ± 0.37	2.16	0.085 ± 0.010	–	–	$13.38^{+3.30}_{-3.15}$
1991G	355	−15.52	64.07 ± 0.95	1.58 ± 0.11	0.85	0.070 ± 0.001	83	0.289	$11.40^{+2.52}_{-2.22}$
1992H	386	−17.92	82.92 ± 0.79	1.49 ± 0.29	0.34	0.126 ± 0.023	–	–	−−
1992ad	225	−−	114.56 ± 1.13	2.83 ± 0.85	0.52	0.056 ± 0.017	–	–	−−
1992ad	286	−−	112.05 ± 1.26	3.72 ± 2.34	0.64	0.063 ± 0.040	–	–	−−
1992ad	287	−−	111.76 ± 1.26	2.70 ± 0.90	0.64	0.083 ± 0.027	–	–	−−
1993K	295	−−	97.57 ± 1.62	1.72 ± 0.11	0.21	0.128 ± 0.005	–	–	$17.60^{+2.40}_{-5.34}$
1996W	252	−−	69.43 ± 1.02	2.28 ± 0.07	1.95	0.063 ± 0.001	–	–	$13.66^{+3.69}_{-3.40}$

Table F: Continued.

SN	Phase (d)	$M_{r,\mathrm{peak}}$ (mag)	H I FWHM (Å)	[Ca II]/[O I]	[Ni II]/[Fe II]	$f_{[\mathrm{O\,I}]}$	Plat. (d)	Slope (10^{-2} mag d^{-1})	M_{ZAMS} ($\mathrm{M}_{\odot}$)
1996W	295	−−	65.30 ± 1.37	2.41 ± 0.10	1.09	0.080 ± 0.002	–	–	$13.66^{+3.69}_{-3.40}$
1997D	207	−14.75	28.29 ± 1.71	2.81 ± 0.68	0.07	0.073 ± 0.001	–	–	$15.77^{+3.09}_{-4.95}$
1997D	350	−14.75	22.72 ± 0.46	1.57 ± 0.11	0.46	0.131 ± 0.001	–	–	$15.77^{+3.09}_{-4.95}$
1999em	317	−17.11	60.71 ± 0.42	3.05 ± 0.13	0.76	0.075 ± 0.001	94	0.169	$12.88^{+2.97}_{-3.03}$
2002hh	396	−−	106.28 ± 1.06	3.58 ± 0.17	0.55	0.056 ± 0.001	200	0.978	$9.71^{+1.62}_{-1.52}$
2003B	275	−15.60	43.68 ± 1.14	1.45 ± 0.05	0.47	0.119 ± 0.001	52	0.710	$17.36^{+2.64}_{-4.99}$
2003gd	130	−16.48	59.52 ± 0.83	1.75 ± 0.10	2.69	0.040 ± 0.001	–	–	$14.04^{+3.31}_{-3.48}$
2003gd	250	−16.48	45.65 ± 0.44	2.06 ± 0.11	0.97	0.066 ± 0.001	–	–	$14.04^{+3.31}_{-3.48}$
2004A	286	−16.68	46.96 ± 0.39	1.36 ± 0.06	0.43	0.075 ± 0.001	86	0.519	$13.81^{+3.50}_{-3.42}$
2004dj	136	−17.45	69.00 ± 1.83	1.10 ± 0.04	0.27	0.045 ± 0.001	50	1.258	$14.78^{+3.65}_{-3.83}$
2004dj	164	−17.45	62.83 ± 1.38	1.79 ± 0.21	0.24	0.033 ± 0.004	50	1.258	$14.78^{+3.65}_{-3.83}$
2004dj	199	−17.45	62.23 ± 1.08	1.32 ± 0.03	0.16	0.055 ± 0.001	50	1.258	$14.78^{+3.65}_{-3.83}$
2004dj	226	−17.45	58.96 ± 0.95	1.37 ± 0.04	0.19	0.067 ± 0.001	50	1.258	$14.78^{+3.65}_{-3.83}$
2004dj	253	−17.45	58.15 ± 0.81	1.67 ± 0.24	0.22	0.064 ± 0.009	50	1.258	$14.78^{+3.65}_{-3.83}$
2004dj	290	−17.45	58.90 ± 0.65	1.51 ± 0.04	0.29	0.090 ± 0.001	50	1.258	$14.78^{+3.65}_{-3.83}$
2004et	162	−17.34	78.16 ± 15.54	3.24 ± 0.08	1.27	0.030 ± 0.001	100	0.657	$12.95^{+2.90}_{-3.07}$
2004et	162	−17.34	78.16 ± 15.54	3.24 ± 0.08	1.27	0.030 ± 0.001	100	0.657	$13.02^{+2.98}_{-3.20}$
2004et	201	−17.34	74.40 ± 23.11	3.38 ± 0.08	1.70	0.045 ± 0.001	100	0.657	$12.95^{+2.90}_{-3.07}$
2004et	201	−17.34	74.40 ± 23.11	3.38 ± 0.08	1.70	0.045 ± 0.001	100	0.657	$13.02^{+2.98}_{-3.20}$
2004et	226	−17.34	69.59 ± 0.53	3.01 ± 0.07	1.07	0.051 ± 0.001	100	0.657	$12.95^{+2.90}_{-3.07}$
2004et	226	−17.34	69.59 ± 0.53	3.01 ± 0.07	1.07	0.051 ± 0.001	100	0.657	$13.02^{+2.98}_{-3.20}$
2004et	258	−17.34	66.56 ± 0.49	3.11 ± 0.09	1.17	0.061 ± 0.001	100	0.657	$12.95^{+2.90}_{-3.07}$
2004et	258	−17.34	66.56 ± 0.49	3.11 ± 0.09	1.17	0.061 ± 0.001	100	0.657	$13.02^{+2.98}_{-3.20}$
2004et	282	−17.34	66.02 ± 0.59	3.24 ± 0.11	1.22	0.073 ± 0.001	100	0.657	$12.95^{+2.90}_{-3.07}$
2004et	282	−17.34	66.02 ± 0.59	3.24 ± 0.11	1.22	0.073 ± 0.001	100	0.657	$13.02^{+2.98}_{-3.20}$
2004et	313	−17.34	64.68 ± 0.50	1.73 ± 0.04	0.79	0.099 ± 0.001	100	0.657	$12.95^{+2.90}_{-3.07}$
2004et	313	−17.34	64.68 ± 0.50	1.73 ± 0.04	0.79	0.099 ± 0.001	100	0.657	$13.02^{+2.98}_{-3.20}$

Table F: Continued.

SN	Phase (d)	$M_{r,\mathrm{peak}}$ (mag)	H I FWHM (Å)	[Ca II]/[O I]	[Ni II]/[Fe II]	$f_{[\mathrm{O\,I}]}$	Plat. (d)	Slope (10^{-2} mag d^{-1})	M_{ZAMS} ($\mathrm{M}_{\odot}$)
2004et	353	−17.34	63.53 ± 0.52	3.33 ± 0.09	1.01	0.092 ± 0.001	100	0.657	$12.95^{+2.90}_{-3.07}$
2004et	353	−17.34	63.53 ± 0.52	3.33 ± 0.09	1.01	0.092 ± 0.001	100	0.657	$13.02^{+2.98}_{-3.20}$
2004et	354	−17.34	63.53 ± 0.52	3.33 ± 0.13	1.01	0.092 ± 0.003	100	0.657	$12.95^{+2.90}_{-3.07}$
2004et	354	−17.34	63.53 ± 0.52	3.33 ± 0.13	1.01	0.092 ± 0.003	100	0.657	$13.02^{+2.98}_{-3.20}$
2005ay	285	−16.27	49.57 ± 0.58	1.24 ± 0.08	0.94	0.078 ± 0.001	91	0.154	$14.15^{+3.41}_{-3.09}$
2005cs	304	−15.66	38.69 ± 0.94	2.76 ± 0.72	1.50	0.083 ± 0.020	113	0.512	$11.21^{+2.17}_{-1.98}$
2005cs	334	−15.66	37.38 ± 0.55	4.52 ± 0.23	1.34	0.058 ± 0.001	113	0.512	$11.21^{+2.17}_{-1.98}$
2007aa	384	−−	53.87 ± 0.57	1.35 ± 0.05	0.88	0.153 ± 0.001	–	–	$15.40^{+4.18}_{-4.03}$
2007it	268	−−	−−	−−	−−	−−	–	–	−−
2007it	268	−15.00	−−	−−	−−	−−	–	–	−−
2007it	268	−−	73.08 ± 1.08	0.76 ± 0.04	1.39	−−	–	–	−−
2007it	268	−15.00	73.08 ± 1.08	0.76 ± 0.04	1.39	−−	–	–	−−
2008cn	340	−−	77.53 ± 0.90	1.78 ± 0.06	0.71	0.115 ± 0.002	–	–	$15.00^{+3.37}_{-4.83}$
2008ex	285	−−	76.37 ± 1.12	1.18 ± 0.16	0.59	0.081 ± 0.010	–	–	$14.64^{+3.16}_{-3.81}$
2009N	411	−16.25	30.40 ± 0.44	3.60 ± 0.42	1.16	0.076 ± 0.009	83	0.407	$10.41^{+1.89}_{-2.00}$
2009dd	232	−17.63	74.10 ± 1.11	1.52 ± 0.04	0.59	0.055 ± 0.001	80	0.231	$13.54^{+2.82}_{-2.72}$
2009dd	408	−17.63	34.30 ± 1.64	2.05 ± 0.39	0.64	0.046 ± 0.008	80	0.231	$13.54^{+2.82}_{-2.72}$
2009ib	219	−16.49	53.75 ± 0.80	1.19 ± 0.06	0.60	0.045 ± 0.001	116	0.377	$17.85^{+2.15}_{-5.31}$
2009ib	262	−16.49	55.94 ± 0.97	0.53 ± 0.03	1.11	0.111 ± 0.001	116	0.377	$17.85^{+2.15}_{-5.31}$
2012A	86	−16.37	85.49 ± 5.57	−−	−−	0.019 ± 0.001	84	1.088	$12.46^{+2.81}_{-3.00}$
2012A	86	−16.37	85.37 ± 9.64	−−	−−	0.023 ± 0.001	84	1.088	$12.46^{+2.81}_{-3.00}$
2012A	408	−16.37	44.84 ± 0.22	1.82 ± 0.21	0.35	0.118 ± 0.013	84	1.088	$12.46^{+2.81}_{-3.00}$
2012aw	369	−17.03	59.56 ± 0.69	1.24 ± 0.06	0.71	0.124 ± 0.001	102	0.361	$14.32^{+3.28}_{-3.29}$
2012ch	357	−−	77.45 ± 1.71	3.38 ± 0.87	1.48	0.085 ± 0.022	–	–	−−
2012ec	403	−16.93	58.09 ± 0.60	0.62 ± 0.08	1.27	0.182 ± 0.010	85	0.629	$16.03^{+3.97}_{-4.59}$
2012ho	168	−−	90.14 ± 15.75	3.98 ± 0.16	0.95	0.028 ± 0.001	–	–	$14.33^{+3.16}_{-3.88}$
2012ho	229	−−	76.47 ± 1.21	3.50 ± 0.11	0.65	0.043 ± 0.001	–	–	$14.33^{+3.16}_{-3.88}$

Table F: Continued.

SN	Phase (d)	$M_{r,\mathrm{peak}}$ (mag)	H I FWHM (Å)	[Ca II]/[O I]	[Ni II]/[Fe II]	$f_{[\mathrm{O\,I}]}$	Plat. (d)	Slope (10^{-2} mag d^{-1})	M_{ZAMS} ($\mathrm{M}_{\odot}$)
2012ho	249	−−	74.21 ± 1.17	2.44 ± 0.08	0.76	0.069 ± 0.001	–	–	$14.33^{+3.16}_{-3.88}$
2012ho	252	−−	74.98 ± 0.48	2.62 ± 0.74	0.60	0.067 ± 0.019	–	–	$14.33^{+3.16}_{-3.88}$
2012ho	265	−−	71.73 ± 1.11	2.44 ± 0.07	0.59	0.071 ± 0.001	–	–	$14.33^{+3.16}_{-3.88}$
2012ho	318	−−	77.70 ± 1.01	3.24 ± 0.48	0.51	0.091 ± 0.012	–	–	$14.33^{+3.16}_{-3.88}$
2012ho	318	−−	77.70 ± 1.01	3.17 ± 0.47	0.51	0.093 ± 0.012	–	–	$14.33^{+3.16}_{-3.88}$
2013am	281	−16.17	35.86 ± 0.93	−−	0.73	−−	81	0.111	−−
2013by	160	−18.76	135.53 ± 8.84	0.60 ± 0.02	157.61	0.061 ± 0.001	67	2.053	$17.86^{+2.14}_{-5.50}$
2013by	160	−18.76	135.53 ± 8.84	0.60 ± 0.02	157.61	0.061 ± 0.001	67	2.053	$17.32^{+2.68}_{-4.97}$
2013by	292	−18.76	110.23 ± 1.43	0.90 ± 0.03	199.45	0.124 ± 0.003	67	2.053	$17.86^{+2.14}_{-5.50}$
2013by	292	−18.76	110.23 ± 1.43	0.90 ± 0.03	199.45	0.124 ± 0.003	67	2.053	$17.32^{+2.68}_{-4.97}$
2013fs	270	−17.63	107.45 ± 0.78	1.46 ± 0.05	1.56	0.140 ± 0.001	69	1.174	$19.93^{+0.07}_{-6.06}$
2014G	137	−18.64	133.74 ± 1.57	1.80 ± 0.10	1.32	0.034 ± 0.001	62	2.194	$18.28^{+1.72}_{-5.15}$
2014G	187	−18.64	115.16 ± 1.47	1.46 ± 0.08	2.30	0.067 ± 0.001	62	2.194	$18.28^{+1.72}_{-5.15}$
2014G	341	−18.64	123.77 ± 2.91	1.12 ± 0.07	2.52	0.177 ± 0.001	62	2.194	$18.28^{+1.72}_{-5.15}$
2014cx	350	−17.33	78.76 ± 2.82	0.76 ± 0.15	0.68	0.196 ± 0.035	82	0.586	−−
2015bs	420	−−	139.59 ± 3.26	0.93 ± 0.18	0.82	0.238 ± 0.043	61	0.492	$20.00^{+0.00}_{-6.82}$
2016X	340	−17.10	114.37 ± 3.39	−−	−−	−−	67	1.311	−−
2016aqf	202	−−	48.05 ± 0.75	1.62 ± 0.10	0.40	0.034 ± 0.001	69	1.601	$12.79^{+2.87}_{-3.08}$
2016aqf	259	−−	44.80 ± 0.58	1.46 ± 0.07	0.31	0.043 ± 0.001	69	1.601	$12.79^{+2.87}_{-3.08}$
2016aqf	285	−−	41.46 ± 1.29	1.75 ± 0.20	0.58	0.063 ± 0.001	69	1.601	$12.79^{+2.87}_{-3.08}$
2016aqf	303	−−	45.15 ± 0.83	1.26 ± 0.08	0.65	0.082 ± 0.001	69	1.601	$12.79^{+2.87}_{-3.08}$
2016aqf	330	−−	43.26 ± 0.54	1.18 ± 0.08	0.40	0.069 ± 0.001	69	1.601	$12.79^{+2.87}_{-3.08}$
2016aqf	351	−−	45.22 ± 1.01	1.23 ± 0.11	0.30	0.088 ± 0.001	69	1.601	$12.79^{+2.87}_{-3.08}$
2016bkv	257	−16.00	25.34 ± 0.43	1.49 ± 0.08	0.44	0.094 ± 0.001	–	–	$9.08^{+1.26}_{-1.08}$
2016bkv	436	−16.00	21.35 ± 0.18	5.27 ± 0.32	0.62	0.059 ± 0.001	–	–	$9.08^{+1.26}_{-1.08}$
2017eaw	250	−17.91	56.08 ± 0.57	2.93 ± 0.10	0.84	0.065 ± 0.002	95	0.645	$13.83^{+3.20}_{-3.23}$
2017ivv	110	−−	147.60 ± 16.67	1.66 ± 0.07	32.78	0.058 ± 0.001	–	–	$20.00^{+0.00}_{-5.47}$

Table F: Continued.

SN	Phase (d)	$M_{r,\mathrm{peak}}$ (mag)	H I FWHM (Å)	[Ca II]/[O I]	[Ni II]/[Fe II]	$f_{[\mathrm{O\,I}]}$	Plat. (d)	Slope (10^{-2} mag d^{-1})	M_{ZAMS} ($\mathrm{M}_{\odot}$)
2017ivv	110	−−	147.60 ± 16.67	1.66 ± 0.07	32.78	0.058 ± 0.001	–	–	$19.69^{+0.31}_{-5.31}$
2017ivv	136	−−	139.78 ± 66.47	1.36 ± 0.04	36.96	0.086 ± 0.001	–	–	$20.00^{+0.00}_{-5.47}$
2017ivv	136	−−	139.78 ± 66.47	1.36 ± 0.04	36.96	0.086 ± 0.001	–	–	$19.69^{+0.31}_{-5.31}$
2017ivv	158	−−	141.56 ± 42.49	1.35 ± 0.05	753.63	0.109 ± 0.001	–	–	$20.00^{+0.00}_{-5.47}$
2017ivv	158	−−	141.56 ± 42.49	1.35 ± 0.05	753.63	0.109 ± 0.001	–	–	$19.69^{+0.31}_{-5.31}$
2017ivv	243	−−	158.72 ± 3.95	1.72 ± 0.06	6.47	0.144 ± 0.002	–	–	$20.00^{+0.00}_{-5.47}$
2017ivv	243	−−	158.72 ± 3.95	1.72 ± 0.06	6.47	0.144 ± 0.002	–	–	$19.69^{+0.31}_{-5.31}$
2017ivv	279	−−	172.71 ± 5.64	1.81 ± 0.08	5.15	0.157 ± 0.001	–	–	$20.00^{+0.00}_{-5.47}$
2017ivv	279	−−	172.71 ± 5.64	1.81 ± 0.08	5.15	0.157 ± 0.001	–	–	$19.69^{+0.31}_{-5.31}$
2017ivv	325	−−	185.67 ± 5.36	1.41 ± 0.07	2.07	0.192 ± 0.001	–	–	$20.00^{+0.00}_{-5.47}$
2017ivv	325	−−	185.67 ± 5.36	1.41 ± 0.07	2.07	0.192 ± 0.001	–	–	$19.69^{+0.31}_{-5.31}$
2017ivv	332	−−	194.44 ± 10.72	1.40 ± 0.09	2.88	0.189 ± 0.009	–	–	$20.00^{+0.00}_{-5.47}$
2017ivv	332	−−	194.44 ± 10.72	1.40 ± 0.09	2.88	0.189 ± 0.009	–	–	$19.69^{+0.31}_{-5.31}$
2018cuf	335	−16.82	77.90 ± 0.85	−−	0.53	−−	72	0.396	−−
2018gj	270	−17.69	93.68 ± 1.91	4.49 ± 0.97	3357.64	0.040 ± 0.009	65	1.214	−−
2018hwm	385	−15.27	34.46 ± 1.92	3.33 ± 0.39	0.69	0.042 ± 0.003	129	0.351	$8.97^{+1.18}_{-0.97}$
2018is	386	−15.29	47.01 ± 3.42	8.69 ± 1.25	0.30	0.085 ± 0.002	84	0.650	$11.67^{+2.31}_{-2.55}$
2020jfo	217	−18.02	75.48 ± 1.14	2.15 ± 0.17	1.44	0.043 ± 0.001	49	1.127	$15.26^{+3.28}_{-4.08}$
2020jfo	256	−18.02	74.45 ± 1.10	1.45 ± 0.17	1.31	0.081 ± 0.007	49	1.127	$15.26^{+3.28}_{-4.08}$
2020jfo	280	−18.02	73.19 ± 1.08	1.70 ± 0.13	1.58	0.082 ± 0.003	49	1.127	$15.26^{+3.28}_{-4.08}$
2020jfo	308	−18.02	73.21 ± 1.25	1.73 ± 0.12	1.43	0.096 ± 0.001	49	1.127	$15.26^{+3.28}_{-4.08}$
2020jfo	351	−18.02	73.88 ± 1.62	1.46 ± 0.12	1.57	0.127 ± 0.003	49	1.127	$15.26^{+3.28}_{-4.08}$
2021dbg	352	−−	109.14 ± 2.28	1.81 ± 0.11	0.80	0.100 ± 0.002	–	–	$13.96^{+3.00}_{-3.71}$
2021gmj	385	−15.85	39.05 ± 0.77	4.26 ± 0.97	0.41	0.065 ± 0.013	86	0.590	−−
2022jox	240	−−	−−	−−	−−	−−	–	–	−−
2022jox	240	−−	65.25 ± 1.51	0.55 ± 0.04	0.60	−−	–	–	−−
2023ixf	260	−17.70	116.06 ± 1.30	1.66 ± 0.05	1.80	0.114 ± 0.001	61	2.282	$18.17^{+1.83}_{-5.28}$

Table F: Continued.

SN	Phase (d)	$M_{r,\mathrm{peak}}$ (mag)	H I FWHM (Å)	[Ca II]/[O I]	[Ni II]/[Fe II]	$f_{[\mathrm{O\,I}]}$	Plat. (d)	Slope (10^{-2} mag d^{-1})	M_{ZAMS} ($\mathrm{M}_{\odot}$)
ZTF19abqhobb	163	−17.59	122.56 ± 5.84	1.29 ± 0.17	0.40	0.035 ± 0.001	–	–	−−
ZTF20aaynrrh	216	−17.48	75.49 ± 1.14	2.14 ± 0.21	1.44	0.043 ± 0.001	–	–	$15.23^{+3.36}_{-4.01}$
ZTF20aaynrrh	256	−17.48	74.47 ± 1.10	1.39 ± 0.14	1.32	0.083 ± 0.001	–	–	$15.23^{+3.36}_{-4.01}$
ZTF20aaynrrh	280	−17.48	73.19 ± 1.08	1.74 ± 0.14	1.59	0.081 ± 0.001	–	–	$15.23^{+3.36}_{-4.01}$
ZTF20aaynrrh	308	−17.48	73.23 ± 1.25	1.75 ± 0.12	1.43	0.095 ± 0.003	–	–	$15.23^{+3.36}_{-4.01}$
ZTF20aaynrrh	351	−17.48	73.88 ± 1.62	1.36 ± 0.11	1.57	0.126 ± 0.003	–	–	$15.23^{+3.36}_{-4.01}$
ZTF20abotkfn	141	−17.10	65.65 ± 1.28	14.49 ± 1.72	0.46	0.028 ± 0.001	–	–	$13.77^{+2.82}_{-2.60}$
ZTF20abotkfn	211	−17.10	59.81 ± 0.72	1.49 ± 0.09	0.50	0.056 ± 0.001	–	–	$13.77^{+2.82}_{-2.60}$
ZTF21abouuat	276	−17.56	81.06 ± 0.76	1.47 ± 0.31	0.37	0.099 ± 0.020	81	0.271	−−
ZTF23aaquhaz	138	−17.53	113.78 ± 14.68	0.84 ± 0.14	0.66	0.070 ± 0.001	–	–	$14.98^{+3.65}_{-4.13}$
ZTF23aaquhaz	310	−17.53	109.72 ± 1.08	1.88 ± 0.30	0.83	0.097 ± 0.015	–	–	$14.98^{+3.65}_{-4.13}$
ZTF23absdcgi	337	−16.73	103.48 ± 4.32	1.24 ± 0.07	0.53	0.167 ± 0.005	–	–	$17.97^{+2.03}_{-4.94}$
ZTF23abvgvab	104	−17.12	115.04 ± 1.12	1.49 ± 0.17	0.79	0.079 ± 0.001	–	–	−−

Table G: Per-spectrum ZAMS mass estimates from the GP inversion. Uncertainties include a 10% systematic added in quadrature.

SN	Phase (days)	$M_{\rm ZAMS}$ ($M_\odot$)
SN1998S	143	$12.04^{+1.29}_{-1.20}$
SN1998S	314	$8.92^{+0.78}_{-0.72}$
SN2004dj	274	$14.86^{+2.95}_{-3.87}$
SN2004et	355	$13.02^{+2.98}_{-3.20}$
SN2013by	287	$17.32^{+2.68}_{-4.97}$
SN2013ej	435	$12.92^{+3.68}_{-3.57}$
SN2015bs	421	$20.00^{+0.00}_{-6.82}$
SN2017ivv	332	$20.00^{+0.00}_{-5.47}$
SN2018zd	182	$13.25^{+2.33}_{-2.20}$
SN2018zd	228	$12.00^{+2.30}_{-1.81}$
SN2018zd	291	$11.77^{+2.43}_{-2.29}$
SN2018zd	306	$14.45^{+3.37}_{-3.71}$
SN2018zd	315	$13.67^{+3.18}_{-3.36}$
SN2018zd	338	$11.47^{+2.47}_{-2.06}$
SN2018zd	399	$12.42^{+2.31}_{-2.87}$
ASASSN15oz	342	$15.74^{+3.34}_{-4.26}$
SN1990E	253	$14.73^{+3.81}_{-3.27}$
SN1990E	269	$16.35^{+3.65}_{-4.33}$
SN1990E	304	$15.70^{+3.18}_{-4.34}$
SN1990E	330	$16.34^{+3.32}_{-5.14}$
SN1990E	330	$16.04^{+3.49}_{-4.84}$
SN1990E	330	$16.34^{+3.32}_{-5.14}$
SN1990E	330	$16.04^{+3.49}_{-4.84}$
SN1990Q	320	$13.38^{+3.30}_{-3.15}$
SN1991G	355	$11.40^{+2.52}_{-2.22}$
SN1992H	386	$13.67^{+3.45}_{-3.69}$
SN1992ad	225	$13.40^{+2.83}_{-2.52}$
SN1992ad	286	$12.84^{+3.46}_{-3.47}$
SN1992ad	287	$14.81^{+3.32}_{-3.81}$
SN1993K	295	$17.60^{+2.40}_{-5.34}$
SN1996W	252	$13.73^{+3.30}_{-3.38}$

Table G: Continued.

SN	Phase (days)	$M_{\rm ZAMS}$ ($M_\odot$)
SN1996W	295	$13.66^{+3.69}_{-3.40}$
SN1997D	207	$15.97^{+4.03}_{-3.90}$
SN1997D	350	$15.77^{+3.09}_{-4.95}$
SN1999em	317	$12.88^{+2.97}_{-3.03}$
SN2002hh	396	$9.71^{+1.62}_{-1.52}$
SN2003B	275	$17.36^{+2.64}_{-4.99}$
SN2003gd	130	$14.12^{+2.41}_{-2.12}$
SN2003gd	250	$14.04^{+3.31}_{-3.48}$
SN2004A	286	$13.81^{+3.50}_{-3.42}$
SN2004dj	136	$14.42^{+2.98}_{-2.68}$
SN2004dj	164	$12.43^{+1.84}_{-1.53}$
SN2004dj	199	$14.00^{+3.18}_{-2.90}$
SN2004dj	226	$14.63^{+3.39}_{-3.18}$
SN2004dj	253	$14.07^{+3.14}_{-3.09}$
SN2004dj	290	$14.78^{+3.65}_{-3.83}$
SN2004et	162	$12.18^{+1.52}_{-1.37}$
SN2004et	201	$13.13^{+2.39}_{-2.05}$
SN2004et	226	$12.96^{+2.56}_{-2.70}$
SN2004et	258	$13.20^{+3.05}_{-2.39}$
SN2004et	282	$14.01^{+2.99}_{-3.61}$
SN2004et	313	$14.97^{+3.37}_{-4.31}$
SN2004et	353	$12.95^{+2.90}_{-3.07}$
SN2004et	354	$12.66^{+3.13}_{-2.88}$
SN2005ay	285	$14.15^{+3.41}_{-3.09}$
SN2005cs	304	$13.73^{+3.45}_{-3.49}$
SN2005cs	334	$11.21^{+2.17}_{-1.98}$
SN2007aa	384	$15.40^{+4.18}_{-4.03}$
SN2008cn	340	$15.00^{+3.37}_{-4.83}$
SN2008ex	285	$14.64^{+3.16}_{-3.81}$
SN2009N	411	$10.41^{+1.89}_{-2.00}$
SN2009dd	232	$13.54^{+2.82}_{-2.72}$
SN2009dd	408	$8.78^{+1.27}_{-0.78}$

Table G: Continued.

SN	Phase (days)	$M_{\rm ZAMS}$ ($M_\odot$)
SN2009ib	219	$12.62^{+2.58}_{-2.31}$
SN2009ib	262	$17.85^{+2.15}_{-5.31}$
SN2012A	86	$12.63^{+1.47}_{-1.11}$
SN2012A	86	$12.30^{+0.98}_{-0.92}$
SN2012A	408	$12.46^{+2.81}_{-3.00}$
SN2012aw	369	$14.32^{+3.28}_{-3.29}$
SN2012ch	357	$12.35^{+2.80}_{-3.09}$
SN2012ec	403	$16.03^{+3.97}_{-4.59}$
SN2012ho	168	$11.84^{+1.46}_{-1.27}$
SN2012ho	229	$12.18^{+2.30}_{-1.98}$
SN2012ho	249	$14.14^{+3.31}_{-3.38}$
SN2012ho	252	$13.85^{+3.40}_{-3.28}$
SN2012ho	265	$14.01^{+3.29}_{-3.21}$
SN2012ho	318	$14.33^{+3.16}_{-3.88}$
SN2012ho	318	$14.07^{+3.50}_{-3.64}$
SN2013by	160	$15.64^{+3.89}_{-3.39}$
SN2013by	292	$17.86^{+2.14}_{-5.50}$
SN2013fs	270	$19.93^{+0.07}_{-6.06}$
SN2014G	137	$13.08^{+2.02}_{-1.80}$
SN2014G	187	$15.97^{+3.33}_{-3.78}$
SN2014G	341	$18.28^{+1.72}_{-5.15}$
SN2014cx	350	$19.23^{+0.77}_{-5.68}$
SN2015bs	420	$19.28^{+0.72}_{-7.38}$
SN2016aqf	202	$11.80^{+1.95}_{-1.61}$
SN2016aqf	259	$11.64^{+2.03}_{-1.68}$
SN2016aqf	285	$12.83^{+2.91}_{-3.14}$
SN2016aqf	303	$13.88^{+2.99}_{-3.30}$
SN2016aqf	330	$11.98^{+2.40}_{-2.25}$
SN2016aqf	351	$12.79^{+2.87}_{-3.08}$
SN2016bkv	257	$16.99^{+3.01}_{-4.43}$
SN2016bkv	436	$9.08^{+1.26}_{-1.08}$
SN2017eaw	250	$13.83^{+3.20}_{-3.23}$

Table G: Continued.

SN	Phase (days)	$M_{\rm ZAMS}$ ($M_\odot$)
SN2017ivv	110	$16.44^{+3.48}_{-3.16}$
SN2017ivv	136	$19.51^{+0.49}_{-4.80}$
SN2017ivv	158	$20.00^{+0.00}_{-5.01}$
SN2017ivv	243	$20.00^{+0.00}_{-4.80}$
SN2017ivv	279	$20.00^{+0.00}_{-6.35}$
SN2017ivv	325	$20.00^{+0.00}_{-5.89}$
SN2017ivv	332	$19.69^{+0.31}_{-5.31}$
SN2018gj	270	$11.13^{+1.71}_{-1.65}$
SN2018hwm	385	$8.97^{+1.18}_{-0.97}$
SN2018is	386	$11.67^{+2.31}_{-2.55}$
SN2020jfo	217	$12.29^{+2.41}_{-2.02}$
SN2020jfo	256	$15.39^{+3.62}_{-4.26}$
SN2020jfo	280	$14.59^{+3.12}_{-4.01}$
SN2020jfo	308	$15.15^{+3.02}_{-3.86}$
SN2020jfo	351	$15.26^{+3.28}_{-4.08}$
SN2021dbg	352	$13.96^{+3.00}_{-3.71}$
SN2021gmj	385	$10.55^{+1.79}_{-1.99}$
SN2023ixf	260	$18.17^{+1.83}_{-5.28}$
ZTF19abqhobb	163	$12.73^{+1.84}_{-1.93}$
ZTF20aaynrrh	216	$12.36^{+2.37}_{-1.93}$
ZTF20aaynrrh	256	$15.65^{+3.39}_{-4.17}$
ZTF20aaynrrh	280	$14.65^{+3.18}_{-3.74}$
ZTF20aaynrrh	308	$14.68^{+3.23}_{-3.99}$
ZTF20aaynrrh	351	$15.23^{+3.36}_{-4.01}$
ZTF20abotkfn	141	$12.41^{+1.46}_{-1.36}$
ZTF20abotkfn	211	$13.77^{+2.82}_{-2.60}$
ZTF21abouuat	276	$16.23^{+3.67}_{-4.16}$
ZTF22abssiet	175	$11.05^{+1.14}_{-0.81}$
ZTF22abssiet	222	$13.62^{+2.84}_{-3.14}$
ZTF22abtjefa	136	$11.82^{+1.40}_{-1.11}$
ZTF22abtjefa	158	$12.56^{+1.72}_{-1.53}$
ZTF22abtjefa	169	$12.28^{+1.72}_{-1.58}$

Table G: Continued.

SN	Phase (days)	$M_{\rm ZAMS}$ ($M_\odot$)
ZTF22abtjefa	215	$12.14^{+2.13}_{-1.99}$
ZTF22abtjefa	282	$12.71^{+3.00}_{-2.58}$
ZTF22abtjefa	332	$13.73^{+3.39}_{-3.25}$
ZTF22abtjefa	366	$12.85^{+2.68}_{-3.05}$
ZTF22abtjefa	393	$13.41^{+3.17}_{-3.15}$
ZTF22abvaetz	391	$8.62^{+0.93}_{-0.62}$
ZTF22abyivoq	258	$11.38^{+1.59}_{-1.85}$
ZTF22abyivoq	287	$11.98^{+2.33}_{-2.44}$
ZTF22abyivoq	340	$11.19^{+2.02}_{-2.11}$
ZTF22abyivoq	369	$11.46^{+2.44}_{-2.42}$
ZTF22abyivoq	439	$11.07^{+2.14}_{-2.18}$
ZTF23aabksje	387	$9.85^{+1.81}_{-1.53}$
ZTF23aabksje	432	$8.44^{+1.05}_{-0.44}$
ZTF23aackjhs	296	$11.89^{+2.77}_{-2.52}$
ZTF23aanxrjm	231	$12.79^{+2.80}_{-2.49}$
ZTF23aanxrjm	264	$10.79^{+1.87}_{-1.41}$
ZTF23aanxrjm	309	$11.08^{+2.03}_{-1.76}$
ZTF23aanxrjm	347	$11.24^{+2.37}_{-2.23}$
ZTF23aaquhaz	138	$17.67^{+2.33}_{-4.31}$
ZTF23aaquhaz	310	$14.98^{+3.65}_{-4.13}$
ZTF23abgmhgw	165	$12.41^{+1.72}_{-1.51}$
ZTF23abgmhgw	210	$12.13^{+2.27}_{-1.89}$
ZTF23abnogui	142	$12.75^{+1.70}_{-1.56}$
ZTF23abnogui	148	$13.43^{+2.06}_{-2.07}$
ZTF23abnogui	172	$14.44^{+3.25}_{-2.63}$
ZTF23abnogui	190	$13.48^{+2.94}_{-2.72}$
ZTF23abnogui	262	$11.60^{+2.31}_{-1.75}$
ZTF23abpbuha	115	$16.93^{+3.07}_{-3.90}$
ZTF23absdcgi	337	$17.97^{+2.03}_{-4.94}$
ZTF23absscow	250	$8.00^{+0.00}_{-0.00}$
ZTF23absscow	342	$10.88^{+2.39}_{-1.71}$
ZTF23abvgvab	104	$18.75^{+1.25}_{-5.04}$

Table H: ECSN diagnostic weights and thresholds.

Diagnostic	Weight	Yes	No
He I λ7065	1.0	SNR $\geq$ 10	SNR $<$ 3 or PeakRatio $<$ 0.10
O I λ7774	1.0	SNR $\geq$ 10	SNR $<$ 3
[C I] λ8727	1.0	SNR $\geq$ 10 and PeakRatio $\geq$ 0.25	PeakRatio $<$ 0.10
Mg I] λ4571	1.0	SNR $\geq$ 10 and PeakRatio $>$ 0.20	PeakRatio $<$ 0.15 or SNR $\leq$ 3
O I λ8447	0.2	SNR $\geq$ 10 or PeakRatio $\geq$ 0.30	SNR $<$ 3 and PeakRatio $<$ 0.30
[Ni II]/[Fe II]	0.5	Ratio $>$ 0.7	Ratio $<$ 0.4
[Ca II]/[O I]	0.5	$--$	Ratio $<$ 1.0

Table G: Continued.

SN	Phase (days)	$M_{\rm ZAMS}$ ($M_\odot$)
ZTF24aaasazz	147	$13.41^{+2.41}_{-2.06}$
ZTF24aaasazz	353	$10.28^{+1.78}_{-1.76}$
ZTF24aabppgn	180	$11.62^{+1.27}_{-1.25}$
ZTF24aaejecr	147	$12.35^{+1.68}_{-1.41}$
ZTF24aaejecr	291	$14.56^{+3.63}_{-3.84}$
ZTF24aaejecr	348	$14.05^{+3.15}_{-3.84}$
ZTF24aaezido	180	$14.03^{+2.98}_{-2.65}$
ZTF24aaplfjd	132	$11.94^{+1.03}_{-1.03}$
ZTF24aaplfjd	184	$11.16^{+1.16}_{-1.18}$
ZTF24aaplfjd	394	$10.50^{+2.00}_{-1.95}$
ZTF24abtczty	149	$16.50^{+3.50}_{-3.79}$
ZTF24abtczty	334	$10.91^{+1.94}_{-2.11}$
ZTF24abtczty	393	$10.51^{+2.50}_{-1.94}$

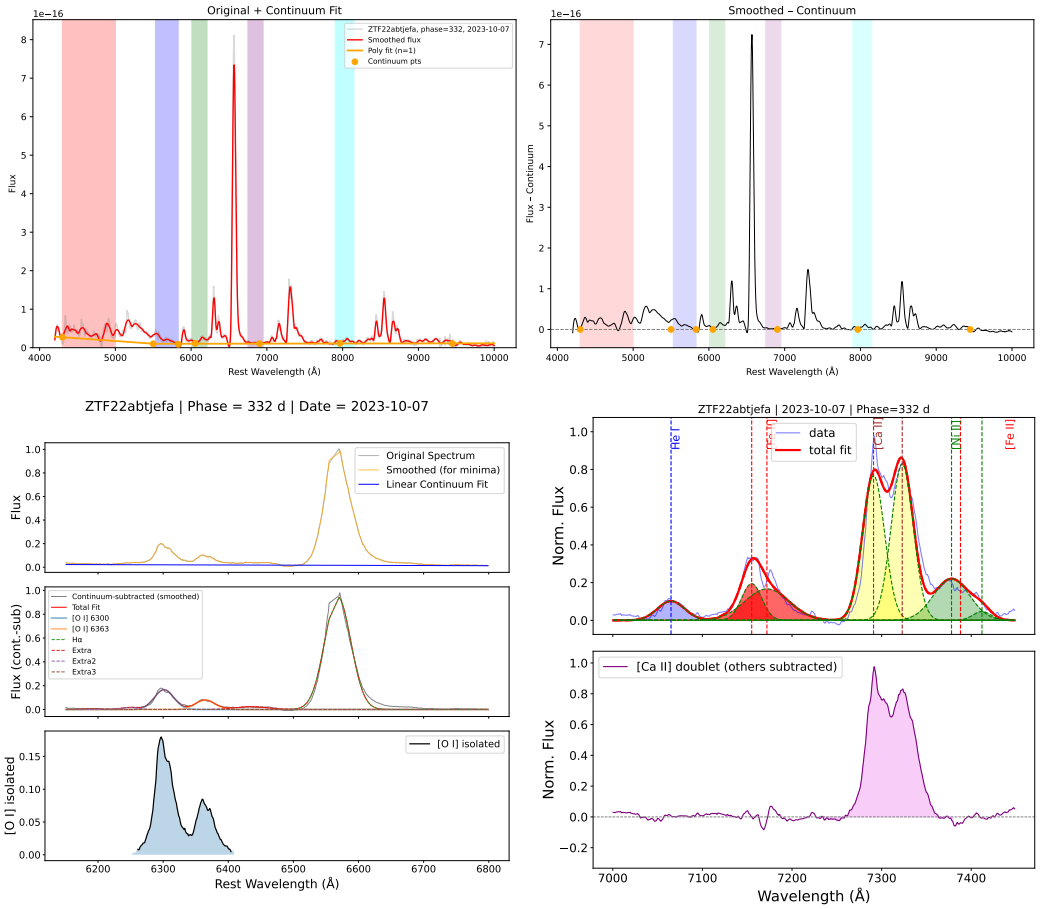

Figure 6.9: Example of the nebular spectral analysis procedure for ZTF22abtjefa/SN 2022aaad at phase 332 d. Top panels show the original rest-frame, extinction-corrected spectrum with the fitted host-galaxy continuum (left) and the continuum-subtracted spectrum (right), with shaded regions indicating the line-poor windows used to define the continuum. Bottom left panels show the isolation of the [O I] $\lambda\lambda$6300, 6363 feature using a local pseudo-continuum defined by minima in the smoothed spectrum, followed by Gaussian fitting to measure the line flux and width. Bottom right panels show the multi-component Gaussian fit to the 7000–7500 Å region and the resulting isolated [Ca II] $\lambda\lambda$7291, 7323 profile after subtracting all other fitted lines.

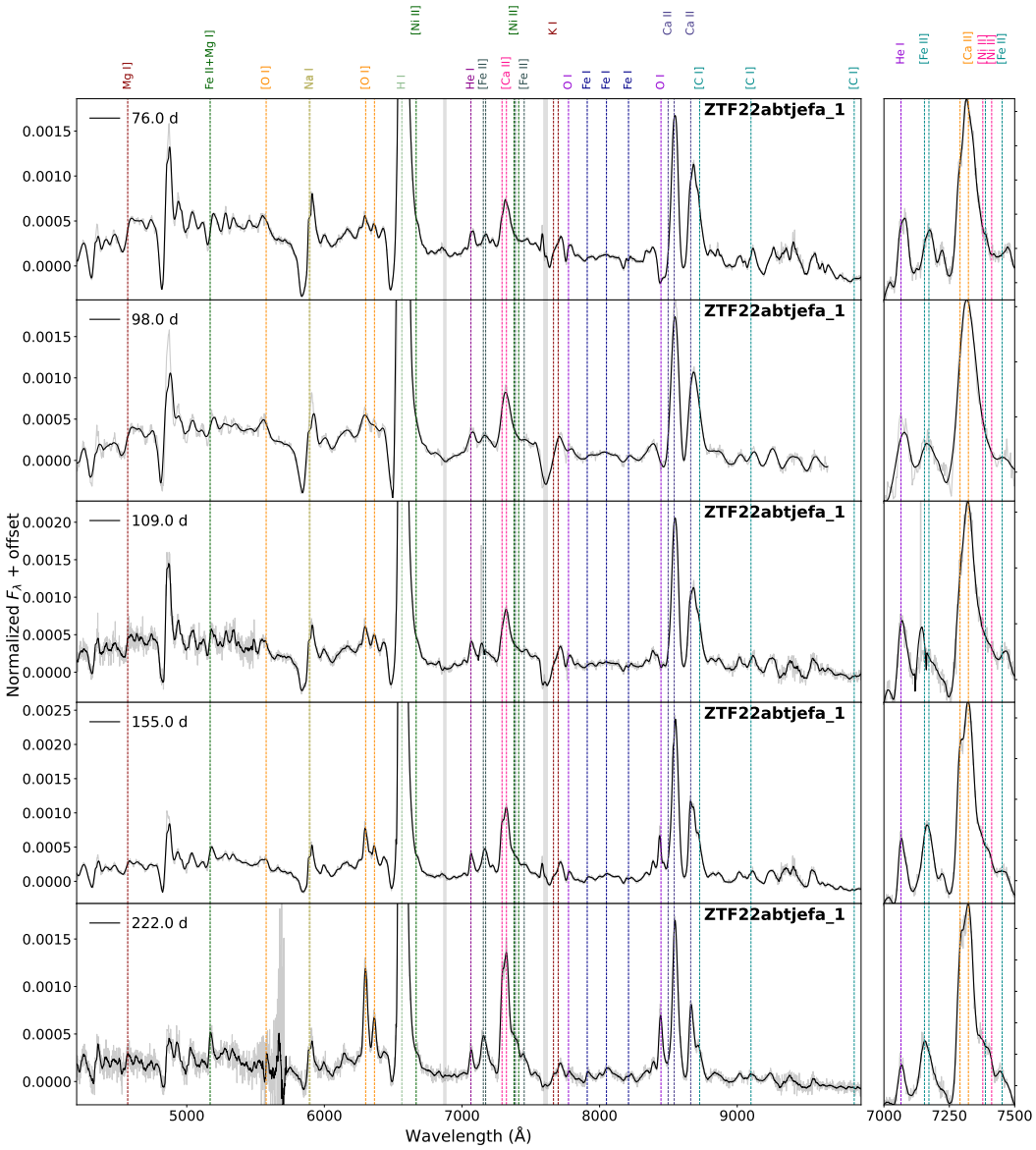

Figure 6.10: Nebular spectra of ZTF22abtjefa/SN 2022aaad.

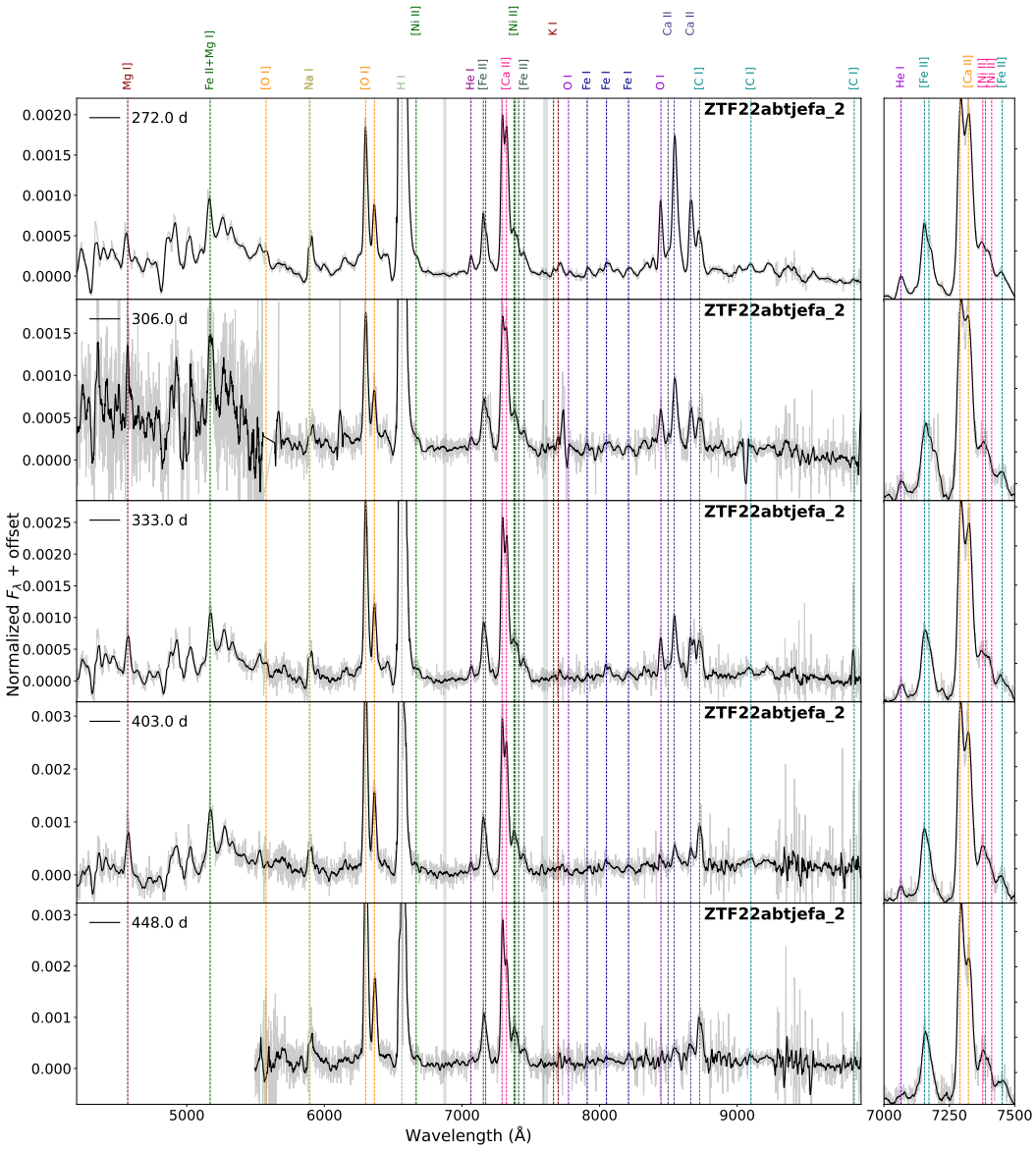

Figure 6.11: Nebular spectra of ZTF22abtjefa/SN 2022aaad.

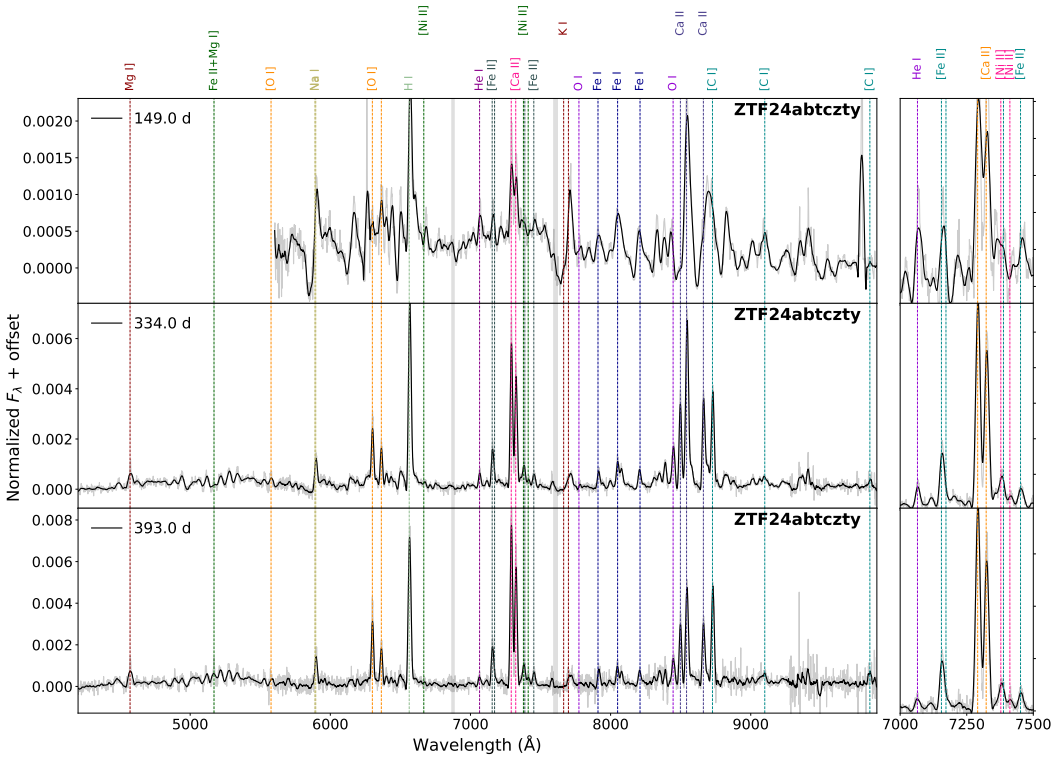

Figure 6.12: Nebular spectra of ZTF24abtczty/SN 2024abfl.

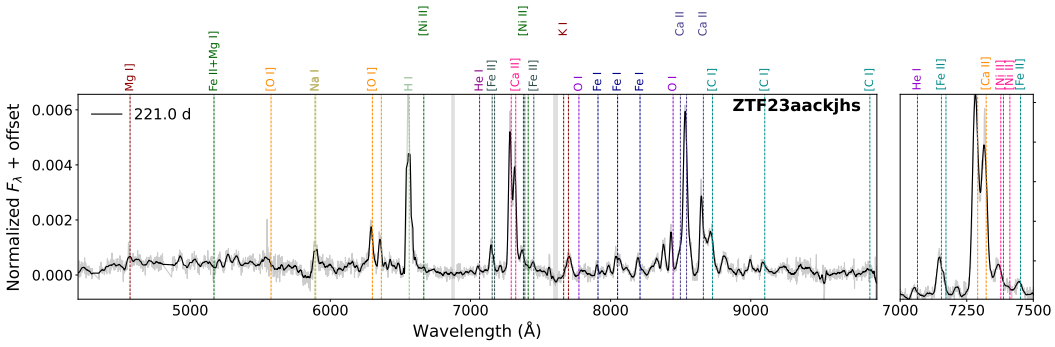

Figure 6.13: Nebular spectra of ZTF23aackjhs/SN 2023bvj.

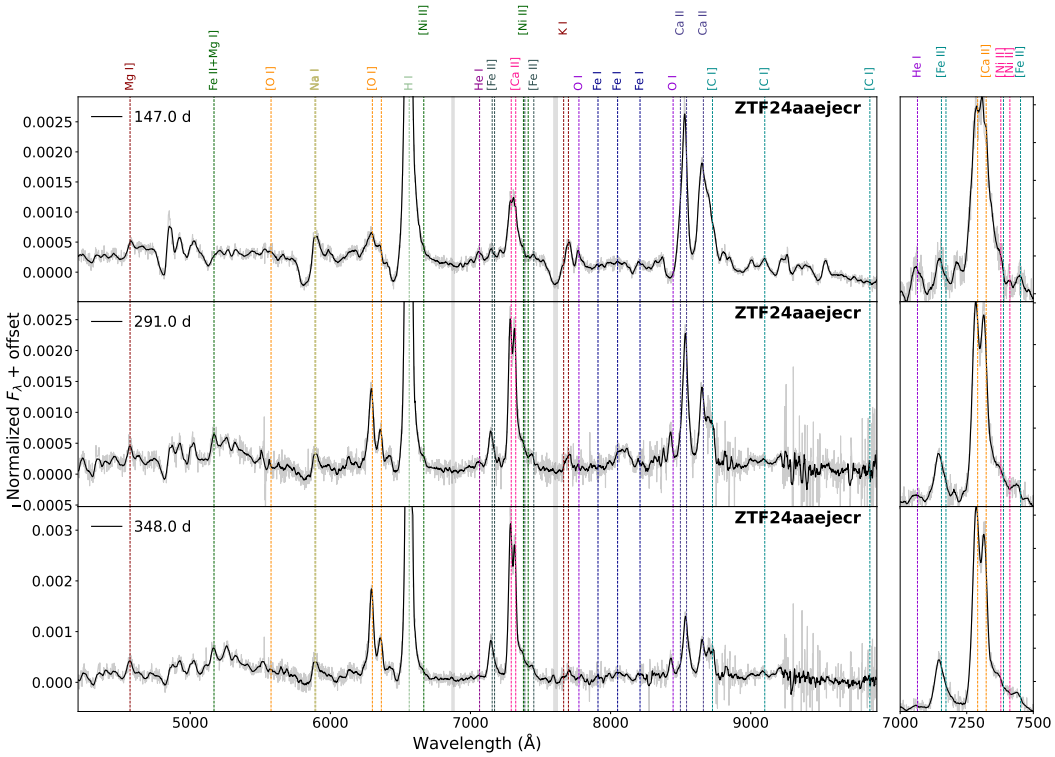

Figure 6.14: Nebular spectra of ZTF24aaejecr/SN 2024btj.

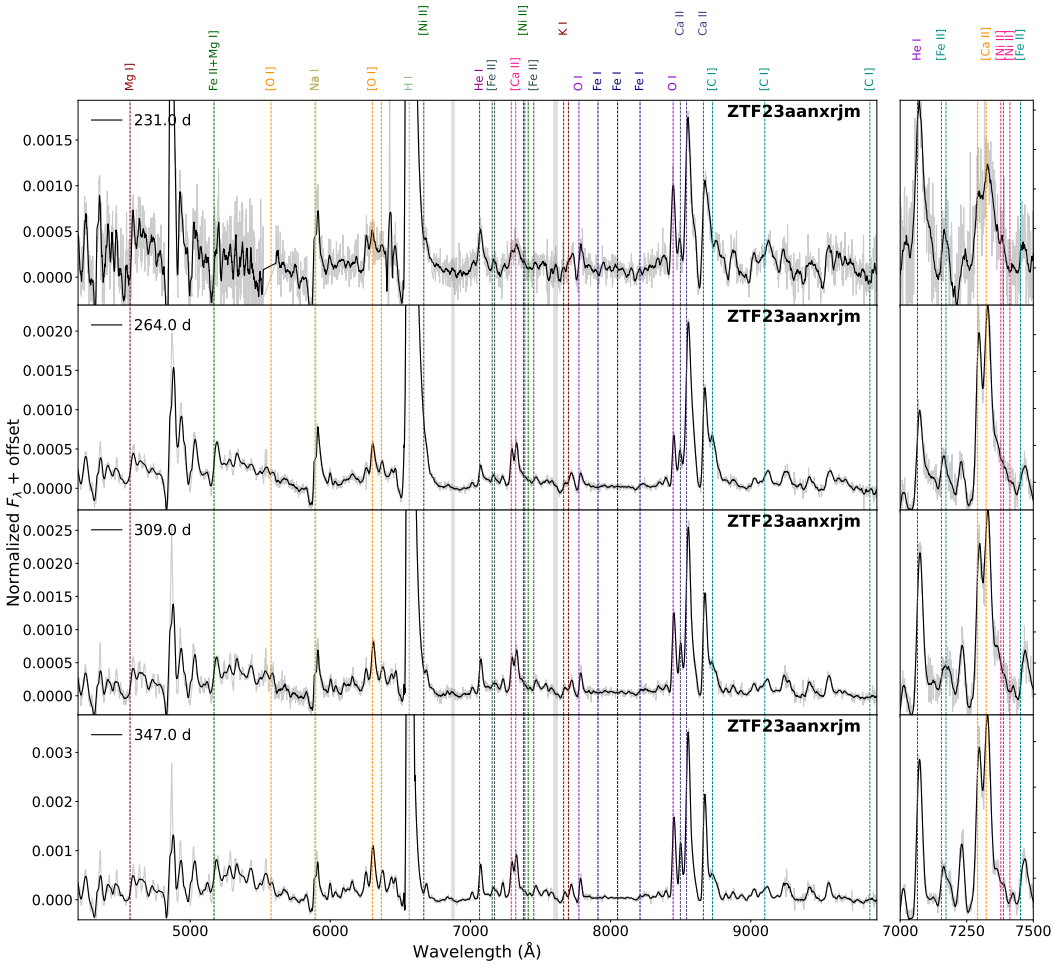

Figure 6.15: Nebular spectra of ZTF23aanxrjm/SN 2023kmk.

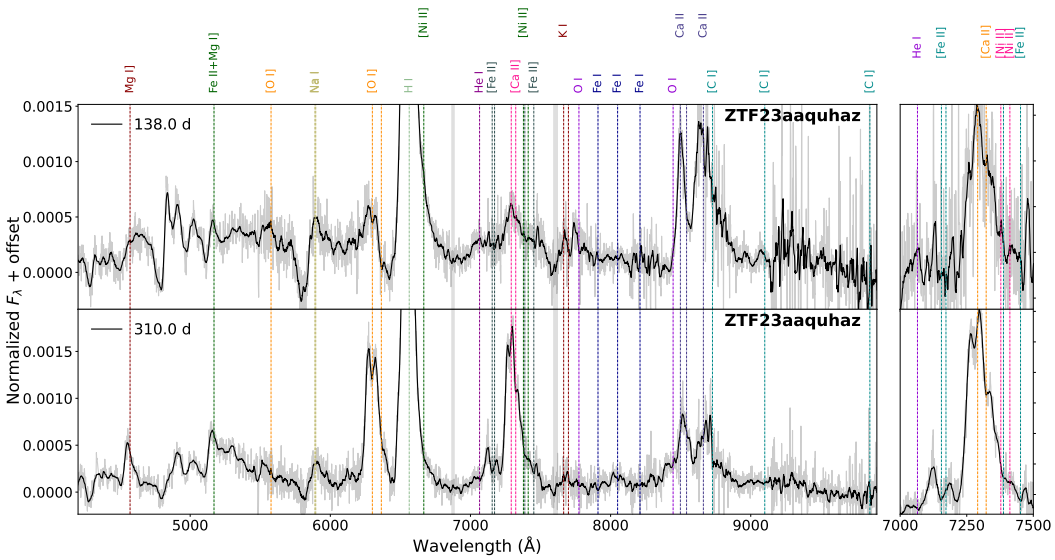

Figure 6.16: Nebular spectra of ZTF23aaquhaz/SN 2023mpz.

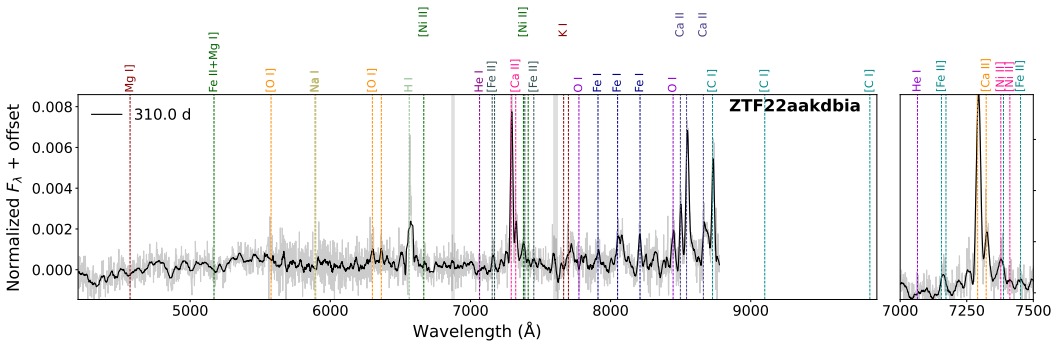

Figure 6.17: Nebular spectra of ZTF22aakdbia/SN 2022jzc.

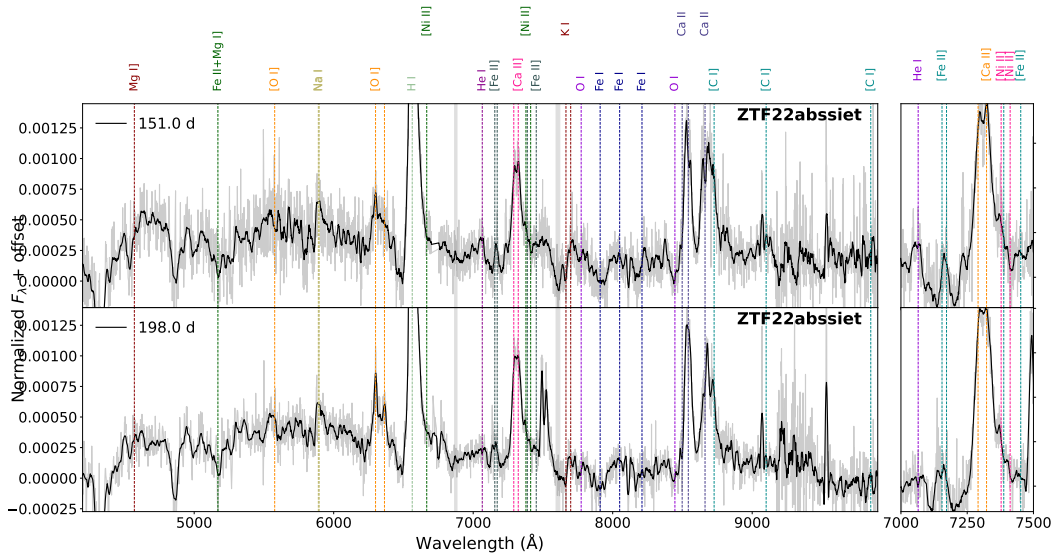

Figure 6.18: Nebular spectra of ZTF22abssiet/SN 2022zmb.

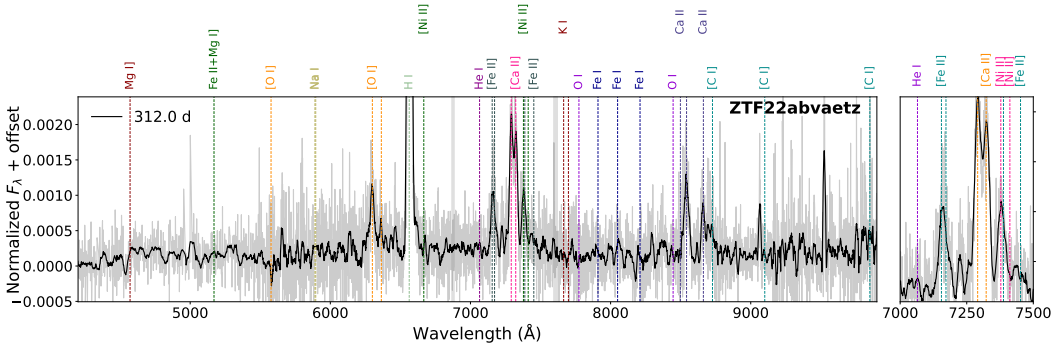

Figure 6.19: Nebular spectra of ZTF22abvaetz/SN 2022aang.

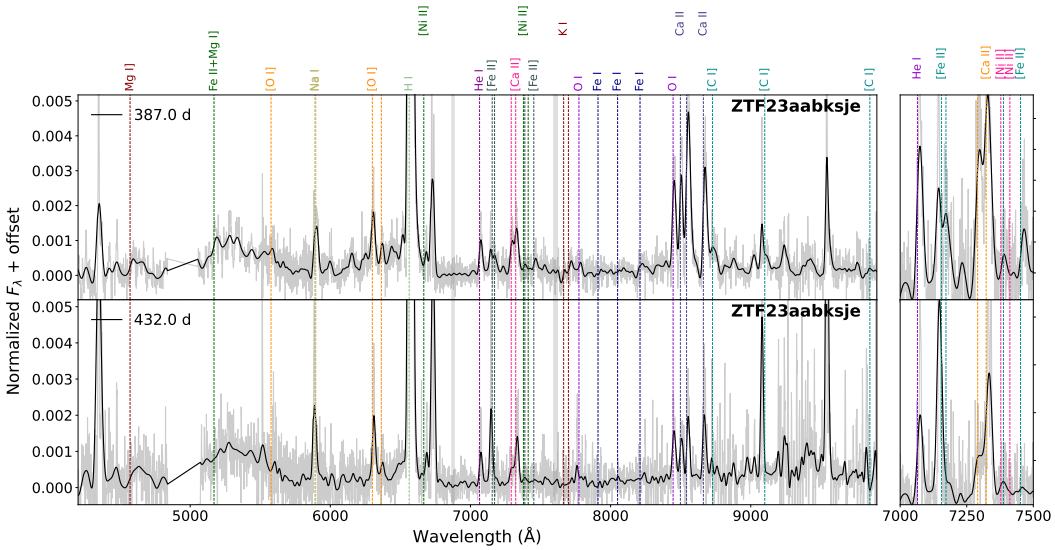

Figure 6.20: Nebular spectra of ZTF23aabksje/SN 2023azx.

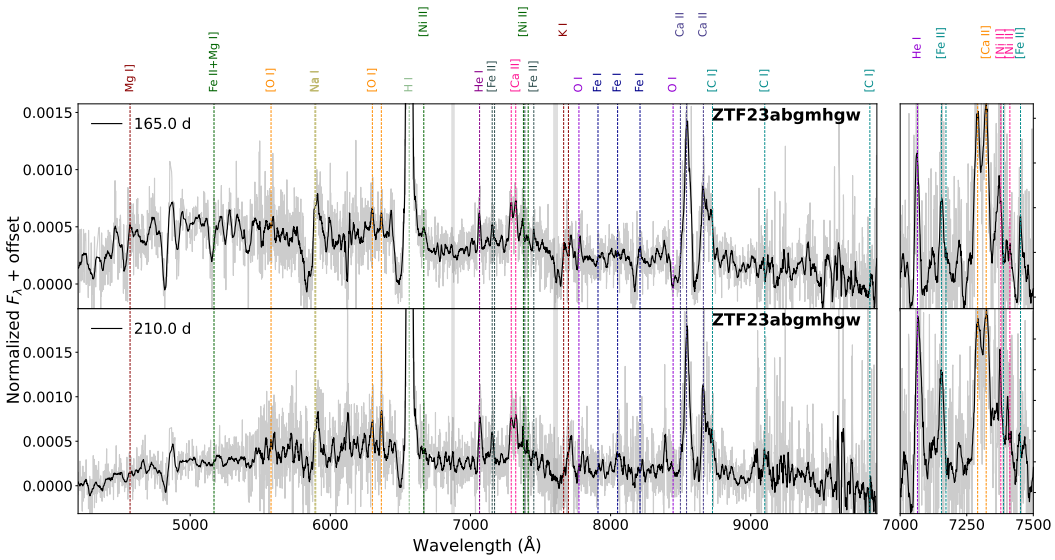

Figure 6.21: Nebular spectra of ZTF23abgmhgw/SN 2023vci.

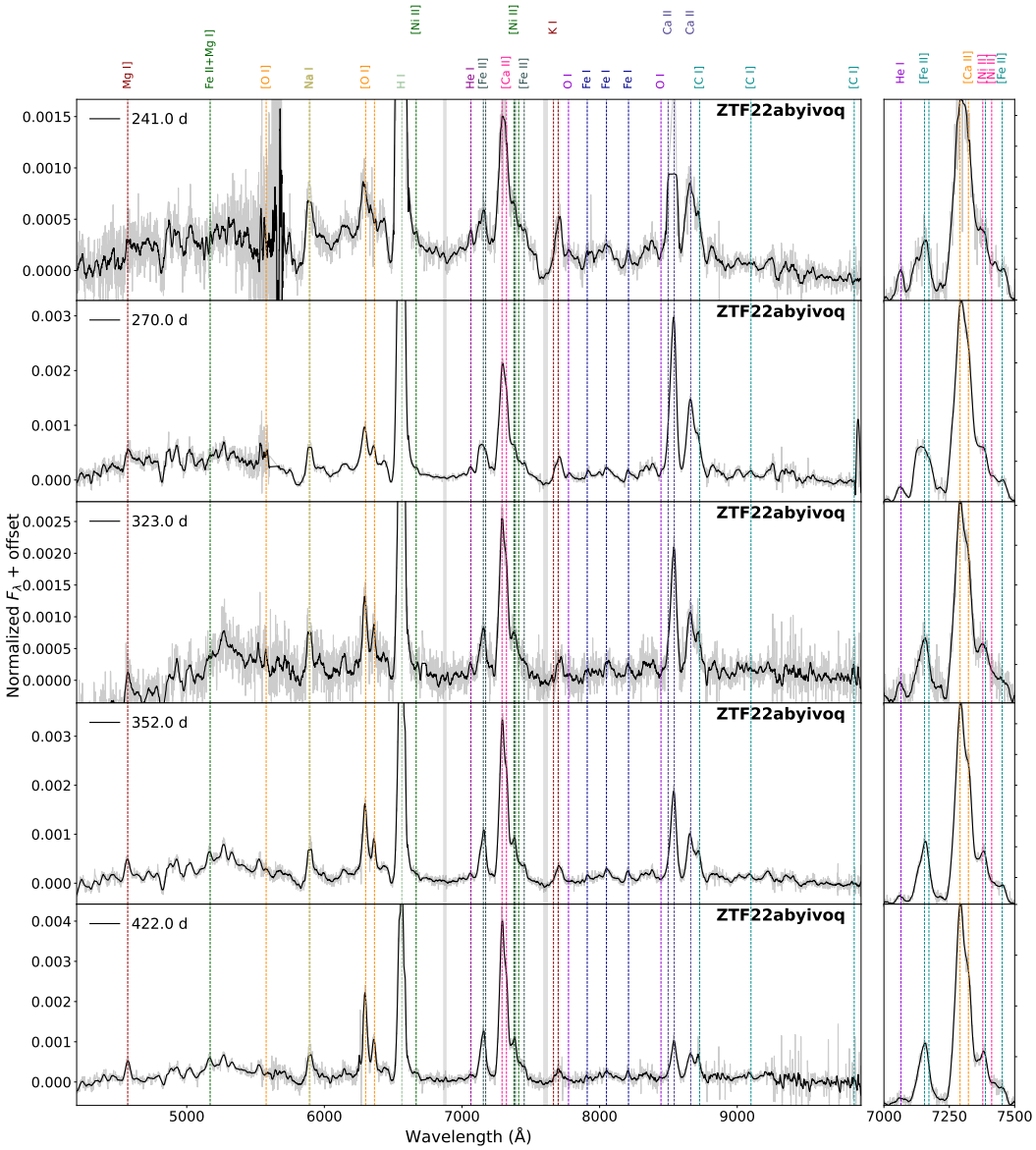

Figure 6.22: Nebular spectra of ZTF22abyivoq/SN 2022acko.

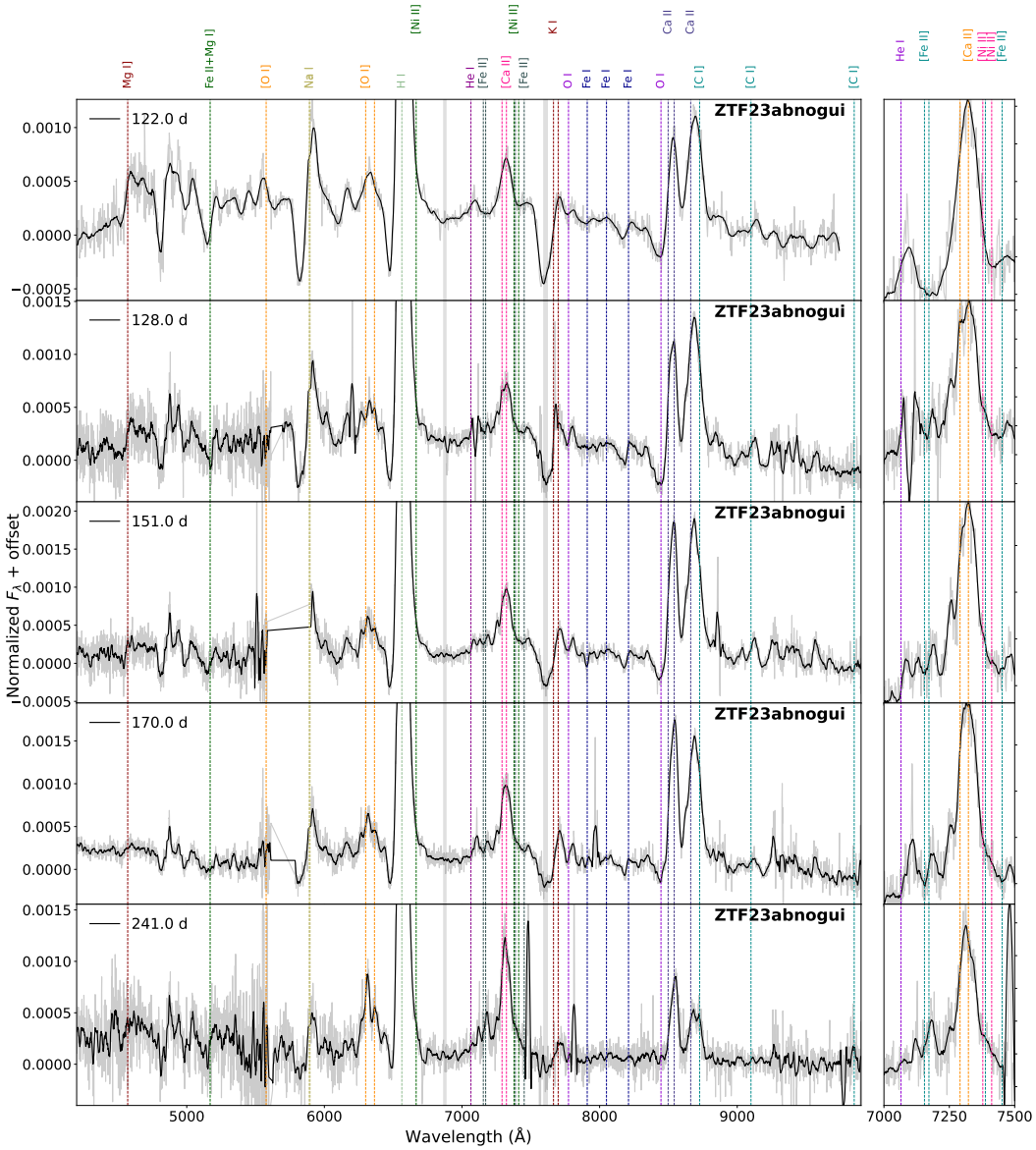

Figure 6.23: Nebular spectra of ZTF23abnogui/SN 2023wcr.

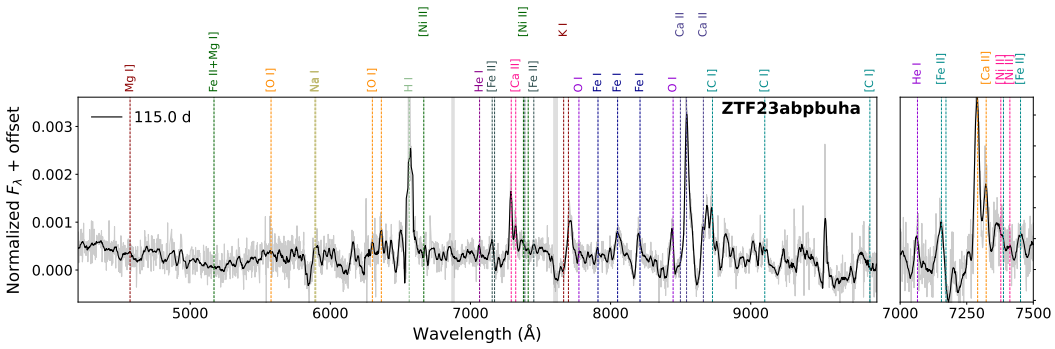

Figure 6.24: Nebular spectra of ZTF23abpbuha/SN 2023usp.

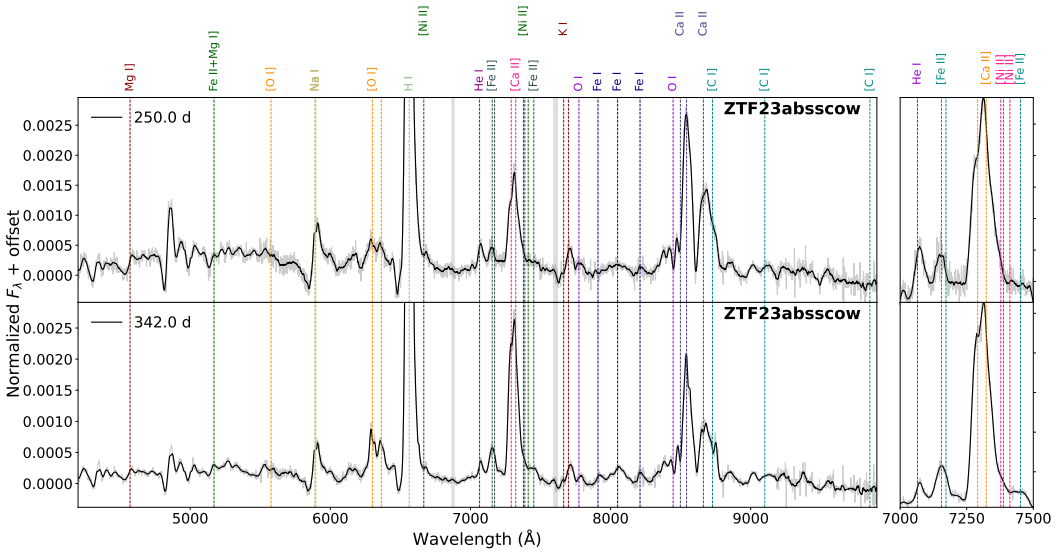

Figure 6.25: Nebular spectra of ZTF23absscow/SN 2023ywa.

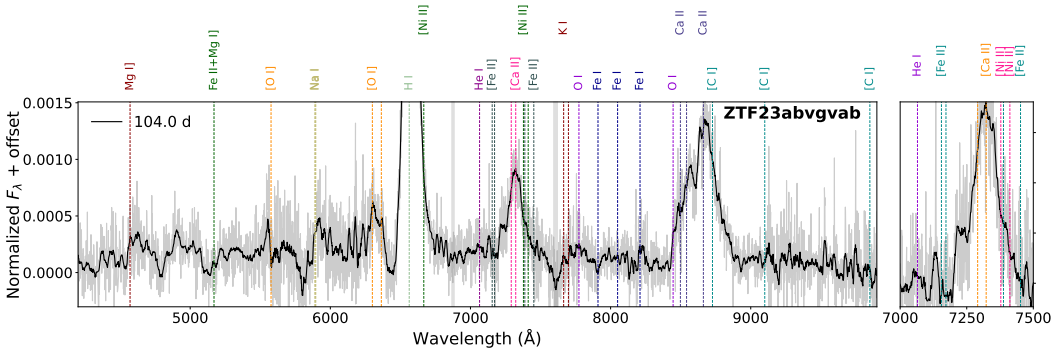

Figure 6.26: Nebular spectra of ZTF23abvgvab/SN 2023abim.

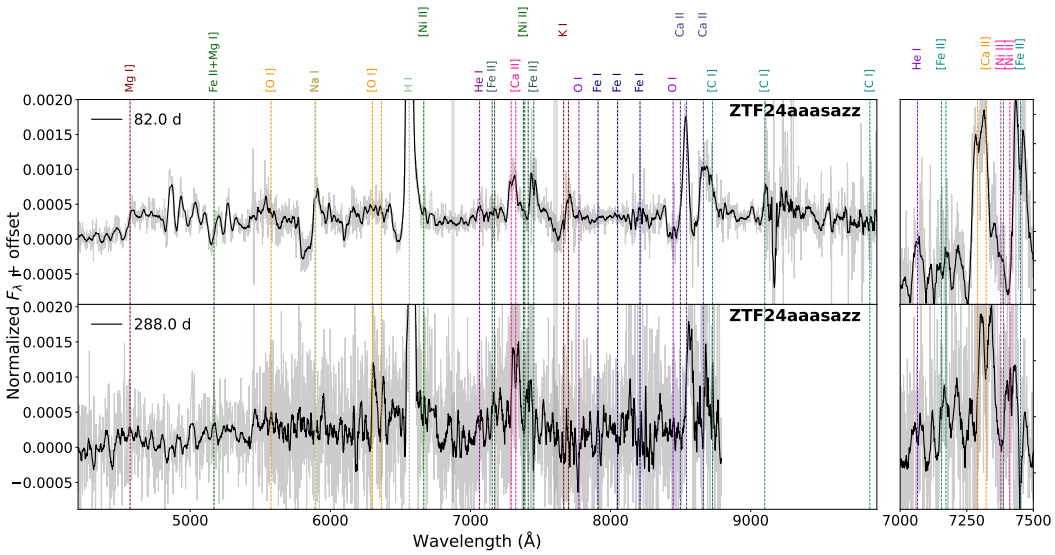

Figure 6.27: Nebular spectra of ZTF24aaasazz/SN 2024ov.

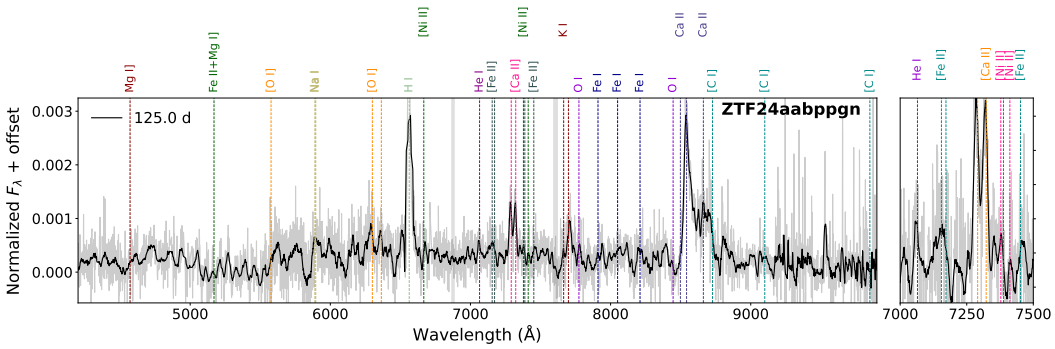

Figure 6.28: Nebular spectra of ZTF24aabppgn/SN 2024wp.

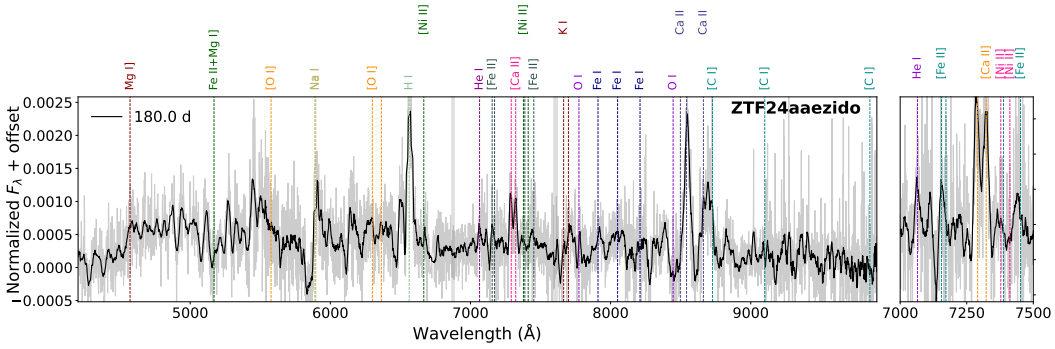

Figure 6.29: Nebular spectra of ZTF24aaezido/SN 2024cro.

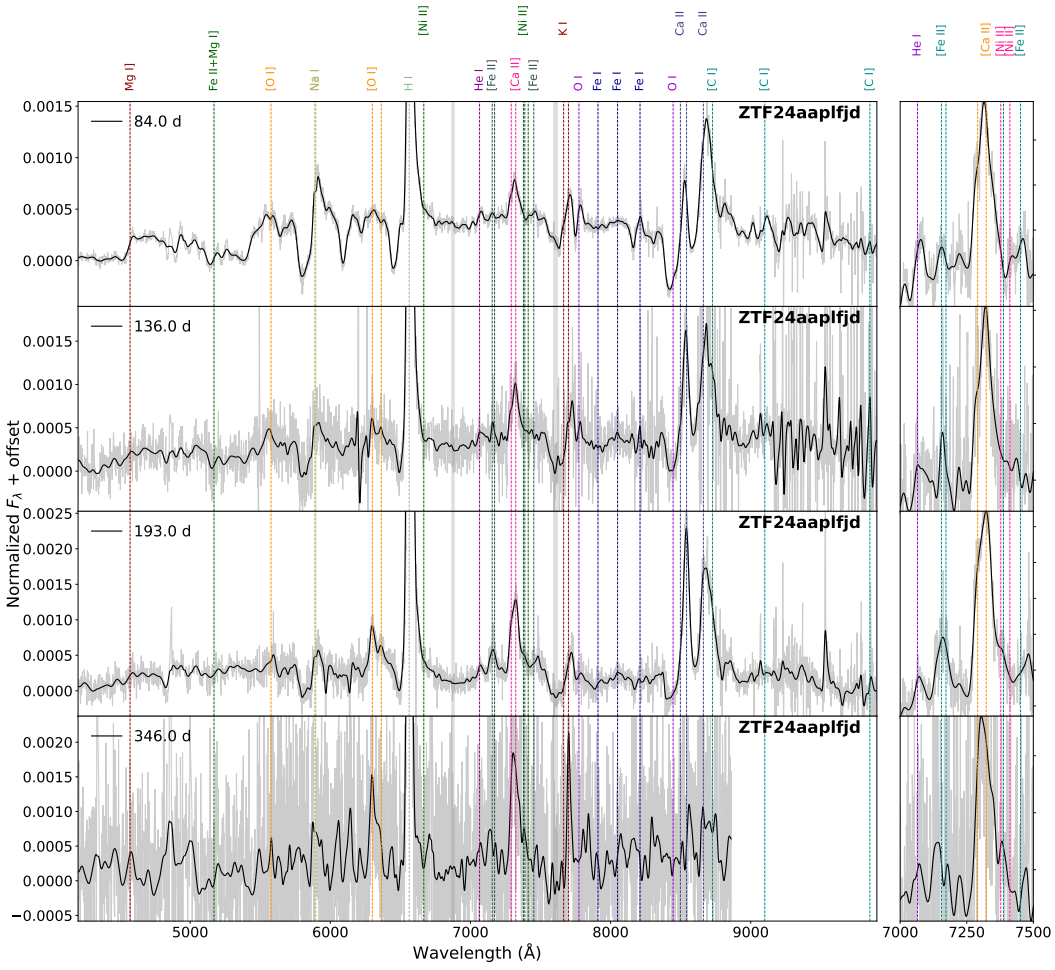

Figure 6.30: Nebular spectra of ZTF24aaplfjd/SN 2024jxm.

Chapter 7

PROBING THE LOW-MASS END OF CORE-COLLAPSE SUPERNOVAE USING A SAMPLE OF STRONGLY-STRIPPED CALCIUM-RICH TYPE IIB SUPERNOVAE FROM THE ZWICKY TRANSIENT FACILITY

Das, K. K., M. M. Kasliwal, et al. (2023). "Probing the Low-mass End of Core-collapse Supernovae Using a Sample of Strongly-stripped Calcium-rich Type IIb Supernovae from the Zwicky Transient Facility". In: *The Astrophysical Journal* 959.1, article 12. DOI: 10.3847/1538-4357/acfeeb.

Kaustav K. Das[1], Mansi M. Kasliwal[1], Christoffer Fremling[1], Sheng Yang[2], Steve Schulze[3], Jesper Sollerman[2], Tawny Sit[1], Kishalay De[4], Anastasios Tzanidakis[1], Daniel A. Perley[5], Shreya Anand[6], Igor Andreoni[7,8,9], C. Barbarino[2], K. Brudge, Andrew Drake[1], Avishay Gal-Yam[10], Russ R. Laher[11], Viraj Karambelkar[1], S. R. Kulkarni[1], Frank J. Masci[11], Michael S. Medford[12,13], Abigail Polin[1], Harrison Reedy[1], Reed Riddle[1], Yashvi Sharma[1], Roger Smith[14], Lin Yan[14], Yi Yang, Yuhan Yao[1]

[1] Cahill Center for Astrophysics, California Institute of Technology, Pasadena, CA 91125, USA

[2] The Oskar Klein Centre, Department of Astronomy, Stockholm University, AlbaNova, SE-10691 Stockholm, Sweden

[3] The Oskar Klein Centre, Department of Physics, Stockholm University, AlbaNova, SE-10691 Stockholm, Sweden

[4] MIT-Kavli Institute for Astrophysics and Space Research, 77 Massachusetts Ave., Cambridge, MA 02139, USA

[5] Astrophysics Research Institute, Liverpool John Moores University, IC2, Liverpool Science Park, Liverpool L3 5RF, UK

[6] Division of Physics, Mathematics and Astronomy, California Institute of Technology, Pasadena, CA 91125, USA

[7] Joint Space-Science Institute, University of Maryland, College Park, MD 20742, USA

[8] Department of Astronomy, University of Maryland, College Park, MD 20742, USA

[9] Astrophysics Science Division, NASA Goddard Space Flight Center, Greenbelt, MD 20771, USA

[10] Department of Particle Physics and Astrophysics, Weizmann Institute of Science, Rehovot 76100, Israel

[11] IPAC, California Institute of Technology, Pasadena, CA 91125, USA

[12] Department of Astronomy, University of California, Berkeley, Berkeley, CA 94720, USA

[13] Lawrence Berkeley National Laboratory, 1 Cyclotron Rd., Berkeley, CA 94720, USA

[14] Caltech Optical Observatories, California Institute of Technology, Pasadena, CA 91125, USA

Abstract

The fate of stars in the zero-age main-sequence (ZAMS) range $\approx 8 - 12$ $M_\odot$ is unclear. They could evolve to form white dwarfs or explode as electron-capture supernovae (SNe) or iron core-collapse SNe (CCSNe). Even though the initial mass function indicates that this mass range should account for over 40% of all CCSNe progenitors, few have been observationally confirmed, likely owing to the faintness and rapid evolution of some of these transients. In this paper, we present a sample of nine Ca-rich/O-poor Type IIb SNe detected by the Zwicky Transient Facility with progenitors likely in this mass range. These sources have a flux ratio of [Ca II] $\lambda\lambda$7291, 7324 to [O I] $\lambda\lambda$6300, 6364 of $\gtrsim 2$ in their nebular spectra. Comparing the measured [O I] luminosity ($\lesssim 10^{39}$erg s^{-1}) and derived oxygen mass (≈ 0.01 $M_\odot$) with theoretical models, we infer that the progenitor ZAMS mass for these explosions is less than 12 $M_\odot$. The ejecta properties ($M_{\rm ej} \lesssim 1$ $M_\odot$ and $E_{\rm kin} \sim 10^{50}$ erg) are also consistent. The low ejecta mass of these sources indicates a class of strongly-stripped SNe that is a transition between the regular stripped-envelope SNe and ultra-stripped SNe. The progenitor could be stripped by a main sequence companion and result in the formation of a neutron star − main sequence binary. Such binaries have been suggested to be progenitors of neutron star − white dwarf systems that could merge within a Hubble time, and be detectable with LISA.

7.1 Introduction

The fate of stars with zero-age main-sequence (ZAMS) masses larger than ≈ 12 $M_\odot$ is reasonably well understood from stellar evolution theory and observations. They form a massive iron core and may explode as a core-collapse supernova (CCSN) once their cores reach the Chandrasekhar mass. However, the fate of less massive stars in the ZAMS range $\approx 8-12$ $M_\odot$ is less clear (e.g., Janka 2012). They might form white dwarfs (WD), explode as electron capture supernovae (ECSNe) with an ONeMg core (e.g., Nomoto 1984, Stockinger et al. 2020), or form an iron core like regular massive stars. Depending on the metallicity and mass loss in binary systems, these stars might undergo violent flashes and power unusual transients before their deaths (Woosley and Heger 2015, Pumo et al. 2009, Podsiadlowski et al. 2004).

We expect that the narrow range of ZAMS masses from $\approx 8-12$ $M_\odot$ should account for a significant fraction of CCSNe, given that the initial mass function (IMF) of stars drops rapidly toward high masses. For a typical IMF, we expect over 40% of the potential CCSN progenitors to reside in this mass range (Sukhbold et al. 2016). However, surprisingly, the number of SNe associated with a low-mass progenitor is small, with most of them being low-luminosity Type II SNe (e.g., Yang et al. 2021, O'Neill et al. 2021, Reguitti et al. 2021, Valerin et al. 2022, Kozyreva et al. 2022). Despite higher abundance in the universe, transients with low-mass progenitors may be missed because they are faint and evolve rapidly. The low mass end of the CCSN population is expected to be under-energetic and possibly underluminous (Melson et al. 2015, Nomoto et al. 1982). Thus, there is likely an observational bias due to the challenge to discover and follow-up of such faint and rapidly-evolving transients. It is difficult to understand the explosion mechanisms and trends for this population due to the small number of detections.

In this paper, we present a sample of Ca-rich Type IIb SNe, with potential progenitor mass lying in this low mass range, detected by the Zwicky Transient Facility (ZTF; Bellm et al. 2019b, Graham et al. 2019). Type IIb is a class of CCSNe whose progenitors initially exhibit hydrogen spectral features that weaken and disappear in the weeks following explosion. Unlike Type II SNe, which are associated with red-supergiant progenitors with ZAMS mass ranging from 8-20 $M_\odot$(see Smartt et al. 2009, 2015, Van Dyk 2017, for a review), the mechanisms that drive the stripping and the regimes in which they dominate are still open questions for Type IIb SNe (e.g., Sravan et al. 2019).

Ca-rich transients are a class of supernovae that are identified by a high [Ca II]/[O I]

flux ratio (> 2) in the nebular phase. Because the oxygen that we see in the nebular phase is formed primarily in the hydrostatic burning phase of the progenitor; its mass depends sensitively on the progenitor mass and is smaller for lower-mass progenitors. Calcium, on the other hand, is synthesized by oxygen burning at a later stage and has a relatively weak dependence on progenitor mass. Thus the Ca/O ratio acts as a tracer for the progenitor mass of core-collapse SNe (Fransson and Chevalier 1989, Jerkstrand et al. 2014a, 2015a, Prentice et al. 2022, Fang et al. 2022, Ergon and Fransson 2022), and a high Ca/O flux ratio implies a lower abundance of oxygen. The typical Type I Ca-rich transients are generally discovered in the outskirts of early-type galaxies (Perets et al. 2011, Kasliwal et al. 2012b, Lunnan et al. 2017). Their old environments make core-collapse SNe unlikely to be the cause for these transients (Perets et al. 2011). However, the SNe in our sample are different from the usual Type I Ca-rich gap transients; they are found in star-forming regions and are classified as Type IIb SNe based on the photospheric spectra.

Recently, SN 2019ehk was proposed to be a Ca-rich Type IIb SN from a low-mass stripped progenitor (De et al. 2021). This is unusual since core-collapse supernovae usually have a low [Ca II]/[O I] ratio. SN 2019ehk was discovered in the galaxy M100 (Grzegorzek 2018, Jacobson-Galán et al. 2020, 2021). Jacobson-Galán et al. (2020) suggested a thermonuclear explosion origin arising from a low-mass hybrid HeCO white dwarf + CO white dwarf merger. However, a core-collapse explosion from a < 10 $M_{\odot}$ ZAMS star could not be ruled out from archival *Hubble Space Telescope* images. Nakaoka et al. (2021) suggested that SN 2019ehk originated in an ultra-stripped core-collapse SN (USSN). However, we do not expect to see hydrogen in an USSN. Thus, Ca-rich IIb events could potentially be strongly-stripped SNe (SSSNe), which is a transition class between the regular stripped-envelope SNe and ultra-stripped SNe.

Here, we present a holistic analysis of the lightcurve and spectral properties for a sample of nine strongly-stripped Ca-rich Type IIbs. This work is useful to describe these potentially common types of transients, understand the fate of the low mass end of CCSNe, and determine the evolutionary pathway for Type IIb SNe. Also, this sample increases the number of Ca-rich Type IIb SNe observed in the literature from one to nine. They could provide observational constraints on SN explosions of low mass He-stars. It can also help probe the distribution of the degree of stripping, understand common envelope evolution, and constrain rates of binary mergers such as NS − WD systems that could be detectable in gravitational waves.

The sample selection and data used are described in Section 7.2. In Section 7.3, we present our analysis of the late-time nebular spectra, photospheric spectra, lightcurves and the host galaxy photometry of the sample. We discuss the inferred progenitor properties, evolutionary pathways and rates in Section 7.4. We provide a brief summary of the results and future goals in Section 7.5.

7.2 Data

Sample Selection

In this work, we use SNe detected by ZTF. ZTF has a 47-square degree field-of-view camera (Dekany et al. 2020) which is mounted on the Palomar 48-inch (P48) Oschin Schmidt telescope. It images the entire Northern sky every ∼2 nights in g and r-bands, with a median depth of around 20.5 mag. We use ZTF discoveries that are part of the Bright Transient Survey (BTS; Fremling et al. 2020) – a magnitude-limited survey aimed at spectroscopically classifying all SNe with peak magnitude brighter than 18.5 mag and the Census of the Local Universe survey (CLU; De et al. 2020b)– a volume-limited survey aimed at classifying all SNe within 200 Mpc whose hosts belong to the CLU galaxy catalog (Cook et al. 2019).

We apply the following selection criteria on the ZTF SN sample obtained from the BTS and CLU surveys (until 31 December 2021):

1. The transient should be classified as a Type IIb SN based on spectra obtained near peak light. We have 94 Type IIb SNe in the BTS + CLU sample.

2. We obtained at least one epoch of late-time nebular spectroscopy (at > 50 rest-frame days post explosion) for events satisfying the above criteria. This was true for 29 of the 94 Type IIb SNe.

3. The [Ca II]/[O I] ratio in the nebular-phase spectrum should be > 2 (Milisavljevic et al. 2017, De et al. 2018a). This is true for 11 SNe out of the 29 SNe for which we have nebular spectra. We excluded two SNe[1] because of poor lightcurve quality. Table A lists the general properties of the nine SNe in the final sample.

Optical photometry

We perform forced PSF photometry on the ZTF difference images via the ZTF forced-photometry service (Masci et al. 2019) in g, r and i bands. For this work, we consider anything less than a 3σ detection an upper limit. The ZTF lightcurves were supplemented with photometry from the Palomar 60-inch telescope (P60; Cenko

[1] SN 2019lsk, SN 2019rta

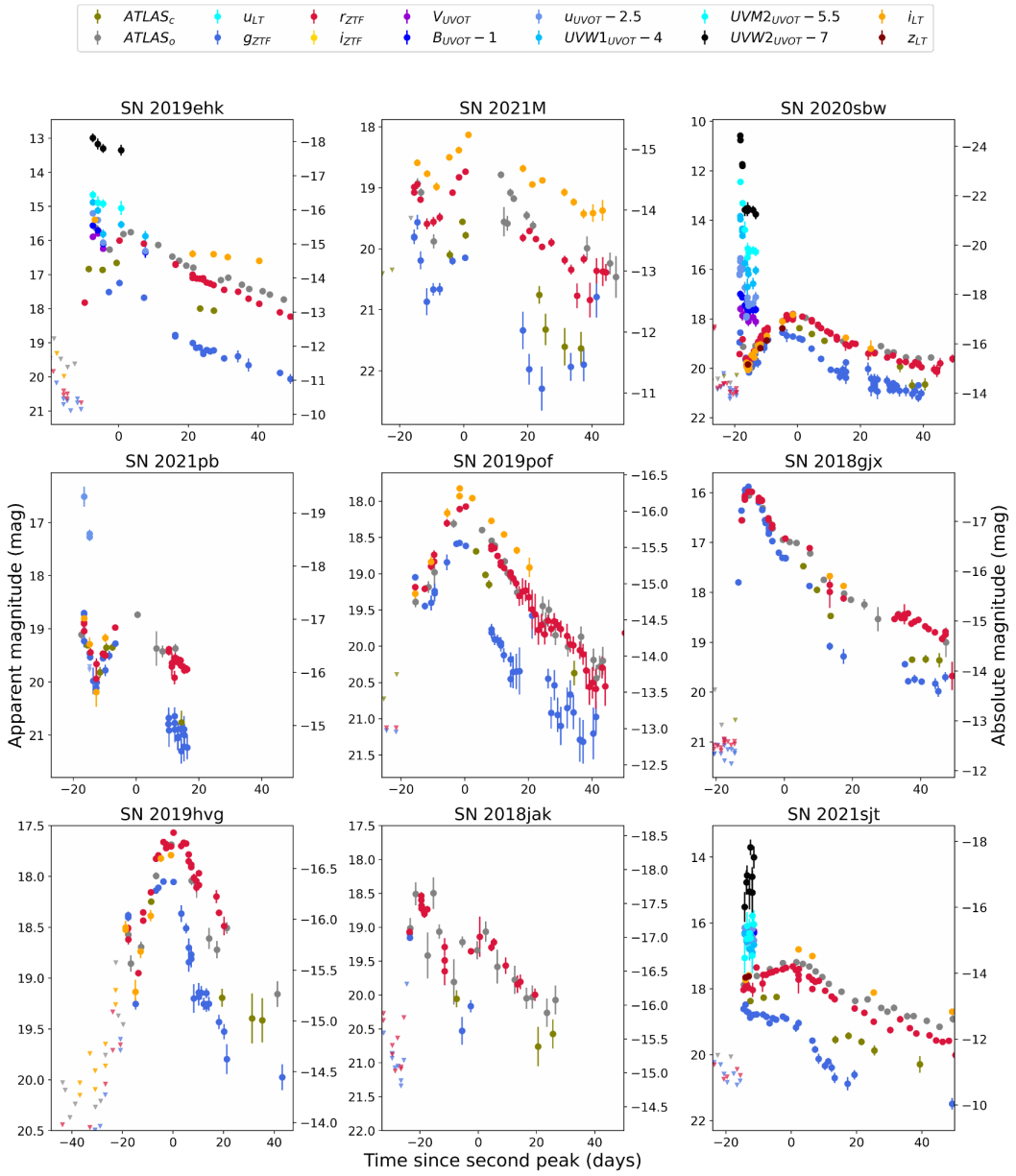

Figure 7.1: Lightcurves for our sample of nine Ca-rich Type IIb SNe. This has forced-photometry from ZTF, ATLAS and follow-up observations from various instruments. See Section 7.2 for further description on the photometry. The left y-axis shows the apparent magnitude (mag) and the right y-axis shows the absolute magnitude (mag), without host extinction correction. The x-axis shows the number of rest-frame days since the second peak.

Table A: Summary of the sample of SNe presented in this work. Subscripts 1 and 2 refer to the peak parameters of the first and second peaks, respectively. The absolute magnitudes are corrected for Milky Way and host-galaxy extinction (see Section 7.3).

ZTF Name	IAU Name	R.A. (hh:mm:ss)	Dec. (dd:mm:ss)	Redshift	t_{max1} (MJD)	M_{r1} (mag)	t_{max2} (MJD)	M_{r2} (mag)	$A_{V,MW}$ (mag)	$A_{V,host}$ (mag)
ZTF19aatesgp	SN2019ehk	12:22:56.14	+15:49:34.0	0.006	58606	-18.2	58616	-17.9	0.1	2.2
ZTF21aaabwfu	SN2021M	14:14:14.72	+35:25:23.1	0.011	59216	-16.8	59231	-17.0	0.1	2.1
ZTF20abwzqzo	SN2020sbw	02:46:03.31	+03:19:47.6	0.023	59088	-16.9	59104	-17.9	0.1	0.7
ZTF21aabxjqr	SN2021pb	09:44:46.80	+51:41:14.6	0.033	59221	-16.9	59238	-16.8	0.0	0.0
ZTF19abxtcio	SN2019pof	01:12:37.87	+33:02:05.7	0.015	58733	-15.6	58749	-16.7	0.2	0.5
ZTF18abwkrbl	SN2018gjx	02:16:15.58	+28:35:28.6	0.012	58379	-17.8	58390	-16.9	0.2	0.0
ZTF19abacxod	SN2019hvg	14:06:01.58	+12:46:50.3	0.018	58654	-16.6	58672	-17.6	0.1	0.8
ZTF18acqxyiq	SN2018jak	09:59:18.19	+34:53:43.7	0.038	58447	-18.1	58467	-17.5	0.0	0.6
ZTF21abjyiiw	SN2021sjt	20:37:19.19	+66:06:23.1	0.005	59403	-16.9	59417	-16.7	1.0	1.9

et al. 2006), the Optical wide field camera on the Liverpool Telescope (LT; Steele et al. 2004), Sinistro and SBIG imagers on the 1-meter class and the Spectral imager on the 2-meter class telescopes operated by Las Cumbres Observatory (LCO; Brown et al. 2013) in g, r and i bands. We also use photometry in u, i, z bands obtained with the LT for a few sources. These data were processed with the automatic image subtraction pipeline FPipe (Fremling et al. 2016) using reference images from the Sloan Digital Sky Survey (SDSS; Ahn et al. 2012) and PanSTARRS (PS1; Chambers et al. 2016). We have early-time UV data from the Ultra-violet Optical Telescope (UVOT; Roming et al. 2005), which is on board the *Neil Gehrels Swift Observatory* (Gehrels et al. 2004). The UVOT data is reduced using HEAsoft[2]. We also use forced-photometry data points from the Asteroid Terrestrial-impact Last Alert System (ATLAS; Tonry et al. 2018, Smith et al. 2020). Figure 7.1 shows a multi-paneled figure of the lightcurves for the SNe in our sample.

Optical spectroscopy

We obtained spectroscopy at multiple epochs for the sources in our sample, with phases varying from one day to over 200 days past the explosion day. One spectrum is obtained near peak luminosity for initial spectroscopic classification. Further spectral follow-up is part of the classification effort of the BTS and CLU surveys. We primarily use the Double Beam Spectrograph (DBSP; Oke and Gunn 1982) on the Palomar 200-inch telescope and the Spectral Energy Distribution Machine (SEDM; Blagorodnova et al. 2018, Rigault et al. 2019) on the Palomar 60 inch telescope for classification. The DBSP spectra reduction pipelines used are described in Bellm and Sesar (2016) and Roberson et al. (2022). The SEDM data reduction pipeline is

[2]https://heasarc.gsfc.nasa.gov/docs/software/heasoft

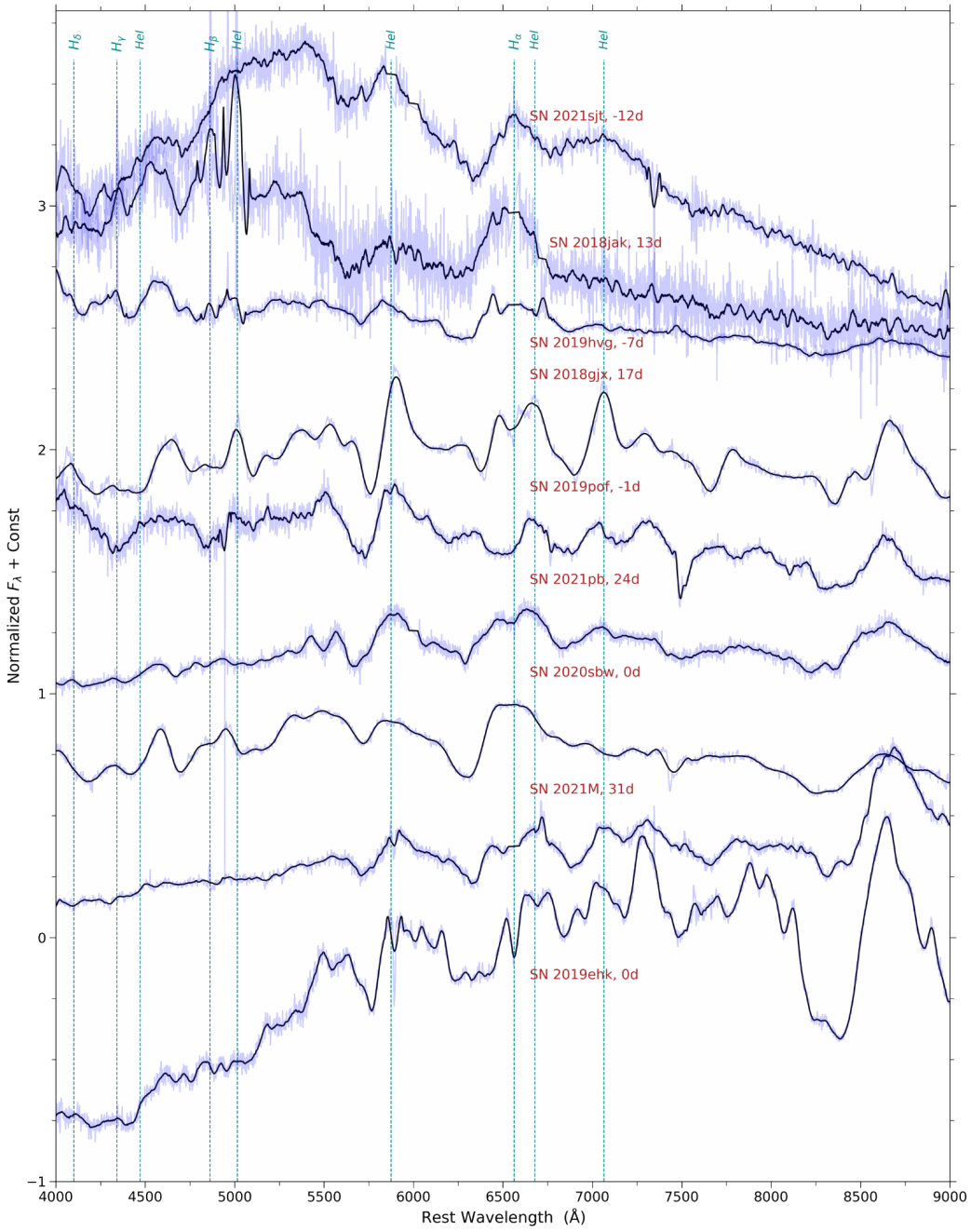

Figure 7.2: Collage of few spectra for the SNe in our sample showing H and He emission lines. The phase of the spectra is measured as the number of rest-frame days since the second peak.

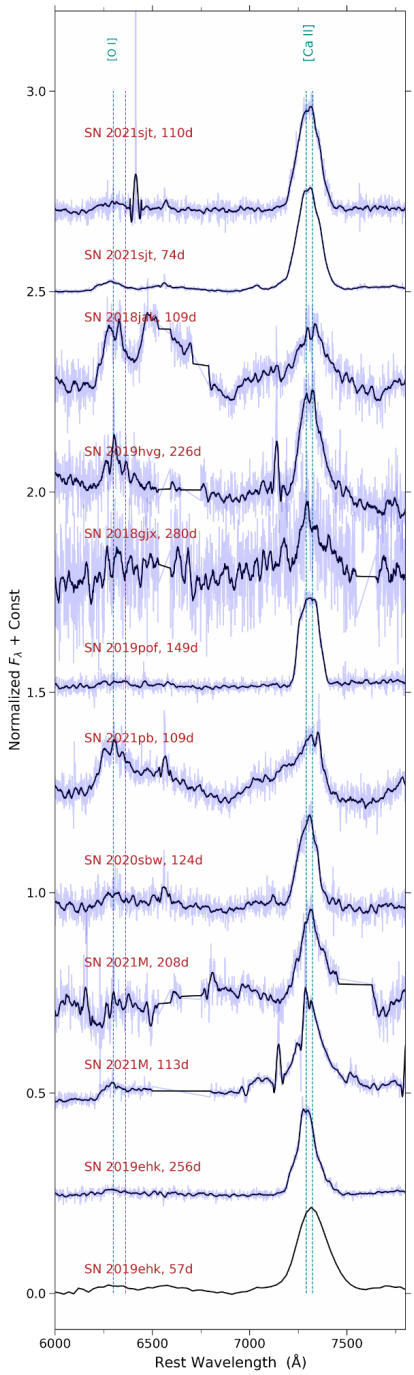

Figure 7.3: Nebular spectra showing the [Ca II] $\lambda\lambda$7291, 7324 and [O I] $\lambda\lambda$6300, 6364 lines. The phase of the spectra is measured as the number of rest-frame days since the second peak.

The spectra with the full wavelength range are shown in Appendix 7.6.

described in Rigault et al. (2019). We also use spectra from the Spectrograph for the Rapid Acquisition of Transients (SPRAT; Piascik et al. 2014) on the Liverpool Telescope, the Alhambra Faint Object Spectrograph and Camera (ALFOSC) on the Nordic Optical Telescope (NOT; Djupvik and Andersen 2010) and the Device Optimized for the LOw RESolution (DOLORES) on the Telescopio Nazionale Galileo (TNG). The SPRAT pipeline is based on the FrodoSpec pipeline (Barnsley et al. 2012). The NOT and TNG data were reduced using the data-reduction pipelines PyNOT[3] and PypeIt (Prochaska et al. 2020a). Late-time nebular-phase spectra were obtained using the Low Resolution Imaging Spectrometer (LRIS) on the Keck I telescope starting $\approx$ 50 days post explosion. For a couple of sources, we obtained multiple epochs of nebular-phase spectra using LRIS. The LRIS spectra were reduced using the automated LPIPE (Perley 2019) pipeline. We used a publicly available LRIS spectrum for SN 2021sjt from 8 July 2021 (Siebert et al. 2021). Table C lists the log of the observed spectra. Figure 7.2 shows one photospheric spectrum obtained for each source and Figure 7.3 shows the obtained nebular spectra.

Host photometry

We obtain science-ready co-added images from the *Galaxy Evolution Explorer* (*GALEX*) general release 6/7 (Martin et al. 2005), Sloan Digital Sky Survey data release 9 (SDSS DR 9; Ahn et al. 2012), the Two Micron All Sky Survey (2MASS; Skrutskie et al. 2006), the Panoramic Survey Telescope and Rapid Response System (Pan-STARRS, PS1) Data Release 1 (Chambers et al. 2016), and preprocessed *WISE* images (Wright et al. 2010) from the unWISE archive (Lang 2014)[4]. The unWISE images are based on the public *WISE* data and from the ongoing NEOWISE-Reactivation mission R3 (Mainzer et al. 2014, Meisner et al. 2017). We measure the brightness of the host galaxies using LAMBDAR[5] (Lambda Adaptive Multi-Band Deblending Algorithm in R; Wright et al. 2016) and the methods described in Schulze et al. (2020). We use the offsets reported by Blanton and Roweis (2007) and Cutri et al. (2013) to convert the 2MASS and unWISE photometry from the Vega system to the AB system.

[3]https://github.com/jkrogager/PyNOT

[4]http://unwise.me

[5]https://github.com/AngusWright/LAMBDAR

7.3 Methods and Analysis

Extinction correction

We need an estimate of the extinction of the SN light due to dust along the line-of-sight to the observer in order to accurately estimate its explosion parameters. Extinction is typically split into two components. The first Galactic component accounts for extinction due to dust within the Milky Way and the second component accounts for extinction external to the Milky Way, mostly attributed to the host galaxy of the SNe. We correct for Galactic extinction by using the reddening maps of Schlafly and Finkbeiner (2011). We use the Cardelli et al. (1989) extinction law and $R_V = 3.1$ for reddening corrections. Accounting for extinction external to our own galaxy is more challenging. In this paper, we use two different approaches to correct for the host-extinction.

First, we use the intrinsic color template from the Carnegie Supernova Project (CSP-I) (Stritzinger et al. 2018). This assumes that Type IIb SNe show similar intrinsic colors after peak. We measure the average difference of our observed colors and the intrinsic template between 0 and 20 days after r-band peak as the excess color due to host extinction. We use $R_V = 3.1$ and Cardelli et al. (1989) extinction law to correct for the reddening. Shock-cooling breakout modeling (described in Section 7.3) provides an opportunity to put an upper limit to the host extinction value. When we use host extinction using the CSP template for SN 2021sjt, we get an unphysically large progenitor envelope radius (R_{env}) of around 1.7×10^6 $R_\odot$. Thus, we need to be cautious while using the intrinsic template given by Stritzinger et al. (2018) based on a sample size of three Type IIb SN.

Second, we use the narrow host-galaxy absorption lines of Na I D. This assumes that there is a relation between host-galaxy sodium absorption lines and the amount of extinction (Poznanski et al. 2012, Stritzinger et al. 2018). To compute the Na I D Equivalent Width (EW), we use spectra obtained with DBSP, ALFOSC, and LRIS, where the signal-to-noise of the spectrum allows the measurement of the EW. To compute A_V, we use $A_V^{host}[mag] = 0.78(\pm 0.15) \times EW_{\mathrm{Na\ I\ D}}[\text{Å}]$ reported in Stritzinger et al. (2018). We note the Na I D EW measurement is not always a reliable tracer of the host extinction. This is particularly true for low-resolution spectra (Poznanski et al. 2011) and in the presence of circumstellar material (Phillips et al. 2013).

The extinction values measured as described are shown in Table B. For the lightcurve analysis done in this paper, we use the average of the extinction values we get from

these methods. We show the color evolution of our objects compared to the Type IIb SNe sample of Taddia et al. (2018) in Figure 7.15.

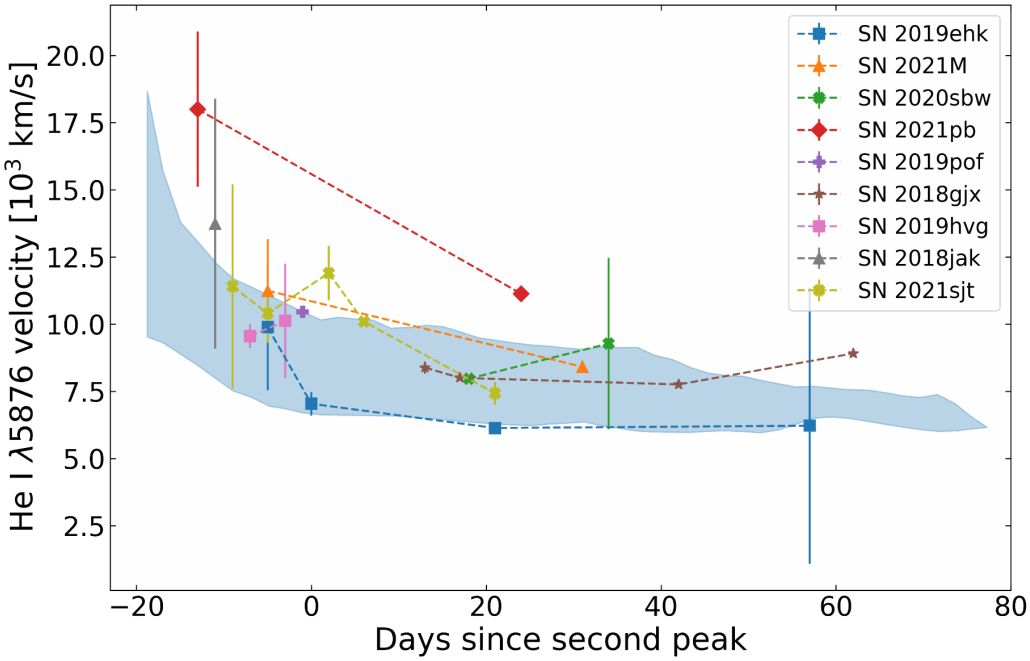

Figure 7.4: The expansion velocity of the He I line for each SN of our sample represented by the filled dots. The blue shaded region shows the 1σ region of the ejecta velocity calculated for a sample of usual Type IIb SNe in Fremling et al. (2018)

Photospheric spectra

As described in Section 7.2, we obtain spectra close to the peak epoch for all the sources. Classifications were done using the `SuperNova Identification` (`SNID`; Blondin and Tonry 2007) code. We used the `superfit` (Howell et al. 2005) code to classify spectra contaminated by the host galaxy. The final classification as Type IIb was made after manual inspection of the emission and absorption lines and the best-fit templates matched from `SNID` or `superfit`.

We determine the expansion velocities of the H I λ6563, He I λ5876, O I λ7774 lines where absorption from these lines could be identified and measurements were possible. To do this, we fit the minima of the absorption part of the P-Cygni profiles of the spectral lines with a polynomial fit (with the polynomial degree manually tuned for each spectrum, but typically 3). The minima of the absorption features are

then used to estimate the expansion velocity. For certain cases, where the spectra are contaminated with galaxy lines or the resolutions is not high, we find the minima of the absorption portion by manual inspection. We list the velocities obtained in Table C. To estimate uncertainties on our measurements, we use a Monte-Carlo approach. We obtain a noise spectrum by subtracting a heavily smoothed version of the spectrum from the original spectrum. To get an estimate of the noise, we then calculate the standard deviation of this noise spectrum. Then, we create simulated noisy spectra by adding noise using a standard gaussian distribution with the standard deviation calculated above. To the heavily smoothed spectra, we add these simulated noise spectra and re-calculate the velocity from the absorption minima for each simulated spectrum. The standard deviation of these measurements is taken as the 1σ uncertainty of our velocity measurements. Fremling et al. (2018) analyzed the spectra of a sample of 55 Type IIb SNe discovered by the Palomar Transient Factory (PTF) and intermediate PTF (iPTF) surveys. We compare the velocities we have with the mean velocities obtained in Fremling et al. (2018) for the He I λ5876 line. From Figure 7.4, we find that the expansion velocities obtained using the He I λ5876 line are consistent with those of typical Type IIb SNe obtained by Fremling et al. (2018).

Nebular spectra

We obtained late-time photometry using the LCO, Keck, P60 and P48 telescopes as recorded in Table D. Since the [Ca II] line lies entirely in the i-band, the interpolated late-time photometry is used to flux calibrate our nebular spectra. When late-time photometry is not available, we extrapolate the lightcurve by assuming a late-time (> 30 days) i-band decline rate of 0.019 ± 0.004 mag/day, based on the average late-time decay of the SESNe tabulated in Wheeler et al. (2015).

We measure the line fluxes by numerical integration of the respective wavelength regions. We add noise (scaled to nearby regions of the continuum) to the line profile and use Monte Carlo sampling of the estimated fluxes to quantify the uncertainties. The measured [Ca II] $\lambda\lambda$7291, 7324 [O I] and $\lambda\lambda$6300, 6364 fluxes and their ratio are shown in Table D.

Modeling lightcurves

Blackbody fit

We estimate the bolometric lightcurve at epochs where at least detections in two filters are available by fitting a blackbody function. For each epoch, we do the

Table B: Summary of the host extinction parameters for our sample.

Source	Telescope + Instrument	Date	Na I D EW (Å)	Avg. Color $(g-r)$ (mag)	$A_{V,\ \mathrm{Na\,I\,D}}$ (mag)	$A_{V,\ \mathrm{color}}$ (mag)	A_V used (mag)
SN 2019ehk	P200+DBSP	13 May 2019	2.99 ± 0.27	0.68 ± 0.03	2.3(0.2)	2.3(0.2)	2.2
	Keck1+LRIS	3 June 2019	2.55 ± 0.43		2.0(0.3)		
SN 2021M	Keck1+LRIS	12 Jan 2021	2.03 ± 0.22	0.95 ± 0.4	1.6(0.2)	3.2(0.3)	2.1
	Keck1+LRIS	17 Feb 2021	2.37 ± 0.21		1.8(0.2)		
	Keck1+LRIS	10 May 2021	2.12 ± 0.24		1.7(0.2)		
	Keck1+LRIS	13 Aug 2021	2.71 ± 0.41		2.1(0.3)		
SN 2020sbw	NOT+ALFOSC	14 Sep 2020	< 0.1	0.51 ± 0.10	< 0.1	1.4(0.1)	0.7
SN 2021pb	–	–	–	–	–	–	0
SN 2019pof	–	–	–	0.38 ± 0.11	–	0.5(0.1)	0.5
SN 2018gjx	–	–	–	–	–	–	0
SN 2019hvg	–	–	–	0.59 ± 0.21	–	0.8(0.1)	0.8
SN 2018jak	Keck1+LRIS	4 Dec 2018	0.8 ± 0.35		0.6(0.3)	–	0.6
SN 2021sjt	Keck1+LRIS	8 July 2021	2.31 ± 0.15	1.1 ± 0.2	1.8(0.1)	3.3(0.3)	1.9
	P200+DBSP	10 July 2021	2.39 ± 0.19		1.9(0.1)		
	P200+DBSP	07 Aug 2021	1.57 ± 0.24		1.2(0.2)		
	Keck1+LRIS	12 Aug 2021	1.50 ± 0.31		1.2(0.2)		

blackbody fit using a Markov Chain Monte-Carlo (MCMC) method using the Python EMCEE package (Foreman-Mackey et al. 2013) to estimate the temperature, radius and bolometric luminosity. We use the 16^{th} and 84^{th} percentiles of the posterior probability distribution as the model uncertainties. The blackbody fits for each source are available in Appendix 7.6.

Modeling the shock cooling powered emission peak

All the sources in our sample have a double-peaked lightcurve, which is usually seen in Type IIb SNe. The timescale of the first peak, the initial blue color and high temperatures indicate that the first peak is dominated by cooling emissions from the shock heated extended envelope (Rabinak and Waxman 2011b, Nakar and Piro 2014, Piro 2015). We note that some of the SNe from our sample do not have well sampled first peaks on both the rising and fading parts. We use the model by Piro et al. (2021) to fit for the shock cooling breakout peak. This model constrains the extended material radius (R_{ext}), mass (M_{ext}), energy (E_{ext}) and the explosion time (t_{exp}). We first select the appropriate epochs of the lightcurve peaks to model as shock cooling and then we fit the multi-band data using the Python EMCEE package. The best-fit values and fits for each source are provided in Table E and Appendix 7.6.

Modeling the radioactively powered lightcurve peak

After fitting the initial cooling peaks in our lightcurves, we use the best-fit parameters to estimate the contribution of the cooling emission to the bolometric lightcurve of each source. We then subtract the cooling component from the bolometric lightcurves obtained from blackbody fitting. The subtracted lightcurves now

Table C: Log of the spectral observations and expansion velocity for few spectral lines in km/s. The phases are measured as the number of rest-frame days since the second peak.

Object	Instrument	Range [Å]	Date	Phase [days]	H I 6563 [km/s]	He I 5876 [km/s]	O I 7774 [km/s]
SN 2021M	P60+SEDM	3500–9220	10 Jan 2021	-7d	18100 ± 4200	–	–
	Keck1+LRIS	3200–10000	12 Jan 2021	-5d	14500 ± 300	11000 ± 1900	–
	Keck1+LRIS	3200–10000	17 Feb 2021	+31d	12400 ± 100	8400 ± 200	3700 ± 300
	Keck1+LRIS	3200–10000	10 May 2021	+113d	–	9100 ± 2700	4700 ± 1600
	Keck1+LRIS	3200–10000	13 Aug 2021	+208d	–	–	2900 ± 900
SN 2020sbw	P200+DBSP	3200–10100	29 Aug 2020	-14d	–	–	–
	P60+SEDM	3500–9220	12 Sep 2020	0d	13400 ± 1000	–	–
	NOT+ALFOSC	3974–9153	14 Sep 2020	+2d	13200 ± 100	7900 ± 100	–
	P60+SEDM	3500–9220	30 Sep 2020	+18d	11400 ± 4100	9300 ± 3200	–
	P60+SEDM	3500–9220	7 Oct 2020	+25d	–	–	–
	NOT+ALFOSC	3974–9153	16 Oct 2020	+34d	13100 ± 200	8900 ± 200	–
	Keck1+LRIS	3200–10000	14 Jan 2021	+124d	–	–	–
SN 2019pof	P60+SEDM	3500–9220	18 Sep 2019	-5d	–	–	–
	P200+DBSP	3200–10100	22 Sep 2019	-1d	15200 ± 600	10400 ± 200	–
	Keck1+LRIS	3200–10000	19 Feb 2020	+149d	–	–	–
SN 2019hvg	P60+SEDM	3500–9220	20 June 2019	-18d	18000 ± 4500	–	–
	P60+SEDM	3500–9220	24 June 2019	-14d	16200 ± 3900	–	–
	P200+DBSP	3200–10100	1 July 2019	-7d	13200 ± 400	9500 ± 400	–
	P60+SEDM	3500–9220	5 July 2019	-3d	12400 ± 900	10100 ± 2100	–
	Keck1+LRIS	3200–10000	19 Feb 2020	+226d	–	–	–
SN 2019ehk	P60+SEDM	3500–9220	8 May 2019	-5d	16500 ± 3200	9900 ± 2300	–
	P200+DBSP	3200–10100	13 May 2019	0d	–	7039 ± 400	–
	Keck1+LRIS	3200–10000	3 June 2019	+21d	–	6100 ± 100	–
	P60+SEDM	3200–10000	9 July 2019	+57d	–	6200 ± 5100	–
	Keck1+LRIS	3200–10000	24 Jan 2020	+256d	–	–	–
SN 2021pb	P60+SEDM	3200–10000	7 Jan 2021	-17d	–	–	–
	Keck1+LRIS	3200–10000	11 Jan 2021	-13d	18400 ± 2900	17900 ± 2900	–
	Keck1+LRIS	3200–10000	17 Feb 2021	+24d	14300 ± 1800	11100 ± 200	9100 ± 800
	Keck1+LRIS	3200–10000	13 May 2021	+109d	–	7900 ± 2900	6100 ± 2000
SN 2018gjx	P60+SEDM	3200–10000	18 Sep 2018	-11d	–	–	–
	NTT+EFOSC2	3200–10000	18 Sep 2018	-11d	–	–	–
	P60+SEDM	3200–10000	12 Oct 2018	+13d	11100 ± 200	8400 ± 200	4000 ± 600
	NOT+ALFOSC	3974–9153	16 Oct 2018	+17d	8300 ± 100	8000 ± 100	3800 ± 100
	Keck1+LRIS	3200–10000	10 Nov 2018	+42d	9400 ± 100	7800 ± 100	4300 ± 100
	TNG+DOLORES	3200–10000	30 Nov 2018	+62d	10500 ± 600	8900 ± 100	7000 ± 400
	Keck1+LRIS	3200–10000	5 Jan 2019	+98d	15100 ± 3400	9300 ± 400	5500 ± 300
	Keck1+LRIS	3200–10000	6 July 2019	+280d	–	–	–
SN 2018jak	Keck1+LRIS	3200–10000	4 Dec 2018	-11d	15800 ± 1700	13700 ± 4600	–
	P60+SEDM	3200–10000	28 Dec 2018	+13d	11000 ± 8400	–	–
	Keck1+LRIS	3200–10000	3 April 2019	+109d	7500 ± 1200	6600 ± 1500	–
SN 2021sjt	Keck1+LRIS	3200–10000	8 July 2021	-14d	10600 ± 1000	–	–
	P60+SEDM	3200–10000	8 July 2021	-14d	–	–	–
	NOT+ALFOSC	3974–9153	8 July 2021	-14d	11600 ± 3300	–	–
	P200+DBSP	3200–10100	10 July 2021	-12d	9900 ± 7600	–	6500 ± 3100
	P60+SEDM	3200–10000	10 July 2021	-12d	–	–	–
	P60+SEDM	3200–10000	13 July 2021	-9d	–	11400 ± 3800	6800 ± 3200
	LT+SPRAT	3200–10000	17 July 2021	-5d	5900 ± 1100	10400 ± 1100	6300 ± 100
	P60+SEDM	3200–10000	24 July 2021	+2d	–	11900 ± 7300	–
	NOT+ALFOSC	3974–9153	28 July 2021	+6d	–	10100 ± 100	5900 ± 200
	P60+SEDM	3200–10000	28 July 2021	+6d	–	12500 ± 3800	7400 ± 2300
	P200+DBSP	3200–10100	7 Aug 2021	+16d	6900 ± 700	–	4300 ± 900
	Keck1+LRIS	3200–10000	12 Aug 2021	+21d	7400 ± 800	7400 ± 200	–
	P60+SEDM	3200–10000	18 Aug 2021	+27d	–	–	–
	P60+SEDM	3200–10000	23 Sep 2021	+63d	–	–	–
	Keck1+LRIS	3200–10000	4 Oct 2021	+74d	–	–	–
	Keck1+LRIS	3200–10000	9 Nov 2021	+110d	–	–	–

correspond to that of the radioactively powered peak. We fit for this peak using two methods. First, we use the analytical model described in Arnett et al. (1989) and Valenti et al. (2008). We attempt to constrain the nickel mass ($M_{\rm Ni}$), characteristic photon diffusion timescale (τ_m) and characteristic γ-ray diffusion timescale (t_o). We use relations from Wheeler et al. (2015) that give the ejecta mass ($M_{\rm ej}$) and kinetic

Table D: Summary of the nebular properties. The phases are measured as the number of rest-frame days since the second peak. We note that the oxygen mass measured here is a lower limit on the oxygen mass in the ejecta. The lower and upper limits of the O mass provided in the 'O mass' column correspond to 4000 K and 3400 K, respectively.

Source	Spectra Tel.+Inst./Phase (days)	Phot. Tel.+Inst./Phase (days)	Phot. mag (mag)	[Ca II]/[O I] flux ratio	[O I] lum. (10^{38} erg s^{-1})	O mass (10^{-2} M$_\odot$)
SN 2019ehk	Keck1+LRIS/256	Keck1+LRIS/280	22.10 ± 0.15	28.58 ± 3.19	1.72 ± 0.17	3.86 – 12.91
SN 2021M	Keck1+LRIS/113	LCOGT 1m/176	21.75 ± 2.19	3.26 ± 1.84	0.15 ± 0.01	0.35 – 1.12
SN 2021M	Keck1+LRIS/208	LCOGT 1m/176	21.75 ± 2.19	4.32 ± 0.22	0.93 ± 0.03	2.25 – 6.58
SN 2020sbw	Keck1+LRIS/124	LCOGT 1m/115	> 20.63	10.37 ± 4.65	< 11.69	< 17.29
SN 2021pb	Keck1+LRIS/109	LCOGT 1m/27	> 20.21	1.73 ± 0.04	< 6.32	< 15.58
SN 2019pof	Keck1+LRIS/149	P48/20	19.02 ± 0.30	32.37 ± 1.47	0.01 ± 0.00	0.04 – 0.10
SN 2018gjx	Keck1+LRIS/102	P60/98	19.61 ± 0.21	2.24 ± 0.51	0.08 ± 0.02	0.16 – 0.64
SN 2019hvg	Keck1+LRIS/226	P48/43	19.35 ± 0.19	3.69 ± 0.48	0.11 ± 0.01	0.25 – 0.79
SN 2018jak	Keck1+LRIS/109	P48/109	> 20.17	1.60 ± 0.13	< 8.57	< 20.78
SN 2021sjt	Keck1+LRIS/110	LCOGT1m/110	19.39 ± 0.20	10.13 ± 0.86	1.15 ± 0.08	2.68 – 8.42

Table E: Summary of the best-fit parameters obtained from shock cooling modeling of the first peak.

ZTF Source	$E_{\rm ext}$ (10^{50}erg)	$R_{\rm ext}$ (R$_\odot$)	$M_{\rm ext}$ (10^{-2} M$_\odot$)	$t_{\rm exp}$ (JD)
SN 2019ehk/ZTF19aatesgp	$3.95^{+0.34}_{-0.32}$	108^{+10}_{-9}	$20.26^{+0.99}_{-0.96}$	$2458602.08^{+0.01}_{-0.01}$
SN 2021M/ZTF21aaabwfu	$7.13^{+1.77}_{-1.91}$	34^{+11}_{-6}	$32.38^{+3.90}_{-4.66}$	$2459213.53^{+0.05}_{-0.02}$
SN 2020sbw/ZTF20abwzqzo	$0.15^{+0.06}_{-0.03}$	2938^{+1103}_{-1334}	$1.68^{+0.34}_{-0.16}$	$2459086.57^{+0.07}_{-0.08}$
SN 2021pb/ZTF21aabxjqr	$4.57^{+0.84}_{-0.71}$	118^{+19}_{-16}	$30.97^{+2.63}_{-2.45}$	$2459218.01^{+0.02}_{-0.01}$
SN 2019pof/ZTF19abxtcio	$0.10^{+0.06}_{-0.03}$	368^{+188}_{-149}	$8.52^{+1.77}_{-1.33}$	$2458730.35^{+0.48}_{-0.25}$
SN 2018gjx/ZTF18abwkrbl	$14.08^{+0.40}_{-0.41}$	47^{+1}_{-1}	$41.00^{+0.86}_{-0.88}$	$2458376.34^{+0.01}_{-0.01}$
SN 2019hvg/ZTF19abacxod	$1.85^{+0.34}_{-0.30}$	121^{+22}_{-18}	$23.36^{+2.05}_{-1.97}$	$2458651.03^{+0.04}_{-0.02}$
SN 2018jak/ZTF18acqxyiq	$9.92^{+0.06}_{-0.12}$	234^{+7}_{-7}	$54.19^{+1.19}_{-1.15}$	$2458442.50^{+0.01}_{-0.01}$
SN 2021sjt/ZTF21abjyiiw	$0.07^{+0.01}_{-0.01}$	1946^{+805}_{-504}	$2.47^{+0.26}_{-0.26}$	$2459400.70^{+0.03}_{-0.01}$

energy in the ejecta ($E_{\rm kin}$) as a function of (τ_m) and photospheric velocity ($v_{\rm ph}$). We obtain $v_{\rm ph}$ measured using the He I line from the photospheric spectra closest to the peak epoch as described in Section 7.3. We also use the lightcurve analytical models from Khatami and Kasen (2019) to derive the explosion parameters. Further details on the model fitting can be found in Appendix B9 in Yao et al. (2020). Table F lists the best-fit parameters. Figures 7.5 and 7.6 show the comparison of the cumulative distribution functions for $M_{\rm Ni}$ and $M_{\rm ej}$ of our sample and the Taddia et al. (2018) sample of Type IIb SNe. A two-sided K-S test of the ejecta mass distribution gives a

Table F: Summary of the best-fit physical parameters obtained by radioactive decay modeling of the second peak of the SNe in our sample. The 'Ar' subscript refers to the Arnett et al. (1989) model while the 'KK' subscript refers to the Khatami and Kasen (2019) model.

Source	$M_{\mathrm{Ni-Ar}}$[6] ($M_\odot$)	$M_{\mathrm{Ni-KK}}$ ($M_\odot$)	$M_{\mathrm{ej-Ar}}$ ($M_\odot$)	$M_{\mathrm{ej-KK}}$ ($M_\odot$)	E_{kin} (10^{51}erg)	t_0 (days)
SN 2019ehk	0.02 – 0.08	0.08	$0.35^{+0.01}_{-0.01}$	0.32	$0.21^{+0.01}_{-0.01}$	$37.79^{+0.98}_{-0.96}$
SN 2021M	0.04 – 0.13	0.14	$1.05^{+0.64}_{-0.54}$	0.79	$0.76^{+0.46}_{-0.39}$	$52.83^{+2.86}_{-2.76}$
SN 2020sbw	0.02 – 0.13	0.14	$0.77^{+0.09}_{-0.07}$	0.57	$0.29^{+0.04}_{-0.03}$	$59.76^{+1.57}_{-1.60}$
SN 2021pb	0.10 – 0.12	0.13	$3.57^{+2.74}_{-0.58}$	2.21	$5.46^{+4.19}_{-0.89}$	$56.84^{+29.20}_{-29.00}$
SN 2019pof	0.01 – 0.03	0.04	$0.77^{+0.37}_{-0.14}$	0.59	$0.46^{+0.22}_{-0.08}$	$40.17^{+1.39}_{-1.44}$
SN 2018gjx	0.04 – 0.05	0.05	$0.20^{+0.02}_{-0.02}$	0.19	$0.08^{+0.00}_{-0.00}$	$59.32^{+1.18}_{-1.13}$
SN 2019hvg	0.02 – 0.13	0.15	$1.15^{+0.08}_{-0.07}$	0.81	$0.56^{+0.04}_{-0.03}$	$47.30^{+3.76}_{-2.90}$
SN 2018jak	0.03 – 0.12	0.11	$0.72^{+0.04}_{-0.04}$	0.62	$0.73^{+0.04}_{-0.04}$	$93.83^{+4.40}_{-6.61}$
SN 2021sjt	0.01 – 0.05	0.05	$1.15^{+0.03}_{-0.03}$	0.83	$0.83^{+0.02}_{-0.02}$	$50.23^{+0.77}_{-0.74}$

p-value < 0.001, thus implying that our sample contains SNe with lower ejecta mass compared to the literature sample of SNe IIb. Our sample indicates that there is an empty phase space with low ejecta mass but high nickel mass and high ejecta mass but low nickel mass (see Figure 7.8). Further analysis on this with a larger sample of Type IIb SNe is left for future work. We plot the lightcurves of the Ca-rich Type IIb SNe sample along with canonical Type IIb SNe from Taddia et al. (2018) in Figure 7.7.

Host Galaxy Spectral Energy Distribution Modeling

We model the spectral energy distributions (SEDs) of the host galaxies with the software package CIGALE (Code Investigating GALaxy Evolution; Burgarella et al. 2005, Noll et al. 2009, Boquien et al. 2019). We use the Chabrier (2003) initial mass function and the Bruzual and Charlot (2003) simple stellar population model to compute the stellar emission. Furthermore, we assume a star-formation history with the following functional form: $t \times \exp(-t/\tau)$, where t is the age of the SFH episode and τ is the e-folding timescale. We fix the CIGALE ionization parameter log U_{ion} as -2. This is used to calculate the nebular emission from the ionized gas in H II regions. We adopt a modified Calzetti et al. (2000a) attenuation curve to model

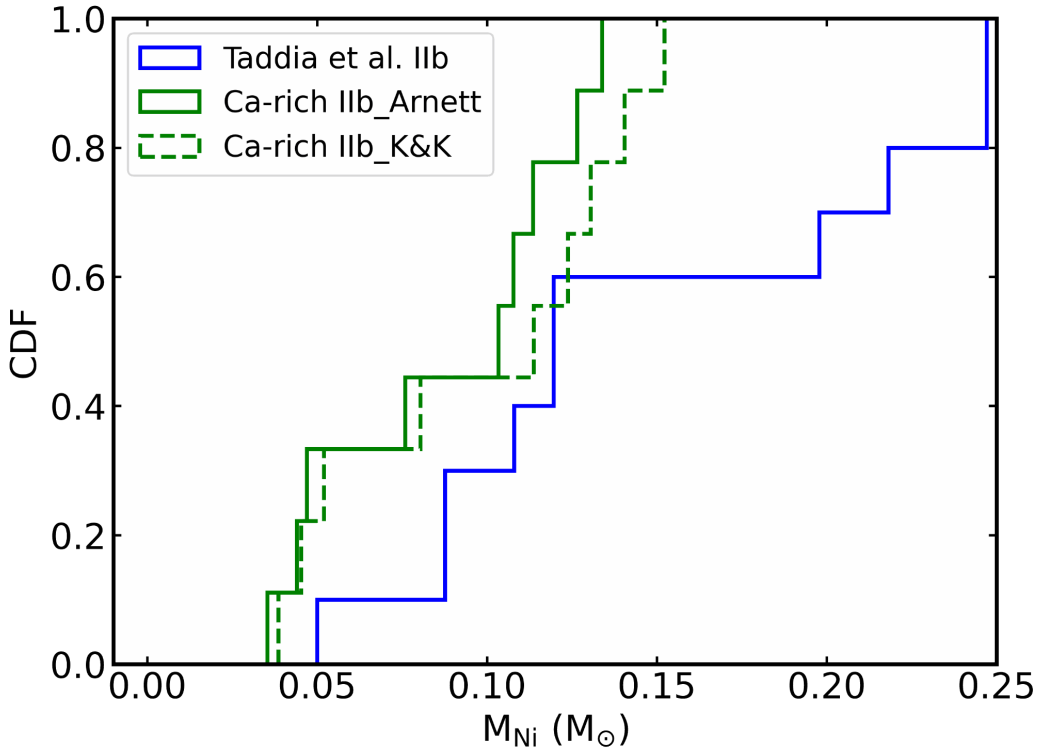

Figure 7.5: ^{56}Ni-mass distribution for our sample of SNe IIb compared to the SN IIb population presented in Taddia et al. (2018).

the dust attenuation. We include dust emission based on the Dale et al. (2014) dust templates. Further details on the different models can be found in Boquien et al. (2019). We generated 24385536 models based on the mentioned configuration, from which we chose the best fit using Bayesian inference. Table I lists the parameters used to generate the models and Table J lists the best-fit parameters for all the host galaxies.

The hosts of all transients were detected in images of the SDSS, Pan-STARRS, and the DESI Imaging Legacy Surveys. Figure 7.9 shows the B-band luminosities of the hosts for our sample. The entire distribution spans a wide range from $M_B \approx -15.7$ mag to $M_B \approx -21.8$ mag. This interval covers the range from $10^{-2}\,L_\star$ to $10\,L_\star$, where $L_\star$ is the knee of the B-band luminosity functions reported in Ilbert et al. (2005), covering the entire parameter space of star-forming galaxies. The majority of the hosts are found in galaxies between a few 10^{-2} and a few $L^\star$. These host properties are identical to hosts of usual CCSNe. This is illustrated by the contours encircling 68, 90 and 95% of the PTF+iPTF CCSN sample (Schulze et al. 2020) that includes 888 objects from all major CCSN classes.

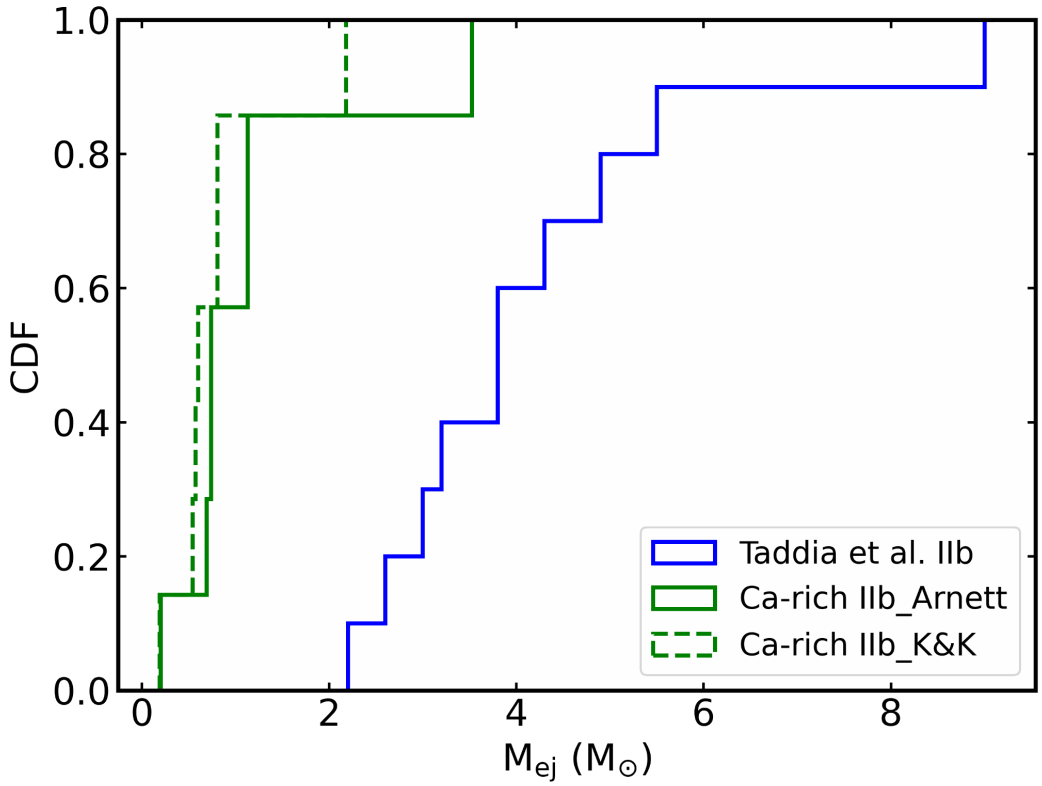

Figure 7.6: Ejecta mass distribution for our sample of SNe IIb compared to the SN IIb population presented in Taddia et al. (2018).

To compare the physical properties of the host galaxies, we present them in the mass-SFR plane (Fig. 7.10). The hosts are located in a narrow region of the parameter space that is occupied by a general population of star-forming galaxies, called the main sequence of star-forming galaxies (indicated by the grey shaded region; Elbaz et al. 2007). A small minority of our SNe occurred in galaxies that lie clearly above the galaxy main sequence and are experiencing a starburst. Like in Figure 7.9, we overlay the 68, 90 and 95% contours of the PTF CCSN host sample. The hosts of regular CCSNe occupy exactly the same parameter space, including the starburst regime (e.g., Taggart and Perley 2021). Most of the host galaxies are actively star-forming, which shows that the core-collapse Ca-rich sample is a different class from the usual Ca-rich sample, which are usually found in the outskirts of quenched galaxies. This is also evident from Figure 7.11, which shows that the projected physical offset distance for Gap Ca-rich thermonuclear transients is systematically higher (p-value = 0.06 for a two-sided K-S test) than that of our Ca-rich Type IIb sample and the general core-collapse population (for the sample presented in De

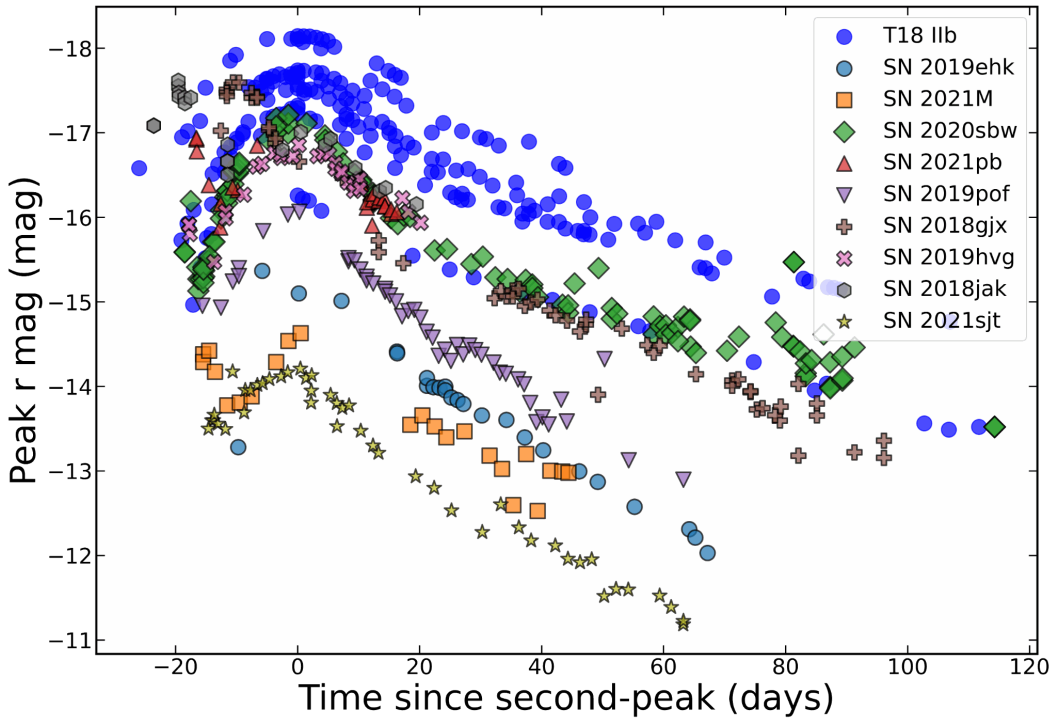

Figure 7.7: Comparison of the lightcurves of the Ca-rich Type IIb SNe in our sample (in filled shapes of different types) with canonical Type IIb SNe lightcurves from Taddia et al. (2018) (in blue circles). The y-axis shows the absolute magnitude (mag), with galactic extinction correction. The x-axis shows the number of rest-frame days since the second peak.

et al. 2020b).

7.4 Discussion

In this paper, we analyze the photometric and spectroscopic properties of the sample of a distinct class of Ca-rich Type IIb SNe. The sources in our sample are all core-collapse and not thermonuclear in origin. This is evident from the presence of photospheric hydrogen in the spectra (see Section 7.3) which suggests $M_H \gtrsim 0.02 - 0.03\ M_\odot$ (Hachinger et al. 2012). The usual Ca-rich Type I events involve CO + He binary WDs progenitors, that are expected to be very deficient in hydrogen ($M_H < 10^{-4} M_\odot$; Podsiadlowski et al. 2003, Zenati et al. 2019). Hence, the formation pathway of our sample is distinct from the thermonuclear Ca-rich gap transients found in old environments. The host galaxy properties described in Section 7.3 are also consistent with that of the core-collapse population exploding in star-forming galaxies. The observed photospheric velocities, which are consistent with canonical stripped-envelop SNe, also rules out the fallback SNe scenario which have an

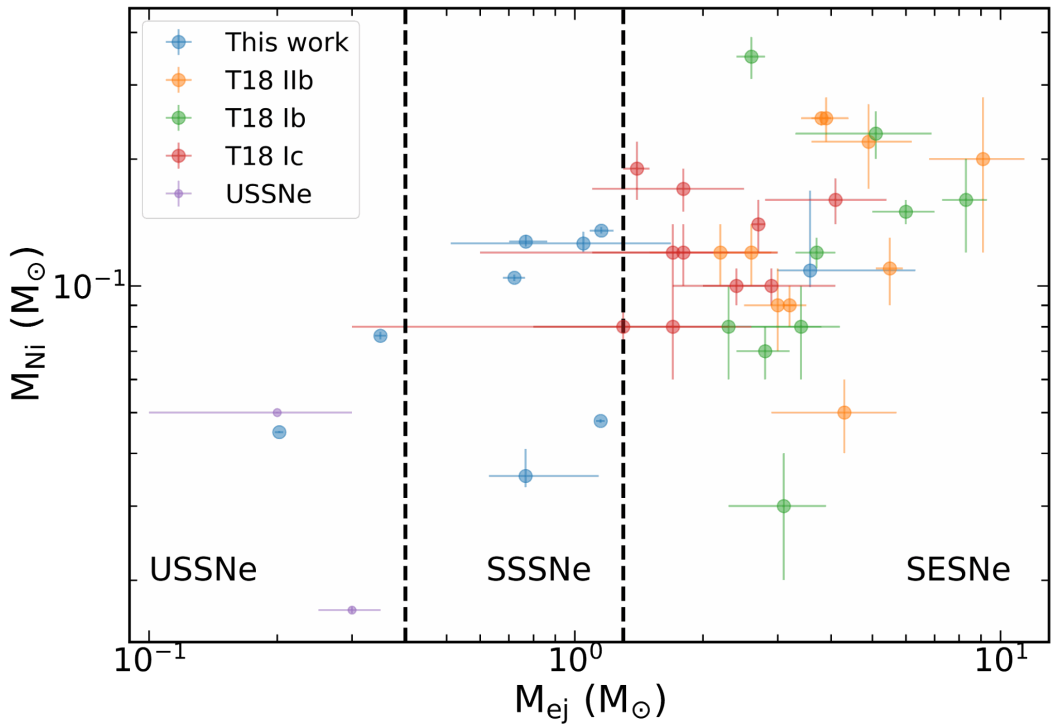

Figure 7.8: Comparison of the ^{56}Ni-mass and the ejecta mass based on the Arnett fit for our sample and usual stripped-envelope Type IIb SNe from Taddia et al. (2018) and USSNe from De et al. (2018a), Yao et al. (2020). We find that the SSSNe in our sample is a transient class between the USSNe and the usual stripped-envelope SNe (SESNe) (rough boundaries indicated by the vertical dashed lined). We also note that there is a region in the parameter-space which is unoccupied by the SESN population.

expected velocity of ~ 3000 km s^{-1} (Moriya et al. 2010). In this section, we discuss the constraints on the progenitors and implications on the progenitor channels for this class.

Constraints on progenitor mass

Constraining progenitor mass using nebular spectra

For all the SNe in our sample, we have at least one nebular spectrum obtained using the Low Resolution Imaging Spectrograph (LRIS) on the Keck I telescope. We calculate the [Ca II]/[O I] flux ratio and the [O I] luminosity using the procedure described in Section 7.3 (see Table D). Next, we use the measured [O I] luminosity to calculate the oxygen abundance and subsequently the progenitor mass. We use the following analytical relation provided in Uomoto (1986) to calculate the minimum O mass required for a given [O I] luminosity: $M_{\rm O}$ =

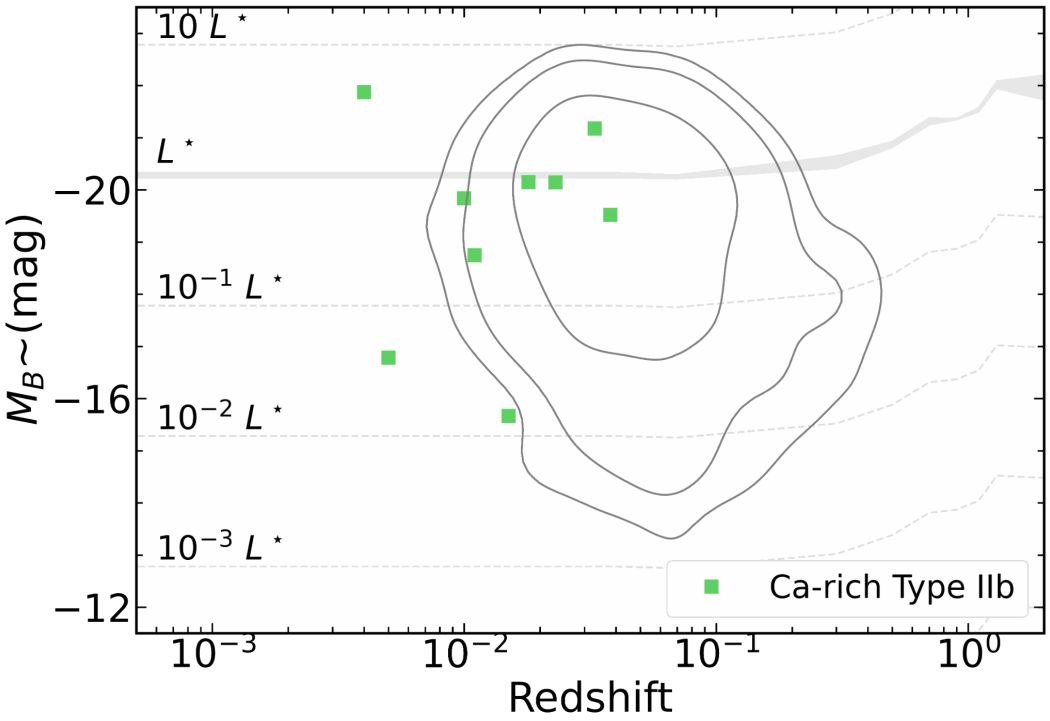

Figure 7.9: The absolute B-band magnitude of CCSN host galaxies as a function of redshift. Our hosts are found in the least-luminous (10^{-3} $L^\star$) to the most luminous star-forming galaxies ($\lesssim$ 5 $L^\star$) ($L^\star$ is the characteristic luminosity of the B-band luminosity function of star-forming galaxies). Most Ca-rich IIb hosts have luminosities of 10^{-2} to a few $L^\star$, similar to regular CCSNe (indicated by the contours encircling 68, 90 and 95% of the PTF+iPTF CCSN sample Schulze et al. 2020). We also indicate the $L^\star$ presented in Faber et al. (2007) and multiples of it with gray.

10^8 (L[O I]/$4\pi D^2_{cm}$) D^2_{Mpc} exp(2.28/T(10^4K)) $M_\odot$, where L[O I] is the luminosity in erg/s of [O I] $\lambda\lambda$6300, 6364. The analytical formula is valid in the high density limit where the electron density is above the [O I] critical density ($\sim 7 \times 10^5 cm^{-3}$), and is estimated to hold in our case for estimated ejecta mass in the range of 0.5 – 2 $M_\odot$. We use typical temperature values estimated from the [O I] emission in other core-collapse SNe of $\approx$ 3500 – 4000 K (Sollerman et al. 1998, Elmhamdi 2011) to get lower limits on the O mass in the range of $\approx$ 0.005 – 0.1 $M_\odot$. The lower and upper limits of the O mass provided in Table D correspond to 4000 K and 3400 K, respectively.

We compare the observed [O I] luminosity and measured oxygen mass lower limits with theoretical models to constrain the progenitor mass. Jerkstrand et al. (2015a) presented the dependence of [O I] luminosity with progenitor mass using detailed nebular phase models of stripped-envelope SNe (see Figure 7.12). We see that the

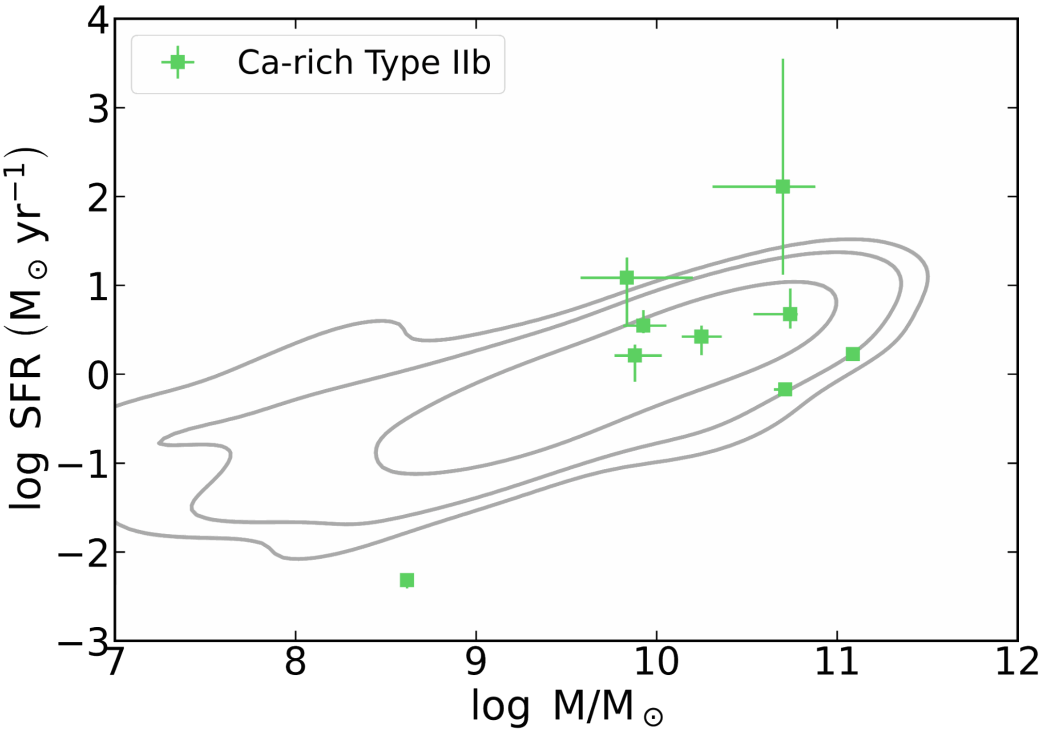

Figure 7.10: The host population in the mass-SFR plane. All sources exploded in star-forming galaxies. This is illustrated by their location with respect to the main sequence of star-forming galaxies (grey-shaded region). The majority of hosts also have properties consistent with those of CCSNe from the PTF+iPTF surveys (grey contours indicate the region encircling 68, 90 and 95% of the sample Schulze et al. 2020)

.

nebular models of progenitors with mass > 12 $M_\odot$ consistently overestimate the [O I] luminosity. This suggests a much lower progenitor core mass for our sample. In Figure 7.13, we plot model tracks showing the steep dependence of O mass on the initial ZAMS mass obtained from canonical core-collapse nebular models (taken from Nomoto et al. 1997, Rauscher et al. 2002, Limongi and Chieffi 2003). We consistently find that the ZAMS mass required to explain the observed O mass lower limits of our sample can be less than 12 $M_\odot$.

Dessart et al. (2021a) presented a set of 1D non-local thermodynamic equilibrium radiative transfer calculations for nebular-phase stripped SNe. In models from He stars with an initial mass >6 $M_\odot$, they find that the [O I] line strength is of comparable or greater strength than [Ca II] lines. The initial helium star mass reflects the mass of the helium core at the time of central helium ignition. In contrast, they show that models from lower mass He stars exhibit a weak [O I], strong [Ca II]. The

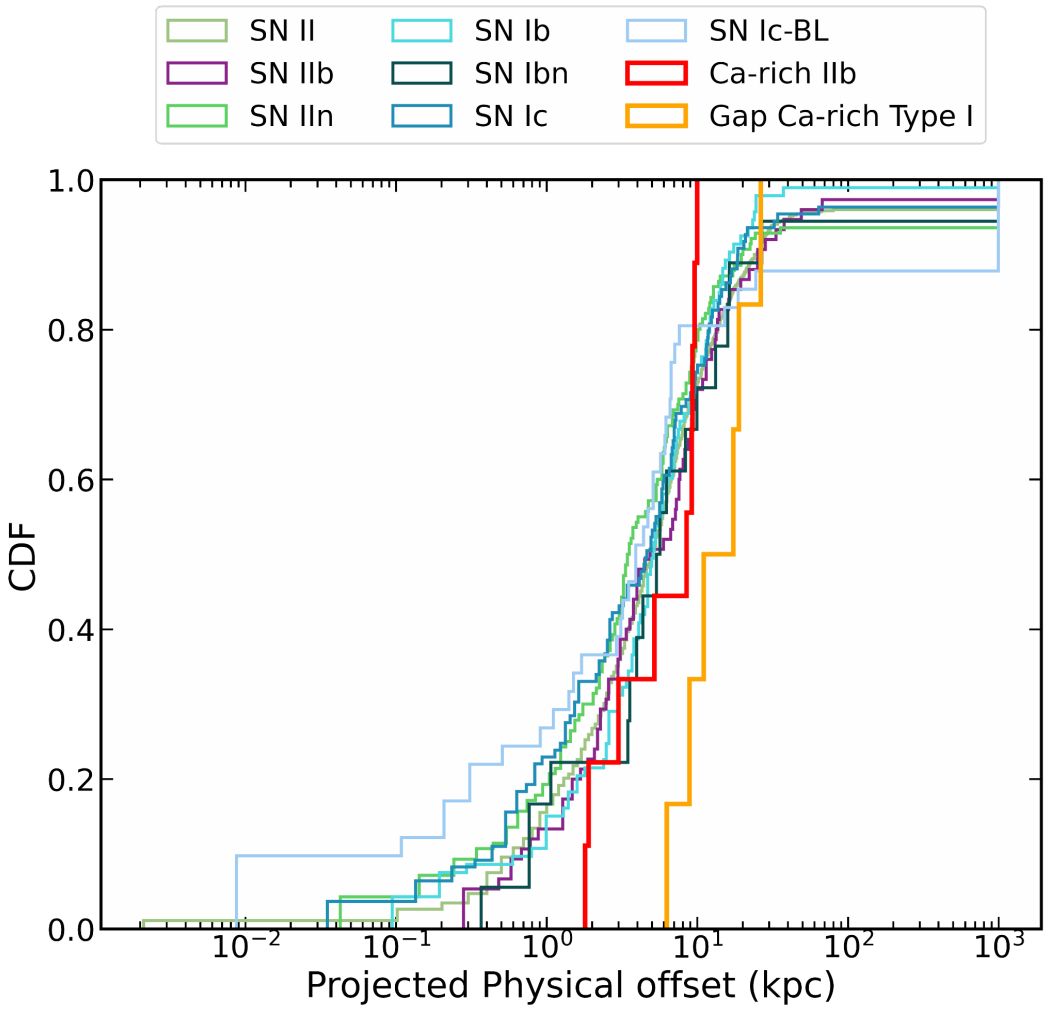

Figure 7.11: The projected physical offset distribution of all the SNe in our sample compared with the distribution for other types of SNe measured in De et al. (2020b). We note that there is a distinct offset from the Gap Ca-rich Type I SNe, known to occur in quenched environments.

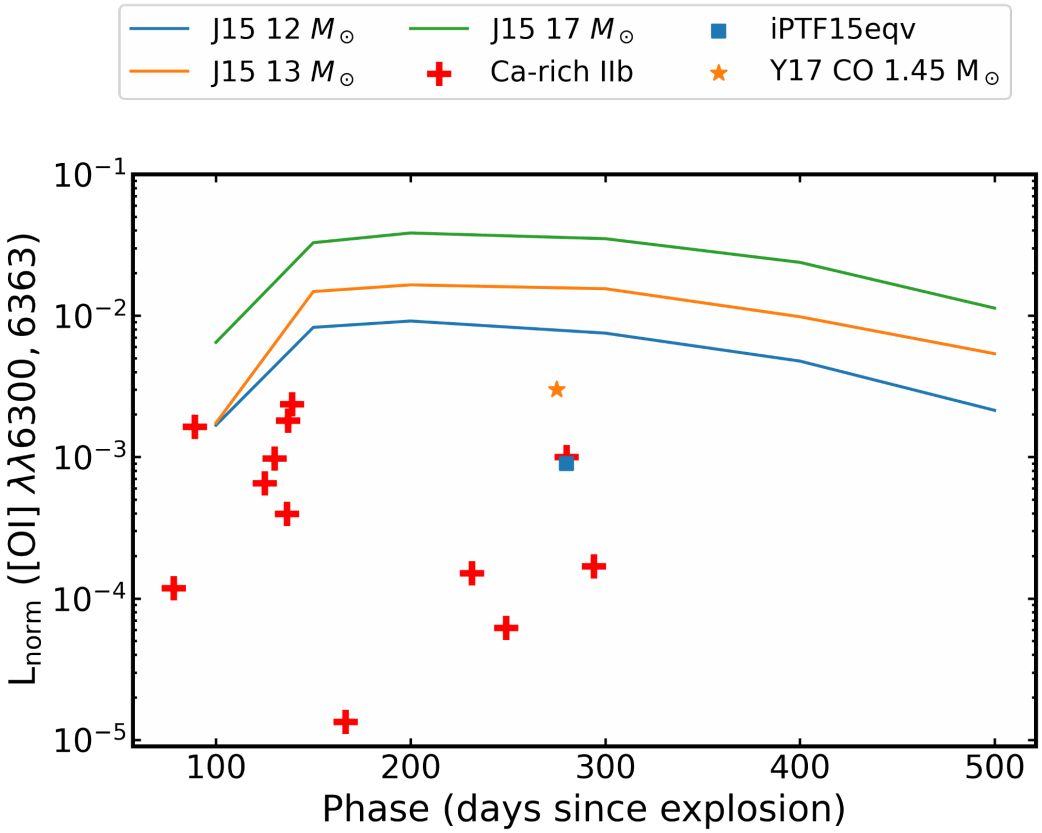

Figure 7.12: The red crosses shows the [O I] luminosities calculated from the nebular spectra for the Ca-rich Type IIb sample. The luminosity is normalized to the ^{56}Co decay energy. We compare these to models of stripped envelope core-collapse SNe from Jerkstrand et al. (2015a). We also show the measured normalized [O I] luminosities from the nucleosynthesis calculations of Yoshida et al. (2017) and the Ca-rich IIb iPTF 15eqv.

high [Ca II]/[O I] flux ratio we observe for our sample is thus consistent with low initial He-star mass. Figure 7.13 compares the measured O mass lower limits for our sample with the synthesized O mass from the He-star progenitor models which assume an evolution in a binary system (Dessart et al. 2021a) and with those arising from single-star models (Sukhbold et al. 2016). In both the binary and single star systems, core collapse is reached with a residual H-rich envelope. Again, we find that the observed oxygen yield is consistent with the lowest ZAMS mass (< 12 M$_\odot$) models for stripped He stars with initial mass less than ~ 3 M$_\odot$. We use the relations in Woosley and Heger (2015) to get the ZAMS mass from the initial He-star mass.

To compare with such low ZAMS masses, we use estimates of the O synthesized for the case of the highly stripped He cores of ultra-stripped SNe. These are modeled

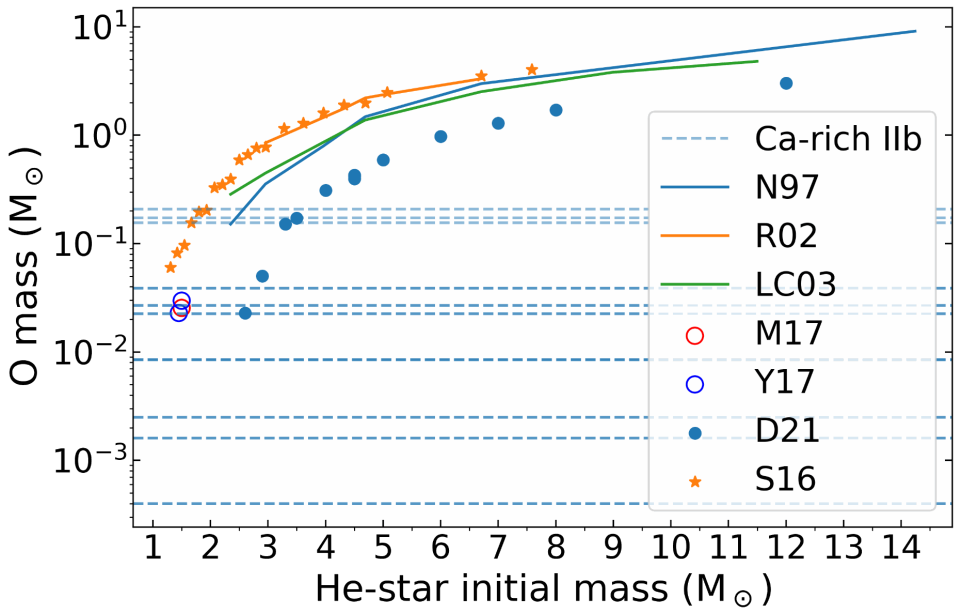

Figure 7.13: The measured O mass lower limits are shown with the horizontal dashed lines. The O yield for the ejecta arising from the He-star progenitor models, which assume an evolution in a binary system (Dessart et al. 2021a) are shown in solid blue dots and those arising from the single-star models (Sukhbold et al. 2016) are shown in filled orange stars. We also plot the O mass for nucleosynthetic models of higher ZAMS stars (Nomoto et al. 1997, Rauscher et al. 2002, Limongi and Chieffi 2003) and for lower ZAMS stars from USSNe models of Yoshida et al. (2017) and Moriya et al. (2017).

as relatively low-mass He stars ($< 3.5\ M_{\odot}$), that are stripped down by a close binary companion, leaving behind CO cores of $\approx 1.45{-}1.6\ M_{\odot}$ at the time of explosion (Tauris et al. 2015). We note that the CO core mass is a good tracer of the progenitor ZAMS as it is insensitive to the binary stripping that occurs in the very late stages of stellar evolution (Fransson and Chevalier 1989, Jerkstrand et al. 2014a, 2015a). We find that the O-yields for such strongly-stripped stars with low CO-core mass are comparable to the low O-yield of sources in our sample (see Figures 7.12 and 7.13).

We caution that we assume that the radioactive power deposited in the O rich shells of the ejecta is released via cooling in the [O I] lines. We note that this is dependent on the presence of impurity species, e.g., Dessart and Hillier (2020) showed that even a small amount of Ca mixed into O-rich regions can dramatically weaken the cooling by [O I]. However, it has been shown that mixing is not significant for core-collapse

SNe. Detailed modeling of core-collapse SNe has shown that [OI] emission arises from the outer O-rich layers produced during the hydrostatic burning phase, while the [Ca II] line is the primary coolant in the Si-rich layers (Jerkstrand et al. 2015a, Dessart and Hillier 2020). Also, Polin et al. (2021) show that pollution of ^{40}Ca even at the 1% level will cause a nebular region to completely cool through [Ca II] emission suggesting that if these ejecta regions were mixed it would be difficult to see any contribution from [O I].

Constraining progenitor mass using lightcurves

We fit the double-peaked lightcurves of the SNe sample using the Piro et al. (2021) and Arnett et al. (1989) models as described in Section 7.3. The best fit parameters of the shock-cooling breakout peak and the radioactive-powered peak such as $M_{\rm Ni}, M_{\rm ej}, E_{\rm kin}, R_{\rm env}$ are tabulated in Tables E and F.

In order to constrain the progenitor properties, we plot the evolutionary track of the predicted ejecta properties as a function of He-star initial mass or initial ZAMS mass from Dessart et al. (2021a). They use He-star models of Woosley (2019) with initial He-star masses spanning the range from 2.6 $M_\odot$ to 13 $M_\odot$ that were evolved to the onset of core collapse. The ejecta properties shown by the solid dots in Figure 7.14 are obtained after performing nebular-phase NLTE steady-state and time-dependent radiative transfer calculations based on prescribed He-star explosion models of Ertl et al. (2020). Depending on the adopted pre-SN mass loss recipe, they give rise to ejecta masses between 0.79 $M_\odot$ and 5.32 $M_\odot$. The ejecta mass values we obtain are consistent with those predicted for the lower end of the He-star mass stars ($<$ 12 $M_\odot$). They report that the lower mass progenitors with initial He-star mass of $\approx$ 2.6 $M_\odot$, calibration to the Crab and realistic 10 $M_\odot$ single star simulations implies an explosion energy of $\sim 10^{51}$ erg. It can be seen from Figure 7.14 that the kinetic energy of our sample is consistently lower than that predicted for ZAMS stars of $\sim$ 12 $M_\odot$. We note that most SNe in our sample have low ejecta mass while having high Ni mass. This could be due to enhanced mass loss rate of the pre SN He star. Dessart et al. (2021a) found that there is a systematic increase in the ^{56}Ni production by a few factors depending on the mass loss rate and the initial mass. The high Ni mass makes an electron-capture core-collapse scenario unlikely as simulations consistently predict an upper limit of $\sim 10^{-2}$ $M_\odot$, that are an order of magnitude lower than those observed for our sample.

It is has been shown from simulations that progenitors of stripped-envelope SNe

with initial masses below 10 $M_{\odot}$ expand to large radii (up to 100 $R_{\odot}$), while more massive progenitors stay compact (e.g., Laplace et al. 2020). Only progenitors with low initial masses in the 8−9 $M_{\odot}$ range can swell enough for renewed interaction with their companion. This is consistent with the envelope radii of our sample, with values lying in the 100−1000 $R_{\odot}$ range. The extent of expansion of a stripped star is critical to understand their fate as the progenitors of core collapse supernovae. The large radii of stripped stars imply that they can potentially fill their Roche lobe again and undergo another phase of mass transfer (Dewi et al. 2002, Dewi and Pols 2003). Additional phases of mass transfer can produce stars with very low envelope masses, possibly explaining the low ejecta mass we observe for our sample.

Strongly stripped-envelope SNe

As discussed in Section 7.4, the ejecta masses observed are consistent with theoretical predictions for stripped He stars with initial mass less than 3 $M_{\odot}$. These occur in tight binaries where a helium star transfers mass to a small companion. The core-collapse of such stellar cores with a small envelope gives rise to low ejecta mass explosions. One way to form such progenitor stars in the stellar evolution theory is through the USSN scenario (Tauris et al. 2013, 2015). These explosions are one of two channels to form double neutron star (DNS) binaries that are compact enough to merge within a Hubble time due to gravitational wave (GW) radiation.

Nakaoka et al. (2021) suggested that the Ca-rich IIb SN 2019ehk originated in an ultra-stripped core-collapse SN. Low-mass progenitors of stripped core-collapse SNe can retain a range of H and He masses depending on the nature of the companion and the initial binary period (Yoon et al. 2010b, Zapartas et al. 2017, Laplace et al. 2020). Presence of hydrogen represents a less extreme case of a 'strongly stripped SN' (ejecta mass $\approx$ 0.6 $M_{\odot}$) from a low mass (ZAMS $\approx$ 9–12 $M_{\odot}$) progenitor, that lost nearly all of its H envelope to stripping in a relatively compact orbit (orbital period $\sim$ 10 days). This is a transition class between the USSNe and the usual SESNe (see Figure 7.8). The progenitor could be stripped by a main sequence companion and resulted in the formation of a compact neutron star – main sequence binary. Such binaries have been suggested to be progenitors of neutron star – white dwarf systems that could merge within a Hubble time, and be detectable with LISA (Toonen et al. 2018).

We compare our estimates of the O yields with that predicted for ultra-stripped SNe (Tauris et al. 2013). We use the nucleosynthetic yields from Moriya et al. (2017),

Yoshida et al. (2017) to estimate the [O I] luminosity in the nebular phase for low-mass CO cores of 1.45−−1.5 $M_\odot$, under different assumptions of the explosion energy and ejecta mass. Figure 7.12 shows that the upper limits on the [O I] luminosity for the low-mass CO core models are similar to the low [O I] luminosity measured for our sample. Also, we find that the O masses estimated in the context of ultra-stripped SNe are consistent with the range estimated for our sample (see Section 7.4),

Ca-rich spectra strengthens the case for a strongly-stripped envelope scenario. Explosion of low-mass He-star progenitors can explain the dominance of Calcium emissions over the oxygen emissions (i.e., deficiency in the oxygen emissions) in the nebular spectra (Kawabata et al. 2010, Maeda et al. 2007, Fang et al. 2019). Also, the rapid evolution seen for our sample is a natural consequence from such a scenario. Such low-mass progenitor explosions are a boundary between the SN explosion (either by a Fe-core collapse or ONeMg-core electron capture) and WD formation, and predicts small ejecta mass, i.e., < 0.5 $M_\odot$ (Tauris et al. 2013, Moriya et al. 2017). These features are consistent with the observational properties of the Ca-rich Type IIb transients.

Thus, we conclude that the ejecta properties of our sample are generally consistent with the expectations for a low-mass (< 2 $M_\odot$) He (or C+O) star explosion corresponding to ZAMS mass of $8 - 12$ $M_\odot$, which defines a boundary between the CCSN explosion and a WD formation. Assuming a residual H mass of ~ 0.1 $M_\odot$, the inferred ejecta mass of our sample of <0.6 $M_\odot$ is consistent with a final CO core mass of $\approx 1.45 - 1.5$ $M_\odot$that collapses to form a ≈ 1.3 $M_\odot$neutron star and ejects ≈ 0.5 $M_\odot$of material. The inferred ejecta mass points to a class of SSSNe that are potential progenitors of NS − WD systems.

Rate estimation

For this work, since all our sources were detected in the BTS survey, we follow the rate estimation analysis adopted by Perley et al. (2020). We discuss the procedure in brief below.

In the case of an ideal survey that is able to scan the entire sky to a given magnitude limit m_{lim}, the volumetric rate can be estimated using

$$R = \frac{1}{t}\sum_{i=1}^{N}\frac{1}{(\frac{4\pi}{3}D^3_{max,i})}, \tag{7.1}$$

where t is the duration of the survey, $D_{max,i}$ is the distance out to which the ith transient can be detected above m_{lim} at peak light in the absence of extinction, given its peak absolute magnitude M_i. However, for practical surveys, there are multiple loss factors one needs to take into account. For this work, we follow the revised equation adopted by Perley et al. (2020):

$$R = \frac{1}{t} \sum_{i=1}^{N} \frac{1}{(\frac{4\pi}{3} D^3_{max,i}) f_{sky} f_{ext} f_{rec} f_{cl,i}}. \tag{7.2}$$

The description of the loss factors and their values used are listed below.

- f_{sky} is the average active survey footprint expressed as a fraction of the full sky. We use $f_{sky} = 0.35$, based on the average active area of the BTS survey of ~ 14400 deg^2.
- f_{ext} is the average reduction in effective survey volume owing to Galactic extinction. We use $f_{ext} = 0.82$, calculated by averaging the reduction in volume associated with the extinction toward each separate ZTF field. We do not correct for host-galaxy extinction.
- f_{rec} is the average recovery efficiency for a detectable transient within the survey footprint: the probability that it is found and included in the sample. We use $f_{rec} = 0.60$. This was measured by calculating the fraction of all events classified as SNe Ia that passed the quality cuts of the ZTF survey.
- $f_{cl,i}$ is the classification efficiency, which may depend on apparent magnitude. We use $f_{cl} = 1.0$ if m < 17.2 mag and $f_{cl} = 0.9$ at m $= 18.5$ mag, with a linear decline in between.

Refer to Perley et al. (2020) for further details on the calculation of the loss parameters. The sample as presented in this paper spans $t = 3.5$ yr of ZTF. We had around 94 sources classified as Type IIb as part of BTS and CLU surveys, out of which we have good quality nebular spectra for 29 Type IIb sources. We use $H_0 = 70$ kms^{-1}Mpc^{-1}. Based on these assumptions and the analysis adopted by Perley et al. (2020), we get a rate of $(5.1^{+6.6}_{-4.5}) \times 10^3$ Gpc^{-3}yr^{-1}. This is $\approx 6^{+12}_{-5}$% of CCSNe and $\approx 22^{+25}_{-19}$% of SNIa assuming a CCSNe rate of $(7.7^{+6.6}_{-4.5}) \times 10^4$ Gpc^{-3}yr^{-1} and SNIa rate of $(2.35 \pm 0.24) \times 10^4$ Gpc^{-3}yr^{-1} calculated using the same procedure. As per present classifications, this is $\approx 22 \pm 6$% of all SESNe and $\approx 44 \pm 31$% of

Type IIb SNe. We note that the rates are based on the present classification status. Also, since these events have low luminosity and are low in number, the associated errors are high. We leave a more accurate rate estimate using a larger sample size and more complete nebular follow-up for future work.

NS-WD merger rates are predicted to be in the range of 3-15% of Type Ia supernova rate (Toonen et al. 2018). The corresponding rates are consistent with that obtained for the Ca-rich Type IIb sample within the large errors, at the low end of the relative rate estimate. Also, the delay time distribution suggests that these mergers are most likely to be found in star-forming galaxies, consistent with the host galaxy properties of our sample.

7.5 Conclusion

We examined the various photometric and spectroscopic properties of the objects in our sample of Ca-rich Type IIb SNe. We find that the observed properties of our sample suggest a class of Strongly-stripped SNe (SSSNe) that form a transition class between the usual Stripped-Envelope SNe (SESNe) and Ultra-Stripped SNe (USSNe) groups. The key takeaways of the paper are:

1. SSSNe are a class of core-collapse SNe which have ejecta mass less than ~ 1 $M_\odot$ but show hydrogen in the ejecta. They have been classified as Type IIb SNe based on the photospheric spectra. The SNe in our sample also shows a high [Ca II]/[O I] flux ratio (≥ 2) in the nebular spectra. Observed properties suggest that the progenitor could be stripped by a main sequence companion and may result in the formation of a compact neutron star – main sequence binary. Such binaries have been suggested to be progenitors of neutron star – white dwarf systems that could merge within a Hubble time, and be detectable with LISA.

2. The ejecta and spectroscopic properties of the class are generally consistent with the expectations for a low-mass ($< 3M_\odot$) He star explosion corresponding to a ZAMS mass less than 12 $M_\odot$. From the low [O I] $\lambda\lambda$6300, 6364 luminosity in the nebular phase spectra, we find that the estimated progenitor oxygen mass lower limits for our sample is in the range $\approx 0.005 - 0.1$ $M_\odot$. For core-collapse SNe models to reproduce our inferred oxygen mass, we infer that the ZAMS mass is less than 12 $M_\odot$. Other measured properties such as the [Ca II]/[O I] ratio, ejecta mass, kinetic energy, envelope radius are also consistent with the $8 - 12$ $M_\odot$ progenitor mass scenario.

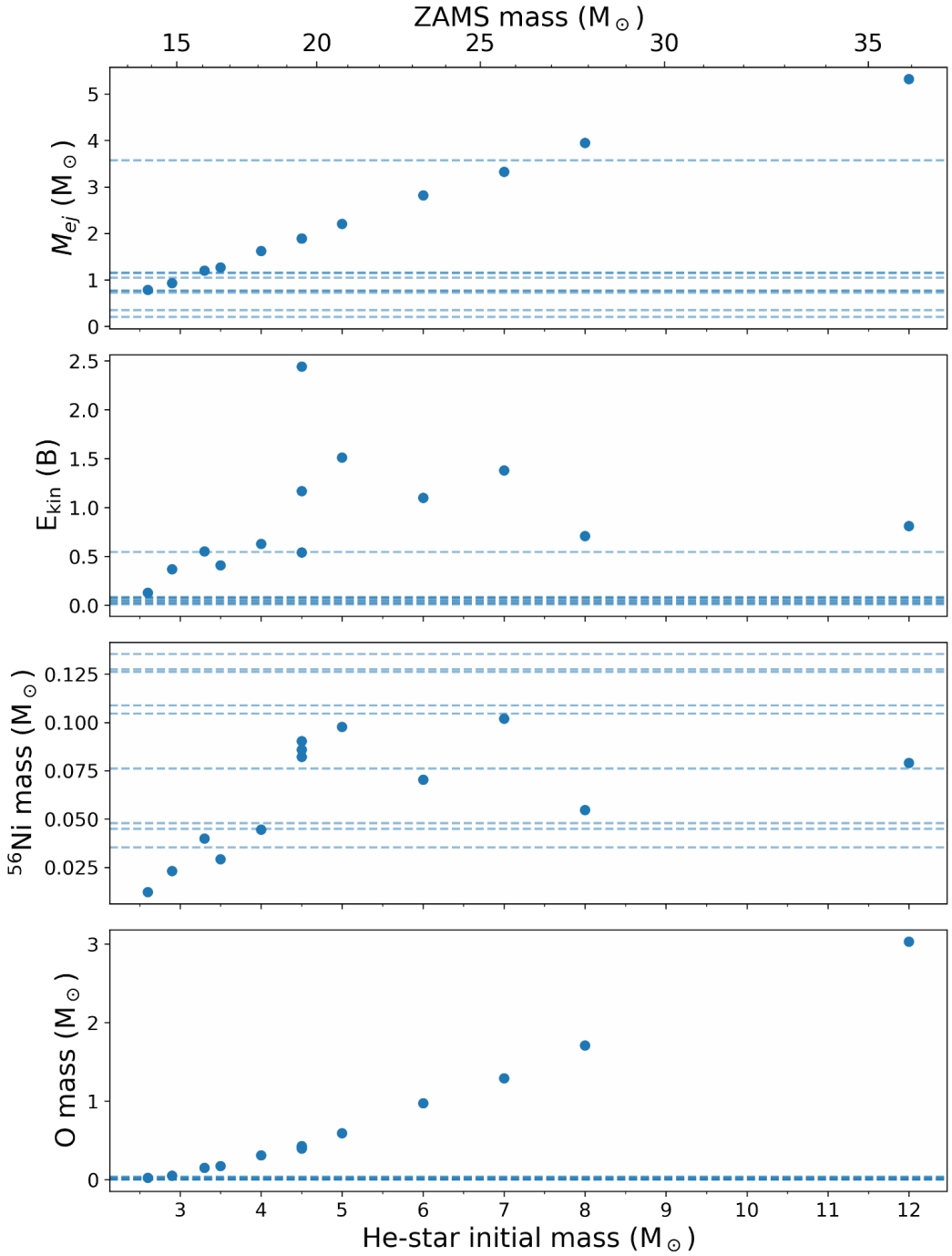

Figure 7.14: Comparison of the ejecta properties we observe (horizontal dashed lines) for our sample with that for the explosion models based on He stars evolved with the nominal mass-loss rate from Dessart et al. (2021a) (solid dots). From top to bottom, we show the ejecta mass $M_{\rm ej}$, ejecta kinetic energy $E_{\rm kin}$, the ^{56}Ni-mass, and the oxygen yield.

3. The presence of photospheric hydrogen suggests $M_H \gtrsim 0.02 - 0.03\ M_\odot$ (Hachinger et al. 2012). The proposed explosion mechanism for the usual Ca-rich Type I events involves CO + He binary WDs progenitors. However they are expected to be very deficient in hydrogen ($M_H < 10^{-4} M_\odot$). Also, the host galaxies of the SSSN class are consistent with star-forming galaxies as they lie in the galaxy main sequence of the mass-SFR plane and have a luminosity range consistent with the hosts for the general Type IIb SN population. Hence, our sample is distinct from the thermonuclear Ca-rich gap transients found in old environments.

Thus, we present a class of SNe that lie in the low mass end of CCSNe and are a transition class between USSNe and the usual SESNe. Observational constraints for such low mass He stars are missing in the literature. This sample provides an opportunity to understand the low mass He star evolution, the extent of binary stripping, and would help in developing theoretical models including nebular spectra for this low mass range. Discovery and follow-up of more members of this class will help obtain a stricter constraint on the rates of these events.

7.6 Data availability

All the photometric and spectroscopic data used in this work can be found here.

The optical photometry and spectroscopy will also be made public through WISeREP, the Weizmann Interactive Supernova Data Repository (Yaron and Gal-Yam 2012a).

Acknowledgements

We thank Adam Burrows for valuable comments on the manuscript. We thank the anonymous referee for their valuable comments that significantly improved the quality of the paper. Based on observations obtained with the Samuel Oschin Telescope 48-inch and the 60-inch Telescope at the Palomar Observatory as part of the Zwicky Transient Facility project. ZTF is supported by the National Science Foundation under Grant No. AST-2034437 and a collaboration including Caltech, IPAC, the Weizmann Institute of Science, the Oskar Klein Center at Stockholm University, the University of Maryland, Deutsches Elektronen-Synchrotron and Humboldt University, the TANGO Consortium of Taiwan, the University of Wisconsin at Milwaukee, Trinity College Dublin, Lawrence Livermore National Laboratories, IN2P3, France, the University of Warwick, the University of Bochum, and Northwestern University.

Operations are conducted by COO, IPAC, and UW.

SED Machine is based upon work supported by the National Science Foundation under Grant No. 1106171.

The ZTF forced-photometry service was funded under the Heising-Simons Foundation grant #12540303 (PI: Graham).

The GROWTH Marshal was supported by the GROWTH project funded by the National Science Foundation under Grant No 1545949.

The data presented here were obtained in part with ALFOSC, which is provided by the Instituto de Astrofisica de Andalucia (IAA) under a joint agreement with the University of Copenhagen and NOT.

The Liverpool Telescope is operated on the island of La Palma by Liverpool John Moores University in the Spanish Observatorio del Roque de los Muchachos of the Instituto de Astrofisica de Canarias with financial support from the UK Science and Technology Facilities Council. Based on observations made with the Italian Telescopio Nazionale Galileo (TNG) operated on the island of La Palma by the Fundación Galileo Galilei of the INAF (Istituto Nazionale di Astrofisica) at the Spanish Observatorio del Roque de los Muchachos of the Instituto de Astrofisica de Canarias.

The W. M. Keck Observatory is operated as a scientific partnership among the California Institute of Technology, the University of California and the National Aeronautics and Space Administration. The Observatory was made possible by the generous financial support of the W. M. Keck Foundation. The authors wish to recognize and acknowledge the very significant cultural role and reverence that the summit of Maunakea has always had within the indigenous Hawaiian community. We are most fortunate to have the opportunity to conduct observations from this mountain. The `ztfquery` code was funded by the European Research Council (ERC) under the European Union's Horizon 2020 research and innovation programme (grant agreement $n°759194-$ USNAC, PI: Rigault).

S. Schulze acknowledges support from the G.R.E.A.T research environment, funded by *Vetenskapsrådet*, the Swedish Research Council, project number 2016-06012.

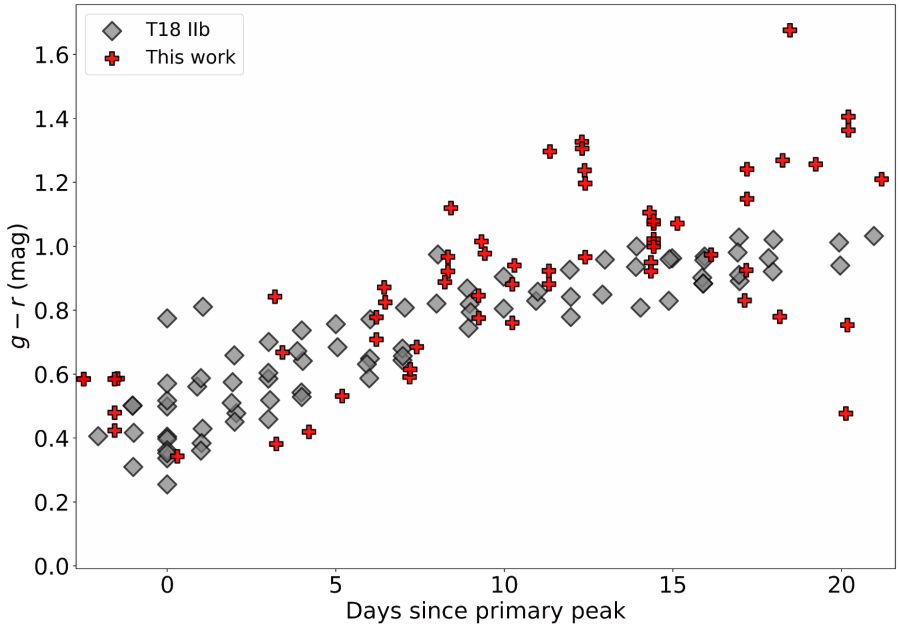

Figure 7.15: The $g - r$ color evolution of the SNe in our sample represented by red crosses compared to the Type IIb SNe sample of Taddia et al. (2018) in gray diamonds.

Appendix

Nebular Spectra

The full-wavelength range nebular spectra are shown in Figure 7.16. The phase of the spectra is measured as the number of rest-frame days since the second peak.

Lightcurve Modeling fits

Figure 7.17 shows a collage of the best-fit lightcurves for the shock cooling model (Piro et al. 2021) fits to the multi-band photometry data. Figure 7.18 shows a collage of the best-fit lightcurves for the radioactive peak model (Arnett et al. 1989) fits to the bolometric luminosity data.

Photometry and spectroscopy data

All the photometry and spectroscopy data are provided as machine-readable tables here.

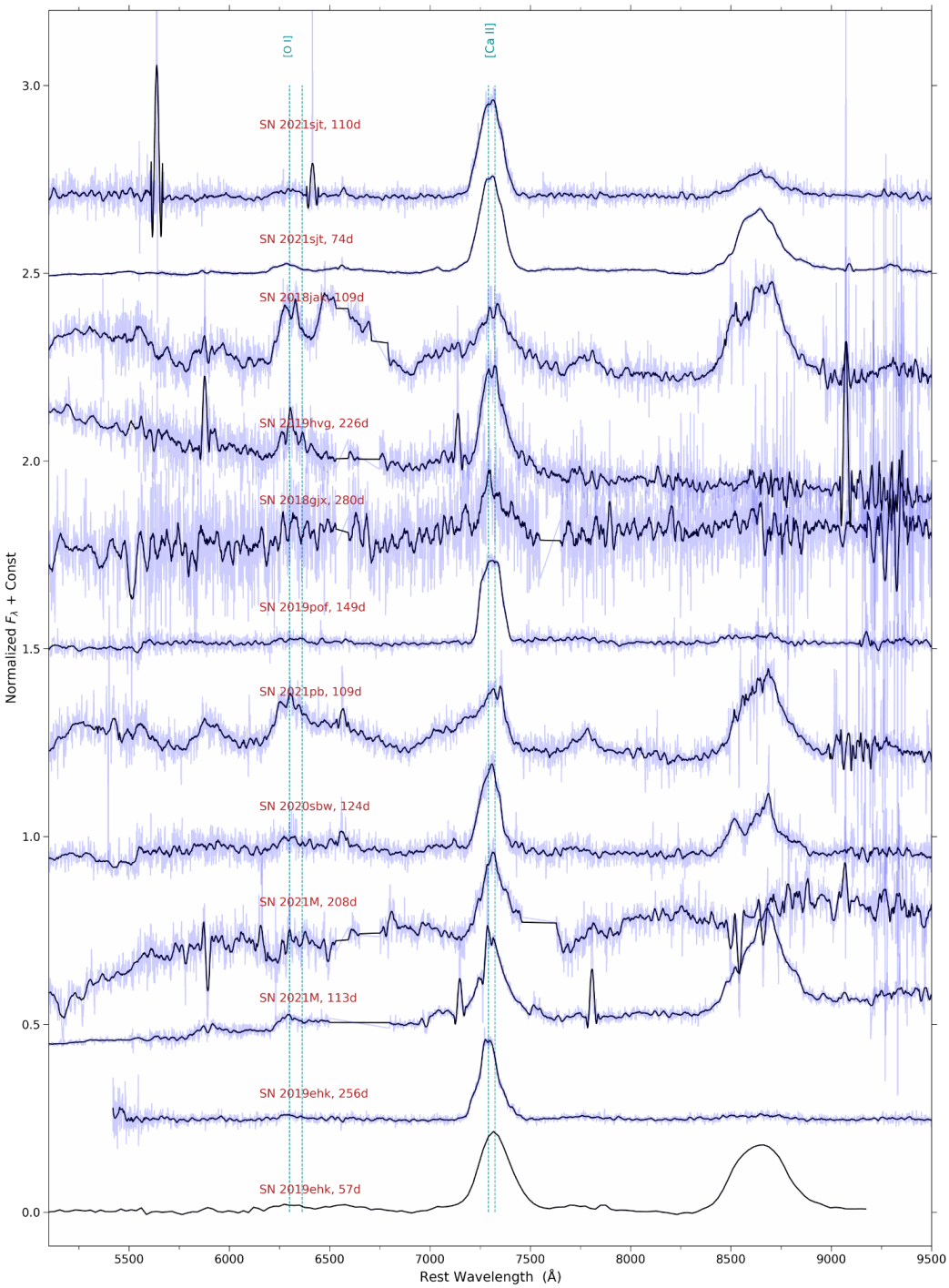

Figure 7.16: The full-wavelength range of the nebular spectra shown in Figure 7.3. The phase of the spectra is measured as the number of rest-frame days since the second peak.

Blackbody fits

All the best-fit parameters including bolometric luminosity, radius and temperature for each object are provided as machine-readable tables here.

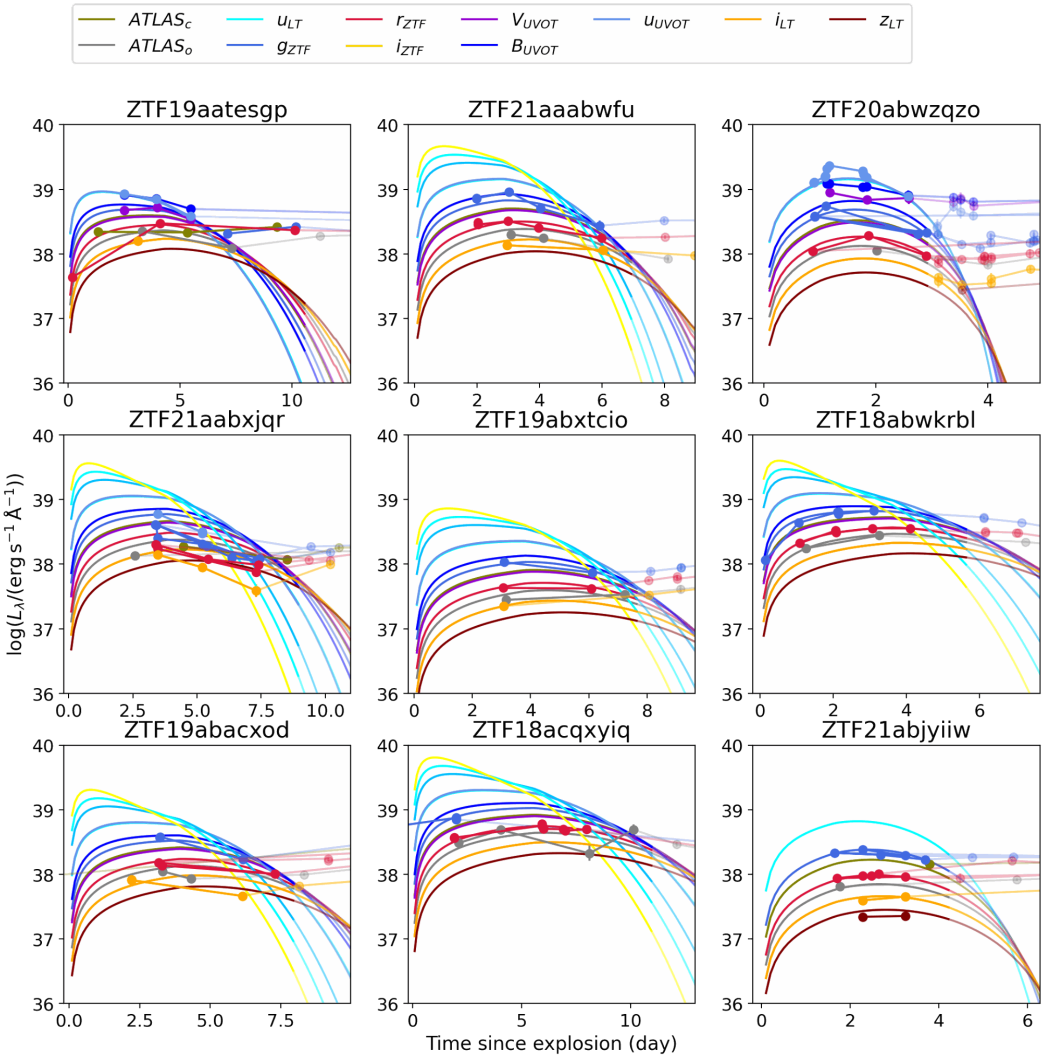

Figure 7.17: Shock cooling model (Piro et al. 2021) fits to multi-band data.

Host galaxy modeling

The models used for CIGALE and the summary of the host-galaxy best-fit parameters are provided in Table I and Table J respectively.

Table G: Summary of the blackbody properties for SN 2021sjt (Truncated). All the best-fit parameters including bolometric luminosity, radius and temperature for each object will be provided as machine-readable tables after publication here.

Phase (days since first detection)	Log Luminosity (erg s^{-1})	Temperature (K)	Radius ($R_\odot$)
2	$42.34^{+0.56}_{-0.21}$	14615^{+12882}_{-4534}	3728^{+2424}_{-1711}
3	$42.10^{+0.02}_{-0.02}$	8449^{+520}_{-438}	8445^{+786}_{-774}
5	$42.08^{+0.01}_{-0.01}$	7118^{+340}_{-321}	11716^{+1013}_{-912}
6	$42.07^{+0.01}_{-0.01}$	6580^{+252}_{-242}	13412^{+1001}_{-912}

Table H: Summary of the photometry data used for SN 2021sjt (Truncated). The photometry and spectroscopy data for each object will be provided as machine-readable tables after publication here.

Source	date (JD)	filter (AB mag)	mag (AB mag)	limiting mag (AB mag)
ZTF21abjyiiw	2459397.43	ztfg	*nan*	20.28
ZTF21abjyiiw	2459400.39	ztfg	*nan*	20.58
ZTF21abjyiiw	2459400.43	ztfr	*nan*	20.18
ZTF21abjyiiw	2459402.35	ztfg	18.58 ± 0.08	19.74
ZTF21abjyiiw	2459402.35	ztfg	18.58 ± 0.08	19.74
ZTF21abjyiiw	2459402.40	ztfr	18.01 ± 0.06	19.36

Table I: The models and fitting parameters used for CIGALE

Galaxy attributes	Brief description
SFH	SFR $\propto \frac{t}{\tau^2}\ exp(-t/\tau)$ τ = 250, 500, 1000, 2000, 4000, 6000, 8000 Myr Age t = 250, 500, 1000, 2000, 4000, 8000, 12000 Myr
SSPs models	BC03 (Bruzual and Charlot 2003) + Chabrier IMF (Chabrier 2003) Stellar metallicity = 0.0004, 0.004, 0.008, 0.02 $Z_{\odot}$
Dust Attenuation	Modified power law curves (Calzetti et al. 2000a) + differential reddening of stars according to age $E(B-V)_{young}$ = 0.0, 0.2, 0.3, 0.5, 0.8, 1.0, 1.5, 2.0, 3.0 $E(B-V)_{old}$ = 0.3, 0.50, 1.0 U$V-bump\ wavelength$ = 217.5 nm U$V-bump\ amplitude$ = 0.0, 1.0, 2.0, 3.0 p$owerlaw\ slope$ = $-0.13, -0.2, -0.5$
Dust emission	Dust templates of Dale et al. (2014) + Energy Balance AGN fraction = 0 alpha = 1.0, 1.5, 2.0, 2.5
Nebular	log U_{ion} = -2.0 emission line width = 300.0 km/s

Table J: Summary of the host-galaxy best-fit parameters

ZTF Name	log Mass ($M_{\odot}$)	log SFR ($M_{\odot}$/yr)	B-band abs. mag (mag)
SN 2019ehk/ZTF19aatesgp	$11.09^{+0.01}_{-0.00}$	$0.23^{+0.01}_{-0.00}$	-21.87
SN 2021M/ZTF21aaabwfu	$9.88^{+0.11}_{-0.15}$	$0.21^{+0.29}_{-0.12}$	-18.75
SN 2020sbw/ZTF20abwzqzo	$10.71^{+0.06}_{-0.01}$	$-0.17^{+0.07}_{-0.01}$	-20.14
SN 2021pb/ZTF21aabxjqr	$10.74^{+0.20}_{-0.04}$	$0.67^{+0.16}_{-0.29}$	-21.17
SN 2019pof/ZTF19abxtcio	$8.62^{+0.01}_{-0.01}$	$-2.32^{+0.09}_{-0.07}$	-15.67
SN 2018gjx/ZTF18abwkrbl	$10.25^{+0.11}_{-0.11}$	$0.42^{+0.21}_{-0.12}$	-19.84
SN 2019hvg/ZTF19abacxod	$9.93^{+0.11}_{-0.13}$	$0.55^{+0.09}_{-0.17}$	-20.15
SN 2018jak/ZTF18acqxyiq	$9.84^{+0.26}_{-0.36}$	$1.09^{+0.55}_{-0.23}$	-19.52
SN 2021sjt/ZTF21abjyiiw	$10.70^{+0.18}_{-0.39}$	$2.11^{+1.44}_{-0.99}$	-16.78

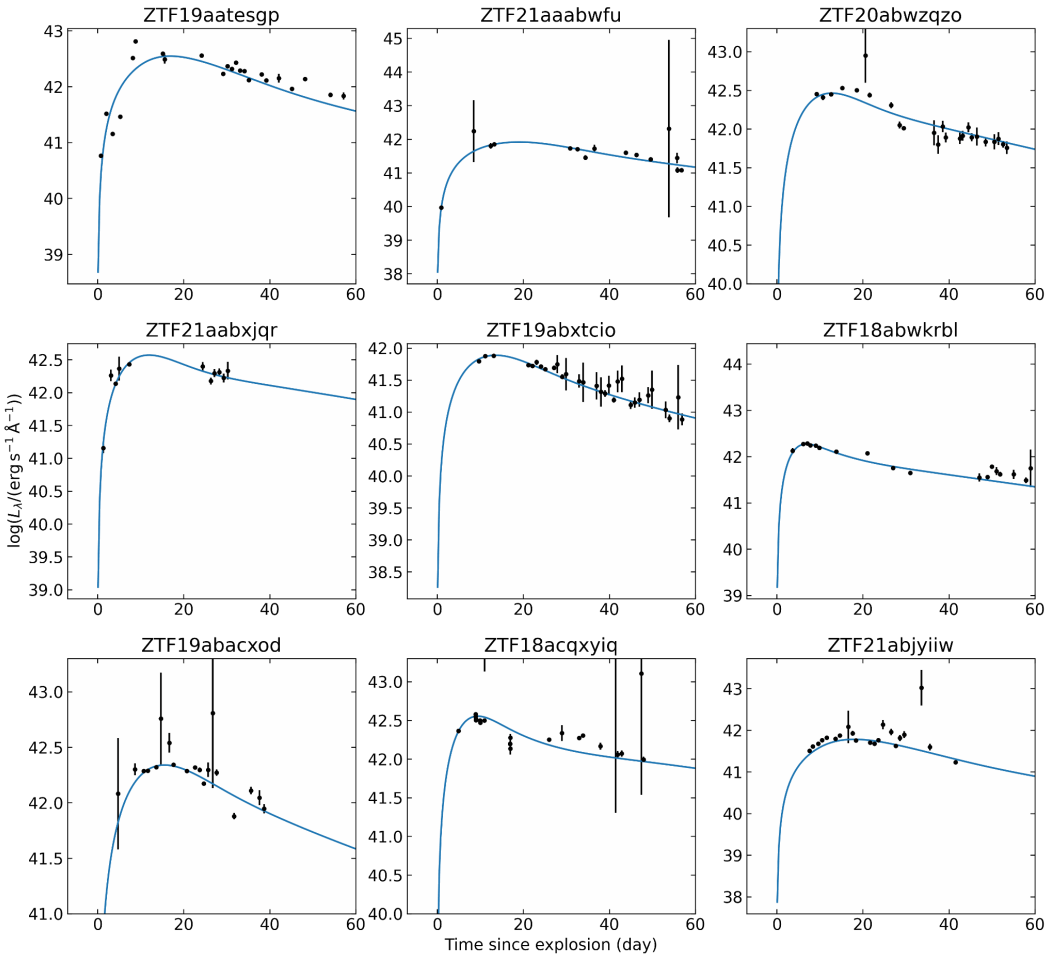

Figure 7.18: Radioactive (Arnett et al. 1989) fits to bolometric luminosity data excluding the data points fit by shock-cooling.

Chapter 8

PROBING PRE-SUPERNOVA MASS LOSS IN DOUBLE-PEAKED TYPE IBC SNE FROM THE ZWICKY TRANSIENT FACILITY

Das, K. K., M. M. Kasliwal, et al. (2024). "Probing Presupernova Mass Loss in Double-peaked Type Ibc Supernovae from the Zwicky Transient Facility". In: *The Astrophysical Journal* 972.1, article 91. DOI: 10.3847/1538-4357/ad595f.

Kaustav K. Das[1], Mansi M. Kasliwal[1], Jesper Sollerman[2], Christoffer Fremling[1], I. Irani[3], Shing-Chi Leung[4], Sheng Yang[2], Samantha Wu[1], Jim Fuller[1], Shreya Anand[1], Igor Andreoni[5,6,7], C. Barbarino[2], Thomas G. Brink[8], Kishalay De[9], Alison Dugas[10], Steven L. Groom[11], George Helou[11], K-Ryan Hinds[12], Anna Y. Q. Ho[13,14,15,16], Viraj Karambelkar[1], S. R. Kulkarni[1], Daniel A. Perley[12], Josiah Purdum[17], Nicolas Regnault[18], Steve Schulze[2], Yashvi Sharma[1], Tawny Sit[19], Niharika Sravan[20], Gokul P. Srinivasaragavan[6], Robert Stein[1], Kirsty Taggart[21], Leonardo Tartaglia[22,23], Anastasios Tzanidakis[1], Avery Wold[11], Lin Yan[17], Yuhan Yao[1], Jeffry Zolkower[17]

[1] Cahill Center for Astrophysics, California Institute of Technology, Pasadena, CA 91125, USA

[2] The Oskar Klein Centre, Department of Astronomy, Stockholm University, AlbaNova, SE-10691 Stockholm, Sweden

[3] Department of Particle Physics and Astrophysics, Weizmann Institute of Science, Rehovot 76100, Israel

[4] Department of Mathematics and Physics, SUNY Polytechnic Institute, Utica, NY 13502, USA

[5] Joint Space-Science Institute, University of Maryland, College Park, MD 20742, USA

[6] Department of Astronomy, University of Maryland, College Park, MD 20742, USA

[7] Astrophysics Science Division, NASA Goddard Space Flight Center, Greenbelt, MD 20771, USA
[8] Department of Astronomy, University of California, Berkeley, CA 94720-3411, USA
[9] MIT-Kavli Institute for Astrophysics and Space Research, 77 Massachusetts Ave., Cambridge, MA 02139, USA
[10] Department of Physics and Astronomy, University of Hawaii, Honolulu, HI 96822, USA
[11] IPAC, California Institute of Technology, Pasadena, CA 91125, USA
[12] Astrophysics Research Institute, Liverpool John Moores University, Liverpool L3 5RF, UK
[13] Miller Institute for Basic Research in Science, Berkeley, CA 94720, USA
[14] Department of Astronomy, University of California, Berkeley, CA 94720, USA
[15] Lawrence Berkeley National Laboratory, Berkeley, CA 94720, USA
[16] Department of Astronomy, Cornell University, Ithaca, NY 14853, USA
[17] Caltech Optical Observatories, California Institute of Technology, Pasadena, CA 91125, USA
[18] LPNHE, CNRS/IN2P3 & Sorbonne Université, 75005 Paris, France
[19] Department of Astronomy, The Ohio State University, Columbus, OH 43210, USA
[20] Department of Physics, Drexel University, Philadelphia, PA 19104, USA
[21] Department of Astronomy and Astrophysics, University of California, Santa Cruz, CA 95064, USA
[22] The Oskar Klein Centre, Department of Astronomy, AlbaNova, SE-10691 Stockholm, Sweden
[23] INAF - Osservatorio Astronomico di Padova, I-35122 Padova, Italy

Abstract

Eruptive mass loss of massive stars prior to supernova (SN) explosion is key to understanding their evolution and end fate. An observational signature of pre-SN mass loss is the detection of an early, short-lived peak prior to the radioactive-powered peak in the lightcurve of the SN. This is usually attributed to the SN shock passing through an extended envelope or circumstellar medium (CSM). Such an early peak is common for double-peaked Type IIb SNe with an extended Hydrogen envelope but is uncommon for normal Type Ibc SNe with very compact progenitors. In this paper, we systematically study a sample of 14 double-peaked Type Ibc SNe

out of 475 Type Ibc SNe detected by the Zwicky Transient Facility. The rate of these events is $\sim 3 - 9\%$ of Type Ibc SNe. A strong correlation is seen between the peak brightness of the first and the second peak. We perform a holistic analysis of this sample's photometric and spectroscopic properties. We find that six SNe have ejecta mass less than 1.5 $M_{\odot}$. Based on the nebular spectra and lightcurve properties, we estimate that the progenitor masses for these are less than ~ 12 $M_{\odot}$. The rest have an ejecta mass > 2.4 $M_{\odot}$ and a higher progenitor mass. This sample suggests that the SNe with low progenitor masses undergo late-time binary mass transfer. Meanwhile, the SNe with higher progenitor masses are consistent with wave-driven mass loss or pulsation-pair instability-driven mass loss simulations.

8.1 Introduction

Most massive stars undergo mass loss during their lifetime. This can affect the star's luminosity, burning lifetime, apparent temperature, Helium-core mass, and impact its end fate. The mass loss has a great influence on the late-time evolution of massive stars and the resultant supernova (SN) (e.g., Smith 2014). Pre-SN mass loss also has an impact on other areas of astronomy since it affects predictions for ionizing radiation, wind feedback from stellar remnants, and the origin of compact stellar remnants.

Early observations of SNe and theoretical models indicate that enhanced mass loss and pre-SN outbursts may occur in progenitors of many types of core-collapse SNe (CCSNe). Different evidence include the direct detection of pre-cursor outbursts (Pastorello et al. 2007, Strotjohann et al. 2015, 2021, 2023, Jacobson-Galán et al. 2022a), bright UV emission in Type IIP SNe at early times (e.g., Morozova et al. 2018, Bostroem et al. 2019b); narrow spectral lines originating from a dense circumstellar medium ionized by the explosion's shock (as in Type IIn, Type Ibn, Type Icn SNe, and Type II SNe e.g., Smith 2017, Pastorello et al. 2008, Perley et al. 2022b, Bruch et al. 2021). Various mechanisms have been proposed to explain this mass loss, like standard nuclear burning instabilities and gravity waves (Arnett and Meakin 2011, Quataert and Shiode 2012b, Wu and Fuller 2021, 2022b, Leung et al. 2021b), silicon deflagration (Woosley and Heger 2015), radiation-driven steady winds (Crowther 2007), pulsation-pair instability driven mass loss (Leung et al. 2019) and binary interactions (Wu and Fuller 2022a).

The detection of the first peak in the lightcurve of a double-peaked SN constitutes an observational signature of circumstellar matter (CSM) or extended envelope around

the progenitor. If strong mass loss occurred shortly before the SN explosion, it would create a layer of CSM around the SN progenitor. The shock cooling emission (i.e., bright post-breakout emission; Rabinak and Waxman 2011b, Nakar and Piro 2014, Piro 2015, Waxman and Katz 2017, Piro et al. 2021, Morag et al. 2023, Khatami and Kasen 2023) is seen as the SN shock passes through this ejected material. This should manifest as an early peak in the SN lightcurve. This is common for Type IIb SNe where the extended material is attributed to the outer He/H envelope. However, the progenitors of Type Ib and Ic SNe (SNe Ibc) are suggested to be very compact Wolf-Rayet (WR) stars or helium stars whose hydrogen envelopes have been stripped off via mass loss (e.g., Yoon 2015). Eruptive mass loss prior to a supernova explosion could provide a medium for the shock to propagate through.

This early peak has been detected in a few Type Ibc SNe in the past. The presence of CSM is likely responsible for the first peak of several peculiar SNe Ic like SN 2006aj (e.g., Modjaz et al. 2006), SN 2010mb (Ben-Ami et al. 2014), iPTF15dtg (Taddia et al. 2016), SN 2020bvc (Ho et al. 2020), and double-peaked superluminous SNe Ic (e.g., PTF12dam; Vreeswijk et al. 2017, LSQ14bdq; Nicholl et al. 2015, Nicholl and Smartt 2016, DES14X3taz; Smith et al. 2016). The double-peak is also seen in a few ordinary Type Ibc SNe: SN LSQ14efd (Barbarino et al. 2017), iPTF 16hgs (De et al. 2018a), SN 2017ein (Xiang et al. 2019), SN 2018lqo (De et al. 2020b), SN 2019ehk (Jacobson-Galán et al. 2020, Nakaoka et al. 2021, De et al. 2021), SNe 2021gno and 2021inl (Jacobson-Galán et al. 2022b), SN 2022oqm (Irani et al. 2022) and ultra-stripped SNe: SN 2019dge (Yao et al. 2020), iPTF14gqr (De et al. 2021). The low number of detections could be because of an observational bias as the detection of these sources requires fast cadence and early follow-up.

Modern high-cadence surveys such as the Zwicky Transient Facility (ZTF; Graham et al. 2019, Bellm et al. 2019b, Masci et al. 2019) act as a discovery engine for such events. In this paper, we present a sample of 17 double-peaked Type Ibc SNe detected by the ZTF. These detections are part of the Census of the Local Universe survey (CLU; De et al. 2020b) and the Bright Transient Survey (BTS; Fremling et al. 2020, Perley et al. 2020). The CLU survey is designed as a volume-limited survey with the objective of classifying all SNe within 200 Mpc, whose host galaxies are part of the CLU galaxy catalog (Cook et al. 2019). BTS is a magnitude-limited survey focused on spectroscopically classifying SNe with a peak magnitude brighter than 18.5 mag. In this paper, we perform a holistic analysis of the lightcurves for both the shock-cooling and the radioactive peaks, as well as for early time, photospheric

and nebular spectra of the sample. Based on the estimated CSM and progenitor properties, we provide constraints on the mass loss and progenitor channels.

The sample selection is described in Section 8.2. We describe the photometric and spectroscopic data in Section 10.2. We present our analysis and results from the spectra and the light curves in Section 10.5. We discuss the inferred progenitor masses in Section 8.5 and the mass-loss scenarios in Section 8.6. We provide a brief summary of the results and future goals in Section 9.5.

8.2 Sample Selection

In this paper, we use SNe observed by the ZTF. The ZTF camera (Dekany et al. 2020) is mounted on the Palomar 48-inch (P48) Oschin Schmidt telescope and has a field of view spanning 47 square degrees. ZTF images the entire Northern sky every ∼2 nights in g and r bands and achieves a median depth of approximately 20.5 mag (Bellm et al. 2019a). We use ZTF discoveries and follow-up spectra that are part of the BTS and CLU surveys.

We apply the following selection criteria on the ZTF SN sample obtained from the BTS and CLU surveys (1 April 2018 to 25 October 2022):

1. The transient should be classified as a stripped-envelope SN (SESN) (Type Ib, Ib-pec, Ibn, Ic, Ic-pec, Icn, Ic-BL, but Type IIb are not included) based on photospheric spectral template matching and manual inspection. As per classification status on 25th October 2022, there are 185 SNe classified as Type Ib, 27 SNe classified as Type Ibn, 176 classified as Type Ic, 59 classified as Type Ic-BL, and 28 SNe classified as Type Ib/c with unclear type (Yang et al. in prep).

2. In our analysis, we utilize the ZTF forced-photometry service developed by Masci et al. (2019) to perform forced photometry in g, r and i bands on the ZTF difference images. We consider 3σ measurements as a threshold. 59 Type Ib/Ibn SNe, 86 Type Ic/Icn/Ic-BL SNe and 47 Type Ib/c SNe (classification not distinguishable between Ib and Ic) have good quality early-time lightcurves, where the gap between the first and second detection as well as the gap between the last non-detection and the first detection is less than 5 days. Hence, we did not miss the first peak for these SNe.

3. We manually inspect the lightcurves of these transients to look for an early bump with a rise and decline or just the decline in either of the ZTF g-band or r-band photometry followed by a second peak. We find 19 such SNe with 10 Type Ib, 4 Type Ic, 3 Type Ic-BL, 2 Type Ib/c. We list the details of the sample in Table B.

4. The early lightcurve decline or rise should be present in at least two filters. There were 2 SNe[1] where we could see an early decline which could correspond to a first peak, but since they were seen only in the *r* or *g* band we do not include them in our sample. The summary of the sources in the sample is provided in Table B.

Thus, the lower and upper limit on the rate of these events is $\sim 17/475 = 3.5\%$ $\sim 17/192 = 8.8\%$ of Type Ibc(BL) SNe respectively.

We note that the time above half maximum of the first peak ($t_{1/2}^{\rm first}$) is < 8 days for fourteen SNe, while three SNe have an unusually long first peak with $t_{1/2}^{\rm first} > 15$ days (see Figure 8.1). The bolometric luminosity for these three sources (SNe 2019cad, 2022hgk, 2021uyv) increases with time for the first peak which is not expected for the shock-cooling phase. Hence, we believe that the powering mechanism for the first peak of these sources is not shock cooling and leave the detailed lightcurve analysis of these SNe for future work.

In Figure 8.2, we look at the interaction times for some stripped-envelope SNe where interactions were observed (Brethauer et al. 2022). We note that our sample shows interaction at earlier times compared with CSM interaction signatures for most SESNe in the literature.

Table A: Steps for selecting our sample. See Section 8.2 for details regarding each step.

Step	Criteria	# Candidates
1	Classified as SESN (except Type IIb)	475
2	Well-sampled early light curve	192
3	Double-peaked	19
4	Candidate has multi-band photometry during the first peak	17

8.3 Data

In this section, we describe the photometric and spectroscopic data used.

Optical photometry

We utilize forced photometry data from the ZTF in the *g*, *r* and *i* bands and from the Asteroid Terrestrial-impact Last Alert System (ATLAS; Tonry et al. 2018, Smith et al. 2020) in the *c* and *o* bands. In addition, photometry data is obtained from

[1]ZTF18acsodbf, ZTF19abzzuhj

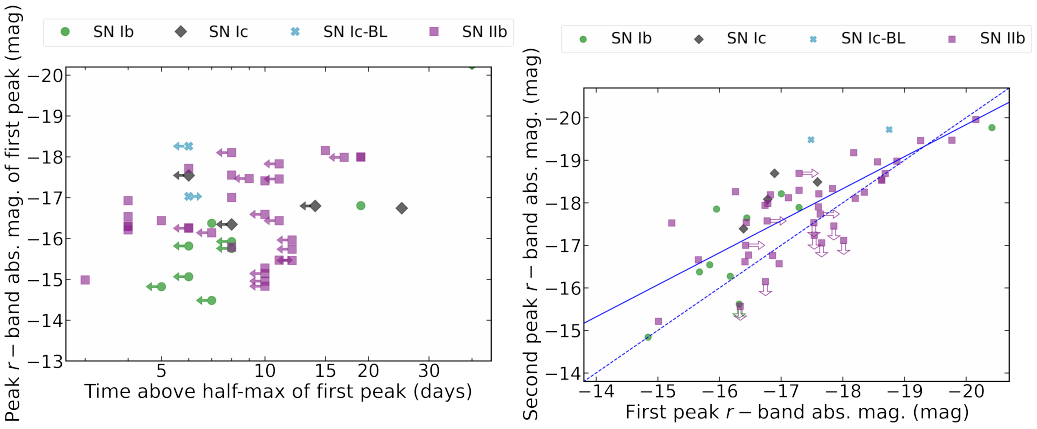

Figure 8.1: *Left:* Parameter space of peak magnitude of the first peak versus time above half maximum of the first peak $t_{1/2}^{\text{first}}$ for all double-peaked SNe observed by ZTF as part of the BTS and CLU surveys. The Type Ibc(BL) SNe in the figure are part of the sample in this work. *Right:* We see a correlation in the peak magnitude of the first and second peaks of the SNe following $M_2 = 0.8 \times M_1 - 4.7$. M_1 and M_2 are the peak magnitudes of the first and second peak respectively. The solid line shows the best-fit linear relation. We can infer from the $y = x$ dashed line that the second peak is brighter than the first peak for most sources. The correlation could imply that the SNe that show double-peaked lightcurves have He-star progenitors that shed their envelope in binary interactions.

the Palomar 60-inch telescope (P60; Cenko et al. 2006), Sinistro imager on the 1-meter class and the Spectral imager on the 2-meter class telescopes operated by Las Cumbres Observatory (LCOGT; Brown et al. 2013), the Liverpool Telescope (LT; Steele et al. 2004) in g, r and i bands. We also obtain u, i, z band photometry for a few sources from the LT. P60 and LT data were processed using the FPipe (Fremling et al. 2016) image subtraction pipeline with Sloan Digital Sky Survey (SDSS; Ahn et al. 2012) and PanSTARRS (PS1; Chambers et al. 2016) reference images. Additionally, we have early-time UV data for some sources acquired from the Ultra-violet Optical Telescope (UVOT; Roming et al. 2005), which is deployed on the *Neil Gehrels Swift Observatory* (Gehrels et al. 2004). UVOT data are reduced using HEAsoft[2]. The photometry data can be found in Appendix 8.10. Figure 8.3 shows the lightcurve of SN 2021gno as an example. We compare the r-band absolute magnitude of the SN with our sample in Figure 8.4. Similar plots for the other SNe can be found in Appendix 8.10. Figure 8.5 shows the lightcurves of all the SNe.

[2]https://heasarc.gsfc.nasa.gov/docs/software/heasoft

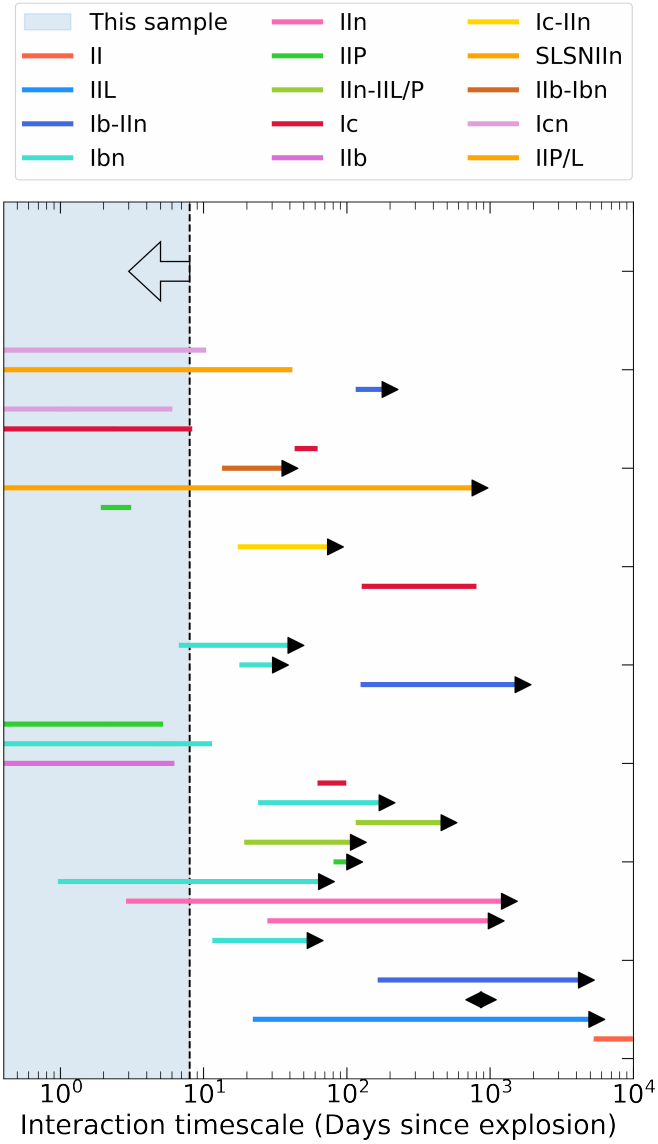

Figure 8.2: The interaction timescale for various SNe in the literature (from data compiled in Brethauer et al. 2022) showing signatures of CSM interaction including SNe Ibc, Ibn, Icn are shown by the colored lines. The blue-shaded region shows the range of timescale of the first peak for our sample consistent with shock-cooling ($t_{1/2}^{\rm first} < 8$ days).

Table B: Summary of the sample of 17 SNe used in this paper. The sources which have been mentioned previously in the literature are labeled with a superscript with a footnote of the list of papers where they were discussed. The absolute magnitudes have been measured by assuming Milky Way extinction ($A_{V,MW}$) and host galaxy extinction ($A_{V,host}$) as described in Section 10.3. Subscripts 1 and 2 refer to the peak parameters of the first peak and second peak respectively.

ZTF Name	IAU Name	R.A. (hh:mm:ss)	Dec. (dd:mm:ss)	Redshift	Type	t_{max1} (MJD)	M_{r1} (mag)	t_{max2} (MJD)	M_{r2} (mag)	$A_{V,MW}$ (mag)	$A_{V,host}$ (mag)
ZTF21aaqhhfu[a]	SN2021gno	12:12:10.29	+13:14:57.0	0.006	Ib	59294	-14.5	59306	-15.2	0.10	0
ZTF21abcgnql	SN2021niq	15:36:06.70	+43:24:21.4	0.018	Ib	59362	-15.1	59371	-15.8	0.07	0
ZTF20abbpkng	SN2020kzs	17:14:55.02	+35:31:13.6	0.037	Ib	58983	-17.5	59009	-18.7	0.08	1.1
ZTF21abccaue	SN2021nng	14:17:22.86	+58:44:58.9	0.040	Ib	59336	-16.5	59381	-18.4	0.03	0.6
ZTF18achcpwu	SN2018ise	07:07:16.74	+64:03:41.8	0.055	Ic	58423	-16.7	58455	-18.6	0.11	0
ZTF18abmxelh	SN2018lqo	16:28:43.25	+41:07:58.6	0.033	Ib	58340	-15.8	58354	-16.4	0.02	0
ZTF21acekmmm	SN2021aabp	23:09:55.08	+09:41:08.9	0.064	Ic-BL	59486	-18.3	59505	-19.1	0.15	0
ZTF21aasuego[a]	SN2021inl	13:01:33.24	+27:49:55.0	0.018	Ib	59311	-14.8	59321	-14.8	0.02	0
ZTF21abdxhgv	SN2021qwm	15:18:25.73	+28:26:04.1	0.070	Ib/c	59369	-17.1	59395	-18.8	0.07	0
ZTF22aapisdk	SN2022nwx	22:15:43.95	+37:16:47.0	0.020	Ib	59755	-15.8	59764	-15.9	0.41	0
ZTF22aasxgjp[b]	SN2022oqm	15:09:08.21	+52:32:05.1	0.011	Ic	59772	-16.3	59785	-17.3	0.05	0
ZTF21aacufip	SN2021vz	15:21:26.85	+36:46:04.0	0.045	Ic	59223	-17.5	59232	-18.4	0.05	0
ZTF22aaezyos	SN2022hgk	14:10:23.70	+44:14:01.2	0.033	Ib	59688	-16.8	59713	-18.0	0.02	0
ZTF21abmlldj	SN2021uvy	00:29:30.87	+12:06:21.0	0.094	Ib	59449	-20.3	59536	-19.6	0.18	0
ZTF18abfcmjw[c]	SN2019dge	17:36:46.74	+50:32:52.1	0.021	Ib	58584	-16.3	58591	-15.6	0.07	0
ZTF20aalxlis[d]	SN2020bvc	14:33:57.01	+40:14:37.6	0.025	Ic-BL	58883	-17.0	58900	-19.0	0.03	0
ZTF19aamsetj[e]	SN2019cad	09:08:42.97	+44:48:46.0	0.028	Ic	58567	-17.9	58594	-19.2	0.05	1.1

[a] Jacobson-Galán et al. (2022b); [b] Irani et al. (2022); [c] Yao et al. (2020); [d] Ho et al. (2020); [e] Gutiérrez et al. (2021).

Optical spectroscopy

We acquired spectroscopy at multiple epochs for the SNe in our sample, covering a range from one day to over 300 days after explosion. Each transient typically has at least one spectrum near peak luminosity for initial classification and additional spectral follow-up was conducted as part of the ZTF surveys. Our primary classification instruments are the Spectral Energy Distribution Machine (SEDM; Blagorodnova et al. 2018) on the Palomar 60-inch telescope and the Double Beam Spectrograph (DBSP; Oke and Gunn 1982) on the Palomar 200-inch telescope. The DBSP spectra is reduced using the reduction pipelines described in Bellm and Sesar (2016) and Roberson et al. (2022). The SEDM data is reduced using the pipeline detailed in Rigault et al. (2019). Additionally, we obtained spectra from the the Alhambra Faint Object Spectrograph and Camera on the Nordic Optical Telescope (NOT; Djupvik and Andersen 2010) and the Spectrograph for the Rapid Acquisition of Transients (SPRAT; Piascik et al. 2014). The NOT data were reduced using the PyNOT[3] and PypeIt (Prochaska et al. 2020a) reduction pipelines, while we use the FrodoSpec pipeline (Barnsley et al. 2012) for reduction of SPRAT data. We obtain late-time nebular-phase spectra with the Low-Resolution Imaging Spectrometer (LRIS; Oke et al. 1995) on the Keck I telescope, with data reduced using the automated LPIPE (Perley 2019) pipeline. The log of the observed spectra can be found in Table L.

[3]https://github.com/jkrogager/PyNOT

Figure 8.6 shows the spectral sequence for SN 2021gno as an example. The spectral sequence of all the sources can be found in Appendix 8.10.

8.4 Methods and Analysis

Extinction correction

For precise estimation of the luminosity and explosion properties of a SN, it is essential to determine the impact of dust extinction along the observer's line of sight. Extinction is commonly divided into two components: the first component represents dust extinction from the Milky Way, while the second component accounts for extinction originating from the SN's host galaxy. To correct for Galactic extinction, we employ the reddening maps provided by Schlafly and Finkbeiner (2011). For reddening corrections, we use the extinction law described by Cardelli et al. (1989) with a value of $R_V = 3.1$.

To estimate the host-galaxy extinction, we measure the equivalent width (EW) of the Na I D absorption feature (Poznanski 2013). We measure a $\mathrm{EW_{Na\,I\,D}}$ of 1.5 Å, 5.5 Å and 0.8 Å for SN 2019cad, SN 2020nng and SN 2021nng, respectively. We do not see Na I D absorption for the other sources in the high signal-to-noise spectra. Thus, we assume zero host extinction for the rest of the sources in our analysis. To compute A_V from the EW measurements, we use $A_\mathrm{V}^\mathrm{host}[\mathrm{mag}] = 0.78 \times EW_{Na\,I\,D}[\text{Å}]$ (Stritzinger et al. 2018). We measure $A_\mathrm{V}^\mathrm{host} = 1.2$ mag for SN 2019cad and $A_\mathrm{V}^\mathrm{host} = 0.6$ mag for SN 2021nng. However, the empirical relation in Stritzinger et al. (2018) is not valid for the high $\mathrm{EW_{Na\,I\,D}}$ measured for SN 2020kzs. Instead, we use the difference in the average color $(g - r)$ of SN 2020kzs with the color expected for typical SNe Ib with no host extinction assuming the intrinsic template for Type Ib SNe provided in Stritzinger et al. (2018). Based on this, we measure $A_\mathrm{V}^\mathrm{host} = 1.1$ mag for SN 2020kzs.

Measuring velocity in Photospheric Spectra

As described in Section 9.2, we obtain spectra soon after explosion for all sources. We use the `SuperNova Identification` (`SNID`; Blondin and Tonry 2007) code for the classifications. For spectra contaminated by host galaxy, we utilized the `superfit` (Howell et al. 2005) code for classification. The final classification as Type Ibc SNe was determined through manual inspection of the emission and absorption lines and the best-fit templates matched from `SNID` or `superfit`.

We measure the expansion velocities of the He I λ5876 and O I λ7774 lines from the absorption part of the P-Cygni profiles of the spectral lines. To do this, we fit a

polynomial function, whose degree is manually tuned for each spectrum (typically 3), to the minima of the P-Cygni profiles. These minima serve as estimates for the expansion velocity. In cases where the spectrum is galaxy lines dominated or has low resolution, we manually inspect the spectrum to determine the minima of the absorption feature. The measured velocities are documented in Table L. We adopt a Monte Carlo approach to estimate the uncertainties in our velocity measurements. We generate a noise spectrum by subtracting a heavily smoothed version of the spectrum from the original spectrum. The standard deviation of this noise spectrum provides an estimate of the noise of the spectrum. Next, we create simulated noisy spectra by adding noise from a standard Gaussian distribution with the calculated standard deviation. We then add these simulated spectra with the heavily smoothed spectra and recalculate the velocities. The 1σ uncertainty in the velocity measurements across all the simulated spectra is considered as the standard deviation. Fremling et al. (2018) analyzed the spectra of a sample of 45 Type Ib SNe, 56 Type Ic SNe, 17 Type Ib/c and 55 Type IIb SNe discovered by the Palomar Transient Factory (PTF) and intermediate PTF (iPTF) surveys. We compare our measured velocities with those from Fremling et al. (2018). From Figure 8.7, we find that the expansion velocities of the He I λ5876 and O I λ7774 lines are consistent with those of canonical Type Ibc SNe.

Measuring Oxygen line flux in Nebular Spectra

We obtained nebular phase spectra for ten sources with Keck and P200. A few of the nebular spectra for SN 2021gno and SN 2021inl were taken from Jacobson-Galán et al. (2022b) as noted in Table C. We use interpolated late-time photometry to flux calibrate our nebular spectra. When late-time photometry is not available, we extrapolate the lightcurve by assuming a late-time (> 30 days) i-band decline rate of 0.019 $\pm$ 0.004 mag/day, based on the average late-time decay of the SESNe tabulated in Wheeler et al. (2015). For each spectrum, we manually set the wavelength regions and measure the line fluxes using trapezoidal integration. Uncertainties in this method are estimated by Monte Carlo sampling of the estimated fluxes by adding noise (scaled to nearby regions of the continuum) to the line profile. Table C presents the measured fluxes of [Ca II] $\lambda\lambda$7291, 7324 and [O I] $\lambda\lambda$6300, 6364, along with their flux ratio.

Modeling light curves

Blackbody fit

We estimate the bolometric light curve for epochs where we have detections in at least two filters by fitting a blackbody function. For each epoch, we use a Python EMCEE package (Foreman-Mackey et al. 2013) to perform a Markov Chain Monte-Carlo (MCMC) analysis in order to estimate the blackbody temperature ($T_{\rm BB}$), radius ($R_{\rm BB}$) and luminosity ($L_{\rm BB}$). The uncertainties of the model parameters are determined by extracting the $16^{\rm th}$ and $84^{\rm th}$ percentiles of the posterior probability distribution. We note that UV coverage is only available for SNe 2020bvc, 2022oqm, 2021gno. For these three SNe, the blackbody fit is done on the available UV−optical photometry. For the rest, the blackbody fit is done on the available optical photometry only. The best-fit parameters can be found in Appendix 8.10.

Fitting Shock Cooling in first-peak

In our sample, all sources exhibit a lightcurve characterized by two distinct peaks. The rapid rise of the first peak, accompanied by an initial blue color and high temperature, indicates that the first peak is likely dominated by cooling emissions from the shock-heated extended envelope (Nakar and Piro 2014, Piro 2015). We plot the peak luminosity versus time above half maxima in Figure 8.1. The same is shown for the first peak of all double-peaked Type IIb SNe (not part of the sample in this work) from BTS+CLU. We note that 43 Type IIb out of 193 Type IIb SNe had detections of two peaks (Das et al. in prep). In the right panel of Figure 8.1, we plot the peak $r-$band magnitude of the first peak vs the peak $r-$band magnitude of the second peak. For the first time, we find that a correlation exists between the peak magnitudes of the first and the second peak. The Pearson correlation coefficient is 0.79 ($p < 10^{-5}$). A similar correlation is also seen for the $g-$band, with a Pearson correlation coefficient of 0.81 ($p < 10^{-5}$). The physical reason for this correlation is not clear. The first peak brightness is primarily dependent on the radius of the progenitor while the peak of the second peak is primarily dependent on the Ni-mass. The correlation could imply that the SNe that show double-peaked lightcurves come from He-star progenitors that shed their envelope in binary interactions. Then, this correlation could be related to the He main sequence (see Figure 5 in Sravan et al. 2020), with the progenitor radius being related to the effective temperature and the Ni-mass being related to the luminosity. This would require that the Ni mass is correlated with the ejecta mass (Lyman et al. 2016). This assumes that

stripped-envelope SNe come from He-stars. Such a correlation could also exist if the first peak is also powered by nickel. This is possible if nickel is not entirely in the core but is also present in the outer envelope. However, it is unlikely that this trace amount of nickel can make a significant contribution to the early luminosity. We note that our survey is biased against sources that have a very faint first peak luminosity.

It is important to note that some of the SNe in our sample do not have well-sampled first peaks in both the rising and fading phases. To fit the multi-band photometry in the shock-cooling phase, we use the model proposed by Piro et al. (2021). This model allows us to determine key parameters, such as the explosion time (t_{exp}), extended material mass (M_{ext}), radius (R_{ext}) and energy (E_{ext}). We use the Python EMCEE package (Foreman-Mackey et al. 2013) to perform a multiband photometry data fitting analysis. We add a systematic error of 50% to account for uncertainties in density and opacity assumptions used in the model. Table D and Appendix 8.10 provide the best-fit values and corresponding fits for each SN.

In Figure 8.8, we compare the best-fit parameters with those for some H-poor SNe for which CSM interactions were detected. This CSM radii cover a wide range of distances from the explosion site, from $\sim 3 \times 10^{13} - 10^{18}$ cm. The range of inferred CSM masses is also broad, spanning from $\sim 10^{-4}$ $M_\odot$ up to tens of $M_\odot$ of material (Figure 8.8). We note that the physical parameters have been estimated with a variety of observational “tracers".

Shock Cooling order-of-magnitude limits for the first-peak

We make the assumption that the layer going through shock cooling has a radius R_{ext} and mass M_{ext}. The expansion timescale is $t_{exp} \sim R_{ext}/v_{ext}$, where v_{ext} is the velocity of this layer. Photons undergo diffusion from this layer within a timescale approximately given by $t_{diff} \sim \tau R_{ext}/c$. The bulk of photons emerge from the layer where $t_{exp} = t_{diff}$ or $\tau \sim c/v_{ext}$.

We assume $\rho \sim M_{ext}/(4\pi R^3/3)$. At a specific radius, the optical depth τ decreases as a result of expansion: $\tau \sim \kappa\rho R$. The radius increases as $R \sim v_{ext}t$, so $\tau \sim 3\kappa M_{ext}/(4\pi(v_{ext}t)^2)$. Setting this equal to c/v_{ext},

$$t \sim \left(\frac{3}{4\pi}\frac{\kappa M_{ext}}{v_{ext}c}\right)^{1/2}. \tag{8.1}$$

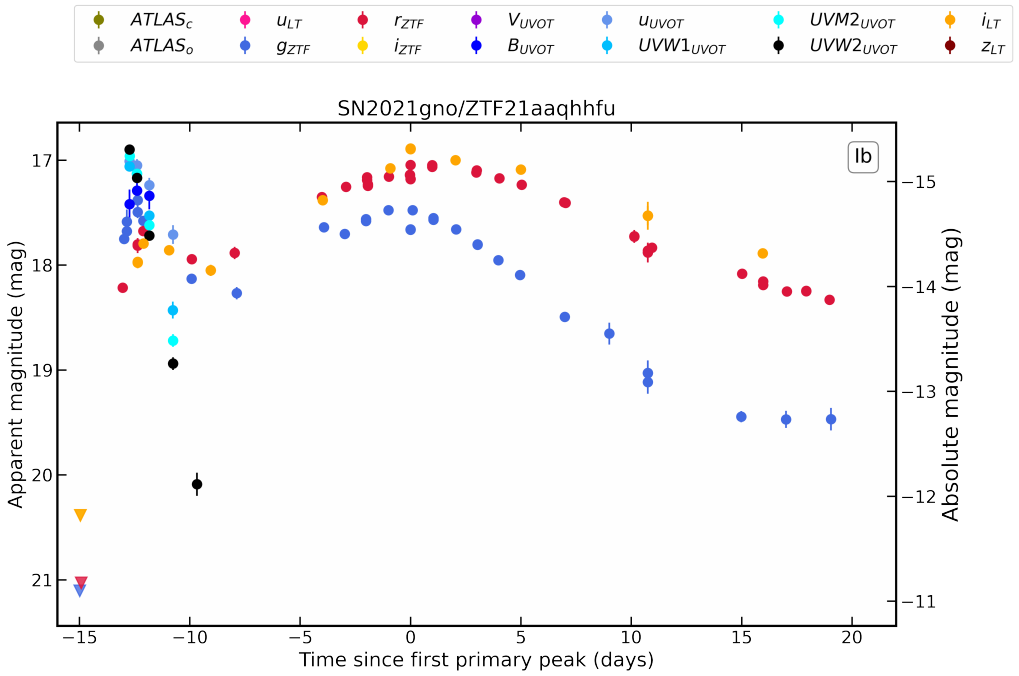

Figure 8.3: Lightcurve of SN 2021gno ($E(B-V)_{\rm MW} = 0.01$). The lightcurves of the other SNe can be found in Appendix 8.10.

We have an upper limit on the time to peak of t_p as the epoch of the first peak calculated from the analytical model described in the previous section. We take $\kappa = 0.2$ cm^{2}g^{-1} for a hydrogen-poor gas and $v_{\rm ext} \sim 0.1c$. Altogether, we find $M_{\rm ext} \sim 0.01 - 1\ M_\odot$. Note that the predicted values are upper limits because the rise time was likely faster than our measurements. The limits are listed in Table E. The values obtained from the analytical model described in the previous section are consistent with the limits obtained.

Next, we estimate the radius $R_{\rm ext}$. If the shock deposits energy $E_{\rm dep}$ into the layer, which then cools from expansion, we can estimate the energy $E_{\rm cool} \sim E_{\rm dep}(R_{\rm ext}/v_{\rm ext}t)$. Thus, the luminosity from cooling is $L_{\rm cool} \sim E_{\rm dep}R_{\rm ext}/v_{\rm ext}t^2$. We assume that the deposited energy is half the kinetic energy $E_{\rm KE}$ of the shock, $E_{\rm dep} = \pi R_{\rm ext}^2 dR \rho v_s^2$, where ρ and dR are the density and width of the layer. Taking $\rho \sim M_{\rm ext}/(4\pi R_{\rm ext}^2 dR)$ and $dR \approx R_{\rm ext}$, we find

$$L_{\rm cool} \sim \frac{v_{\rm ext}R_{\rm ext}M_{\rm ext}}{4t^2}. \tag{8.2}$$

Taking the above $M_{\rm ext}$, t_p values, $v_{\rm ext} = 0.1c$, and lower limits on the peak luminosity from the bolometric blackbody fits, we find $R_{\rm ext}$ in the range $\approx 10 - 200\ R_\odot$. We

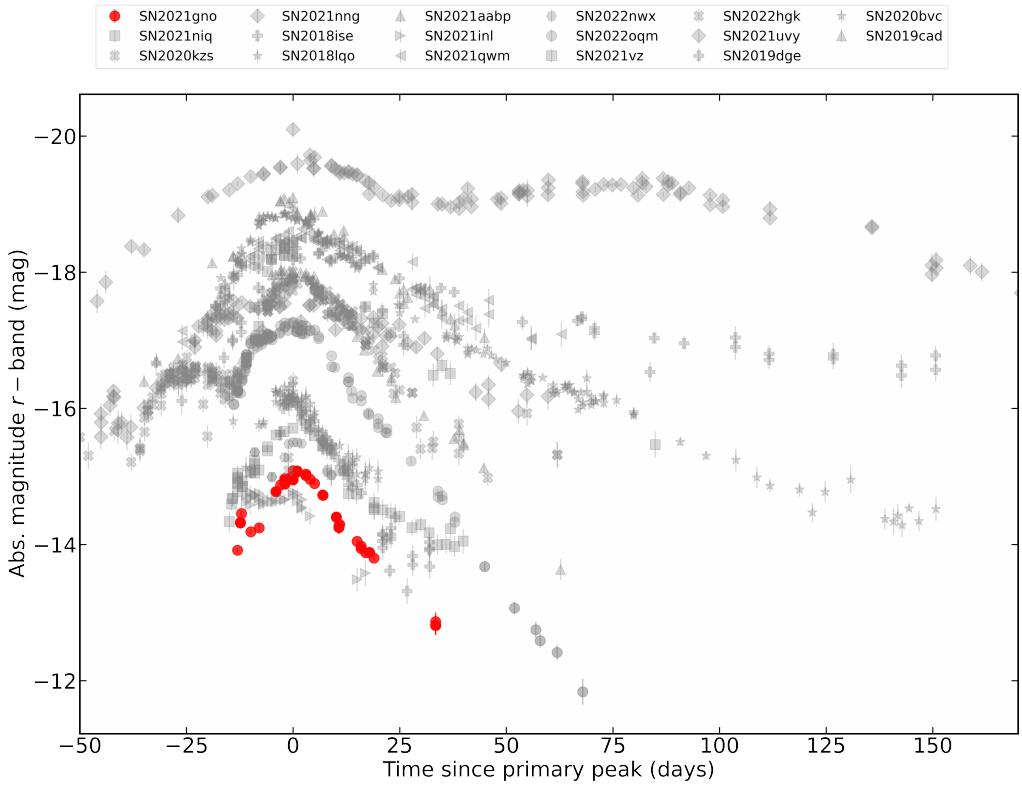

Figure 8.4: Comparison of the r-band absolute magnitude light curve of SN 2021gno to the other sources in the sample. The comparison for the other sources can be found in Appendix 8.10.

can only measure a lower limit on the radius because the true peak luminosity is likely higher than what we can measure.

The limits are listed in Table E. The values obtained from the analytical model described in the previous section are consistent with the limits obtained.

Ruling out Shock breakout from CSM for the first-peak

In this section, we conduct a rough estimation to determine if the rise time and peak luminosity can be accounted for a model in which shock interaction powers the light curve ("wind shock breakout").

The shock crossing timescale is $t_{\rm cross} \sim R_{\rm CSM}/v_s$, which is ~ 0.01 day, assuming shock velocity ($v_s \approx 0.1c$) for the observed radius range, which is around two orders of magnitude less than the observed timescale. The estimated limits are listed in Table F.

The shock heats the CSM with an energy density that is roughly half of the kinetic

energy of the shock, so the energy density of the CSM $\sim (1/2)(\rho v_s^2/2)$. The luminosity is the total energy deposited divided by $t_{\rm cross}$,

$$L_{\rm BO} \sim \frac{v_s^3}{4}\frac{dM}{dR}, \tag{8.3}$$

which is $> 10^{44}$erg, again a few orders higher than the observations, assuming a constant density.

Therefore, considering shock velocities $(0.1c)$ comparable to the observed expansion of the photospheric radius, Table F indicates that we would require higher values for M_{CSM} than what is expected for unbound CSM. Thus we rule out this as a possible explanation for the early bump.

Modeling the radioactively powered second-peak

In this section, we describe the modeling of the second peak of the SNe. First, we estimate the contribution of the cooling emission to the bolometric luminosity using the best-fit parameters obtained in Section 8.4. This cooling component is then subtracted from the bolometric lightcurves obtained through blackbody fitting. We employ two methods to fit the peak, assuming it is powered by radioactive decay. Firstly, we apply the analytical model outlined in Arnett et al. (1989), Valenti et al. (2008), and Wheeler et al. (2015). Using this model, we constrain the characteristic photon diffusion timescale (τ_m), characteristic γ-ray diffusion timescale (t_o) and nickel mass ($M_{\rm Ni}$). Additionally, we use relations from Wheeler et al. (2015) that provide the kinetic energy in the ejecta ($E_{\rm kin}$) and the ejecta mass ($M_{\rm ej}$) as functions of photospheric velocity ($v_{\rm ph}$) and (τ_m). We use the $v_{\rm ph}$ measured using the average He I line and O I velocity from the photospheric spectra within 5 days of the second peak epoch for Type Ib and Type Ic(BL) SNe respectively listed in Section 8.4. If there are no velocity measurements available from spectra within 5 days of the second peak, we assume an average velocity of 8000 km s^{-1}. For SN 2020bvc, we use $v_{\rm ph} = 18000$ km s^{-1} derived in Ho et al. (2020). Secondly, we use the lightcurve analytical models given in Khatami and Kasen (2019) to estimate the various explosion parameters. Further details on the model fitting can be found in Yao et al. (2020) (their Appendix B). Figure 10.12 shows the parameter space occupied by these transients with ejecta mass varying from $\approx 0.2 - 7\ M_\odot$ and nickel mass varying from $0.01 - 0.5\ M_\odot$. For SN 2021inl, we note that the estimated ejecta mass and kinetic energy values are higher than those estimated in Jacobson-Galán et al. (2022b) as they used a lower photospheric velocity of 7500 km s^{-1}, instead of

14350 km s^{-1} used in this work. We compare the ejecta mass and nickel mass with those from Taddia et al. (2018) in Figure 10.12. The best fit parameters and fits are provided in Table G and Appendix 8.10.

8.5 Constraining progenitor mass

The late-time evolution of a star, including pre-SN mass loss is strongly dependent on the progenitor mass. In this section, we try to provide rough estimates of the progenitor mass based on the nebular spectra and the lightcurves.

We have at least one nebular spectrum for ten SNe obtained using LRIS on the Keck I telescope. Using the procedure described in Section 8.4, we calculate the [Ca II] $\lambda\lambda$7291, 7324 to [O I] $\lambda\lambda$6300, 6364 flux ratio and determine the [O I] $\lambda\lambda$6300, 6364 fluxes (Table C). Next, we use these [O I] luminosity measurements to compute the oxygen abundance and, subsequently, the progenitor mass. To determine the minimum required oxygen mass for a given [O I] luminosity, we use the analytical relation in Uomoto (1986). This analytical formula is applicable where the electron density is higher than $\sim 7\times10^5$ cm^{-3}. This is estimated to be valid for our case, with ejecta mass in the range of $0.3-6$ $M_\odot$. We use temperature values of $\approx 3500-4000$ K estimated in other core-collapse SNe from the [O I] emission (Sollerman et al. 1998, Elmhamdi 2011). Using this, we get an estimate of O mass in our sample in the range of $\approx 0.001-1$ $M_\odot$(see Table C).

We use these O-mass estimates to constrain the progenitor mass. To achieve this, we refer to the work of Dessart et al. (2021a), who conducted 1D non-local thermodynamic equilibrium radiative transfer calculations specifically for nebular-phase stripped SNe. Strong [Ca II] and weak [O I] emission is predicted for lower mass He stars. The high [Ca II]/[O I] flux ratio we observe for SNe 2021gno, 2021inl, 2022nwx, 2022oqm, 2018lqo in our sample is indicative of a low initial He-star mass progenitor. In Figure 8.10, we present a comparison of the measured O mass in our sample and the synthesized O mass obtained from He-star progenitor models from both binary evolution (Dessart et al. 2021a) and single-star models (Sukhbold et al. 2016). Of the 14 SNe consistent with shock-cooling, we find that the SNe with progenitor mass less than 12 $M_\odot$ are SNe 2019dge, 2021gno, 2021inl, 2022nwx, 2022oqm, 2018lqo. To determine the progenitor mass from the He-star mass, we use the relation provided in Woosley and Heger (2015).

In order to make a comparison with such low progenitor masses, we also consider estimates of the O synthesized in the case of ultra-stripped SNe (USSNe). USSNe

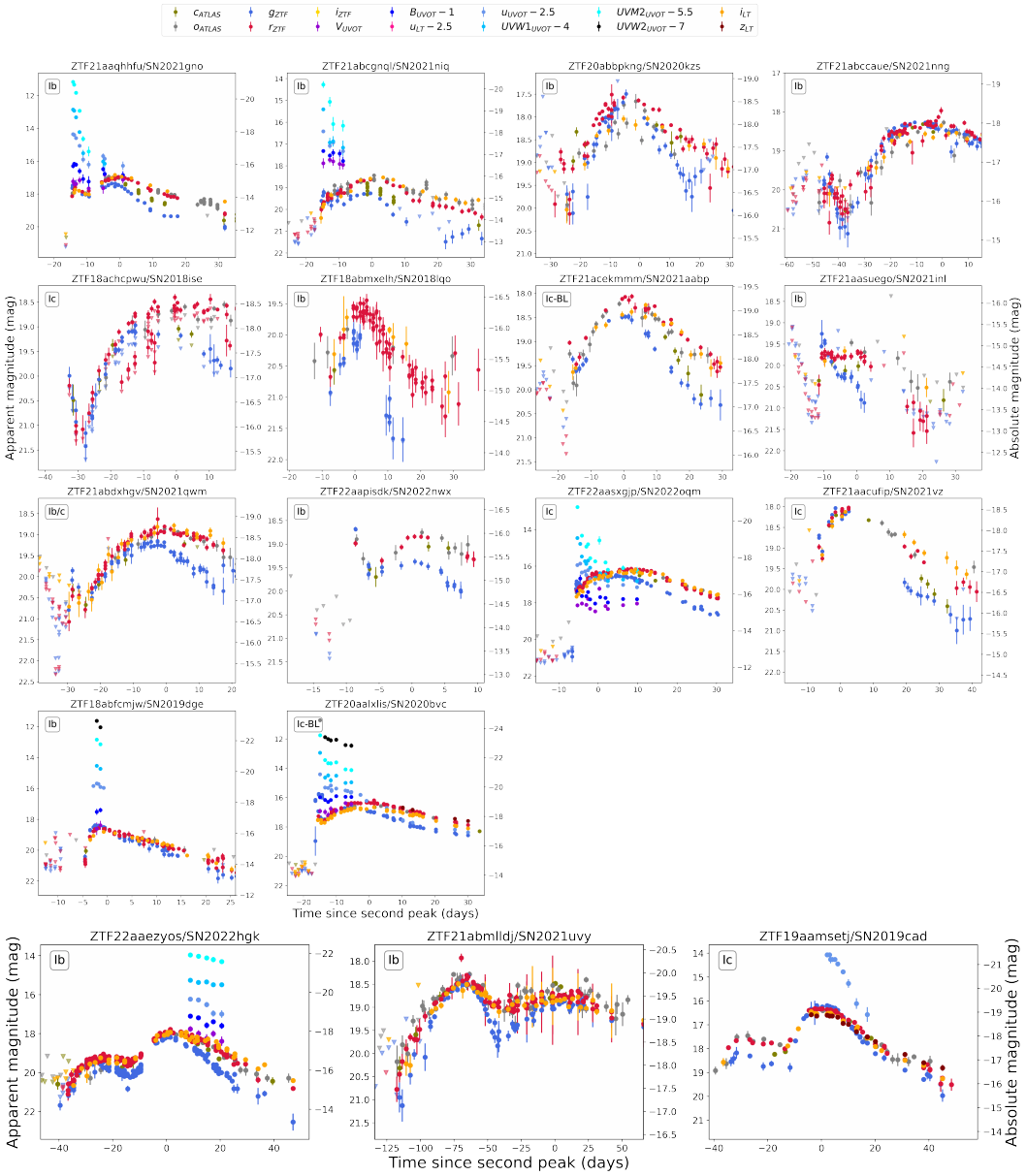

Figure 8.5: *Top:* Lightcurves of double-peaked Type Ibc SNe in our sample, obtained through forced-photometry from ZTF, ATLAS, and follow-up observations from various instruments. Further details on the photometry can be found in Section 9.2. The left y-axis represents the apparent magnitude (mag), while the right y-axis shows the absolute magnitude (mag). The absolute magnitude measurements assume Milky Way and host extinction values from Table B. The x-axis shows the number of rest-frame days since the epoch of the second peak. *Bottom:* The three SNe in the bottom panel have an unusually long first peak with $t_{1/2}^{\text{first}} > 15$ days. We leave the detailed lightcurve analysis of these SNe for future work.

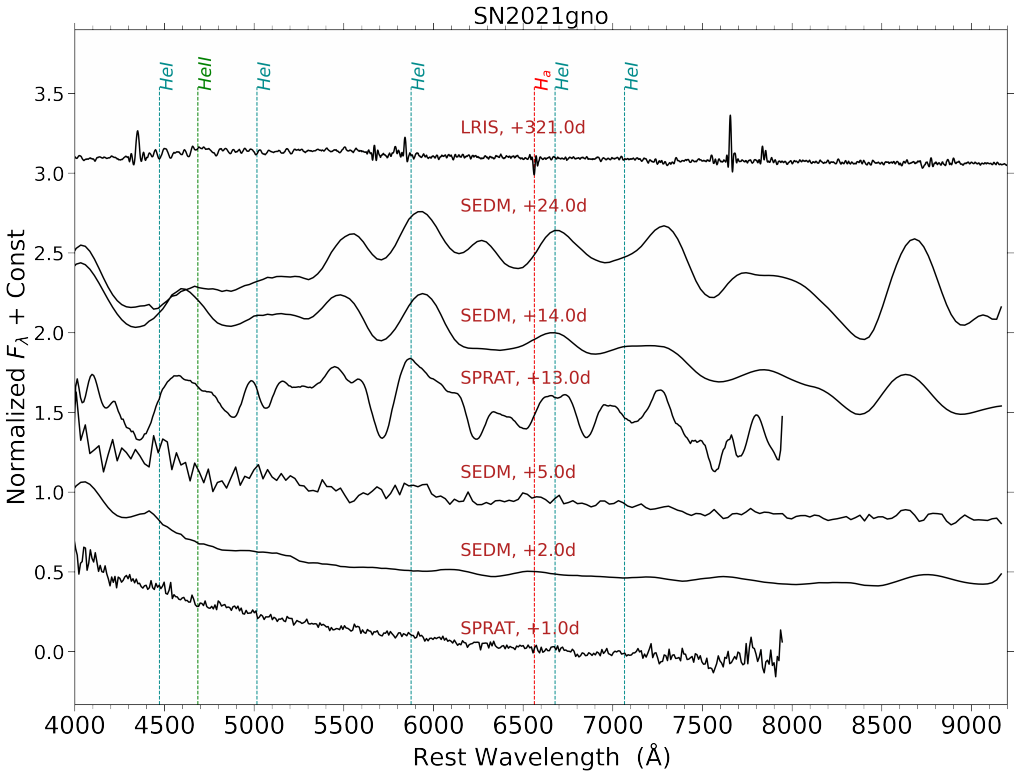

Figure 8.6: Spectral sequence for SN 2021gno (Type Ib) taken as part of the ZTF and CLU surveys. See Section 8.4 for details on the spectra obtained. Spectral sequence for the other sources can be found in Appendix 8.10.

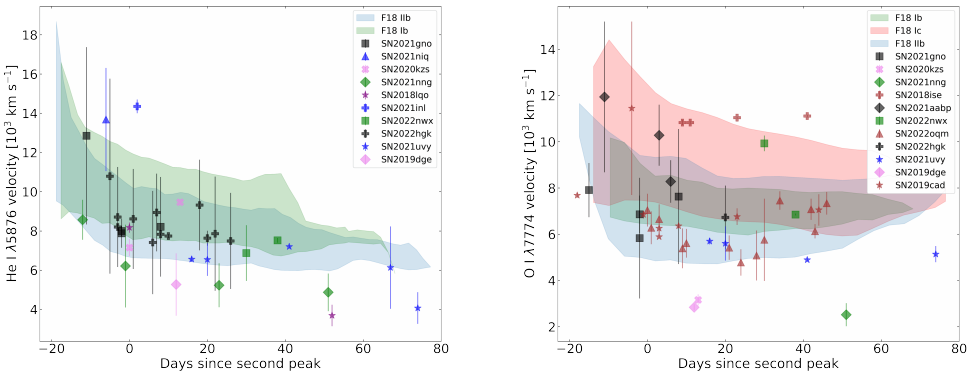

Figure 8.7: *Left:* The filled shapes represent the expansion velocity of the He I λ5876 line for each SN in our sample. The blue-shaded region indicates the 1σ range of the ejecta velocities calculated for a sample of canonical Type IIb and Type Ibc SNe from Fremling et al. (2018). *Right:* The filled shapes represent the expansion velocity of the O I λ7774 line for each SN in our sample. Again, the blue-shaded region represents the 1σ range of the ejecta velocities calculated for a sample of normal Type IIb and Type Ibc SNe from Fremling et al. (2018).

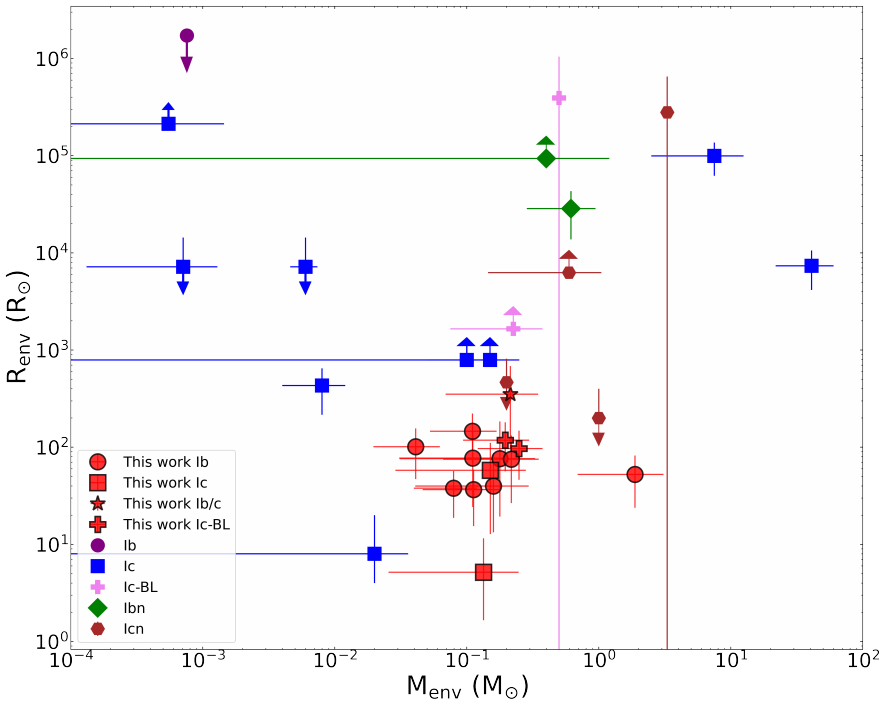

Figure 8.8: Comparison of the CSM parameters of the sample in this paper with CSM properties of other SNe in the literature (from Brethauer et al. 2022). We note that the physical parameters have been estimated with a variety of observational "tracers" and hence probe different regions of the CSM.

arise from low-mass He stars ($< 3.5\ M_\odot$) that have been highly stripped by a binary companion in a close orbit, leaving behind CO cores with approximate masses ranging from 1.45 to 1.6 $M_\odot$ at the time of the explosion (Tauris et al. 2015). It is worth noting that the CO core mass serves as a reliable indicator of the ZAMS mass, as it remains unaffected by binary stripping (Fransson and Chevalier 1989, Jerkstrand et al. 2014a, 2015a). We find that the O-yields for the CO-cores of USSNe are higher than five SNe in our sample (see Figure 8.10).

We caution that these measurements assume that the radioactive energy deposited in the O-rich shells is primarily released through cooling in the [O I] lines. However, presence of impurity species can affect the [O I] luminosities. E.g., Dessart and Hillier (2020) showed that if Ca is mixed into the O-rich regions, the [O I] line emissions are weakened. Nevertheless, extensive studies on CCSNe have indicated that mixing is not significant in these events. Detailed modeling of CCSNe has

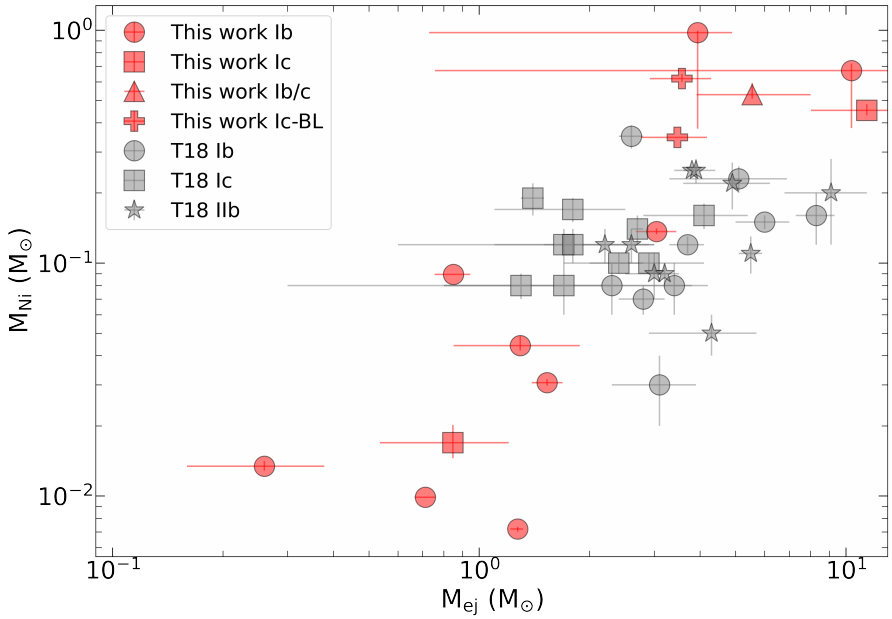

Figure 8.9: The distribution of measured ^{56}Ni mass vs ejecta mass for SNe in this sample compared to normal Type Ibc, IIb SNe from Taddia et al. (2018).

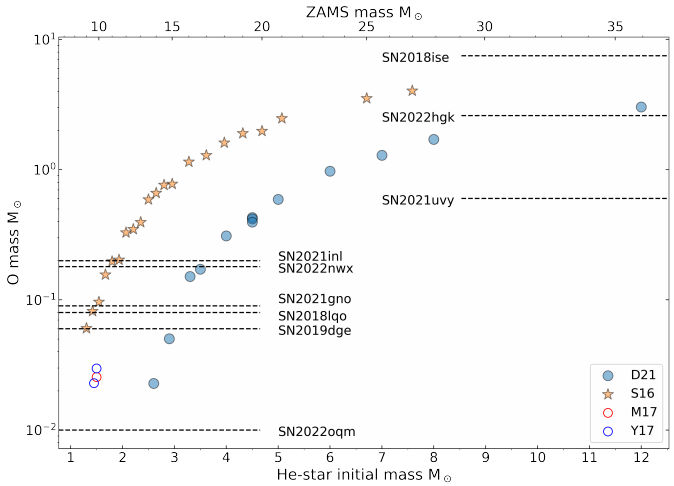

Figure 8.10: The O mass measurements are depicted by horizontal dashed lines. The O yields from the He-star progenitor models, assuming binary evolution (Dessart et al. 2021a), are represented by solid blue dots. The O yields from the single-star models (Sukhbold et al. 2016) are indicated by filled orange stars. Additionally, we show the O mass predictions from nucleosynthetic models of lower ZAMS stars from USSNe models by Yoshida et al. (2017) and Moriya et al. (2017).

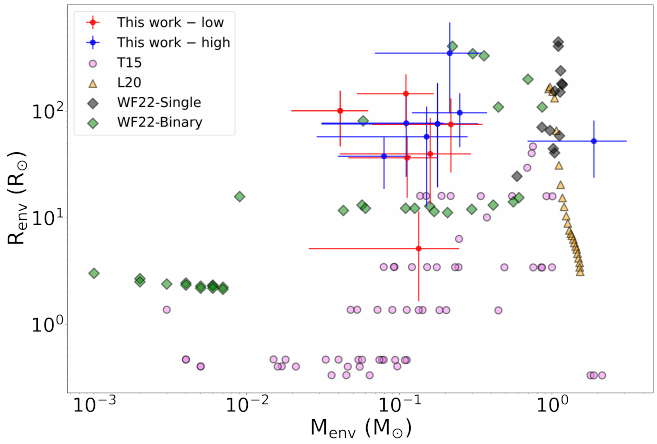

Figure 8.11: Comparison of the envelope parameters derived using analytical shock-cooling model as described in Section 8.4 (in red cross) with *bound* envelope properties from various binary and single star models (WF22; Wu and Fuller 2022a), (L20; Laplace et al. 2020) and (T15; Tauris et al. 2015). The SNe with low progenitor masses ($\lesssim$ 12 $M_\odot$) and higher progenitor masses are shown in red and blue respectively.

revealed that the [Ca II] lines are the primary coolant in the Si-rich layers while the emission from [O I] originates from the outer layers rich in oxygen, formed during the hydrostatic burning phase (Jerkstrand et al. 2015a, Dessart and Hillier 2020). Additionally, Polin et al. (2021) have demonstrated that even a contamination of 1% level of ^{40}Ca can cool a nebular region entirely through [Ca II] emission. Thus, if these ejecta regions were mixed, it would be challenging to observe the emission of [O I] line.

We note that the low ejecta mass ($\lesssim$ 1.5 $M_\odot$) for SNe 2021gno, 2021inl, 2022nwx, 2018lqo, 2021niq are consistent with those predicted for the lower end of the He-star mass stars based on predicted ejecta properties of H-poor stars (e.g., Dessart et al. 2021a). Nebular spectra estimates for all the above SNe are also consistent with low ZAMS mass, except for SN 2021niq for which we don't have any nebular spectrum. Also, for SN 2022oqm, the ejecta mass is not consistent with the progenitor mass estimate from the nebular spectra. In this paper, we consider SN 2021gno, SN 2021niq, SN 2021inl, SN 2022nwx, SN 2018lqo, SN 2019dge as potential SNe with progenitor masses less than ~12 $M_\odot$.

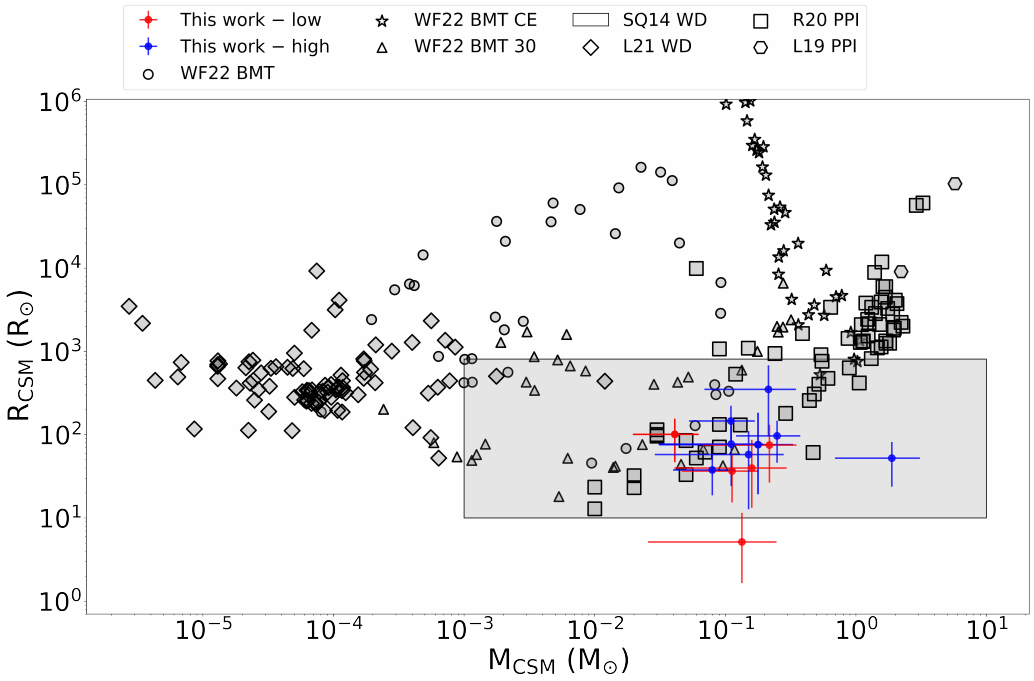

Figure 8.12: Comparison of the envelope parameters derived using analytical shock-cooling model as described in Section 8.4 (in red cross) with *unbound* CSM predictions from various pre-SN mass-loss models: late-time stable binary mass transfer (BMT; Wu and Fuller 2022a), late-time unstable binary mass transfer via common envelope (BMT CE; Wu and Fuller 2022a), late-time binary mass transfer with shock breakout at optical depth ~ 30 (BMT 30; Wu and Fuller 2022a), wave-driven mass loss (WD; Leung et al. 2021a, Shiode and Quataert 2014), pulsation-pair instability driven mass loss (PPI; Renzo et al. 2020, Leung et al. 2019). The SNe with low progenitor masses ($\lesssim 12\ M_\odot$) and higher progenitor masses are shown in red and blue respectively.

8.6 Mass-loss scenarios

In the previous sections, we presented the results from the analysis of our double-peaked Type Ibc(BL) sample that included lightcurve and spectral properties. In this section, we try to understand the physical process that gave rise to the first peak. The early bump is most likely due to interaction with the external stellar material that is part of the extended bound envelope of a massive star or unbound material ejected in a pre-SN mass loss event. There are other evidences for CSM interaction for some of the SNe in our sample. For example, Jacobson-Galán et al. (2022b) measured a CSM mass of $0.3 - 1.6 \times 10^{-3}\ M_\odot$ that extends upto 5×10^{14} cm. Luminous x-Ray and radio counterparts were observed for SN 2020bvc (Ho et al. 2020). Irani et al. (2022) predicts the presence of C/O-rich CSM at $2 - 5 \times 10^{14}$ cm based on early-time

spectra. Similarly, early-time spectra for SN 2019dge (Yao et al. 2020) was used to constrain the distance of He-rich CSM at $\gtrsim 3 \times 10^{13}$ cm. The sample provides a unique opportunity to understand the origin of the CSM from late-time stellar evolution. There are different theoretical models for possible pre-SN mass loss. In this section, we explore these scenarios and compare them to the observations.

Pre-SN mass loss for progenitor masses $\lesssim$ 12 $M_\odot$

Low mass binary He-stars

We know that the majority ($\sim 70\%$) of young massive stars live in interacting binary systems (Mason et al. 1998, Sana et al. 2012). Recent evidence suggests that Type Ibc SNe form when less massive stars are stripped due to a binary companion (e.g., Podsiadlowski et al. 1992). These stripped stars are formed when they lose their hydrogen envelopes through case B mass transfer (MT) after hydrogen burning. The stripped stars with $M_{He} \lesssim 4\ M_\odot$ expand again and lose a significant amount of their He envelope through Case BC MT. This results in stars with low pre-collapse masses which can explain the inferred M_{ej} of the sources with low progenitor mass and low ejecta mass constraints.

There have been attempts to model the case BB MT to make predictions for mass loss and the final fate of the progenitor (Tauris et al. 2013, 2015, Yoon et al. 2010a, Laplace et al. 2020). However, these do not predict the significant CSM that we infer in our observations. However, Wu and Fuller (2022a) find that when the O/Ne-core burning is taken into account, He-stars of masses $\approx 2.5 - 3\ M_\odot$ rapidly re-expand. As a result, they undergo high rates of binary MT weeks to decades before core-collapse. In *Part A* and *Part B*, we look at the possible cases where the shock passes through this re-expanded bound material before and after the late-time MT. In *Part C*, we look at the possible case where the shock passes through the unbound material ejected as part of the late-time MT.

Part A: Bound stellar material before late-time binary mass transfer

Stripped stars with initial masses $2.5\ M_\odot \lesssim M_{He} \lesssim 3\ M_\odot$ expand by two orders of magnitude during C-burning beginning $\sim 10^5$ years before core-collapse. Wu and Fuller (2022b) found that the radius can expand to $\sim 200\ R_\odot$ for low mass He-stars during O/Ne-burning.

We investigate if the low-luminosity first bumps we see for those with low progenitor mass be produced as the shock from the core-collapse passes through this bound

puffed-up stellar envelope. We can see from Table H that the models for single star evolution from Wu and Fuller (2022a) can puff up to a radius that is consistent with what is calculated from the shock-cooling modeling.

Based on the density profiles of these stars (see Figure 8.15), we assume the material at $r > R_{max}/3$ (Nakar and Piro 2014) is the bounded envelope responsible for the early bump, where R_{max} is the radial distance of the star where the density drops below 10^{-7}g cm^{-3}. We also compare the bound envelope properties of binary and single stars from Laplace et al. (2020), Tauris et al. (2015) with those calculated for our sample in Figure 9.12. We find that the expected envelope mass for these models is $\sim 1.2\ M_{\odot}$, an order of magnitude greater than the observed values.

We also note that the above scenario would require that the star will not interact afterward with the binary companion after undergoing Case B mass transfer. This is possible when the binary stars have very large periods so that the Roche-lobe is not filled during the expansion. Wu and Fuller (2022a) find that the highest-mass models $M_{He} \geq 2.8\ M_{\odot}$ with orbital period (P_{orb}) = 100 day do not expand enough to fill their Roche lobes.

However, in these cases, it is more likely that the substantial radius expansion of the stripped stars suggests the possibility of them reoccupying their Roche lobes and experiencing subsequent phases of mass transfer (Dewi et al. 2002, Dewi and Pols 2003, Ivanova et al. 2003). Additional phases of mass transfer can produce stars with low envelope masses, possibly explaining the low ejecta mass we observe for those with low progenitor mass. We discuss this in the next part.

Part B: Bound stellar material after late-time binary mass transfer

Wu and Fuller (2022a) calculated the mass-loss rates from the late-time binary transfer described earlier and the accumulated mass loss at P_{orb} = 1, 10, and 100 days. After the late-time mass transfer, the final masses range between $\sim$ 1.4–2.9 $M_{\odot}$. As these models reach Si-burning with final masses $\geq 1.4\ M_{\odot}$, they are expected to undergo core collapse. Assuming $M_{NS} = 1.4\ M_{\odot}$, the implied SN ejecta masses are $\lesssim 1.5\ M_{\odot}$. The density profiles of these stars after the late-time mass transfer are shown in Appendix 8.10. The envelope radius of most of these binary stars, especially those with P_{orb} = 10 days, is consistent with the observed values (see Table I and Figure 9.12). Using these density profiles and the same procedure used in the previous section, we get an envelope mass range of 0.01–0.1 $M_{\odot}$, which is consistent with the measured mass.

But for those stars which have lost mass through the late-time mass transfer, there should be another sign of interaction when the shock passes through the unbound CSM. It is possible that we did not have high enough cadence spectra to look for these interactions or that any interaction contribution to the lightcurve was too small compared to the Ni-powered lightcurve.

Part C: Unbound stellar material after late time transfer

Wu and Fuller (2022a) assume that shells of expelled material form at a distribution of radii around the binary system as a result of the late-time MT. To estimate the properties of this CSM they perform a mass-weighted average of these radii to calculate the characteristic CSM radius. They calculate the total CSM mass in each system as the integrated mass loss rate at core collapse.

We note that the shock-cooling breakout radius is expected to be smaller than the mass-weighted radius reported in Wu and Fuller (2022a). Here, we calculate the CSM radius assuming the shock breakouts at an optical depth ($\tau \sim 3c/v_s \sim 30$). We assume a CSM wind-density profile of the form $\rho = Kr^{-2}$ (used in e.g., Ofek et al. 2010, Chevalier and Irwin 2011), where r is the distance from the progenitor. $K \equiv \dot{M}/(4\pi v_{\rm w})$ is the wind density parameter, $v_{\rm w}$ is the wind velocity, and $\dot{M}$ is the mass-loss rate. $\rm R_{out}$ is the maximum distance of the unbound CSM ejected during the late-time MT. If we assume that the shock breakout occurs at an optical depth ($\tau \sim 30$):

$$\tau(r) = \int_{r}^{\rm R_{out}} \kappa\rho dr = \kappa K\left(\frac{1}{r} - \frac{1}{\rm R_{out}}\right) \approx \frac{c}{v_s} \tag{8.4}$$

we get the shock-breakout radius ($r_{\rm SBO}$) as:

$$r_{\rm SBO} = \frac{R_d \rm R_{out}}{R_d + \rm R_{out}} \tag{8.5}$$

, where $R_d \equiv \frac{\kappa K v_S}{c}$ (see Chevalier and Irwin 2011). From Figure 8.12, we see that the shock-cooling breakout radius (SCB-30) from most models is consistent with our observations.

These models have small SN ejecta masses $\lesssim 1.5\ M_\odot$, assuming an NS mass of $M_{\rm NS} = 1.4\ M_\odot$ consistent with the measured ejecta masses for SN 2021gno, SN 2021niq, SN 2021inl, SN 2022nwx, SN 2018lqo, SN 2019dge in our sample. We compare the CSM properties for these with those predicted from the late-time MT simulations (see Figure 8.12). We also show the CSM properties expected in case of unstable MT, which leads to a common envelope event (see Wu and

Fuller 2022b for details). We find that the CSM properties across both scenarios are consistent with the CSM masses ($\sim 0.01 - 1\ M_\odot$) and radii ($\sim 10^{11} - 10^{13}$ cm) inferred for those SNe with low ejecta mass.

However, as mentioned earlier, the late-time mass transfer only occurs for the low progenitor mass SNe. To explain the CSM properties for sources with high ejecta mass, we turn to other pre-SN mass-loss models.

Pre-SN mass loss for higher progenitor masses

Wave heating process in hydrogen-poor stars

Wave-driven mass loss (Quataert and Shiode 2012a, Shiode and Quataert 2014, Fuller 2017, Fuller and Ro 2018, Wu and Fuller 2021, Leung et al. 2021a) occur when convective motions in the massive star's core excite internal gravity waves during its late-phase nuclear burning. These gravity waves propagate through the radiative core and transmit some percentage of its energy into the envelope via acoustic waves, which can be sufficient to eject a substantial amount of mass.

We compare the CSM properties with mass-loss models in Leung et al. (2021b) in Figure 8.12. The wave heating process in massive hydrogen-poor stars was investigated by Leung et al. (2021b), who surveyed a range of stellar models with main sequence progenitor masses from $20 - 70\ M_\odot$ and metallicity from 0.002 to 0.02. Most of these models predict CSM masses less than $\sim 10^{-2}\ M_\odot$. The low mass makes just wave driven-driven mass loss an unlikely explanation for all the observed CSM masses. However, a few models predict somewhat higher wave energy fluxes, have larger ejected mass ($\sim 10^{-2}\ M_\odot$) or have a very large $R_{\rm CSM} \sim 10^{14}$ cm. These are models with large wave energies or long wave heating time scales, respectively. It requires the merger of nearby burning shells, in their models the carbon and helium shells. The merging of the two shells allows gravity waves to propagate across the star with a lower evanescence. However, numerical models show that such a phenomenon only occurs at individual masses of massive stars rather than a robust mass range. This may be consistent with the rarity of SNe observed in this work.

We find that the CSM properties predicted in Shiode and Quataert (2014) are consistent with our observations (see Figure 8.12). Shiode and Quataert (2014) predicts that wave excitation and damping during Si-burning can inflate nominally compact Wolf-Rayet progenitors to $10^{-3} - 1\ M_\odot$ of the envelope of Wolf-Rayet stars to tens to hundreds of $R_\odot$. These findings indicate that certain supernova (SN)

progenitors, often characterized by their compact nature, including those associated with Type Ibc SNe, exhibit a shock cooling signature that differs considerably from conventional assumptions. The authors predict that the outcome of wave energy deposition during silicon fusion in Wolf-Rayet (WR) progenitors would probably manifest as a core-collapse SN classified spectroscopically as Type Ibc (i.e., a compact star), but displaying early thermal emission reminiscent of extended stellar envelopes, which is observed as an early bump in our sample. However, we note that their estimates do not involve hydrodynamical simulations.

Pulsation Pair Instablility

For very massive stars ($M_{\rm ZAMS} = 80-140\ M_{\odot}$), the electron-positron pair instability (PPI) drives explosive O-burning and mass ejection, which accounts for an outburst of $\sim$ 0.1 to tens of $M_{\odot}$(Woosley 2019, Leung et al. 2019, Renzo et al. 2020). Pulsation-induced mass loss relies on the electron–positron pair-creation catastrophe which happens in very massive stars (Heger and Woosley 2002). The star can experience several mass-loss events, depending on the available carbon and oxygen in the core (Woosley 2017, Leung and Fuller 2020).

In Figure 8.12, we plot the predicted CSM properties for the PPI-driven mass loss from Renzo et al. (2020), Leung et al. (2019). The models center around $M_{\rm CSM} \sim 0.01 - 10\ M_{\odot}$ and $R_{\rm CSM} \sim 10^{11} - 10^{15}$ cm. These are consistent with the observed CSM properties for our sample (see Figure 8.12). The objects in this work are consistent with the lower mass PPISNe reported in the literature near a He core mass $\sim$ 40 $M_{\odot}$ (or ZAMS mass $\sim$ 80 $M_{\odot}$). We notice that the PPISN model will be in tension for the objects with a low ejecta mass reported in this work. Given the high progenitor mass for PPISN ($80-140\ M_{\odot}$), and the production ^{56}Ni, which indicates a robust explosion, if a spherical explosion is considered the ejecta mass would be much larger. Most PPISN models predict that the star will collapse into a black hole. The low ejecta mass could be explained if most of the star's mass falls into the black hole and only a small fraction of the mass is ejected during the SN explosion. It is also possible that the aspherical explosion plays a role here. Through a jet-like energy deposition, only matter along the jet opening angle acquires the energy deposition, thus the necessary energy deposition and the corresponding ejecta mass can be substantially lower even when the progenitor mass is high. Then, a relatively lower amount of energy is needed for the same ejecta velocity. The aspherical shape may lead to strong polarity in the optical signals,

which can be checked for such sources in the future. Further samples along the trend may provide further evidence for PPISN being a robust production mechanism for low-mass CSM. However, given its high progenitor mass which is less common in the stellar population according to the Salpeter relation, further comparison with the canonical supernova rate will be important to check the compatibility of this picture with the stellar statistics. If we assume a Salpeter IMF, roughly $\sim 2.3\%$ of CCSNe should undergo PPI, which is roughly consistent with the rate predicted for the double-peaked Type Ibc SNe in Section 8.2.

Wolf-Rayet+Red Super Giant wind mass loss

One possibility is that the progenitors of our observed sources underwent a typical phase of Red Super Giant (RSG) with line-driven wind mass loss. Assuming a wind velocity (v_w) of ≈ 10 km s^{-1}, the expected mass-loss rates range from $\dot{M} \approx 10^{-6}$ $M_\odot$ yr^{-1} to $\dot{M} \approx 10^{-3}$ $M_\odot$ yr^{-1} (e.g., de Jager et al. 1988, Marshall et al. 2004, van Loon et al. 2005).

Subsequently, there is a relatively brief phase of Wolf-Rayet (WR), characterized by higher wind velocities of a few 1000 km s^{-1} and mass-loss rates around $\sim 10^{-5}$ $M_\odot$ yr^{-1} (e.g., Crowther 2007). It is a possibility that the stellar progenitor explodes as a Type Ibc supernova within the bubble formed by its own WR winds interacting with the prior RSG wind phase. However, the documented cases of WR-RSG wind-wind interaction are associated with "bubbles" at typical distances of $\sim 10^{19}$ cm (Marston 1997), significantly farther than the few $< 10^{15}$ cm distances inferred for our sources. For our sample, the proximity of the CSM shell implies an extremely short WR phase with a duration of $\sim 10^3$ ($v \sim 1000$ km s^{-1}) yrs, conflicting with the $\sim 10^5$ yr duration of the WR phase expected in the case of isolated massive stars. For such a short lifespan, assuming a mass loss rate of $\sim 10^{-5}$ $M_\odot$yr^{-1}, the mass loss will be around 0.01 $M_\odot$, which is an order or so less than what we observe. Thus, wind loss from WR+RSG is not consistent with our observations.

White dwarf progenitor

In the earlier sections, we discussed the presence of the early shock-cooling signatures as originating from the extended envelope or CSM of a massive progenitor star. However, we note that an early excess in the lightcurve is also possible in the context of a white dwarf. Such scenarios include white dwarf systems that involve companion interaction through Roche-lobe overflow (Magee et al. 2020,

Kasen 2010), clumpy nickel distribution in the ejecta (Magee and Maguire 2020), CSM interaction (Piro and Morozova 2016). The ejecta mass and oxygen mass measured for SN 2021gno, SN 2021niq, SN 2021inl, SN 2019dge, SN 2018lqo are within the mass limit for a white dwarf. Based on the strong [Ca II] emission lines in the nebular spectra, SN 2021gno, SN 2021inl, SN 2018lqo and SN 2022oqm could belong to the thermonuclear group of Ca-rich gap transients, which result from explosive burning of He shells on the surface of low mass white dwarfs (De et al. 2020b). Jacobson-Galán et al. (2022b) favored a low-mass hybrid He/C/O + C/O WD binary progenitor system for SN 2021gno and SN 2021inl based on the environment of their explosion sites. The disruption of a C/O WD by a heavier WD companion is favored for SN 2022oqm in Irani et al. (2022). Detailed spectral and lightcurve analysis in the context of the various white dwarf progenitor channels is left for future work.

8.7 Summary and Future Goals

1. We present a sample of 17 double-peaked Type Ibc(BL) SNe from ZTF. This was selected from a sample of 475 SNe classified as Ibc(BL) as part of the ZTF and CLU surveys. Out of these 475 SNe, there were 144 SNe with well-sampled early light curves. The rate of this sample is $\sim 3-9\%$ of Type Ibc(BL) SNe.

   The first peak is likely produced after the shockwave runs through an extended envelope, and the layer cools (the "shock cooling" phase). Type Ibc SNe are thought to arise from compact stars, so the envelope is more likely to be stellar material that was ejected in some mass-loss episode.

2. The peak magnitude of the first peak range from -14.2 to -20.1. We find that the peak magnitude of the first peak and second peak are correlated as $M_2 = 0.8 \times M_1 - 4.7$ where M_1, M_2 are the peak magnitudes of the first and second peak, respectively. The correlation could imply that the SNe that show double-peaked lightcurves have He-star progenitors that shed their envelope in binary interactions. The photospheric velocities of the SNe in our sample are consistent with those of canonical Type Ibc SNe.

3. Based on nebular spectra and lightcurve properties, we divide our sample into two groups: six SNe − SN 2021gno, SN 2018lqo, SN 2021inl, SN 2022nwx, SN 2019dge, SN 2021niq − with progenitor mass less than $\sim 12\ M_\odot$ and ejecta mass less than $1.5\ M_\odot$ and the rest with higher progenitor mass.

4. The observed CSM properties for SNe with low progenitor and ejecta mass might be explained as due to the binary evolution of low-mass He stars due to late-time mass transfer. The observed CSM properties of SNe with higher ejecta mass are consistent with certain models of wave-driven mass loss due to Si-burning or pulsation-pair instability-driven mass loss.

The sample presented in this paper will enable detailed modeling of the progenitor and supernova, offering insights into their mass-loss histories and envelope structures and thus inform stellar evolution models. The investigation of double-peaked Type Ibc supernovae and the mechanisms behind pre-supernova mass loss have implications across multiple areas of astronomy. These findings have the potential to alter predictions related to ionizing radiation and wind feedback from stellar populations, thereby influencing conclusions about star formation rates and initial mass functions in galaxies beyond our own. Moreover, these discoveries impact our understanding of the origins of diverse compact stellar remnants and shape the way we utilize supernovae as tools for studying stellar evolution throughout cosmic history

While analytical modeling of shock-cooling provides a good estimate of the CSM properties, it might not be able to take into account detailed nuances such as variable opacities, densities, etc. The exact structure of the CSM and its impact on the explosion light curve require detailed hydrodynamics and radiative transfer calculations which we leave for future work.

It is also important to understand the implication of the missing early bump in the majority of Type Ibc SN in understanding the multiplicity of stars, binary evolution, and the extent of stripping in compact binaries including common envelope evolution. Further theoretical work to study this is left for future work.

This sample shows that shock-cooling emission may be very common in H-poor SNe. We might be missing many of them because of poor early-time cadence. Early observations with future wide-field UV surveys such as ULTRASAT (Sagiv et al. 2014, Shvartzvald et al. 2023) and UVEX (Kulkarni et al. 2021) will be critical for the discovery and study of these SNe. Also, X-ray and radio follow-up observations (Matsuoka and Maeda 2020, Kashiyama et al. 2022) of H-poor SNe with well-sampled early optical light curves will help better constrain the mass-loss mechanisms.

8.8 Data availability

All the photometric and spectroscopic data used in this work will be available here after publication.

The optical photometry and spectroscopy will also be made public through WISeREP, the Weizmann Interactive Supernova Data Repository (Yaron and Gal-Yam 2012a).

8.9 Acknowldegement

We thank Anthony L. Piro for insightful discussions and comments. We would also like to thank Daniel Brethauer for providing the data used in Brethauer et al. (2022). Based on observations obtained with the Samuel Oschin Telescope 48-inch and the 60-inch Telescope at the Palomar Observatory as part of the Zwicky Transient Facility project. ZTF is supported by the National Science Foundation under Grant No. AST-2034437 and a collaboration including Caltech, IPAC, the Weizmann Institute of Science, the Oskar Klein Center at Stockholm University, the University of Maryland, Deutsches Elektronen-Synchrotron and Humboldt University, the TANGO Consortium of Taiwan, the University of Wisconsin at Milwaukee, Trinity College Dublin, Lawrence Livermore National Laboratories, IN2P3, France, the University of Warwick, the University of Bochum, and Northwestern University. Operations are conducted by COO, IPAC, and UW.

SED Machine is based upon work supported by the National Science Foundation under Grant No. 1106171.

The ZTF forced-photometry service was funded under the Heising-Simons Foundation grant #12540303 (PI: Graham).

The GROWTH Marshal was supported by the GROWTH project funded by the National Science Foundation under Grant No 1545949.

The data presented here were obtained in part with ALFOSC, which is provided by the Instituto de Astrofisica de Andalucia (IAA) under a joint agreement with the University of Copenhagen and NOT.

The Liverpool Telescope is operated on the island of La Palma by Liverpool John Moores University in the Spanish Observatorio del Roque de los Muchachos of the Instituto de Astrofisica de Canarias with financial support from the UK Science and Technology Facilities Council. Based on observations made with the Italian Telescopio Nazionale Galileo (TNG) operated on the island of La Palma by the

Table C: Summary of the nebular properties.

Source	Spectra Tel.+Inst.	Phase (days since primary peak)	[Ca II]/[O I] flux ratio	[O I] lum. (10^{38} erg s^{-1})	O mass ($M_\odot$)
ZTF21aaqhhfu/SN 2021gno[a]	Keck + LRIS	84	8.97 ± 1.79	3.9 ± 0.4	0.1 – 0.3
ZTF18achcpwu/SN 2018ise	Keck + LRIS	120	0.93 ± 0.08	303.45 ± 12.11	7.5 – 20.0
ZTF18abmxelh/SN 2018lqo	Keck + LRIS	52	> 50	< 1.6	< 0.1
ZTF21aasuego/SN 2021inl[a]	Keck + LRIS	111	4.39 ± 0.88	8.2 ± 0.4	0.2 – 0.6
ZTF22aapisdk/SN 2022nwx	Keck + LRIS	86	10.95 ± 1.15	7.62 ± 0.90	0.2 – 0.5
ZTF22aasxgjp/SN 2022oqm	P200 + DBSP	74	> 22	< 0.17	< 0.01
ZTF22aaezyos/SN 2022hgk	Keck + LRIS	75	1.13 ± 0.04	104 ± 1.4	2.6 – 7.4
ZTF21abmlldj/SN 2021uvy	Keck + LRIS	426	3.38 ± 0.15	81 ± 8	0.6 – 3.1
ZTF18abfcmjw/SN 2019dge	Keck + LRIS	83	1.22 ± 0.19	2.44 ± 0.33	0.06 – 0.1

[a] From Jacobson-Galán et al. (2022b).

Fundación Galileo Galilei of the INAF (Istituto Nazionale di Astrofisica) at the Spanish Observatorio del Roque de los Muchachos of the Instituto de Astrofisica de Canarias.

The W. M. Keck Observatory is operated as a scientific partnership among the California Institute of Technology, the University of California and the National Aeronautics and Space Administration. The Observatory was made possible by the generous financial support of the W. M. Keck Foundation. The authors wish to recognize and acknowledge the very significant cultural role and reverence that the summit of Maunakea has always had within the indigenous Hawaiian community. We are most fortunate to have the opportunity to conduct observations from this mountain. The `ztfquery` code was funded by the European Research Council (ERC) under the European Union's Horizon 2020 research and innovation programme (grant agreement $n°759194-$ USNAC, PI: Rigault).

Shing-Chi Leung acknowledges support by the National Science Foundation under Grant AST-2316807.

Table D: Shock cooling modeling

Source	E_{ext} ($\times 10^{49}$ erg)	R_{ext} $R_\odot$	M_{ext} ($\times 10^{-2} M_\odot$)	t_{exp} JD
ZTF21aaqhhfu/SN2021gno	$0.70^{+0.06}_{-0.06}$	$101.19^{+8.32}_{-7.43}$	$4.10^{+0.9}_{-0.9}$	$59292.29^{+0.05}_{-0.05}$
ZTF21abcgnql/SN2021niq	$4.71^{+1.00}_{-0.86}$	$36.64^{+7.67}_{-5.82}$	$11.26^{+1.02}_{-1.01}$	$59355.80^{+0.10}_{-0.12}$
ZTF20abbpkng/SN2020kzs	$34.24^{+33.39}_{-20.59}$	$76.11^{+139.24}_{-37.44}$	$17.79^{+6.28}_{-5.80}$	$58980.47^{+0.31}_{-0.50}$
ZTF21abccaue/SN2021nng	$93.44^{+4.84}_{-9.73}$	$52.40^{+6.67}_{-4.83}$	$188.21^{+26.63}_{-24.96}$	$59333.35^{+0.26}_{-0.35}$
ZTF18achcpwu/SN2018ise	$23.42^{+25.90}_{-10.53}$	$57.76^{+77.12}_{-61.14}$	$15.08^{+12.93}_{-12.20}$	$58420.81^{+0.81}_{-0.96}$
ZTF18abmxelh/SN2018lqo	$7.57^{+3.38}_{-2.80}$	$75.29^{+75.72}_{-59.76}$	$21.77^{+13.34}_{-15.13}$	$58336.50^{+0.50}_{-0.35}$
ZTF21acekmmm/SN2021aabp	$79.40^{+4.47}_{-4.41}$	$96.79^{+53.49}_{-52.93}$	$24.90^{+12.61}_{-12.81}$	$59484.01^{+0.02}_{-0.01}$
ZTF21aasuego/SN2021inl	$3.90^{+2.91}_{-2.38}$	$39.85^{+73.71}_{-33.17}$	$15.94^{+13.53}_{-11.87}$	$59308.66^{+0.26}_{-0.77}$
ZTF21abdxhgv/SN2021qwm	$12.62^{+9.28}_{-5.45}$	$350.65^{+488.49}_{-334.14}$	$21.41^{+13.34}_{-14.49}$	$59366.17^{+0.60}_{-0.68}$
ZTF22aapisdk/SN2022nwx	$45.39^{+36.30}_{-29.55}$	$5.16^{+10.20}_{-4.43}$	$13.39^{+11.27}_{-10.84}$	$59754.55^{+0.21}_{-0.43}$
ZTF22aasxgjp/SN2022oqm	$15.58^{+0.15}_{-0.15}$	$37.81^{+0.41}_{-0.39}$	$7.94^{+1.1}_{-2.3}$	$59770.23^{+0.1}_{-0.2}$
ZTF21aacufip/SN2021vz	$46.36^{+25.01}_{-18.70}$	$77.29^{+99.91}_{-67.37}$	$11.10^{+8.35}_{-8.02}$	$59221.50^{+0.33}_{-0.33}$
ZTF18abfcmjw/SN2019dge	$5.73^{+0.25}_{-0.27}$	$146.04^{+79.39}_{-78.92}$	$11.05^{+6.17}_{-6.16}$	$58580.25^{+0.02}_{-0.02}$
ZTF20aalxlis/SN2020bvc	$67.18^{+2.94}_{-3.31}$	$118.21^{+65.45}_{-64.20}$	$19.55^{+10.13}_{-10.18}$	$58881.00^{+0.3}_{-0.3}$

Table E: Order of magnitude shock-cooling CSM estimates

Source	M_{CSM} ($M_\odot$)	R_{CSM} ($R_\odot$)
SN 2021gno	0.02	10
SN 2021niq	0.20	10
SN 2020kzs	0.53	20
SN 2021nng	0.06	40
SN 2018ise	0.05	60
SN 2018lqo	1.23	10
SN 2021aabp	0.34	60
SN 2021inl	0.04	10
SN 2021qwm	0.07	220
SN 2022nwx	0.03	10
SN 2022oqm	0.01	30
SN 2021vz	0.28	1030
SN 2022hgk	0.18	20
SN 2021uvy	11.31	260
SN 2019dge	0.06	30
SN 2020bvc	0.01	210
SN 2019cad	0.86	20

Table F: Order of magnitude shock-breakout CSM estimates

Source	M_{CSM} (10^{-3} $M_\odot$)	R_{CSM} ($R_\odot$)
SN 2021gno	0.19	5900
SN 2021niq	0.11	19400
SN 2020kzs	0.13	3100
SN 2021nng	0.69	10800
SN 2018ise	1.13	9400
SN 2018lqo	0.03	47400
SN 2021aabp	0.40	25000
SN 2021inl	0.15	8900
SN 2021qwm	3.45	11300
SN 2022nwx	0.22	6800
SN 2022oqm	1.26	4700
SN 2021vz	8.12	22500
SN 2022hgk	0.15	18500
SN 2021uvy	0.31	143700
SN 2019dge	0.53	10800
SN 2020bvc	7.26	5000
SN 2019cad	0.1	39500

Table G: Summary of the best-fit physical parameters obtained from radioactive-decay modeling of the second peak of the SNe in our sample. The 'Ar' subscript refers to the Arnett et al. (1989) model, while the 'KK' subscript refers to the Khatami and Kasen (2019) model. The photospheric velocity is estimated as described in Section 8.4.

Source	$M_{\mathrm{Ni-Ar}}$ ($0.01\ M_\odot$)	$M_{\mathrm{Ni-KK}}$ ($0.01\ M_\odot$)	τ_m (days)	Velocity (km s^{-1})	$M_{\mathrm{ej-Ar}}$ ($M_\odot$)	$M_{\mathrm{ej-KK}}$ ($M_\odot$)	E_{kin} (10^{51} erg)	t_0 (days)
SN2021gno	$1.01^{+0.11}_{-0.11}$	1.09	$8.99^{+0.01}_{-0.01}$	7940 ± 500	$0.71^{+0.05}_{-0.05}$	0.53	$0.27^{+0.03}_{-0.04}$	$38.57^{+2.72}_{-3.68}$
SN2021niq	$4.42^{+0.49}_{-0.49}$	5.20	$12.07^{+1.45}_{-0.89}$	8000 ± 1600	$1.29^{+0.59}_{-0.44}$	0.88	$0.49^{+0.13}_{-0.07}$	$50.24^{+33.85}_{-15.88}$
SN2020kzs	$13.66^{+1.50}_{-1.50}$	18.31	$19.59^{+0.69}_{-0.62}$	7150 ± 430	$3.04^{+0.40}_{-0.37}$	1.68	$0.93^{+0.07}_{-0.06}$	$60.55^{+2.68}_{-2.60}$
SN2021nng	$67.09^{+4.70}_{-29.11}$	72.17	$38.76^{+1.00}_{-13.86}$	6210 ± 2110	$10.35^{+4.06}_{-9.60}$	2.85	$2.38^{+0.12}_{-1.40}$	$44.81^{+28.06}_{-2.37}$
SN2018ise	$45.24^{+2.86}_{-2.15}$	100.36	$35.83^{+2.10}_{-1.77}$	8000 ± 1600	$11.40^{+3.65}_{-3.37}$	6.05	$4.35^{+0.53}_{-0.42}$	$88.85^{+7.83}_{-10.36}$
SN2018lqo	$3.06^{+0.34}_{-0.34}$	3.61	$13.00^{+0.45}_{-0.40}$	8170 ± 260	$1.53^{+0.16}_{-0.14}$	0.99	$0.61^{+0.04}_{-0.04}$	$37.60^{+2.15}_{-2.10}$
SN2021aabp	$61.94^{+2.92}_{-2.10}$	76.66	$17.69^{+0.63}_{-0.48}$	10280 ± 1320	$3.57^{+0.72}_{-0.65}$	1.95	$2.25^{+0.16}_{-0.12}$	$41.16^{+2.28}_{-2.48}$
SN2021inl	$0.72^{+0.08}_{-0.08}$	0.77	$8.94^{+0.04}_{-0.09}$	14350 ± 350	$1.27^{+0.04}_{-0.06}$	0.91	$1.56^{+0.02}_{-0.03}$	$23.89^{+2.73}_{-2.20}$
SN2021qwm	$52.86^{+6.37}_{-2.11}$	82.22	$25.00^{+2.87}_{-1.22}$	8000 ± 1600	$5.55^{+2.46}_{-1.64}$	2.92	$2.12^{+0.51}_{-0.20}$	$68.20^{+13.49}_{-12.05}$
SN2022nwx	$1.69^{+0.19}_{-0.19}$	1.16	$9.77^{+1.02}_{-0.86}$	8000 ± 1600	$0.85^{+0.36}_{-0.31}$	0.36	$0.32^{+0.07}_{-0.05}$	$13.06^{+1.48}_{-1.22}$
SN2022oqm	$8.94^{+0.98}_{-0.98}$	10.18	$10.73^{+0.04}_{-0.04}$	6660 ± 690	$0.85^{+0.09}_{-0.09}$	0.60	$0.23^{+0.00}_{-0.00}$	$36.51^{+0.18}_{-0.18}$
SN2021vz	$97.55^{+10.73}_{-59.80}$	34.23	$21.07^{+0.43}_{-7.99}$	8000 ± 1600	$3.94^{+0.95}_{-3.21}$	0.68	$1.50^{+0.06}_{-0.92}$	$14.60^{+16.20}_{-0.54}$
SN2019dge	$1.34^{+0.15}_{-0.15}$	1.40	$5.41^{+0.65}_{-0.53}$	8000 ± 1600	$0.26^{+0.12}_{-0.10}$	0.23	$0.10^{+0.03}_{-0.02}$	$21.77^{+0.65}_{-0.65}$
SN2020bvc	$34.65^{+3.81}_{-3.81}$	40.44	$13.18^{+0.03}_{-0.03}$	18000 ± 3600	$3.47^{+0.71}_{-0.71}$	2.18	$6.70^{+0.03}_{-0.03}$	$41.84^{+0.16}_{-0.16}$

Table H: Bound stellar material properties of single star.

Initial mass ($M_\odot$)	R_{max} ($R_\odot$)	Mass ($> R_{max}/3$) ($M_\odot$)	Mass ($> 5\ R_\odot$) ($M_\odot$)
2.51	446.68	1.09	1.10
2.55	407.38	1.09	1.10
2.58	154.88	1.04	1.04
2.62	239.88	1.14	1.14
2.65	151.36	1.12	1.13
2.68	181.97	1.15	1.16
2.72	177.83	1.17	1.17
2.75	70.79	0.82	0.73
2.79	66.07	0.93	0.87
2.82	44.67	1.01	0.92
2.86	40.74	1.04	0.94
2.90	58.88	1.09	1.02
2.92	24.55	0.55	0.20

Table I: Bound stellar material properties after binary mass transfer

Initial mass ($M_\odot$)	Period (days)	R_{max} ($R_\odot$)	Mass ($> R_{max}/3$) ($M_\odot$)	Mass ($> 5\ R_\odot$) ($M_\odot$)
2.51	100	79.43	0.00	0.00
2.55	100	81.28	0.06	0.05
2.58	100	407.38	0.22	0.22
2.62	100	346.74	0.30	0.30
2.65	100	109.65	0.44	0.44
2.68	100	331.13	0.35	0.36
2.72	100	199.53	0.69	0.70
2.75	100	109.65	0.85	0.85
2.51	10	15.85	0.01	0.00
2.55	10	13.18	0.06	0.02
2.58	10	12.30	0.06	0.01
2.62	10	11.75	0.04	0.00
2.65	10	12.30	0.11	0.04
2.68	10	12.30	0.12	0.05
2.72	10	12.88	0.16	0.06
2.75	10	11.48	0.17	0.05
2.79	10	11.22	0.21	0.07
2.82	10	12.02	0.30	0.10
2.86	10	13.18	0.40	0.14
2.90	10	14.13	0.56	0.25
2.92	10	15.49	0.60	0.26

Table I: Continued...

Initial mass ($M_\odot$)	Period (days)	R_{max} ($R_\odot$)	Mass ($> R_{max}/3$) ($M_\odot$)	Mass ($> 5\ R_\odot$) ($M_\odot$)
2.51	1	2.69	0.00	0.00
2.55	1	3.02	0.00	0.00
2.58	1	2.51	0.00	0.00
2.62	1	2.40	0.00	0.00
2.65	1	2.45	0.00	0.00
2.68	1	2.34	0.01	0.00
2.72	1	2.34	0.00	0.00
2.75	1	2.29	0.01	0.00
2.79	1	2.29	0.01	0.00
2.82	1	2.24	0.01	0.00
2.86	1	2.19	0.01	0.00
2.90	1	2.19	0.01	0.00
2.92	1	2.14	0.01	0.00

8.10 Appendix

The complete datasets in Appendices 8.10, 8.10, 8.10, 8.10, and 8.10 can be found in Zenodo (DOI: 10.5281/zenodo.11505429) and GitHub[4].

Photometry Data

Summary of the photometry data used for SN 2018lqo (Truncated) is provided in Table J. The photometry data for all sources are provided as machine-readable tables in Zenodo viaDOI: 10.5281/zenodo.11505429.

Lightcurves

The lightcurves of all sources can be found in Zenodo viaDOI: 10.5281/zenodo.11505429.

Spectra

The spectra of all sources are provided as machine-readable tables in Zenodo viaDOI: 10.5281/zenodo.11505429.

Blackbody Fits

Summary of the blackbody properties for SN 2018lqo (Truncated) is provided in Table K. All the best-fit parameters including bolometric luminosity, radius and temperature for each object are provided as machine-readable tables in Zenodo viaDOI: 10.5281/zenodo.11505429.

First-peak fits

Figure 8.13 shows a collage of the best-fit lightcurves for the shock cooling model (Piro et al. 2021) fits to the multi-band photometry data.

Second-peak fits

Figure 8.14 shows a collage of the best-fit lightcurves for the radioactive peak model (Arnett and Meakin 2011) fits to the bolometric luminosity data.

Spectral log

The spectral log and the velocity measurements are listed in Table L.

[4] `https://github.com/kaustavkdas/doublepeaked_Ibc`

Table J: Summary of the photometry data used for SN 2018lqo (Truncated).

Date (JD)	filter	instrument	mag (AB mag)	limiting mag (AB mag)
2458340.68	r	P48+ZTF	20.11 ± 0.17	20.31
2458343.66	r	P48+ZTF	20.68 ± 0.23	20.64
2458343.68	g	P48+ZTF	20.98 ± 0.37	20.71
2458346.66	g	P48+ZTF	20.49 ± 0.30	20.49
2458346.68	r	P48+ZTF	20.16 ± 0.16	20.53
2458346.68	r	P48+ZTF	20.16 ± 0.16	20.53
2458347.76	r	P60+SEDM	20.02 ± 0.05	21.69
2458347.76	r	P60+SEDM	20.06 ± 0.04	99.00
2458347.76	g	P60+SEDM	20.40 ± 0.06	21.81
2458347.76	g	P60+SEDM	20.47 ± 0.07	99.00
2458347.76	i	P60+SEDM	19.92 ± 0.10	21.48
2458347.76	i	P60+SEDM	19.92 ± 0.53	99.00
2458348.68	i	P48+ZTF	19.82 ± 0.23	19.94
2458350.65	r	P48+ZTF	19.68 ± 0.16	20.45

Density profile of He-stars used in the late-time mass transfer models

The density profiles of the single He-stars of different masses before late-time mass transfer used in Section 8.6 are shown in Figure 8.15. The density profiles of the bound material of the stars after mass transfer can be found in Zenodo viaDOI: 10.5281/zenodo.11505429.

Table K: Summary of the blackbody properties for SN 2018lqo (Truncated).

Phase (days since first detection)	Log Luminosity (erg s^{-1})	Temperature (K)	Radius ($R_\odot$)
3.17	$41.55^{+0.11}_{-0.07}$	7048^{+3206}_{-1691}	6197^{+4753}_{-2832}
4.33	$41.67^{+0.50}_{-0.10}$	7197^{+10256}_{-1965}	6751^{+5648}_{-4616}
6.17	$41.76^{+0.05}_{-0.04}$	5908^{+1167}_{-915}	11467^{+5377}_{-3439}
7.26	$41.76^{+0.01}_{-0.01}$	6165^{+250}_{-244}	10699^{+942}_{-836}
8.24	$41.90^{+0.54}_{-0.11}$	5171^{+10212}_{-1856}	15557^{+29245}_{-11786}
10.21	$41.93^{+0.02}_{-0.02}$	5880^{+405}_{-382}	14321^{+2247}_{-1852}
11.22	$41.92^{+0.03}_{-0.02}$	5384^{+443}_{-391}	16918^{+3269}_{-2683}
12.21	$41.93^{+0.03}_{-0.03}$	5955^{+635}_{-544}	13900^{+3299}_{-2635}
20.22	$41.90^{+0.28}_{-0.16}$	3633^{+712}_{-683}	36441^{+39393}_{-15074}
21.17	$41.72^{+0.01}_{-0.01}$	4195^{+70}_{-70}	22190^{+1028}_{-917}
22.22	$41.76^{+0.08}_{-0.07}$	3926^{+391}_{-358}	26476^{+8634}_{-6183}
25.18	$42.00^{+0.40}_{-0.22}$	3175^{+609}_{-630}	53509^{+77779}_{-24058}

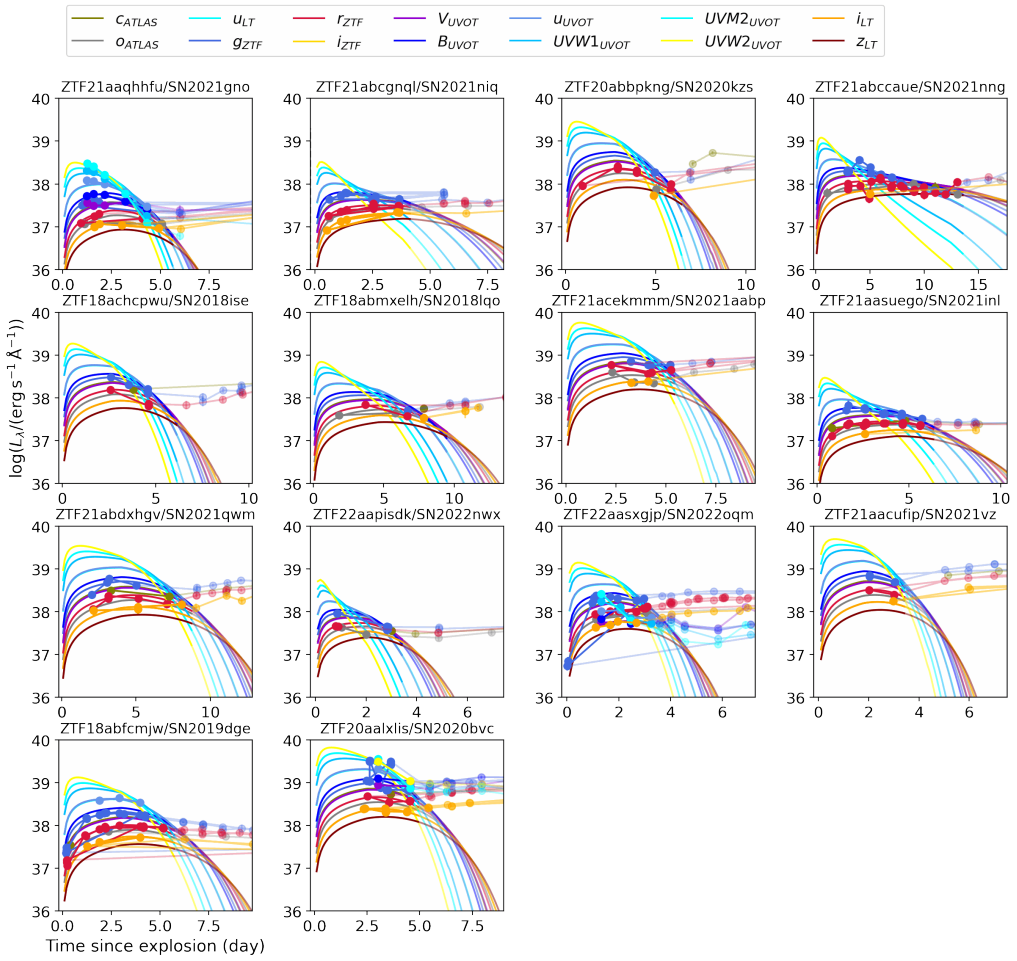

Figure 8.13: Shock cooling model (Piro et al. 2021) fits to multi-band data.

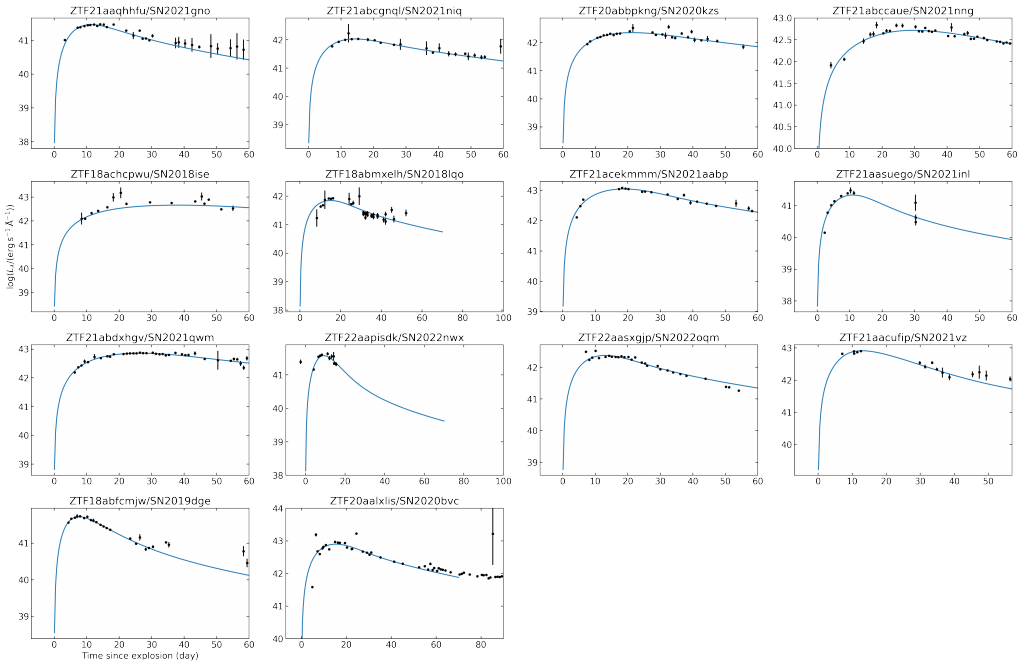

Figure 8.14: Radioactive (Arnett et al. 1989) fits to bolometric luminosity data.

Table L: Spectral log and ejecta velocity measurements.

Source	Date	Phase (days)	Inst.	He I λ5876 (km s^{-1})	O I λ7774 (km s^{-1})
ZTF21aaqhhfu/SN 2021gno	2021-03-20	-15.0	SPRAT	–	7910 ± 1170
ZTF21aaqhhfu/SN 2021gno	2021-03-21	-14.0	SEDM	–	–
ZTF21aaqhhfu/SN 2021gno	2021-03-24	-11.0	SEDM	12850 ± 4520	–
ZTF21aaqhhfu/SN 2021gno	2021-04-02	-2.0	SPRAT	8000 ± 260	6860 ± 810
ZTF21aaqhhfu/SN 2021gno	2021-04-02	-2.0	SEDM	7880 ± 740	5830 ± 2610
ZTF21aaqhhfu/SN 2021gno	2021-04-12	8.0	SEDM	8210 ± 2540	7630 ± 2920
ZTF21aaqhhfu/SN 2021gno	2022-02-04	306.0	LRIS	–	–
ZTF21abcgnql/SN 2021niq	2021-05-31	-6.0	DBSP	13680 ± 2630	–
ZTF21abcgnql/SN 2021niq	2022-04-13	310.0	LRIS	–	–
ZTF20abbpkng/SN 2020kzs	2020-06-01	-9.0	SEDM	–	–

* The full version of this table is available in machine-readable format in the online journal. A portion is shown here for guidance regarding its form and function.

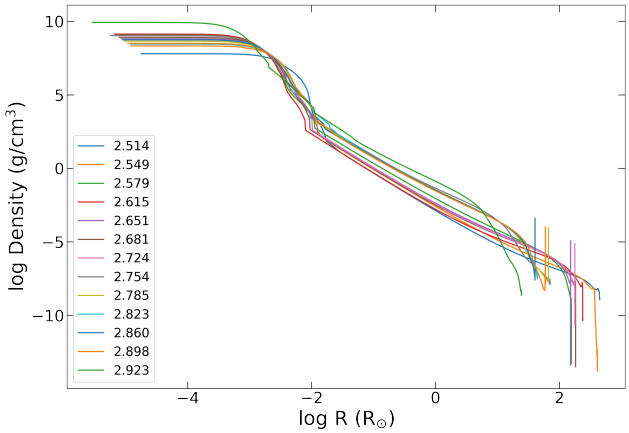

Figure 8.15: Density profile of the single He-stars of different masses before late-time mass transfer used in Section 8.6.

Chapter 9

SN 2023ZAW: AN ULTRA-STRIPPED, NICKEL-POOR SUPERNOVA FROM A LOW-MASS PROGENITOR

Das, K. K., C. Fremling, et al. (2024). "SN 2023zaw: An Ultrastripped, Nickel-poor Supernova from a Low-mass Progenitor". In: *The Astrophysical Journal Letters* 969.1, article L11. DOI: 10.3847/2041-8213/ad527a.

Kaustav K. Das[1], Christoffer Fremling[2], Mansi M. Kasliwal[1], Steve Schulze[3], Jesper Sollerman[4], Viraj Karambelkar[1], Sam Rose[1], Shreya Anand[1], Igor Andreoni[5,6,7], Marie Aubert[8], Sean J. Brennan[4], S. Bradley Cenko[5,7], Michael W. Coughlin[9], B. O'Connor[10], Kishalay De[11], Jim Fuller[1], Matthew Graham[1], Erica Hammerstein[6], Annastasia Haynie[12,13], K-Ryan Hinds[14], Io Kleiser[1], S. R. Kulkarni[1], Zeren Lin[1], Chang Liu[15,3], Ashish A. Mahabal[16,17], Christopher Martin[1], Adam A. Miller[15,3], James D. Neill[1], Daniel A. Perley[14], Priscila J. Pessi[4], Nikolaus Z. Prusinski[1], Josiah Purdum[2], Vikram Ravi[1], Ben Rusholme[1], Samantha Wu[1], Avery Wold[1], Lin Yan[2]

[1] Cahill Center for Astrophysics, California Institute of Technology, Pasadena, CA 91125, USA

[2] Caltech Optical Observatories, California Institute of Technology, Pasadena, CA 91125, USA

[3] Center for Interdisciplinary Exploration and Research in Astrophysics (CIERA), Northwestern University, Evanston, IL 60201, USA

[4] The Oskar Klein Centre, Department of Astronomy, Stockholm University, AlbaNova, SE-10691 Stockholm, Sweden

[5] Joint Space-Science Institute, University of Maryland, College Park, MD 20742, USA

[6] Department of Astronomy, University of Maryland, College Park, MD 20742, USA

[7] Astrophysics Science Division, NASA Goddard Space Flight Center, Greenbelt, MD 20771, USA

[8] Université Clermont-Auvergne, CNRS, LPCA, 63000 Clermont-Ferrand, France
[9] School of Physics and Astronomy, University of Minnesota, Minneapolis, MN 55455, USA
[10] McWilliams Center for Cosmology and Astrophysics, Carnegie Mellon University, Pittsburgh, PA 15213, USA
[11] MIT-Kavli Institute for Astrophysics and Space Research, 77 Massachusetts Ave., Cambridge, MA 02139, USA
[12] Department of Physics and Astronomy, University of Southern California, Los Angeles, CA 90089, USA
[13] The Observatories of the Carnegie Institution for Science, Pasadena, CA 91101, USA
[14] Astrophysics Research Institute, Liverpool John Moores University, Liverpool L3 5RF, UK
[15] Department of Physics and Astronomy, Northwestern University, Evanston, IL 60208, USA
[16] Division of Physics, Mathematics and Astronomy, California Institute of Technology, Pasadena, CA 91125, USA
[17] Center for Data Driven Discovery, California Institute of Technology, Pasadena, CA 91125, USA

Abstract

We present SN 2023zaw − a sub-luminous ($M_r = -16.7$ mag) and rapidly-evolving supernova ($t_{1/2,r} = 4.9$ days), with the lowest nickel mass ($\approx 0.002\ M_\odot$) measured among all stripped-envelope supernovae discovered to date. The photospheric spectra are dominated by broad He I and Ca NIR emission lines with velocities of $\sim 10\,000 - 12\,000$ km s^{-1}. The late-time spectra show prominent narrow He I emission lines at ∼1000 km s^{-1}, indicative of interaction with He-rich circumstellar material. SN 2023zaw is located in the spiral arm of a star-forming galaxy. We perform radiation-hydrodynamical and analytical modeling of the lightcurve by fitting with a combination of shock-cooling emission and nickel decay. The progenitor has a best-fit envelope mass of $\approx 0.2\ M_\odot$ and an envelope radius of $\approx 50\ R_\odot$. The extremely low nickel mass and low ejecta mass ($\approx 0.5\ M_\odot$) suggest an ultra-stripped SN, which originates from a mass-losing low mass He-star (ZAMS mass < 10 $M_\odot$) in a close binary system. This is a channel to form double neutron star systems, whose merger is detectable with LIGO. SN 2023zaw underscores the existence of a previously undiscovered population of extremely low nickel mass (< 0.005 $M_\odot$)

stripped-envelope supernovae, which can be explored with deep and high-cadence transient surveys.

9.1 Introduction

Modern wide-field and high-cadence transient surveys such as the Zwicky Transient Facility (ZTF; Bellm et al. 2019b, Graham et al. 2019) and the Asteroid Terrestrial-impact Last Alert System (ATLAS; Tonry et al. 2018, Smith et al. 2020) have expanded the discovery space of unusual supernovae (SNe). The class of rapidly-evolving, faint SNe constitutes such a population of peculiar SNe that evolve on the shortest timescales of a few days and have a peak absolute magnitude fainter than -17 mag. There are only a handful of well-studied examples in the literature – SN 2005ek (Drout et al. 2013), SN 2010X (Kasliwal et al. 2010), iPTF14gqr (De et al. 2018a), SN 2018kzr (McBrien et al. 2019), SN 2019dge (Yao et al. 2020), SN 2019wxt (Shivkumar et al. 2023, Agudo et al. 2023), SN 2019bkc (Prentice et al. 2020, Chen et al. 2020), and SN 2022agco (Yan et al. 2023).

Despite advances in understanding the photometric and spectroscopic diversity, their progenitors and powering mechanisms remain unknown. The various theoretical scenarios include ultra-stripped core-collapse SNe of massive stars that lead to binary neutron star systems (Tauris et al. 2013, 2015), non-terminal thermonuclear detonations of a helium shell on the surface of a white dwarf called a '.Ia' SN (Bildsten et al. 2007, Shen et al. 2010), shock-cooling of H-poor stars with an extended envelope (Kleiser and Kasen 2014, Kleiser et al. 2018), fallback in a core-collapse SN (Zhang et al. 2008, Moriya et al. 2010), accretion-induced collapse of a white dwarf (Dessart et al. 2007), electron-capture SN (Moriya and Eldridge 2016), and neutron-star white-dwarf mergers (Margalit and Metzger 2016).

In this paper, we present SN 2023zaw – a Type Ib SN with the lowest nickel mass measured among all stripped-envelope SNe discovered to date. The late-time spectra are dominated by narrow He I emission lines, suggestive of interaction with He-rich circumstellar material (CSM). SN 2023zaw exhibits the most rapid rise and fade time among all stripped-envelope SNe in the literature. Additionally, it is the nearest SN among all fast and faint SNe in the literature. The photometric and spectroscopic properties suggest that it is an ultra-stripped SN, originating from a progenitor with an initial mass $< 10\ M_{\odot}$, which likely formed a neutron star.

9.2 Discovery and follow-up observations

Discovery

SN 2023zaw (ZTF23absbqun) was discovered with the ZTF camera (Dekany et al. 2020), which is mounted on the 48-inch Samuel Oschin Telescope at the Palomar Observatory. It was first detected at $\alpha = 04^{h}29^{m}20.235^{s}$, $\delta = +70°25'37.52''$ (J2000) on December 7, 2023 at 05:34:06 UTC and reported to the Transient Name Server[1] (Sollerman 2023). At the time of discovery, the AB apparent magnitude in the $g-$band was 19.34 ± 0.15 mag. The transient stood out due to its faintness and extremely fast evolution (see Figure 10.3). It was also flagged as a fast transient candidate by the ZTFReST framework for kilonova and fast transient discovery (Andreoni et al. 2021) and was saved as part of the magnitude-limited (Bright Transient Survey; Fremling et al. 2020) and volume-limited (Census of the Local Universe; De et al. 2020b) surveys of ZTF.

SN 2023zaw is located in the UGC 03048 galaxy at a redshift of $z = 0.0101$ (Springob et al. 2005). It is located on the edge of one of its spiral arms (see Figure 9.1). The angular separation from the nucleus of the galaxy is 21.44″, which corresponds to a physical separation of 4.36 kpc. We correct for the Virgo, Great Attractor, and Shapley supercluster infall (Mould et al. 2000) based on the NASA Extragalactic Database object page (NED)[2] for UGC 03048. We adopt a Hubble-flow distance of 43.9 ± 3.1 Mpc, which corresponds to a distance modulus of 33.21 ± 0.15 mag.

Optical photometry

We obtained multiple epochs of g, r and $i-$band photometry with the ZTF camera. The images were reduced using the ZTF image analysis pipeline (Masci et al. 2019). We also perform forced photometry at the location of the transient for the ZTF images in the gri bands. We obtained c and o-band photometry from the forced-photometry service of the Asteroid Terrestrial-impact Last Alert System (ATLAS; Tonry et al. 2018, Smith et al. 2020, Shingles et al. 2021). We took regular cadence multiband photometry in the g, r, i and z bands with the Optical Imager (IO:O) at the 2.0 m robotic Liverpool Telescope (Steele et al. 2004). In addition, photometric data was obtained with the Rainbow Camera on the automated Palomar 60-inch telescope (P60; Cenko et al. 2006). LT and P60 images were processed using the FPipe (Fremling et al. 2016) image subtraction pipeline with PanSTARRS (PS1;

[1] https://www.wis-tns.org/

[2] https://ned.ipac.caltech.edu/

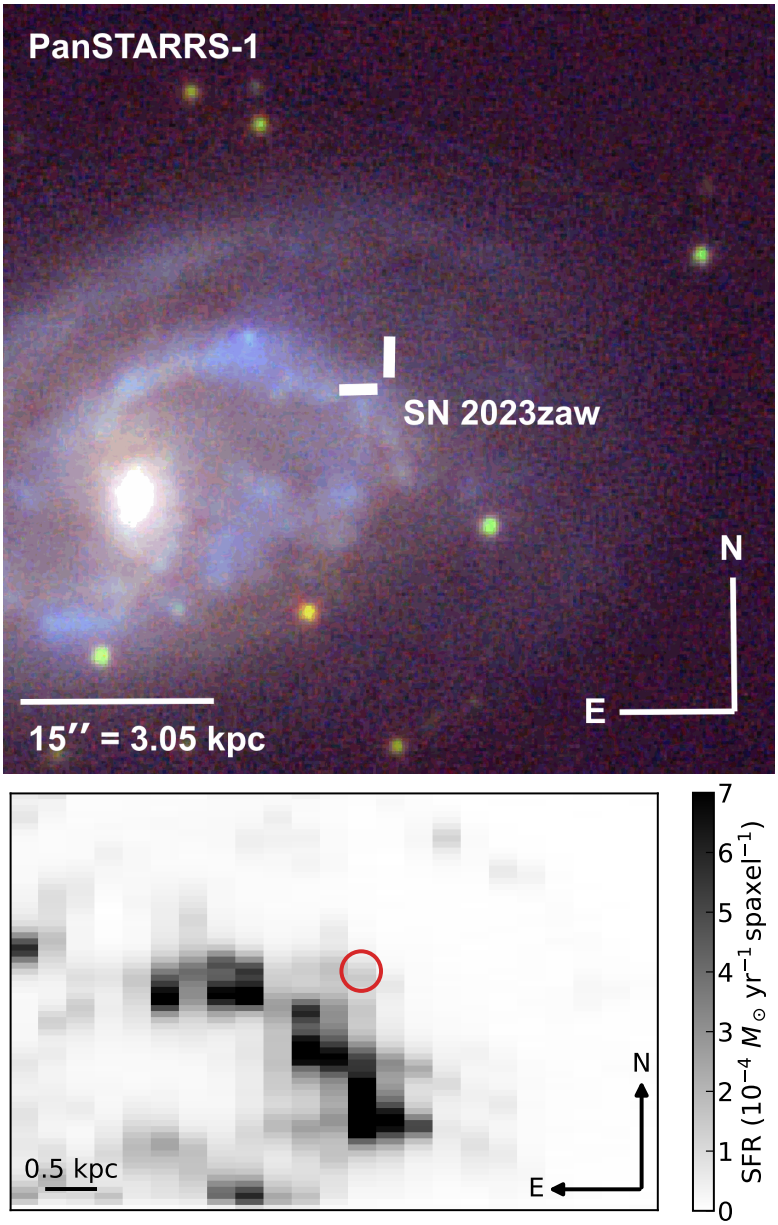

Figure 9.1: *Left:* Pan-STARRS image of the host-galaxy of SN 2023zaw, UGC 03048 in the *grizy* filters. The location of the transient is indicated by the white cross at the center. *Right:* Star-formation rate (SFR) map of the environment around SN 2023zaw (see Section 9.3). SN 2023zaw (position marked by the red circle) exploded in a star-forming region of the host galaxy close to regions of more vigorously star-forming regions. The image has a size of 4.1×6.7 kpc. The SFR scale is not corrected for attenuation.

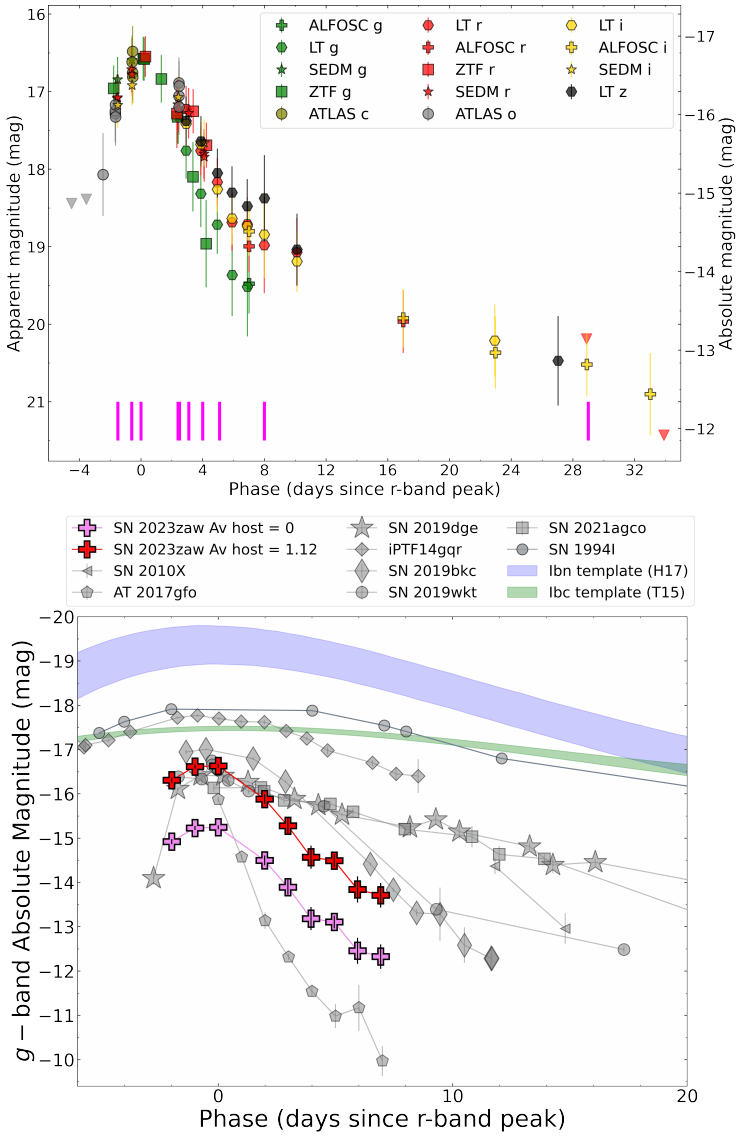

Figure 9.2: *Left:* The multiband lightcurve collage of SN 2023zaw. The x-axis shows rest-frame days since the r-band peak (MJD = 60287.7). The photometry data has been corrected for Milky Way ($A_{V,MW}$ = 0.77 mag) and host extinction ($A_{V,host}$ = 1.12 mag) as described in Section 10.3. The vertical magenta lines represent epochs of spectral observations. *Right:* The g-band lightcurve of SN 2023zaw compared with other fast-evolving transients in the literature – fast-declining Type I SNe – SN 2010X (Kasliwal et al. 2010), SN 2019bkc (Prentice et al. 2020, Chen et al. 2020), the kilonova AT 2017gfo (Abbott et al. 2017), ultra-stripped SN candidates – SN 2019dge (Yao et al. 2020), iPTF14gqr (De et al. 2018c), SN 2019wxt (Shivkumar et al. 2023, Agudo et al. 2023), SN 2022agco (Yan et al. 2023). We also compare with Type Ibc and Type Ibn SN lightcurve templates from Taddia et al. (2015) and Hosseinzadeh et al. (2017a), respectively.

Chambers et al. 2016) reference images. The Alhambra Faint Object Spectrograph and Camera (ALFOSC) at the 2.5m Nordic Optical Telescope was used to obtain g, r, and $i-$band photometry. The ALFOSC data was reduced using the PyNOT[3] pipeline. The collage of all the multi-band lightcurves is shown in Figure 10.4. The photometry data is listed in Table A1.

Optical spectroscopy

We acquired four epochs of spectroscopy with the Spectral Energy Distribution Machine (SEDM; Blagorodnova et al. 2018) on the Palomar 60-inch telescope. The SEDM data was reduced using the pipeline described in Rigault et al. (2019) and Kim et al. (2022). We obtained three epochs of spectroscopy with the Low-Resolution Imaging Spectrometer (LRIS; Oke et al. 1995) on the Keck I telescope, with data reduced using the automated LPIPE (Perley 2019) pipeline. The Alhambra Faint Object Spectrograph and Camera (ALFOSC) instrument at the 2.5m Nordic Optical Telescope was used to obtain one epoch of low-resolution spectrum, which was reduced using the PyNOT[4] pipeline. We took one spectrum with the Binospec spectrograph (Fabricant et al. 2019) on the Multiple Mirror Telescope, which was reduced using the `PypeIt` package (Prochaska et al. 2020, Prochaska et al. 2020b). We used the Keck Cosmic Web Imager (KCWI; Martin et al. 2010, Morrissey et al. 2018a) to obtain spectra of the transient and its host environment. This was reduced using the KCWI data reduction pipeline[5]. We also show one spectrum observed with the Gemini-GMOS instrument from the Transient Name Server[6]. The collage of all the spectra is shown in Figure 10.5 and the spectroscopy log can be found in Table A2.

9.3 Methods and analysis

Extinction Correction

We correct for Milky Way extinction using the dust maps from Schlafly and Finkbeiner (2011). Along the line of sight of SN 2023zaw, $E(B-V) = 0.25$ mag. For reddening corrections, we use the extinction law in Cardelli et al. (1989) with $R_V = 3.1$.

For host extinction correction, we use the Na I D absorption lines of the host-galaxy (Poznanski et al. 2012, Stritzinger et al. 2018). We measure an equivalent width of

[3]https://github.com/jkrogager/PyNOT
[4]https://github.com/jkrogager/PyNOT
[5]https://kcwi-drp.readthedocs.io
[6]https://www.wis-tns.org/

1.5 ± 0.2 Å, from the KCWI spectrum obtained at a phase of +2.5 days past r-band peak. To compute A_V, we use $A_V^{\rm host}[\rm mag] = 0.78(\pm 0.15) \times EW_{\rm Na\,I\,D}[\text{Å}]$ (Stritzinger et al. 2018). We note that there are caveats in using the Na I D EW measurement to estimate host extinction, especially for low-resolution spectra (Poznanski et al. 2011) and in the presence of circumstellar material (Phillips et al. 2013).

We plot the $g - r$ and $r - i$ colors of SN 2023zaw before and after host extinction correction in Figure A2 and compare with other rapidly evolving transients and the SN Ib color template from Stritzinger et al. (2018).

Explosion epoch estimation

We fit for the $r-$band maximum epoch with a polynomial fit to the $r-$band photometry and obtain a peak magnitude of -16.7 mag and peak MJD of 60287.7. All phases mentioned in the paper will be in rest frame days measured from this $r-$band peak epoch. The last non-detection before the first detection was on 60283 MJD (-4.7 days), with an upper limit of -14.8 mag in the $o-$band. We perform a power-law fit to the r-band data prior to the maximum epoch to estimate the explosion epoch. We find that the explosion epoch is 60284.4 ± 0.5 MJD (-3.3 ± 0.5 days).

Lightcurve properties

In Figures 10.4 and 9.10, we compare the $g-$ and $r-$band evolution of SN 2023zaw to other fast-evolving and subluminous transients in the literature – fast-declining Type I SNe – SN 2005ek (Drout et al. 2013), SN 2010X (Kasliwal et al. 2010), SN 2018kzr (McBrien et al. 2019), SN 2019bkc (Prentice et al. 2020, Chen et al. 2020), the kilonova AT 2017gfo (Abbott et al. 2017), ultra-stripped SN candidates – SN 2019dge (Yao et al. 2020), iPTF14gqr (De et al. 2018c), SN 2019wxt (Shivkumar et al. 2023, Agudo et al. 2023), SN 2022agco (Yan et al. 2023). We also compare with lightcurve templates for Type Ibn (Hosseinzadeh et al. 2017a) and Type Ibc SNe (Taddia et al. 2015). SN 2023zaw is much fainter and faster evolving than the typical Type Ibn or Ibc SN. However, we note that some Type Ibn/Icn SNe also show rapid evolution: LSQ13ccw (Hosseinzadeh et al. 2017a), SN 2023emq (Pursiainen et al. 2023). We fit a polynomial to the lightcurves and measure the rise time and fade time as the duration above the half-maximum of the peak. SN 2023zaw has a rise time ($t_{\rm rise}^{1/2}$) of 1.8 days and a decline time ($t_{\rm dec}^{1/2}$) of 3.1 days. The time above half maximum of the peak is shorter than for all other fast-evolving faint transients in the literature (see Figures 10.4, 10.3, and 9.10). The lightcurve declines by 2.7 mag in 10 days in the $r-$band and by 2.7 mag in 6 days in the $g-$band. SN 2023zaw is only slower

than kilonova AT 2017gfo and has a comparable decline timescale to SN 2019bkc and SN 2018kzr. In the $r-$band, SN 2023zaw has a very sharp initial decline of $\sim$ 0.28 mag day^{-1} followed by a transition to a relatively slower decline rate of $\sim$ 0.07 mag day^{-1} after $\sim$10 days since peak. In the g band, SN 2023zaw shows a very sharp initial decline of $\sim$ 0.44 mag day^{-1} till 10 days post-peak. The peak absolute magnitude in the r band before and after host-extinction correction is -15.6 mag and -16.7 mag respectively. In the $g-$band, the peak absolute magnitude before and after host-extinction correction is -15.2 mag and -16.6 mag respectively. We compare the time above half maximum and the absolute luminosity of SN 2023zaw to a sample of SESNe detected by ZTF and other fast and faint SNe in the literature in Figure 10.3. SN 2023zaw shows the fastest evolution among all transients at similar luminosities.

Spectral Properties

In the early SEDM spectra taken before $r-$band peak, we see a blue, featureless continuum. We see multiple broad helium lines – He I $\lambda\lambda$5876, 6678, 7065, in the subsequent spectra. The expansion velocity measured from the absorption in the P-Cygni profile of the He I lines evolved from 12,000 to 9700 km s^{-1} from 0 days to 8 days post-peak. These He I absorption lines resemble those seen in Type Ib SNe and we obtain a decent fit to Type Ib SNe at similar or later phases using the `SuperNova Identification` (`SNID`; Blondin and Tonry 2007) code. This is consistent with the initial classification made by Gillanders et al. (2023). There is also a redshifted component to the He I λ5876 line profile in the spectrum taken at +8 and +29 days, probably due to asymmetrical ejecta. He I line velocities drop to $\sim$ 3000 km s^{-1} at a phase of 29 days. Prominent narrow He I emission lines can be seen in the LRIS spectra obtained at 29 and 61 days after peak. The FWHM velocities of the He I emission lines in the latest LRIS spectrum are $\sim$ 1050 $\pm$ 100 km s^{-1}.

In the photospheric phase, we do not see any broad O I λ7774 emission line, which is common in stripped-envelope SNe. We also see broad, high-velocity lines of the Ca II NIR triplet at $\sim$ 12,000 km s^{-1} as early as 2 days after peak. Such high-velocity early Ca NIR absorption lines are not seen in other fast-evolving SNe (see Figure 9.3). Also, unlike other rapid-declining SNe, SN 2023zaw does not reach nebular phase even at 29 days after peak. Broad nebular lines such as [O I] $\lambda\lambda$6300, 6364, Ca II NIR triplet are also not seen in the latest LRIS spectrum taken at +61 days.

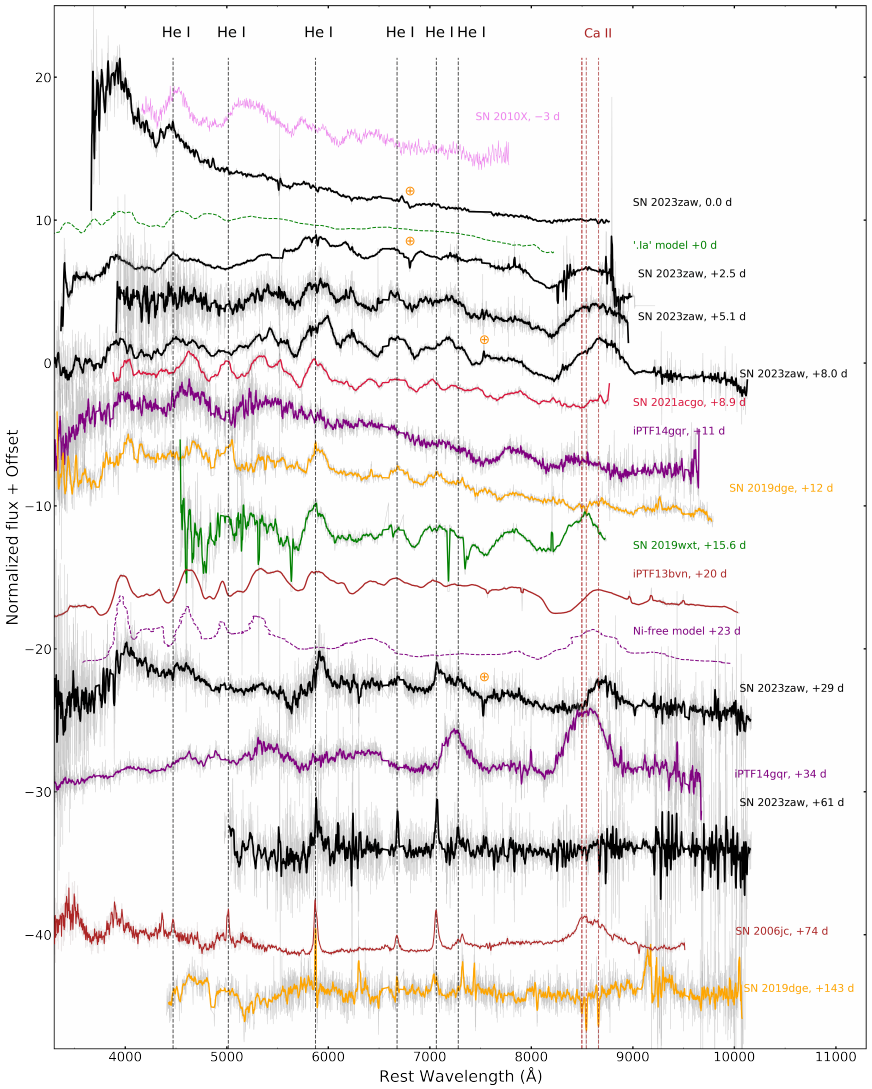

Figure 9.3: The spectra of SN 2023zaw (in black) compared with other fast-evolving transients in the literature – fast-declining Type I SNe – SN 2010X (Kasliwal et al. 2010), ultra-stripped SNe candidates – SN 2019dge (Yao et al. 2020), iPTF14gqr (De et al. 2018c), SN 2019wxt (Shivkumar et al. 2023, Agudo et al. 2023), SN 2022agco (Yan et al. 2023), canonical Type Ib SN – iPTF14bvn (Fremling et al. 2018), Type Ibn – SN 2006jc (Foley et al. 2007). We also compare with theoretical predictions for '.Ia' SNe (Shen et al. 2010) and nickel-free SN models (Kleiser and Kasen 2014). The spectra are corrected for Milky Way and host extinction. The x-axis represents the rest wavelength. The He I and Ca II emission lines are shown in dashed vertical lines. The telluric absorption features are indicated by the $\oplus$ symbol.

Bolometric Lightcurve

We bin the data in intervals of one day and fit with the Planck blackbody function where there are detections in at least three filters. We perform the fit using the Python EMCEE package (Foreman-Mackey et al. 2013). The blackbody temperature, radius and luminosity thus obtained are shown in Table E. The errors in the model parameters are determined by extracting the 16^{th} and 84^{th} percentiles of the posterior probability distribution. For the later epochs, where we have photometry in only one band, we use the extrapolated blackbody temperatures obtained by fitting an exponential decay function to the temperature data from previous epochs. The temperature stays roughly constant at $\approx$ 4000 K. For these later epochs, we also estimate the bolometric luminosity as νL_ν. These estimates agree with each other within 3σ, with the latter method slightly underestimating the bolometric luminosity as expected.

We plot the best-fit blackbody parameters and compare these with other ultra-stripped SN candidates in Figure 9.4. We can see that the bolometric light curve of SN 2023zaw is similar in peak brightness to the other SNe but has a faster decline rate within the first 10 days after r-band peak. The decline of the bolometric luminosity slows down after around 6 days post-peak. The photospheric radius increases up to 4 days post-peak, reaching a maximum of ~10 000 $R_\odot$. The temperature decreases over time, from a maximum of ~17 000 K on day 0 to ~4000 K on day 8.

Modeling the lightcurve

Radiation-Hydrodynamics Modeling

We use the pre-supernova model grid presented in Wu and Fuller (2022a). This grid was produced through binary evolution of He-stars with an initial mass of 2.5 $M_\odot$ − 3 $M_\odot$ evolved up to silicon burning using the Modules for Experiments in Stellar Astrophysics code (MESA; Paxton et al. 2010). The binary systems evolved in Wu and Fuller (2022a) include orbital periods of 1, 10, and 100 days. Predictions of the properties of the unbound CSM in the vicinity of each pre-supernova model were also produced. In this work we compare our data to both models with and without unbound CSM.

We use the SuperNova Explosion code (SNEC; Morozova et al. 2015) to explode the grid of pre-supernova stellar models described above. First, we exploded all models in the grid using a thermal bomb with $E_{kin} = 0.4 \times 10^{51}$ erg, and $M_{Ni} = 0.0035\ M_\odot$, with ^{56}Ni mixed all the way through the remaining star after mass excision of 1.4 $M_\odot$

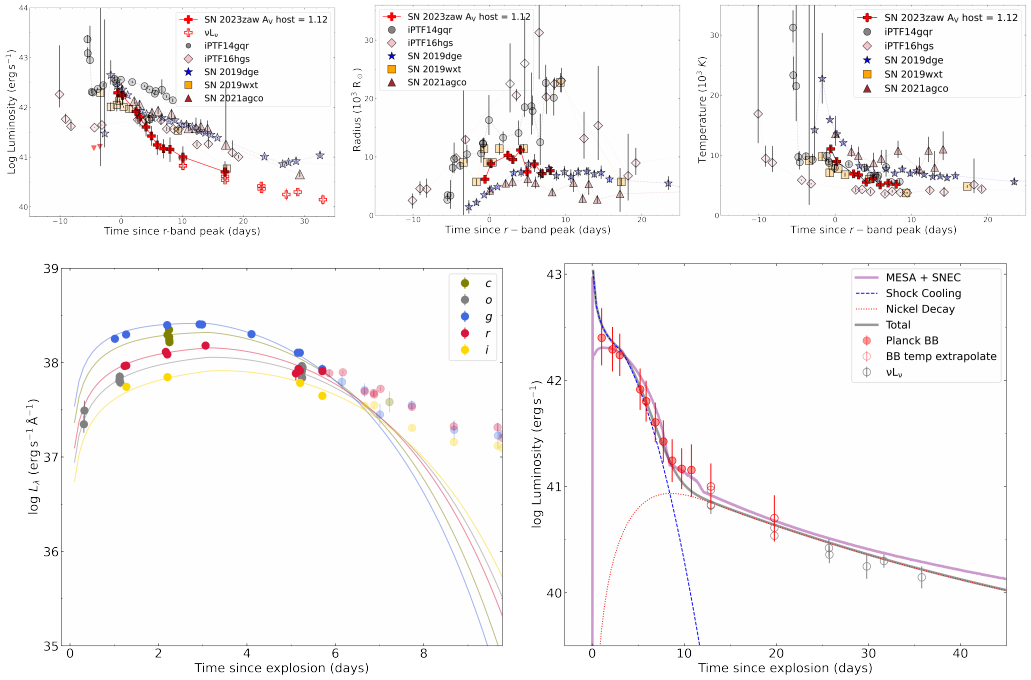

Figure 9.4: *Top:* Comparison of the bolometric luminosity, best-fit radius, and temperature evolution of SN 2023zaw from the blackbody fits described in Section 9.3 with ultra-stripped SN candidates: SN 2019dge (Yao et al. 2020), iPTF14gqr (De et al. 2018c), SN 2019wxt (Shivkumar et al. 2023, Agudo et al. 2023), and SN 2022agco (Yan et al. 2023). *Bottom left:* Shock-cooling emission model fit to the early-phase multiband light curve as described in Section 9.3. *Bottom right:* Best fits for bolometric luminosity with radiation-hydrodynamics and analytical models as described in Section 9.3.

in the center.

The resulting bolometric lightcurves and expansion velocities were then compared to our data on SN 2023zaw. We find that the model Wu and Fuller (2022a) produced from a He-star with an initial mass of 2.651 $M_\odot$ and an orbit period of 100 days reproduces the overall behavior seen in our data well, including the expansion velocities. Other models fail to reproduce both the early cooling-phase of the bolometric lightcurve (governed by the radius and mass in the bound envelope) or the late-time decline rate (governed by the total ejecta mass). To produce our best-fitting MESA+SNEC model shown in Figure 9.4, we modified the bound envelope radius of the raw MESA model so that it extends to $\approx 50\ R_\odot$, by cutting the model grid appropriately (compared to $\approx 110\ R_\odot$ in the raw model). This would correspond to an orbital period between 10 and 100 days. We also modified the mass excision in the center to be 1.3 $M_\odot$. These modifications result in the explosion parameters

$E_{kin} = 0.4 \times 10^{51}$ erg, $M_{Ni} = 0.0035\ M_\odot$, with complete mixing of ^{56}Ni through the ejecta, which has a total mass of $M_{ej} = 0.56\ M_\odot$, including the bound envelope. Models including the unbound CSM predicted by Wu and Fuller (2022a) are largely inconsistent with our data. The luminosity during the first week can be similar to what we observe if the explosion energy is adjusted to be low ($< 0.1 \times 10^{51}$ erg). However, such models are inconsistent (too bright) at later times and inconsistent with the overall decay rate.

Analytical Modeling

The bolometric luminosity declines at a rapid rate for the first $\sim$ 6 days after peak (see Figure 9.4). Radioactivity alone is unable to power this early-time luminosity under the constraint that the ejecta mass must be greater than the nickel mass. The peak luminosity of 2.5×10^{42} erg s^{-1} and timescale of evolution ($\approx$ 4.9 days) falls in the forbidden region of nickel-powered lightcurves (see Figure 1 in Kasen 2017). Instead, we model this early lightcurve as being powered by shock-cooling emission from the shock-heated bound or unbound extended stellar material. We use the shock-cooling emission model presented in Piro et al. (2021) to fit the early-time multiband photometry. We obtain a good fit for all the filters for photometry up to 6 days past peak (Figure 9.4). The explosion time is constrained to be -2.7 ± 0.2 days before the peak. Based on the fit, we find that the best-fit envelope mass is $0.20 \pm 0.01\ M_\odot$ and envelope radius is $55 \pm 11\ R_\odot$. This is comparable to the envelope properties measured from shock-cooling emission modeling in other Type Ibc SNe (see Figure 9.11). The envelope properties of SN 2023zaw are also consistent with theoretical models for bound and unbound stellar material (Figure 9.12).

For estimating the Ni mass, we first subtract the contribution of the shock cooling emission estimated above from the bolometric luminosity, which we then assume to be entirely powered by radioactive decay. We use the analytical expression for a Ni-powered bolometric lightcurve provided in Arnett et al. (1989), Valenti et al. (2008), and Wheeler et al. (2015). Further details on the model fitting can be found in Yao et al. (2020, their Appendix B). Based on the fit, we find that the required Ni-mass to power the supernova is $0.24 \pm 0.14 \times 10^{-2}\ M_\odot$. We measure a photon diffusion timescale (τ_m) of $6.21^{+0.11}_{-0.11}$ days and characteristic γ-ray diffusion timescale (t_o) of $36.04^{+3.41}_{-2.74}$ days.

We assume that the photospheric velocity is $\sim$ 12000 km s^{-1}, as assumed from the He I absorption lines in the ALFOSC spectrum taken at $r-$band peak. We use an

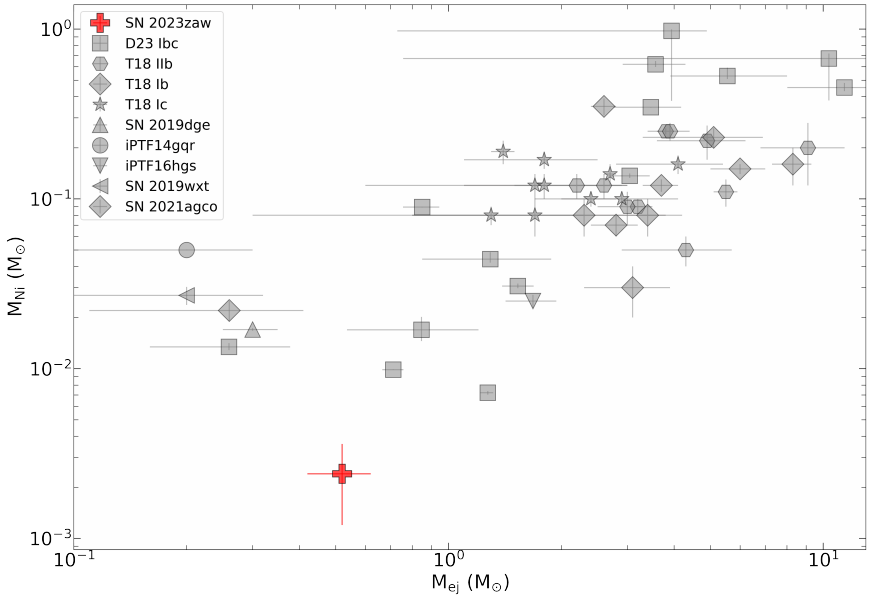

Figure 9.5: We compare the estimated ejecta mass and nickel mass with Type Ibc SNe from Taddia et al. (2018), double-peaked Type Ibc SNe from Das et al. (2023b) and other ultra-stripped SN candidates – SN 2019dge (Yao et al. 2020), iPTF14gqr (De et al. 2018c), SN 2019wxt (Shivkumar et al. 2023, Agudo et al. 2023), SN 2022agco (Yan et al. 2023). The red plus sign denotes the best-fit parameters by fitting shock cooling emission + nickel decay to the lightcurve after host-extinction correction.

opacity (κ) value of 0.07 cm^2 g^{-1}, appropriate for H-poor SNe (Taddia et al. 2018). We estimate the ejecta mass using the following relation: $\tau_m = \left(\frac{2\kappa M_{ej}}{13.8 c v_{phot}}\right)^{1/2}$, which gives $M_{ej} \approx 0.52^{+0.02}_{-0.02} \times \left(\frac{v_{phot}}{12000\ km/s}\right) M_\odot$. The calculated explosion kinetic energy is $\approx 4.82^{+0.18}_{-0.18} \times 10^{50}$ erg s^{-1}.

These explosion parameters are an order of magnitude lower than for regular Type Ibc SNe. The estimated ejecta mass is comparable to other ultra-stripped SNe in the literature while the Ni-mass is smaller by a factor of ~5. The rapid light curve decline is explained by the low ejecta mass, which allows γ-rays to escape already a few days after the peak. Overall, SN 2023zaw occupies a unique location in the phase space plot of nickel mass versus ejecta mass (see Figure 10.12). For comparison, we also plot the nickel and ejecta masses estimated for a sample of stripped-envelope SNe from Taddia et al. (2018) and double-peaked Type Ibc SNe from Das et al. (2023b). We note that the double-peaked SN 2021inl (Jacobson-Galán et al. 2022b,

Table A: Comparison of explosion properties of SN 2023zaw with ultra-stripped SN candidates – SN 2019dge (Yao et al. 2020), iPTF14gqr (De et al. 2018c), iPTF16hgs (De et al. 2018b), SN 2019wxt (Shivkumar et al. 2023, Agudo et al. 2023), SN 2022agco (Yan et al. 2023).

Source	Redshift	Host Type	$r-$band Peak (mag)	$M_{\rm ej}$ ($M_\odot$)	$M_{\rm Ni}$ (10^{-2} $M_\odot$)	$R_{\rm ext}$ (10^{13} cm)	$M_{\rm ext}$ (10^{-2} $M_\odot$)
SN 2023zaw	0.0101	Spiral	-16.7 ± 0.1	$0.52^{+0.02}_{-0.02}$	$0.24^{+0.02}_{-0.02}$	$0.4^{+0.1}_{-0.1}$	$19.53^{+0.99}_{-0.98}$
SN 2021agco	0.01056	Spiral	-16.2 ± 0.24	$0.26^{+0.04}_{-0.02}$	$2.2^{+0.2}_{-0.3}$	$0.55^{+0.18}_{-0.14}$	$10.04^{+1.87}_{-1.05}$
AT 2019wxt	0.036	Compact	-16.6 ± 0.4	$0.20^{+0.12}_{-0.11}$	$2.7^{+0.33}_{-0.18}$	$35.8^{+4.06}_{-3.68}$	$3.55^{+0.12}_{-0.11}$
SN 2019dge	0.021	Compact	-16.3 ± 0.2	$0.30^{+0.02}_{-0.02}$	$1.6^{+0.04}_{-0.03}$	$1.2^{+0.06}_{-0.05}$	$9.71^{+0.28}_{-0.27}$
iPTF14gqr	0.063	Spiral	-17.5 ± 0.2	$0.20^{-0.10}_{+0.10}$	$5.0^{+0.14}_{-0.15}$	$6.1^{+8.73}_{-3.18}$	$2.59^{+0.46}_{-0.34}$
iPTF16hgs	0.017	Spiral	-15.5 ± 0.2	$1.68^{+0.28}_{-0.25}$	$2.5^{+0.20}_{-0.22}$	$2.6^{+14.08}_{-1.80}$	$9.27^{+3.40}_{-2.48}$

Das et al. 2023b) is the other SN with Ni-mass < 0.01 $M_\odot$.

We also use the analytical models given in Khatami and Kasen (2019) to obtain a nickel mass estimate of $\approx 2.5 \times 10^{-2}$ $M_\odot$ and an ejecta mass estimate of ≈ 0.45 $M_\odot$.

Host galaxy environment

We observed SN 2023zaw and its immediate environment with the integral-field unit KCWI (Section 9.2). These data allow us to address two outstanding questions: i) did SN 2023zaw explode in a star-forming region, and ii) how high is the host attenuation along the line of sight towards SN 2023zaw?

We cleanly detect emission lines from a star-forming region at the SN position in the unbinned KCWI data. To measure the properties of the star-forming region, we extract the SN spectrum using a 4×4-px aperture, tie the flux scale to our g- and i-band photometry, and extract the flux of Hα-Hγ, [O II]$\lambda\lambda$3729,3729, [O III]$\lambda\lambda$4959,5007, [N II]$\lambda\lambda$6548,6584, and [S II]$\lambda\lambda$6717,6731 by fitting each line with a Gaussian. All measurements are summarised in Table B.

We infer the attenuation by ionised gas from the flux ratio between Hβ and Hγ (Momcheva et al. 2013). Using the Calzetti et al. (2000b) attenuation model, we measure $E(B-V)_{\rm gas} = 0.58 \pm 0.20$ mag, which translates to a stellar continuum colour excess of 0.26 ± 0.09 mag. This value is comparable to the reddening inferred from the Na I D absorption lines (Section 10.3) and corroborates that the line of sight is suffering from significant host attenuation.

We note that the stellar populations near SN 2023zaw are evolved, and their spectra show conspicuous Balmer absorption lines. This could introduce a bias into the

observed Balmer decrement. To quantify the impact, we centre a box annulus on the SN position and extract a spectrum from the blue KCWI data between 2 to 4 px from the SN position. We fit the stellar continuum with the stellar population fitting code FIREFLY version 1.0.3 (Wilkinson et al. 2017, Neumann et al. 2022), utilising the stellar population models from Maraston et al. (2020) and assuming the Kroupa initial mass function (IMF), a spectral resolution of 1000–1250 appropriate for our spectroscopic observation (Morrissey et al. 2018b) and a velocity dispersion of 130 ± 20 km s^{-1}. The best-fit yields an $E(B-V)_{\rm star}$ of 0.36 mag, comparable to the value at the explosion site. Henceforth, we use $E(B-V)_{\rm gas} = 0.58 \pm 0.20$ mag to characterise the properties of the star-forming region further.

The attenuation-corrected Hα flux of 1.2×10^{-14} erg cm^{-2} s^{-1} translates to a star-formation rate of $1.4^{+1.2}_{-0.6} \times 10^{-2}$ $M_\odot$ yr^{-1} utilising the relationship between the Hα luminosity and the star-formation rate from Kennicutt (1998) and the scaling factor from Madau and Dickinson (2014) to convert from the Salpeter to the Chabrier IMF in the Kennicutt (1998) relation. The error estimate includes the uncertainty of the flux measurements, the gas-phase attenuation and the luminosity distance of SN 2023zaw's host galaxy. We stress that the large SFR error reflects the uncertainty in the attenuation correction, not a low precision of the Hα flux measurement (Table B).

Detecting emission lines from hydrogen, nitrogen and oxygen also allows us to measure the metallicity of the star-forming region. Using the O3N2 metallicity indicator and the calibration from Curti et al. (2017), we infer a metallicity of 1.18 $\pm$ 0.02 solar (statistical error), adopting a solar oxygen abundance of 8.67 (Asplund et al. 2009).

Next, we draw our attention to SN 2023zaw's neighbourhood. Figure 9.1 shows a map of the star-formation activity out to a distance of 6.7 kpc from SN 2023zaw's location. This image was generated from the KCWI data. First, we extracted a 20-Å-wide image centred on the wavelength of Hα. Then, we extracted two additional 20-Å-wide images from emission-line free regions adjacent to Hα and interpolated between them to remove the galaxy/SN flux at the wavelength of Hα. Finally, the intensity scale was corrected for MW extinction, scaled to the SN photometry and converted to star-formation rate as we did for the explosion site. The SFRs in Figure 9.1 are strict lower limits. They account for neither host attenuation nor stellar Balmer absorption lines.

The explosion site, marked by the blue circle in Figure 9.1, is located near the

outskirts of a larger region with ongoing star-formation activity. Although the level of star formation activity at the explosion site is in the lower half of the intensity distribution, this star-forming region extends much farther. Inspecting the neighbouring spaxels reveals that the star-formation activity extends to regions of even less intensity. Thus, the location of SN 2023zaw favors a massive star progenitor, but it does not rule out a thermonuclear origin.

9.4 Discussion: Progenitor and evolutionary pathway

In this section, we discuss the possible progenitors and evolutionary pathways for SN 2023zaw.

Thermonuclear '.Ia' SN

In the '.Ia' SN scenario, the progenitor is a white dwarf in a close binary ($P_{orb} < 1$ hour) system, accreting helium from its companion. They have a tenth of the ejecta mass and explosion energy of a normal Type Ia supernova (Bildsten et al. 2007). We compare the r-band lightcurve and bolometric luminosity with '.Ia' SN models from Shen et al. (2010) in Figure 9.6. The peak luminosities range from $0.5 - 5 \times 10^{42}$ erg s^{-1} or peak bolometric magnitudes from -15.5 to -18 mag, consistent with SN 2023zaw. We highlight the best-fit '.Ia' SN bolometric lightcurve which is an excellent fit to the early-time data before host-extinction correction. Prominent He I features from unburnt He are predicted, which is consistent with the spectra of SN 2023zaw. We note that the absence of broad O I λ7774 and the presence of Ca II NIR lines at early phases resemble the spectra of SN 2010X (Kasliwal et al. 2010) which is a '.Ia' SN candidate (see Figure 9.3). However, the fact that the decline of the r-band lightcurve slows down after $\sim$ 10 days post-peak, is not consistent with the '.Ia' SN models (Shen et al. 2010).

Accretion-induced collapse (AIC) of white dwarf

O-Ne white dwarfs collapse to form a neutron star when it approaches Chandrasekhar mass. Numerical simulations predict very low explosion energy ($\sim 0.5 \times 10^{49}$ erg). We compare the bolometric lightcurve prediction from Darbha et al. (2010) with SN 2023zaw in Figure 9.6. The predicted peak luminosity is $\sim$ 10 times fainter than that observed for SN 2023zaw. The models do not predict the late-time tail seen in SN 2023zaw. The nickel mass predicted in AIC models ($\lesssim 0.001\ M_{\odot}$) is slightly smaller than that estimated for SN 2023zaw. The ejecta velocities predicted for AIC explosions are very high ($\sim$ 0.1c), which is not consistent with SN 2023zaw.

White dwarf – neutron star/black hole merger

Spectroscopic models of WD-NS/BH mergers (Gillanders et al. 2020) predict that the ejecta should be rich in intermediate elements such as O, Mg, S. This is not consistent with the observed spectra for SN 2023zaw.

Nickel free core-collapse supernova

A potential powering mechanism for a fast-evolving, low-Ni mass SN is the 'Ni-free' SN scenario (Kleiser and Kasen 2014, Kleiser et al. 2018). In this case, the supernova is not powered by decay of radionuclides like ^{56}Ni but is instead powered by shock-interactions with an extended hydrogen-poor circumstellar medium (CSM). We compare the r-band lightcurve and bolometric luminosity of SN 2023zaw with Ni-free SN models from Kleiser et al. (2018) in Figure 9.6. If there is a significant amount of Ni present ($> 0.05\ M_{\odot}$), it shows up as a second peak in the model lightcurves, which is not seen for SN 2023zaw. The models with 0 or 0.01 $M_{\odot}$ of nickel produce bright and short-lived peaks. However, none of the lightcurves can explain the rapid rise and the slower-evolving late-time lightcurve tail of SN 2023zaw.

Electron-capture SN

The low nickel mass is consistent with super Asymptotic Giant Branch (sAGB) progenitor stars with an O-Ne-Mg core that explodes as an electron-capture supernova (ECSN). However, a sAGB star has a hydrogen-rich envelope. Since, the spectra do not show hydrogen, a binary system is necessary, where the hydrogen has been stripped off through Roche-lobe overflow or common envelope ejection. Stripped-envelope ECSN models in Moriya and Eldridge (2016) predict ejecta mass of $\sim 0.3 - 0.6\ M_{\odot}$, nickel mass of $\sim 0.003\ M_{\odot}$, and explosion energy of 10^{50} erg, which is consistent with SN 2023zaw. Enhanced production of calcium is predicted for these SN, which is also consistent with the broad Ca emission lines seen in SN 2023zaw, as early as 2 days after peak. We compared the theoretical lightcurves from Moriya and Eldridge (2016) with SN 2023zaw in Figure 9.6. The predicted peak bolometric luminosities ($\sim 10^{41}$ erg s^{-1}) are ~ 10 times fainter than the peak luminosity measured for SN 2023zaw.

Ultra-stripped core-collapse supernova from a low-mass progenitor embedded in a He-rich CSM

An ultra-stripped SN (Tauris et al. 2015) is a possible channel for the formation of double neutron-star systems. They arise from a binary star system where a He-star undergoes a high degree of stripping by its smaller companion, such that the remaining ejecta mass is $< 1\ M_{\odot}$. The nickel mass is also expected to be quite low ($\sim 0.01\ M_{\odot}$). Due to the low nickel and ejecta mass, the lightcurves are expected to be faint and show fast evolution. The multiband lightcurve and bolometric properties of SN 2023zaw are consistent with an ultra-stripped SN scenario (Figures 10.4, 9.4 and 9.10). We compare the measured ejecta and nickel mass for SN 2023zaw with other ultra-stripped SN candidates in the literature in Table A and Figure 10.12. The estimated ejecta mass is comparable with other ultra-stripped SN candidates, while the nickel mass is a factor of ~ 5 lower. We could also reproduce the observed lightcurve by using ultra-stripped SN progenitor models evolved with MESA and exploded using SNEC (see Section 9.3).

Implication of narrow He I lines in the late-time spectra

The presence of narrow He I emission lines in the late-time spectra at 30 and 60 days post-peak implies the presence of a He-rich dense CSM shell, which is consistent with the predictions of ultra-stripped SN models. We note that we do not see prominent narrow He I emission lines in the spectra taken prior to 9 days after peak. It is likely the broad He I lines from the ejecta dominate over the narrow CSM emission lines in the initial days. But if there is actually no CSM interaction till +8 days, we can constrain the CSM shell to be at $\sim 10^{15}$ cm, which is consistent with the short-period binary models from Wu and Fuller (2022a). While the mass transfer model in Wu and Fuller (2022a) assumes that the stellar material lost through the L2 point is distributed spherically, a torus-like distribution of the CSM is also likely (Pejcha et al. 2016, Lu et al. 2023). The viewing angle will strongly influence the observed spectral line widths. In this scenario, the early spectra do not show narrow lines as the CSM is engulfed in the SN ejecta, similar to the model described in Andrews and Smith (2018) for iPTF14hls. Once the photosphere recedes, the CSM is accelerated by the collision of the ejecta to intermediate velocities of ≈ 1000 km s^{-1}. In this scenario, the absence of narrow lines in the ALFOSC spectrum taken at +0 days can be explained if the CSM is confined within 10^{14} cm, which is consistent with the majority of binary mass transfer models in Wu and Fuller (2022a). We note that the CSM interaction does not show up as an additional bump in the optical

lightcurve. This could be explained by a very low mass He-rich CSM, which is consistent with the estimated low progenitor and ejecta masses. If CSM interaction does contribute significantly to the luminosity, the nickel mass we estimate should be considered as an upper limit.

Implication of very low nickel mass

Observations and parametrized 1D models of massive star explosions suggest that typically $\sim 0.05\ M_{\odot}$ Ni should be ejected from a core-collapse SN. Anderson (2019) and Meza and Anderson (2020) measured the Ni-mass for a sample of Type II and Type Ibc SNe in the literature and found that the Ni-mass synthesized in SESNe was significantly higher than for Type II SNe. The lowest Ni-mass in their Type Ibc sample was $0.015\ M_{\odot}$, and 25% of all Type II SNe has a Ni-mass below this limit. However, this might be due to an observational bias as low Ni-mass SESNe are harder to detect as they are likely to be faint as well as fast-evolving. The extremely low amount of Ni-mass in SN 2023zaw ($\sim 0.002\ M_{\odot}$) could imply a fallback event, where most of the Ni produced in the core-collapse immediately fall into the newly formed black hole (Turatto et al. 1998, Sollerman 2002, Balberg et al. 2000). However, the observed high velocities do not favor this scenario.

The other explanation is that the progenitor's initial mass lies in the low-mass end of core-collapse SN progenitors, as stars with low-mass iron cores produce a low amount of Ni. Stockinger et al. (2020) and Sandoval et al. (2021) obtained $\sim$ 0.002-0.005 $M_{\odot}$ Ni mass for a 9.6 $M_{\odot}$ progenitor. More recent 3D simulations (Burrows et al. 2024) estimate $0.002 - 0.006\ M_{\odot}$ Ni-mass for a 9 $M_{\odot}$ ZAMS mass progenitor and $> 0.01\ M_{\odot}$ for progenitors with initial mass greater than 9.25 $M_{\odot}$. We note that these models are not for stripped-envelope SNe. However, if they undergo mass-loss after He-core burning, the core evolution of a star is decoupled from the envelope evolution and the nickel mass is expected to be the same. The amount of Ni synthesized in ultra-stripped models for low-mass CO stars is $\lesssim 0.01\ M_{\odot}$ (Moriya et al. 2017, Sawada et al. 2022), which is consistent with our estimate for SN 2023zaw.

9.5 Conclusion

In this paper, we have presented the observations and analysis of an unusual stellar explosion – SN 2023zaw. It has the lowest nickel mass among all stripped-envelope SNe discovered so far. SN 2023zaw also shows the fastest evolution among all

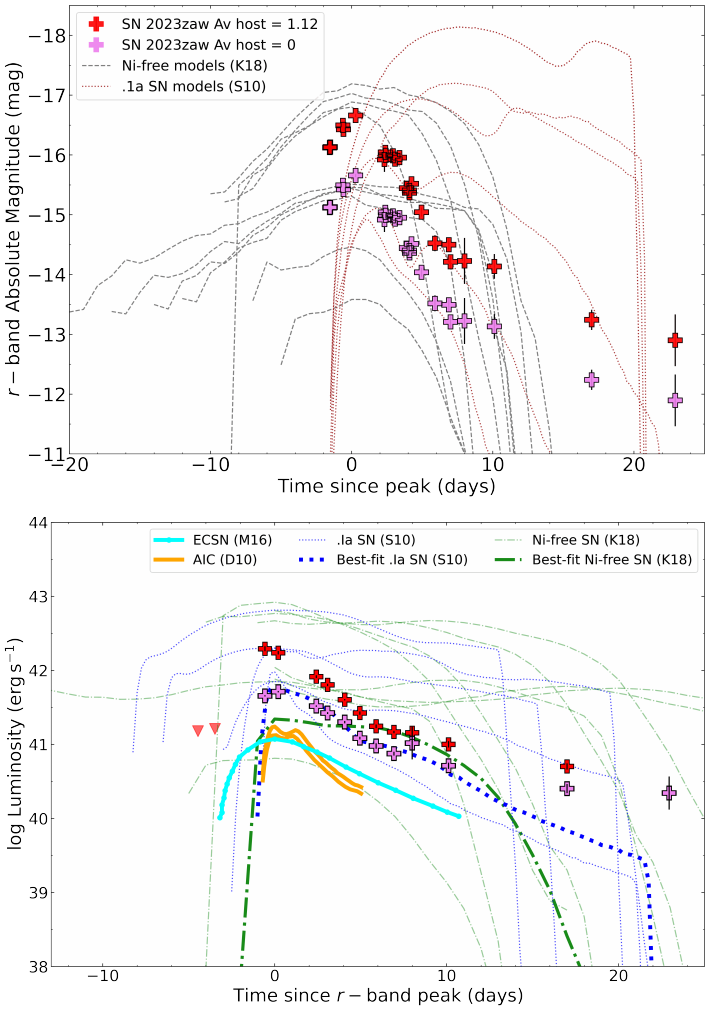

Figure 9.6: Comparison of the $r-$band and bolometric luminosity of SN 2023zaw with theoretical models for '.Ia' SNe (Shen et al. 2010), nickel-free SNe (Kleiser et al. 2018), electron-capture SN (Moriya and Eldridge 2016), and accretion-induced collapse of white dwarf (Darbha et al. 2010). The bold blue and green lines indicate the best-fit '.Ia' and nickel-free SN models, respectively.

stripped-envelope SNe, with a time above half maximum of 4.9 days in the $r-$band. The photospheric spectra show broad He I emission lines. It also shows broad Ca NIR emission lines as early as 2 days after peak.

We performed radiation-hydrodynamical and analytical modeling of the lightcurve by fitting with a combination of shock-cooling emission and nickel decay. The early-time lightcurve fits well with shock-cooling emission, with an envelope mass of $\approx 0.2\ M_{\odot}$and an envelope radius of $\approx 50\ R_{\odot}$. The estimated ejecta and nickel masses are $\approx 0.5\ M_{\odot}$ and $\approx 0.002\ M_{\odot}$ respectively.

We interpret SN 2023zaw as an ultra-stripped SN from a low-mass He-star – compact object binary. The late-time evolution of the He-star results in an extended He-rich envelope. There is also spectral evidence for thick He-rich CSM, likely from pre-SN mass loss episodes from late-time Roche lobe overflow. The very low nickel mass, ejecta mass, and explosion energy can only be explained by a progenitor with an initial mass less than around $10\ M_{\odot}$.

The late-time spectra show prominent narrow He I at a FWHM velocity of ~ 1000 km s^{-1}, indicating the presence of He-rich CSM. It is unclear if CSM interaction also provides a powering mechanism for SN 2023zaw. A number of other models for faint and rapidly evolving transients such as the nickel-free SN, accretion induced collapse, electron capture supernova were ruled out based on the peak luminosity and the presence of a late-time tail in the lightcurve of SN 2023zaw. The excess luminosity might be explained if the luminosity is boosted by CSM interaction. In this case, the estimated nickel mass should be treated as an upper limit. Including CSM interaction modeling in the future will help conclusively favor or rule out these scenarios. Also, late-time multi-wavelength follow-up will provide useful diagnostics in determining the CSM properties, the pre-SN mass-loss mechanism, and the evolutionary channel (Matsuoka and Maeda 2020, Kashiyama et al. 2022).

Spectroscopic modeling is currently missing for most of the theoretical scenarios for producing faint and rapid transients. Detailed modeling is required to explain some unusual spectroscopic features of SN 2023zaw such as – the presence of strong Ca NIR lines close to peak, redshifted component of He I λ5876 emission line, not reaching nebular phase till 30 days in spite of the low ejecta mass, the emergence of narrow He I emission lines and the absence of [Ca II], [O I] and Ca NIR emission lines in the nebular phase.

The extremely low nickel mass of SN 2023zaw gives rise to the question – what is the

lowest nickel mass that is synthesized in a stripped-envelope SN? Current literature shows that the nickel mass measured in stripped-envelope SNe is significantly higher than in Type II SNe (Anderson 2019). It is likely that this is due to an observational bias, as SESNe with low nickel masses are likely to be faint and fast evolving and hence harder to detect, classify, and follow-up. SN 2023zaw underscores the existence of this undiscovered population of low nickel mass SESNe ($< 0.005\ M_{\odot}$) with progenitor masses in the low mass end of core-collapse SNe ($< 10\ M_{\odot}$). A systematic study of the lowest-nickel mass stripped-envelope SNe, including their rates and the nickel mass distribution of low-luminosity SESNe will be explored in future work. Candidates for such low nickel mass stripped-envelope SNe include double peaked Type Ibc SNe such as SN 2021inl (Jacobson-Galán et al. 2022b, Das et al. 2023b), rapidly-evolving ($t_{1/2,r} < 10$ days) Type IIb SNe (e.g., Ho et al. 2023, Das et al. 2023a, Fremling et al. in prep), rapidly-declining H-poor SNe such as SN 2020ghq (Wang et al. in prep). For SNe with extremely low Ni-mass, the shock cooling emission is likely to dominate over nickel decay. The ultra-stripped SNe candidates in the literature show an early luminosity excess that is powered by shock-cooling. Future wide-field UV surveys such as ULTRASAT (Sagiv et al. 2014, Shvartzvald et al. 2023), UVEX (Kulkarni et al. 2021), and deep ground-based surveys such as LSST (Ivezić et al. 2008) in synergy with high-cadenced surveys such as ZTF will provide an exciting opportunity to explore this phase space.

9.6 Data availability

All the photometric and spectroscopic data used in this work will be made available on GitHub after publication.

The optical photometry and spectroscopy will also be made public through WISeREP, the Weizmann Interactive Supernova Data Repository (Yaron and Gal-Yam 2012a).

9.7 Acknowldegement

KKD acknowledges support from the Schwartz Reisman Collaborative Science Program, which is supported by the Gerald Schwartz and Heather Reisman Foundation.

M.W.C acknowledges support from the National Science Foundation with grant numbers PHY-2308862 and PHY-2117997.

S. Schulze is partially supported by LBNL Subcontract NO. 7707915.

Based on observations obtained with the Samuel Oschin Telescope 48-inch and

the 60-inch Telescope at the Palomar Observatory as part of the Zwicky Transient Facility project. ZTF is supported by the National Science Foundation under Grant No. AST-2034437 and a collaboration including Caltech, IPAC, the Oskar Klein Center at Stockholm University, the University of Maryland, University of California, Berkeley, the University of Wisconsin at Milwaukee, University of Warwick, Ruhr University, Cornell University, Northwestern University and Drexel University. Operations are conducted by COO, IPAC, and UW.

SED Machine is based upon work supported by the National Science Foundation under Grant No. 1106171.

The ZTF forced-photometry service was funded under the Heising-Simons Foundation grant #12540303 (PI: Graham).

The Gordon and Betty Moore Foundation, through both the Data-Driven Investigator Program and a dedicated grant, provided critical funding for SkyPortal.

This research has made use of the NASA/IPAC Extragalactic Database (NED), which is funded by the National Aeronautics and Space Administration and operated by the California Institute of Technology.

The data presented here were obtained in part with ALFOSC, which is provided by the Instituto de Astrofisica de Andalucia (IAA) under a joint agreement with the University of Copenhagen and NOT.

The Liverpool Telescope is operated on the island of La Palma by Liverpool John Moores University in the Spanish Observatorio del Roque de los Muchachos of the Instituto de Astrofisica de Canarias with financial support from the UK Science and Technology Facilities Council. Based on observations made with the Italian Telescopio Nazionale Galileo (TNG) operated on the island of La Palma by the Fundación Galileo Galilei of the INAF (Istituto Nazionale di Astrofisica) at the Spanish Observatorio del Roque de los Muchachos of the Instituto de Astrofisica de Canarias.

The W. M. Keck Observatory is operated as a scientific partnership among the California Institute of Technology, the University of California and the National Aeronautics and Space Administration. The Observatory was made possible by the generous financial support of the W. M. Keck Foundation. The authors wish to recognize and acknowledge the very significant cultural role and reverence that the summit of Maunakea has always had within the indigenous Hawaiian community.

We are most fortunate to have the opportunity to conduct observations from this mountain.

MMT Observatory access was supported by Northwestern University and the Center for Interdisciplinary Exploration and Research in Astrophysics (CIERA).

9.8 Appendix

Timescale - Luminosity phase space

In Figure 10.3, we compare the time above half maximum and peak luminosity of SN 2023zaw with stripped-envelope supernovae and other fast-evolving transients in the literature with rise and decline time constraints.

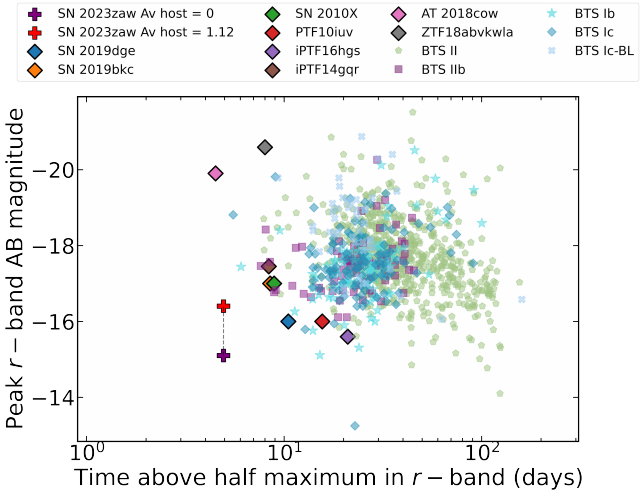

Figure 9.7: We compare the time above half maximum and peak luminosity of SN 2023zaw with stripped-envelope supernovae from the BTS experiment (Perley et al. 2020). For sources with two peaks in the $r-$band lightcurve, the second peak is used. We also compare with other fast-evolving transients – SN 2019dge (Yao et al. 2020), SN 2019bkc (Prentice et al. 2020, Chen et al. 2020), iPTF14gqr (De et al. 2018c), iPTF16hgs (De et al. 2018b), AT 2018cow (Perley et al. 2019), ZTF18abvkwla or AT2023abbd (Ho et al. 2020).

Host galaxy emission lines

Table B shows the emission line flux measurements of the star-forming region at the SN site.

Table B: Emission line flux measurements of the star-forming region at the SN site.

Transition	Flux $(10^{-17}\,\mathrm{erg\,cm^{-2}\,s^{-1}})$
[O II] $\lambda\lambda$ 3726,3729	61.10 ± 5.23
[O III] λ 4959	4.63 ± 0.15
[O III] λ 5007	13.90 ± 0.46
Hγ	14.83 ± 1.20
Hβ	42.48 ± 2.51
[N II] λ 6549	26.04 ± 1.27
Hα	203.98 ± 6.74
[N II] λ 6584	78.12 ± 3.81
[S II] λ 6718	40.84 ± 1.61
[S II] λ 6732	28.69 ± 1.43

Note. No measurement is corrected for reddening.

Photometry Data

A truncated version of the photometry table is shown in Table A1. All the photometric and spectroscopic data used in this work will be made available on GitHub after publication.

Spectroscopy Collage

A collage all the spectra of SN 2023zaw is shown in Figure 10.5.

Spectroscopy Log

The spectroscopy log is shown in Table A2.

Color Evolution Plot

The $g - r$ and $r - i$ color evolution of SN 2023zaw compared to other SNe in the literature is shown in Figure A2.

Lightcurve comparison

In Figure 9.10, we compare the $r-$band lightcurve of SN 2023zaw with other fast-evolving transients in the literature.

Blackbody best-fit parameters

The summary of the best-fit blackbody properties can be found in Table E.

Table C: Truncated photometry data for SN 2023zaw. The full machine-readable version will be made available on GitHub after publication. The photometry data has been corrected for Milky Way extinction.

MJD	Phase[a]	Instrument	Filter	AB Magnitude
60285	−2	ATLAS	*o*	19.33 ± 0.26
60285	−2	P48	*g*	18.34 ± 0.06
60285	−2	ATLAS	*o*	18.16 ± 0.07
60285	−2	SEDM	*r*	18.09 ± 0.07
60285	−2	SEDM	*g*	18.23 ± 0.05
60285	−2	SEDM	*r*	18.08 ± 0.04
60285	−2	SEDM	*i*	17.91 ± 0.06
60286	−1	SEDM	*r*	17.72 ± 0.06
60286	−1	SEDM	*g*	17.98 ± 0.05
60286	−1	SEDM	*r*	17.78 ± 0.04
60286	−1	SEDM	*i*	17.65 ± 0.02
60286	−1	ATLAS	*c*	17.88 ± 0.05
60287	0	P48	*g*	17.96 ± 0.05
60287	0	P48	*g*	17.97 ± 0.04

[a] Days since *r*-band peak (MJD = 60287.7).

Table D: Spectroscopy log.

Date	Phase[a]	Instrument
Dec 12 2023	−1.5	SEDM
Dec 08 2023	−0.6	SEDM
Dec 09 2023	0.0	ALFOSC
Dec 11 2023	+2.4	SEDM
Dec 12 2023	+2.5	KCWI
Dec 12 2023	+3.1	SEDM
Dec 13 2023	+4.0	GMOS
Dec 14 2023	+5.1	Binospec
Dec 17 2023	+8.0	LRIS
Jan 07 2024	+29.0	LRIS
Feb 07 2024	+61.0	LRIS

[a] Days since *r*-band peak (MJD = 60287.7).

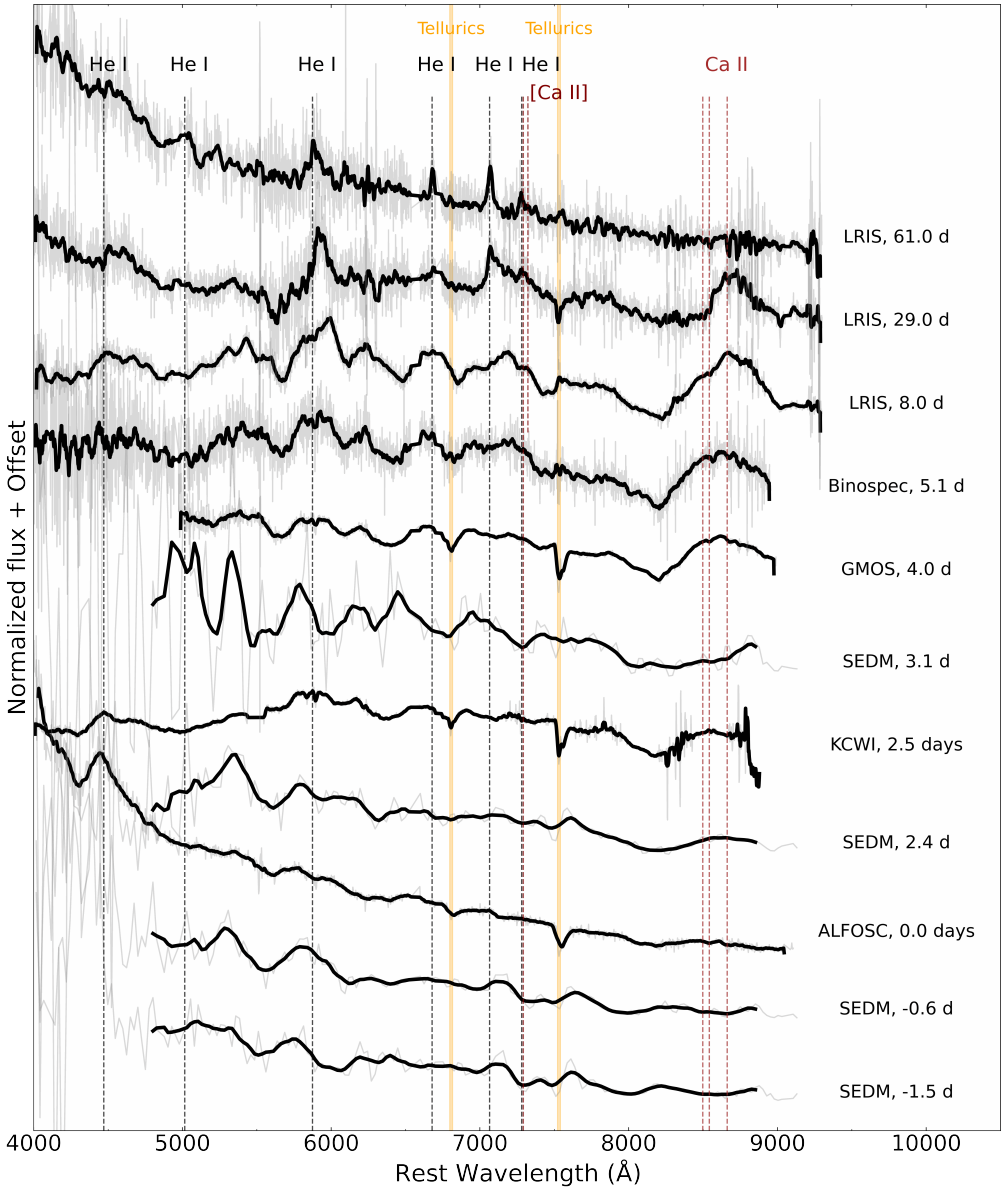

Figure 9.8: Spectral sequence for SN 2023zaw. The phases are in rest-frame days since the r-band peak (MJD = 60287.7). See Section 9.2 for details on the obtained spectra.

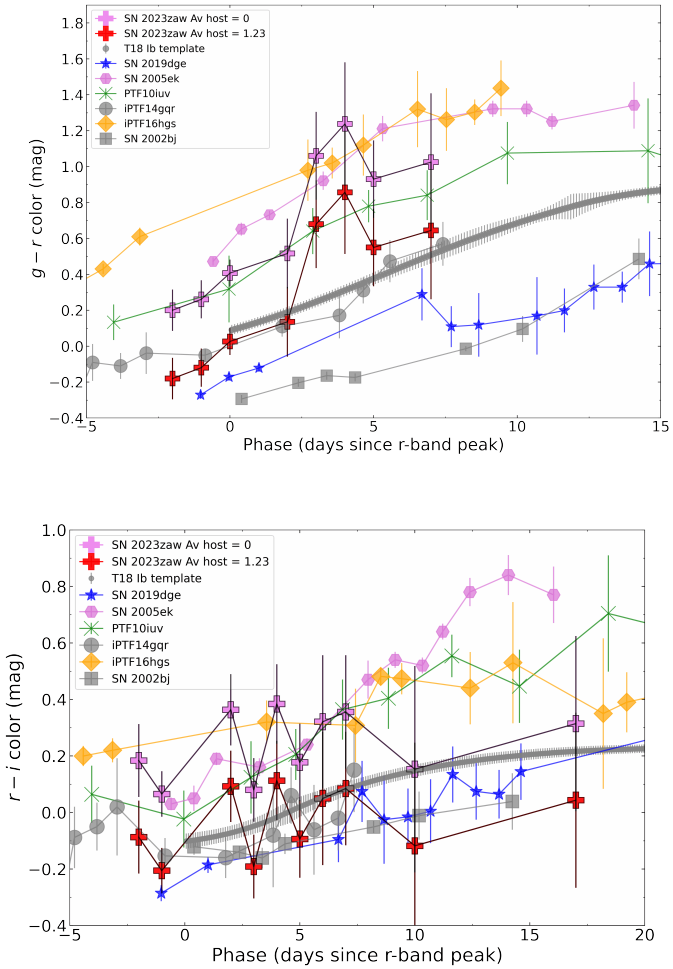

Figure 9.9: The $g-r$ (*left*) and $r-i$ (*right*) color evolution of SN 2023zaw compared to other fast transients – SN 2005ek (Drout et al. 2013), SN 2019dge (Yao et al. 2020), iPTF14gqr (De et al. 2018c), iPTF14hgs (De et al. 2018b). The gray line shows the intrinsic color template for Type Ib SNe from Stritzinger et al. (2018).

Comparison of envelope properties

We compare the envelope properties of SN 2023zaw with USSNe candidates and Type Ibn SNe in Figure 9.11. We compare the envelope properties of SN 2023zaw with theoretical models for bound and unbound stellar material in Figure 9.12.

Priors and Corner plots

The priors and corner plots for shock-cooling emission and radioactive decay model fitting are shown in Tables F, G and Figure 9.13.

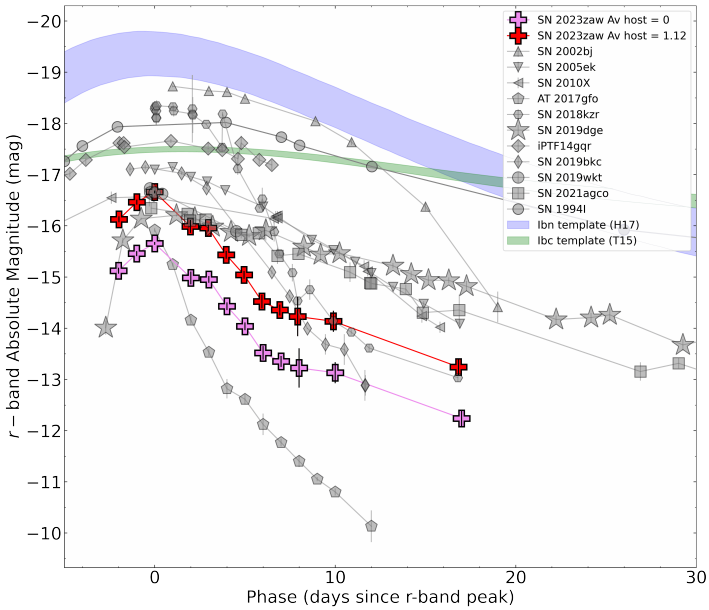

Figure 9.10: The $r-$band lightcurve of SN 2023zaw compared with other fast-evolving transients in the literature – fast-declining Type I SNe – SN 2010X (Kasliwal et al. 2010), SN 2019bkc (Prentice et al. 2020, Chen et al. 2020), the kilonova AT 2017gfo (Abbott et al. 2017), ultra-stripped SN candidates – SN 2019dge (Yao et al. 2020), iPTF14gqr (De et al. 2018c), SN 2019wxt (Shivkumar et al. 2023, Agudo et al. 2023), SN 2022agco (Yan et al. 2023).

Table E: Summary of the blackbody properties for SN 2023zaw. A machine-readable version of this table will be made available on GitHub after publication.

Phase (days)	Log Luminosity (erg s^{-1})	Temperature (K)	Radius ($R_\odot$)
−2	$42.40^{+0.10}_{-0.08}$	15620^{+1850}_{-1440}	3500^{+360}_{-360}
−1	$42.29^{+0.03}_{-0.03}$	11050^{+510}_{-490}	6180^{+340}_{-320}
0	$42.24^{+0.02}_{-0.02}$	8960^{+500}_{-460}	8820^{+760}_{-700}
2	$41.92^{+0.02}_{-0.02}$	6900^{+340}_{-330}	10270^{+860}_{-750}
3	$41.80^{+0.02}_{-0.02}$	6710^{+300}_{-280}	9530^{+710}_{-670}
4	$41.60^{+0.01}_{-0.01}$	5520^{+230}_{-210}	11190^{+880}_{-830}
5	$41.42^{+0.02}_{-0.02}$	6100^{+380}_{-340}	7440^{+790}_{-720}
6	$41.24^{+0.02}_{-0.03}$	5060^{+470}_{-430}	8780^{+1710}_{-1360}
7	$41.17^{+0.02}_{-0.02}$	5370^{+320}_{-290}	7140^{+870}_{-760}
8	$41.16^{+0.07}_{-0.08}$	5160^{+10}_{-10}	7640^{+590}_{-660}
10	$41.00^{+0.04}_{-0.05}$	5070^{+10}_{-10}	6630^{+310}_{-330}
17	$40.70^{+0.04}_{-0.04}$	5000^{+10}_{-10}	4830^{+220}_{-240}

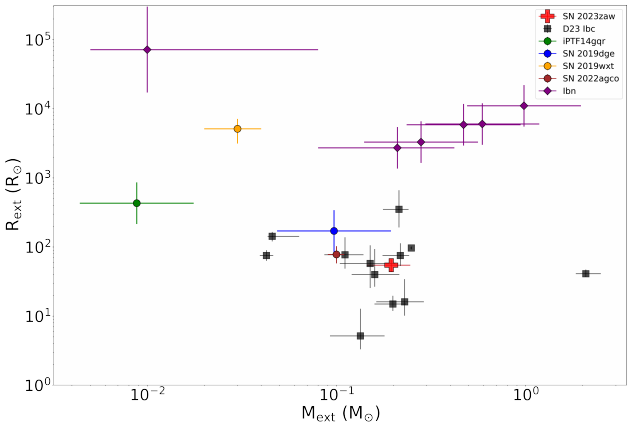

Figure 9.11: The envelope properties of SN 2023zaw (red cross) compared with double-peaked Type Ibc SNe (black squares) from Das et al. (2023b), USSN candidates (circles) – iPTF14gqr, SN 2019dge, SN 2019wxt, SN 2022agco (De et al. 2018c, Yao et al. 2020, Shivkumar et al. 2023, Agudo et al. 2023, Yan et al. 2023), and Type Ibn SNe (purple diamonds) – SN 2006jc, SN 2019wep, SN 2019up, SN 2012jpk, SN 2019deh, LSQ13ddu (Anupama et al. 2009, Pellegrino et al. 2022b, Clark et al. 2020).

Table F: Priors used for shock-cooling emission model fitting described in Section 9.3.

Parameter	Prior
$\log R_{\rm ext}$	$\mathcal{U}(-5, 25)$
$\log M_{\rm ext}$	$\mathcal{U}(-4, 1)$
$E_{\rm ext,49}$	$\mathcal{U}(0.1, 100)$

Table G: Priors used for nickel decay model fitting described in Section 9.3.

Parameter	Prior
$\tau_{\rm m}$	$\mathcal{U}(1, 20)$
$\log M_{\rm Ni}$	$\mathcal{U}(-4, 0)$
t_0	$\mathcal{U}(2, 100)$

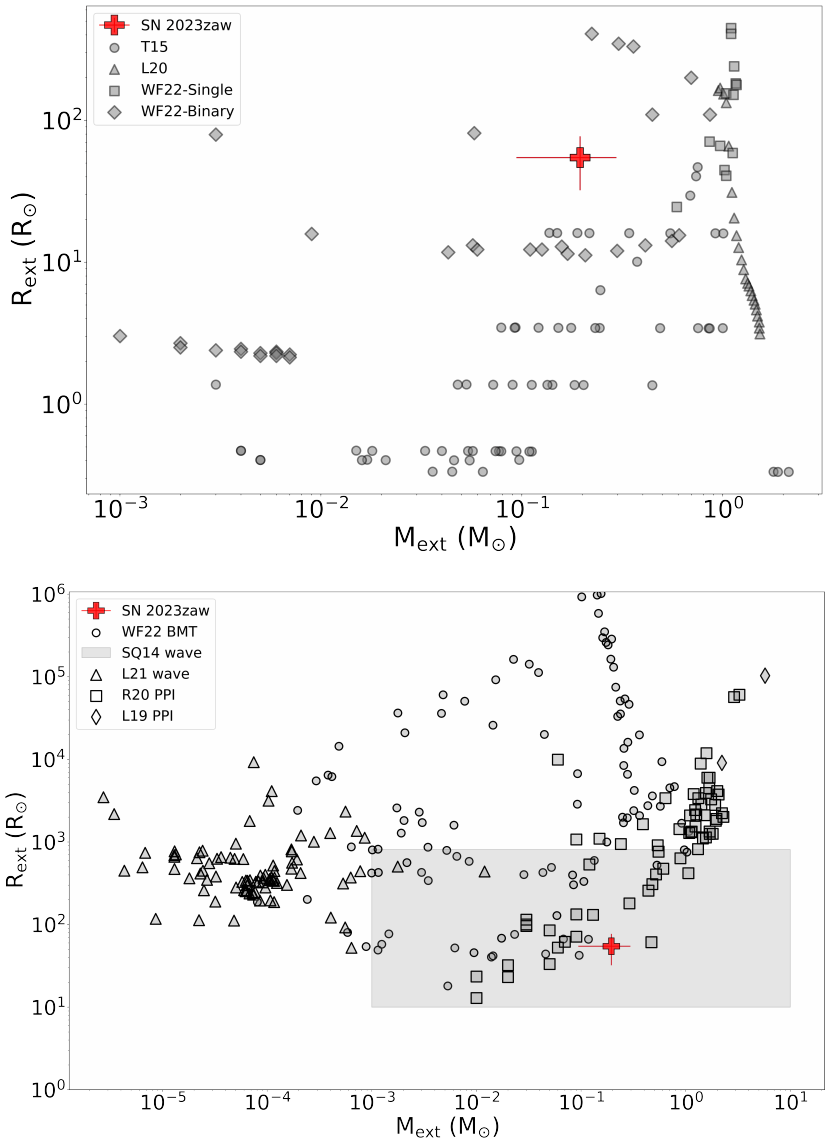

Figure 9.12: *Left:* Comparison of the envelope properties of SN 2023zaw with theoretical models for *bound* stellar material – binary and single star models from Wu and Fuller (2022a) (WF22), Laplace et al. (2020) (L20) and Tauris et al. (2015) (T15). *Right:* Comparison of the the envelope properties of SN 2023zaw with theoretical models for *unbound* stellar material – late-time binary mass transfer (BMT; Wu and Fuller 2022a), wave-driven mass loss (Leung et al. 2021a, Shiode and Quataert 2014), pulsation-pair instability driven mass loss (PPI; Renzo et al. 2020, Leung et al. 2019).

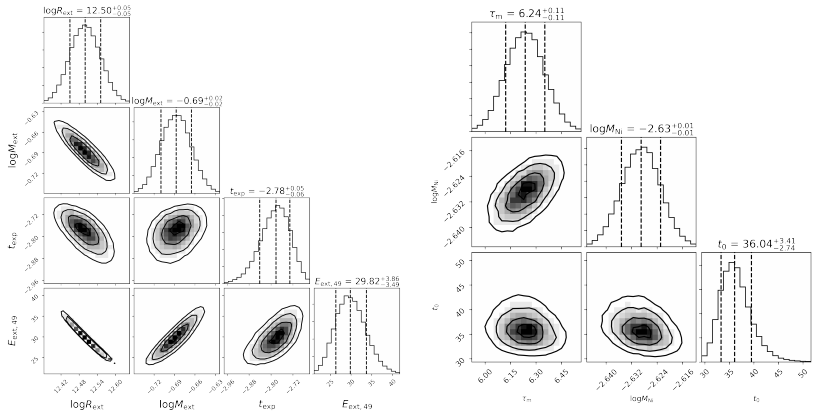

Figure 9.13: Corner plots showing the posterior constraints of the model parameters in the shock-cooling emission (left) and radioactive decay (right) models described in Section 9.3.

Chapter 10

SN 2018ERX: A FAST-EVOLVING, DUST-REDDENED TYPE ICN SUPERNOVA WITH BROAD C II EMISSION LINES

Das, K. K., A. Gangopadhyay, et al. (2026). "SN 2018erx: A fast-evolving, dust-reddened Type Icn supernova with broad C II emission lines". In: Submitted to *Publications of the Astronomical Society of the Pacific*. arXiv: 2605.24811.

Abstract

We present the discovery and characterization of SN 2018erx (ZTF18abkmbpy), a fast-evolving, unusually red, interacting stripped-envelope supernova. Spectroscopically, SN 2018erx exhibits prominent broad C II emission with characteristic widths of $\sim 3800\,\mathrm{km\,s^{-1}}$, consistent with interaction with a carbon-rich circumstellar medium (CSM) and a Type Icn core-collapse SN classification.

Photometrically, SN 2018erx evolves exceptionally rapidly, rising from half-maximum to peak in 2.1 d and declining back in 3.1 d, placing it among the fastest-evolving core-collapse supernovae observed. Semi-analytical CSM-interaction modeling favors a compact, shell-like CSM with $M_{\mathrm{CSM}} \approx 0.3\,M_\odot$, an inner radius of $R_0 \approx 0.7$ AU, and a very low ejecta mass of $M_{\mathrm{ej}} \approx 0.11\,M_\odot$. The radioactive yield is likewise small, with a ^{56}Ni mass $\lesssim (3\text{–}5) \times 10^{-3}\,M_\odot$, placing SN 2018erx at the low end of the H-poor stripped-envelope SN distribution. At +29 d after peak, we detect a near-infrared excess consistent with pre-existing local circumstellar dust and infer a hot-dust mass of $M_{\mathrm{d}} \sim 10^{-6}$–$10^{-5}\,M_\odot$. Taken together, the rapid evolution, strong local reddening, carbon-rich emission, and evidence for pre-existing dust point to a multi-component circumstellar environment consisting of a dense inner interaction region produced by enhanced pre-SN mass loss ($\dot{M} \sim 10^{-3}$–$10^{-4}\,M_\odot\,\mathrm{yr^{-1}}$) and an outer dusty layer at $R \gtrsim 4 \times 10^{16}$ cm, produced by an earlier mass-loss episode roughly 10–200 yr before core collapse. These properties favor an ultra-stripped core-collapse explosion of a low-mass He star in a binary system that underwent late-time Case BC mass transfer or Si-flash-induced mass loss. Fallback-modified Wolf–Rayet collapse or a merger-driven mass-loss episode remain plausible alternatives. These observations provide rare insight into the mass-loss history of stripped-envelope SNe, indicate that SN 2018erx-like events may be efficient sites of dust formation, and suggest that dust-enshrouded explosions of this kind may be

systematically underrepresented in optical surveys.

10.1 Introduction

Wide-field, high-cadence time-domain surveys have transformed the study of explosive transients by enabling the systematic discovery of rare and fast-evolving events. Facilities such as the Zwicky Transient Facility (ZTF; Bellm et al. 2019b, Graham et al. 2019, Dekany et al. 2020, Masci et al. 2019) and the Asteroid Terrestrial-impact Last Alert System (ATLAS; Tonry et al. 2018, Smith et al. 2020) now deliver large samples of core-collapse supernovae (SNe) with well-sampled photometric coverage and spectroscopy. One of the most important outcomes of this observational shift has been the growing realization that the final months to years of massive-star evolution can be extraordinarily dynamic. In many events, the explosion is accompanied by clear evidence for substantial circumstellar material (CSM) in the immediate environment, implying intense pre-SN mass loss. When the SN ejecta collide with this dense CSM, kinetic energy is efficiently converted into radiation, reshaping the light curve and imprinting narrow or intermediate-width emission features on the spectrum.

Among the diverse interaction-powered transients, the interacting stripped-envelope (SE) SNe are particularly valuable because they probe mass loss after hydrogen removal, when the progenitor has already transitioned to a compact helium star or Wolf–Rayet (WR)-like object (Smith 2014). Classical SESNe (Types IIb/Ib/Ic) are understood as explosions of stars that have lost most or all of their hydrogen-rich envelopes through wind or binary stripping. Their progenitor may also have recently expelled dense material that remains sufficiently close to the star to contribute to the luminosity. The best-known subclass in this category is the Type Ibn SNe, defined by the presence of narrow helium emission lines (often with P-Cygni profiles) and weak or absent hydrogen features, signaling interaction with He-rich CSM (e.g., Pastorello et al. 2008, Hosseinzadeh et al. 2017a, Farias et al. 2025). The newly established Type Icn SN class extends this picture further. These events show narrow or intermediate-width carbon and nitrogen lines (commonly high-ionization species at early phases), while lacking strong H and He features, pointing to interaction with H/He-poor and likely C/O-rich material. Only six confirmed SNe Icn have been published to date—SN 2019hgp, SN 2019jc, SN 2021csp, SN 2021ckj, SN 2022ann and SN 2023xgo (Gal-Yam et al. 2022a, Pellegrino et al. 2022a, Perley et al. 2022b, Nagao et al. 2023, Davis et al. 2023, Gangopadhyay et al. 2025). Even within this small sample, the class exhibits substantial diversity in luminosity, timescale, and

line morphology (Pellegrino et al. 2022a, Nagao et al. 2023, Davis et al. 2023), suggesting that more than one progenitor pathway may contribute to the observed phenomenology.

The progenitor systems and mass-loss histories that give rise to SNe Ibn and SNe Icn remain uncertain. A natural interpretation is that both SNe Ibn and SNe Icn are linked to WR-like progenitors, with apparent compositional differences reflecting the surface chemistry of the star at the time of mass loss (e.g., WN-like for He-rich material versus WC/WO-like for C/O-rich material), together with variations in the geometry, timing, and density of the pre-SN outflow (Gal-Yam et al. 2022a, Perley et al. 2022a). Lightcurve modeling of many normal SESNe often implies ejecta masses of only a few solar masses, frequently below expectations for single-star WR progenitors, motivating binary stripping as a dominant channel for producing SE explosions (e.g., Drout et al. 2013, Lyman et al. 2016, Prentice et al. 2019, Taddia et al. 2018, Barbarino et al. 2021, Dessart et al. 2022). In the most rapidly evolving events, the characteristic diffusion times can be so short that the inferred ejecta masses fall well below $\sim 1\ M_{\odot}$, reminiscent of "ultra-stripped" explosions, which are binary-stripped He-stars with $M_{\rm ej} < 1\ M_{\odot}$ in compact binaries (e.g., Tauris et al. 2013, 2015). In this regime, even modest amounts of nearby CSM can dramatically influence the observed lightcurve, and interaction-powered models have been shown to reproduce the fast and luminous peaks of several rapidly evolving transients (Pellegrino et al. 2022a, Wu and Fuller 2022a, Moriya et al. 2025). Whether interacting SESNe preferentially arise from classical WR stars with enhanced pre-SN mass loss and fallback to a compact object, from low-mass helium stars in close binaries undergoing extreme late-stage stripping or from a mixture of these possibilities remains an open question. Another interesting progenitor channel was recently suggested by Wu et al. (2024), Moriya et al. (2026), which suggests that white dwarf mergers can also lead to the formation of He and C+O dense CSM in SNe Ibn/Icn.

Several SNe Ibn/Icn have also exhibited strong evidence for dust formation or for pre-existing dust in the immediate environment. The prototypical SN 2006jc showed a steepening optical light-curve decline accompanied by the emergence of a near-infrared (NIR) excess, a combination widely interpreted as due to rapid dust condensation in the post-shock cool dense shell (e.g., Anupama et al. 2009). Similar dust-related behaviour has been suggested in other members of the Type Ibn class, including SN 2010al and the slowly evolving OGLE-2012-SN-006 (Gan et al.

2021). More recently, Yamanaka and Nagayama (2025) reported a pronounced and persistent NIR excess in SN 2023xgo (classified as a Type Ibn/Icn event) lasting from ∼15 to 100 days, which they interpret as a NIR echo from pre-existing circumstellar carbon dust. These cases motivate to consider local dust as an important ingredient when interpreting unusually red interacting SESNe such as SN 2018erx.

In this paper, we present SN 2018erx (ZTF18abkmbpy), a fast-evolving interacting SESN discovered by the Zwicky Transient Facility (ZTF). Its lightcurve shows an exceptionally rapid rise and decline, placing it among the fastest H-poor SNe and overlapping with the regime of rapidly evolving stripped-envelope transients (e.g., Drout et al. 2014, De et al. 2018c, Yao et al. 2020, Das et al. 2024a). Prior to extinction correction, SN 2018erx is unusually red and optically faint for an interacting stripped-envelope event. Its spectra reveal prominent broad C II emission lines, linking it to the emerging Type Icn class, for which only six events are currently known. A late-time NIR excess further suggests the presence of pre-existing local circumstellar dust.

Taken together, these properties make SN 2018erx a rare but important event for understanding how rapid evolution, carbon-rich CSM interaction, and dust obscuration shape the observed stripped-envelope SN population. The combination of a dense inner CSM and a more extended dusty CSM component provides a direct probe of multi-epoch mass loss in heavily stripped progenitors. The carbon-rich environment also provides favorable conditions for efficient dust formation and growth. These results suggest that some fast, low-luminosity, low-^{56}Ni explosions may be underrepresented in current optical samples, especially if they are additionally dimmed by local dust extinction. SN 2018erx therefore provides rare insight into stripped progenitor systems, their recent mass-loss history, and possible observational biases affecting the discovery of interacting stripped-envelope explosions.

The paper is organized as follows. In Section 10.2, we describe the discovery of SN 2018erx and summarize the photometric and spectroscopic follow-up observations. Section 10.3 presents the extinction analysis. Section 10.4 details the observed photometric and spectroscopic properties, including comparisons with literature transients. In Section 10.5, our analysis and modeling. In Section 10.6, we discuss the progenitor and evolutionary pathways. We summarize our conclusions in Section 10.7.

10.2 Discovery and follow-up observations

Discovery and host-galaxy

SN 2018erx was discovered with the ZTF camera (Dekany et al. 2020) on the 48-inch Samuel Oschin Telescope at Palomar Observatory. The source was first detected at $\alpha = 17^{\rm h}05^{\rm m}14.284^{\rm s}$, $\delta = +56°13'00.11''$ (J2000) on 2018 August 3 at 07:52:19 UT and reported to the Transient Name Server[1] as SN 2018erx (Fremling 2018). At discovery, the transient had an AB magnitude of $r_{\rm ZTF} = 18.7$ mag. A pre-discovery ZTF image obtained on 2018 July 31 shows no source at the transient position down to a 5σ limiting magnitude of $r_{\rm ZTF} > 20.6$ mag, implying that the rise occurred within the preceding few days.

SN 2018erx is projected on the galaxy CGCG 277−025 (NED position $\alpha = 17^{\rm h}05^{\rm m}13.9592^{\rm s}$, $\delta = +56°13'10.462''$, J2000). We adopt a host-galaxy redshift of $z = 0.02938$, measured from the narrow nebular emission lines in our Keck/LRIS spectrum at the SN position. Assuming a flat ΛCDM cosmology (Planck Collaboration et al. 2020) with $H_0 = 67.7$ km s^{-1} Mpc^{-1}, $\Omega_{\rm m} = 0.31$, this corresponds to a luminosity distance of $D_L = 133.1$ Mpc and a distance modulus of $\mu = 35.62$ mag. We ignore explicit corrections for peculiar motions for galaxies at this distance. Assuming a characteristic peculiar velocity of $\sim$ 300 km s^{-1}, the resulting uncertainty in the distance modulus is $\lesssim 0.1$ mag. The transient is offset by $10.7''$ from CGCG 277−025, corresponding to a projected separation of ~ 6.5 kpc at this distance.

We note that CGCG 277−025 also hosted the Type Ib SN 2018cfh, discovered earlier in 2018 only a few weeks before SN 2018erx. The two events therefore constitute a near-contemporaneous "sibling" SN pair in the same host galaxy (e.g., Biswas et al. 2022, Dhawan et al. 2025). The same galaxy has since produced another core-collapse event, the Type IIb SN 2025abku (Das et al. 2025a).

Optical and near-infrared photometry

We obtained multiple epochs of g- and r-band photometry with the ZTF camera on the Palomar 48-inch Oschin telescope (Dekany et al. 2020). The images were processed with the ZTF image analysis pipeline (Masci et al. 2019), and we performed forced photometry at the transient position on the ZTF difference images in the gri bands. We also carried out follow-up optical imaging with the 2.0 m robotic Liverpool Telescope (Steele et al. 2004), obtaining regular-cadence photometry in

[1] https://www.wis-tns.org/object/2018erx/discovery-cert

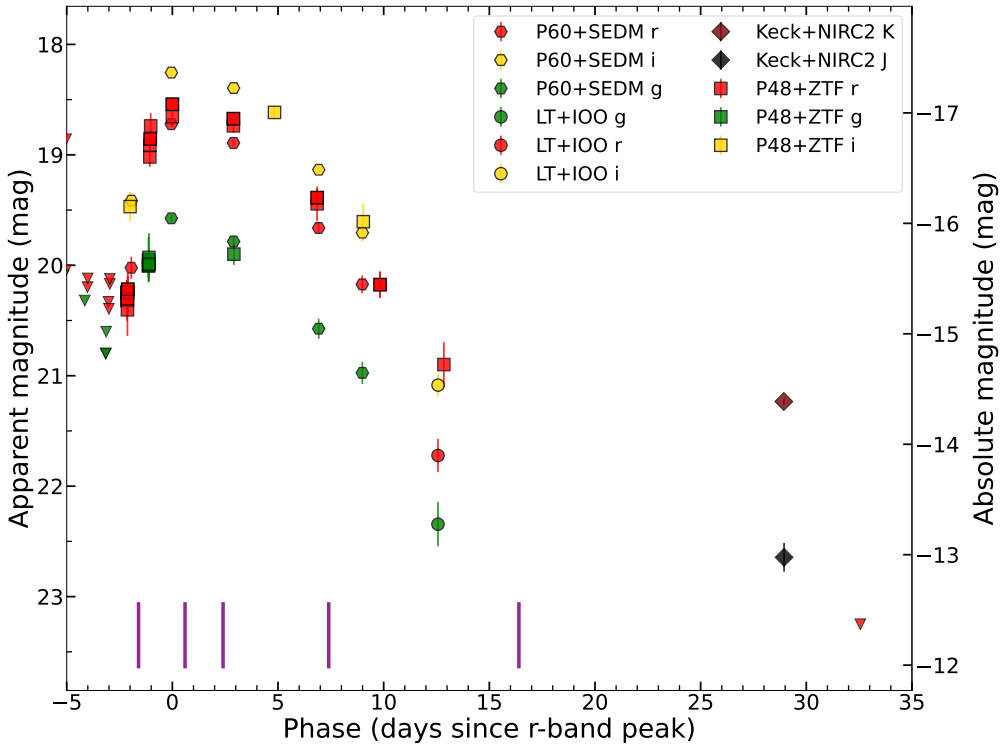

Figure 10.1: Multi-band optical and near-infrared lightcurves of SN 2018erx. The left axis shows the observed apparent magnitudes, while the right axis indicates the corresponding absolute magnitudes. Both axes are corrected for Milky Way extinction, but no correction for host or circumstellar dust extinction has been applied. The phase is given in rest-frame days relative to the epoch of r-band maximum. Downward triangles denote nondetections. The epochs of spectroscopic observations are indicated by vertical purple lines.

the g, r, and i bands. Further multi-band optical photometry in g, r, and i was obtained with the Rainbow Camera on the automated Palomar 60-inch telescope (P60; Cenko et al. 2006). The P60 images were processed with the FPipe image-subtraction pipeline (Fremling et al. 2016) using Pan-STARRS1 (PS1; Chambers et al. 2016) reference images. Near-infrared imaging was obtained in the J and K bands with NIRC2 behind the Keck II adaptive optics system.[2] The NIRC2 data were reduced using the pipeline described in De et al. (2020a). The full set of optical and near-infrared lightcurves is shown in Figure 10.1, and the photometry is listed in Table A1. All phases are quoted relative to rest-frame r-band maximum (58334.4 MJD) unless otherwise stated.

[2]https://www2.keck.hawaii.edu/inst/nirc2/

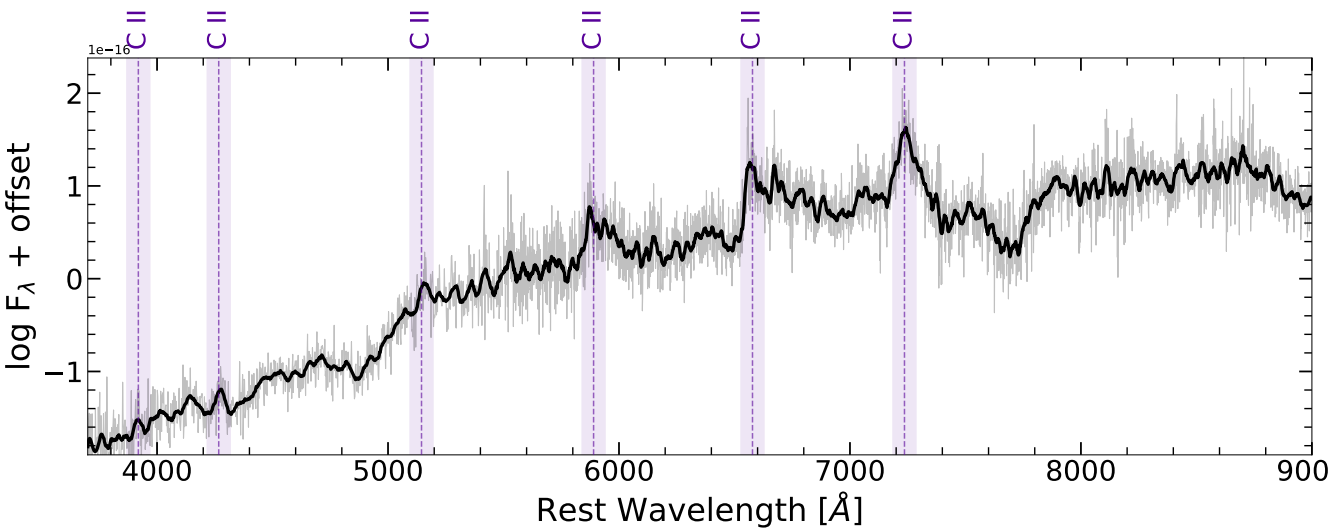

Figure 10.2: Keck/LRIS spectrum of SN 2018erx obtained at a phase of +2.4 days (rest-frame) relative to r-band maximum. The grey line shows the original spectrum, while the black curve indicates a smoothed version. The purple shaded regions mark the wavelengths of prominent C II $\lambda\lambda$4267, 5145, 5890, 6578, and 7236 emission lines.

Optical and near-infrared spectroscopy

We observed the spectral evolution of SN 2018erx, spanning from discovery through the following month. An initial spectrum was taken on the discovery date (2018 August 3) with the Spectral Energy Distribution Machine (SEDM; Blagorodnova et al. 2018) on the Palomar 60-inch telescope (with two exposures obtained that night), followed by optical spectroscopy with the Double Spectrograph (DBSP; Oke and Gunn 1982) on the Palomar 200-inch Hale telescope on 2018 August 4. We obtained an additional optical spectrum with the Low-Resolution Imaging Spectrometer (LRIS; Oke et al. 1995) on Keck I on 2018 August 8. Continued monitoring was carried out with DBSP on 2018 August 12 and 2018 August 21. Finally, we obtained a late-time Keck/LRIS spectrum on 2025 August 19 to characterize the host-galaxy contribution at the transient position.

The DBSP spectra were reduced following the procedures described by Bellm and Sesar (2016) and Roberson et al. (2022), the SEDM data were reduced using the pipeline described by Rigault et al. (2019), and the LRIS spectra were reduced using the LPIPE pipeline (Perley 2019).

The photometry and spectroscopy were coordinated through the Global Relay of Observatories Watching Transients Happen (GROWTH) Marshal (Kasliwal et al. 2019)

and the `Fritz` Marshal (van der Walt et al. 2019, Coughlin et al. 2023), both of which are web portals designed for vetting and coordinating transient follow-up observations.

Figure 10.2 shows an early-time spectrum of SN 2018erx, highlighting the prominent C II emission features that characterize the event. The spectroscopy log is provided in Table A2. All photometry and spectroscopy data will be made publicly available on Zenodo and WISeREP (Yaron and Gal-Yam 2012b) after publication.

10.3 Extinction correction

We correct all photometry and spectra for Milky Way foreground extinction using the dust maps of Schlafly and Finkbeiner (2011). Along the line of sight to SN 2018erx we adopt $E(B-V)_{\rm MW} = 0.02$ mag. All reddening corrections are applied with the Cardelli et al. (1989) extinction law assuming $R_V = 3.1$.

Host-galaxy extinction constraints from narrow features

No prominent narrow Na I D absorption lines were seen in the spectra of SN 2018erx. To estimate any host-galaxy reddening, we also use the Balmer decrement measured from narrow nebular emission lines in our Keck/LRIS long-slit spectrum taken ∼2572 d after r-band peak (Fig. A1). At this late epoch, any direct contribution from the SN or ongoing SN–CSM interaction should be negligible, so we interpret the narrow Balmer emission as arising from the local host-galaxy environment at the SN position. After shifting the spectrum to the host rest frame ($z = 0.0294$), we subtract a locally fitted linear continuum in the 4000–5400 Å region (excluding windows around the Balmer lines) and measure line fluxes for Hγ and Hβ by integrating the continuum-subtracted spectrum within ±20 Å of the line centers. We then compare the observed ratio $(\mathrm{H}\gamma/\mathrm{H}\beta)_{\rm obs}$ to the intrinsic Case B recombination value $(\mathrm{H}\gamma/\mathrm{H}\beta)_0 = 0.469$, appropriate for photoionized gas at $T \sim 10^4$ K and low electron density (e.g., Momcheva et al. 2013). The implied color excess in AB mag is

$$E(B-V)_{\rm gas} = \frac{2.5}{k(\mathrm{H}\gamma) - k(\mathrm{H}\beta)} \log_{10}\left[\frac{(\mathrm{H}\gamma/\mathrm{H}\beta)_0}{(\mathrm{H}\gamma/\mathrm{H}\beta)_{\rm obs}}\right], \tag{10.1}$$

where $k(\lambda) = A_\lambda / E(B-V)$ is evaluated from the Cardelli et al. (1989) law. For $R_V = 3.1$ we adopt $k(\mathrm{H}\beta) = 4.60$ and $k(\mathrm{H}\gamma) = 5.12$, and convert to visual attenuation via $A_V^{\rm host} = R_V\, E(B-V)_{\rm gas}$. We measure $(\mathrm{H}\gamma/\mathrm{H}\beta_{\rm obs} = 0.459$, consistent with the intrinsic Case B value within uncertainties, implying no significant host-galaxy reddening.

We therefore find no compelling evidence for significant large-scale host-galaxy extinction from either narrow Na I D absorption or the Balmer decrement. However, Balmer-decrement estimates can be affected by underlying stellar Balmer absorption, slit losses, residual calibration uncertainties, and the narrow nebular lines need not trace the same dust column that attenuates the transient continuum if the emitting gas is not strictly co-spatial with the SN or if additional dust is local to the progenitor system. Likewise, extinction estimates based on the equivalent width of narrow Na I D are uncertain, particularly in low-resolution spectra (Poznanski et al. 2011) and in the presence of circumstellar material (Phillips et al. 2013).

Effective reddening implied by the red continuum and early ionized-carbon features

Blackbody fits to the early-time optical SED of SN 2018erx, corrected only for Milky Way extinction, yield characteristic temperatures of only $\sim$ 4000 K if no additional extinction is applied (see Section 10.5). Such low temperatures are difficult to reconcile with the early spectroscopic appearance of the SN, which shows prominent C II features and a Type Icn-like interaction spectrum. We therefore interpret the observed red optical colors as reflecting substantial effective attenuation of an intrinsically hotter continuum, rather than the true color temperature of the emitting region.

This interpretation is also supported by comparison with other Type Icn SNe. Published events with analogous early-time ionized-carbon features show blue continua and characteristic blackbody temperatures of order 10^4 K or higher at comparable phases (Pellegrino et al. 2022a, Perley et al. 2022b, Nagao et al. 2023, Davis et al. 2023), while radiative-transfer models of hot carbon-rich stripped-envelope explosions produce optical C II features near maximum light at photospheric temperatures of $\sim 12,000$ K (Dessart 2019). Motivated by the temperatures inferred for Type Icn SNe and by spectral models that produce C II features at $T \sim 12,000$ K, we adopt a fiducial intrinsic continuum temperature of $T_{\rm C} = 12,000$ K and a conservative range of 10,000–15, 000 K.

Close to the epoch of the MJD 58333.8 LRIS spectrum, the absolute magnitudes corrected for MW extinction are $M_g = -15.8$, $M_r = -16.7$, and $M_i = -17.2$, which give observed colors of $(M_g - M_r)_{\rm obs} = 0.9$ mag and $(M_r - M_i)_{\rm obs} = 0.5$ mag. We approximate the intrinsic optical continuum by a blackbody with color temperature $T_{\rm C}$ and evaluate flux ratios at the effective wavelengths of the gri filters, λ_g =

0.477 μm, $\lambda_r = 0.623$ μm, and $\lambda_i = 0.763$ μm, using the Planck function:

$$B_\nu(\nu, T) = \frac{2h\nu^3}{c^2} \frac{1}{\exp(h\nu/kT) - 1}. \tag{10.2}$$

In the AB system, the monochromatic blackbody color between two bands X and Y is

$$(X - Y)_{\rm BB}(T_{\rm C}) \simeq -2.5 \log_{10}\left[\frac{B_\nu(\nu_X, T_{\rm C})}{B_\nu(\nu_Y, T_{\rm C})}\right], \tag{10.3}$$

where $\nu_X = c/\lambda_X$.

Across the adopted temperature range, the corresponding blackbody colors are $(M_g - M_r)_{\rm BB} \approx -0.04$ to -0.25 mag and $(M_r - M_i)_{\rm BB} \approx -0.14$ to -0.25 mag. Adopting a Cardelli extinction law with $R_V = 3.1$, the relevant color coefficients are $R_g - R_r = 1.005$ and $R_r - R_i = 0.673$. Matching the de-reddened colors to the blackbody colors gives

$$E(B - V)_{gr} = \frac{(M_g - M_r)_{\rm obs} - (M_g - M_r)_{\rm BB}}{1.005}, \tag{10.4}$$

$$E(B - V)_{ri} = \frac{(M_r - M_i)_{\rm obs} - (M_r - M_i)_{\rm BB}}{0.673}. \tag{10.5}$$

Across this temperature range, both color combinations yield similar values,

$$E(B - V) \simeq 1.0\text{–}1.2 \text{ mag}. \tag{10.6}$$

Using $T_{\rm C} = 12{,}000$ K as a fiducial intrinsic continuum temperature, we obtain an effective reddening estimate of $E(B - V) \simeq 1.05$ mag, corresponding to $A_V \simeq 3.3$ mag for $R_V = 3.1$. This estimate is robust to within ± 0.1 mag in $E(B - V)$, corresponding to ± 0.3 mag in A_V, across the adopted temperature range.

Consistency with CSM-interaction lightcurve modeling

As an independent check, we allow the effective extinction to vary freely in our multi-band CSM-interaction modeling with `redback` (Sarin et al. 2024, Chatzopoulos et al. 2012, 2013) (see Sect. 10.5). In this framework, the model SED is approximated as a blackbody (with a temperature floor) and an attenuation parameter $A_V^{\rm eff}$ is inferred simultaneously with the interaction parameters. The posterior favors substantial attenuation,

$$A_V^{\rm eff} \simeq 3.15^{+0.05}_{-0.05} \text{ mag}, \tag{10.7}$$

consistent with the C II-motivated color-temperature estimate. Given the strong and internally consistent evidence for significant effective attenuation from the early-time colors and the CSM-interaction fit, we adopt $A_V^{\rm eff} \simeq 3.3$ mag, together with $E(B-V)_{\rm MW} = 0.02$ mag, for extinction corrections throughout this work. This choice also brings the color evolution of SN 2018erx into agreement with that of other interacting SESNe (Figure A2).

Consistency with the inferred dust properties

In the previous subsections, we inferred a large effective attenuation, $A_V^{\rm eff} \simeq 3.2$–3.3 mag, from the lightcurve and the presence of C II features, despite the absence of strong host-ISM reddening diagnostics (narrow Na I D absorption and the Balmer decrement). This motivates a local circumstellar dust origin for much of the extinction. Here we assess whether an attenuation of this magnitude is quantitatively consistent with the dust component implied by the observed NIR excess.

For a foreground dust screen, extinction and optical depth are related by

$$A_V = 2.5 \log_{10}(e)\, \tau_V \simeq 1.086\, \tau_V, \tag{10.8}$$

where τ_V is the V-band extinction optical depth (absorption + scattering). Writing $\tau_V = \kappa_V \Sigma_{\rm d}$ in terms of the dust surface density $\Sigma_{\rm d}$ and the V-band mass extinction coefficient κ_V (e.g., Draine 2011), and approximating the dust as residing in a geometrically thin shell at radius $R_{\rm d}$ that subtends a solid-angle covering fraction f_Ω of 4π, the characteristic dust column through the dusty regions is

$$\Sigma_{\rm d} \simeq \frac{M_{\rm d}}{4\pi f_\Omega R_{\rm d}^2}. \tag{10.9}$$

Combining these relations gives

$$A_V \simeq 1.086\, \kappa_V \frac{M_{\rm d}}{4\pi f_\Omega R_{\rm d}^2}. \tag{10.10}$$

Solving for the required dust mass yields

$$\begin{aligned} M_{\rm d} \simeq 8.6 \times 10^{-6} &\left(\frac{A_V}{3.3\ {\rm mag}}\right)\left(\frac{R_{\rm d}}{3\times10^{15}\ {\rm cm}}\right)^2 \\ &\times \left(\frac{\kappa_V}{2\times10^4\ {\rm cm^2\, g^{-1}}}\right)^{-1}\left(\frac{f_\Omega}{1}\right) M_\odot, \end{aligned} \tag{10.11}$$

where the normalization $\kappa_V \simeq 2\times10^4$ cm$^2\, g^{-1}$ is representative of carbonaceous (see Section 10.5) ISM-like grain populations at optical wavelengths (e.g., Draine 2003, Zubko et al. 2004).

Equation (10.11) shows that if the extinction-producing dust lies at a radius of order a few $\times 10^{15}$ cm (comparable to the effective emitting scale inferred for the hot NIR component in Section 10.5), only $\sim 10^{-6}$–$10^{-5}\,M_\odot$ of dust is required to produce $A_V \sim 3$ mag for plausible optical opacities. This is comparable to the order-of-magnitude dust mass inferred from the JK emission under optically thin assumptions (Section 10.5) and to the lower end of dust masses inferred in other interacting stripped-envelope SNe (e.g., Anupama et al. 2009, Gan et al. 2021, Yamanaka and Nagayama 2025). An extinction of $A_V \sim 3$ mag is therefore not extreme from a dust-mass perspective. More generally, the required dust mass scales as $M_\mathrm{d} \propto R_\mathrm{d}^2\, f_\Omega/\kappa_V$, so a clumpy or aspherical distribution ($f_\Omega < 1$) can yield substantial line-of-sight attenuation without requiring a globally massive dust shell. Taken together, the NIR-inferred dust properties and the color-based extinction estimate are mutually consistent with a circumstellar dust origin for the attenuation.

10.4 Observed properties

Explosion epoch estimation

For SN 2018erx, we constrain the explosion epoch using the best-fitting CSM interaction model (see Section 10.5), which yields $t_\mathrm{exp} = 58328.19^{+0.04}_{-0.04}$ MJD. The ZTF lightcurve includes a last r-band non-detection at MJD 58331.17 with a limiting magnitude of $r > 20.4$ mag, followed by the first r-band detection at MJD 58331.18 with $r = 20.3$ mag in the ZTF forced-photometry light curve.

Lightcurve properties of SN 2018erx

The multi-band light curve of SN 2018erx, shown in Figure 10.1, spans $\sim$−3 to +30 d relative to r-band maximum. To estimate the peak date and magnitude, we interpolate the photometry with a Gaussian process implemented in `GEORGE` (Ambikasaran et al. 2015) using a Matérn-3/2 kernel. The GP fit yields an r-band maximum at MJD 58334.4 with $r = 18.32 \pm 0.17$ mag. We measure the light-curve width in flux space relative to half-maximum: the rest-frame rise time from 50% of peak flux to maximum is 2.1 d, and the corresponding fade time from maximum back to 50% of peak flux is 3.1 d. The rapid post-peak evolution is also reflected in $\Delta m_{15,r} = 2.9$ mag. These values place SN 2018erx among the fastest-evolving events in the SESN and Type Ibn/Icn populations (Hosseinzadeh et al. 2017a, Farias et al. 2025, Pellegrino et al. 2022b), and comparable to other rapidly evolving stripped-envelope transients (Drout et al. 2014). This is illustrated in Figure 10.3, where SN 2018erx occupies a short-timescale region of parameter

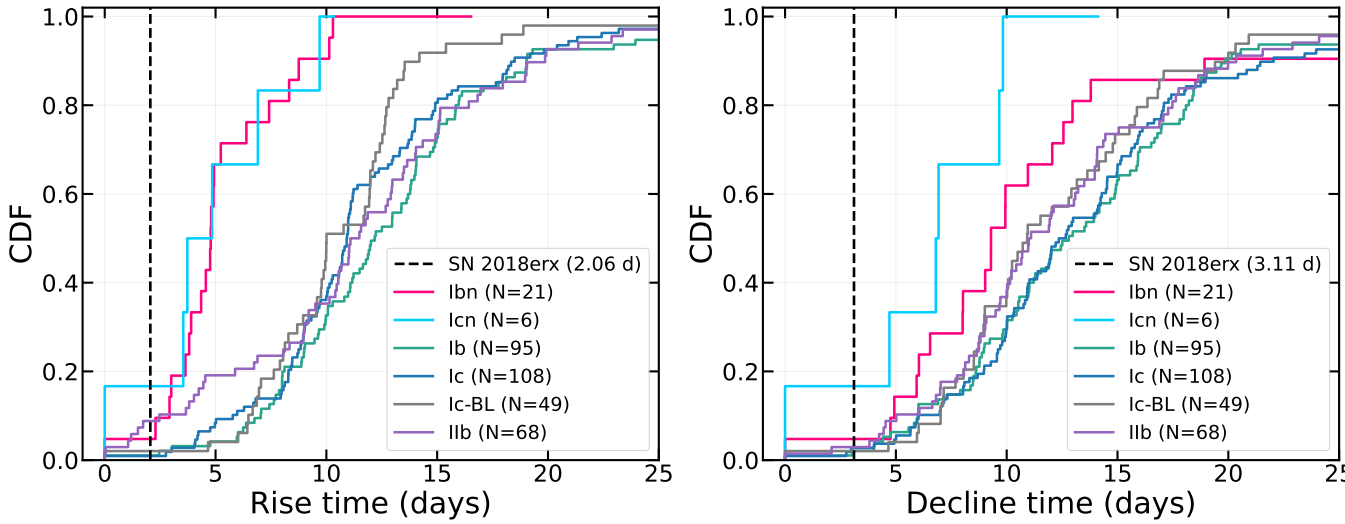

Figure 10.3: Cumulative distribution functions (CDFs) of rise time (left) and decline time (right) for stripped-envelope SN subclasses from the ZTF Bright Transient Survey (BTS) sample, while the SNe Icn sample combines the BTS SNe Icn with SN 2019jc, SN 2021ckj, SN 2023qre, and SN 2023rau. The vertical dashed line indicates the measured values for SN 2018erx, showing that it lies among the most rapidly evolving events relative to the broader populations of SNe Ib, Ic, Ic-BL, and IIb.

space relative to the broader stripped-envelope SN population. The estimated r-band decline rates over the intervals 0–10 and 10–20 d after maximum are 0.16 ± 0.01 and 0.09 ± 0.01 mag d^{-1}, respectively, faster than the mean weighted decline rate of the SN Ibn sample in Farias et al. (2025). The cumulative distributions shown in Figure 10.3 also indicate that SN 2018erx is among the most rapidly evolving events relative to the Bright Transient Survey (BTS) populations of SNe Ib, Ic, Ic-BL, and IIb. In addition to the unusually rapid optical evolution, SN 2018erx also exhibits a pronounced late-time near-infrared excess. At $\sim$+29 d, the transient is detected in both the J and K bands with very red $(J - K)$ color, indicating the presence of a hot dust component. We analyze the inferred dust properties in Section 10.5.

Comparison of the lightcurve with literature transients

Using the distance adopted in Section 10.2, we construct the absolute-magnitude r-band light curve of SN 2018erx and compare it with rapidly evolving transients and stripped-envelope SNe from the literature (Figure 10.4). We further summarize its location in peak-luminosity versus timescale space in Figure 10.3.

To place SN 2018erx in context, our comparison sample includes rapidly evolv-

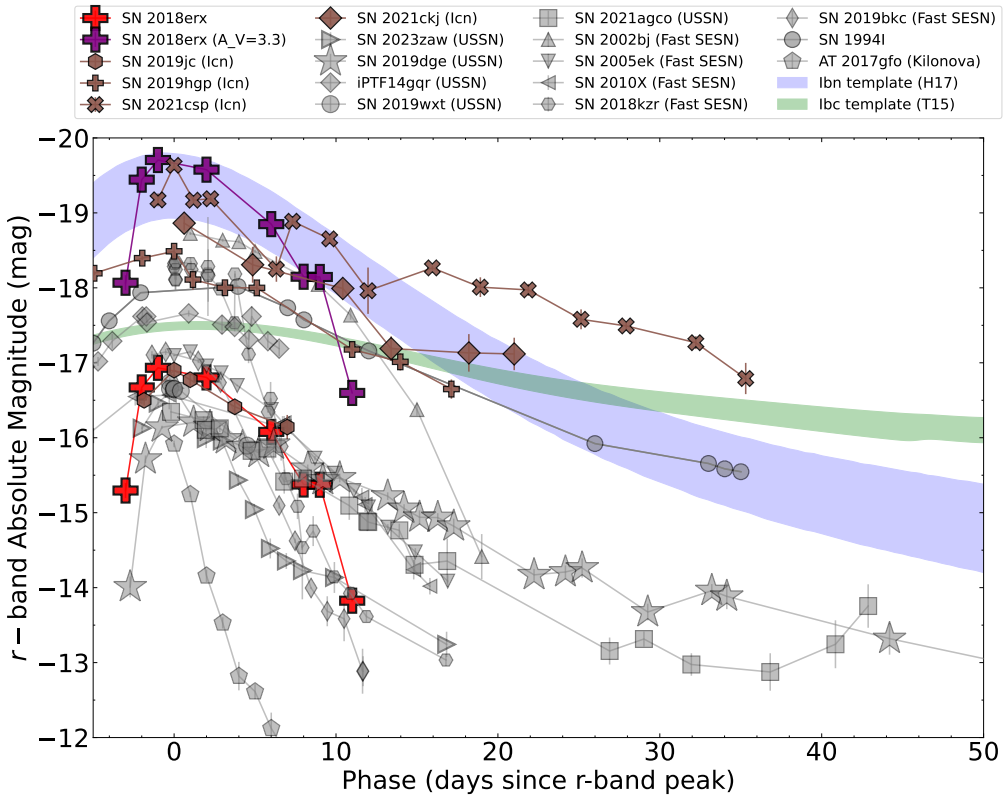

Figure 10.4: r-band absolute-magnitude lightcurve of SN 2018erx compared with rapidly evolving transients and SESNe from the literature. Red symbols show SN 2018erx assuming no host extinction ($A_V = 0$), while purple symbols show the extinction-corrected lightcurve adopting $A_V = 3.3$ mag. For comparison, lightcurves of several fast transients and interacting SESNe (colored markers) and a broader sample of stripped-envelope SNe (gray markers) are shown. The shaded regions indicate template lightcurves for SNe Ibn (G17; Hosseinzadeh et al. 2017a) and SNe Ibc (T15; Taddia et al. 2015). SN 2018erx evolves on a significantly faster timescale than typical SESNe.

ing hydrogen-poor transients such as SNe 2002bj (Poznanski et al. 2010), 2005ek (Drout et al. 2013), 2010X (Kasliwal et al. 2010), 2018kzr (McBrien et al. 2019), 2019dge (Yao et al. 2020), iPTF14gqr (De et al. 2018c), 2019bkc (Prentice et al. 2020, Chen et al. 2020), 2019wxt (Agudo et al. 2023, Shivkumar et al. 2023), and 2021agco (Yan et al. 2023), together with the well-studied Type Ic SN 1994I (Richmond et al. 1996) and representative template light curves of SNe Ibn and SNe Ibc (Hosseinzadeh et al. 2017a, Taddia et al. 2015). Several of these objects, in particular SNe 2002bj, 2005ek, 2010X, 2019wxt, and 2021agco, occupy a similar fast-timescale regime. Motivated by our interaction modeling, which favors a low ejecta mass, we also compare SN 2018erx with transients proposed to arise from ultra-stripped explosions, including SNe 2019dge (Yao et al. 2020), 2023zaw (Das et al. 2024a), 2021agco (Yan et al. 2023), and iPTF14gqr (De et al. 2018c). For completeness, we further include AT2017gfo, the electromagnetic counterpart of GW170817 (Abbott et al. 2017, Villar et al. 2017), which is not a core-collapse event but provides a useful benchmark for extremely rapid photometric evolution.

We estimate the r-band peak using a Gaussian-process interpolation with a Matérn-3/2 kernel, obtaining an observed peak absolute magnitude of $M_r = -17.29 \pm 0.17$ mag. Prior to any host-extinction correction, SN 2018erx would therefore be among the faintest members of the interacting SESN population and is roughly two magnitudes fainter than the mean SN Ibn/Icn templates, despite having similarly rapid rise and decline times. Adopting the effective host attenuation inferred in Section 10.3, $A_V = 3.3$ mag, and a Cardelli et al. (1989) law with $R_V = 3.1$, the corresponding extinction in the r band is $A_r \simeq 2.87$ mag. This shifts the intrinsic peak to $M_r \approx -20.16$ mag. Thus, while the uncorrected light curve would place SN 2018erx among the faintest interacting SESNe, the extinction-corrected luminosity moves it into the luminous end of the Ibn/Icn-like population, while preserving its exceptionally short timescale.

Optical and near-infrared spectral properties of SN 2018erx

Figure 10.5 shows the spectroscopic evolution of SN 2018erx from −1.6 d to +16.4 d relative to r-band maximum. The spectra shown are corrected for the host redshift but are not corrected for extinction from the Milky Way or the host galaxy along the line of sight. The earliest spectra exhibit a remarkably red continuum. Such a red continuum could arise either from substantial dust extinction along the line of sight or from an intrinsically red spectral energy distribution (Sasdelli et al. 2016).

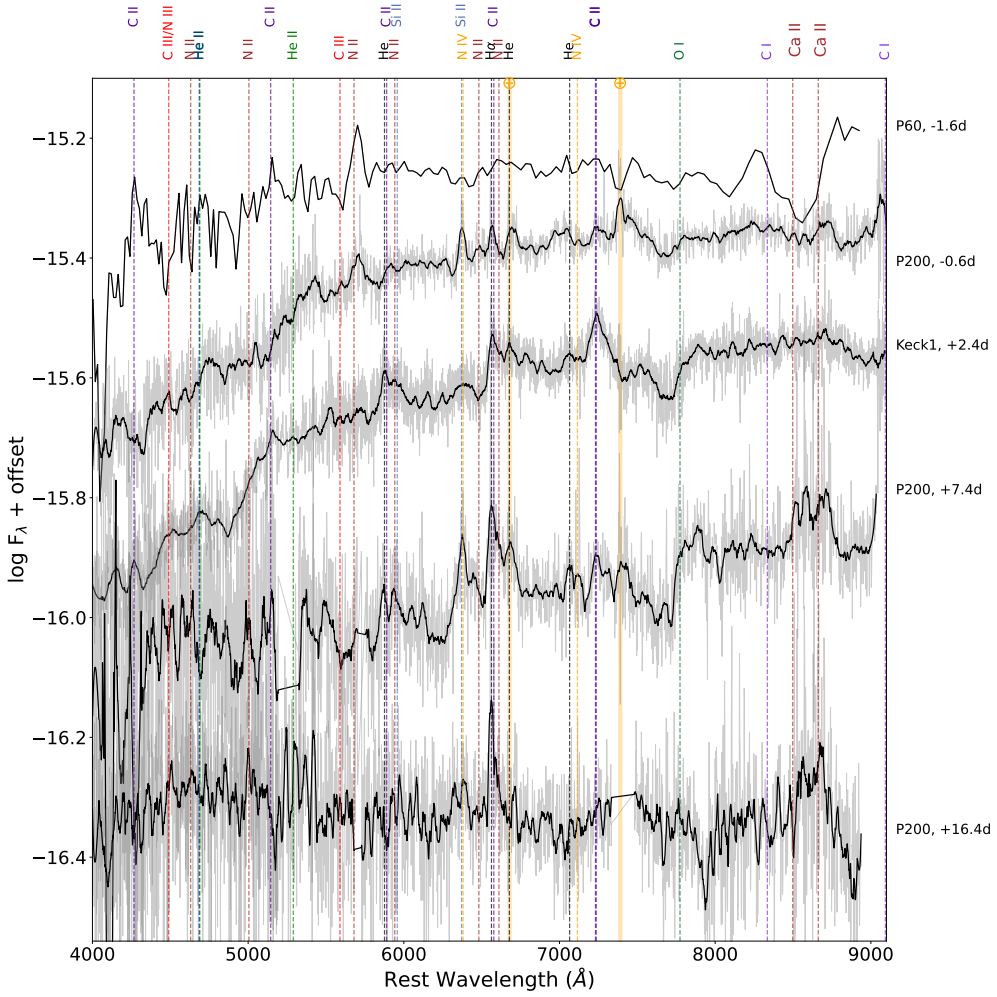

Figure 10.5: Spectral evolution of SN 2018erx from −1.6 to +16.4 days relative to *r*-band maximum. The spectra are shown in the host-galaxy rest frame and have been vertically offset for clarity. The gray lines show the original spectra, while the black curves indicate smoothed versions. Indentifications of prominent lines are marked with dashed vertical lines, including C II, He I, N II, N III, O I, and Ca II.

No unambiguous signatures of flash ionization are identified in the early spectra. Rather than exhibiting the rapidly fading, transient emission features typically associated with flash-ionized infant supernovae, the spectra obtained between −1.6 d and +2.4 d show comparatively long-lived absorption and emission features of C II, N II, Si II, and O I, which strengthen with time. Weak He I λ5876 and λ6678 emission is also detected over this interval. The prevalence of lower-ionization species may point either to a cooler ejecta environment, consistent with the blackbody temperature evolution shown in Fig. 10.8, or to a softer ionizing continuum.

At later epochs, from +2.4 d to +16.4 d, the C II features strengthen significantly, particularly the transitions at λ5890, λ6578, and λ7236. Lines of N II and O I remain visible throughout this period, while the Ca II near-infrared triplet becomes progressively stronger with time. The overall strengthening of C II features, together with the rapid photometric evolution (Section 10.2), supports a classification of SN 2018erx as a Type Icn SN. An important characteristic of SN 2018erx is the detection of He I lines at multiple stages of its evolution. This distinguishes it from previously studied SNe Icn, including SN 2019hgp and SN 2021csp, which did not show clear He I features. The presence of helium in SN 2018erx thus points to additional diversity within the SN Icn population.

Comparison of spectra with literature transients

To further assess the spectral classification of SN 2018erx, we compare its earliest high-quality optical spectrum, the +2.4 d Keck/LRIS spectrum, with representative Type Ibn and Type Icn events (Figure 10.6). Among the SNe Ibn, we consider SNe 2010al (Pastorello et al. 2015), 2011hw (Pastorello et al. 2015), 2019uo (Gangopadhyay et al. 2020), and 2019wep (Gangopadhyay et al. 2022). For the Type Icn comparison sample, we use SNe 2019hgp (Gal-Yam et al. 2022b), 2021ckj (Nagao et al. 2023), and 2021csp (Perley et al. 2022a). All comparison spectra are corrected for redshift, and where available they are also corrected for the adopted host extinction.

The overall comparison favors a Type Icn classification for SN 2018erx. Its spectrum is dominated by prominent C II emission features, with clear detections at $\lambda\lambda$4629, 5145, 5706, 5890, 6578, and 7236, and shows the closest resemblance to the Type Icn SN 2021csp. In particular, the strong carbon features and the absence of the narrow, helium-dominated emission spectrum typical of classical SNe Ibn argue that the CSM interacting with SN 2018erx is H/He-poor and carbon rich. Weak He I λ5876

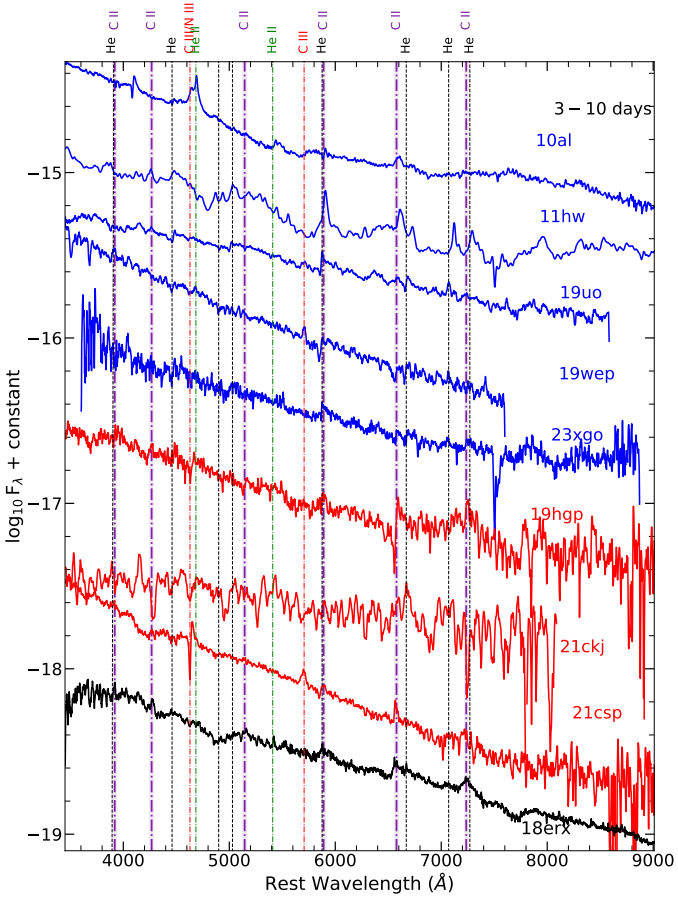

Figure 10.6: Comparison of the +2.4 day Keck/LRIS spectrum of SN 2018erx (black) with representative spectra of Type Ibn (blue) and Type Icn (red) supernovae at phases of ∼ 3–10 days relative to peak. The spectra are shown in the rest frame and vertically offset for clarity. Dashed vertical lines mark the wavelengths of prominent spectral features, including C II, He I, He II, N II, N III, and Ca II.

and λ6678 are present, but they do not dominate the spectrum. We therefore classify SN 2018erx as a Type Icn supernova, while noting that it may retain some residual helium seen in other SNe Icn (Perley et al. 2022a).

This classification is further supported by the velocity-space comparison of the strongest C II lines (Figure 10.7). We compare the profiles of C II λ7236, λ6587, and λ5890 in SN 2018erx with those of the Type Icn events SN 2022ann and SN 2019hgp. The line profiles of SN 2018erx are broadly similar in both width and shape to those of the comparison Type Icn events, reinforcing the interpretation that its intermediate-width carbon emission arises from interaction with a carbon-rich CSM. Compared to SN 2021csp, whose C II lines display narrow P-Cygni structure, the C II features in SN 2018erx are smoother and somewhat broader, with

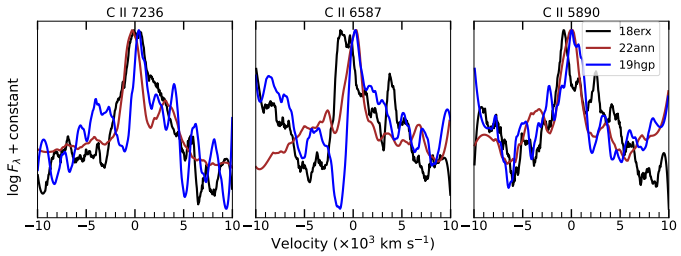

Figure 10.7: Velocity profiles of prominent C II emission lines in SN 2018erx compared with representative Type Icn supernovae. The panels show the regions around C II λ7236, λ6587, and λ5890. Spectra are plotted in velocity space relative to the rest wavelength of each transition. The spectrum of SN 2018erx (black) is compared with those of the Type Icn events SN 2022ann (red) and SN 2019hgp (blue). The similar line widths and profiles highlight the strong C II emission characteristic of carbon-rich interacting SESNe.

characteristic FWHM of order ∼3500–4000 km s^{-1}. We do not detect the very narrow component of C II, typically observed in interacting SNe and tracing slow unshocked CSM ($v \lesssim$ 100–200 km s^{-1}). This may be attributed to either insufficient spectral resolution to resolve such a feature, rapid photoionization of the pre-shock CSM by the intense SN radiation field, or a geometrically confined and tenuous circumstellar environment in which narrow-line emission falls below the detection threshold and sometimes can be caused by radiative acceleration suppressing narrow lines.

10.5 Analysis and Results

Blackbody SED fitting

We construct spectral energy distributions (SEDs) by binning the multi-band photometry into 1-day (rest-frame) intervals. For each epoch with detections in at least three filters, we fit a Planck blackbody function to the SED and infer the effective temperature ($T_{\rm bb}$) and photospheric radius ($R_{\rm bb}$). We sample the posterior distribution using the Python package `emcee` (Foreman-Mackey et al. 2013). The corresponding bolometric luminosity is then computed as

$$L_{\rm bb} = 4\pi R_{\rm bb}^2 \sigma T_{\rm bb}^4. \tag{10.12}$$

where σ denotes the Stefan–Boltzmann constant. We report the median posterior values in Table A3, with uncertainties corresponding to the 16th and 84th percentiles.

Figure 10.8 shows the temporal evolution of the inferred blackbody parameters for SN 2018erx, while the corresponding numerical values are listed in Table A3. Black

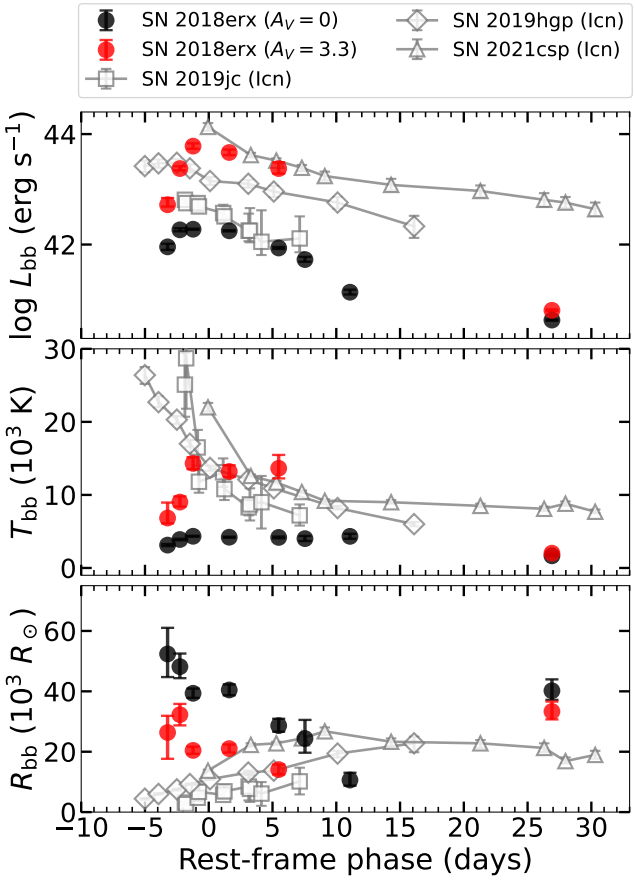

Figure 10.8: Evolution of the blackbody parameters derived from multi-band photometry of SN 2018erx. Top: bolometric luminosity (L_{bb}); middle: blackbody temperature (T_{bb}); bottom: blackbody radius (R_{bb}) as a function of rest-frame phase relative to r-band maximum. Black symbols show results obtained assuming no host extinction ($A_V = 0$), while brown symbols correspond to extinction-corrected values adopting $A_V = 3.3$ mag. Correcting for the inferred host attenuation significantly increases the inferred temperature and luminosity while reducing the emitting radius near peak.

symbols show results obtained assuming no host extinction ($A_V = 0$), while brown symbols correspond to extinction-corrected values adopting $A_V = 3.3$ mag. Correcting for the inferred host attenuation significantly increases the inferred temperature and luminosity while reducing the emitting radius near peak.

Without any host-extinction correction, SN 2018erx reaches a peak bolometric luminosity of $\log(L_{\rm bb}/{\rm erg\,s^{-1}}) \approx 42.3$ near maximum light. The luminosity then declines rapidly to $\log(L_{\rm bb}/{\rm erg\,s^{-1}}) \approx 41.1$ by ∼10 d after peak and to ≈ 40.6 by the latest epoch at ∼27 d. In this case the inferred temperature remains relatively cool, with $T_{\rm bb} \approx (4.0\text{–}4.5) \times 10^3$ K during the first ∼10 d after peak, before dropping to $\sim 1.6 \times 10^3$ K at the final epoch. The corresponding radius is large around maximum, $R_{\rm bb} \sim (4\text{–}6) \times 10^4\,R_\odot$, decreases to $\sim 10^4\,R_\odot$ by ∼+11 d, and remains of order a few $\times 10^4\,R_\odot$ at the latest epoch.

Applying the preferred host attenuation of $A_V = 3.3$ mag yields a markedly different and more physically plausible SED evolution. The peak luminosity increases to $\log(L_{\rm bb}/{\rm erg\,s^{-1}}) \simeq 43.8$, declines to ≃ 43.4 by ∼+6 d, and reaches ≃ 40.8 by ∼+27 d. The inferred radius is $R_{\rm bb} \simeq (2\text{–}3) \times 10^4\,R_\odot$ around peak and contracts to $\sim 1.4 \times 10^4\,R_\odot$ by ∼+6 d. The temperature correspondingly rises from $T_{\rm bb} \simeq 7 \times 10^3$ K at ∼-4 d to $\simeq (1.3\text{–}1.5) \times 10^4$ K near maximum, remains near $\simeq 1.3\text{–}1.4 \times 10^4$ K through the first week, and cools to $\sim 2 \times 10^3$ K at the latest epoch. These early-time temperatures are broadly consistent with the hot continuum typically associated with optical C II in SN spectra. The inferred blackbody radius of $R_{\rm bb} \simeq (2\text{–}3) \times 10^4\,R_\odot$ ($\simeq 1.4 \times 10^{15}$–$2.1 \times 10^{15}$ cm; ≃ 93–140 AU) near peak is inconsistent with a bare stellar photosphere and instead points to an optically thick, geometrically confined circumstellar envelope at scales of $\sim 10^2$ AU, consistent with pre-SN mass loss or an LBV-like eruption occurring years to decades prior to explosion. The subsequent contraction to $R_{\rm bb} \sim 1.4 \times 10^4\,R_\odot$ ($\sim 9.7 \times 10^{14}$ cm; ∼ 65 AU) by ∼+6 d, combined with the rising photospheric temperature toward maximum light, is consistent with the forward shock propagating through and progressively consuming the optically thick CSM, reducing the effective photospheric radius as the swept-up shell becomes increasingly optically thin. Crucially, at $t \sim +6$ d the blackbody radius remains significantly larger than the inferred ejecta radius of $R_{\rm ej} \simeq (1.66\text{–}1.97) \times 10^{14}$ cm (≃ 11–13 AU), confirming that the photosphere is still embedded within the overlying unshocked CSM at this epoch.

Overall, the extinction-corrected fits are more consistent with the spectroscopic evidence for a hot radiation field, whereas the uncorrected fits imply temperatures

that are too low to naturally explain the observed high-ionization features.

CSM-interaction lightcurve semi-analytical modeling

We model the multi-band lightcurve using the semi-analytic circumstellar interaction framework of Chatzopoulos et al. (2012, 2013), as implemented in `redback` (Sarin et al. 2024). The model assumes that the observed luminosity is powered by conversion of kinetic energy into radiation at the forward and reverse shocks, followed by diffusion through an optically thick CSM. The CSM is described by a power-law density profile,

$$\rho_{\rm csm}(r) = q\, r^{-\eta}, \qquad q \equiv \rho_0\, r_0^{\eta}, \tag{10.13}$$

where r_0 is the inner CSM radius and $\rho_0 \equiv \rho_{\rm csm}(r_0)$ is the density at r_0. For a given $M_{\rm csm}$, the outer edge of the CSM follows from mass conservation,

$$M_{\rm csm} = \int_{r_0}^{R_{\rm csm}} 4\pi r^2 \rho_{\rm csm}(r)\, dr = \frac{4\pi q}{3-\eta}\left(R_{\rm csm}^{3-\eta} - r_0^{3-\eta}\right), \tag{10.14}$$

The corresponding optically thick CSM mass is

$$M_{\rm csm,th} = \frac{4\pi q}{3-\eta}\left(r_{\rm ph}^{3-\eta} - r_0^{3-\eta}\right), \tag{10.15}$$

where $r_{\rm ph}$ is the photospheric radius within the CSM. Following Chatzopoulos et al. (2012, 2013), we adopt an outer ejecta density profile index $n = 12$ (Matzner and McKee 1999) and inner slope $\delta = 0$ (shell-like CSM structure). The shock-crossing time of the optically thick CSM, $t_{\rm sh}$, is computed using the self-similar shock solutions and tabulated constants of Chatzopoulos et al. (2012, 2013), and we define the diffusion time through the optically thick CSM as

$$t_{\rm diff} = \left(\frac{2\,\kappa\, M_{\rm csm,th}}{13.7\, c\, v_{\rm ej}}\right)^{1/2}. \tag{10.16}$$

For each model evaluation, we convert the bolometric luminosity and photospheric radius into broad-band fluxes using a blackbody spectral energy distribution with a temperature floor,

$$T = \max\left[\left(\frac{L}{4\pi\sigma r_{\rm ph}^2}\right)^{1/4}, T_{\rm floor}\right],$$

and include host extinction as a free parameter, $A_V^{\rm host}$. We fix the redshift to $z = 0.0294$ and adopt Gaussian priors on the opacity parameters, centered at

$\kappa = 0.07\ \mathrm{cm^2\,g^{-1}}$ and $\kappa_\gamma = 0.03\ \mathrm{cm^2\,g^{-1}}$, each with a width of 0.001, effectively treating both opacities as constant. We use log-uniform priors on $M_{\rm ej}$, $M_{\rm csm}$, $v_{\rm ej}$, ρ, r_0, and $T_{\rm floor}$, and uniform priors on η, t_0, and $A_V^{\rm host}$. Specifically, the ejecta mass and CSM mass are allowed to vary over 0.1–15 $\mathrm{M_\odot}$ and 10^{-3}–15 $\mathrm{M_\odot}$, respectively, while the ejecta velocity spans 10^3–5×10^4 km s^{-1}. The inner CSM radius is assigned a log-uniform prior over 0.1–100 AU, and the density at the inner radius is given a log-uniform prior over 10^{-15}–10^{-9} g cm^{-3}. The CSM density profile index is assigned a uniform prior between $\eta = 0$, corresponding to a shell-like configuration, and $\eta = 2$, corresponding to a steady wind. Posterior sampling is performed using nested sampling (Feroz et al. 2009) with the `dynesty` package (Speagle 2020), adopting the `rslice` sampling method.

The priors and the best-fit parameters are summarized in Table A and Table B, respectively. The resulting multi-band lightcurve fit is shown in Figure 10.9. The quoted 1σ uncertainties reflect only the formal statistical errors derived from the fitting procedure and do not account for systematic or model-dependent uncertainties. We note that $\mathrm{r_0}$ and ρ_0 are driven toward the boundaries of the explored parameter space (see Figure 10.10).

We find that a CSM mass of $M_{\rm CSM} \simeq 0.30^{+0.01}_{-0.01}\,\mathrm{M_\odot}$ provides a good reproduction of the observed lightcurves when coupled with an ejecta mass of $M_{\rm ej} \simeq 0.11^{+0.03}_{-0.01}\,\mathrm{M_\odot}$ and an interaction onset at an inner CSM radius of $R_0 \equiv r_0 \simeq 0.66^{+1.60}_{-0.47}$ AU. The fit further prefers substantial host extinction, $A_V \simeq 3.15^{+0.05}_{-0.05}$ mag. The comparatively low ejecta mass is broadly consistent with expectations for ultra-stripped explosions from low-mass helium stars in close binary systems (Das et al. 2024a, Wu and Fuller 2022b).

Compared with literature interaction-modeling results for SNe Ibn and SNe Icn (e.g., Pellegrino et al. 2022b, Farias et al. 2025), SN 2018erx occupies the low-mass end of both the ejecta-mass and CSM-mass distributions (Figure 10.11). In the R_0–$M_{\rm CSM}$ plane, it lies well below the bulk of the SN Ibn population, indicating a more compact inner CSM radius at comparable CSM mass, while remaining broadly consistent with the compact radii inferred for the small number of modeled SN Icn events. The cumulative-distribution comparison likewise shows that $M_{\rm ej}$, $M_{\rm CSM}$, and CSM density for SN 2018erx fall toward the lower end of the Type Ibn distribution, yet remain within the range spanned by both the Type Ibn and Icn samples. The CSM model fitted ejecta velocity, $v_{\rm ej} \simeq 1.5\times10^4$ km s^{-1}, lies toward the higher end of the SN Ibn distribution and is comparable to values inferred for SNe Icn, suggesting a

faster-moving, lower-mass ejecta component more reminiscent of stripped-envelope explosions with little residual helium.

The inferred CSM density profile, characterized by a shallow power-law slope $\eta \simeq 0.05^{+0.06}_{-0.32}$, is the most distinctive feature of SN 2018erx within the broader Type Ibn/Icn population. This value is indicative of a shell-like, approximately constant-density CSM configuration, in stark contrast to the $\eta = 2$ profile expected for a steady stellar wind. While Farias et al. (2025) report that a subset of SNe Ibn exhibit shell-like CSM geometries, the majority of events in their sample are better described by wind-like density profiles with $\eta \sim 2$. Among SNe Icn, the modeled sample remains small, but the available results suggest similarly compact and dense CSM configurations, with some events also preferring shallower density slopes (Pellegrino et al. 2022b).

Taken together, the combination of small R_0, high CSM density, low ejecta mass, high ejecta velocity, and a nearly flat density profile disfavors a canonical steady-state WR wind as the dominant pre-explosion mass-loss mechanism. Instead, these properties are more naturally explained by a brief, intense episode of mass ejection in the years to decades prior to explosion, forming a confined, shell-like CSM. Such behavior is more consistent with binary-driven mass transfer or common-envelope interaction than with the continuous radiatively-driven outflows associated with isolated WR stars. We return to this point in Section 10.6, where we argue that the full set of observational and modeling constraints for SN 2018erx collectively favor a binary progenitor channel over a single massive-star scenario.

To relate the fitted parameters to an approximate CSM outer radius, we adopt a power-law density profile

$$\rho(r) = \rho_0 \left(\frac{r}{R_0}\right)^{-\eta}, \qquad R_0 \le r \le R_{\rm out}, \tag{10.17}$$

where ρ_0 is the density at the inner edge ($\rho_0 \simeq 9.56^{+2.50}_{-1.12} \times 10^{-13}\,\mathrm{g\,cm^{-3}}$). The total CSM mass then satisfies

$$M_{\rm CSM} = 4\pi \int_{R_0}^{R_{\rm out}} \rho(r)\, r^2\, dr = \frac{4\pi \rho_0 R_0^3}{3-\eta} \left[\left(\frac{R_{\rm out}}{R_0}\right)^{3-\eta} - 1 \right], \tag{10.18}$$

for $\eta \neq 3$. Inverting Eq. (10.18) gives

$$R_{\rm out} = R_0 \left[1 + \frac{(3-\eta)\, M_{\rm CSM}}{4\pi \rho_0 R_0^3} \right]^{1/(3-\eta)}. \tag{10.19}$$

Table A: Priors and constraints adopted for the `redback` CSM interaction fit.

Parameter	Prior type	Range / Value
z	fixed	0.0294
$M_{\rm ej}$ [$M_\odot$]	log-uniform	[0.1, 15]
$v_{\rm ej}$ [km s^{-1}]	log-uniform	[10^3, 5×10^4]
$M_{\rm CSM}$ [$M_\odot$]	log-uniform	[10^{-3}, 15]
η	uniform	[0, 2]
ρ [g cm^{-3}]	log-uniform	[10^{-15}, 10^{-9}]
r_0 [AU]	log-uniform	[10^{-1}, 10^2]
$T_{\rm floor}$ [K]	log-uniform	[10^2, 10^4]
t_0 [MJD]	uniform	[58321.18, 58331.18]
A_V [mag]	uniform	[0, 5]
κ [cm^2 g^{-1}]	Gaussian	0.07 ± 0.001
κ_γ [cm^2 g^{-1}]	Gaussian	0.03 ± 0.001
$t_{\rm diff}/t_{\rm shock}$	constraint	[0.1, 0.8]
$r_{\rm ph}/r_{\rm CSM}$	constraint	[0, 1]
$r_0/r_{\rm ph}$	constraint	[0, 1]

Table B: Posterior median values and 68% credible intervals (16th and 84th percentiles) for the CSM interaction model parameters.

Parameter	Value
$M_{\rm ej}$ [$M_\odot$]	$0.111^{+0.034}_{-0.009}$
$M_{\rm CSM}$ [$M_\odot$]	$0.299^{+0.006}_{-0.006}$
$v_{\rm ej}$ [km s^{-1}]	$(1.56^{+0.03}_{-0.03})\times10^4$
η	$0.045^{+0.064}_{-0.033}$
ρ [g cm^{-3}]	$(9.56^{+2.58}_{-1.12})\times10^{-13}$
r_0 [AU]	$0.66^{+1.60}_{-0.47}$
$T_{\rm floor}$ [K]	6242^{+290}_{-281}
t_0 [MJD]	$58328.19^{+0.01}_{-0.01}$
A_V [mag]	$3.15^{+0.05}_{-0.05}$

Using the posterior median values, we obtain

$$R_{\rm out} \simeq 5.6\times10^{14}\ {\rm cm} \simeq 37\ {\rm AU}. \tag{10.20}$$

The inferred CSM therefore extends from $R_0 \sim 0.6$ AU to ~ 40 AU.

CSM radial extent based on spectroscopy

The spectra of SN 2018erx show prominent intermediate-width C II emission and related interaction signatures (Figures 10.5 and 10.7), indicating that the line-forming region is associated with shocked circumstellar gas. These features can therefore be used to place order-of-magnitude constraints on the radial extent of the CSM.

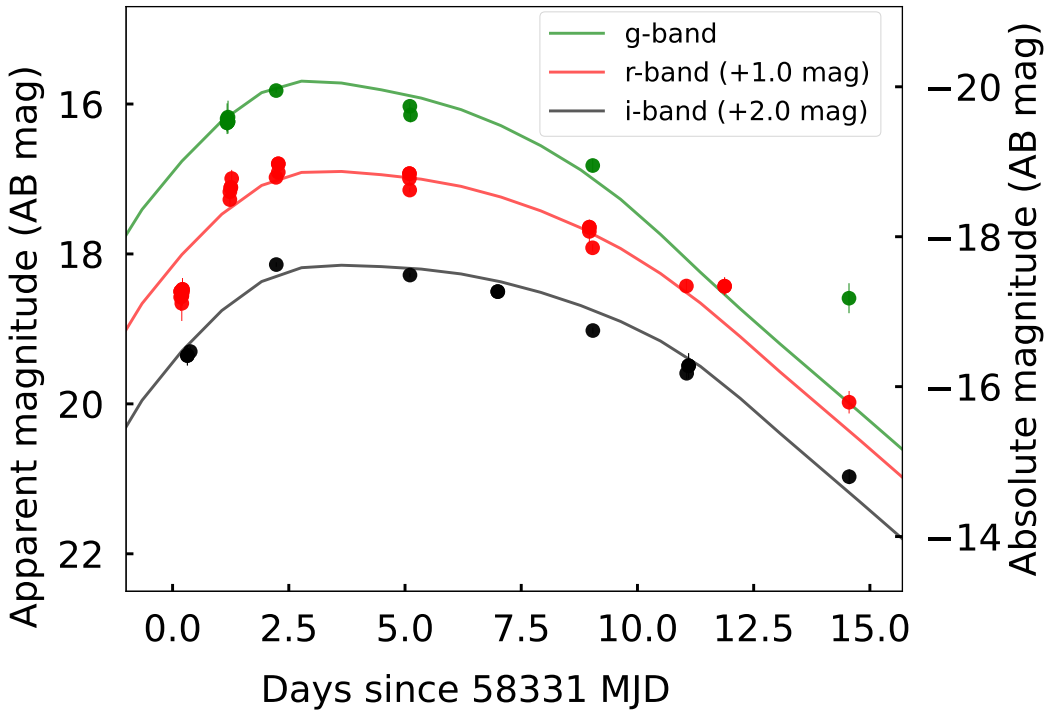

Figure 10.9: Multi-band light-curve fit of SN 2018erx using the CSM-interaction model implemented in `redback`. The observed photometry in the g, r, and i bands is shown as colored points, while the solid curves represent the best-fitting model.

We detect clear interaction signatures already in the first spectrum at MJD 58334, corresponding to roughly 6 d after the explosion epoch inferred in Section 10.4. This implies that the fastest interaction front, identified with the outer ejecta or the forward shock, must have reached the inner edge of the CSM by that time.

For this estimate, we adopt a characteristic ejecta velocity of $v_{\rm ej} \simeq 5200$ km s^{-1} from the P-Cygni absorption minima. This gives

$$R_{\rm CSM,\,inner} \lesssim v_{\rm ej}\,\Delta t \simeq 18\ {\rm AU}, \tag{10.21}$$

consistent with an extended circumstellar envelope at the time of interaction. Interaction-related C II absorption/emission remains visible as late as MJD 58351, about 23 d after explosion. This indicates that CSM-processed material continues to contribute to the line-forming region at least until that epoch. Using the same velocity then gives a conservative lower limit on the outer extent of the line-forming CSM,

$$R_{\rm CSM,\,outer} \gtrsim v_{\rm ej}\,\Delta t \simeq 70\ {\rm AU}. \tag{10.22}$$

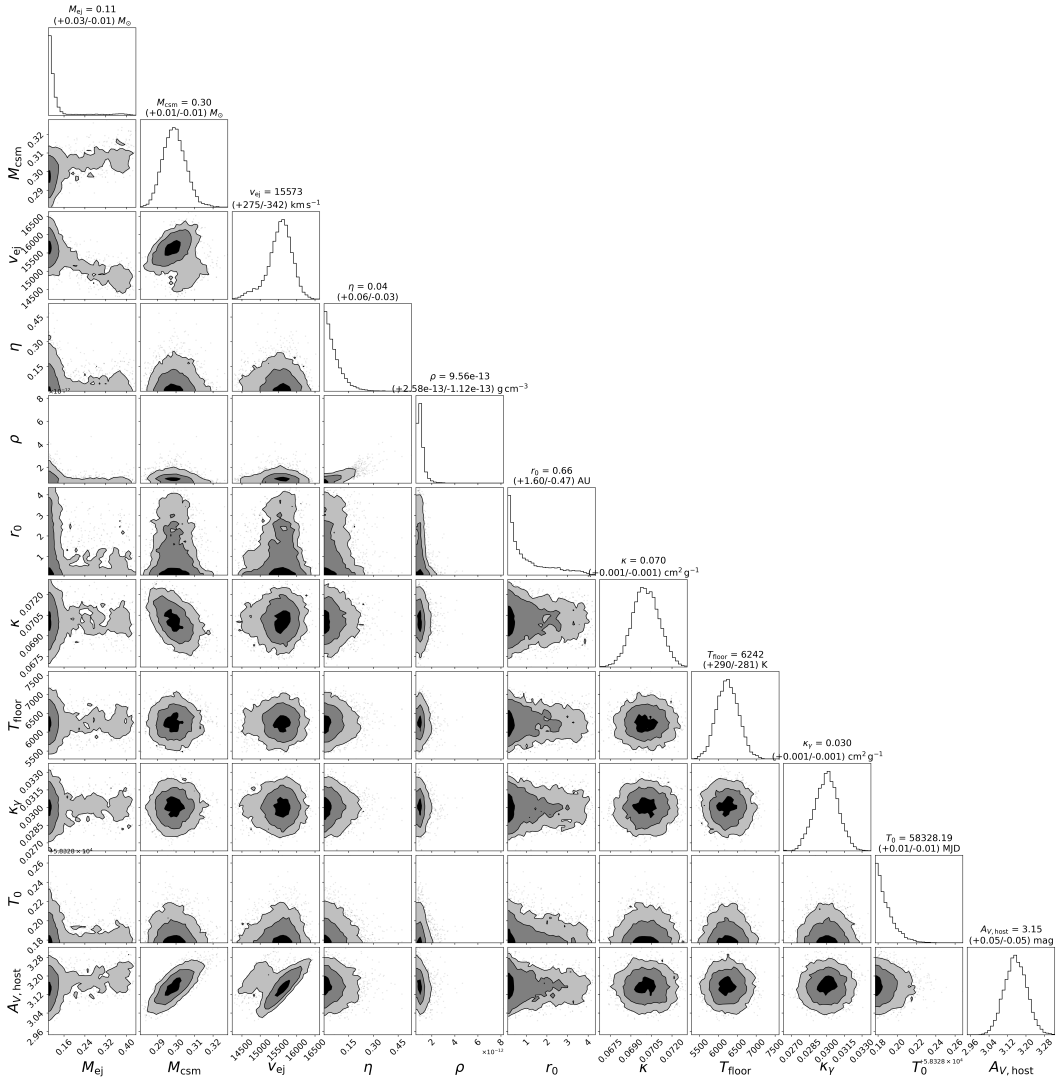

Figure 10.10: Corner plot showing the posterior distributions of the CSM-interaction model parameters obtained from the `redback` fit to the multi-band lightcurve of SN 2018erx. The diagonal panels show the marginalized posterior distributions, while the off-diagonal panels show the parameter covariances. The dashed lines indicate the median values and 1σ credible intervals.

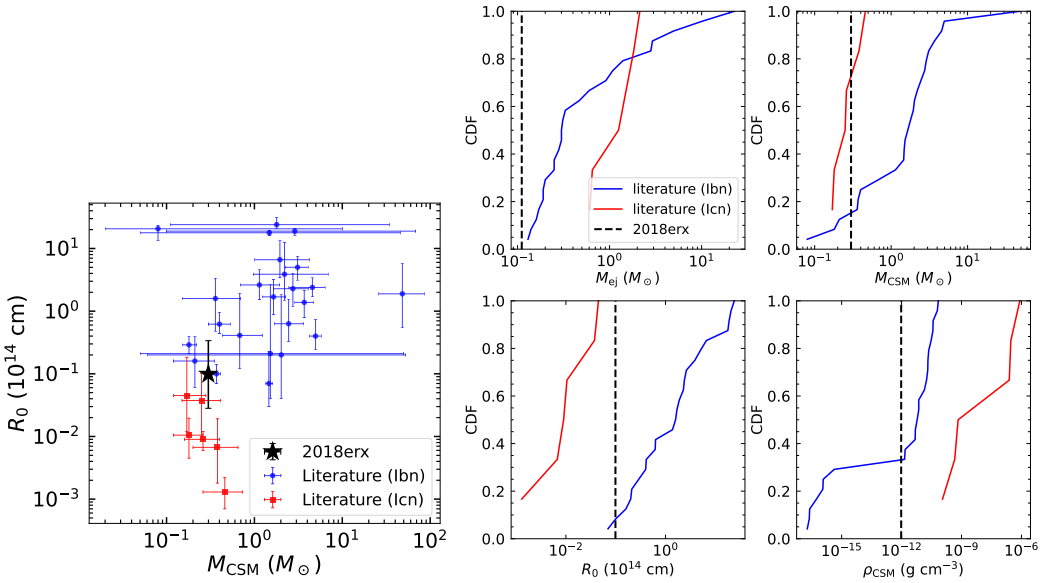

Figure 10.11: Comparison of the circumstellar interaction parameters inferred for SN 2018erx with literature samples of Type Ibn/Icn SNe. Left: Inner CSM radius R_0 versus CSM mass $M_{\rm CSM}$. The black star marks the values inferred for SN 2018erx from the `redback` interaction modeling, while blue and red symbols show literature estimates for SNe Ibn and SNe Icn, respectively. Right: Cumulative distribution functions (CDFs) of the inferred interaction parameters ($M_{\rm ej}$, $M_{\rm CSM}$, R_0, $v_{\rm ej}$, and $\rho_{\rm CSM}$) for literature samples of SNe Ibn (blue) and SNe Icn (green). The dashed vertical line indicates the corresponding value for SN 2018erx.

These spectroscopic constraints are broadly consistent with the lightcurve modeling. The interaction fit yields an inner CSM radius of $R_0 \simeq 0.56$ AU, comfortably below the spectroscopic upper limit on the inner edge, while the outer radius inferred from the best-fit CSM parameters is $R_{\rm out} \sim 40$ AU, comparable to the spectroscopic lower limit above.

Order-of-magnitude CSM mass estimate from ejecta–CSM interaction

We provide an independent, order-of-magnitude estimate of the CSM mass by treating the early emission as powered by kinetic energy dissipated in a strongly inelastic ejecta–CSM collision. Here we explicitly distinguish the *pre-shock* CSM speed ($v_{\rm w}$) from the *post-shock* bulk speed of the swept-up shell ($v_{\rm shell}$) inferred from the absorption.

Consider an outer ejecta layer of mass $M_{{\rm ej},i}$ moving at $v_{\rm ej}$ that impacts a CSM shell of mass $M_{\rm CSM}$ moving at a pre-shock speed $v_{\rm w}$. In the perfectly inelastic limit, the shocked ejecta and swept-up CSM merge into a single shell (e.g. a cooled dense

shell) moving at a common post-shock velocity $v_{\rm shell}$. Conservation of momentum gives

$$(M_{{\rm ej},i} + M_{\rm CSM})\, v_{\rm shell} = M_{{\rm ej},i}\, v_{\rm ej} + M_{\rm CSM}\, v_{\rm w}, \tag{10.23}$$

or equivalently

$$v_{\rm shell} - v_{\rm w} = \frac{M_{{\rm ej},i}}{M_{{\rm ej},i} + M_{\rm CSM}}\,(v_{\rm ej} - v_{\rm w}). \tag{10.24}$$

The kinetic energy dissipated in the collision is the difference between the initial and final kinetic energies,

$$\begin{aligned}\Delta E &= \frac{1}{2}\, M_{{\rm ej},i}\, v_{\rm ej}^2 + \frac{1}{2}\, M_{\rm CSM}\, v_{\rm w}^2 - \frac{1}{2}\,(M_{{\rm ej},i} + M_{\rm CSM})\, v_{\rm shell}^2 \\ &= \frac{1}{2}\,\frac{M_{{\rm ej},i}\, M_{\rm CSM}}{M_{{\rm ej},i} + M_{\rm CSM}}\,(v_{\rm ej} - v_{\rm w})^2.\end{aligned} \tag{10.25}$$

Using Eq. (10.24) to eliminate the mass ratio yields a convenient expression in terms of the observable post-shock velocity:

$$\Delta E = \frac{1}{2}\, M_{\rm CSM}\,(v_{\rm ej} - v_{\rm w})\,(v_{\rm shell} - v_{\rm w}). \tag{10.26}$$

For the order-of-magnitude estimate we adopt $v_{\rm w} \ll v_{\rm shell}$, so that

$$\Delta E \simeq \frac{1}{2}\, M_{\rm CSM}\, v_{\rm ej}\, v_{\rm shell}. \tag{10.27}$$

If the interaction region is radiative on the relevant timescale, a fraction $\epsilon \leq 1$ of the dissipated energy emerges as radiation, $E_{\rm rad} \simeq \epsilon\, \Delta E$. Solving Eq. (10.26) for the CSM mass gives

$$M_{\rm CSM} \simeq \frac{2\, E_{\rm rad}}{\epsilon\,(v_{\rm ej} - v_{\rm w})\,(v_{\rm shell} - v_{\rm w})} \;\approx\; \frac{2\, E_{\rm rad}}{\epsilon\, v_{\rm ej}\, v_{\rm shell}} \quad (v_{\rm w} \ll v_{\rm shell}). \tag{10.28}$$

Adopting $v_{\rm ej} \simeq 5200$ km s^{-1} from the P-Cygni absorption minima, we estimate the post-shock velocity from the C II λ7238 emission feature. After fitting a local continuum within ± 50 Å of line center and modeling the line profile with Gaussian and Lorentzian functions, we infer a characteristic velocity of $v_{\rm shell} = 3900 \pm 100$ km s^{-1}, which we interpret as the bulk speed of the post-shock swept-up shell. We thus obtain

$$\begin{aligned}M_{\rm CSM} \simeq 4.9 \times 10^{-1}\, \epsilon^{-1} &\left(\frac{E_{\rm rad}}{10^{50}\ {\rm erg}}\right)\left(\frac{v_{\rm ej}}{5200\ {\rm km\ s^{-1}}}\right)^{-1} \\ &\times \left(\frac{v_{\rm shell}}{3900\ {\rm km\ s^{-1}}}\right)^{-1}\ {\rm M_\odot}.\end{aligned} \tag{10.29}$$

The inferred deceleration also fixes the interacting mass ratio. From Eq. (10.23), for $v_{\rm w} \ll v_{\rm shell}$ one finds

$$\frac{M_{\rm CSM}}{M_{{\rm ej},i}} \simeq \left(\frac{v_{\rm ej}}{v_{\rm shell}}\right) - 1 \approx 0.33, \tag{10.30}$$

so the swept-up CSM mass is comparable to the interacting ejecta-layer mass for the adopted velocities, consistent with the regime of efficient dissipation. This estimate should be interpreted as an order-of-magnitude scale. If the interaction is not fully radiative on the observed timescale, $\epsilon < 1$ increases the inferred $M_{\rm CSM}$. Thus, for reasonable choices of ϵ and $E_{\rm rad}$, this order-of-magnitude estimate is broadly consistent with the CSM mass inferred from the `redback` interaction fit ($M_{\rm CSM} \simeq 0.31\ M_\odot$), given the large systematic uncertainties inherent in the simplified inelastic-collision picture.

Mass-loss-rate estimates for the inner CSM

Below we estimate the characteristic mass-loss scale associated with the inner CSM: one based on the observed luminosity and spectroscopic line width, and a second based on the the best-fit CSM model.

Based on spectroscopy

If the observed luminosity is powered primarily by kinetic-energy dissipation at the ejecta–CSM interaction shock, the corresponding mass-loss rate can be estimated as

$$\dot{M} = \frac{2 L v_w}{\epsilon\, v_{\rm shell}^3}, \tag{10.31}$$

where $\epsilon \leq 1$ is the efficiency with which shock kinetic energy is converted into radiation, v_w is the pre-SN outflow velocity, $v_{\rm shell}$ is the velocity of the post-shock shell, and L is the bolometric luminosity.

The outflow velocity is not directly measured in SN 2018erx, so we consider two representative values: $v_w = 100\,{\rm km\ s^{-1}}$, appropriate for a slower eruptive or binary-driven outflow, and $v_w = 1000\,{\rm km\ s^{-1}}$, characteristic of a WR-like wind. To estimate the post-shock velocity, we analyze the C II λ7238 emission feature. After fitting a local continuum within ±50 Å of line center, we model the profile with Gaussian and Lorentzian functions and infer a characteristic velocity of $v_{\rm shell} = 3900 \pm 100\,{\rm km\ s^{-1}}$.

Adopting $\epsilon = 0.5$, we obtain characteristic mass-loss rates of

$$\dot{M} \approx 4.7 \times 10^{-4}\ M_\odot\ {\rm yr}^{-1}$$

for $v_w = 100$ km s^{-1}, and

$$\dot{M} \approx 4.7 \times 10^{-3}\, M_\odot\, \mathrm{yr}^{-1}$$

for $v_w = 1000$ km s^{-1}.

Effective mass-loss rate from the CSM model fitting

Although the best-fit density profile is shell-like rather than a steady wind, it is still useful to quote an "effective" mass-loss rate by identifying the fitted density normalization ρ_0 at R_0 with that of a stationary wind:

$$\dot{M}_{\mathrm{eff}} = 4\pi R_0^2 \rho_0 v_w. \tag{10.32}$$

Using the posterior median values of R_0 and ρ_0, and adopting a fiducial WR-like velocity of $v_w = 1000$ km s^{-1}, we find

$$\dot{M}_{\mathrm{eff}} \sim 1.9 \times 10^{-3}\, M_\odot\, \mathrm{yr}^{-1}.$$

This should be interpreted only as a characteristic rate at the inner CSM radius, not as evidence for a long-lived steady wind.

The spectroscopic and model-based estimates are broadly consistent at the order-of-magnitude level. For $v_w = 1000$ km s^{-1}, the luminosity-based estimate exceeds the effective rate inferred from the CSM fit by a factor of a few; given the different assumptions involved, this level of agreement is reasonable. Both approaches therefore indicate a dense and enhanced pre-SN mass-loss episode.

Upper limits on the ^{56}Ni mass in SN 2018erx from the rapidly fading lightcurve

At late phases, the luminosity of core-collapse SNe is often powered by radioactive decay. In events with a well-detected nebular tail, the ^{56}Ni mass can be inferred by comparing the late-time bolometric luminosity to the expected ^{56}Co decay power. For SN 2018erx, however, the available photometry does not reveal a clear ^{56}Co-powered tail. We therefore treat the luminosity measured at the last blackbody epoch as an upper limit on the contribution from radioactive decay and derive corresponding upper limits on M_{Ni}.

For an initial ^{56}Ni mass M_{Ni}, the instantaneous radioactive power from the full ^{56}Ni $\rightarrow$ ^{56}Co $\rightarrow$ ^{56}Fe decay chain is

$$L_{\mathrm{rad}}(t) = f_{\mathrm{dep}}(t) \left(\frac{M_{\mathrm{Ni}}}{M_\odot} \right) \epsilon_{\mathrm{rad}}(t), \tag{10.33}$$

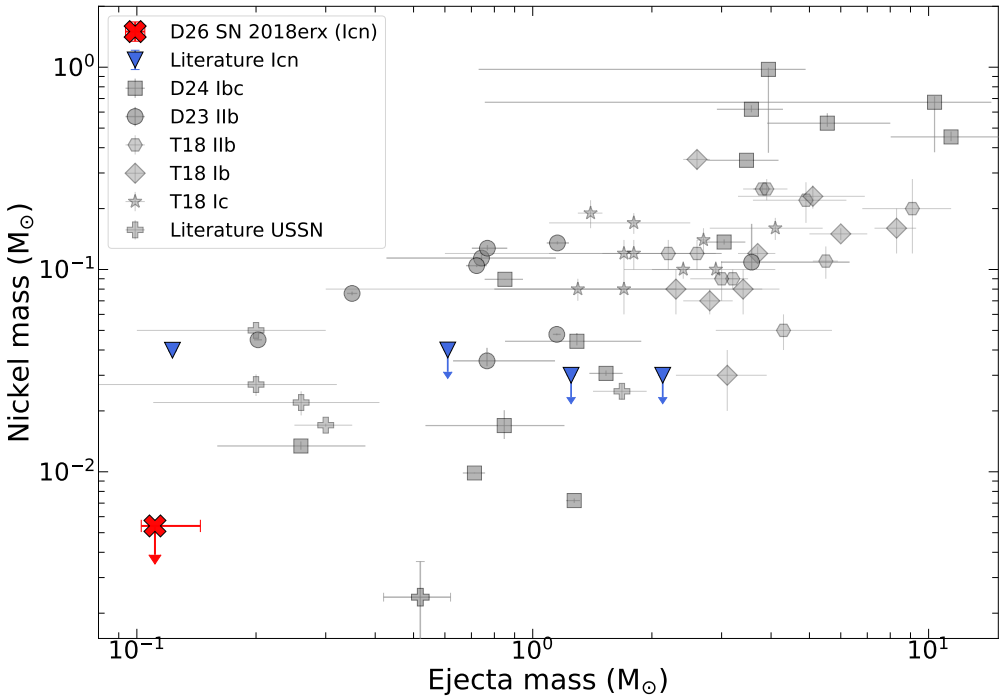

Figure 10.12: Comparison of the ^{56}Ni mass ($M_{\rm Ni}$) and ejecta mass ($M_{\rm ej}$) of SN 2018erx with SESNe from the literature. The red symbol marks SN 2018erx, while blue triangles denote Type Icn events (Pellegrino et al. 2022b). The arrow indicates that the inferred ^{56}Ni mass is an upper limit. Gray symbols show literature measurements for other SESN subclasses from D24 (Das et al. 2023b), D23 (Das et al. 2023a), and T18 (Taddia et al. 2018), as well as ultra-stripped SN candidates (USSN) from Das et al. (2024a). SN 2018erx occupies the regime of both low ejecta mass and low ^{56}Ni mass.

where

$$\epsilon_{\rm rad}(t) = 6.45 \times 10^{43} e^{-t/8.8\,\rm d} + 1.45 \times 10^{43} e^{-t/111.3\,\rm d} \quad \rm erg\ s^{-1}. \tag{10.34}$$

Here t is the rest-frame time since explosion, the first term represents heating from ^{56}Ni decay, and the second term represents heating from ^{56}Co decay. The factor $f_{\rm dep}(t)$ accounts for incomplete deposition of the radioactive energy; for complete trapping, $f_{\rm dep} = 1$.

Requiring $L_{\rm rad}(t_{\rm last}) \leq L_{\rm bb}(t_{\rm last})$ gives

$$M_{\rm Ni} \leq \frac{L_{\rm bb}(t_{\rm last})}{f_{\rm dep}(t_{\rm last})\,\epsilon_{\rm rad}(t_{\rm last})} M_\odot. \tag{10.35}$$

The last blackbody epoch that passes our quality cut occurs at phase +27.7 d relative to r-band maximum, corresponding to $t_{\rm last} \simeq 34$ d after explosion. Assuming com-

plete trapping, the no-host-extinction luminosity at this epoch, $\log L_{\rm bb}(\mathrm{erg\ s^{-1}}) = 40.63$, gives

$$M_{\rm Ni} \lesssim 3.5 \times 10^{-3}\ M_{\odot}. \tag{10.36}$$

For the high-extinction case, the corresponding limit is

$$M_{\rm Ni} \lesssim 5.4 \times 10^{-3}\ M_{\odot}. \tag{10.37}$$

These limits should be interpreted cautiously, since the last blackbody epoch is likely dominated at by hot dust or reprocessed emission rather than a clean nebular radioactive tail as discussed in Section 10.5. We therefore write the more general limit as

$$M_{\rm Ni} \lesssim \left(\frac{f_{\rm rad}}{f_{\rm dep}}\right) M_{\rm Ni,trap}, \tag{10.38}$$

where $M_{\rm Ni,trap}$ is the complete-trapping value above, $f_{\rm rad} \leq 1$ is the fraction of the observed late-time luminosity actually powered by radioactive decay, and $f_{\rm dep} \leq 1$ is the radioactive-energy deposition fraction. Incomplete γ-ray trapping increases the inferred upper limit by a factor $f_{\rm dep}^{-1}$, whereas any contribution from circumstellar interaction, an infrared echo, or hot dust reprocessing reduces the radioactive fraction of the luminosity and therefore lowers the allowed ^{56}Ni mass. For ordinary SESN-like values $T_0 \sim 50$–150 d, $f_{\rm dep}(34\ \mathrm{d}) \simeq 0.89$–$1.00$, so the complete-trapping limits remain nearly unchanged if $f_{\rm rad} = 1$. Even in a more weakly trapped, low-ejecta-mass configuration with $f_{\rm dep} \sim 0.5$, the inferred limit would increase only by a factor of ~ 2. Thus, the two correction factors may partially compensate each other, and the inferred ^{56}Ni limits are likely to remain close to the complete-trapping estimates above, i.e. $M_{\rm Ni} \sim$ few $\times\ 10^{-3}\ M_{\odot}$.

Dust

Dust Properties from the Near-Infrared Excess

SN 2018erx exhibits a clear NIR excess at +27 d in addition to its unusually red optical continuum. Because the early-time spectra simultaneously show high-ionization carbon features (requiring a hot radiation field), the red continuum is difficult to reconcile with a genuinely cool photosphere alone, and instead naturally points to dust absorption and re-emission. In interacting SESNe, dust signatures can originate from (i) pre-existing circumstellar dust that survives the SN flash and produces an infrared echo, and/or (ii) newly formed dust condensing rapidly in the dense, cooling post-shock region (the cool dense shell; CDS). Both pathways have been invoked for interacting SESNe, most famously in the Type Ibn SN 2006jc (Foley

et al. 2007, Anupama et al. 2009), and more recently in SN 2023xgo (Gangopadhyay et al. 2025, Yamanaka and Nagayama 2025). Below we use the NIR excess to obtain order-of-magnitude constraints on the characteristic dust temperature, an effective emitting size, and the dust mass.

At the epoch of our NIR detection, the measured absolute magnitudes are $M_K = -14.25$ and $M_J = -12.83$, giving $(J-K)_{\rm AB} = 1.42$ mag and therefore

$$\frac{F_{\nu,J}}{F_{\nu,K}} = 10^{-0.4(J-K)_{\rm AB}} \simeq 0.270. \tag{10.39}$$

If the emission is dominated by optically thin thermal dust emission, then

$$F_\nu \propto \kappa_\nu \, B_\nu(T_{\rm d}), \tag{10.40}$$

where κ_ν is the dust mass absorption coefficient at frequency ν. The observed color then constrains the dust temperature through

$$\frac{F_{\nu,J}}{F_{\nu,K}} = \frac{\kappa_J}{\kappa_K} \, \frac{B_\nu(\nu_J, T_{\rm d})}{B_\nu(\nu_K, T_{\rm d})}. \tag{10.41}$$

For an order-of-magnitude estimate we take $\kappa_J/\kappa_K \simeq 1$ (a weak dependence in the near-IR for typical grain models), which yields a color temperature

$$T_{\rm d} \simeq 1.66 \times 10^3 \ {\rm K}. \tag{10.42}$$

We adopt a conservative range $T_{\rm d} \sim (1.5\text{–}2.0) \times 10^3$ K for the hot component traced by J and K. This temperature is close to the condensation/sublimation temperature of carbonaceous grains, consistent with a carbon-rich circumstellar environment as implied by the Type Icn-like spectral signatures.

If the NIR excess arises from an IR echo (i.e., dust at radii comparable to or larger than the sublimation scale; see below), the emitting dust is expected to be optically thin in the near-IR for the small dust masses implied by the data. For a dust mass $M_{\rm d}$ distributed over a shell of radius $R_{\rm d}$ and covering fraction f_Ω, the characteristic K-band optical depth is $\tau_K \sim \kappa_K M_{\rm d}/(4\pi f_\Omega R_{\rm d}^2)$, which is $\ll 1$ for $R_{\rm d} \gtrsim$ few$\times 10^{16}$ cm unless the dust is extremely clumped or confined to a very small solid angle.

In the optically thin limit, the monochromatic luminosity is

$$L_{\nu,K} \simeq 4\pi \, \kappa_K \, M_{\rm d} \, B_\nu(\nu_K, T_{\rm d}), \tag{10.43}$$

where κ_K is the dust mass absorption coefficient at 2.2 μm. For spherical grains of radius a and bulk density $\rho_{\rm b}$,

$$\kappa_\nu(a) = \frac{3\, Q_{\rm abs}(\nu, a)}{4 a \rho_{\rm b}}, \tag{10.44}$$

where $Q_{\rm abs}(\nu, a)$ is the dimensionless absorption efficiency, i.e., the ratio of the absorption cross section to the geometric cross section of a grain. The above expression is equivalent to the commonly used grain-based form

$$M_{\rm d} = \frac{4}{3}\,\frac{a\rho_{\rm b}}{Q_{\rm abs}(\nu, a)}\,\frac{F_\nu d^2}{B_\nu(\nu, T_{\rm d})}, \tag{10.45}$$

where F_ν is the observed flux density at distance d. For representative carbonaceous grains ($a \sim 0.1$ μm, $\rho_{\rm b} \sim 2.2$ g cm^{-3}), $Q_{\rm abs}$ of order a few $\times 0.1$ at ~ 2 μm corresponds to $\kappa_K \sim 10^4$ cm^2 g^{-1}, which we adopt as a fiducial value.

Solving for the dust mass gives

$$M_{\rm d} \simeq \frac{L_{\nu,K}}{4\pi\,\kappa_K\,B_\nu(\nu_K, T_{\rm d})}. \tag{10.46}$$

Adopting $\kappa_K = 10^4$ cm^2 g^{-1} yields

$$M_{\rm d} \simeq 1.2 \times 10^{-6}\,M_\odot \left(\frac{\kappa_K}{10^4\ {\rm cm^2\ g^{-1}}}\right)^{-1}, \tag{10.47}$$

for $T_{\rm d} = 1.66{\times}10^3$ K. The dominant systematic uncertainty is the poorly known near-IR opacity, together with the uncertainty in $T_{\rm d}$ from the two-band color. Allowing $T_{\rm d} = 1500$–2000 K and $\kappa_K = 10^3$–10^4 cm^2 g^{-1}, we obtain

$$M_{\rm d} \sim 6 \times 10^{-7}\text{–}2 \times 10^{-5}\,M_\odot \tag{10.48}$$

for the hot dust component traced by the J- and K-band photometry.

For grains in radiative equilibrium with a central source of luminosity L, the distance at which dust reaches temperature $T_{\rm d}$ is approximately

$$R(T_{\rm d}) \simeq \left[\frac{L}{16\pi\sigma T_{\rm d}^4}\,\frac{\langle Q_{\rm abs}\rangle_{\rm in}}{\langle Q_{\rm abs}\rangle_{\rm out}}\right]^{1/2}, \tag{10.49}$$

where $\langle Q_{\rm abs}\rangle_{\rm in}$ and $\langle Q_{\rm abs}\rangle_{\rm out}$ are absorption efficiencies averaged over the incident (UV/optical) and emitted (IR) spectra. Using this radiative-equilibrium relation, the dust survival radius is

$$R_{\rm sub} \approx 4.6 \times 10^{16} \left(\frac{L_{\rm pk}}{10^{43.8}\ {\rm erg\ s^{-1}}}\right)^{1/2} \left(\frac{T_{\rm sub}}{1800\ {\rm K}}\right)^{-2}\ {\rm cm}.$$

For the extinction-corrected peak luminosity, $\log(L_{\rm pk}/{\rm erg\,s^{-1}}) \simeq 43.8$, this gives $R_{\rm sub} \approx 4.6 \times 10^{16}$ cm ≈ 3100 AU, implying a distinct outer dusty component in addition to the compact inner CSM responsible for the rapid interaction.

10.6 Discussion

Dust origin scenario

Here we explore the possible origin of the hot dust responsible for the near-infrared emission in SN 2018erx. Our inferred $T_{\rm d} \sim$ 1500–2000 K is comparable to temperatures reported for hot dust components in other interacting SESNe (Gan et al. 2021, Yamanaka and Nagayama 2025). In SN 2006jc, the emergence of a red/NIR excess and contemporaneous spectroscopic changes were interpreted as rapid dust formation in the post-shock region, establishing that dust can condense on timescales of only weeks in a dense He-rich CSM interaction environment (Smith et al. 2008). More recently, NIR and optical monitoring of the transitional Type Ibn/Icn SN 2023xgo revealed a prominent NIR excess persisting from ∼15–100 d (Yamanaka and Nagayama 2025), with SED modelling favouring carbon dust at $T_{\rm d} \approx 1600 \pm 100$ K and an inferred dust mass of $\sim 10^{-4}\,M_{\odot}$. That work argues that the NIR excess is best explained as an IR echo from pre-existing circumstellar carbon dust located outside the shocked CDS. In the Type Ibn SN OGLE-2012-SN-006, early optical–NIR SED modelling similarly favours a pre-existing dust shell, with dust temperatures of ∼1200–1300 K and substantially larger inferred dust masses ($\sim 5 \times 10^{-4}$–$2 \times 10^{-3}\,M_{\odot}$) (Gan et al. 2021).

Thus, the hot dust mass we infer for SN 2018erx, $M_{\rm d} \sim 10^{-6}$–$10^{-5}\,M_{\odot}$, lies toward the low end of the distribution, broadly comparable to the small dust masses or upper limits reported for several SNe Ibn, and well below the $\sim 10^{-4}$–$10^{-3}\,M_{\odot}$ values inferred for SN 2023xgo and OGLE-2012-SN-006. We caution that our two-band estimate constrains only the hot dust component emitting in J and K; any cooler dust peaking at longer wavelengths would increase the total dust mass. Mid-IR photometry is therefore required to robustly constrain the full dust mass budget. If a fraction $f_{\rm d} \sim 1\%$ of the expelled material condensed into dust, the inferred $M_{\rm d} \sim 6 \times 10^{-7}$–$2 \times 10^{-5}\,M_{\odot}$ implies that the total mass expelled in the dusty circumstellar layer was of order 6×10^{-5}–$2 \times 10^{-3}\,M_{\odot}$.

If the NIR excess is powered by a pre-existing IR echo, we estimated earlier that the dust responsible for the observed hot component must lie at radii of at least a few $\times 10^{16}$ cm unless it is substantially shielded by optically thick gas or confined to dense clumps. This radius corresponds to a light-travel time of $R_{\rm sub}/c \sim$ 10–20 d and an echo duration of order $2R_{\rm sub}/c \sim$ 20–40 d for a thin shell, naturally consistent with the observations for SN 2018erx.

This in turn places a lower limit on when the dusty circumstellar layer was expelled

prior to explosion. For a characteristic outflow velocity $v_{\rm w}$,

$$t_{\rm ej} \gtrsim \frac{R_{\rm sub}}{v_{\rm w}} \approx 15 \left(\frac{R_{\rm sub}}{4.6 \times 10^{16}\ {\rm cm}}\right) \left(\frac{v_{\rm w}}{10^3\ {\rm km\,s^{-1}}}\right)^{-1}\ {\rm yr}. \tag{10.50}$$

Thus, for WR-like outflow speeds ($v_{\rm w} \sim 1000\ {\rm km\,s^{-1}}$), the dusty layer must have been launched at least ∼10–20 yr before core collapse, while for slower outflows ($v_{\rm w} \sim 100\ {\rm km\,s^{-1}}$) the corresponding timescale becomes ∼100–200 yr. These estimates support a picture in which SN 2018erx is embedded in a structured, multi-epoch CSM: a compact inner C-rich component on $\lesssim$ tens-of-AU scales powers the rapid interaction, while an additional dusty component at much larger radii produces the large effective attenuation and the NIR excess. The fact that the optical lightcurve and spectra are already strongly reddened at the earliest observed epochs, together with line-profile asymmetries consistent with preferential attenuation of the receding side, strongly favors pre-existing circumstellar dust over dust formed only after explosion.

Progenitor and evolutionary pathway

SN 2018erx is one of the faintest members of the SN Ibn/Icn sub-class. It rises and declines quickly with rise time and decline time of 2.1 d and 3.1 d respectively. Any viable progenitor scenario must account simultaneously for (i) the signatures of interaction with H/He-poor and likely C-rich material, and (ii) the small characteristic mass and compact spatial scale implied by our interaction fit. In particular, the `redback` CSM-interaction posteriors for SN 2018erx favor $M_{\rm ej} = 0.11^{+0.03}_{-0.01}\ M_\odot$ and $M_{\rm CSM} = 0.30^{+0.01}_{-0.01}\ M_\odot$. These values place SN 2018erx in a regime where the CSM mass is comparable to the ejecta mass, such that strong deceleration and efficient conversion of kinetic energy into radiation are expected. In addition, the rapidly fading light curve constrains the radioactive yield to be very small, with an upper limit of $M_{\rm Ni} \lesssim 5.4 \times 10^{-3}\ M_\odot$ placing SN 2018erx at the low end of both the ejecta-mass and ^{56}Ni-mass distributions among other SESNe (Taddia et al. 2018, Das et al. 2023a,b, 2024a, Pellegrino et al. 2022b) (Figure 10.12).

Below, we consider three broad progenitor and explosion pathways that could plausibly reproduce the observed and inferred properties of SN 2018erx: (1) an interaction-boosted ultra-stripped core-collapse supernova, (2) the core collapse of a more massive WC/WO Wolf–Rayet star, potentially involving fallback, and (3) a merger-powered transient involving a compact object and a stripped massive star.

Ultra-stripped SN of a low-mass He-star

SN 2018erx is consistent with a rapidly evolving, H-poor SN powered by the core-collapse of an ultra-stripped progenitor embedded in dense, nearby C-rich CSM. In the standard ultra-stripped channel, binary interaction removes almost the entire H-rich envelope and subsequently erodes much of the remaining He-rich layers during late Roche-lobe overflow (Case BB/BC mass transfer) onto a compact companion, leaving behind a low-mass pre-SN core and therefore a very small ejecta mass at explosion (e.g., Tauris et al. 2013, 2015).

Despite allowing a very broad prior range (0.1–15 $M_\odot$), the fit for SN 2018erx favors a low ejecta mass, $M_{\rm ej} = 0.11^{+0.03}_{-0.01}\ M_\odot$ (Table B). This places SN 2018erx firmly in the same ejecta-mass regime as well-studied ultra-stripped candidates such as iPTF 14gqr ($M_{\rm ej} \sim 0.2\ M_\odot$; De et al. 2018c), SN 2019dge ($M_{\rm ej} \sim 0.4\ M_\odot$; Yao et al. 2020), and SN 2023zaw ($M_{\rm ej} \sim 0.5\ M_\odot$; Das et al. 2024a), and far below the typical $M_{\rm ej} \sim 1$–$5\ M_\odot$ inferred for most SNe Ib/c (e.g., Taddia et al. 2018). Such a small ejecta mass strongly suggests a progenitor that was stripped efficiently by a close companion rather than a single massive WR star retaining a more substantial CO core at collapse. Such a low value of ejecta mass has been seen previously for SN 2023xgo (SN Ibn/Icn; $M_{\rm ej} \sim 0.12\ M_\odot$). While interaction complicates a purely radioactive interpretation, the low inferred $M_{\rm ej}$ itself is difficult to reconcile with a standard high-mass single-star channel.

At the same time, the fit favors a substantial circumstellar mass, $M_{\rm CSM} = 0.30^{+0.01}_{-0.01}\ M_\odot$ (Table B). This is few times the ejecta mass, with $M_{\rm CSM}/M_{\rm ej} \sim 2.7$. Such a mass ratio is a qualitatively important regime for interaction: once the swept-up CSM mass approaches the ejecta mass, strong deceleration is expected and a significant fraction of the kinetic energy can be converted into radiation. In that limit, the emergent luminosity is governed primarily by shock interaction rather than radioactive heating, even if the underlying explosion is intrinsically faint. The parameter combination inferred for SN 2018erx therefore naturally places it in an interaction-dominated regime.

This configuration closely resembles the scenario explored by Moriya et al. (2025), who demonstrate that an ultra-stripped explosion embedded in sufficiently massive nearby CSM can appear observationally as a luminous, H-poor interaction-powered transient. In their models, a pre-SN mass-ejection episode triggered by violent late burning produces CSM whose mass can rival or exceed that of the ejecta. The underlying mechanism is related to degenerate silicon flashes expected near

the low-mass boundary for iron-core collapse. In mass-losing helium-star models, Woosley (2019) show that helium cores of $M_{\rm He} \simeq 2.5$–$3.2\ M_\odot$ can undergo off-center silicon ignition under partially degenerate conditions, launching shocks that eject a substantial fraction of the remaining envelope. The resulting shell masses span ~ 0.02–$0.7\ M_\odot$, with characteristic ejection speeds of order 10^2–10^3 km s^{-1} and delays of tens of days between the flash and final collapse. These parameters naturally place dense material at radii $R \sim 10^{14}$–10^{15} cm by the time of explosion. The best-fit $M_{\rm CSM} \approx 0.3\ M_\odot$ for SN 2018erx lies comfortably within this predicted shell-mass range, and the inferred compact CSM configuration is consistent with a mass-ejection episode occurring only months to years before core collapse. While the data do not uniquely require a silicon-flash origin, the overall scale of the inferred CSM mass and radius is at least compatible with this picture.

The fitted CSM density scale and inner radius further support a compact, recently ejected structure. The posterior medians, $\rho_0 = (9.56^{+2.58}_{-1.12}) \times 10^{-13}$ g cm^{-3} and $r_0 = 0.66^{+1.60}_{-0.47}$ AU, set the scale for an optically thick, relatively compact CSM beginning just outside the progenitor. Approximating the CSM as a dense shell with mass $M_{\rm CSM} \sim 0.3\ M_\odot$ and characteristic density ρ_0 implies an outer radius of order a few $\times 10^{14}$ cm (tens of AU). This is far smaller than the 10^{16}–10^{17} cm scales typical of long-lived interaction in SNe IIn, yet entirely consistent with the confined, nearby CSM inferred for fast H-poor interaction events. For outflow speeds of $\sim$ 100–1000 km s^{-1}, such radii correspond to ejection occurring months to a few years before collapse, naturally pointing to very late-stage binary evolution. This aligns well with the calculations of Wu and Fuller (2022b), who model stripped helium stars through advanced burning and find that helium cores of $\simeq 2.5$–$3\ M_\odot$ can re-expand during O/Ne burning, triggering extreme late-stage mass transfer in close binaries. They obtain mass-transfer rates $\dot{M} \gtrsim 10^{-2}\ M_\odot\ {\rm yr}^{-1}$ beginning weeks to decades before collapse, and show that either stable mass loss from the system or unstable transfer leading to a common-envelope ejection can produce CSM masses $\sim 10^{-2}$–$1\ M_\odot$ at radii $\sim 10^{13}$–10^{16} cm. The posterior medians for SN 2018erx ($M_{\rm CSM} \simeq 0.3\ M_\odot$ and characteristic radii $\sim 10^{14}$–10^{15} cm) fall well within these predicted ranges (Figure A3). The mass-loss rates obtained from spectroscopy are also well within this range (Section 10.5). The spectroscopically derived $\dot{M}$ (Section 10.5) is consistent with ejection occurring months to a few years before collapse. The dust shell, sitting at larger radii, likely traces an earlier, distinct mass-loss episode – possibly a prior phase of stable Roche-lobe overflow or a partial common-envelope interaction – predating the terminal stripping event by decades to

centuries. The consistency in mass scale and spatial extent suggests that the dense CSM around SN 2018erx could plausibly arise from the same late-stage binary processes that produce ultra-stripped explosions.

Core collapse of a massive WC/WO Wolf–Rayet star

A WC/WO progenitor remains attractive for SN 2018erx because it naturally explains the carbon-rich circumstellar environment implied by the strong intermediate-width C II emission and, plausibly, the carbonaceous dust indicated by the NIR excess. In particular, a WC/WO-like surface composition provides a straightforward route to H/He-poor, C/O-rich CSM, unlike lower-mass stripped progenitors for which the origin of carbon-rich outflows is less direct (e.g., Gal-Yam et al. 2022a, Perley et al. 2022a, Pellegrino et al. 2022b). The outer dusty layer inferred from the NIR echo in SN 2018erx is also not, by itself, problematic for such a progenitor: for WR-like outflow speeds, the dust-survival radius implies ejection on a timescale of order ∼10–20 yr before core collapse, while the hot dust mass implies only a modest total dusty outflow mass.

The difficulty lies instead in the inner interaction region. Our modeling requires $M_{\rm CSM} \approx 0.3\,M_\odot$, $R_0 \approx 0.7$ AU, $R_{\rm out} \sim 40$ AU, and a nearly constant-density profile ($\eta \approx 0$), i.e. a compact shell rather than a steady r^{-2} wind. Placing $\sim 0.3\,M_\odot$ within $\sim 6\times10^{14}$ cm implies characteristic mass-loss rates of order $\dot{M} \sim 0.1$–$1\,M_\odot\,{\rm yr}^{-1}$ for $v_w \sim 10^2$–10^3 km s^{-1}, far above canonical steady WR wind values (e.g., Crowther 2007). Likewise, the shell-like density structure inferred here is unlike the wind-like CSM expected from a long-lived WR outflow. In this sense, a standard single-star WC/WO wind is difficult to reconcile with SN 2018erx; if the progenitor was WR-like at collapse, the data require an unusually violent pre-SN ejection episode, strong binary mediation, or both.

A second tension is the explosion scale itself. The inferred ejecta mass, $M_{\rm ej} \approx 0.11\,M_\odot$, is far below that expected from a normal successful explosion of a massive WC/WO star, which would typically retain a substantially larger CO core at collapse. Thus, while a WC/WO-like surface composition remains an appealing explanation for the carbon-rich CSM, the combined requirements of a compact shell-like CSM and a very low ejecta mass argue against a simple steady-wind WR channel. If SN 2018erx did originate from a massive WR progenitor, then fallback or some other mechanism for suppressing the effective ejecta mass is likely required (see next subsection).

A partially successful (fallback) explosion and jet-driven outflow

In fallback SN scenarios, the explosion energy is insufficient to unbind the entire star; the inner layers fall back onto the compact remnant, reducing both the effective ejecta mass and the ^{56}Ni yield (e.g., Woosley et al. 1993, Moriya et al. 2010). A jet launched during or after collapse (Khokhlov et al. 1999, MacFadyen and Woosley 1999, MacFadyen et al. 2001) can still imprint broad features even if the bulk explosion is weak, linking some SNe Icn/Ibn to peculiar Ic-BL-like events with low ^{56}Ni yields (e.g., Fraser et al. 2021, Perley et al. 2022b, Pellegrino et al. 2022b). In the context of SN 2018erx, fallback offers a coherent explanation for the combination of low ejecta mass, weak radioactive output, and low expansion velocities, while remaining compatible with a WC/WO progenitor and hence a carbon-rich circumstellar environment.

For SN 2018erx, the inferred $M_{\rm ej} \approx 0.11\ M_\odot$ and $M_{\rm Ni} \lesssim 5.4 \times 10^{-3}\ M_\odot$ lie firmly in the regime expected for strong fallback, where a significant fraction of the initially ejected material fails to escape. The observed photospheric velocity of $\sim 5200\ {\rm km\ s^{-1}}$ is also consistent with a low-energy explosion in which the surviving ejecta expand more slowly than in typical stripped-envelope SNe.

However, the compact, shell-like CSM ($M_{\rm CSM} \approx 0.3\ M_\odot$, $R_{\rm out} \sim 40$ AU, $\eta \approx 0$) still requires a brief and intense pre-SN mass ejection episode, as steady WR winds cannot deposit $\sim 0.3\ M_\odot$ at such small radii. Fallback therefore constrains the explosion outcome, but does not by itself explain the origin of the dense nearby CSM, and is most naturally combined with a binary-mediated mass-loss channel.

Merger-powered fast transients involving a compact object

A merger-powered scenario is appealing for SN 2018erx primarily because it can naturally produce the structured, asymmetric, and multi-epoch circumstellar environment implied by the data. The event appears to require both a dense inner shell on sub-AU to tens-of-AU scales, which powers the rapid interaction, and a distinct outer dusty layer at radii of at least a few $\times 10^{16}$ cm ($M_{\rm d} \sim 10^{-6}$–$10^{-5}\ M_\odot$), which accounts for the strong effective attenuation ($A_V \simeq 3.3$ mag) and the NIR echo. In particular, delayed mergers between a stripped WR star and a compact object (neutron star or black hole) provide a physically motivated channel, in which the WR star is tidally disrupted and accreted, driving a disk-wind outflow and shaping both the inner and outer CSM (Metzger 2022).

The merger picture is also attractive because it does not require the inner CSM to resemble a steady wind. In SN 2018erx the inferred shell-like density profile ($\eta \approx 0.05$), compact inner radius ($R_0 \approx 0.7$ AU), and relatively high CSM density ($\rho_0 \approx 9.6 \times 10^{-13}$ g cm^{-3}) are more suggestive of a confined mass ejection than of a long-lived outflow. The implied characteristic mass-loss rate, $\dot{M} \sim 10^{-3}\ M_\odot\ \mathrm{yr}^{-1}$ (Section 10.5), is orders of magnitude above canonical WR wind values, yet consistent with rates expected during a common-envelope or dynamical mass-transfer episode. In this sense, merger-related ejection or common-envelope clearing may better match the geometry of the inferred CSM than a canonical WR wind. If the stripped star involved in the merger were WC/WO-like, the carbon-rich line spectrum and carbonaceous dust would also follow naturally.

The main limitation is that current merger models are not yet tied closely enough to the specific parameter combination inferred for SN 2018erx. It remains unclear whether they generically produce an effective ejecta mass as low as $M_{\mathrm{ej}} \sim 0.11\ M_\odot$ together with $M_{\mathrm{CSM}} \sim 0.3\ M_\odot$ at radii of only tens of AU, while also reproducing Type Icn-like intermediate-width C II emission. We also lack independent observational evidence for merger or engine signatures such as luminous X-ray or radio emission, long-lived central-engine activity, or extreme late-time asymmetry, although the available follow-up is not deep enough to exclude them. We therefore regard merger-powered models as plausible, particularly for explaining the CSM geometry and the presence of a distinct dusty outer layer, but not yet uniquely required by the present data.

10.7 Conclusion

We have presented optical and near-infrared observations of SN 2018erx (ZTF18abkmbpy), a fast-evolving and unusually red interacting SESN discovered by ZTF. Photometrically, SN 2018erx rises to peak in ~ 2 d and declines at 0.16 ± 0.01 mag d^{-1} over the first 10 d, placing it among the most rapidly evolving hydrogen-poor SNe and overlapping with the parameter space of rapidly evolving stripped-envelope transients. Spectroscopically, it exhibits prominent, relatively broad C II emission with characteristic widths of ~ 3800 km s^{-1}, consistent with interaction between the SN ejecta and a carbon-rich CSM and favoring a Type Icn classification. Semi-analytical CSM-interaction modeling indicates a compact, shell-like CSM with $M_{\mathrm{CSM}} \approx 0.3\ M_\odot$ interacting with low-mass ejecta of $M_{\mathrm{ej}} \approx 0.11\ M_\odot$ at velocities of $v_{\mathrm{ej}} \approx 1.5 \times 10^4$ km s^{-1}, while the late-time luminosity constrains the ^{56}Ni mass to $\lesssim (3\text{–}5) \times 10^{-3}\ M_\odot$. The estimated near-constant density profile ($\eta \approx 0.05$) and

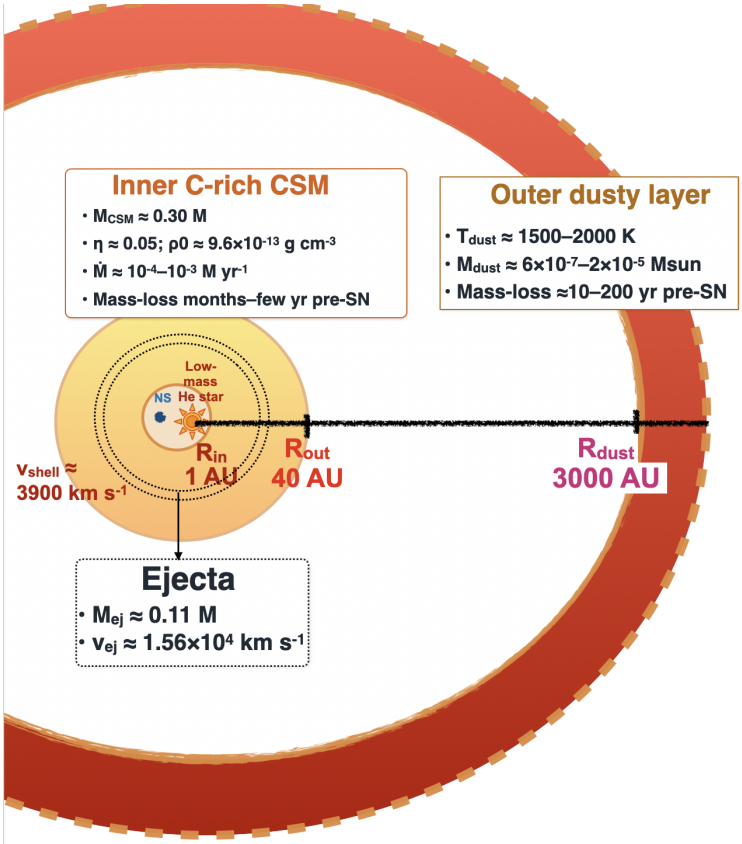

Figure 10.13: Schematic illustration of the CSM environment inferred for SN 2018erx from the lightcurve and spectral modeling. The figure summarizes the compact C-rich inner CSM responsible for the rapid interaction, together with the more extended dusty component inferred from the strong extinction and late-time near-infrared excess.

high inner density ($\rho_0 \approx 9.6\times10^{-13}$ g cm^{-3}) disfavor a steady WR wind and instead point to a brief, intense mass-ejection episode in the final years before collapse, most naturally explained by late-stage binary interaction. The strong continuum reddening ($A_V \simeq 3.3$ mag) and near-infrared excess at +27 d, corresponding to a hot dust component at $T_{\rm d} \sim$ 1500–2000 K with inferred mass $M_{\rm d} \sim 10^{-6}$–$10^{-5}\,M_\odot$, point to local circumstellar dust. The dust sublimation radius ($R_{\rm sub} \approx 4.6\times10^{16}$ cm) implies that this outer dusty layer was ejected $\sim$ 10–200 yr before core collapse, representing an earlier mass-loss episode distinct from that of the compact inner CSM. Together, the rapid evolution, low ejecta mass, modest radioactive yield, and evidence for compact CSM interaction place SN 2018erx in a sparsely populated region of the interacting SESN phase space.

The inferred properties are most naturally consistent with an interaction-boosted

ultra-stripped core-collapse explosion in a close binary system. In particular, the very low ejecta mass ($M_{\rm ej} \sim 0.11\ M_\odot$), very small radioactive yield ($M_{\rm Ni} \lesssim (3–5) \times 10^{-3}\ M_\odot$), rapid photometric evolution, and compact dense CSM with a mass comparable to that of the ejecta are all consistent with a progenitor stripped to a low-mass core via binary interaction, followed by a final episode of intense mass loss through Case BC evolution or a silicon-flash-driven ejection shortly before collapse. At the same time, the carbon-rich circumstellar environment is not uniquely diagnostic of this channel. A WC/WO progenitor provides a direct route to C-rich gas and dust, but a steady Wolf–Rayet wind struggles to produce the inferred combination of low ^{56}Ni mass, compact shell-like CSM with an approximately constant density profile, and such a small ejecta mass without invoking an additional eruptive mass-loss episode and/or strong fallback. A fallback-modified WR explosion can account for the low effective ejecta mass and suppressed ^{56}Ni production, yet it does not by itself explain the origin of the dense nearby shell required by the interaction. Merger- or compact-object-powered scenarios remain plausible because they can generate a structured, multi-epoch circumstellar environment, including both the compact inner shell and the older dusty outer material. These scenarios also naturally accommodate the high inferred mass-loss rates and shell-like geometry. However, current models do not yet demonstrate that they reproduce the full combination of low ejecta mass, low nickel yield, compact CSM, and Type Icn-like spectroscopic properties observed in SN 2018erx. Overall, the ultra-stripped interpretation provides the most self-consistent explanation of the full parameter set, while WR/fallback and merger-driven channels remain viable alternatives that likely require more detailed modelling.

Looking ahead, distinguishing between an interaction-boosted ultra-stripped explosion, a fallback-modified Wolf–Rayet collapse forming a black hole, or a merger/engine-driven scenario will require more detailed modelling and substantially deeper late-time observations. In particular, very deep optical and near-infrared tail photometry is essential to measure or tightly constrain any ^{56}Co-powered decay. This will allow us to separate a zero nickel yield from a merely low ^{56}Ni mass. Late-time spectroscopy is equally important, as nebular line diagnostics can directly probe the inner ejecta composition, progenitor mass, and the persistence or shutdown of circumstellar interaction.

The detection of local circumstellar dust in SN 2018erx raises a broader question about the role of dust in the interacting SESN population. While dust signatures

have been identified in individual Type Ibn and Icn events (e.g., SN 2006jc, OGLE-2012-SN-006, SN 2023xgo), they are not seen in all cases. This likely reflects a combination of factors. The dust may be distributed in a clumpy or aspherical configuration, so that it does not lie along every line of sight. In other events, the total dust mass may simply be too low to produce a detectable signature at optical wavelengths. Observational biases also play an important role: heavily dust-reddened events like SN 2018erx appear intrinsically faint in the optical before extinction correction, making them easier to miss or misclassify in optical surveys. Multi-epoch near- and mid-infrared monitoring will be crucial to fully characterize this dust component. Type Icn SNe, with their dense and carbon-rich C/O-dominated circumstellar environments, may represent especially favorable conditions for efficient dust condensation and growth, making them promising targets for JWST follow-up. Robust modeling will connect dust formation to the progenitor's final mass-loss history and, more broadly, these carbon-rich environments provide a direct probe of whether core-collapse SNe can significantly contribute to the cosmic dust budget.

Finally, SN 2018erx adds to the growing evidence that stripped-envelope explosions with very low ^{56}Ni masses may be underrepresented in current samples. Previous studies have suggested a discrepancy between nickel yields in stripped-envelope SNe and Type II SNe (Anderson 2019), possibly driven by observational bias. SN 2018erx reinforces the emerging picture that low-nickel, low-ejecta-mass events are faint and evolve rapidly, and may only be discovered or classified when their peak luminosity is boosted by circumstellar interaction or shock cooling. Similarly, SN 2018erx shows that sufficiently high dust extinction can make a Type Icn SN appear optically faint and unusually red, suggesting that dustier members of the class may be systematically missed in optical surveys. Future deep surveys such as LSST (Ivezić et al. 2008) and Roman, combined with high-cadence surveys such as ZTF, will be transformative in uncovering this hidden population.

10.8 Data availability

All photometry and spectroscopy data will be made publicly available on Zenodo and WISeREP (Yaron and Gal-Yam 2012b) after publication.

10.9 Acknowledgements

Based on observations obtained with the Samuel Oschin Telescope 48-inch and the 60-inch Telescope at the Palomar Observatory as part of the Zwicky Transient Facility project. ZTF is supported by the National Science Foundation under Grant

No. AST-1440341 and a collaboration including Caltech, IPAC, the Weizmann Institute of Science, the Oskar Klein Center at Stockholm University, the University of Maryland, the University of Washington, Deutsches Elektronen-Synchrotron and Humboldt University, Los Alamos National Laboratories, the TANGO Consortium of Taiwan, the University of Wisconsin at Milwaukee, and Lawrence Berkeley National Laboratories. Operations are conducted by COO, IPAC, and UW.

SED Machine is based upon work supported by the National Science Foundation under Grant No. 1106171

The ZTF forced-photometry service was funded under the Heising-Simons Foundation grant 12540303 (PI: Graham).

The Gordon and Betty Moore Foundation, through both the Data-Driven Investigator Program and a dedicated grant, provided critical funding for SkyPortal.

M.W.C. acknowledges support from the National Science Foundation with grant numbers PHY-2117997, PHY-2308862 and PHY-2409481.

D. T. is supported by Harvard University through the Institute for Theory and Computation Fellowship.

The Gordon and Betty Moore Foundation, through both the Data-Driven Investigator Program and a dedicated grant, provided critical funding for SkyPortal .

This research has made use of the NASA/IPAC Extragalactic Database (NED), which is funded by the National Aeronautics and Space Administration and operated by the California Institute of Technology.

The Liverpool Telescope is operated on the island of La Palma by Liverpool John Moores University in the Spanish Observatorio del Roque de los Muchachos of the Instituto de Astrofisica de Canarias with financial support from the UK Science and Technology Facilities Council.

The W. M. Keck Observatory is operated as a scientific partnership among the California Institute of Technology, the University of California and the National Aeronautics and Space Administration. The Observatory was made possible by the generous financial support of the W. M. Keck Foundation. The authors wish to recognize and acknowledge the very significant cultural role and reverence that the summit of Maunakea has always had within the indigenous Hawaiian community. We are most fortunate to have the opportunity to conduct observations from this mountain.

Software: Global Relay of Observatories Watching Transients Happen Marshal (GROWTH; Kasliwal et al. 2019) and the Fritz SkyPortal Marshal (Duev et al. 2019, Van der Walt et al. 2019, Coughlin et al. 2023). Astropy (Astropy Collaboration et al. 2013), Matplotlib (Hunter 2007)

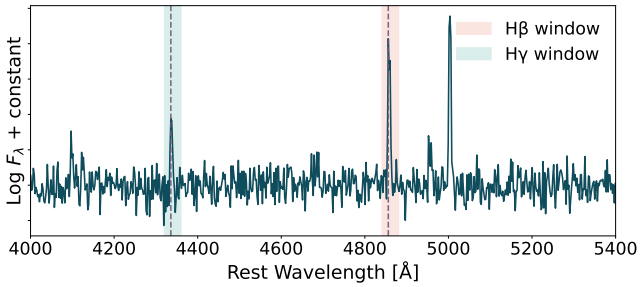

Figure A1: Measurement of the Balmer decrement in the host-galaxy spectrum at the position of SN 2018erx using a late-time Keck/LRIS observation. The continuum-subtracted host spectrum used to measure the line fluxes. The shaded regions mark the wavelength windows used to integrate the Hβ and Hγ emission lines.

Appendix

Table A1: Photometry after MW extinction correction.

Phase (d)	MJD	Instrument	Filter	AB mag	Phase (d)	MJD	Instrument	Filter	AB mag
-2.15	58331.17716	P48+ZTF	*r*	20.32 ± 0.18	0.00	58333.32784	P48+ZTF	*r*	18.54 ± 0.04
-2.15	58331.17716	P48+ZTF	*r*	20.25 ± 0.11	2.89	58336.21634	P48+ZTF	*r*	18.74 ± 0.06
-2.15	58331.17716	P48+ZTF	*r*	20.25 ± 0.11	2.89	58336.21634	P48+ZTF	*r*	18.67 ± 0.03
-2.13	58331.20277	P48+ZTF	*r*	20.40 ± 0.24	2.89	58336.21634	P48+ZTF	*r*	18.67 ± 0.03
-2.13	58331.20277	P48+ZTF	*r*	20.30 ± 0.14	2.89	58336.22250	P60	*r*	18.89 ± 0.03
-2.13	58331.20277	P48+ZTF	*r*	20.30 ± 0.14	2.90	58336.22530	P60	*g*	19.78 ± 0.05
-2.11	58331.21819	P48+ZTF	*r*	20.25 ± 0.18	2.90	58336.22810	P60	*i*	18.40 ± 0.03
-2.11	58331.21819	P48+ZTF	*r*	20.22 ± 0.12	2.91	58336.24016	P48+ZTF	*g*	19.90 ± 0.10
-2.11	58331.21819	P48+ZTF	*r*	20.22 ± 0.12	4.83	58338.16157	P48+ZTF	*i*	18.62 ± 0.06
-2.00	58331.32586	P48+ZTF	*i*	19.47 ± 0.13	6.85	58340.17862	P48+ZTF	*r*	19.44 ± 0.16
-1.94	58331.38350	P60	*r*	20.02 ± 0.10	6.85	58340.17862	P48+ZTF	*r*	19.39 ± 0.08
-1.94	58331.38900	P60	*i*	19.42 ± 0.07	6.85	58340.17862	P48+ZTF	*r*	19.39 ± 0.08
-1.13	58332.20088	P48+ZTF	*g*	20.00 ± 0.11	6.92	58340.25020	P60	*r*	19.66 ± 0.05
-1.13	58332.20088	P48+ZTF	*g*	19.95 ± 0.20	6.93	58340.25300	P60	*g*	20.57 ± 0.09
-1.13	58332.20088	P48+ZTF	*g*	20.00 ± 0.11	6.93	58340.25570	P60	*i*	19.14 ± 0.04
-1.11	58332.22079	P48+ZTF	*g*	19.99 ± 0.10	8.99	58342.31620	P60	*r*	20.17 ± 0.08
-1.11	58332.22079	P48+ZTF	*g*	19.93 ± 0.22	8.99	58342.31900	P60	*g*	20.97 ± 0.10
-1.11	58332.22079	P48+ZTF	*g*	19.99 ± 0.10	8.99	58342.32170	P60	*i*	19.71 ± 0.08
-1.07	58332.26127	P48+ZTF	*r*	19.02 ± 0.09	9.04	58342.36434	P48+ZTF	*i*	19.61 ± 0.17
-1.07	58332.26127	P48+ZTF	*r*	18.91 ± 0.05	9.83	58343.15726	P48+ZTF	*r*	20.18 ± 0.12
-1.05	58332.28213	P48+ZTF	*r*	18.86 ± 0.05	9.83	58343.15726	P48+ZTF	*r*	20.18 ± 0.12
-1.05	58332.28213	P48+ZTF	*r*	18.86 ± 0.05	12.57	58345.89690	LT+IOO	*g*	22.34 ± 0.20
-1.03	58332.30164	P48+ZTF	*r*	18.74 ± 0.12	12.57	58345.89890	LT+IOO	*r*	21.72 ± 0.15
-0.05	58333.27800	P60	*r*	18.72 ± 0.02	12.57	58345.90090	LT+IOO	*i*	21.09 ± 0.10
-0.05	58333.28090	P60	*g*	19.57 ± 0.03	12.85	58346.17784	P48+ZTF	*r*	20.90 ± 0.20
-0.04	58333.28360	P60	*i*	18.26 ± 0.03	28.94	58362.26390	Keck	*K*	21.23 ± 0.03
0.00	58333.32784	P48+ZTF	*r*	18.65 ± 0.09	28.95	58362.27590	Keck	*J*	22.64 ± 0.13
0.00	58333.32784	P48+ZTF	*r*	18.54 ± 0.04					

Table A2: Spectroscopy log

Date	Phase (d)	Telescope/Instrument
2018-08-03	-1.6	P60/SEDM
2018-08-04	-0.6	P200/DBSP
2018-08-07	+2.4	Keck-I/LRIS
2018-08-12	+7.4	P200/DBSP
2018-08-21	+16.4	P200/DBSP
2018-09-02	+29.4	Keck-II/NIRES
2025-08-19	+2572.7	Keck-I/LRIS

Table A3: Blackbody evolution of SN 2018erx before and after extinction correction. Blank entries did not pass the quality cut $\sigma_{L_{\rm bb}}/L_{\rm bb} < 1$ because their best-fit luminosity uncertainties are too large.

Phase	Before correction ($A_V = 0$)			After correction ($A_V = 3.3$)		
(days)	$\log L_{\rm bb}$ (erg s^{-1})	$T_{\rm bb}$ (K)	$R_{\rm bb}$ ($R_\odot$)	$\log L_{\rm bb}$ (erg s^{-1})	$T_{\rm bb}$ (K)	$R_{\rm bb}$ ($R_\odot$)
-3.3	$41.96^{+0.06}_{-0.06}$	3130^{+150}_{-140}	52380^{+8650}_{-7650}	$42.72^{+0.12}_{-0.03}$	6840^{+2120}_{-730}	26370^{+5530}_{-8720}
-2.3	$42.27^{+0.03}_{-0.03}$	3900^{+100}_{-100}	48180^{+4340}_{-3810}	$43.38^{+0.04}_{-0.03}$	9020^{+770}_{-610}	32270^{+3560}_{-3550}
-1.3	$42.28^{+0.01}_{-0.01}$	4340^{+60}_{-60}	39350^{+1570}_{-1510}	$43.78^{+0.05}_{-0.05}$	14320^{+840}_{-790}	20440^{+1240}_{-1140}
1.7	$42.25^{+0.01}_{-0.01}$	4210^{+70}_{-70}	40450^{+1850}_{-1750}	$43.67^{+0.05}_{-0.05}$	13200^{+840}_{-750}	21030^{+1360}_{-1300}
5.6	$41.94^{+0.02}_{-0.02}$	4180^{+120}_{-120}	28640^{+2280}_{-2010}	$43.38^{+0.11}_{-0.09}$	13650^{+1830}_{-1390}	14090^{+1640}_{-1620}
7.8	$41.73^{+0.05}_{-0.04}$	4010^{+370}_{-330}	24370^{+6160}_{-4700}	...	...	...
11.4	$41.14^{+0.05}_{-0.04}$	4330^{+350}_{-330}	10620^{+2430}_{-1860}	...	...	...
27.7	$40.63^{+0.01}_{-0.01}$	1660^{+60}_{-70}	40200^{+3770}_{-3020}	$40.81^{+0.02}_{-0.02}$	2020^{+100}_{-100}	33330^{+3290}_{-2620}

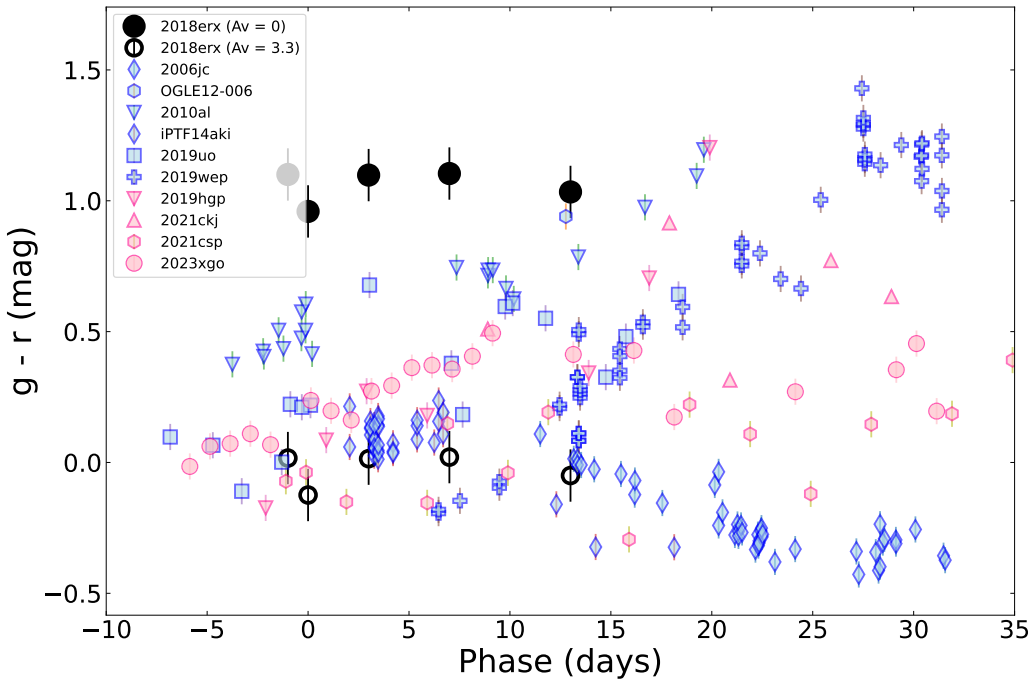

Figure A2: Evolution of the optical color $(g - r)$ for SN 2018erx compared with Type Ibn (blue symbols) and Type Icn (pink symbols) supernovae from the literature. Filled black circles show the observed colors of SN 2018erx assuming no host extinction ($A_V = 0$), while open black circles show the extinction-corrected values adopting $A_V = 3.3$ mag. Phases are given relative to r-band maximum. Compared to the comparison samples, SN 2018erx exhibits unusually red colors if no host extinction is applied, while the extinction-corrected colors are broadly consistent with the color evolution of other interacting SESNe.

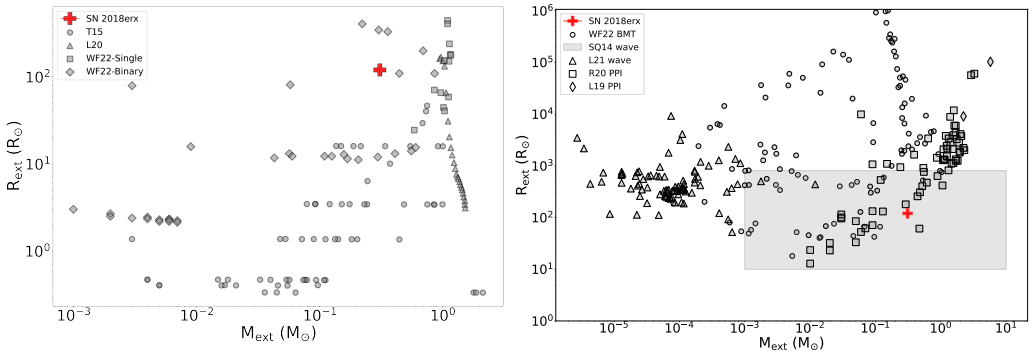

Figure A3: Comparison of the envelope properties of SN 2018erx with theoretical models for *bound* stellar material – binary and single star models from Wu and Fuller (2022a) (WF22), Laplace et al. (2020) (L20) and Tauris et al. (2015) (T15). *Right:* Comparison of the the envelope properties of SN 2023zaw with theoretical models for *unbound* stellar material – late-time binary mass transfer (BMT; Wu and Fuller 2022a), wave-driven mass loss (Leung et al. 2021a, Shiode and Quataert 2014), pulsation-pair instability driven mass loss (PPI; Renzo et al. 2020, Leung et al. 2019).

Chapter 11

CONCLUSION

11.1 Summary

Constraining the fate of stars near the low-mass end of core collapse requires spectroscopically complete, volume-limited SN samples. This thesis is built around that goal. Its observational foundation is provided by the Zwicky Transient Facility (ZTF), whose wide-field, high-cadence survey enables the discovery of nearby SNe, including intrinsically faint and rapidly evolving events. Within this framework, I contributed to Phase II of the Census of the Local Universe (CLU), helping classify around 1750 transients within 150 Mpc. I also worked on the commissioning and science-validation of the Next Generation Palomar Spectrograph (NGPS), whose improved throughput and efficiency addressed the poor spectroscopic completeness of the faintest transients discovered by ZTF (Chapter II). These gains were realized in the Complete Astronomical Transient Survey within 150 Mpc (CATS150), where my work contributed to achieving a spectroscopic completeness of 97.2% for local ZTF transients down to 20 mag (Chapter III). Together, these efforts provide the observational backbone for the results presented in this thesis.

The main results of this thesis, organized by chapter, are as follows:

- **Chapter IV:** I constructed the largest systematic sample of Type IIP supernovae assembled to date and measured the luminosity function of the hydrogen-rich population. This places the clearest observational limits so far on very low-luminosity end of Type IIP explosions: fewer than 1.5% of Type IIP SNe are fainter than -14.5 mag, while LLIIP SNe constitute only 8^{+1}_{-2}% of all core-collapse supernovae (Das et al. 2025c). This shows that faint hydrogen-rich explosions do not hide a large missing population, and that the unresolved discrepancy between core-collapse supernova rates and star-formation rates cannot be explained by LLIIP SNe alone.

- **Chapter V:** I presented the largest systematic study of lightcurve properties of Type IIP supernovae from a volume-limited survey. Many LLIIP SNe show positive plateau slopes, suggesting smaller progenitor radii and distinct density structures. A small number of objects with steep plateau-to-tail drops

stand out as promising candidates for black-hole fallback. I showed that LLIIP SNe occupy the low-^{56}Ni, low-explosion-energy, and low-mass end of the H-rich population, consistent with the lowest-mass RSG/sAGB core-collapse progenitors.

- **Chapter VI:** I used the first systematic nebular sample of LLIIP SNe to search for electron-capture explosions from sAGB progenitors. Only two objects satisfy the conservative criteria adopted here for ECSN classification. If ECSNe arise predominantly through this channel, we infer an upper limit on the ECSN rate of $\lesssim (5\text{–}8) \times 10^2\,\mathrm{Gpc^{-3}\,yr^{-1}}$. This corresponds to a narrow sAGB progenitor mass window of $\Delta M_{\mathrm{sAGB}} \lesssim 0.02\text{–}0.06\ M_\odot$, substantially smaller than predicted by many stellar-evolution models.

- **Chapter VII:** I identified a Ca-rich Type IIb population occupying a strongly stripped regime intermediate between canonical Type IIb/Ib/Ic supernovae and the most extreme ultra-stripped explosions. Despite retaining a small amount of hydrogen at the time of collapse, these events evolve faster and have lower ejecta masses than typical Type Ibc supernovae, with weak oxygen emission indicating low-mass progenitors. Their properties point to binary progenitor systems with a low-mass He star undergoing strong stripping, potentially producing compact remnants in close orbits that may be detectable with gravitational-wave observatories such as LISA.

- **Chapter VIII:** I constructed the first systematic sample of double-peaked Type Ibc supernovae, showing that early shock-cooling emission from extended material is present in a measurable fraction of otherwise compact hydrogen-poor explosions. Their lightcurves and nebular spectroscopy point to late-stage expansion or recent mass loss in low-mass helium stars before collapse.

- **Chapter IX:** I presented the discovery and characterization of SN 2023zaw, an unusually faint and rapidly evolving stripped-envelope supernova with an inferred nickel mass of only $M_{\mathrm{Ni}} \approx 0.002\ M_\odot$, the lowest measured for any stripped-envelope supernova to date. This object demonstrates that stripped-envelope explosions can reach radioactive yields comparable to, or even below, those of the faintest Type II events. It could form compact binary remnants that may merge within a Hubble timescale, and points to a potentially hidden

population of such events that would be missed without early shock-cooling emission.

- **Chapter X:** Through SN 2018erx, I showed that this low-mass stripped sequence extends to a more extreme mass-loss regime. Its fast evolution, low ejecta mass, compact carbon-rich circumstellar material, local pre-existing dust, and very low radioactive yield indicate that some faint stripped-envelope explosions are powered primarily by dense circumstellar interaction. Heavily dust-reddened events like SN 2018erx may therefore be missed in optical surveys, and may only be detected or classified when their luminosity is enhanced by circumstellar interaction.

11.2 Missing supernovae from 8–12 $M_\odot$ progenitors: tension with a Salpeter-like IMF

A central synthesis emerging from this thesis is that even after accounting for both the hydrogen-rich and stripped-envelope channels identified here, the observed faint population still falls short of the number of explosions expected from 8–12 $M_\odot$ progenitors under a standard Salpeter-like initial mass function. LLIIP SNe contribute only 8^{+1}_{-2}% of all core-collapse supernovae (Das et al. 2025c), while the low-mass stripped channels presented in this thesis each likely contribute at only the percent level (Figure 11.2). This discrepancy points to multiple possible explanations, which we outline below.

Theoretical explanations. One possibility is that the effective lower-mass boundary for successful core collapse is somewhat higher than is often assumed. Under a Salpeter initial mass function, the interval 9.5–12 $M_\odot$ would account for only $\sim$ 20–25% of all core-collapse supernovae, much closer to the contribution currently inferred from the known faint channels than the canonical 8–12 $M_\odot$ range. This may indicate that some stars near the nominal lower boundary never reach the conditions required for collapse and instead end their lives as massive white dwarfs.

Another possibility is that some stars do collapse, but produce either very weak explosions with substantial fallback or direct collapse into a black hole with little optical display (Burrows and Vartanyan 2021, Antoni et al. 2025).

Binary evolution adds another layer of uncertainty. Stellar mergers and mass gain can shift stars that began in the 8–12 $M_\odot$ range into effectively more massive progenitors

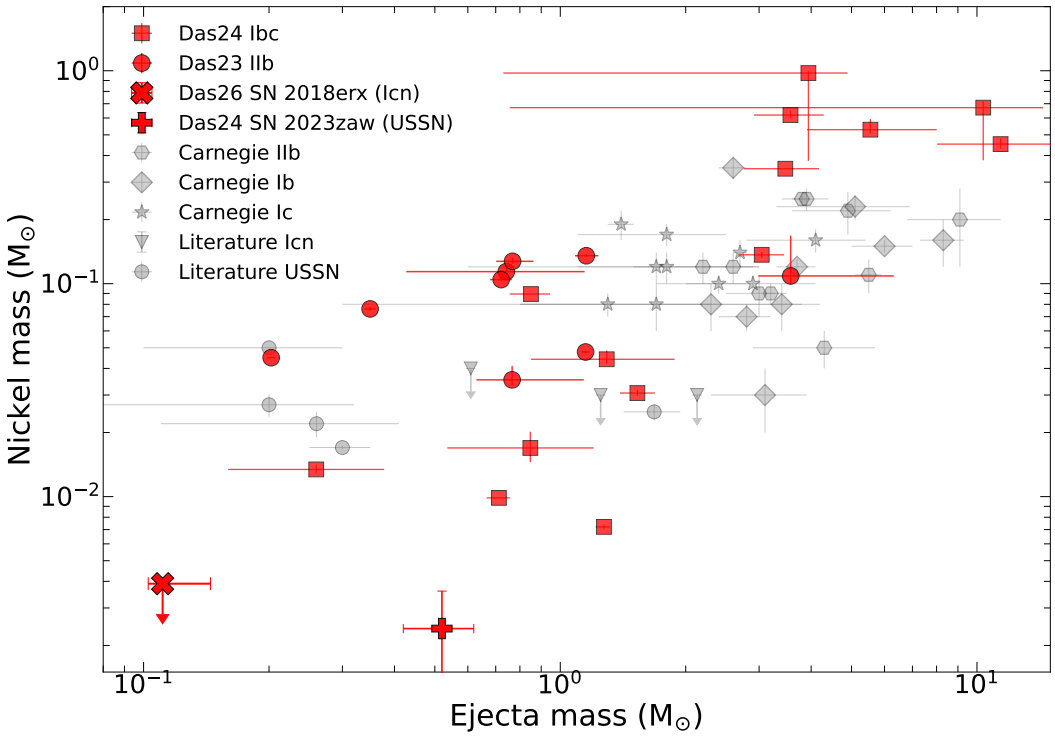

Figure 11.1: This thesis progressively fills the ejecta-mass/56Ni-mass phase space toward the low-mass, low-nickel end for stripped-envelope SNe. The gray symbols represent literature measurements for Type Ib/Ic supernovae from the Carnegie Supernova Project (Taddia et al. 2018), together with candidate ultra-stripped supernovae (USSNe) from the literature, including iPTF14gqr (De et al. 2018c), SN 2019dge (Yao et al. 2020), SN 2019wxt (Shivkumar et al. 2023, Agudo et al. 2023), and SN 2022agco (Yan et al. 2023). Type Icn SNe are taken from Pellegrino et al. (2022a). The colored symbols highlight objects analyzed in this thesis. Taken together, these objects extend the observed distribution into the previously sparsely populated regime of low ejecta mass and low ^{56}Ni mass.

before explosion. In that case, the resulting supernovae may appear brighter and more massive than would be expected from isolated low-mass stars, masking their original position near the lower-mass boundary (Sana et al. 2012, Zapartas et al. 2019, 2021).

Observational explanations. Spectroscopic completeness remains poorest at the faint end, and very low-luminosity explosions fainter than about -13 mag remain difficult to discover and classify beyond the very local universe. ZTF is sensitive only to $\sim$ 25 Mpc for transients fainter than -12 mag and to $\sim$ 40 Mpc for those fainter than -13 mag. A still fainter population of nearby core-collapse explosions may therefore remain hidden below the effective limits of current optical surveys.

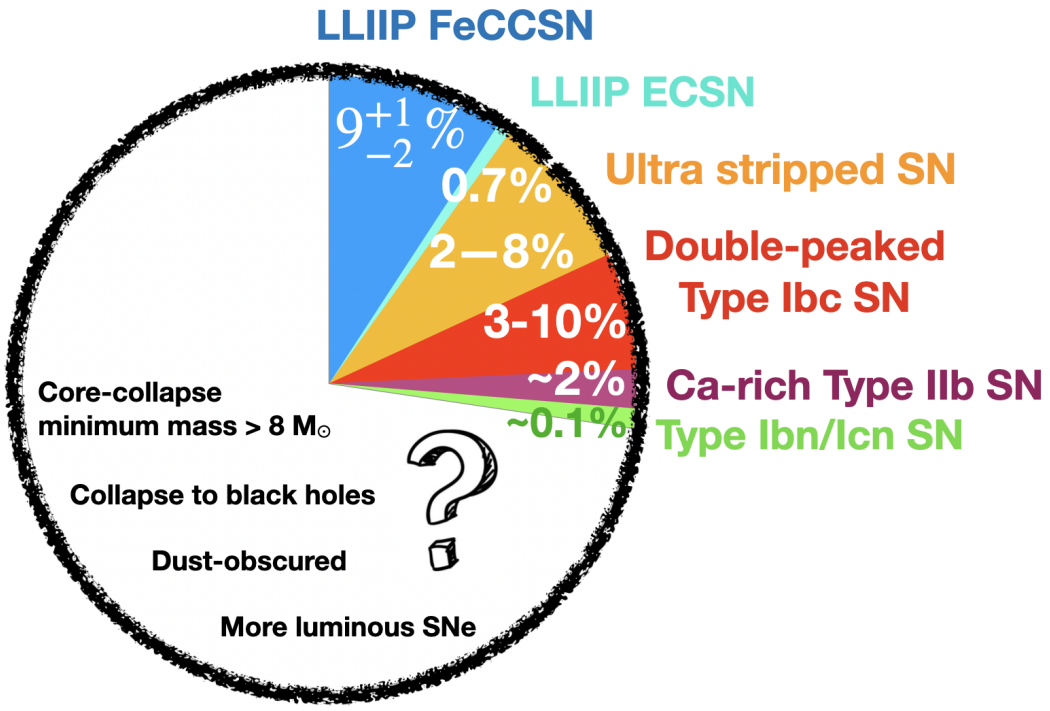

Figure 11.2: Missing supernovae from 8–12 $M_\odot$ progenitors. The observed fractions of low-luminosity and stripped-envelope channels (colored wedges) fall short of expectations from a Salpeter initial mass function combined with the cosmic star-formation rate, indicating that a significant fraction of low-mass core-collapse events remain unaccounted for.

Dust obscuration is likely another important contributor. Current estimates suggest that a substantial fraction ($\sim$ 10–60%) of nearby core-collapse supernovae are missed by optical surveys because they occur in highly extinguished environments (Mattila et al. 2012, Jencson et al. 2019b, Fox et al. 2021). Events such as SPIRITS16tn, which is consistent with a heavily obscured low-luminosity Type II supernova, show that some low-energy explosions may preferentially occur behind large dust columns (Jencson et al. 2019b).

A further observational possibility is that some low-mass progenitors do not appear as classical faint Type IIP supernovae at all, but instead explode as other classes of transients. Some low-mass explosions may even appear in more luminous classes when their lightcurves are boosted by circumstellar interaction. In addition, super-AGB stars in the $\sim$ 7–9 $M_\odot$ range may contribute to the population of intermediate-luminosity red transients (ILRTs) (Nomoto 1984, Botticella et al. 2009, Adams et al. 2016, Jencson et al. 2019a, Rose et al. 2024, Valerin et al. 2025). Current rate

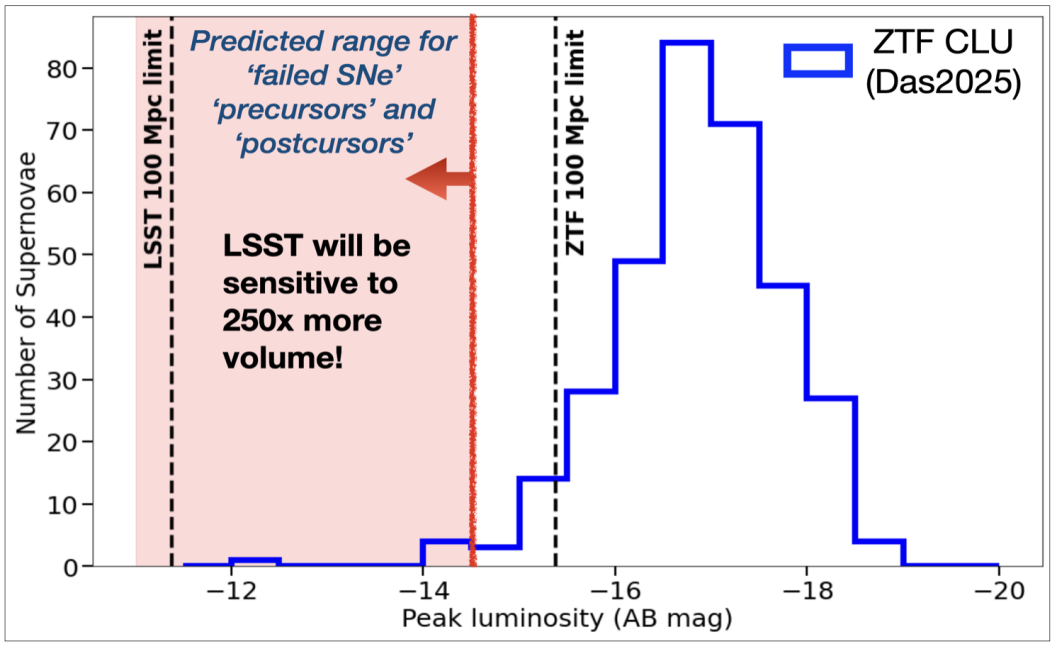

Figure 11.3: LSST will probe the faint end of the core-collapse supernova luminosity function to significantly larger distances, increasing the accessible volume by a factor of $\sim$ 250 and enabling a systematic census of the faintest explosion channels. The shaded region indicates the predicted luminosity range of failed supernova "precursors" and "postcursors," which remain largely unexplored with current surveys. The vertical dashed line marks the approximate sensitivity limit of ZTF within 100 Mpc. The blue histogram shows the ZTF CLU volume-limited sample (Das et al. 2025b).

estimates, however, suggest that ILRTs account for only a few percent of the overall core-collapse population (Karambelkar et al. 2023), and so are unlikely to close the full gap on their own.

The most likely resolution is therefore not a single missing channel, but some combination of revised stellar-fate boundaries, binary redistribution into other supernova classes, dust obscuration, and a population of intrinsically faint or failed explosions that remains below present survey limits. Distinguishing among these possibilities is the main next step opened by this thesis.

11.3 Future

Massive stars ($> 8\,M_\odot$) shape the Universe through their radiation, winds, and explosive deaths, leaving behind neutron stars and black holes. More than 80% of massive stars reside in binaries, where mass transfer, envelope stripping, and mergers profoundly alter their evolution and remnants (Sana et al. 2012). However,

we still lack a coherent framework linking binary interaction to the final outcomes of massive stars.

The ideal experiment—tracking a supernova from pre-explosion activity through the explosion and into the late-time phase that reveals the compact remnant—has long been out of reach, as both the precursor signatures and late-time emission are intrinsically faint. The results of this thesis highlight this missing regime, particularly at low luminosities, where key evolutionary channels may remain undetected. With the depth of next-generation surveys such as LSST, it will become possible to probe these phases systematically. In particular, LSST will detect transients as faint as $M_r \approx -11.5$ mag out to $\sim$ 100 Mpc, opening the discovery space for the faintest explosions and enabling a more complete census of massive-star outcomes.

In this context, the following sections outline three central questions that define the next step in this field: (I.) Can we predict when a massive binary star will explode? (II.) What powers the explosion and late-time rebrightenings of massive binaries? (III.) Which massive binaries form black holes?

I. Can we predict when a massive binary star will explode? The next leap in time-domain astronomy is predicting when a star will explode. In interacting binaries, a low-mass helium star can expand late in life, transfer mass, and drive luminous outflows before collapse (Tsuna et al. 2024). Detecting such pre-supernova activity would enable forecasts of core collapse and directly connect binary evolution to the explosion. Only one stripped star has been observed with pre-supernova spectroscopy, and only a handful have been detected photometrically prior to explosion (Brennan et al. 2024). This regime will become increasingly accessible with the sensitivity of upcoming surveys such as LSST.

As part of CLU classifications, we obtained a sequence of spectra more than 100 days before explosion for the transient that became SN 2023fyq, representing the earliest pre-explosion spectroscopy of any supernova to date. As illustrated by SN 2023fyq, significant progress in linking binary progenitors to explosions will come from pre-supernova spectroscopy, which reveals emission and absorption features absent in impostor events. The luminosity and color evolution of such activity constrain mass-loss rates and circumbinary outflows, while spectra diagnose composition and geometry. While it remains unclear whether a universal, repeatable precursor signature exists, the systematic discovery and characterization of pre-supernova activity will place strong empirical constraints on how massive binaries lose mass in their final stages and on the physical conditions that lead to core collapse.

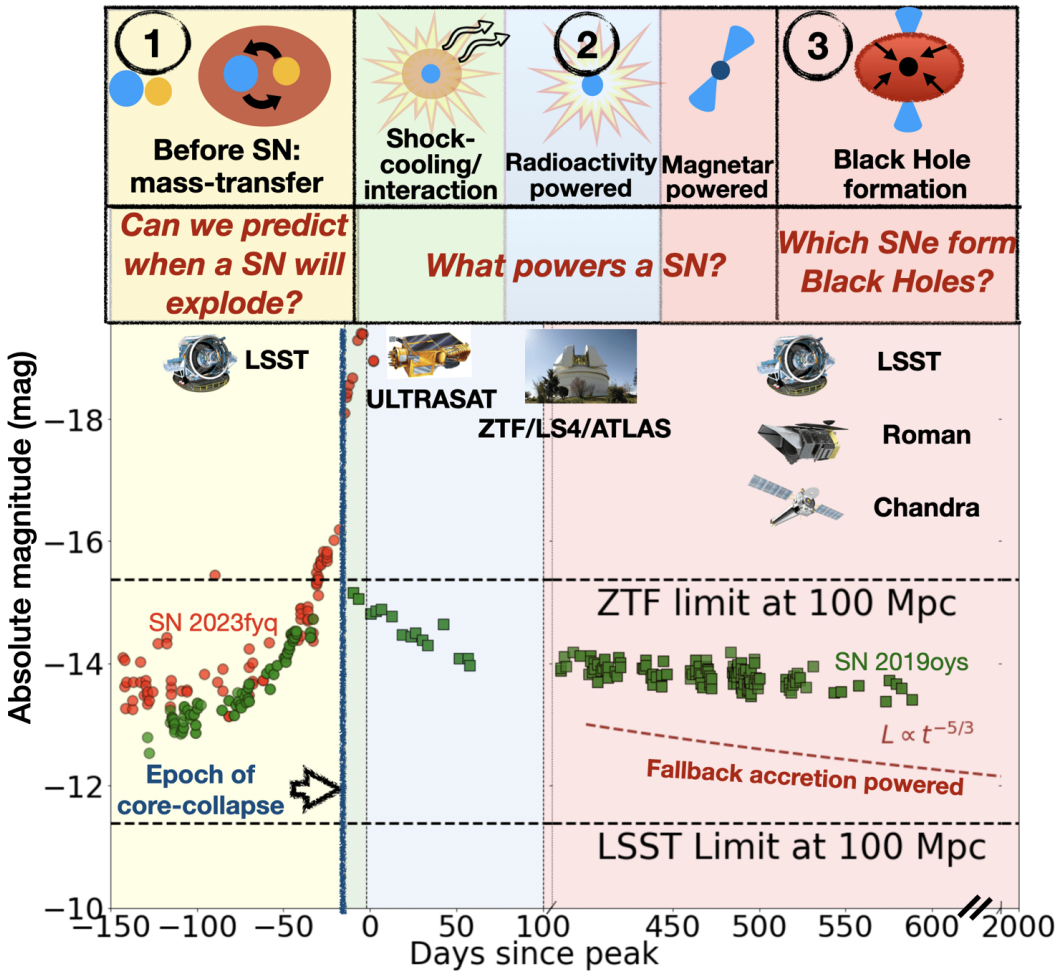

Figure 11.4: Three future directions that build directly on this thesis: identifying precursor activity before explosion, mapping the full power budget of stripped-envelope supernovae, and constraining which explosions form black holes. Horizontal dashed lines indicate approximate ZTF and Rubin/LSST single-epoch depth limits at 100 Mpc.

II: What powers stripped-envelope supernovae and their late-time rebrightenings? Binary interaction not only determines when a star explodes, but also how the resulting supernova is powered. Most stripped-envelope supernovae (SESNe) are powered by the radioactive decay of ^{56}Ni synthesized during the explosion; however, the results of this thesis suggest that faint, nickel-poor events remain underrepresented in existing samples. The CATS150 dataset provides a substantial step forward, and will enable a systematic mapping of the low-^{56}Ni end of the SESN population. Coupled with binary stellar-evolution and radiative-transfer models, this will help connect ejecta mass, nickel yield, and explosion energy to the binary parameters that shape the progenitor.

Beyond the ^{56}Ni-powered phase, a growing class of late-time rebrightening supernovae shows that some stripped-envelope explosions receive renewed energy injection months to years after explosion. These events provide a direct probe of both pre-supernova mass loss and compact remnant activity. In some systems, the rebrightening is likely powered by circumstellar interaction, as the shock encounters shells of material lost shortly before collapse; the timing, luminosity, and line widths then constrain the radius, mass, and density of the expelled material, offering a time-resolved record of binary mass loss.

In other cases, the late-time emission may instead reflect central-engine power, such as magnetar spin-down or fallback accretion onto the compact remnant. Both channels are expected to produce long-lived signatures that can remain relatively faint compared to ordinary supernova emission, placing them naturally in the low-luminosity regime.

Future deep, high-cadence surveys will therefore be essential for identifying these events systematically. In this context, LSST will be especially powerful, extending sensitivity to faint, long-duration transients and enabling a volume-limited census of late-time rebrightening supernovae that can constrain the mechanisms powering stripped-envelope explosions.

III: Which massive binaries form black holes? The results of this thesis, particularly the constraints on the luminosity function and the faint end of the core-collapse population, suggest that a class of intrinsically faint explosions may still be missing from existing samples. Such events are natural candidates for black hole formation, either through fallback or direct collapse. Identifying and characterizing these channels is therefore essential for completing the observational picture of massive star outcomes.

Gravitational-wave detections have established that stellar-mass black holes (3–100 $M_\odot$) are common, yet direct observational constraints on their formation in supernovae remain limited. In binary black hole mergers formed through isolated binary evolution, both black holes originate from progenitor stars that have lost their hydrogen envelopes through mass transfer. Such stripping is expected to significantly modify the pre-supernova core structure, and therefore the explosion outcome and remnant mass (e.g., Schneider et al. 2023). Determining which stripped-envelope supernovae produce black holes is thus key to linking supernova outcomes to binary evolution, informing population-synthesis models, and interpreting compact-object merger rates observed by LIGO–Virgo–KAGRA. However, the observational signa-

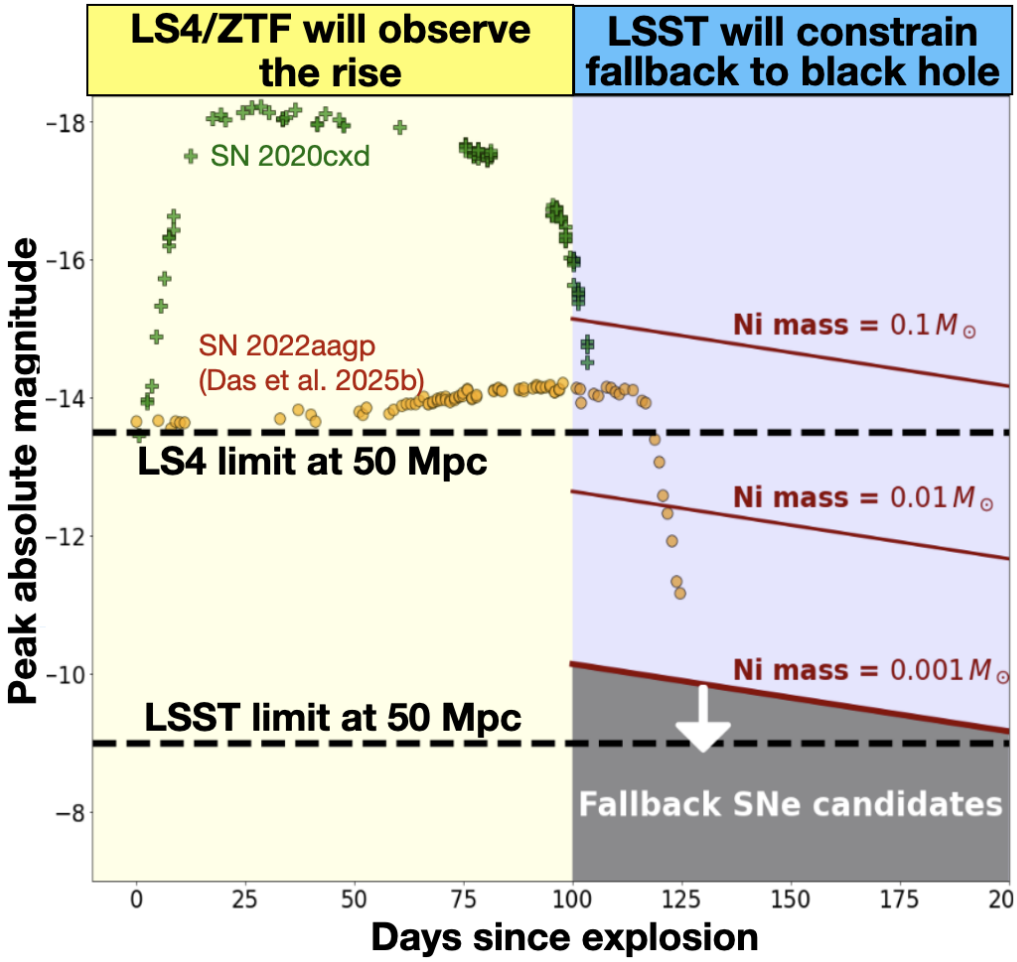

Figure 11.5: Schematic illustration of the discovery space for faint and fallback-powered core-collapse supernovae. The left panel shows the early-time lightcurve evolution, where higher-cadence surveys such as LS4 and ZTF are well suited to capture the rise and peak of low-luminosity events. The right panel highlights the late-time regime, where LSST can probe the declining lightcurves and constrain fallback onto compact remnants, including black hole formation. The dashed lines mark representative detection limits at 50 Mpc, demonstrating that LSST will uniquely access the regime of extremely low-luminosity, fallback-powered events that are largely inaccessible to current surveys.

tures of black hole formation during or after a supernova are intrinsically faint and have therefore remained difficult to detect in existing samples.

Two primary observational channels are expected. In fallback supernovae, a significant fraction of the inner ejecta falls back onto the compact remnant, leading to black hole formation. Because ^{56}Ni is synthesized in these innermost layers, it is among the first material to return, resulting in little or no radioactive tail. The absence of

a ^{56}Ni-powered tail therefore provides a key diagnostic of fallback. In Chapter V (Das et al. 2025e), I identified two archival candidates of this kind, although the depth of current surveys precluded confirmation. In contrast, failed supernovae may occur when a massive star collapses directly into a black hole without launching a successful explosion, producing only a weak, low-energy transient. Such events are expected to be long-lived ($\gtrsim$ 100–200 days), intrinsically faint ($\sim$100 times fainter than ordinary supernovae), and likely to fall below the sensitivity limits of most current optical surveys, as illustrated by the two strongest candidates: NGC 6946-BH1 and M31-2014-DS1 (Adams et al. 2017, De et al. 2026, Antoni and Quataert 2023, Antoni et al. 2025). Future deep, wide-field surveys such as LSST, in synergy with higher-cadence surveys like ZTF and the La Silla Schmidt Southern Survey (LS4; Miller et al. 2025), will be essential for identifying these channels and constraining the rate of black hole formation in supernovae.

BIBLIOGRAPHY

B. P. Abbott, R. Abbott, T. D. Abbott, F. Acernese, K. Ackley, C. Adams, T. Adams, P. Addesso, R. X. Adhikari, V. B. Adya, C. Affeldt, M. Afrough, B. Agarwal, M. Agathos, K. Agatsuma, N. Aggarwal, O. D. Aguiar, L. Aiello, A. Ain, P. Ajith, B. Allen, G. Allen, A. Allocca, P. A. Altin, A. Amato, A. Ananyeva, S. B. Anderson, W. G. Anderson, S. V. Angelova, S. Antier, S. Appert, K. Arai, M. C. Araya, J. S. Areeda, N. Arnaud, K. G. Arun, S. Ascenzi, G. Ashton, M. Ast, S. M. Aston, P. Astone, D. V. Atallah, P. Aufmuth, C. Aulbert, K. AultONeal, C. Austin, A. Avila-Alvarez, S. Babak, P. Bacon, M. K. M. Bader, S. Bae, P. T. Baker, F. Baldaccini, G. Ballardin, S. W. Ballmer, S. Banagiri, J. C. Barayoga, S. E. Barclay, B. C. Barish, D. Barker, K. Barkett, F. Barone, B. Barr, L. Barsotti, M. Barsuglia, D. Barta, S. D. Barthelmy, J. Bartlett, I. Bartos, R. Bassiri, A. Basti, J. C. Batch, M. Bawaj, J. C. Bayley, M. Bazzan, B. Bécsy, C. Beer, M. Bejger, I. Belahcene, A. S. Bell, B. K. Berger, G. Bergmann, J. J. Bero, C. P. L. Berry, D. Bersanetti, A. Bertolini, J. Betzwieser, S. Bhagwat, R. Bhandare, I. A. Bilenko, G. Billingsley, C. R. Billman, J. Birch, R. Birney, O. Birnholtz, S. Biscans, S. Biscoveanu, A. Bisht, M. Bitossi, C. Biwer, M. A. Bizouard, J. K. Blackburn, J. Blackman, C. D. Blair, D. G. Blair, R. M. Blair, S. Bloemen, O. Bock, N. Bode, M. Boer, G. Bogaert, A. Bohe, F. Bondu, E. Bonilla, R. Bonnand, B. A. Boom, R. Bork, V. Boschi, S. Bose, K. Bossie, Y. Bouffanais, A. Bozzi, C. Bradaschia, P. R. Brady, M. Branchesi, J. E. Brau, T. Briant, A. Brillet, M. Brinkmann, V. Brisson, P. Brockill, J. E. Broida, A. F. Brooks, D. A. Brown, D. D. Brown, S. Brunett, C. C. Buchanan, A. Buikema, T. Bulik, H. J. Bulten, A. Buonanno, D. Buskulic, C. Buy, R. L. Byer, M. Cabero, L. Cadonati, G. Cagnoli, C. Cahillane, J. Calderón Bustillo, T. A. Callister, E. Calloni, J. B. Camp, M. Canepa, P. Canizares, K. C. Cannon, H. Cao, J. Cao, C. D. Capano, E. Capocasa, F. Carbognani, S. Caride, M. F. Carney, J. Casanueva Diaz, C. Casentini, S. Caudill, M. Cavaglià, F. Cavalier, R. Cavalieri, G. Cella, C. B. Cepeda, P. Cerdá-Durán, G. Cerretani, E. Cesarini, S. J. Chamberlin, M. Chan, S. Chao, P. Charlton, E. Chase, E. Chassande-Mottin, D. Chatterjee, K. Chatziioannou, B. D. Cheeseboro, H. Y. Chen, X. Chen, Y. Chen, H.-P. Cheng, H. Chia, A. Chincarini, A. Chiummo, T. Chmiel, H. S. Cho, M. Cho, J. H. Chow, N. Christensen, Q. Chu, A. J. K. Chua, S. Chua, A. K. W. Chung, S. Chung, and G. Ciani. Multi-messenger Observations of a Binary Neutron Star Merger. *ApJ*, 848(2):L12, Oct. 2017. doi: 10.3847/2041-8213/aa91c9.

S. M. Adams, C. S. Kochanek, J. L. Prieto, X. Dai, B. J. Shappee, and K. Z. Stanek. Almost gone: SN 2008S and NGC 300 2008OT-1 are fainter than their progenitors. *MNRAS*, 460(2):1645–1657, Aug. 2016. doi: 10.1093/mnras/stw1059.

S. M. Adams, C. S. Kochanek, J. R. Gerke, K. Z. Stanek, and X. Dai. The search for failed supernovae with the Large Binocular Telescope: confirmation of a

disappearing star. *MNRAS*, 468(4):4968–4981, July 2017. doi: 10.1093/mnras/stx816.

I. Agudo, L. Amati, T. An, F. E. Bauer, S. Benetti, M. G. Bernardini, R. Beswick, K. Bhirombhakdi, T. de Boer, M. Branchesi, S. J. Brennan, E. Brocato, M. D. Caballero-García, E. Cappellaro, N. Castro Rodríguez, A. J. Castro-Tirado, K. C. Chambers, E. Chassande-Mottin, S. Chaty, T. W. Chen, A. Coleiro, S. Covino, F. D'Ammando, P. D'Avanzo, V. D'Elia, A. Fiore, A. Flörs, M. Fraser, S. Frey, C. Frohmaier, M. Fulton, L. Galbany, C. Gall, H. Gao, J. García-Rojas, G. Ghirlanda, S. Giarratana, J. H. Gillanders, M. Giroletti, B. P. Gompertz, M. Gromadzki, K. E. Heintz, J. Hjorth, Y. D. Hu, M. E. Huber, A. Inkenhaag, L. Izzo, Z. P. Jin, P. G. Jonker, D. A. Kann, E. C. Kool, R. Kotak, G. Leloudas, A. J. Levan, C. C. Lin, J. D. Lyman, E. A. Magnier, K. Maguire, I. Mandel, B. Marcote, D. Mata Sánchez, S. Mattila, A. Melandri, M. J. Michałowski, J. Moldon, M. Nicholl, A. Nicuesa Guelbenzu, S. R. Oates, F. Onori, M. Orienti, R. Paladino, Z. Paragi, M. Perez-Torres, E. Pian, G. Pignata, S. Piranomonte, J. Quirola-Vásquez, F. Ragosta, A. Rau, S. Ronchini, A. Rossi, R. Sánchez-Ramírez, O. S. Salafia, S. Schulze, S. J. Smartt, K. W. Smith, J. Sollerman, S. Srivastav, R. L. C. Starling, D. Steeghs, H. F. Stevance, N. R. Tanvir, V. Testa, M. A. P. Torres, A. Valeev, S. D. Vergani, D. Vescovi, R. Wainscost, D. Watson, K. Wiersema, Ł. Wyrzykowski, J. Yang, S. Yang, and D. R. Young. Panning for gold, but finding helium: Discovery of the ultra-stripped supernova SN 2019wxt from gravitational-wave follow-up observations. *A&A*, 675:A201, July 2023. doi: 10.1051/0004-6361/202244751.

C. P. Ahn, R. Alexandroff, C. Allende Prieto, S. F. Anderson, T. Anderton, B. H. Andrews, É. Aubourg, S. Bailey, E. Balbinot, R. Barnes, and et al. The Ninth Data Release of the Sloan Digital Sky Survey: First Spectroscopic Data from the SDSS-III Baryon Oscillation Spectroscopic Survey. *ApJS*, 203:21, Dec. 2012. doi: 10.1088/0067-0049/203/2/21.

B. Ailawadhi, R. Dastidar, K. Misra, R. Roy, D. Hiramatsu, D. A. Howell, T. G. Brink, W. Zheng, L. Galbany, M. Shahbandeh, I. Arcavi, C. Ashall, K. A. Bostroem, J. Burke, T. Chapman, Dimple, A. V. Filippenko, A. Gangopadhyay, A. Ghosh, A. M. Hoffman, G. Hosseinzadeh, C. Jennings, V. K. Jha, A. Kumar, E. Karamehmetoglu, C. McCully, E. McGinness, T. E. Müller-Bravo, Y. S. Murakami, S. B. Pandey, C. Pellegrino, L. Piscarreta, J. Rho, M. Stritzinger, J. Sunseri, S. D. Van Dyk, and L. Yadav. Photometric and spectroscopic analysis of the Type II SN 2020jfo with a short plateau. *MNRAS*, 519(1):248–270, Feb. 2023. doi: 10.1093/mnras/stac3234.

S. Ambikasaran, D. Foreman-Mackey, L. Greengard, D. W. Hogg, and M. O'Neil. Fast Direct Methods for Gaussian Processes. *IEEE Transactions on Pattern Analysis and Machine Intelligence*, 38:252, June 2015. doi: 10.1109/TPAMI.2015.2448083.

J. P. Anderson. A meta-analysis of core-collapse supernova ^{56}Ni masses. *A&A*, 628: A7, Aug. 2019. doi: 10.1051/0004-6361/201935027.

J. P. Anderson, L. Dessart, C. P. Gutierrez, M. Hamuy, N. I. Morrell, M. Phillips, G. Folatelli, M. D. Stritzinger, W. L. Freedman, S. González-Gaitán, P. McCarthy, N. Suntzeff, and J. Thomas-Osip. Analysis of blueshifted emission peaks in Type II supernovae. *MNRAS*, 441(1):671–680, June 2014a. doi: 10.1093/mnras/stu610.

J. P. Anderson, S. González-Gaitán, M. Hamuy, C. P. Gutiérrez, M. D. Stritzinger, F. Olivares E., M. M. Phillips, S. Schulze, R. Antezana, L. Bolt, A. Campillay, S. Castellón, C. Contreras, T. de Jaeger, G. Folatelli, F. Förster, W. L. Freedman, L. González, E. Hsiao, W. Krzemiński, K. Krisciunas, J. Maza, P. McCarthy, N. I. Morrell, S. E. Persson, M. Roth, F. Salgado, N. B. Suntzeff, and J. Thomas-Osip. Characterizing the V-band Light-curves of Hydrogen-rich Type II Supernovae. *ApJ*, 786(1):67, May 2014b. doi: 10.1088/0004-637X/786/1/67.

J. P. Anderson, L. Dessart, C. P. Gutiérrez, T. Krühler, L. Galbany, A. Jerkstrand, S. J. Smartt, C. Contreras, N. Morrell, M. M. Phillips, M. D. Stritzinger, E. Y. Hsiao, S. González-Gaitán, C. Agliozzo, S. Castellón, K. C. Chambers, T.-W. Chen, H. Flewelling, C. Gonzalez, G. Hosseinzadeh, M. Huber, M. Fraser, C. Inserra, E. Kankare, S. Mattila, E. Magnier, K. Maguire, T. B. Lowe, J. Sollerman, M. Sullivan, D. R. Young, and S. Valenti. The lowest-metallicity type II supernova from the highest-mass red supergiant progenitor. *Nature Astronomy*, 2:574–579, May 2018. doi: 10.1038/s41550-018-0458-4.

I. Andreoni, M. W. Coughlin, E. C. Kool, M. M. Kasliwal, H. Kumar, V. Bhalerao, A. S. Carracedo, A. Y. Q. Ho, P. T. H. Pang, D. Saraogi, K. Sharma, V. Shenoy, E. Burns, T. Ahumada, S. Anand, L. P. Singer, D. A. Perley, K. De, U. C. Fremling, E. C. Bellm, M. Bulla, A. Crellin-Quick, T. Dietrich, A. Drake, D. A. Duev, A. Goobar, M. J. Graham, D. L. Kaplan, S. R. Kulkarni, R. R. Laher, A. A. Mahabal, D. L. Shupe, J. Sollerman, R. Walters, and Y. Yao. Fast-transient Searches in Real Time with ZTFReST: Identification of Three Optically Discovered Gamma-Ray Burst Afterglows and New Constraints on the Kilonova Rate. *ApJ*, 918(2): 63, Sept. 2021. doi: 10.3847/1538-4357/ac0bc7.

J. E. Andrews and N. Smith. Strong late-time circumstellar interaction in the peculiar supernova iPTF14hls. *MNRAS*, 477(1):74–79, June 2018. doi: 10.1093/mnras/sty584.

J. E. Andrews, B. E. K. Sugerman, G. C. Clayton, J. S. Gallagher, M. J. Barlow, J. Clem, B. Ercolano, J. Fabbri, M. Meixner, M. Otsuka, D. L. Welch, and R. Wesson. Photometric and Spectroscopic Evolution of the IIP SN 2007it to Day 944. *ApJ*, 731(1):47, Apr. 2011. doi: 10.1088/0004-637X/731/1/47.

J. E. Andrews, J. Pearson, G. Hosseinzadeh, K. A. Bostroem, Y. Dong, M. Shrestha, J. E. Jencson, D. J. Sand, S. Valenti, E. Hoang, D. Janzen, M. J. Lundquist, N. Meza, S. Wyatt, S. W. Jha, C. Simpson, J. Farah, E. Padilla Gonzalez, D. A.

Howell, C. McCully, M. Newsome, C. Pellegrino, and G. Terreran. SN 2022jox: An Extraordinarily Ordinary Type II SN with Flash Spectroscopy. *ApJ*, 965(1): 85, Apr. 2024. doi: 10.3847/1538-4357/ad2a49.

A. Antoni and E. Quataert. Numerical simulations of the random angular momentum in convection - II. Delayed explosions of red supergiants following 'failed' supernovae. *MNRAS*, 525(1):1229–1245, Oct. 2023. doi: 10.1093/mnras/stad2328.

A. Antoni, Y.-F. Jiang, and E. Quataert. Radiation Hydrodynamic Simulations of Low-Energy Explosions of Red and Yellow Supergiants. *arXiv e-prints*, art. arXiv:2509.16308, Sept. 2025. doi: 10.48550/arXiv.2509.16308.

G. C. Anupama, D. K. Sahu, U. K. Gurugubelli, T. P. Prabhu, N. Tominaga, M. Tanaka, and K. Nomoto. Optical photometry and spectroscopy of the Type Ibn supernova SN 2006jc until the onset of dust formation. *MNRAS*, 392(2):894–903, Jan. 2009. doi: 10.1111/j.1365-2966.2008.14129.x.

I. Arcavi, A. Gal-Yam, O. Yaron, A. Sternberg, I. Rabinak, E. Waxman, M. M. Kasliwal, R. M. Quimby, E. O. Ofek, A. Horesh, S. R. Kulkarni, A. V. Filippenko, J. M. Silverman, S. B. Cenko, W. Li, J. S. Bloom, M. Sullivan, P. E. Nugent, D. Poznanski, E. Gorbikov, B. J. Fulton, D. A. Howell, D. Bersier, A. Riou, S. Lamotte-Bailey, T. Griga, J. G. Cohen, S. Hachinger, D. Polishook, D. Xu, S. Ben-Ami, I. Manulis, E. S. Walker, K. Maguire, Y.-C. Pan, T. Matheson, P. A. Mazzali, E. Pian, D. B. Fox, N. Gehrels, N. Law, P. James, J. M. Marchant, R. J. Smith, C. J. Mottram, R. M. Barnsley, M. T. Kandrashoff, and K. I. Clubb. SN 2011dh: Discovery of a Type IIb Supernova from a Compact Progenitor in the Nearby Galaxy M51. *ApJ*, 742(2):L18, Dec. 2011. doi: 10.1088/2041-8205/742/2/L18.

I. Arcavi, A. Gal-Yam, S. B. Cenko, D. B. Fox, D. C. Leonard, D.-S. Moon, D. J. Sand, A. M. Soderberg, M. Kiewe, O. Yaron, A. B. Becker, R. Scheps, G. Birenbaum, D. Chamudot, and J. Zhou. Caltech Core-Collapse Project (CCCP) Observations of Type II Supernovae: Evidence for Three Distinct Photometric Subtypes. *ApJ*, 756(2):L30, Sept. 2012. doi: 10.1088/2041-8205/756/2/L30.

W. D. Arnett and C. Meakin. Toward Realistic Progenitors of Core-collapse Supernovae. *ApJ*, 733(2):78, June 2011. doi: 10.1088/0004-637X/733/2/78.

W. D. Arnett, J. N. Bahcall, R. P. Kirshner, and S. E. Woosley. Supernova 1987A. *ARA&A*, 27:629–700, 1989. doi: 10.1146/annurev.aa.27.090189.003213.

M. Asplund, N. Grevesse, A. J. Sauval, and P. Scott. The Chemical Composition of the Sun. *ARA&A*, 47(1):481–522, Sept. 2009. doi: 10.1146/annurev.astro.46.060407.145222.

Astropy Collaboration, T. P. Robitaille, E. J. Tollerud, P. Greenfield, M. Droettboom, E. Bray, T. Aldcroft, M. Davis, A. Ginsburg, A. M. Price-Whelan, W. E. Kerzendorf, A. Conley, N. Crighton, K. Barbary, D. Muna, H. Ferguson, F. Grollier,

M. M. Parikh, P. H. Nair, H. M. Unther, C. Deil, J. Woillez, S. Conseil, R. Kramer, J. E. H. Turner, L. Singer, R. Fox, B. A. Weaver, V. Zabalza, Z. I. Edwards, K. Azalee Bostroem, D. J. Burke, A. R. Casey, S. M. Crawford, N. Dencheva, J. Ely, T. Jenness, K. Labrie, P. L. Lim, F. Pierfederici, A. Pontzen, A. Ptak, B. Refsdal, M. Servillat, and O. Streicher. Astropy: A community Python package for astronomy. *A&A*, 558:A33, Oct. 2013. doi: 10.1051/0004-6361/201322068.

S. Balberg, L. Zampieri, and S. L. Shapiro. Black Hole Emergence in Supernovae. *ApJ*, 541(2):860–882, Oct. 2000. doi: 10.1086/309472.

C. Barbarino, M. T. Botticella, M. Dall'Ora, M. Della Valle, S. Benetti, J. D. Lyman, S. J. Smartt, I. Arcavi, C. Baltay, D. Bersier, M. Dennefeld, N. Ellman, M. Fraser, A. Gal-Yam, G. Hosseinzadeh, D. A. Howell, C. Inserra, E. Kankare, G. Leloudas, K. Maguire, C. McCully, A. Mitra, R. McKinnon, F. Olivares E., G. Pignata, D. Rabinowitz, S. Rostami, K. W. Smith, M. Sullivan, S. Valenti, O. Yaron, and D. Young. LSQ14efd: observations of the cooling of a shock break-out event in a type Ic Supernova. *MNRAS*, 471(2):2463–2480, Oct. 2017. doi: 10.1093/mnras/stx1709.

C. Barbarino, J. Sollerman, F. Taddia, C. Fremling, E. Karamehmetoglu, I. Arcavi, A. Gal-Yam, R. Laher, S. Schulze, P. Wozniak, and L. Yan. Type Ic supernovae from the (intermediate) Palomar Transient Factory. *A&A*, 651:A81, July 2021. doi: 10.1051/0004-6361/202038890.

B. L. Barker, C. E. Harris, M. L. Warren, E. P. O'Connor, and S. M. Couch. Connecting the Light Curves of Type IIP Supernovae to the Properties of Their Progenitors. *ApJ*, 934(1):67, July 2022a. doi: 10.3847/1538-4357/ac77f3.

B. L. Barker, C. E. Harris, M. L. Warren, E. P. O'Connor, and S. M. Couch. Connecting the Light Curves of Type IIP Supernovae to the Properties of Their Progenitors. *ApJ*, 934(1):67, July 2022b. doi: 10.3847/1538-4357/ac77f3.

S. Barmentloo, A. Jerkstrand, K. Iwamoto, I. Hachisu, K. Nomoto, J. Sollerman, and S. Woosley. Nebular nitrogen line emission in stripped-envelope supernovae - a new progenitor mass diagnostic. *MNRAS*, 533(2):1251–1280, Sept. 2024. doi: 10.1093/mnras/stae1811.

R. M. Barnsley, R. J. Smith, and I. A. Steele. A fully automated data reduction pipeline for the FRODOSpec integral field spectrograph. *Astronomische Nachrichten*, 333(2):101–117, Feb. 2012. doi: 10.1002/asna.201111634.

E. C. Bellm and B. Sesar. pyraf-dbsp: Reduction pipeline for the Palomar Double Beam Spectrograph. Astrophysics Source Code Library, Feb. 2016.

E. C. Bellm, S. R. Kulkarni, T. Barlow, U. Feindt, M. J. Graham, A. Goobar, T. Kupfer, C.-C. Ngeow, P. Nugent, E. Ofek, T. A. Prince, R. Riddle, R. Walters, and Q.-Z. Ye. The Zwicky Transient Facility: Surveys and Scheduler. *PASP*, 131 (6):068003, June 2019a. doi: 10.1088/1538-3873/ab0c2a.

E. C. Bellm, S. R. Kulkarni, M. J. Graham, R. Dekany, R. M. Smith, R. Riddle, F. J. Masci, G. Helou, T. A. Prince, S. M. Adams, C. Barbarino, T. Barlow, J. Bauer, R. Beck, J. Belicki, R. Biswas, N. Blagorodnova, D. Bodewits, B. Bolin, V. Brinnel, T. Brooke, B. Bue, M. Bulla, R. Burruss, S. B. Cenko, C.-K. Chang, A. Connolly, M. Coughlin, J. Cromer, V. Cunningham, K. De, A. Delacroix, V. Desai, D. A. Duev, G. Eadie, T. L. Farnham, M. Feeney, U. Feindt, D. Flynn, A. Franckowiak, S. Frederick, C. Fremling, A. Gal-Yam, S. Gezari, M. Giomi, D. A. Goldstein, V. Z. Golkhou, A. Goobar, S. Groom, E. Hacopians, D. Hale, J. Henning, A. Y. Q. Ho, D. Hover, J. Howell, T. Hung, D. Huppenkothen, D. Imel, W.-H. Ip, Ž. Ivezić, E. Jackson, L. Jones, M. Juric, M. M. Kasliwal, S. Kaspi, S. Kaye, M. S. P. Kelley, M. Kowalski, E. Kramer, T. Kupfer, W. Landry, R. R. Laher, C.-D. Lee, H. W. Lin, Z.-Y. Lin, R. Lunnan, M. Giomi, A. Mahabal, P. Mao, A. A. Miller, S. Monkewitz, P. Murphy, C.-C. Ngeow, J. Nordin, P. Nugent, E. Ofek, M. T. Patterson, B. Penprase, M. Porter, L. Rauch, U. Rebbapragada, D. Reiley, M. Rigault, H. Rodriguez, J. van Roestel, B. Rusholme, J. van Santen, S. Schulze, D. L. Shupe, L. P. Singer, M. T. Soumagnac, R. Stein, J. Surace, J. Sollerman, P. Szkody, F. Taddia, S. Terek, A. Van Sistine, S. van Velzen, W. T. Vestrand, R. Walters, C. Ward, Q.-Z. Ye, P.-C. Yu, L. Yan, and J. Zolkower. The Zwicky Transient Facility: System Overview, Performance, and First Results. *PASP*, 131(995):018002, Jan. 2019b. doi: 10.1088/1538-3873/aaecbe.

S. Ben-Ami, A. Gal-Yam, P. A. Mazzali, O. Gnat, M. Modjaz, I. Rabinak, M. Sullivan, L. Bildsten, D. Poznanski, O. Yaron, I. Arcavi, J. S. Bloom, A. Horesh, M. M. Kasliwal, S. R. Kulkarni, P. E. Nugent, E. O. Ofek, D. Perley, R. Quimby, and D. Xu. SN 2010mb: Direct Evidence for a Supernova Interacting with a Large Amount of Hydrogen-free Circumstellar Material. *ApJ*, 785(1):37, Apr. 2014. doi: 10.1088/0004-637X/785/1/37.

S. Benetti, M. Turatto, S. Balberg, L. Zampieri, S. L. Shapiro, E. Cappellaro, K. Nomoto, T. Nakamura, P. A. Mazzali, and F. Patat. The fading of supernova 1997D. *MNRAS*, 322(2):361–368, Apr. 2001. doi: 10.1046/j.1365-8711.2001.04122.x.

M. C. Bersten and M. Hamuy. Bolometric Light Curves for 33 Type II Plateau Supernovae. *ApJ*, 701(1):200–208, Aug. 2009. doi: 10.1088/0004-637X/701/1/200.

L. Bildsten, K. J. Shen, N. N. Weinberg, and G. Nelemans. Faint Thermonuclear Supernovae from AM Canum Venaticorum Binaries. *ApJ*, 662(2):L95–L98, June 2007. doi: 10.1086/519489.

R. Biswas et al. Two c's in a pod: cosmology-independent measurement of the type ia supernova colour-luminosity relation with a sibling pair. *MNRAS*, 509: 5340–5354, 2022.

C. S. Black, D. Milisavljevic, R. Margutti, R. A. Fesen, D. Patnaude, and S. Parker. The Transition of a Type IIL Supernova into a Supernova Remnant: Late-time

Observations of SN 2013by. *ApJ*, 848(1):5, Oct. 2017. doi: 10.3847/1538-4357/aa8999.

N. Blagorodnova, J. D. Neill, R. Walters, S. R. Kulkarni, C. Fremling, S. Ben-Ami, R. G. Dekany, J. R. Fucik, N. Konidaris, R. Nash, C.-C. Ngeow, E. O. Ofek, D. O' Sullivan, R. Quimby, A. Ritter, and K. E. Vyhmeister. The SED Machine: A Robotic Spectrograph for Fast Transient Classification. *PASP*, 130(3):035003, Mar. 2018. doi: 10.1088/1538-3873/aaa53f.

E. L. Blanton, B. P. Schmidt, R. P. Kirshner, C. H. Ford, F. R. Chromey, and W. Herbst. Observations of the Type II-P SN 1991G in NGC 4088. *AJ*, 110:2868, Dec. 1995. doi: 10.1086/117735.

M. R. Blanton and S. Roweis. K-Corrections and Filter Transformations in the Ultraviolet, Optical, and Near-Infrared. *AJ*, 133(2):734–754, Feb 2007. doi: 10.1086/510127.

S. Blondin and J. L. Tonry. Determining the Type, Redshift, and Phase of a Supernova Spectrum. In T. di Salvo, G. L. Israel, L. Piersant, L. Burderi, G. Matt, A. Tornambe, and M. T. Menna, editors, *The Multicolored Landscape of Compact Objects and Their Explosive Origins*, volume 924 of *American Institute of Physics Conference Series*, pages 312–321, Aug. 2007. doi: 10.1063/1.2774875.

R. Bollig, N. Yadav, D. Kresse, H.-T. Janka, B. Müller, and A. Heger. Self-consistent 3D Supernova Models From -7 Minutes to +7 s: A 1-bethe Explosion of a 19 $M_\odot$ Progenitor. *ApJ*, 915(1):28, July 2021. doi: 10.3847/1538-4357/abf82e.

M. Boquien, D. Burgarella, Y. Roehlly, V. Buat, L. Ciesla, D. Corre, A. K. Inoue, and H. Salas. CIGALE: a python Code Investigating GALaxy Emission. *A&A*, 622:A103, Feb. 2019. doi: 10.1051/0004-6361/201834156.

E. Bordier, A. J. Frost, H. Sana, M. Reggiani, A. Mérand, A. Rainot, M. C. Ramírez-Tannus, and W. J. de Wit. The origin of close massive binaries in the M17 star-forming region. *A&A*, 663:A26, July 2022. doi: 10.1051/0004-6361/202141849.

S. Bose, B. Kumar, F. Sutaria, B. Kumar, R. Roy, V. K. Bhatt, S. B. Pandey, H. C. Chandola, R. Sagar, K. Misra, and S. Chakraborti. Supernova 2012aw - a high-energy clone of archetypal Type IIP SN 1999em. *MNRAS*, 433(3):1871–1891, Aug. 2013. doi: 10.1093/mnras/stt864.

S. Bose, F. Sutaria, B. Kumar, C. Duggal, K. Misra, P. J. Brown, M. Singh, V. Dwarkadas, D. G. York, S. Chakraborti, H. C. Chandola, J. Dahlstrom, A. Ray, and M. Safonova. SN 2013ej: A Type IIL Supernova with Weak Signs of Interaction. *ApJ*, 806(2):160, June 2015. doi: 10.1088/0004-637X/806/2/160.

K. A. Bostroem, S. Valenti, A. Horesh, V. Morozova, N. P. M. Kuin, S. Wyatt, A. Jerkstrand, D. J. Sand, M. Lundquist, M. Smith, M. Sullivan, G. Hosseinzadeh, I. Arcavi, E. Callis, R. Cartier, A. Gal-Yam, L. Galbany, C. Gutiérrez, D. A.

Howell, C. Inserra, E. Kankare, K. M. López, C. McCully, G. Pignata, A. L. Piro, Ó. Rodríguez, S. J. Smartt, K. W. Smith, O. Yaron, and D. R. Young. Signatures of circumstellar interaction in the Type IIL supernova ASASSN-15oz. *MNRAS*, 485(4):5120–5141, June 2019a. doi: 10.1093/mnras/stz570.

K. A. Bostroem, S. Valenti, A. Horesh, V. Morozova, N. P. M. Kuin, S. Wyatt, A. Jerkstrand, D. J. Sand, M. Lundquist, M. Smith, M. Sullivan, G. Hosseinzadeh, I. Arcavi, E. Callis, R. Cartier, A. Gal-Yam, L. Galbany, C. Gutiérrez, D. A. Howell, C. Inserra, E. Kankare, K. M. López, C. McCully, G. Pignata, A. L. Piro, Ó. Rodríguez, S. J. Smartt, K. W. Smith, O. Yaron, and D. R. Young. Signatures of circumstellar interaction in the Type IIL supernova ASASSN-15oz. *MNRAS*, 485(4):5120–5141, June 2019b. doi: 10.1093/mnras/stz570.

K. A. Bostroem, L. Dessart, D. J. Hillier, M. Lundquist, J. E. Andrews, D. J. Sand, Y. Dong, S. Valenti, J. Haislip, E. T. Hoang, G. Hosseinzadeh, D. Janzen, J. E. Jencson, S. W. Jha, V. Kouprianov, J. Pearson, N. E. Meza Retamal, D. E. Reichart, M. Shrestha, C. Ashall, E. Baron, P. J. Brown, J. M. DerKacy, J. Farah, L. Galbany, J. I. González Hernández, E. Green, P. Hoeflich, D. A. Howell, L. A. Kwok, C. McCully, T. E. Müller-Bravo, M. Newsome, E. P. Gonzalez, C. Pellegrino, J. Rho, M. Rowe, M. Schwab, M. Shahbandeh, N. Smith, J. Strader, G. Terreran, S. D. Van Dyk, and S. Wyatt. SN 2022acko: The First Early Far-ultraviolet Spectra of a Type IIP Supernova. *ApJ*, 953(2):L18, Aug. 2023. doi: 10.3847/2041-8213/ace31c.

M. T. Botticella, A. Pastorello, S. J. Smartt, W. P. S. Meikle, S. Benetti, R. Kotak, E. Cappellaro, R. M. Crockett, S. Mattila, M. Sereno, F. Patat, D. Tsvetkov, J. T. van Loon, D. Abraham, I. Agnoletto, R. Arbour, C. Benn, G. di Rico, N. Elias-Rosa, D. L. Gorshanov, A. Harutyunyan, D. Hunter, V. Lorenzi, F. P. Keenan, K. Maguire, J. Mendez, M. Mobberley, H. Navasardyan, C. Ries, V. Stanishev, S. Taubenberger, C. Trundle, M. Turatto, and I. M. Volkov. SN 2008S: an electron-capture SN from a super-AGB progenitor? *MNRAS*, 398(3):1041–1068, Sept. 2009. doi: 10.1111/j.1365-2966.2009.15082.x.

M. T. Botticella, S. J. Smartt, R. C. Kennicutt, E. Cappellaro, M. Sereno, and J. C. Lee. A comparison between star formation rate diagnostics and rate of core collapse supernovae within 11 Mpc. *A&A*, 537:A132, Jan. 2012. doi: 10.1051/0004-6361/201117343.

S. J. Brennan, J. Sollerman, I. Irani, S. Schulze, P. Chen, K. K. Das, K. De, C. Fransson, A. Gal-Yam, A. Gkini, K. R. Hinds, R. Lunnan, D. Perley, Y. J. Qin, R. Stein, J. Wise, L. Yan, E. A. Zimmerman, S. Anand, R. J. Bruch, R. Dekany, A. J. Drake, C. Fremling, B. Healy, V. Karambelkar, M. M. Kasliwal, M. Kong, S. R. Kulkarni, F. J. Masci, R. S. Post, J. Purdum, R. M. Rich, and A. Wold. Spectroscopic observations of progenitor activity 100 days before a Type Ibn supernova. *A&A*, 684:L18, Apr. 2024. doi: 10.1051/0004-6361/202449350.

D. Brethauer, R. Margutti, D. Milisavljevic, M. F. Bietenholz, R. Chornock, D. L. Coppejans, F. D. Colle, A. Hajela, G. Terreran, F. Vargas, L. DeMarchi, C. Harris, W. V. Jacobson-Galán, A. Kamble, D. Patnaude, and M. C. Stroh. Seven Years of Coordinated Chandra-NuSTAR Observations of SN 2014C Unfold the Extreme Mass-loss History of Its Stellar Progenitor. *ApJ*, 939(2):105, Nov. 2022. doi: 10.3847/1538-4357/ac8b14.

T. M. Brown, N. Baliber, F. B. Bianco, M. Bowman, B. Burleson, P. Conway, M. Crellin, É. Depagne, J. De Vera, B. Dilday, D. Dragomir, M. Dubberley, J. D. Eastman, M. Elphick, M. Falarski, S. Foale, M. Ford, B. J. Fulton, J. Garza, E. L. Gomez, M. Graham, R. Greene, B. Haldeman, E. Hawkins, B. Haworth, R. Haynes, M. Hidas, A. E. Hjelstrom, D. A. Howell, J. Hygelund, T. A. Lister, R. Lobdill, J. Martinez, D. S. Mullins, M. Norbury, J. Parrent, R. Paulson, D. L. Petry, A. Pickles, V. Posner, W. E. Rosing, R. Ross, D. J. Sand, E. S. Saunders, J. Shobbrook, A. Shporer, R. A. Street, D. Thomas, Y. Tsapras, J. R. Tufts, S. Valenti, K. Vander Horst, Z. Walker, G. White, and M. Willis. Las Cumbres Observatory Global Telescope Network. *PASP*, 125(931):1031, Sept. 2013. doi: 10.1086/673168.

R. J. Bruch, A. Gal-Yam, S. Schulze, O. Yaron, Y. Yang, M. Soumagnac, M. Rigault, N. L. Strotjohann, E. Ofek, J. Sollerman, F. J. Masci, C. Barbarino, A. Y. Q. Ho, C. Fremling, D. Perley, J. Nordin, S. B. Cenko, S. Adams, I. Adreoni, E. C. Bellm, N. Blagorodnova, M. Bulla, K. Burdge, K. De, S. Dhawan, A. J. Drake, D. A. Duev, A. Dugas, M. Graham, M. L. Graham, I. Irani, J. Jencson, E. Karamehmetoglu, M. Kasliwal, Y.-L. Kim, S. Kulkarni, T. Kupfer, J. Liang, A. Mahabal, A. A. Miller, T. A. Prince, R. Riddle, Y. Sharma, R. Smith, F. Taddia, K. Taggart, R. Walters, and L. Yan. A Large Fraction of Hydrogen-rich Supernova Progenitors Experience Elevated Mass Loss Shortly Prior to Explosion. *ApJ*, 912 (1):46, May 2021. doi: 10.3847/1538-4357/abef05.

R. J. Bruch, A. Gal-Yam, O. Yaron, P. Chen, N. L. Strotjohann, I. Irani, E. Zimmerman, S. Schulze, Y. Yang, Y.-L. Kim, M. Bulla, J. Sollerman, M. Rigault, E. Ofek, M. Soumagnac, F. J. Masci, C. Fremling, D. Perley, J. Nordin, S. B. Cenko, A. Y. Q. Ho, S. Adams, I. Adreoni, E. C. Bellm, N. Blagorodnova, K. Burdge, K. De, R. G. Dekany, S. Dhawan, A. J. Drake, D. A. Duev, M. Graham, M. L. Graham, J. Jencson, E. Karamehmetoglu, M. M. Kasliwal, S. Kulkarni, A. A. Miller, J. D. Neill, T. A. Prince, R. Riddle, B. Rusholme, Y. Sharma, R. Smith, N. Sravan, K. Taggart, R. Walters, and L. Yan. The Prevalence and Influence of Circumstellar Material around Hydrogen-rich Supernova Progenitors. *ApJ*, 952 (2):119, Aug. 2023. doi: 10.3847/1538-4357/acd8be.

S. W. Bruenn, E. J. Lentz, W. R. Hix, A. Mezzacappa, J. A. Harris, O. E. B. Messer, E. Endeve, J. M. Blondin, M. A. Chertkow, E. J. Lingerfelt, P. Marronetti, and K. N. Yakunin. The Development of Explosions in Axisymmetric Ab Initio Core-collapse Supernova Simulations of 12-25 M Stars. *ApJ*, 818(2):123, Feb. 2016. doi: 10.3847/0004-637X/818/2/123.

S. W. Bruenn, A. Sieverding, E. J. Lentz, T. Sukhbold, W. R. Hix, L. N. Huk, J. A. Harris, O. E. B. Messer, and A. Mezzacappa. Comparison of the Core-collapse Evolution of Two Nearly Equal-mass Progenitors. *ApJ*, 947(1):35, Apr. 2023. doi: 10.3847/1538-4357/acbb65.

G. Bruzual and S. Charlot. Stellar population synthesis at the resolution of 2003. *MNRAS*, 344:1000–1028, Oct. 2003. doi: 10.1046/j.1365-8711.2003.06897.x.

F. Bufano, S. Benetti, M. Turatto, L. Zampieri, A. Gal-Yam, A. Pastorello, N. Elias-Rosa, M. Dolci, G. Valentini, and E. Cappellaro. Type II-Plateau Supernova 2005ay: an extensive study from Ultraviolet to Near-Infrared. In T. di Salvo, G. L. Israel, L. Piersant, L. Burderi, G. Matt, A. Tornambe, and M. T. Menna, editors, *The Multicolored Landscape of Compact Objects and Their Explosive Origins*, volume 924 of *American Institute of Physics Conference Series*, pages 271–276. AIP, Aug. 2007. doi: 10.1063/1.2774869.

D. Burgarella, V. Buat, and J. Iglesias-Páramo. Star formation and dust attenuation properties in galaxies from a statistical ultraviolet-to-far-infrared analysis. *MNRAS*, 360(4):1413–1425, July 2005. doi: 10.1111/j.1365-2966.2005.09131.x.

A. Burrows and D. Vartanyan. Core-collapse supernova explosion theory. *Nature*, 589(7840):29–39, Jan. 2021. doi: 10.1038/s41586-020-03059-w.

A. Burrows, D. Radice, and D. Vartanyan. Three-dimensional supernova explosion simulations of 9-, 10-, 11-, 12-, and 13-$M_\odot$ stars. *MNRAS*, 485(3):3153–3168, May 2019. doi: 10.1093/mnras/stz543.

A. Burrows, D. Radice, D. Vartanyan, H. Nagakura, M. A. Skinner, and J. C. Dolence. The overarching framework of core-collapse supernova explosions as revealed by 3D FORNAX simulations. *MNRAS*, 491(2):2715–2735, Jan. 2020. doi: 10.1093/mnras/stz3223.

A. Burrows, T. Wang, and D. Vartanyan. Physical Correlations and Predictions Emerging from Modern Core-collapse Supernova Theory. *ApJ*, 964(1):L16, Mar. 2024. doi: 10.3847/2041-8213/ad319e.

Y. Z. Cai, A. Pastorello, M. Fraser, M. T. Botticella, N. Elias-Rosa, L. Z. Wang, R. Kotak, S. Benetti, E. Cappellaro, M. Turatto, A. Reguitti, S. Mattila, S. J. Smartt, C. Ashall, S. Benitez, T. W. Chen, A. Harutyunyan, E. Kankare, P. Lundqvist, P. A. Mazzali, A. Morales-Garoffolo, P. Ochner, G. Pignata, S. J. Prentice, T. M. Reynolds, X. W. Shu, M. D. Stritzinger, L. Tartaglia, G. Terreran, L. Tomasella, S. Valenti, G. Valerin, G. J. Wang, X. F. Wang, L. Borsato, E. Callis, G. Cannizzaro, S. Chen, E. Congiu, M. Ergon, L. Galbany, A. Gal-Yam, X. Gao, M. Gromadzki, S. Holmbo, F. Huang, C. Inserra, K. Itagaki, Z. Kostrzewa-Rutkowska, K. Maguire, S. Margheim, S. Moran, F. Onori, A. Sagués Carracedo, K. W. Smith, J. Sollerman, A. Somero, B. Wang, and D. R. Young. Intermediate-luminosity red transients: Spectrophotometric properties

and connection to electron-capture supernova explosions. *A&A*, 654:A157, Oct. 2021. doi: 10.1051/0004-6361/202141078.

E. Callis, M. Fraser, A. Pastorello, S. Dong, S. J. Brennan, P. Chen, S. Bose, T. Reynolds, L. Salmon, P. Jonker, S. Benetti, M. Berton, G. Cannizzaro, E. Cappellaro, E. Congiu, S. Dyrbye, D. Eappachen, N. Elias-Rosa, M. Gromadzki, C. P. Gutiérrez, S. Holmbo, T. W. S. Holoien, K. Itagaki, E. Kankare, S. Mattila, R. Mutel, P. Ochner, R. S. Post, J. Prieto, A. Reguitti, T. Roth, J. Ryon, A. Sagués-Carracedo, B. J. Shappee, A. Siviero, K. G. Stassun, M. Stritzinger, L. Tomasella, S. Villanueva, Jr., T. Wevers, and P. Wiggins. How low can you go? SN 2018zd as a low-mass Fe core-collapse supernova. *arXiv e-prints*, art. arXiv:2109.12943, Sept. 2021. doi: 10.48550/arXiv.2109.12943.

D. Calzetti, L. Armus, R. C. Bohlin, A. L. Kinney, J. Koornneef, and T. Storchi-Bergmann. The Dust Content and Opacity of Actively Star-forming Galaxies. *ApJ*, 533:682–695, Apr. 2000a. doi: 10.1086/308692.

D. Calzetti, L. Armus, R. C. Bohlin, A. L. Kinney, J. Koornneef, and T. Storchi-Bergmann. The Dust Content and Opacity of Actively Star-forming Galaxies. *ApJ*, 533(2):682–695, Apr. 2000b. doi: 10.1086/308692.

E. Cappellaro, M. T. Botticella, G. Pignata, A. Grado, L. Greggio, L. Limatola, M. Vaccari, A. Baruffolo, S. Benetti, F. Bufano, M. Capaccioli, E. Cascone, G. Covone, D. De Cicco, S. Falocco, M. Della Valle, M. Jarvis, L. Marchetti, N. R. Napolitano, M. Paolillo, A. Pastorello, M. Radovich, P. Schipani, S. Spiro, L. Tomasella, and M. Turatto. Supernova rates from the SUDARE VST-OmegaCAM search. I. Rates per unit volume. *A&A*, 584:A62, Dec. 2015. doi: 10.1051/0004-6361/201526712.

J. A. Cardelli, G. C. Clayton, and J. S. Mathis. The Relationship between Infrared, Optical, and Ultraviolet Extinction. *ApJ*, 345:245, Oct. 1989. doi: 10.1086/167900.

S. B. Cenko, D. B. Fox, D.-S. Moon, F. A. Harrison, S. R. Kulkarni, J. R. Henning, C. D. Guzman, M. Bonati, R. M. Smith, R. P. Thicksten, M. W. Doyle, H. L. Petrie, A. Gal-Yam, A. M. Soderberg, N. L. Anagnostou, and A. C. Laity. The Automated Palomar 60 Inch Telescope. *PASP*, 118:1396–1406, Oct. 2006. doi: 10.1086/508366.

G. Chabrier. Galactic Stellar and Substellar Initial Mass Function. *PASP*, 115:763–795, July 2003. doi: 10.1086/376392.

K. C. Chambers, E. A. Magnier, N. Metcalfe, H. A. Flewelling, M. E. Huber, C. Z. Waters, L. Denneau, P. W. Draper, D. Farrow, D. P. Finkbeiner, C. Holmberg, J. Koppenhoefer, P. A. Price, A. Rest, R. P. Saglia, E. F. Schlafly, S. J. Smartt, W. Sweeney, R. J. Wainscoat, W. S. Burgett, S. Chastel, T. Grav, J. N. Heasley, K. W. Hodapp, R. Jedicke, N. Kaiser, R.-P. Kudritzki, G. A. Luppino, R. H. Lupton, D. G. Monet, J. S. Morgan, P. M. Onaka, B. Shiao, C. W. Stubbs, J. L. Tonry,

R. White, E. Bañados, E. F. Bell, R. Bender, E. J. Bernard, M. Boegner, F. Boffi, M. T. Botticella, A. Calamida, S. Casertano, W.-P. Chen, X. Chen, S. Cole, N. Deacon, C. Frenk, A. Fitzsimmons, S. Gezari, V. Gibbs, C. Goessl, T. Goggia, R. Gourgue, B. Goldman, P. Grant, E. K. Grebel, N. C. Hambly, G. Hasinger, A. F. Heavens, T. M. Heckman, R. Henderson, T. Henning, M. Holman, U. Hopp, W.-H. Ip, S. Isani, M. Jackson, C. D. Keyes, A. M. Koekemoer, R. Kotak, D. Le, D. Liska, K. S. Long, J. R. Lucey, M. Liu, N. F. Martin, G. Masci, B. McLean, E. Mindel, P. Misra, E. Morganson, D. N. A. Murphy, A. Obaika, G. Narayan, M. A. Nieto-Santisteban, P. Norberg, J. A. Peacock, E. A. Pier, M. Postman, N. Primak, C. Rae, A. Rai, A. Riess, A. Riffeser, H. W. Rix, S. Röser, R. Russel, L. Rutz, E. Schilbach, A. S. B. Schultz, D. Scolnic, L. Strolger, A. Szalay, S. Seitz, E. Small, K. W. Smith, D. R. Soderblom, P. Taylor, R. Thomson, A. N. Taylor, A. R. Thakar, J. Thiel, D. Thilker, D. Unger, Y. Urata, J. Valenti, J. Wagner, T. Walder, F. Walter, S. P. Watters, S. Werner, W. M. Wood-Vasey, and R. Wyse. The Pan-STARRS1 Surveys. *arXiv e-prints*, Dec. 2016.

E. Chatzopoulos, J. C. Wheeler, and J. Vinko. Generalized Semi-analytical Models of Supernova Light Curves. *ApJ*, 746(2):121, Feb. 2012. doi: 10.1088/0004-637X/746/2/121.

E. Chatzopoulos, J. C. Wheeler, J. Vinko, Z. L. Horvath, and A. Nagy. Analytical Light Curve Models of Superluminous Supernovae: χ^2-minimization of Parameter Fits. *ApJ*, 773(1):76, Aug. 2013. doi: 10.1088/0004-637X/773/1/76.

P. Chen, S. Dong, M. D. Stritzinger, S. Holmbo, J. Strader, C. S. Kochanek, E. W. Peng, S. Benetti, D. Bersier, S. Brownsberger, D. A. H. Buckley, M. Gromadzki, S. Moran, A. Pastorello, E. Aydi, S. Bose, T. Connor, K. Boutsia, F. Di Mille, N. Elias-Rosa, K. D. French, T. W. S. Holoien, S. Mattila, B. J. Shappee, A. A. Stark, and S. J. Swihart. The Most Rapidly Declining Type I Supernova 2019bkc/ATLAS19dqr. *ApJ*, 889(1):L6, Jan. 2020. doi: 10.3847/2041-8213/ab62a4.

R. A. Chevalier and C. M. Irwin. Shock Breakout in Dense Mass Loss: Luminous Supernovae. *ApJ*, 729(1):L6, Mar. 2011. doi: 10.1088/2041-8205/729/1/L6.

R. Chornock, A. V. Filippenko, W. Li, and J. M. Silverman. Large Late-Time Asphericities in Three Type IIP Supernovae. *ApJ*, 713(2):1363–1375, Apr. 2010. doi: 10.1088/0004-637X/713/2/1363.

P. Clark, K. Maguire, C. Inserra, S. Prentice, S. J. Smartt, C. Contreras, G. Hosseinizadeh, E. Y. Hsiao, E. Kankare, M. Kasliwal, P. Nugent, M. Shahbandeh, C. Baltay, D. Rabinowitz, I. Arcavi, C. Ashall, C. R. Burns, E. Callis, T.-W. Chen, T. Diamond, M. Fraser, D. A. Howell, E. Karamehmetoglu, R. Kotak, J. Lyman, N. Morrell, M. Phillips, G. Pignata, M. Pursiainen, J. Sollerman, M. Stritzinger, M. Sullivan, and D. Young. LSQ13ddu: a rapidly evolving stripped-envelope supernova with early circumstellar interaction signatures. *MNRAS*, 492(2):2208–2228, Feb. 2020. doi: 10.1093/mnras/stz3598.

A. Clocchiatti, S. Benetti, J. C. Wheeler, W. Wren, J. Boisseau, E. Cappellaro, M. Turatto, F. Patat, D. A. Swartz, R. P. Harkness, M. S. Brotherton, B. Wills, P. Hemenway, M. Cornell, M. Frueh, and M. B. Kaiser. A Study of SN 1992H in NGC 5377. *AJ*, 111:1286, Mar. 1996. doi: 10.1086/117874.

C. Colling, P. Hennebelle, S. Geen, O. Iffrig, and F. Bournaud. Impact of galactic shear and stellar feedback on star formation. *A&A*, 620:A21, Dec. 2018. doi: 10.1051/0004-6361/201833161.

D. O. Cook, M. M. Kasliwal, A. Van Sistine, D. L. Kaplan, J. S. Sutter, T. Kupfer, D. L. Shupe, R. R. Laher, F. J. Masci, D. A. Dale, B. Sesar, P. R. Brady, L. Yan, E. O. Ofek, D. H. Reitze, and S. R. Kulkarni. Census of the Local Universe (CLU) Narrowband Survey. I. Galaxy Catalogs from Preliminary Fields. *ApJ*, 880(1):7, July 2019. doi: 10.3847/1538-4357/ab2131.

D. O. Cook, J. M. Mazzarella, G. Helou, A. Alcala, T. X. Chen, R. Ebert, C. Frayer, J. Kim, T. Lo, B. F. Madore, P. M. Ogle, M. Schmitz, L. P. Singer, S. Terek, J. Valladon, and X. Wu. Completeness of the NASA/IPAC Extragalactic Database (NED) Local Volume Sample. *ApJS*, 268(1):14, Sept. 2023. doi: 10.3847/1538-4365/acdd06.

M. W. Coughlin, J. S. Bloom, G. Nir, S. Antier, T. J. du Laz, S. van der Walt, A. Crellin-Quick, T. Culino, D. A. Duev, D. A. Goldstein, B. F. Healy, V. Karambelkar, J. Lilleboe, K. M. Shin, L. P. Singer, T. Ahumada, S. Anand, E. C. Bellm, R. Dekany, M. J. Graham, M. M. Kasliwal, I. Kostadinova, R. W. Kiendrebeogo, S. R. Kulkarni, S. Jenkins, N. LeBaron, A. A. Mahabal, J. D. Neill, B. Parazin, J. Peloton, D. A. Perley, R. Riddle, B. Rusholme, J. van Santen, J. Sollerman, R. Stein, D. Turpin, A. Wold, C. Amat, A. Bonnefon, A. Bonnefoy, M. Flament, F. Kerkow, S. Kishore, S. Jani, S. K. Mahanty, C. Liu, L. Llinares, J. Makarison, A. Olliéric, I. Perez, L. Pont, and V. Sharma. A Data Science Platform to Enable Time-domain Astronomy. *ApJS*, 267(2):31, Aug. 2023. doi: 10.3847/1538-4365/acdee1.

R. M. Crockett, S. J. Smartt, A. Pastorello, J. J. Eldridge, A. W. Stephens, J. R. Maund, and S. Mattila. On the nature of the progenitors of three Type II-P supernovae: 2004et, 2006my and 2006ov. *MNRAS*, 410(4):2767–2786, Feb. 2011. doi: 10.1111/j.1365-2966.2010.17652.x.

P. A. Crowther. Physical Properties of Wolf-Rayet Stars. *ARA&A*, 45(1):177–219, Sept. 2007. doi: 10.1146/annurev.astro.45.051806.110615.

M. Curti, G. Cresci, F. Mannucci, A. Marconi, R. Maiolino, and S. Esposito. New fully empirical calibrations of strong-line metallicity indicators in star-forming galaxies. *MNRAS*, 465(2):1384–1400, Feb. 2017. doi: 10.1093/mnras/stw2766.

R. M. Cutri, E. L. Wright, T. Conrow, J. W. Fowler, P. R. M. Eisenhardt, C. Grillmair, J. D. Kirkpatrick, F. Masci, H. L. McCallon, S. L. Wheelock, S. Fajardo-Acosta, L. Yan, D. Benford, M. Harbut, T. Jarrett, S. Lake, D. Leisawitz, M. E. Ressler,

S. A. Stanford, C. W. Tsai, F. Liu, G. Helou, A. Mainzer, D. Gettings, A. Gonzalez, D. Hoffman, K. A. Marsh, D. Padgett, M. F. Skrutskie, R. P. Beck, M. Papin, and M. Wittman. Explanatory Supplement to the AllWISE Data Release Products. Technical report, Nov. 2013.

D. A. Dale, G. Helou, G. E. Magdis, L. Armus, T. Díaz-Santos, and Y. Shi. A Two-parameter Model for the Infrared/Submillimeter/Radio Spectral Energy Distributions of Galaxies and Active Galactic Nuclei. *ApJ*, 784(1):83, Mar. 2014. doi: 10.1088/0004-637X/784/1/83.

C. B. D'Andrea, M. Sako, B. Dilday, J. A. Frieman, J. Holtzman, R. Kessler, K. Konishi, D. P. Schneider, J. Sollerman, J. C. Wheeler, N. Yasuda, D. Cinabro, S. Jha, R. C. Nichol, H. Lampeitl, M. Smith, D. W. Atlee, B. Bassett, F. J. Castander, A. Goobar, R. Miquel, J. Nordin, L. Östman, J. L. Prieto, R. Quimby, A. G. Riess, and M. Stritzinger. Type II-P Supernovae from the SDSS-II Supernova Survey and the Standardized Candle Method. *ApJ*, 708(1):661–674, Jan. 2010. doi: 10.1088/0004-637X/708/1/661.

S. Darbha, B. D. Metzger, E. Quataert, D. Kasen, P. Nugent, and R. Thomas. Nickel-rich outflows produced by the accretion-induced collapse of white dwarfs: light curves and spectra. *MNRAS*, 409(2):846–854, Dec. 2010. doi: 10.1111/j.1365-2966.2010.17353.x.

K. Das, A. Mehla, C. Fremling, and M. Kasliwal. ZTF Transient Classification Report for 2025-10-27. *Transient Name Server Classification Report*, 2025-4328: 1, Oct. 2025a.

K. K. Das, M. M. Kasliwal, C. Fremling, S. Yang, S. Schulze, J. Sollerman, T. Sit, K. De, A. Tzanidakis, D. A. Perley, S. Anand, I. Andreoni, C. Barbarino, K. Brudge, A. Drake, A. Gal-Yam, R. R. Laher, V. Karambelkar, S. R. Kulkarni, F. J. Masci, M. S. Medford, A. Polin, H. Reedy, R. Riddle, Y. Sharma, R. Smith, L. Yan, Y. Yang, and Y. Yao. Probing the Low-mass End of Core-collapse Supernovae Using a Sample of Strongly-stripped Calcium-rich Type IIb Supernovae from the Zwicky Transient Facility. *ApJ*, 959(1):12, Dec. 2023a. doi: 10.3847/1538-4357/acfeeb.

K. K. Das, M. M. Kasliwal, J. Sollerman, C. Fremling, I. Irani, S.-C. Leung, S. Yang, S. Wu, J. Fuller, S. Anand, I. Andreoni, C. Barbarino, T. G. Brink, K. De, A. Dugas, S. L. Groom, G. Helou, K.-R. Hinds, A. Y. Q. Ho, V. Karambelkar, S. R. Kulkarni, D. A. Perley, J. Purdum, N. Regnault, S. Schulze, Y. Sharma, T. Sit, G. P. Srinivasaragavan, R. Stein, K. Taggart, L. Tartaglia, A. Tzanidakis, A. Wold, L. Yan, Y. Yao, and J. Zolkower. Probing pre-supernova mass loss in double-peaked Type Ibc supernovae from the Zwicky Transient Facility. *arXiv e-prints*, art. arXiv:2306.04698, June 2023b. doi: 10.48550/arXiv.2306.04698.

K. K. Das, C. Fremling, M. M. Kasliwal, S. Schulze, J. Sollerman, V. Karambelkar, S. Rose, S. Anand, I. Andreoni, M. Aubert, S. J. Brennan, S. B. Cenko,

M. W. Coughlin, B. O'Connor, K. De, J. Fuller, M. Graham, E. Hammerstein, A. Haynie, K.-R. Hinds, I. Kleiser, S. R. Kulkarni, Z. Lin, C. Liu, A. A. Mahabal, C. Martin, A. A. Miller, J. D. Neill, D. A. Perley, P. J. Pessi, N. Z. Prusinski, J. Purdum, V. Ravi, B. Rusholme, S. Wu, A. Wold, and L. Yan. SN 2023zaw: An Ultrastripped, Nickel-poor Supernova from a Low-mass Progenitor. *ApJ*, 969(1): L11, July 2024a. doi: 10.3847/2041-8213/ad527a.

K. K. Das, C. Fremling, M. M. Kasliwal, S. Schulze, J. Sollerman, V. Karambelkar, S. Rose, S. Anand, I. Andreoni, M. Aubert, S. J. Brennan, S. B. Cenko, M. W. Coughlin, B. O'Connor, K. De, J. Fuller, M. Graham, E. Hammerstein, A. Haynie, K. R. Hinds, I. Kleiser, S. R. Kulkarni, Z. Lin, C. Liu, A. A. Mahabal, C. Martin, A. A. Miller, J. D. Neill, D. A. Perley, P. J. Pessi, N. Z. Prusinski, J. Purdum, V. Ravi, B. Rusholme, S. Wu, A. Wold, and L. Yan. SN 2023zaw: An Ultrastripped, Nickel-poor Supernova from a Low-mass Progenitor. *ApJ*, 969(1): L11, July 2024b. doi: 10.3847/2041-8213/ad527a.

K. K. Das, M. M. Kasliwal, J. Sollerman, C. Fremling, I. Irani, S.-C. Leung, S. Yang, S. Wu, J. Fuller, S. Anand, I. Andreoni, C. Barbarino, T. G. Brink, K. De, A. Dugas, S. L. Groom, G. Helou, K. R. Hinds, A. Y. Q. Ho, V. Karambelkar, S. R. Kulkarni, D. A. Perley, J. Purdum, N. Regnault, S. Schulze, Y. Sharma, T. Sit, N. Sravan, G. P. Srinivasaragavan, R. Stein, K. Taggart, L. Tartaglia, A. Tzanidakis, A. Wold, L. Yan, Y. Yao, and J. Zolkower. Probing Presupernova Mass Loss in Double-peaked Type Ibc Supernovae from the Zwicky Transient Facility. *ApJ*, 972(1):91, Sept. 2024c. doi: 10.3847/1538-4357/ad595f.

K. K. Das, M. M. Kasliwal, C. Fremling, J. Sollerman, D. A. Perley, K. De, A. Tzanidakis, T. Sit, S. Adams, S. Anand, T. Ahumuda, I. Andreoni, S. Brennan, T. Brink, R. J. Bruch, P. Chen, M. R. Chu, D. O. Cook, S. Covarrubias, A. Dahiwale, N. Earley, A. Y. Q. Ho, A. Gal-Yam, A. Gangopadhyay, E. Hammerstein, K.-R. Hinds, V. Karambelkar, Y. Kong, S. R. Kulkarni, T. Jegou du Laz, C. Liu, W. Meynardie, A. A. Miller, G. Nir, K. C. Patra, P. J. Pessi, R. M. Rich, N. Rehemtulla, S. Rose, B. Rusholme, S. Schulze, Y. Sharma, A. Singh, R. Smith, R. Stein, M. Sharma Mandigo-Stoba, N. L. Strotjohann, Y.-J. Qin, J. Wise, A. Wold, L. Yan, Y. Yang, Y. Yao, and E. Zimmerman. Low-Luminosity Type IIP Supernovae from the Zwicky Transient Facility Census of the Local Universe. I: Luminosity Function, Volumetric Rate. *arXiv e-prints*, art. arXiv:2502.19493, Feb. 2025b. doi: 10.48550/arXiv.2502.19493.

K. K. Das, M. M. Kasliwal, C. Fremling, J. Sollerman, D. A. Perley, K. De, A. Tzanidakis, T. Sit, S. Adams, S. Anand, T. Ahumuda, I. Andreoni, S. Brennan, T. Brink, R. J. Bruch, P. Chen, M. R. Chu, D. O. Cook, S. Covarrubias, A. Dahiwale, N. Earley, A. Y. Q. Ho, A. Gal-Yam, A. Gangopadhyay, E. Hammerstein, K. R. Hinds, V. Karambelkar, Y. Kong, S. R. Kulkarni, T. Jegou du Laz, C. Liu, W. Meynardie, A. A. Miller, G. Nir, K. C. Patra, P. J. Pessi, R. M. Rich, N. Rehemtulla, S. Rose, B. Rusholme, S. Schulze, Y. Sharma, A. Singh, R. Smith, R. Stein, M. S. Mandigo-Stoba, N. L. Strotjohann, Y.-J. Qin, J. Wise,

A. Wold, L. Yan, Y. Yang, Y. Yao, and E. Zimmerman. Low-luminosity Type IIP Supernovae from the Zwicky Transient Facility Census of the Local Universe. I. Luminosity Function, Volumetric Rate. *PASP*, 137(4):044203, Apr. 2025c. doi: 10.1088/1538-3873/adcaeb.

K. K. Das, M. M. Kasliwal, T. J. D. Laz, S. Covarrubias, C. Fremling, W. Jacobson-Galan, S. Rose, Y. Qin, D. Cook, J. Sollerman, A. Gangopadhay, A. Singh, I. Andreoni, J. Carney, D. Perley, K. Hinds, N. Rehemtulla, A. A. Miller, and S. Schulze. ZTF Complete Astronomical Transient Survey within 150 Mpc (CATS150). *Transient Name Server AstroNote*, 64:1, Feb. 2025d.

K. K. Das, M. M. Kasliwal, J. Sollerman, C. Fremling, T. J. Moriya, K.-R. Hinds, D. A. Perley, E. C. Bellm, T. X. Chen, E. P. O'Connor, M. W. Coughlin, W. V. Jacobson-Galan, A. Gangopadhyay, M. Graham, S. R. Kulkarni, J. Purdum, N. Sarin, S. Schulze, A. Singh, D. Tsuna, and A. Wold. Low-Luminosity Type IIP Supernovae from the Zwicky Transient Facility Census of the Local Universe. II: Lightcurve Analysis. *arXiv e-prints*, art. arXiv:2506.20068, June 2025e. doi: 10.48550/arXiv.2506.20068.

R. Dastidar, K. Misra, S. Valenti, D. J. Sand, A. Pastorello, A. Reguitti, G. Pignata, S. Benetti, S. Bose, A. Gangopadhyay, M. Singh, L. Tomasella, J. E. Andrews, I. Arcavi, C. Ashall, C. Bilinski, K. A. Bostroem, D. A. H. Buckley, G. Cannizzaro, L. Chomiuk, E. Congiu, S. Dong, Y. Dong, N. Elias-Rosa, M. Fraser, C. Gall, M. Gromadzki, D. Hiramatsu, G. Hosseinzadeh, D. A. Howell, E. Y. Hsiao, C. McCully, N. Smith, and J. Strader. SN 2018is: a low-luminosity Type IIP supernova with narrow hydrogen emission lines at early phases. *arXiv e-prints*, art. arXiv:2501.01530, Jan. 2025.

K. W. Davis, K. Taggart, S. Tinyanont, R. J. Foley, V. A. Villar, L. Izzo, C. R. Angus, M. J. Bustamante-Rosell, D. A. Coulter, N. Earl, D. Farias, J. Hjorth, M. E. Huber, D. O. Jones, P. L. Kelly, C. D. Kilpatrick, D. Langeroodi, H.-Y. Miao, C. M. Pellegrino, E. Ramirez-Ruiz, C. L. Ransome, S. Rest, M. R. Siebert, G. Terreran, I. M. Thornton, S. K. Yadavalli, G. R. Zeimann, K. Auchettl, C. R. Bom, T. G. Brink, J. Burke, Y. Camacho-Neves, K. C. Chambers, T. J. L. de Boer, L. DeMarchi, A. V. Filippenko, L. Galbany, C. Gall, H. Gao, F. R. Herpich, D. A. Howell, W. V. Jacobson-Galan, S. W. Jha, A. Kanaan, N. Khetan, L. A. Kwok, Z. Lai, C. Larison, C.-C. Lin, K. C. Loertscher, E. A. Magnier, C. McCully, P. McGill, M. Newsome, E. Padilla Gonzalez, Y.-C. Pan, A. Rest, J. Rho, T. Ribeiro, A. Santos, W. Schoenell, S. N. Sharief, K. W. Smith, R. J. Wainscoat, Q. Wang, Y. Zenati, and W. Zheng. SN 2022ann: a Type Icn supernova from a dwarf galaxy that reveals helium in its circumstellar environment. *MNRAS*, 523(2):2530–2550, Aug. 2023. doi: 10.1093/mnras/stad1433.

K. De, M. M. Kasliwal, T. Cantwell, Y. Cao, S. B. Cenko, A. Gal-Yam, J. Johansson, A. Kong, S. R. Kulkarni, R. Lunnan, F. Masci, M. Matuszewski, K. P. Mooley, J. D. Neill, P. E. Nugent, E. O. Ofek, Y. Perrott, U. D. Rebbapragada, A. Rubin,

D. O' Sullivan, and O. Yaron. iPTF 16hgs: A Double-peaked Ca-rich Gap Transient in a Metal-poor, Star-forming Dwarf Galaxy. *ApJ*, 866(1):72, Oct. 2018a. doi: 10.3847/1538-4357/aadf8e.

K. De, M. M. Kasliwal, T. Cantwell, Y. Cao, S. B. Cenko, A. Gal-Yam, J. Johansson, A. Kong, S. R. Kulkarni, R. Lunnan, F. Masci, M. Matuszewski, K. P. Mooley, J. D. Neill, P. E. Nugent, E. O. Ofek, Y. Perrott, U. D. Rebbapragada, A. Rubin, D. O' Sullivan, and O. Yaron. iPTF 16hgs: A Double-peaked Ca-rich Gap Transient in a Metal-poor, Star-forming Dwarf Galaxy. *ApJ*, 866(1):72, Oct. 2018b. doi: 10.3847/1538-4357/aadf8e.

K. De, M. M. Kasliwal, E. O. Ofek, T. J. Moriya, J. Burke, Y. Cao, S. B. Cenko, G. B. Doran, G. E. Duggan, R. P. Fender, C. Fransson, A. Gal-Yam, A. Horesh, S. R. Kulkarni, R. R. Laher, R. Lunnan, I. Manulis, F. Masci, P. A. Mazzali, P. E. Nugent, D. A. Perley, T. Petrushevska, A. L. Piro, C. Rumsey, J. Sollerman, M. Sullivan, and F. Taddia. A hot and fast ultra-stripped supernova that likely formed a compact neutron star binary. *Science*, 362:201–206, Oct. 2018c. doi: 10.1126/science.aas8693.

K. De, M. J. Hankins, M. M. Kasliwal, A. M. Moore, E. O. Ofek, S. M. Adams, M. C. B. Ashley, A.-N. Babul, A. Bagdasaryan, K. B. Burdge, J. Burnham, R. G. Dekany, A. Declacroix, A. Galla, T. Greffe, D. Hale, J. E. Jencson, R. M. Lau, A. Mahabal, D. McKenna, M. Sharma, P. L. Shopbell, R. M. Smith, J. Soon, J. Sokoloski, R. Soria, and T. Travouillon. Palomar Gattini-IR: Survey Overview, Data Processing System, On-sky Performance and First Results. *PASP*, 132 (1008):025001, Feb. 2020a. doi: 10.1088/1538-3873/ab6069.

K. De, M. M. Kasliwal, A. Tzanidakis, U. C. Fremling, S. Adams, R. Aloisi, I. Andreoni, A. Bagdasaryan, E. C. Bellm, L. Bildsten, C. Cannella, D. O. Cook, A. Delacroix, A. Drake, D. Duev, A. Dugas, S. Frederick, A. Gal-Yam, D. Goldstein, V. Z. Golkhou, M. J. Graham, D. Hale, M. Hankins, G. Helou, A. Y. Q. Ho, I. Irani, J. E. Jencson, D. L. Kaplan, S. Kaye, S. R. Kulkarni, T. Kupfer, R. R. Laher, R. Leadbeater, R. Lunnan, F. J. Masci, A. A. Miller, J. D. Neill, E. O. Ofek, D. A. Perley, A. Polin, T. A. Prince, E. Quataert, D. Reiley, R. L. Riddle, B. Rusholme, Y. Sharma, D. L. Shupe, J. Sollerman, L. Tartaglia, R. Walters, L. Yan, and Y. Yao. The Zwicky Transient Facility Census of the Local Universe. I. Systematic Search for Calcium-rich Gap Transients Reveals Three Related Spectroscopic Subclasses. *ApJ*, 905(1):58, Dec. 2020b. doi: 10.3847/1538-4357/abb45c.

K. De, U. C. Fremling, A. Gal-Yam, O. Yaron, M. M. Kasliwal, and S. R. Kulkarni. The Peculiar Ca-rich SN2019ehk: Evidence for a Type IIb Core-collapse Supernova from a Low-mass Stripped Progenitor. *ApJ*, 907(1):L18, Jan. 2021. doi: 10.3847/2041-8213/abd627.

K. De, M. MacLeod, J. E. Jencson, E. Lovegrove, A. Antoni, E. Kara, M. M. Kasliwal, R. M. Lau, A. Loeb, M. Masterson, A. M. Meisner, C. Panagiotou,

E. Quataert, and R. Simcoe. Disappearance of a massive star in the Andromeda Galaxy due to formation of a black hole. *Science*, 391(6786):689–693, Feb. 2026. doi: 10.1126/science.adt4853.

T. de Jaeger, J. P. Anderson, L. Galbany, S. González-Gaitán, M. Hamuy, M. M. Phillips, M. D. Stritzinger, C. Contreras, G. Folatelli, C. P. Gutiérrez, E. Y. Hsiao, N. Morrell, N. B. Suntzeff, L. Dessart, and A. V. Filippenko. Observed Type II supernova colours from the Carnegie Supernova Project-I. *MNRAS*, 476(4): 4592–4616, June 2018. doi: 10.1093/mnras/sty508.

T. de Jaeger, W. Zheng, B. E. Stahl, A. V. Filippenko, T. G. Brink, A. Bigley, K. Blanchard, P. K. Blanchard, J. Bradley, S. K. Cargill, C. Casper, S. B. Cenko, S. Channa, B. Y. Choi, K. I. Clubb, B. E. Cobb, D. Cohen, M. de Kouchkovsky, M. Ellison, E. Falcon, O. D. Fox, K. Fuller, M. Ganeshalingam, C. Gould, M. L. Graham, G. Halevi, K. T. Hayakawa, J. Hestenes, M. P. Hyland, B. Jeffers, N. Joubert, M. T. Kandrashoff, P. L. Kelly, H. Kim, M. Kim, S. Kumar, E. J. Leonard, G. Z. Li, T. B. Lowe, P. Lu, M. Mason, K. J. McAllister, J. C. Mauerhan, M. Modjaz, J. Molloy, D. A. Perley, K. Pina, D. Poznanski, T. W. Ross, I. Shivvers, J. M. Silverman, C. Soler, S. Stegman, S. Taylor, K. Tang, A. Wilkins, X. Wang, X. Wang, H. Yuk, S. Yunus, and K. D. Zhang. The Berkeley sample of Type II supernovae: BVRI light curves and spectroscopy of 55 SNe II. *MNRAS*, 490(2): 2799–2821, Dec. 2019a. doi: 10.1093/mnras/stz2714.

T. de Jaeger, W. Zheng, B. E. Stahl, A. V. Filippenko, T. G. Brink, A. Bigley, K. Blanchard, P. K. Blanchard, J. Bradley, S. K. Cargill, C. Casper, S. B. Cenko, S. Channa, B. Y. Choi, K. I. Clubb, B. E. Cobb, D. Cohen, M. de Kouchkovsky, M. Ellison, E. Falcon, O. D. Fox, K. Fuller, M. Ganeshalingam, C. Gould, M. L. Graham, G. Halevi, K. T. Hayakawa, J. Hestenes, M. P. Hyland, B. Jeffers, N. Joubert, M. T. Kandrashoff, P. L. Kelly, H. Kim, M. Kim, S. Kumar, E. J. Leonard, G. Z. Li, T. B. Lowe, P. Lu, M. Mason, K. J. McAllister, J. C. Mauerhan, M. Modjaz, J. Molloy, D. A. Perley, K. Pina, D. Poznanski, T. W. Ross, I. Shivvers, J. M. Silverman, C. Soler, S. Stegman, S. Taylor, K. Tang, A. Wilkins, X. Wang, X. Wang, H. Yuk, S. Yunus, and K. D. Zhang. The Berkeley sample of Type II supernovae: BVRI light curves and spectroscopy of 55 SNe II. *MNRAS*, 490(2): 2799–2821, Dec. 2019b. doi: 10.1093/mnras/stz2714.

C. de Jager, H. Nieuwenhuijzen, and K. A. van der Hucht. Mass loss rates in the Hertzsprung-Russell diagram. *A&AS*, 72:259–289, Feb. 1988.

R. Dekany, R. M. Smith, R. Riddle, M. Feeney, M. Porter, D. Hale, J. Zolkower, J. Belicki, S. Kaye, J. Henning, R. Walters, J. Cromer, A. Delacroix, H. Rodriguez, D. J. Reiley, P. Mao, D. Hover, P. Murphy, R. Burruss, J. Baker, M. Kowalski, K. Reif, P. Mueller, E. Bellm, M. Graham, and S. R. Kulkarni. The Zwicky Transient Facility: Observing System. *PASP*, 132(1009):038001, Mar. 2020. doi: 10.1088/1538-3873/ab4ca2.

L. Dessart. Simulations of light curves and spectra for superluminous Type Ic supernovae powered by magnetars. *A&A*, 621:A141, Jan. 2019. doi: 10.1051/0004-6361/201834535.

L. Dessart and D. J. Hillier. Distance determinations using type II supernovae and the expanding photosphere method. *A&A*, 439:671–685, Aug. 2005. doi: 10.1051/0004-6361:20053217.

L. Dessart and D. J. Hillier. Radiative-transfer modeling of nebular-phase type II supernovae. Dependencies on progenitor and explosion properties. *A&A*, 642: A33, Oct. 2020. doi: 10.1051/0004-6361/202038148.

L. Dessart, A. Burrows, E. Livne, and C. D. Ott. Magnetically Driven Explosions of Rapidly Rotating White Dwarfs Following Accretion-Induced Collapse. *ApJ*, 669(1):585–599, Nov. 2007. doi: 10.1086/521701.

L. Dessart, D. J. Hillier, T. Sukhbold, S. E. Woosley, and H. T. Janka. Nebular phase properties of supernova Ibc from He-star explosions. *A&A*, 656:A61, Nov. 2021a. doi: 10.1051/0004-6361/202141927.

L. Dessart, D. J. Hillier, T. Sukhbold, S. E. Woosley, and H. T. Janka. The explosion of 9-29 $M_{\odot}$ stars as Type II supernovae: Results from radiative-transfer modeling at one year after explosion. *A&A*, 652:A64, Aug. 2021b. doi: 10.1051/0004-6361/202140839.

L. Dessart, D. J. Hillier, and H. Kuncarayakti. Helium stars exploding in circumstellar material and the origin of Type Ibn supernovae. *A&A*, 658:A130, Feb. 2022. doi: 10.1051/0004-6361/202142436.

L. Dessart, C. P. Gutiérrez, A. Ercolino, H. Jin, and N. Langer. A sequence of Type Ib, IIb, II-L, and II-P supernovae from binary-star progenitors with varying initial separations. *A&A*, 685:A169, May 2024. doi: 10.1051/0004-6361/202349066.

L. Dessart, R. Kotak, W. Jacobson-Galan, K. Das, C. Fremling, M. Kasliwal, Y.-J. Qin, and S. Rose. An optical to infrared study of type II SN2024ggi at nebular times. *arXiv e-prints*, art. arXiv:2507.05803, July 2025. doi: 10.48550/arXiv.2507.05803.

J. D. M. Dewi and O. R. Pols. The late stages of evolution of helium star-neutron star binaries and the formation of double neutron star systems. *MNRAS*, 344(2): 629–643, Sept. 2003. doi: 10.1046/j.1365-8711.2003.06844.x.

J. D. M. Dewi, O. R. Pols, G. J. Savonije, and E. P. J. van den Heuvel. The evolution of naked helium stars with a neutron star companion in close binary systems. *MNRAS*, 331(4):1027–1040, Apr. 2002. doi: 10.1046/j.1365-8711.2002.05257.x.

S. Dhawan et al. Ztf sn ia dr2: Cosmology-independent constraints on supernova standardization from sibling pairs. *A&A*, 702:A190, 2025.

A. A. Djupvik and J. Andersen. The Nordic Optical Telescope. In *Highlights of Spanish Astrophysics V*, volume 14 of *Astrophysics and Space Science Proceedings*, page 211, Jan. 2010. doi: 10.1007/978-3-642-11250-8_21.

C. L. Doherty, P. Gil-Pons, L. Siess, J. C. Lattanzio, and H. H. B. Lau. Super- and massive AGB stars - IV. Final fates - initial-to-final mass relation. *MNRAS*, 446 (3):2599–2612, Jan. 2015. doi: 10.1093/mnras/stu2180.

Y. Dong, S. Valenti, K. A. Bostroem, D. J. Sand, J. E. Andrews, L. Galbany, S. W. Jha, Y. Eweis, L. Kwok, E. Y. Hsiao, S. Davis, P. J. Brown, H. Kuncarayakti, K. Maeda, J. Rho, R. C. Amaro, J. P. Anderson, I. Arcavi, J. Burke, R. Dastidar, G. Folatelli, J. Haislip, D. Hiramatsu, G. Hosseinzadeh, D. A. Howell, J. Jencson, V. Kouprianov, M. Lundquist, J. D. Lyman, C. McCully, K. Misra, D. E. Reichart, S. F. Sánchez, N. Smith, X. Wang, L. Wang, and S. Wyatt. Supernova 2018cuf: A Type IIP Supernova with a Slow Fall from Plateau. *ApJ*, 906(1):56, Jan. 2021. doi: 10.3847/1538-4357/abc417.

B. T. Draine. Interstellar Dust Grains. *ARA&A*, 41:241–289, Jan. 2003. doi: 10.1146/annurev.astro.41.011802.094840.

B. T. Draine. *Physics of the Interstellar and Intergalactic Medium*. 2011.

A. J. Drake, S. G. Djorgovski, M. J. Graham, A. Mahabal, R. Williams, J. L. Prieto, M. Catelan, E. C. Beshore, S. M. Larson, E. Christensen, J. Brimacombe, G. H. Marion, and J. Irwin. Supernova 2012ch = Psn J15060254+4125327. *Central Bureau Electronic Telegrams*, 3118:1, May 2012.

M. R. Drout, A. M. Soderberg, P. A. Mazzali, J. T. Parrent, R. Margutti, D. Milisavljevic, N. E. Sanders, R. Chornock, R. J. Foley, R. P. Kirshner, A. V. Filippenko, W. Li, P. J. Brown, S. B. Cenko, S. Chakraborti, P. Challis, A. Friedman, M. Ganeshalingam, M. Hicken, C. Jensen, M. Modjaz, H. B. Perets, J. M. Silverman, and D. S. Wong. The Fast and Furious Decay of the Peculiar Type Ic Supernova 2005ek. *ApJ*, 774(1):58, Sept. 2013. doi: 10.1088/0004-637X/774/1/58.

M. R. Drout, R. Chornock, A. M. Soderberg, N. E. Sanders, R. McKinnon, A. Rest, R. J. Foley, D. Milisavljevic, R. Margutti, E. Berger, M. Calkins, W. Fong, S. Gezari, M. E. Huber, E. Kankare, R. P. Kirshner, C. Leibler, R. Lunnan, S. Mattila, G. H. Marion, G. Narayan, A. G. Riess, K. C. Roth, D. Scolnic, S. J. Smartt, J. L. Tonry, W. S. Burgett, K. C. Chambers, K. W. Hodapp, R. Jedicke, N. Kaiser, E. A. Magnier, N. Metcalfe, J. S. Morgan, P. A. Price, and C. Waters. Rapidly Evolving and Luminous Transients from Pan-STARRS1. *ApJ*, 794(1): 23, Oct. 2014. doi: 10.1088/0004-637X/794/1/23.

G. Duchêne and A. Kraus. Stellar Multiplicity. *ARA&A*, 51(1):269–310, Aug. 2013. doi: 10.1146/annurev-astro-081710-102602.

D. A. Duev, A. Mahabal, F. J. Masci, M. J. Graham, B. Rusholme, R. Walters, I. Karmarkar, S. Frederick, M. M. Kasliwal, U. Rebbapragada, and C. Ward.

Real-bogus classification for the Zwicky Transient Facility using deep learning. *arXiv e-prints*, July 2019.

K. Ebinger, S. Curtis, C. Fröhlich, M. Hempel, A. Perego, M. Liebendörfer, and F.-K. Thielemann. PUSHing Core-collapse Supernovae to Explosions in Spherical Symmetry. II. Explodability and Remnant Properties. *ApJ*, 870(1):1, Jan. 2019. doi: 10.3847/1538-4357/aae7c9.

D. Elbaz, E. Daddi, D. Le Borgne, M. Dickinson, D. M. Alexander, R. R. Chary, J. L. Starck, W. N. Brandt, M. Kitzbichler, E. MacDonald, M. Nonino, P. Popesso, D. Stern, and E. Vanzella. The reversal of the star formation-density relation in the distant universe. *A&A*, 468(1):33–48, June 2007. doi: 10.1051/0004-6361:20077525.

J. J. Eldridge, L. Xiao, E. R. Stanway, N. Rodrigues, and N. Y. Guo. Supernova lightCURVE POPulation Synthesis I: Including interacting binaries is key to understanding the diversity of type II supernova lightcurves. *PASA*, 35:e049, Dec. 2018. doi: 10.1017/pasa.2018.47.

J. J. Eldridge, N. Y. Guo, N. Rodrigues, E. R. Stanway, and L. Xiao. Supernova lightCURVE POPulation Synthesis II: Validation against supernovae with an observed progenitor. *PASA*, 36:e041, Nov. 2019. doi: 10.1017/pasa.2019.31.

N. Elias-Rosa, S. D. Van Dyk, W. Li, N. Morrell, S. Gonzalez, M. Hamuy, A. V. Filippenko, J.-C. Cuillandre, R. J. Foley, and N. Smith. On the Progenitor of the Type II-Plateau SN 2008cn in NGC 4603. *ApJ*, 706(2):1174–1183, Dec. 2009. doi: 10.1088/0004-637X/706/2/1174.

N. Elias-Rosa, S. D. Van Dyk, W. Li, J. M. Silverman, R. J. Foley, M. Ganeshalingam, J. C. Mauerhan, E. Kankare, S. Jha, A. V. Filippenko, J. E. Beckman, E. Berger, J.-C. Cuillandre, and N. Smith. The Massive Progenitor of the Possible Type II-Linear Supernova 2009hd in Messier 66. *ApJ*, 742(1):6, Nov. 2011. doi: 10.1088/0004-637X/742/1/6.

A. Elmhamdi. Oxygen Issue in Core Collapse Supernovae. *Acta Astron.*, 61(2): 179–198, June 2011.

A. Elmhamdi, I. J. Danziger, N. Chugai, A. Pastorello, M. Turatto, E. Cappellaro, G. Altavilla, S. Benetti, F. Patat, and M. Salvo. Photometry and spectroscopy of the Type IIP SN 1999em from outburst to dust formation. *MNRAS*, 338(4): 939–956, Feb. 2003. doi: 10.1046/j.1365-8711.2003.06150.x.

M. Ergon and C. Fransson. Spectral modelling of Type IIb Supernovae. *arXiv e-prints*, art. arXiv:2206.11014, June 2022.

T. Ertl, H. T. Janka, S. E. Woosley, T. Sukhbold, and M. Ugliano. A Two-parameter Criterion for Classifying the Explodability of Massive Stars by the Neutrino-driven Mechanism. *ApJ*, 818(2):124, Feb. 2016. doi: 10.3847/0004-637X/818/2/124.

T. Ertl, S. E. Woosley, T. Sukhbold, and H. T. Janka. The Explosion of Helium Stars Evolved with Mass Loss. *ApJ*, 890(1):51, Feb. 2020. doi: 10.3847/1538-4357/ab6458.

S. M. Faber, C. N. A. Willmer, C. Wolf, D. C. Koo, B. J. Weiner, J. A. Newman, M. Im, A. L. Coil, C. Conroy, M. C. Cooper, M. Davis, D. P. Finkbeiner, B. F. Gerke, K. Gebhardt, E. J. Groth, P. Guhathakurta, J. Harker, N. Kaiser, S. Kassin, M. Kleinheinrich, N. P. Konidaris, R. G. Kron, L. Lin, G. Luppino, D. S. Madgwick, K. Meisenheimer, K. G. Noeske, A. C. Phillips, V. L. Sarajedini, R. P. Schiavon, L. Simard, A. S. Szalay, N. P. Vogt, and R. Yan. Galaxy Luminosity Functions to z$_\sim$1 from DEEP2 and COMBO-17: Implications for Red Galaxy Formation. *ApJ*, 665(1):265–294, Aug. 2007. doi: 10.1086/519294.

D. Fabricant, R. Fata, H. Epps, T. Gauron, M. Mueller, J. Zajac, S. Amato, J. Barberis, H. Bergner, P. Brennan, W. Brown, I. Chilingarian, J. Geary, V. Kradinov, B. McLeod, M. Smith, and D. Woods. Binospec: A Wide-field Imaging Spectrograph for the MMT. *PASP*, 131(1001):075004, July 2019. doi: 10.1088/1538-3873/ab1d78.

Q. Fang, K. Maeda, H. Kuncarayakti, F. Sun, and A. Gal-Yam. A hybrid envelope-stripping mechanism for massive stars from supernova nebular spectroscopy. *Nature Astronomy*, 3:434–439, Mar. 2019. doi: 10.1038/s41550-019-0710-6.

Q. Fang, K. Maeda, H. Kuncarayakti, M. Tanaka, K. S. Kawabata, T. Hattori, K. Aoki, T. J. Moriya, and M. Yamanaka. Statistical Properties of the Nebular Spectra of 103 Stripped-envelope Core-collapse Supernovae. *ApJ*, 928(2):151, Apr. 2022. doi: 10.3847/1538-4357/ac4f60.

Q. Fang, K. Maeda, H. Ye, T. J. Moriya, and T. Matsumoto. Diversity in Hydrogen-rich Envelope Mass of Type II Supernovae. I. Plateau Phase Light-curve Modeling. *ApJ*, 978(1):35, Jan. 2025. doi: 10.3847/1538-4357/ad8b19.

T. Faran, D. Poznanski, A. V. Filippenko, R. Chornock, R. J. Foley, M. Ganeshalingam, D. C. Leonard, W. Li, M. Modjaz, E. Nakar, F. J. D. Serduke, and J. M. Silverman. Photometric and spectroscopic properties of Type II-P supernovae. *MNRAS*, 442(1):844–861, July 2014a. doi: 10.1093/mnras/stu955.

T. Faran, D. Poznanski, A. V. Filippenko, R. Chornock, R. J. Foley, M. Ganeshalingam, D. C. Leonard, W. Li, M. Modjaz, E. Nakar, F. J. D. Serduke, and J. M. Silverman. Photometric and spectroscopic properties of Type II-P supernovae. *MNRAS*, 442(1):844–861, July 2014b. doi: 10.1093/mnras/stu955.

D. Farias, C. Gall, V. A. Villar, K. Auchettl, K. M. de Soto, A. Gagliano, W. B. Hoogendam, G. Narayan, A. Sedgewick, S. K. Yadavalli, Y. Zenati, C. R. Angus, K. W. Davis, J. Hjorth, W. V. Jacobson-Galán, D. O. Jones, C. D. Kilpatrick, M. J. Bustamante Rosell, D. A. Coulter, G. Dimitriadis, R. J. Foley, A. Gangopadhyay, H. Gao, M. E. Huber, L. Izzo, J. L. Johnson, A. L. Piro, A. Rest, C. Rojas-Bravo, M. R. Siebert, K. Taggart, and S. Tinyanont. Characterization of type Ibn SNe.

arXiv e-prints, art. arXiv:2511.12362, Nov. 2025. doi: 10.48550/arXiv.2511.12362.

F. Feroz, M. P. Hobson, and M. Bridges. MULTINEST: an efficient and robust Bayesian inference tool for cosmology and particle physics. *MNRAS*, 398(4): 1601–1614, Oct. 2009. doi: 10.1111/j.1365-2966.2009.14548.x.

L. Ferrari, G. Folatelli, K. Ertini, H. Kuncarayakti, and J. E. Andrews. Progenitor mass and ejecta asymmetry of supernova 2023ixf from nebular spectroscopy. *A&A*, 687:L20, July 2024. doi: 10.1051/0004-6361/202450440.

R. J. Foley, N. Smith, M. Ganeshalingam, W. Li, R. Chornock, and A. V. Filippenko. SN 2006jc: A Wolf-Rayet Star Exploding in a Dense He-rich Circumstellar Medium. *ApJ*, 657(2):L105–L108, Mar. 2007. doi: 10.1086/513145.

D. Foreman-Mackey, D. W. Hogg, D. Lang, and J. Goodman. emcee: The MCMC Hammer. *PASP*, 125:306, Mar. 2013. doi: 10.1086/670067.

F. Förster, T. J. Moriya, J. C. Maureira, J. P. Anderson, S. Blinnikov, F. Bufano, G. Cabrera-Vives, A. Clocchiatti, T. de Jaeger, P. A. Estévez, L. Galbany, S. González-Gaitán, G. Gräfener, M. Hamuy, E. Y. Hsiao, P. Huentelemu, P. Huijse, H. Kuncarayakti, J. Martínez, G. Medina, F. Olivares E., G. Pignata, A. Razza, I. Reyes, J. San Martín, R. C. Smith, E. Vera, A. K. Vivas, A. de Ugarte Postigo, S. C. Yoon, C. Ashall, M. Fraser, A. Gal-Yam, E. Kankare, L. Le Guillou, P. A. Mazzali, N. A. Walton, and D. R. Young. The delay of shock breakout due to circumstellar material evident in most type II supernovae. *Nature Astronomy*, 2: 808, Sept. 2018. doi: 10.1038/s41550-018-0563-4.

O. D. Fox, H. Khandrika, D. Rubin, C. Casper, G. Z. Li, T. Szalai, L. Armus, A. V. Filippenko, M. F. Skrutskie, L. Strolger, and S. D. Van Dyk. A Spitzer survey for dust-obscured supernovae. *MNRAS*, 506(3):4199–4209, Sept. 2021. doi: 10.1093/mnras/stab1740.

C. Fransson and R. A. Chevalier. Late Emission from Supernovae: A Window on Stellar Nucleosynthesis. *ApJ*, 343:323, Aug. 1989. doi: 10.1086/167707.

M. Fraser, K. Takáts, A. Pastorello, S. J. Smartt, S. Mattila, M. T. Botticella, S. Valenti, M. Ergon, J. Sollerman, I. Arcavi, S. Benetti, F. Bufano, R. M. Crockett, I. J. Danziger, A. Gal-Yam, J. R. Maund, S. Taubenberger, and M. Turatto. On the Progenitor and Early Evolution of the Type II Supernova 2009kr. *ApJ*, 714 (2):L280–L284, May 2010. doi: 10.1088/2041-8205/714/2/L280.

M. Fraser, M. Ergon, J. J. Eldridge, S. Valenti, A. Pastorello, J. Sollerman, S. J. Smartt, I. Agnoletto, I. Arcavi, S. Benetti, M. T. Botticella, F. Bufano, A. Campillay, R. M. Crockett, A. Gal-Yam, E. Kankare, G. Leloudas, K. Maguire, S. Mattila, J. R. Maund, F. Salgado, A. Stephens, S. Taubenberger, and M. Turatto. SN 2009md: another faint supernova from a low-mass progenitor. *MNRAS*, 417(2): 1417–1433, Oct. 2011. doi: 10.1111/j.1365-2966.2011.19370.x.

M. Fraser, J. R. Maund, S. J. Smartt, R. Kotak, A. Lawrence, A. Bruce, S. Valenti, F. Yuan, S. Benetti, T. W. Chen, A. Gal-Yam, C. Inserra, and D. R. Young. On the progenitor of the Type IIP SN 2013ej in M74. *MNRAS*, 439:L56–L60, Mar. 2014. doi: 10.1093/mnrasl/slt179.

M. Fraser, M. D. Stritzinger, S. J. Brennan, A. Pastorello, Y. Cai, A. L. Piro, C. Ashall, P. Brown, C. R. Burns, N. Elias-Rosa, R. Kotak, A. V. Filippenko, L. Galbany, E. Y. Hsiao, S. W. Jha, A. Reguitti, J.-j. Zhang, S. Moran, N. Morrell, B. J. Shappee, L. Tomasella, J. P. Anderson, T. Barna, P. Ochner, M. M. Phillips, M. Tucker, X. Wang, E. Baron, S. Benetti, M. C. Bersten, T. G. Brink, Y. Camacho-Neves, S. Davis, K. G. Dettman, G. Folatelli, C. P. Gutierrez, P. Hoflich, T. W. S. Holoien, E. Kankare, S. Kumar, J. Lu, P. Mazzali, S. Taubenberger, S. Tinyanont, H. Kuncarayakti, L. Kwok, M. Shahbandeh, N. B. Suntzeff, S. Yan, Y. Yang, and W. Zheng. SN 2021csp – the explosion of a stripped envelope star within a H and He-poor circumstellar medium. *arXiv e-prints*, art. arXiv:2108.07278, Aug. 2021. doi: 10.48550/arXiv.2108.07278.

C. Fremling. ZTF Transient Discovery Report for 2018-08-07. *Transient Name Server Discovery Report*, 2018-1120:1, Aug. 2018.

C. Fremling, J. Sollerman, F. Taddia, M. Ergon, M. Fraser, E. Karamehmetoglu, S. Valenti, A. Jerkstrand, I. Arcavi, F. Bufano, N. Elias Rosa, A. V. Filippenko, D. Fox, A. Gal-Yam, D. A. Howell, R. Kotak, P. Mazzali, D. Milisavljevic, P. E. Nugent, A. Nyholm, E. Pian, and S. Smartt. PTF12os and iPTF13bvn. Two stripped-envelope supernovae from low-mass progenitors in NGC 5806. *A&A*, 593:A68, Sept. 2016. doi: 10.1051/0004-6361/201628275.

C. Fremling, J. Sollerman, M. M. Kasliwal, S. R. Kulkarni, C. Barbarino, M. Ergon, E. Karamehmetoglu, F. Taddia, I. Arcavi, S. B. Cenko, K. Clubb, A. De Cia, G. Duggan, A. V. Filippenko, A. Gal-Yam, M. L. Graham, A. Horesh, G. Hosseinzadeh, D. A. Howell, D. Kuesters, R. Lunnan, T. Matheson, P. E. Nugent, D. A. Perley, R. M. Quimby, and C. Saunders. Oxygen and helium in stripped-envelope supernovae. *A&A*, 618:A37, Oct. 2018. doi: 10.1051/0004-6361/201731701.

C. Fremling, A. A. Miller, Y. Sharma, A. Dugas, D. A. Perley, K. Taggart, J. Sollerman, A. Goobar, M. L. Graham, J. D. Neill, J. Nordin, M. Rigault, R. Walters, I. Andreoni, A. Bagdasaryan, J. Belicki, C. Cannella, E. C. Bellm, S. B. Cenko, K. De, R. Dekany, S. Frederick, V. Z. Golkhou, M. J. Graham, G. Helou, A. Y. Q. Ho, M. M. Kasliwal, T. Kupfer, R. R. Laher, A. Mahabal, F. J. Masci, R. Riddle, B. Rusholme, S. Schulze, D. L. Shupe, R. M. Smith, S. van Velzen, L. Yan, Y. Yao, Z. Zhuang, and S. R. Kulkarni. The Zwicky Transient Facility Bright Transient Survey. I. Spectroscopic Classification and the Redshift Completeness of Local Galaxy Catalogs. *ApJ*, 895(1):32, May 2020. doi: 10.3847/1538-4357/ab8943.

J. Fuller. Pre-supernova outbursts via wave heating in massive stars - I. Red supergiants. *MNRAS*, 470(2):1642–1656, Sept. 2017. doi: 10.1093/mnras/stx1314.

J. Fuller and S. Ro. Pre-supernova outbursts via wave heating in massive stars - II. Hydrogen-poor stars. *MNRAS*, 476(2):1853–1868, May 2018. doi: 10.1093/mnras/sty369.

A. Gal-Yam, R. Bruch, S. Schulze, Y. Yang, D. A. Perley, I. Irani, J. Sollerman, E. C. Kool, M. T. Soumagnac, O. Yaron, N. L. Strotjohann, E. Zimmerman, C. Barbarino, S. R. Kulkarni, M. M. Kasliwal, K. De, Y. Yao, C. Fremling, L. Yan, E. O. Ofek, C. Fransson, A. V. Filippenko, W. Zheng, T. G. Brink, C. M. Copperwheat, R. J. Foley, J. Brown, M. Siebert, G. Leloudas, A. L. Cabrera-Lavers, D. Garcia-Alvarez, A. Marante-Barreto, S. Frederick, T. Hung, J. C. Wheeler, J. Vinkó, B. P. Thomas, M. J. Graham, D. A. Duev, A. J. Drake, R. Dekany, E. C. Bellm, B. Rusholme, D. L. Shupe, I. Andreoni, Y. Sharma, R. Riddle, J. van Roestel, and N. Knezevic. A WC/WO star exploding within an expanding carbon-oxygen-neon nebula. *Nature*, 601(7892):201–204, Jan. 2022a. doi: 10.1038/s41586-021-04155-1.

A. Gal-Yam, R. Bruch, S. Schulze, Y. Yang, D. A. Perley, I. Irani, J. Sollerman, E. C. Kool, M. T. Soumagnac, O. Yaron, N. L. Strotjohann, E. Zimmerman, C. Barbarino, S. R. Kulkarni, M. M. Kasliwal, K. De, Y. Yao, C. Fremling, L. Yan, E. O. Ofek, C. Fransson, A. V. Filippenko, W. Zheng, T. G. Brink, C. M. Copperwheat, R. J. Foley, J. Brown, M. Siebert, G. Leloudas, A. L. Cabrera-Lavers, D. Garcia-Alvarez, A. Marante-Barreto, S. Frederick, T. Hung, J. C. Wheeler, J. Vinkó, B. P. Thomas, M. J. Graham, D. A. Duev, A. J. Drake, R. Dekany, E. C. Bellm, B. Rusholme, D. L. Shupe, I. Andreoni, Y. Sharma, R. Riddle, J. van Roestel, and N. Knezevic. A WC/WO star exploding within an expanding carbon-oxygen-neon nebula. *Nature*, 601(7892):201–204, Jan. 2022b. doi: 10.1038/s41586-021-04155-1.

L. Galbany, M. Hamuy, M. M. Phillips, N. B. Suntzeff, J. Maza, T. de Jaeger, T. Moraga, S. González-Gaitán, K. Krisciunas, N. I. Morrell, J. Thomas-Osip, W. Krzeminski, L. González, R. Antezana, M. Wishnjewski, P. McCarthy, J. P. Anderson, C. P. Gutiérrez, M. Stritzinger, G. Folatelli, C. Anguita, G. Galaz, E. M. Green, C. Impey, Y.-C. Kim, S. Kirhakos, M. A. Malkan, J. S. Mulchaey, A. C. Phillips, A. Pizzella, C. F. Prosser, B. P. Schmidt, R. A. Schommer, W. Sherry, L.-G. Strolger, L. A. Wells, and G. M. Williger. UBVRIz Light Curves of 51 Type II Supernovae. *AJ*, 151(2):33, Feb. 2016. doi: 10.3847/0004-6256/151/2/33.

W.-P. Gan, S.-Q. Wang, and E.-W. Liang. The Study of Dust Formation of Four Type Ibn Supernovae. *ApJ*, 914(2):125, June 2021. doi: 10.3847/1538-4357/abfbdf.

A. Gangopadhyay, K. Misra, D. Hiramatsu, S.-Q. Wang, G. Hosseinzadeh, X. Wang, S. Valenti, J. Zhang, D. A. Howell, I. Arcavi, G. C. Anupama, J. Burke, R. Dastidar, K. Itagaki, B. Kumar, B. Kumar, L. Li, C. McCully, J. Mo, S. B. Pandey, C. Pellegrino, H. Sai, D. K. Sahu, P. Sanwal, A. Singh, M. Singh, J. Zhang, T. Zhang, and X. Zhang. Flash Ionization Signatures in the Type Ibn Supernova SN 2019uo. *ApJ*, 889(2):170, Feb. 2020. doi: 10.3847/1538-4357/ab6328.

A. Gangopadhyay, K. Misra, G. Hosseinzadeh, I. Arcavi, C. Pellegrino, X. Wang, D. Andrew Howell, J. Burke, J. Zhang, K. Kawabata, M. Singh, R. Dastidar, D. Hiramatsu, C. McCully, J. Mo, Z. Chen, and D. Xiang. Evolution of a Peculiar Type Ibn Supernova SN 2019wep. *ApJ*, 930(2):127, May 2022. doi: 10.3847/1538-4357/ac6187.

A. Gangopadhyay, J. Sollerman, K. Tsalapatas, K. Maeda, N. Dukiya, S. Schulze, C. Fransson, N. Sarin, P. J. Pessi, M. Singh, J. Wise, T. Nakaoka, A. Singh, R. Dastidar, M. Kawabata, Y.-J. Qin, K. K. Das, D. Perley, C. Fremling, K. Taguchi, K. R. Hinds, R. Lunnan, R. S. Teja, M. Dubey, B. Ailawadhi, S. Banerjee, K. S. Kawabata, K. Misra, D. K. Sahu, S. J. Brennan, M. M. Kasliwal, A. Y. C. Q. Ho, A. Bochenek, B. Rusholme, R. R. Laher, R. Smith, J. Purdum, and N. Sravan. SN 2023xgo: Helium-rich Type Icn or Carbon-Flash Type Ibn supernova? *MNRAS*, Sept. 2025. doi: 10.1093/mnras/staf1517.

N. Gehrels, G. Chincarini, P. Giommi, K. O. Mason, J. A. Nousek, A. A. Wells, N. E. White, S. D. Barthelmy, D. N. Burrows, L. R. Cominsky, K. C. Hurley, F. E. Marshall, P. Mészáros, P. W. A. Roming, L. Angelini, L. M. Barbier, T. Belloni, S. Campana, P. A. Caraveo, M. M. Chester, O. Citterio, T. L. Cline, M. S. Cropper, J. R. Cummings, A. J. Dean, E. D. Feigelson, E. E. Fenimore, D. A. Frail, A. S. Fruchter, G. P. Garmire, K. Gendreau, G. Ghisellini, J. Greiner, J. E. Hill, S. D. Hunsberger, H. A. Krimm, S. R. Kulkarni, P. Kumar, F. Lebrun, N. M. Lloyd-Ronning, C. B. Markwardt, B. J. Mattson, R. F. Mushotzky, J. P. Norris, J. Osborne, B. Paczynski, D. M. Palmer, H. S. Park, A. M. Parsons, J. Paul, M. J. Rees, C. S. Reynolds, J. E. Rhoads, T. P. Sasseen, B. E. Schaefer, A. T. Short, A. P. Smale, I. A. Smith, L. Stella, G. Tagliaferri, T. Takahashi, M. Tashiro, L. K. Townsley, J. Tueller, M. J. L. Turner, M. Vietri, W. Voges, M. J. Ward, R. Willingale, F. M. Zerbi, and W. W. Zhang. The Swift Gamma-Ray Burst Mission. *ApJ*, 611(2):1005–1020, Aug. 2004. doi: 10.1086/422091.

J. H. Gillanders, S. A. Sim, and S. J. Smartt. AT2018kzr: the merger of an oxygen-neon white dwarf and a neutron star or black hole. *MNRAS*, 497(1):246–262, Sept. 2020. doi: 10.1093/mnras/staa1822.

J. H. Gillanders, M. Huber, K. Chambers, S. J. Smartt, S. Srivastav, T. W. Chen, M. Fulton, T. Moore, K. W. Smith, D. R. Young, and M. Nicholl. Spectroscopic classification of the rapidly-evolving transient AT2023zaw as a SN Ib. *Transient Name Server AstroNote*, 341:1, Dec. 2023.

J. A. Goldberg and L. Bildsten. The Value of Progenitor Radius Measurements for Explosion Modeling of Type II-Plateau Supernovae. *ApJ*, 895(2):L45, June 2020. doi: 10.3847/2041-8213/ab9300.

J. A. Goldberg, L. Bildsten, and B. Paxton. Inferring Explosion Properties from Type II-Plateau Supernova Light Curves. *ApJ*, 879(1):3, July 2019. doi: 10.3847/1538-4357/ab22b6.

G. Gómez and R. López. The Canarias Database of Nearby Type II Supernovae. *AJ*, 120(1):367–381, July 2000. doi: 10.1086/301419.

M. J. Graham, S. R. Kulkarni, E. C. Bellm, S. M. Adams, C. Barbarino, N. Blagorodnova, D. Bodewits, B. Bolin, P. R. Brady, S. B. Cenko, C.-K. Chang, M. W. Coughlin, K. De, G. Eadie, T. L. Farnham, U. Feindt, A. Franckowiak, C. Fremling, S. Gezari, S. Ghosh, D. A. Goldstein, V. Z. Golkhou, A. Goobar, A. Y. Q. Ho, D. Huppenkothen, Ž. Ivezić, R. L. Jones, M. Juric, D. L. Kaplan, M. M. Kasliwal, M. S. P. Kelley, T. Kupfer, C.-D. Lee, H. W. Lin, R. Lunnan, A. A. Mahabal, A. A. Miller, C.-C. Ngeow, P. Nugent, E. O. Ofek, T. A. Prince, L. Rauch, J. van Roestel, S. Schulze, L. P. Singer, J. Sollerman, F. Taddia, L. Yan, Q.-Z. Ye, P.-C. Yu, T. Barlow, J. Bauer, R. Beck, J. Belicki, R. Biswas, V. Brinnel, T. Brooke, B. Bue, M. Bulla, R. Burruss, A. Connolly, J. Cromer, V. Cunningham, R. Dekany, A. Delacroix, V. Desai, D. A. Duev, M. Feeney, D. Flynn, S. Frederick, A. Gal-Yam, M. Giomi, S. Groom, E. Hacopians, D. Hale, G. Helou, J. Henning, D. Hover, L. A. Hillenbrand, J. Howell, T. Hung, D. Imel, W.-H. Ip, E. Jackson, S. Kaspi, S. Kaye, M. Kowalski, E. Kramer, M. Kuhn, W. Landry, R. R. Laher, P. Mao, F. J. Masci, S. Monkewitz, P. Murphy, J. Nordin, M. T. Patterson, B. Penprase, M. Porter, U. Rebbapragada, D. Reiley, R. Riddle, M. Rigault, H. Rodriguez, B. Rusholme, J. van Santen, D. L. Shupe, R. M. Smith, M. T. Soumagnac, R. Stein, J. Surace, P. Szkody, S. Terek, A. Van Sistine, S. van Velzen, W. T. Vestrand, R. Walters, C. Ward, C. Zhang, and J. Zolkower. The Zwicky Transient Facility: Science Objectives. *PASP*, 131(1001):078001, July 2019. doi: 10.1088/1538-3873/ab006c.

GRAVITY Collaboration, M. Karl, O. Pfuhl, F. Eisenhauer, R. Genzel, R. Grellmann, M. Habibi, R. Abuter, M. Accardo, A. Amorim, N. Anugu, G. Ávila, M. Benisty, J.-P. Berger, N. Blind, H. Bonnet, P. Bourget, W. Brandner, R. Brast, A. Buron, A. Caratti O Garatti, F. Chapron, Y. Clénet, C. Collin, V. Coudé Du Foresto, W.-J. de Wit, T. de Zeeuw, C. Deen, F. Delplancke-Ströbele, R. Dembet, F. Derie, J. Dexter, G. Duvert, M. Ebert, A. Eckart, M. Esselborn, P. Fédou, G. Finger, P. Garcia, C. E. Garcia Dabo, R. Garcia Lopez, F. Gao, É. Gendron, S. Gillessen, F. Gonté, P. Gordo, U. Grözinger, P. Guajardo, S. Guieu, P. Haguenauer, O. Hans, X. Haubois, M. Haug, F. Haußmann, T. Henning, S. Hippler, M. Horrobin, A. Huber, Z. Hubert, N. Hubin, G. Jakob, L. Jochum, L. Jocou, A. Kaufer, S. Kellner, S. Kendrew, L. Kern, P. Kervella, M. Kiekebusch, R. Klein, R. Köhler, J. Kolb, M. Kulas, S. Lacour, V. Lapeyrère, B. Lazareff, J.-B. Le Bouquin, P. Léna, R. Lenzen, S. Lévêque, C.-C. Lin, M. Lippa, Y. Magnard, L. Mehrgan, A. Mérand, T. Moulin, E. Müller, F. Müller, U. Neumann, S. Oberti, T. Ott, L. Pallanca, J. Panduro, L. Pasquini, T. Paumard, I. Percheron, K. Perraut, G. Perrin, A. Pflüger, T. P. Duc, P. M. Plewa, D. Popovic, S. Rabien, A. Ramírez, J. Ramos, C. Rau, M. Riquelme, G. Rodríguez-Coira, R.-R. Rohloff, A. Rosales, G. Rousset, J. Sanchez-Bermudez, S. Scheithauer, M. Schöller, N. Schuhler, J. Spyromilio, O. Straub, C. Straubmeier, E. Sturm, M. Suarez, K. R. W. Tristram, N. Ventura, F. Vincent, I. Waisberg, I. Wank, F. Widmann, E. Wieprecht, M. Wiest,

E. Wiezorrek, M. Wittkowski, J. Woillez, B. Wolff, S. Yazici, D. Ziegler, and G. Zins. Multiple star systems in the Orion nebula. *A&A*, 620:A116, Dec. 2018. doi: 10.1051/0004-6361/201833575.

J. Grzegorzek. PSH Transient Discovery Report for 2018-05-05. *Transient Name Server Discovery Report*, 2018-582:1, May 2018.

J. Guillochon, J. Parrent, L. Z. Kelley, and R. Margutti. An Open Catalog for Supernova Data. *ApJ*, 835(1):64, Jan. 2017. doi: 10.3847/1538-4357/835/1/64.

Y. Guo, C. Liu, L. Wang, J. Wang, B. Zhang, K. Ji, Z. Han, and X. Chen. The statistical properties of early-type stars from LAMOST DR8. *A&A*, 667:A44, Nov. 2022. doi: 10.1051/0004-6361/202244300.

U. K. Gurugubelli, D. K. Sahu, G. C. Anupama, and N. K. Chakradhari. Photometric and spectroscopic evolution of type II-P supernova SN 2004A. *Bulletin of the Astronomical Society of India*, 36(2):79–97, Sept. 2008.

C. P. Gutiérrez, J. P. Anderson, M. Hamuy, S. González-Gaitan, L. Galbany, L. Dessart, M. D. Stritzinger, M. M. Phillips, N. Morrell, and G. Folatelli. Type II Supernova Spectral Diversity. II. Spectroscopic and Photometric Correlations. *ApJ*, 850(1):90, Nov. 2017a. doi: 10.3847/1538-4357/aa8f42.

C. P. Gutiérrez, J. P. Anderson, M. Hamuy, N. Morrell, S. González-Gaitan, M. D. Stritzinger, M. M. Phillips, L. Galbany, G. Folatelli, L. Dessart, C. Contreras, M. Della Valle, W. L. Freedman, E. Y. Hsiao, K. Krisciunas, B. F. Madore, J. Maza, N. B. Suntzeff, J. L. Prieto, L. González, E. Cappellaro, M. Navarrete, A. Pizzella, M. T. Ruiz, R. C. Smith, and M. Turatto. Type II Supernova Spectral Diversity. I. Observations, Sample Characterization, and Spectral Line Evolution. *ApJ*, 850(1):89, Nov. 2017b. doi: 10.3847/1538-4357/aa8f52.

C. P. Gutiérrez, A. Pastorello, A. Jerkstrand, L. Galbany, M. Sullivan, J. P. Anderson, S. Taubenberger, H. Kuncarayakti, S. González-Gaitán, P. Wiseman, C. Inserra, M. Fraser, K. Maguire, S. Smartt, T. E. Müller-Bravo, I. Arcavi, S. Benetti, D. Bersier, S. Bose, K. A. Bostroem, J. Burke, P. Chen, T.-W. Chen, M. Della Valle, S. Dong, A. Gal-Yam, M. Gromadzki, D. Hiramatsu, T. W.-S. Holoien, G. Hosseinzadeh, D. A. Howell, E. Kankare, C. S. Kochanek, C. McCully, M. Nicholl, G. Pignata, J. L. Prieto, B. Shappee, K. Taggart, L. Tomasella, S. Valenti, and D. R. Young. SN 2017ivv: two years of evolution of a transitional Type II supernova. *MNRAS*, 499(1):974–992, Nov. 2020. doi: 10.1093/mnras/staa2763.

C. P. Gutiérrez, M. C. Bersten, M. Orellana, A. Pastorello, K. Ertini, G. Folatelli, G. Pignata, J. P. Anderson, S. Smartt, M. Sullivan, M. Pursiainen, C. Inserra, N. Elias-Rosa, M. Fraser, E. Kankare, S. Moran, A. Reguitti, T. M. Reynolds, M. Stritzinger, J. Burke, C. Frohmaier, L. Galbany, D. Hiramatsu, D. A. Howell, H. Kuncarayakti, S. Mattila, T. Müller-Bravo, C. Pellegrino, and M. Smith.

The double-peaked Type Ic supernova 2019cad: another SN 2005bf-like object. *MNRAS*, 504(4):4907–4922, July 2021. doi: 10.1093/mnras/stab1009.

J. Gutiérrez, R. Canal, and E. García-Berro. The gravitational collapse of ONe electron-degenerate cores and white dwarfs: The role of ^{24}Mg and ^{12}C revisited. *A&A*, 435(1):231–237, May 2005. doi: 10.1051/0004-6361:20042254.

S. Hachinger, P. A. Mazzali, S. Taubenberger, W. Hillebrandt, K. Nomoto, and D. N. Sauer. How much H and He is 'hidden' in SNe Ib/c? - I. Low-mass objects. *MNRAS*, 422(1):70–88, May 2012. doi: 10.1111/j.1365-2966.2012.20464.x.

M. Hamuy. Observed and Physical Properties of Core-Collapse Supernovae. *ApJ*, 582(2):905–914, Jan. 2003. doi: 10.1086/344689.

A. Heger and S. E. Woosley. The Nucleosynthetic Signature of Population III. *ApJ*, 567(1):532–543, Mar. 2002. doi: 10.1086/338487.

G. Helou, B. F. Madore, M. Schmitz, M. D. Bicay, X. Wu, and J. Bennett. The NASA/IPAC extragalactic database. In M. A. Albrecht and D. Egret, editors, *Databases and On-line Data in Astronomy*, volume 171 of *Astrophysics and Space Science Library*, pages 89–106, Jan. 1991. doi: 10.1007/978-94-011-3250-3_10.

M. A. Hendry, S. J. Smartt, J. R. Maund, A. Pastorello, L. Zampieri, S. Benetti, M. Turatto, E. Cappellaro, W. P. S. Meikle, R. Kotak, M. J. Irwin, P. G. Jonker, L. Vermaas, R. F. Peletier, H. van Woerden, K. M. Exter, D. L. Pollacco, S. Leon, S. Verley, C. R. Benn, and G. Pignata. A study of the Type II-P supernova 2003gd in M74. *MNRAS*, 359(3):906–926, May 2005. doi: 10.1111/j.1365-2966.2005.08928.x.

M. A. Hendry, S. J. Smartt, R. M. Crockett, J. R. Maund, A. Gal-Yam, D.-S. Moon, S. B. Cenko, D. W. Fox, R. P. Kudritzki, C. R. Benn, and R. Østensen. SN 2004A: another Type II-P supernova with a red supergiant progenitor. *MNRAS*, 369(3): 1303–1320, July 2006. doi: 10.1111/j.1365-2966.2006.10374.x.

K.-R. Hinds, D. Perley, J. Sollerman, A. Miller, C. Fremling, T. Moriya, K. Das, Y.-J. Qin, E. Bellm, X. T. Chen, M. Coughlin, W. Jacobson-Gal\'an, M. Kasliwal, S. Kulkarni, A. Mahabal, F. Masci, Priscila, J. Pessi, J. N. Purdum, R. Riddle, A. Singh, R. Smith, and N. Sravan. Inferring CSM Properties of Type II SNe Using a Magnitude-Limited ZTF Sample. *arXiv e-prints*, art. arXiv:2503.19969, Mar. 2025. doi: 10.48550/arXiv.2503.19969.

D. Hiramatsu, D. A. Howell, S. D. Van Dyk, J. A. Goldberg, K. Maeda, T. J. Moriya, N. Tominaga, K. Nomoto, G. Hosseinzadeh, I. Arcavi, C. McCully, J. Burke, K. A. Bostroem, S. Valenti, Y. Dong, P. J. Brown, J. E. Andrews, C. Bilinski, G. G. Williams, P. S. Smith, N. Smith, D. J. Sand, G. S. Anand, C. Xu, A. V. Filippenko, M. C. Bersten, G. Folatelli, P. L. Kelly, T. Noguchi, and K. Itagaki. The electron-capture origin of supernova 2018zd. *Nature Astronomy*, 5:903–910, June 2021a. doi: 10.1038/s41550-021-01384-2.

D. Hiramatsu, D. A. Howell, S. D. Van Dyk, J. A. Goldberg, K. Maeda, T. J. Moriya, N. Tominaga, K. Nomoto, G. Hosseinzadeh, I. Arcavi, C. McCully, J. Burke, K. A. Bostroem, S. Valenti, Y. Dong, P. J. Brown, J. E. Andrews, C. Bilinski, G. G. Williams, P. S. Smith, N. Smith, D. J. Sand, G. S. Anand, C. Xu, A. V. Filippenko, M. C. Bersten, G. Folatelli, P. L. Kelly, T. Noguchi, and K. Itagaki. The electron-capture origin of supernova 2018zd. *Nature Astronomy*, 5:903–910, June 2021b. doi: 10.1038/s41550-021-01384-2.

A. Y. Q. Ho, S. R. Kulkarni, D. A. Perley, S. B. Cenko, A. Corsi, S. Schulze, R. Lunnan, J. Sollerman, A. Gal-Yam, S. Anand, C. Barbarino, E. C. Bellm, R. J. Bruch, E. Burns, K. De, R. Dekany, A. Delacroix, D. A. Duev, D. D. Frederiks, C. Fremling, D. A. Goldstein, V. Z. Golkhou, M. J. Graham, D. Hale, M. M. Kasliwal, T. Kupfer, R. R. Laher, J. Martikainen, F. J. Masci, J. D. Neill, A. Ridnaia, B. Rusholme, V. Savchenko, D. L. Shupe, M. T. Soumagnac, N. L. Strotjohann, D. S. Svinkin, K. Taggart, L. Tartaglia, L. Yan, and J. Zolkower. SN 2020bvc: A Broad-line Type Ic Supernova with a Double-peaked Optical Light Curve and a Luminous X-Ray and Radio Counterpart. *ApJ*, 902(1):86, Oct. 2020. doi: 10.3847/1538-4357/aba630.

A. Y. Q. Ho, D. A. Perley, A. Gal-Yam, R. Lunnan, J. Sollerman, S. Schulze, K. K. Das, D. Dobie, Y. Yao, C. Fremling, S. Adams, S. Anand, I. Andreoni, E. C. Bellm, R. J. Bruch, K. B. Burdge, A. J. Castro-Tirado, A. Dahiwale, K. De, R. Dekany, A. J. Drake, D. A. Duev, M. J. Graham, G. Helou, D. L. Kaplan, V. Karambelkar, M. M. Kasliwal, E. C. Kool, S. R. Kulkarni, A. A. Mahabal, M. S. Medford, A. A. Miller, J. Nordin, E. Ofek, G. Petitpas, R. Riddle, Y. Sharma, R. Smith, A. J. Stewart, K. Taggart, L. Tartaglia, A. Tzanidakis, and J. M. Winters. A Search for Extragalactic Fast Blue Optical Transients in ZTF and the Rate of AT2018cow-like Transients. *ApJ*, 949(2):120, June 2023. doi: 10.3847/1538-4357/acc533.

A. M. Hopkins and J. F. Beacom. On the Normalization of the Cosmic Star Formation History. *ApJ*, 651(1):142–154, Nov. 2006. doi: 10.1086/506610.

S. Horiuchi, J. F. Beacom, C. S. Kochanek, J. L. Prieto, K. Z. Stanek, and T. A. Thompson. The Cosmic Core-collapse Supernova Rate Does Not Match the Massive-star Formation Rate. *ApJ*, 738(2):154, Sept. 2011. doi: 10.1088/0004-637X/738/2/154.

S. Horiuchi, J. F. Beacom, M. S. Bothwell, and T. A. Thompson. Effects of Stellar Rotation on Star Formation Rates and Comparison to Core-collapse Supernova Rates. *ApJ*, 769(2):113, June 2013. doi: 10.1088/0004-637X/769/2/113.

G. Hosseinzadeh, I. Arcavi, S. Valenti, C. McCully, D. A. Howell, J. Johansson, J. Sollerman, A. Pastorello, S. Benetti, Y. Cao, S. B. Cenko, K. I. Clubb, A. Corsi, G. Duggan, N. Elias-Rosa, A. V. Filippenko, O. D. Fox, C. Fremling, A. Horesh, E. Karamehmetoglu, M. Kasliwal, G. H. Marion, E. Ofek, D. Sand, F. Taddia, W. Zheng, M. Fraser, A. Gal-Yam, C. Inserra, R. Laher, F. Masci, U. Rebbapragada, S. Smartt, K. W. Smith, M. Sullivan, J. Surace, and P. Woźniak. Type Ibn

Supernovae Show Photometric Homogeneity and Spectral Diversity at Maximum Light. *ApJ*, 836(2):158, Feb. 2017a. doi: 10.3847/1538-4357/836/2/158.

G. Hosseinzadeh, I. Arcavi, S. Valenti, C. McCully, D. A. Howell, J. Johansson, J. Sollerman, A. Pastorello, S. Benetti, Y. Cao, S. B. Cenko, K. I. Clubb, A. Corsi, G. Duggan, N. Elias-Rosa, A. V. Filippenko, O. D. Fox, C. Fremling, A. Horesh, E. Karamehmetoglu, M. Kasliwal, G. H. Marion, E. Ofek, D. Sand, F. Taddia, W. Zheng, M. Fraser, A. Gal-Yam, C. Inserra, R. Laher, F. Masci, U. Rebbapragada, S. Smartt, K. W. Smith, M. Sullivan, J. Surace, and P. Woźniak. Type Ibn Supernovae Show Photometric Homogeneity and Spectral Diversity at Maximum Light. *ApJ*, 836:158, Feb. 2017b. doi: 10.3847/1538-4357/836/2/158.

G. Hosseinzadeh, S. Valenti, C. McCully, D. A. Howell, I. Arcavi, A. Jerkstrand, D. Guevel, L. Tartaglia, L. Rui, J. Mo, X. Wang, F. Huang, H. Song, T. Zhang, and K. Itagaki. Short-lived Circumstellar Interaction in the Low-luminosity Type IIP SN 2016bkv. *ApJ*, 861(1):63, July 2018. doi: 10.3847/1538-4357/aac5f6.

D. A. Howell, M. Sullivan, K. Perrett, T. J. Bronder, I. M. Hook, P. Astier, E. Aubourg, D. Balam, S. Basa, R. G. Carlberg, S. Fabbro, D. Fouchez, J. Guy, H. Lafoux, J. D. Neill, R. Pain, N. Palanque-Delabrouille, C. J. Pritchet, N. Regnault, J. Rich, R. Taillet, R. Knop, R. G. McMahon, S. Perlmutter, and N. A. Walton. Gemini Spectroscopy of Supernovae from the Supernova Legacy Survey: Improving High-Redshift Supernova Selection and Classification. *ApJ*, 634 (2):1190–1201, Dec. 2005. doi: 10.1086/497119.

B. Hsu, N. Smith, J. A. Goldberg, K. A. Bostroem, G. Hosseinzadeh, D. J. Sand, J. Pearson, D. Hiramatsu, J. E. Andrews, E. R. Beasor, Y. Dong, J. Farah, L. Galbany, S. Gomez, E. Padilla Gonzalez, C. P. Gutiérrez, D. A. Howell, R. Könyves-Tóth, C. McCully, M. Newsome, M. Shrestha, G. Terreran, V. A. Villar, and X. Wang. One Year of SN 2023ixf: Breaking Through the Degenerate Parameter Space in Light-Curve Models with Pulsating Progenitors. *arXiv e-prints*, art. arXiv:2408.07874, Aug. 2024. doi: 10.48550/arXiv.2408.07874.

F. Huang, X. Wang, L. Zampieri, M. L. Pumo, I. Arcavi, P. J. Brown, M. L. Graham, A. V. Filippenko, W. Zheng, G. Hosseinzadeh, D. A. Howell, C. McCully, L. Rui, S. Valenti, T. Zhang, J. Zhang, K. Zhang, and L. Wang. Optical and Ultraviolet Observations of the Very Young Type IIP SN 2014cx in NGC 337. *ApJ*, 832(2): 139, Dec. 2016. doi: 10.3847/0004-637X/832/2/139.

F. Huang, X.-F. Wang, G. Hosseinzadeh, P. J. Brown, J. Mo, J.-J. Zhang, K.-C. Zhang, T.-M. Zhang, D.-A. Howell, I. Arcavi, C. McCully, S. Valenti, L.-M. Rui, H. Song, D.-F. Xiang, W.-X. Li, H. Lin, and L.-F. Wang. SN 2016X: a type II-P supernova with a signature of shock breakout from explosion of a massive red supergiant. *MNRAS*, 475(3):3959–3973, Apr. 2018. doi: 10.1093/mnras/sty066.

J. D. Hunter. Matplotlib: A 2d graphics environment. *Computing In Science & Engineering*, 9(3):90–95, 2007. doi: 10.1109/MCSE.2007.55.

O. Ilbert, L. Tresse, E. Zucca, S. Bardelli, S. Arnouts, G. Zamorani, L. Pozzetti, D. Bottini, B. Garilli, V. Le Brun, O. Le Fèvre, D. Maccagni, J. P. Picat, R. Scaramella, M. Scodeggio, G. Vettolani, A. Zanichelli, C. Adami, M. Arnaboldi, M. Bolzonella, A. Cappi, S. Charlot, T. Contini, S. Foucaud, P. Franzetti, I. Gavignaud, L. Guzzo, A. Iovino, H. J. McCracken, B. Marano, C. Marinoni, G. Mathez, A. Mazure, B. Meneux, R. Merighi, S. Paltani, R. Pello, A. Pollo, M. Radovich, M. Bondi, A. Bongiorno, G. Busarello, P. Ciliegi, F. Lamareille, Y. Mellier, P. Merluzzi, V. Ripepi, and D. Rizzo. The VIMOS-VLT deep survey. Evolution of the galaxy luminosity function up to z = 2 in first epoch data. *A&A*, 439(3):863–876, Sep 2005. doi: 10.1051/0004-6361:20041961.

C. Inserra, A. Pastorello, M. Turatto, M. L. Pumo, S. Benetti, E. Cappellaro, M. T. Botticella, F. Bufano, N. Elias-Rosa, A. Harutyunyan, S. Taubenberger, S. Valenti, and L. Zampieri. Moderately luminous Type II supernovae. *A&A*, 555:A142, July 2013. doi: 10.1051/0004-6361/201220496.

I. Irani, P. Chen, J. Morag, S. Schulze, A. Gal-Yam, N. L. Strotjohann, O. Yaron, E. A. Zimmerman, A. Sharon, D. A. Perley, J. Sollerman, A. Tohuvavohu, K. K. Das, M. M. Kasliwal, R. Bruch, T. G. Brink, W. Zheng, K. C. Patra, S. S. Vasylyev, A. V. Filippenko, Y. Yang, M. J. Graham, J. S. Bloom, J. Purdum, R. R. Laher, A. Wold, Y. Sharma, L. Lacroix, and M. S. Medford. SN 2022oqm – a Ca-rich explosion of a compact progenitor embedded in C/O circumstellar material. *arXiv e-prints*, art. arXiv:2210.02554, Oct. 2022.

I. Irani, J. Morag, A. Gal-Yam, E. Waxman, S. Schulze, J. Sollerman, K. R. Hinds, D. A. Perley, P. Chen, N. L. Strotjohann, O. Yaron, E. A. Zimmerman, R. Bruch, E. O. Ofek, M. T. Soumagnac, Y. Yang, S. L. Groom, F. J. Masci, M. Aubert, R. Riddle, E. C. Bellm, and D. Hale. The Early Ultraviolet Light Curves of Type II Supernovae and the Radii of Their Progenitor Stars. *ApJ*, 970(1):96, July 2024. doi: 10.3847/1538-4357/ad3de8.

K. Itagaki, T. Noguchi, S. Nakano, T. Yusa, N. Wada, L. Elenin, I. Molotov, J. Brimacombe, K. Takaki, R. Itoh, K. Kawaguchi, K. S. Kawabata, I. Ueno, Y. Moritani, H. Akitaya, T. Urano, M. Yamanaka, J.-J. Zhang, X.-L. Zhao, X.-F. Wang, L.-F. Wang, J. M. Silverman, J. Vinko, R. Quimby, J. C. Wheeler, E. Chatzopoulos, J. T. Parrent, G. H. Marion, D. Milisavljevic, and S. Rostopchin. Supernova 2012ho in MCG -01-57-21 = Psn J22401702-0225341. *Central Bureau Electronic Telegrams*, 3338:1, Dec. 2012.

N. Ivanova, K. Belczynski, V. Kalogera, F. A. Rasio, and R. E. Taam. The Role of Helium Stars in the Formation of Double Neutron Stars. *ApJ*, 592(1):475–485, July 2003. doi: 10.1086/375578.

Ž. Ivezić, J. A. Tyson, E. Acosta, R. Allsman, S. F. Anderson, J. Andrew, R. Angel, T. Axelrod, J. D. Barr, A. C. Becker, J. Becla, C. Beldica, R. D. Blandford, J. S. Bloom, K. Borne, W. N. Brandt, M. E. Brown, J. S. Bullock, D. L. Burke, S. Chandrasekharan, S. Chesley, C. F. Claver, A. Connolly, K. H. Cook, A. Cooray, K. R.

Covey, C. Cribbs, R. Cutri, G. Daues, F. Delgado, H. Ferguson, E. Gawiser, J. C. Geary, P. Gee, M. Geha, R. R. Gibson, D. K. Gilmore, W. J. Gressler, C. Hogan, M. E. Huffer, S. H. Jacoby, B. Jain, J. G. Jernigan, R. L. Jones, M. Juric, S. M. Kahn, J. S. Kalirai, J. P. Kantor, R. Kessler, D. Kirkby, L. Knox, V. L. Krabbendam, S. Krughoff, S. Kulkarni, R. Lambert, D. Levine, M. Liang, K. Lim, R. H. Lupton, P. Marshall, S. Marshall, M. May, M. Miller, D. J. Mills, D. G. Monet, D. R. Neill, M. Nordby, P. O'Connor, J. Oliver, S. S. Olivier, K. Olsen, R. E. Owen, J. R. Peterson, C. E. Petry, F. Pierfederici, S. Pietrowicz, R. Pike, P. A. Pinto, R. Plante, V. Radeka, A. Rasmussen, S. T. Ridgway, W. Rosing, A. Saha, T. L. Schalk, R. H. Schindler, D. P. Schneider, G. Schumacher, J. Sebag, L. G. Seppala, I. Shipsey, N. Silvestri, J. A. Smith, R. C. Smith, M. A. Strauss, C. W. Stubbs, D. Sweeney, A. Szalay, J. J. Thaler, D. Vanden Berk, L. Walkowicz, M. Warner, B. Willman, D. Wittman, S. C. Wolff, W. M. Wood-Vasey, P. Yoachim, H. Zhan, and for the LSST Collaboration. LSST: from Science Drivers to Reference Design and Anticipated Data Products. *ArXiv e-prints*, May 2008.

W. V. Jacobson-Galán, R. Margutti, C. D. Kilpatrick, D. Hiramatsu, H. Perets, D. Khatami, R. J. Foley, J. Raymond, S.-C. Yoon, A. Bobrick, Y. Zenati, L. Galbany, J. Andrews, P. J. Brown, R. Cartier, D. L. Coppejans, G. Dimitriadis, M. Dobson, A. Hajela, D. A. Howell, H. Kuncarayakti, D. Milisavljevic, M. Rahman, C. Rojas-Bravo, D. J. Sand, J. Shepherd, S. J. Smartt, H. Stacey, M. Stroh, J. J. Swift, G. Terreran, J. Vinko, X. Wang, J. P. Anderson, E. A. Baron, E. Berger, P. K. Blanchard, J. Burke, D. A. Coulter, L. DeMarchi, J. M. DerKacy, C. Fremling, S. Gomez, M. Gromadzki, G. Hosseinzadeh, D. Kasen, L. Kriskovics, C. McCully, T. E. Müller-Bravo, M. Nicholl, A. Ordasi, C. Pellegrino, A. L. Piro, A. Pál, J. Ren, A. Rest, R. M. Rich, H. Sai, K. Sárneczky, K. J. Shen, P. Short, M. R. Siebert, C. Stauffer, R. Szakáts, X. Zhang, J. Zhang, and K. Zhang. SN 2019ehk: A Double-peaked Ca-rich Transient with Luminous X-Ray Emission and Shock-ionized Spectral Features. *ApJ*, 898(2):166, Aug. 2020. doi: 10.3847/1538-4357/ab9e66.

W. V. Jacobson-Galán, R. Margutti, C. D. Kilpatrick, J. Raymond, E. Berger, P. K. Blanchard, A. Bobrick, R. J. Foley, S. Gomez, G. Hosseinzadeh, D. Milisavljevic, H. Perets, G. Terreran, and Y. Zenati. Late-time Observations of Calcium-rich Transient SN 2019ehk Reveal a Pure Radioactive Decay Power Source. *ApJ*, 908 (2):L32, Feb. 2021. doi: 10.3847/2041-8213/abdebc.

W. V. Jacobson-Galán, L. Dessart, D. O. Jones, R. Margutti, D. L. Coppejans, G. Dimitriadis, R. J. Foley, C. D. Kilpatrick, D. J. Matthews, S. Rest, G. Terreran, P. D. Aleo, K. Auchettl, P. K. Blanchard, D. A. Coulter, K. W. Davis, T. J. L. de Boer, L. DeMarchi, M. R. Drout, N. Earl, A. Gagliano, C. Gall, J. Hjorth, M. E. Huber, A. L. Ibik, D. Milisavljevic, Y. C. Pan, A. Rest, R. Ridden-Harper, C. Rojas-Bravo, M. R. Siebert, K. W. Smith, K. Taggart, S. Tinyanont, Q. Wang, and Y. Zenati. Final Moments. I. Precursor Emission, Envelope Inflation, and Enhanced Mass Loss Preceding the Luminous Type II Supernova 2020tlf. *ApJ*, 924(1):15, Jan. 2022a. doi: 10.3847/1538-4357/ac3f3a.

W. V. Jacobson-Galán, P. Venkatraman, R. Margutti, D. Khatami, G. Terreran, R. J. Foley, R. Angulo, C. R. Angus, K. Auchettl, P. K. Blanchard, A. Bobrick, J. S. Bright, D. Brout, K. C. Chambers, C. D. Couch, D. A. Coulter, K. Clever, K. W. Davis, T. J. L. de Boer, L. DeMarchi, S. A. Dodd, D. O. Jones, J. Johnson, C. D. Kilpatrick, N. Khetan, Z. Lai, D. Langeroodi, C. C. Lin, E. A. Magnier, D. Milisavljevic, H. B. Perets, J. D. R. Pierel, J. Raymond, S. Rest, A. Rest, R. Ridden-Harper, K. J. Shen, M. R. Siebert, C. Smith, K. Taggart, S. Tinyanont, F. Valdes, V. A. Villar, Q. Wang, S. K. Yadavalli, Y. Zenati, and A. Zenteno. The Circumstellar Environments of Double-peaked, Calcium-strong Transients 2021gno and 2021inl. *ApJ*, 932(1):58, June 2022b. doi: 10.3847/1538-4357/ac67dc.

W. V. Jacobson-Galán, L. Dessart, K. W. Davis, C. D. Kilpatrick, R. Margutti, R. J. Foley, R. Chornock, G. Terreran, D. Hiramatsu, M. Newsome, E. Padilla Gonzalez, C. Pellegrino, D. A. Howell, A. V. Filippenko, J. P. Anderson, C. R. Angus, K. Auchettl, K. A. Bostroem, T. G. Brink, R. Cartier, D. A. Coulter, T. de Boer, M. R. Drout, N. Earl, K. Ertini, J. R. Farah, D. Farias, C. Gall, H. Gao, M. A. Gerlach, F. Guo, A. Haynie, G. Hosseinzadeh, A. L. Ibik, S. W. Jha, D. O. Jones, D. Langeroodi, N. LeBaron, E. A. Magnier, A. L. Piro, S. I. Raimundo, A. Rest, S. Rest, R. M. Rich, C. Rojas-Bravo, H. Sears, K. Taggart, V. A. Villar, R. J. Wainscoat, X. F. Wang, A. R. Wasserman, S. Yan, Y. Yang, J. Zhang, and W. Zheng. Final Moments. II. Observational Properties and Physical Modeling of Circumstellar-material-interacting Type II Supernovae. *ApJ*, 970(2):189, Aug. 2024. doi: 10.3847/1538-4357/ad4a2a.

W. V. Jacobson-Galán, L. Dessart, K. W. Davis, K. A. Bostroem, C. D. Kilpatrick, R. Margutti, A. V. Filippenko, R. J. Foley, R. Chornock, G. Terreran, D. Hiramatsu, M. Newsome, E. Padilla Gonzalez, C. Pellegrino, D. A. Howell, J. P. Anderson, C. R. Angus, K. Auchettl, T. G. Brink, R. Cartier, D. A. Coulter, T. de Boer, M. R. Drout, N. Earl, K. Ertini, J. R. Farah, D. Farias, C. Gall, H. Gao, M. A. Gerlach, F. Guo, A. Haynie, G. Hosseinzadeh, A. L. Ibik, S. W. Jha, D. O. Jones, D. Langeroodi, N. LeBaron, E. A. Magnier, A. L. Piro, S. I. Raimundo, A. Rest, S. Rest, R. M. Rich, C. Rojas-Bravo, H. Sears, K. Taggart, V. A. Villar, R. J. Wainscoat, X.-F. Wang, A. R. Wasserman, S. Yan, Y. Yang, J. Zhang, and W. Zheng. Final Moments III: Explosion Properties and Progenitor Constraints of CSM-Interacting Type II Supernovae. *arXiv e-prints*, art. arXiv:2505.04698, May 2025a. doi: 10.48550/arXiv.2505.04698.

W. V. Jacobson-Galán, L. Dessart, K. W. Davis, K. A. Bostroem, C. D. Kilpatrick, R. Margutti, A. V. Filippenko, R. J. Foley, R. Chornock, G. Terreran, D. Hiramatsu, M. Newsome, E. Padilla Gonzalez, C. Pellegrino, D. A. Howell, J. P. Anderson, C. R. Angus, K. Auchettl, T. G. Brink, R. Cartier, D. A. Coulter, T. de Boer, M. R. Drout, N. Earl, K. Ertini, J. R. Farah, D. Farias, C. Gall, H. Gao, M. A. Gerlach, F. Guo, A. Haynie, G. Hosseinzadeh, A. L. Ibik, S. W. Jha, D. O. Jones, D. Langeroodi, N. LeBaron, E. A. Magnier, A. L. Piro, S. I. Raimundo, A. Rest, S. Rest, R. Michael Rich, C. Rojas-Bravo, H. Sears, K. Taggart, V. A.

Villar, R. J. Wainscoat, X.-F. Wang, A. R. Wasserman, S. Yan, Y. Yang, J. Zhang, and W. Zheng. Final Moments. III. Explosion Properties and Progenitor Constraints of CSM-interacting Type II Supernovae. *ApJ*, 992(1):100, Oct. 2025b. doi: 10.3847/1538-4357/adfa23.

J. Jäger, Zoltán, J. Vinkó, B. I. Bíró, T. Hegedüs, T. Borkovits, S. Jäger, Zoltán, A. P. Nagy, L. Molnár, and L. Kriskovics. A low-luminosity core-collapse supernova very similar to SN 2005cs. *MNRAS*, 496(3):3725–3740, Aug. 2020. doi: 10.1093/mnras/staa1743.

H.-T. Janka. Explosion Mechanisms of Core-Collapse Supernovae. *Annual Review of Nuclear and Particle Science*, 62(1):407–451, Nov. 2012. doi: 10.1146/annurev-nucl-102711-094901.

H. T. Janka, B. Müller, F. S. Kitaura, and R. Buras. Dynamics of shock propagation and nucleosynthesis conditions in O-Ne-Mg core supernovae. *A&A*, 485(1):199–208, July 2008. doi: 10.1051/0004-6361:20079334.

J. E. Jencson, S. M. Adams, H. E. Bond, S. D. van Dyk, M. M. Kasliwal, J. Bally, N. Blagorodnova, K. De, C. Fremling, Y. Yao, A. Fruchter, D. Rubin, C. Barbarino, J. Sollerman, A. A. Miller, E. K. S. Hicks, M. A. Malkan, I. Andreoni, E. C. Bellm, R. Buchheim, R. Dekany, M. Feeney, S. Frederick, A. Gal-Yam, R. D. Gehrz, M. Giomi, M. J. Graham, W. Green, D. Hale, M. J. Hankins, M. Hanson, G. Helou, A. Y. Q. Ho, T. Hung, M. Jurić, M. R. Kendurkar, S. R. Kulkarni, R. M. Lau, F. J. Masci, J. D. Neill, K. Quin, R. L. Riddle, B. Rusholme, F. Sims, N. Smith, R. M. Smith, M. T. Soumagnac, Y. Tachibana, S. Tinyanont, R. Walters, S. Watson, and R. E. Williams. Discovery of an Intermediate-luminosity Red Transient in M51 and Its Likely Dust-obscured, Infrared-variable Progenitor. *ApJ*, 880(2):L20, Aug. 2019a. doi: 10.3847/2041-8213/ab2c05.

J. E. Jencson, M. M. Kasliwal, S. M. Adams, H. E. Bond, K. De, J. Johansson, V. Karambelkar, R. M. Lau, S. Tinyanont, S. D. Ryder, A. M. Cody, F. J. Masci, J. Bally, N. Blagorodnova, S. Castellón, C. Fremling, R. D. Gehrz, G. Helou, C. D. Kilpatrick, P. A. Milne, N. Morrell, D. A. Perley, M. M. Phillips, N. Smith, S. D. van Dyk, and R. E. Williams. The SPIRITS Sample of Luminous Infrared Transients: Uncovering Hidden Supernovae and Dusty Stellar Outbursts in Nearby Galaxies. *ApJ*, 886(1):40, Nov. 2019b. doi: 10.3847/1538-4357/ab4a01.

A. Jerkstrand, C. Fransson, and C. Kozma. The ^{44}Ti-powered spectrum of SN 1987A. *A&A*, 530:A45, June 2011. doi: 10.1051/0004-6361/201015937.

A. Jerkstrand, C. Fransson, K. Maguire, S. Smartt, M. Ergon, and J. Spyromilio. The progenitor mass of the Type IIP supernova SN 2004et from late-time spectral modeling. *A&A*, 546:A28, Oct. 2012. doi: 10.1051/0004-6361/201219528.

A. Jerkstrand, S. J. Smartt, M. Fraser, C. Fransson, J. Sollerman, F. Taddia, and R. Kotak. The nebular spectra of SN 2012aw and constraints on stellar nucle-

osynthesis from oxygen emission lines. *MNRAS*, 439(4):3694–3703, Apr. 2014a. doi: 10.1093/mnras/stu221.

A. Jerkstrand, S. J. Smartt, M. Fraser, C. Fransson, J. Sollerman, F. Taddia, and R. Kotak. The nebular spectra of SN 2012aw and constraints on stellar nucleosynthesis from oxygen emission lines. *MNRAS*, 439(4):3694–3703, Apr. 2014b. doi: 10.1093/mnras/stu221.

A. Jerkstrand, M. Ergon, S. J. Smartt, C. Fransson, J. Sollerman, S. Taubenberger, M. Bersten, and J. Spyromilio. Late-time spectral line formation in Type IIb supernovae, with application to SN 1993J, SN 2008ax, and SN 2011dh. *A&A*, 573:A12, Jan. 2015a. doi: 10.1051/0004-6361/201423983.

A. Jerkstrand, S. J. Smartt, J. Sollerman, C. Inserra, M. Fraser, J. Spyromilio, C. Fransson, T.-W. Chen, C. Barbarino, M. Dall'Ora, M. T. Botticella, M. Della Valle, A. Gal-Yam, S. Valenti, K. Maguire, P. Mazzali, and L. Tomasella. Super-solar Ni/Fe production in the Type IIP SN 2012ec. *MNRAS*, 448(3):2482–2494, Apr. 2015b. doi: 10.1093/mnras/stv087.

A. Jerkstrand, S. J. Smartt, J. Sollerman, C. Inserra, M. Fraser, J. Spyromilio, C. Fransson, T.-W. Chen, C. Barbarino, M. Dall'Ora, M. T. Botticella, M. Della Valle, A. Gal-Yam, S. Valenti, K. Maguire, P. Mazzali, and L. Tomasella. Super-solar Ni/Fe production in the Type IIP SN 2012ec. *MNRAS*, 448(3):2482–2494, Apr. 2015c. doi: 10.1093/mnras/stv087.

A. Jerkstrand, T. Ertl, H. T. Janka, E. Müller, T. Sukhbold, and S. E. Woosley. Emission line models for the lowest mass core-collapse supernovae - I. Case study of a 9 $M_{\odot}$ one-dimensional neutrino-driven explosion. *MNRAS*, 475(1): 277–305, Mar. 2018. doi: 10.1093/mnras/stx2877.

L. Jiang, T. M. Tauris, W.-C. Chen, and J. Fuller. Novel Model of an Ultra-stripped Supernova Progenitor of a Double Neutron Star. *ApJ*, 920(2):L36, Oct. 2021. doi: 10.3847/2041-8213/ac2cc9.

S. Jones, R. Hirschi, K. Nomoto, T. Fischer, F. X. Timmes, F. Herwig, B. Paxton, H. Toki, T. Suzuki, G. Martínez-Pinedo, Y. H. Lam, and M. G. Bertolli. Advanced Burning Stages and Fate of 8-10 M $_{\odot}$ Stars. *ApJ*, 772(2):150, Aug. 2013. doi: 10.1088/0004-637X/772/2/150.

S. Jones, B. Côté, F. K. Röpke, and S. Wanajo. A New Model for Electron-capture Supernovae in Galactic Chemical Evolution. *ApJ*, 882(2):170, Sept. 2019. doi: 10.3847/1538-4357/ab384e.

V. R. Karambelkar, M. M. Kasliwal, N. Blagorodnova, J. Sollerman, R. Aloisi, S. G. Anand, I. Andreoni, T. G. Brink, R. Bruch, D. Cook, K. K. Das, K. De, A. Drake, A. V. Filippenko, C. Fremling, G. Helou, A. Ho, J. Jencson, D. Jones, R. R. Laher, F. J. Masci, K. C. Patra, J. Purdum, A. Reedy, T. Sit, Y. Sharma, A. Tzanidakis, S. J. van der Walt, Y. Yao, and C. Zhang. Volumetric Rates of Luminous Red

Novae and Intermediate-luminosity Red Transients with the Zwicky Transient Facility. *ApJ*, 948(2):137, May 2023. doi: 10.3847/1538-4357/acc2b9.

D. Kasen. Seeing the Collision of a Supernova with Its Companion Star. *ApJ*, 708 (2):1025–1031, Jan. 2010. doi: 10.1088/0004-637X/708/2/1025.

D. Kasen. Unusual Supernovae and Alternative Power Sources. In A. W. Alsabti and P. Murdin, editors, *Handbook of Supernovae*, page 939. 2017. doi: 10.1007/978-3-319-21846-5_32.

D. Kasen and S. E. Woosley. Type II Supernovae: Model Light Curves and Standard Candle Relationships. *ApJ*, 703(2):2205–2216, Oct. 2009. doi: 10.1088/0004-637X/703/2/2205.

K. Kashiyama, R. Sawada, and Y. Suwa. X-Raying the Birth of Binary Neutron Stars and Neutron Star-Black Hole Binaries. *ApJ*, 935(2):86, Aug. 2022. doi: 10.3847/1538-4357/ac7ff7.

M. M. Kasliwal, S. R. Kulkarni, A. Gal-Yam, O. Yaron, R. M. Quimby, E. O. Ofek, P. Nugent, D. Poznanski, J. Jacobsen, A. Sternberg, I. Arcavi, D. A. Howell, M. Sullivan, D. J. Rich, P. F. Burke, J. Brimacombe, D. Milisavljevic, R. Fesen, L. Bildsten, K. Shen, S. B. Cenko, J. S. Bloom, E. Hsiao, N. M. Law, N. Gehrels, S. Immler, R. Dekany, G. Rahmer, D. Hale, R. Smith, J. Zolkower, V. Velur, R. Walters, J. Henning, K. Bui, and D. McKenna. Rapidly Decaying Supernova 2010X: A Candidate "Ia" Explosion. *ApJ*, 723(1):L98–L102, Nov. 2010. doi: 10.1088/2041-8205/723/1/L98.

M. M. Kasliwal, S. R. Kulkarni, A. Gal-Yam, P. E. Nugent, M. Sullivan, L. Bildsten, O. Yaron, H. B. Perets, I. Arcavi, S. Ben-Ami, V. B. Bhalerao, J. S. Bloom, S. B. Cenko, A. V. Filippenko, D. A. Frail, M. Ganeshalingam, A. Horesh, D. A. Howell, N. M. Law, D. C. Leonard, W. Li, E. O. Ofek, D. Polishook, D. Poznanski, R. M. Quimby, J. M. Silverman, A. Sternberg, and D. Xu. Calcium-rich Gap Transients in the Remote Outskirts of Galaxies. *ApJ*, 755:161, Aug. 2012a. doi: 10.1088/0004-637X/755/2/161.

M. M. Kasliwal, S. R. Kulkarni, A. Gal-Yam, P. E. Nugent, M. Sullivan, L. Bildsten, O. Yaron, H. B. Perets, I. Arcavi, S. Ben-Ami, V. B. Bhalerao, J. S. Bloom, S. B. Cenko, A. V. Filippenko, D. A. Frail, M. Ganeshalingam, A. Horesh, D. A. Howell, N. M. Law, D. C. Leonard, W. Li, E. O. Ofek, D. Polishook, D. Poznanski, R. M. Quimby, J. M. Silverman, A. Sternberg, and D. Xu. Calcium-rich Gap Transients in the Remote Outskirts of Galaxies. *ApJ*, 755(2):161, Aug. 2012b. doi: 10.1088/0004-637X/755/2/161.

M. M. Kasliwal, E. Nakar, L. P. Singer, D. L. Kaplan, D. O. Cook, A. Van Sistine, R. M. Lau, C. Fremling, O. Gottlieb, J. E. Jencson, S. M. Adams, U. Feindt, K. Hotokezaka, S. Ghosh, D. A. Perley, P.-C. Yu, T. Piran, J. R. Allison, G. C. Anupama, A. Balasubramanian, K. W. Bannister, J. Bally, J. Barnes, S. Barway, E. Bellm, V. Bhalerao, D. Bhattacharya, N. Blagorodnova, J. S. Bloom, P. R.

Brady, C. Cannella, D. Chatterjee, S. B. Cenko, B. E. Cobb, C. Copperwheat, A. Corsi, K. De, D. Dobie, S. W. K. Emery, P. A. Evans, O. D. Fox, D. A. Frail, C. Frohmaier, A. Goobar, G. Hallinan, F. Harrison, G. Helou, T. Hinderer, A. Y. Q. Ho, A. Horesh, W.-H. Ip, R. Itoh, D. Kasen, H. Kim, N. P. M. Kuin, T. Kupfer, C. Lynch, K. Madsen, P. A. Mazzali, A. A. Miller, K. Mooley, T. Murphy, C.-C. Ngeow, D. Nichols, S. Nissanke, P. Nugent, E. O. Ofek, H. Qi, R. M. Quimby, S. Rosswog, F. Rusu, E. M. Sadler, P. Schmidt, J. Sollerman, I. Steele, A. R. Williamson, Y. Xu, L. Yan, Y. Yatsu, C. Zhang, and W. Zhao. Illuminating gravitational waves: A concordant picture of photons from a neutron star merger. *Science*, 358(6370):1559–1565, 2017. ISSN 0036-8075. doi: 10.1126/science.aap9455. URL https://science.sciencemag.org/content/358/6370/1559.

M. M. Kasliwal, C. Cannella, A. Bagdasaryan, T. Hung, U. Feindt, L. P. Singer, M. Coughlin, C. Fremling, R. Walters, D. Duev, R. Itoh, and R. M. Quimby. The GROWTH Marshal: A Dynamic Science Portal for Time-domain Astronomy. *PASP*, 131(3):038003, Mar. 2019. doi: 10.1088/1538-3873/aafbc2.

M. M. Kasliwal, C. Fremling, L. Yan, K. Das, F. Verdi, J. Zmudzinas, C. Martin, E. Kirby, S. Xue, L. Ho, G. Herczeg, X. Wu, Z. Hu, H. Ji, M. Matuszewski, R. Bertz, D. Hale, H. Rodriguez, A. Boden, R. Dekany, R. Smith, D. Reiley, R. Nash, J. Milburn, D. Neill, J. Brugger, R. Zarzaca, B. Weber, and C. Shapiro. The First Science Spectrum with the Next Generation Palomar Spectrograph (NGPS): Classification of ZTF24abrfcqd as a Type Ia Supernova. *Transient Name Server AstroNote*, 340:1, Nov. 2024.

K. S. Kawabata, K. Maeda, K. Nomoto, S. Taubenberger, M. Tanaka, J. Deng, E. Pian, T. Hattori, and K. Itagaki. A massive star origin for an unusual helium-rich supernova in an elliptical galaxy. *Nature*, 465(7296):326–328, May 2010. doi: 10.1038/nature09055.

J. Kennicutt, Robert C. Star Formation in Galaxies Along the Hubble Sequence. *ARA&A*, 36:189–232, Jan. 1998. doi: 10.1146/annurev.astro.36.1.189.

D. Khatami and D. Kasen. The Landscape of Thermal Transients from Supernova Interacting with a Circumstellar Medium. *arXiv e-prints*, art. arXiv:2304.03360, Apr. 2023. doi: 10.48550/arXiv.2304.03360.

D. K. Khatami and D. N. Kasen. Physics of Luminous Transient Light Curves: A New Relation between Peak Time and Luminosity. *ApJ*, 878(1):56, June 2019. doi: 10.3847/1538-4357/ab1f09.

A. M. Khokhlov, P. A. Höflich, E. S. Oran, J. C. Wheeler, L. Wang, and A. Y. Chtchelkanova. Jet-induced Explosions of Core Collapse Supernovae. *ApJ*, 524 (2):L107–L110, Oct. 1999. doi: 10.1086/312305.

C. D. Kilpatrick, R. J. Foley, W. V. Jacobson-Galán, A. L. Piro, S. J. Smartt, M. R. Drout, A. Gagliano, C. Gall, J. Hjorth, D. O. Jones, K. S. Mandel, R. Margutti,

E. Ramirez-Ruiz, C. L. Ransome, V. A. Villar, D. A. Coulter, H. Gao, D. J. Matthews, K. Taggart, and Y. Zenati. SN 2023ixf in Messier 101: A Variable Red Supergiant as the Progenitor Candidate to a Type II Supernova. *ApJ*, 952(1): L23, July 2023. doi: 10.3847/2041-8213/ace4ca.

Y. L. Kim, M. Rigault, J. D. Neill, M. Briday, Y. Copin, J. Lezmy, N. Nicolas, R. Riddle, Y. Sharma, M. Smith, J. Sollerman, and R. Walters. New Modules for the SEDMachine to Remove Contaminations from Cosmic Rays and Non-target Light: BYECR and CONTSEP. *PASP*, 134(1032):024505, Feb. 2022. doi: 10.1088/1538-3873/ac50a0.

O. S. Kirsebom, S. Jones, D. F. Strömberg, G. Martínez-Pinedo, K. Langanke, F. K. Röpke, B. A. Brown, T. Eronen, H. O. U. Fynbo, M. Hukkanen, A. Idini, A. Jokinen, A. Kankainen, J. Kostensalo, I. Moore, H. Möller, S. T. Ohlmann, H. Penttilä, K. Riisager, S. Rinta-Antila, P. C. Srivastava, J. Suhonen, W. H. Trzaska, and J. ńystö. Discovery of an Exceptionally Strong β -Decay Transition of ^{20}F and Implications for the Fate of Intermediate-Mass Stars. *Phys. Rev. Lett.*, 123(26):262701, Dec. 2019. doi: 10.1103/PhysRevLett.123.262701.

F. S. Kitaura, H. T. Janka, and W. Hillebrandt. Explosions of O-Ne-Mg cores, the Crab supernova, and subluminous type II-P supernovae. *A&A*, 450(1):345–350, Apr. 2006. doi: 10.1051/0004-6361:20054703.

I. K. W. Kleiser and D. Kasen. Rapidly fading supernovae from massive star explosions. *MNRAS*, 438(1):318–328, Feb. 2014. doi: 10.1093/mnras/stt2191.

I. K. W. Kleiser, D. Kasen, and P. C. Duffell. Models of bright nickel-free supernovae from stripped massive stars with circumstellar shells. *MNRAS*, 475(3):3152–3164, Apr. 2018. doi: 10.1093/mnras/stx3321.

H. A. Kobulnicky, D. C. Kiminki, M. J. Lundquist, J. Burke, J. Chapman, E. Keller, K. Lester, E. K. Rolen, E. Topel, A. Bhattacharjee, R. A. Smullen, C. A. Vargas Álvarez, J. C. Runnoe, D. A. Dale, and M. M. Brotherton. Toward Complete Statistics of Massive Binary Stars: Penultimate Results from the Cygnus OB2 Radial Velocity Survey. *ApJS*, 213(2):34, Aug. 2014. doi: 10.1088/0067-0049/213/2/34.

C. S. Kochanek, R. Khan, and X. Dai. On Absorption by Circumstellar Dust, with the Progenitor of SN 2012aw as a Case Study. *ApJ*, 759(1):20, Nov. 2012. doi: 10.1088/0004-637X/759/1/20.

I. Kondo, T. Sumi, N. Koshimoto, N. J. Rattenbury, D. Suzuki, and D. P. Bennett. Prediction of Planet Yields by the PRime-focus Infrared Microlensing Experiment Microlensing Survey. *AJ*, 165(6):254, June 2023. doi: 10.3847/1538-3881/acccf9.

A. Kozyreva, E. Nakar, and R. Waldman. The role of radioactive nickel in shaping the plateau phase of Type II supernovae. *MNRAS*, 483(1):1211–1223, Feb. 2019. doi: 10.1093/mnras/sty3185.

A. Kozyreva, P. Baklanov, S. Jones, G. Stockinger, and H.-T. Janka. Synthetic observables for electron-capture supernovae and low-mass core collapse supernovae. *MNRAS*, 503(1):797–814, May 2021. doi: 10.1093/mnras/stab350.

A. Kozyreva, H.-T. Janka, D. Kresse, S. Taubenberger, and P. Baklanov. Low-luminosity type IIP supermnovae: SN 2005cs and SN 2020cxd as very low-energy iron core-collapse explosions. *MNRAS*, 514(3):4173–4189, Aug. 2022. doi: 10.1093/mnras/stac1518.

S. R. Kulkarni, F. A. Harrison, B. W. Grefenstette, H. P. Earnshaw, I. Andreoni, D. A. Berg, J. S. Bloom, S. B. Cenko, R. Chornock, J. L. Christiansen, M. W. Coughlin, A. Wuollet Criswell, B. Darvish, K. K. Das, K. De, L. Dessart, D. Dixon, B. Dorsman, K. El-Badry, C. Evans, K. E. S. Ford, C. Fremling, B. T. Gansicke, S. Gezari, Y. Gotberg, G. M. Green, M. J. Graham, M. Heida, A. Y. Q. Ho, A. D. Jaodand, C. M. Johns-Krull, M. M. Kasliwal, M. Lazzarini, W. Lu, R. Margutti, D. C. Martin, D. C. Masters, B. McKernan, S. M. Nissanke, B. Parazin, D. A. Perley, E. S. Phinney, A. L. Piro, G. Raaijmakers, A. C. Rodriguez, P. Senchyna, L. P. Singer, J. J. Spake, K. G. Stassun, D. Stern, H. I. Teplitz, D. R. Weisz, and Y. Yao. Science with the Ultraviolet Explorer (UVEX). *arXiv e-prints*, art. arXiv:2111.15608, Nov. 2021.

D. Lang. unWISE: Unblurred Coadds of the WISE Imaging. *AJ*, 147:108, May 2014. doi: 10.1088/0004-6256/147/5/108.

E. Laplace, Y. Götberg, S. E. de Mink, S. Justham, and R. Farmer. The expansion of stripped-envelope stars: Consequences for supernovae and gravitational-wave progenitors. *A&A*, 637:A6, May 2020. doi: 10.1051/0004-6361/201937300.

D. C. Leonard, A. V. Filippenko, M. Ganeshalingam, F. J. D. Serduke, W. Li, B. J. Swift, A. Gal-Yam, R. J. Foley, D. B. Fox, S. Park, J. L. Hoffman, and D. S. Wong. A non-spherical core in the explosion of supernova SN 2004dj. *Nature*, 440(7083):505–507, Mar. 2006. doi: 10.1038/nature04558.

S.-C. Leung and J. Fuller. Hydrodynamic Simulations of Pre-supernova Outbursts in Red Supergiants: Asphericity and Mass Loss. *ApJ*, 900(2):99, Sept. 2020. doi: 10.3847/1538-4357/abac5d.

S.-C. Leung, K. Nomoto, and S. Blinnikov. Pulsational Pair-instability Supernovae. I. Pre-collapse Evolution and Pulsational Mass Ejection. *ApJ*, 887(1):72, Dec. 2019. doi: 10.3847/1538-4357/ab4fe5.

S.-C. Leung, J. Fuller, and K. Nomoto. Fast Blue Optical Transients Due to Circumstellar Interaction and the Mysterious Supernova SN 2018gep. *ApJ*, 915(2): 80, July 2021a. doi: 10.3847/1538-4357/abfcbe.

S.-C. Leung, S. Wu, and J. Fuller. Wave-driven Mass Loss of Stripped Envelope Massive Stars: Progenitor-dependence, Mass Ejection, and Supernovae. *ApJ*, 923 (1):41, Dec. 2021b. doi: 10.3847/1538-4357/ac2c63.

E. M. Levesque, P. Massey, K. A. G. Olsen, B. Plez, E. Josselin, A. Maeder, and G. Meynet. The Effective Temperature Scale of Galactic Red Supergiants: Cool, but Not As Cool As We Thought. *ApJ*, 628(2):973–985, Aug. 2005. doi: 10.1086/430901.

W. Li, S. D. Van Dyk, A. V. Filippenko, J.-C. Cuillandre, S. Jha, J. S. Bloom, A. G. Riess, and M. Livio. Identification of the Red Supergiant Progenitor of Supernova 2005cs: Do the Progenitors of Type II-P Supernovae Have Low Mass? *ApJ*, 641 (2):1060–1070, Apr. 2006. doi: 10.1086/499916.

W. Li, J. Leaman, R. Chornock, A. V. Filippenko, D. Poznanski, M. Ganeshalingam, X. Wang, M. Modjaz, S. Jha, R. J. Foley, and N. Smith. Nearby supernova rates from the Lick Observatory Supernova Search - II. The observed luminosity functions and fractions of supernovae in a complete sample. *MNRAS*, 412:1441–1472, Apr. 2011. doi: 10.1111/j.1365-2966.2011.18160.x.

M. Limongi and A. Chieffi. Evolution, Explosion, and Nucleosynthesis of Core-Collapse Supernovae. *ApJ*, 592(1):404–433, July 2003. doi: 10.1086/375703.

H. Lin, X. Wang, J. Zhang, S. Yan, D. Xiang, T. Zhang, X. Zhao, X. Zhang, H. Sai, L. Rui, J. Mo, G. Xi, F. Huang, X. Li, Y. Cai, W. Lin, J. Lin, C. Wu, J. Zhang, Z. Chen, Z. Li, W. Li, L. Li, K. Zhang, C. Miao, J. Chen, Z. Fan, J. Fu, S. Qian, H. Wu, X.-B. Wu, J. Yan, H. Zhang, J. Zhang, L. Zhang, J. Zheng, and Q. Zhai. A spectral data release for 104 type II supernovae from the Tsinghua Supernova group. *MNRAS*, 528(2):3092–3129, Feb. 2024. doi: 10.1093/mnras/stae144.

S. M. Lisakov, L. Dessart, D. J. Hillier, R. Waldman, and E. Livne. A study of the low-luminosity Type II-Plateau supernova 2008bk. *MNRAS*, 466(1):34–48, Apr. 2017. doi: 10.1093/mnras/stw3035.

I. I. Litvinova and D. K. Nadezhin. Hydrodynamical Models of Type-II Supernovae. *Ap&SS*, 89(1):89–113, Jan. 1983. doi: 10.1007/BF01008387.

N. P. Lourie, J. W. Baker, R. S. Burruss, M. Egan, G. Fżrész, D. Frostig, A. A. Garcia-Zych, N. Ganciu, K. Haworth, E. Hinrichsen, M. M. Kasliwal, V. R. Karambelkar, A. Malonis, R. A. Simcoe, and J. Zolkower. The wide-field infrared transient explorer (WINTER). In C. J. Evans, J. J. Bryant, and K. Motohara, editors, *Ground-based and Airborne Instrumentation for Astronomy VIII*, volume 11447 of *Society of Photo-Optical Instrumentation Engineers (SPIE) Conference Series*, page 114479K, Dec. 2020. doi: 10.1117/12.2561210.

W. Lu, J. Fuller, E. Quataert, and C. Bonnerot. On rapid binary mass transfer - I. Physical model. *MNRAS*, 519(1):1409–1424, Feb. 2023. doi: 10.1093/mnras/stac3621.

R. Lunnan, M. M. Kasliwal, Y. Cao, L. Hangard, O. Yaron, J. T. Parrent, C. McCully, A. Gal-Yam, J. S. Mulchaey, S. Ben-Ami, A. V. Filippenko, C. Fremling, A. S. Fruchter, D. A. Howell, J. Koda, T. Kupfer, S. R. Kulkarni, R. Laher, F. Masci,

P. E. Nugent, E. O. Ofek, M. Yagi, and L. Yan. Two New Calcium-rich Gap Transients in Group and Cluster Environments. *ApJ*, 836(1):60, Feb. 2017. doi: 10.3847/1538-4357/836/1/60.

J. D. Lyman, D. Bersier, and P. A. James. Bolometric corrections for optical light curves of core-collapse supernovae. *MNRAS*, 437(4):3848–3862, Feb. 2014. doi: 10.1093/mnras/stt2187.

J. D. Lyman, A. J. Levan, P. A. James, C. R. Angus, R. P. Church, M. B. Davies, and N. R. Tanvir. Hubble Space Telescope observations of the host galaxies and environments of calcium-rich supernovae. *MNRAS*, 458(2):1768–1777, May 2016. doi: 10.1093/mnras/stw477.

A. I. MacFadyen and S. E. Woosley. Collapsars: Gamma-Ray Bursts and Explosions in "Failed Supernovae". *ApJ*, 524(1):262–289, Oct. 1999. doi: 10.1086/307790.

A. I. MacFadyen, S. E. Woosley, and A. Heger. Supernovae, Jets, and Collapsars. *ApJ*, 550(1):410–425, Mar. 2001. doi: 10.1086/319698.

P. Madau and M. Dickinson. Cosmic Star-Formation History. *ARA&A*, 52:415–486, Aug. 2014. doi: 10.1146/annurev-astro-081811-125615.

K. Maeda, K. Kawabata, M. Tanaka, K. Nomoto, N. Tominaga, T. Hattori, T. Minezaki, T. Kuroda, T. Suzuki, J. Deng, P. A. Mazzali, and E. Pian. SN 2006aj Associated with XRF 060218 at Late Phases: Nucleosynthesis Signature of a Neutron Star-driven Explosion. *ApJ*, 658(1):L5–L8, Mar. 2007. doi: 10.1086/513564.

M. R. Magee and K. Maguire. An investigation of ^{56}Ni shells as the source of early light curve bumps in type Ia supernovae. *A&A*, 642:A189, Oct. 2020. doi: 10.1051/0004-6361/202037870.

M. R. Magee, K. Maguire, R. Kotak, S. A. Sim, J. H. Gillanders, S. J. Prentice, and K. Skillen. Determining the ^{56}Ni distribution of type Ia supernovae from observations within days of explosion. *A&A*, 634:A37, Feb. 2020. doi: 10.1051/0004-6361/201936684.

K. Maguire, E. Di Carlo, S. J. Smartt, A. Pastorello, D. Y. Tsvetkov, S. Benetti, S. Spiro, A. A. Arkharov, G. Beccari, M. T. Botticella, E. Cappellaro, S. Cristallo, M. Dolci, N. Elias-Rosa, M. Fiaschi, D. Gorshanov, A. Harutyunyan, V. M. Larionov, H. Navasardyan, A. Pietrinferni, G. Raimondo, G. di Rico, S. Valenti, G. Valentini, and L. Zampieri. Optical and near-infrared coverage of SN 2004et: physical parameters and comparison with other Type IIP supernovae. *MNRAS*, 404(2):981–1004, May 2010. doi: 10.1111/j.1365-2966.2010.16332.x.

K. Maguire, A. Jerkstrand, S. J. Smartt, C. Fransson, A. Pastorello, S. Benetti, S. Valenti, F. Bufano, and G. Leloudas. Constraining the physical properties of Type II-Plateau supernovae using nebular phase spectra. *MNRAS*, 420(4):3451–3468, Mar. 2012. doi: 10.1111/j.1365-2966.2011.20276.x.

A. Mahabal, U. Rebbapragada, R. Walters, F. J. Masci, N. Blagorodnova, J. van Roestel, Q.-Z. Ye, R. Biswas, K. Burdge, C.-K. Chang, D. A. Duev, V. Z. Golkhou, A. A. Miller, J. Nordin, C. Ward, S. Adams, E. C. Bellm, D. Branton, B. Bue, C. Cannella, A. Connolly, R. Dekany, U. Feindt, T. Hung, L. Fortson, S. Frederick, C. Fremling, S. Gezari, M. Graham, S. Groom, M. M. Kasliwal, S. Kulkarni, T. Kupfer, H. W. Lin, C. Lintott, R. Lunnan, J. Parejko, T. A. Prince, R. Riddle, B. Rusholme, N. Saunders, N. Sedaghat, D. L. Shupe, L. P. Singer, M. T. Soumagnac, P. Szkody, Y. Tachibana, K. Tirumala, S. van Velzen, and D. Wright. Machine Learning for the Zwicky Transient Facility. *PASP*, 131(3): 038002, Mar. 2019. doi: 10.1088/1538-3873/aaf3fa.

A. Mainzer, J. Bauer, R. M. Cutri, T. Grav, J. Masiero, R. Beck, P. Clarkson, T. Conrow, J. Dailey, P. Eisenhardt, B. Fabinsky, S. Fajardo-Acosta, J. Fowler, C. Gelino, C. Grillmair, I. Heinrichsen, M. Kendall, J. D. Kirkpatrick, F. Liu, F. Masci, H. McCallon, C. R. Nugent, M. Papin, E. Rice, D. Royer, T. Ryan, P. Sevilla, S. Sonnett, R. Stevenson, D. B. Thompson, S. Wheelock, D. Wiemer, M. Wittman, E. Wright, and L. Yan. Initial Performance of the NEOWISE Reactivation Mission. *ApJ*, 792(1):30, Sept. 2014. doi: 10.1088/0004-637X/792/1/30.

C. Maraston, L. Hill, D. Thomas, R. Yan, Y. Chen, J. Lian, T. Parikh, J. Neumann, S. Meneses-Goytia, M. Bershady, N. Drory, D. Bizyaev, A. Concas, J. Brownstein, D. Lazarz, G. Stringfellow, and K. Stassun. Stellar population models based on the SDSS-IV MaStar library of stellar spectra - I. Intermediate-age/old models. *MNRAS*, 496(3):2962–2997, Aug. 2020. doi: 10.1093/mnras/staa1489.

B. Margalit and B. D. Metzger. Time-dependent models of accretion discs with nuclear burning following the tidal disruption of a white dwarf by a neutron star. *MNRAS*, 461(2):1154–1176, Sept. 2016. doi: 10.1093/mnras/stw1410.

J. R. Marshall, J. T. van Loon, M. Matsuura, P. R. Wood, A. A. Zijlstra, and P. A. Whitelock. Asymptotic giant branch superwind speed at low metallicity. *MNRAS*, 355(4):1348–1360, Dec. 2004. doi: 10.1111/j.1365-2966.2004.08417.x.

A. P. Marston. A Survey of Nebulae around Galactic Wolf-Rayet Stars in the Southern Sky. III. Survey Completion and Conclusions. *ApJ*, 475(1):188–193, Jan. 1997. doi: 10.1086/303534.

C. Martin, A. Moore, P. Morrissey, M. Matuszewski, S. Rahman, S. Adkins, and H. Epps. The Keck Cosmic Web Imager. In I. S. McLean, S. K. Ramsay, and H. Takami, editors, *Ground-based and Airborne Instrumentation for Astronomy III*, volume 7735 of *Society of Photo-Optical Instrumentation Engineers (SPIE) Conference Series*, page 77350M, July 2010. doi: 10.1117/12.858227.

D. C. Martin, J. Fanson, D. Schiminovich, P. Morrissey, P. G. Friedman, T. A. Barlow, T. Conrow, R. Grange, P. N. Jelinsky, B. Milliard, O. H. W. Siegmund, L. Bianchi, Y.-I. Byun, J. Donas, K. Forster, T. M. Heckman, Y.-W. Lee, B. F.

Madore, R. F. Malina, S. G. Neff, R. M. Rich, T. Small, F. Surber, A. S. Szalay, B. Welsh, and T. K. Wyder. The Galaxy Evolution Explorer: A Space Ultraviolet Survey Mission. *ApJ*, 619(1):L1–L6, Jan 2005. doi: 10.1086/426387.

L. Martinez, M. C. Bersten, J. P. Anderson, S. González-Gaitán, F. Förster, and G. Folatelli. Progenitor properties of type II supernovae: fitting to hydrodynamical models using Markov chain Monte Carlo methods. *A&A*, 642:A143, Oct. 2020. doi: 10.1051/0004-6361/202038393.

L. Martinez, J. P. Anderson, M. C. Bersten, M. Hamuy, S. González-Gaitán, M. Orellana, M. Stritzinger, M. M. Phillips, C. P. Gutiérrez, C. Burns, T. de Jaeger, K. Ertini, G. Folatelli, F. Förster, L. Galbany, P. Hoeflich, E. Y. Hsiao, N. Morrell, P. J. Pessi, and N. B. Suntzeff. Type II supernovae from the Carnegie Supernova Project-I. III. Understanding SN II diversity through correlations between physical and observed properties. *A&A*, 660:A42, Apr. 2022a. doi: 10.1051/0004-6361/202142555.

L. Martinez, M. C. Bersten, J. P. Anderson, M. Hamuy, S. González-Gaitán, F. Förster, M. Orellana, M. Stritzinger, M. M. Phillips, C. P. Gutiérrez, C. Burns, C. Contreras, T. de Jaeger, K. Ertini, G. Folatelli, L. Galbany, P. Hoeflich, E. Y. Hsiao, N. Morrell, P. J. Pessi, and N. B. Suntzeff. Type II supernovae from the Carnegie Supernova Project-I. II. Physical parameter distributions from hydrodynamical modelling. *A&A*, 660:A41, Apr. 2022b. doi: 10.1051/0004-6361/202142076.

F. J. Masci, R. R. Laher, B. Rusholme, D. L. Shupe, S. Groom, J. Surace, E. Jackson, S. Monkewitz, R. Beck, D. Flynn, S. Terek, W. Landry, E. Hacopians, V. Desai, J. Howell, T. Brooke, D. Imel, S. Wachter, Q.-Z. Ye, H.-W. Lin, S. B. Cenko, V. Cunningham, U. Rebbapragada, B. Bue, A. A. Miller, A. Mahabal, E. C. Bellm, M. T. Patterson, M. Jurić, V. Z. Golkhou, E. O. Ofek, R. Walters, M. Graham, M. M. Kasliwal, R. G. Dekany, T. Kupfer, K. Burdge, C. B. Cannella, T. Barlow, A. Van Sistine, M. Giomi, C. Fremling, N. Blagorodnova, D. Levitan, R. Riddle, R. M. Smith, G. Helou, T. A. Prince, and S. R. Kulkarni. The Zwicky Transient Facility: Data Processing, Products, and Archive. *PASP*, 131(1):018003, Jan. 2019. doi: 10.1088/1538-3873/aae8ac.

F. J. Masci, R. R. Laher, B. Rusholme, D. Shupe, R. Paladini, S. Groom, A. Wold, A. A. Miller, and A. Drake. A New Forced Photometry Service for the Zwicky Transient Facility. *arXiv e-prints*, art. arXiv:2305.16279, May 2023. doi: 10.48550/arXiv.2305.16279.

B. D. Mason, T. J. Henry, W. I. Hartkopf, T. ten Brummelaar, and D. R. Soderblom. A Multiplicity Survey of Chromospherically Active and Inactive Stars. *AJ*, 116 (6):2975–2983, Dec. 1998. doi: 10.1086/300654.

T. Matsuoka and K. Maeda. Radio Emission from Ultra-stripped Supernovae as Diagnostics for Properties of the Remnant Double Neutron Star Binaries. *ApJ*, 898(2):158, Aug. 2020. doi: 10.3847/1538-4357/ab9c1b.

S. Mattila, S. J. Smartt, J. J. Eldridge, J. R. Maund, R. M. Crockett, and I. J. Danziger. VLT Detection of a Red Supergiant Progenitor of the Type II-P Supernova 2008bk. *ApJ*, 688(2):L91, Dec. 2008. doi: 10.1086/595587.

S. Mattila, T. Dahlen, A. Efstathiou, E. Kankare, J. Melinder, A. Alonso-Herrero, M. Á. Pérez-Torres, S. Ryder, P. Väisänen, and G. Östlin. Core-collapse Supernovae Missed by Optical Surveys. *ApJ*, 756(2):111, Sept. 2012. doi: 10.1088/0004-637X/756/2/111.

C. D. Matzner and C. F. McKee. The Expulsion of Stellar Envelopes in Core-Collapse Supernovae. *ApJ*, 510(1):379–403, Jan. 1999. doi: 10.1086/306571.

J. R. Maund and S. J. Smartt. The Disappearance of the Progenitors of Supernovae 1993J and 2003gd. *Science*, 324(5926):486, Apr. 2009. doi: 10.1126/science.1170198.

J. R. Maund, S. J. Smartt, and I. J. Danziger. The progenitor of SN 2005cs in the Whirlpool Galaxy. *MNRAS*, 364(1):L33–L37, Nov. 2005. doi: 10.1111/j.1745-3933.2005.00100.x.

J. R. Maund, M. Fraser, S. J. Smartt, M. T. Botticella, C. Barbarino, M. Childress, A. Gal-Yam, C. Inserra, G. Pignata, D. Reichart, B. Schmidt, J. Sollerman, F. Taddia, L. Tomasella, S. Valenti, and O. Yaron. Supernova 2012ec: identification of the progenitor and early monitoring with PESSTO. *MNRAS*, 431:L102–L106, Apr. 2013. doi: 10.1093/mnrasl/slt017.

J. R. Maund, S. Mattila, E. Ramirez-Ruiz, and J. J. Eldridge. A new precise mass for the progenitor of the Type IIP SN 2008bk. *MNRAS*, 438(2):1577–1592, Feb. 2014. doi: 10.1093/mnras/stt2296.

O. R. McBrien, S. J. Smartt, T.-W. Chen, C. Inserra, J. H. Gillanders, S. A. Sim, A. Jerkstrand, A. Rest, S. Valenti, R. Roy, M. Gromadzki, S. Taubenberger, A. Flörs, M. E. Huber, K. C. Chambers, A. Gal-Yam, D. R. Young, M. Nicholl, E. Kankare, K. W. Smith, K. Maguire, I. Mandel, S. Prentice, Ó. Rodríguez, J. Pineda Garcia, C. P. Gutiérrez, L. Galbany, C. Barbarino, P. S. J. Clark, J. Sollerman, S. R. Kulkarni, K. De, D. A. H. Buckley, and A. Rau. SN2018kzr: A Rapidly Declining Transient from the Destruction of a White Dwarf. *ApJ*, 885 (1):L23, Nov. 2019. doi: 10.3847/2041-8213/ab4dae.

A. M. Meisner, D. Lang, and D. J. Schlegel. Full-depth Coadds of the WISE and First-year NEOWISE-reactivation Images. *AJ*, 153:38, Jan 2017. doi: 10.3847/1538-3881/153/1/38.

T. Melson, H.-T. Janka, and A. Marek. Neutrino-driven Supernova of a Low-mass Iron-core Progenitor Boosted by Three-dimensional Turbulent Convection. *ApJ*, 801(2):L24, Mar. 2015. doi: 10.1088/2041-8205/801/2/L24.

B. D. Metzger. Luminous Fast Blue Optical Transients and Type Ibn/Icn SNe from Wolf-Rayet/Black Hole Mergers. *ApJ*, 932(2):84, June 2022. doi: 10.3847/1538-4357/ac6d59.

N. Meza and J. P. Anderson. Stripped-envelope core-collapse supernova ^{56}Ni masses. Persistently larger values than supernovae type II. *A&A*, 641:A177, Sept. 2020. doi: 10.1051/0004-6361/201937113.

N. Meza-Retamal, Y. Dong, K. A. Bostroem, S. Valenti, L. Galbany, J. Pearson, G. Hosseinzadeh, J. E. Andrews, D. J. Sand, J. E. Jencson, D. Janzen, M. J. Lundquist, E. T. Hoang, S. Wyatt, P. J. Brown, D. A. Howell, M. Newsome, E. Padilla Gonzalez, C. Pellegrino, G. Terreran, V. Kouprianov, D. Hiramatsu, S. W. Jha, N. Smith, J. Haislip, D. E. Reichart, M. Shrestha, F. F. Rosales-Ortega, T. G. Brink, A. V. Filippenko, W. Zheng, and Y. Yang. Circumstellar Interaction Signatures in the Low-luminosity Type II SN 2021gmj. *ApJ*, 971(2):141, Aug. 2024. doi: 10.3847/1538-4357/ad4d55.

D. Milisavljevic, D. J. Patnaude, J. C. Raymond, M. R. Drout, R. Margutti, A. Kamble, R. Chornock, J. Guillochon, N. E. Sanders, J. T. Parrent, L. Lovisari, I. V. Chilingarian, P. Challis, R. P. Kirshner, M. T. Penny, K. Itagaki, J. J. Eldridge, and T. J. Moriya. iPTF15eqv: Multiwavelength Exposé of a Peculiar Calcium-rich Transient. *ApJ*, 846(1):50, Sept. 2017. doi: 10.3847/1538-4357/aa7d9f.

A. A. Miller, N. S. Abrams, G. Aldering, S. Anand, C. R. Angus, I. Arcavi, C. Baltay, F. E. Bauer, D. Brethauer, J. S. Bloom, H. Bommireddy, M. Catelan, R. Chornock, P. Clark, T. E. Collett, G. Dimitriadis, S. Faris, F. Förster, A. Franckowiak, C. Frohmaier, L. Galbany, R. B. Galleguillos, A. Goobar, O. Graur, C. P. Gutiérrez, S. Hall, E. Hammerstein, K. R. Herner, I. M. Hook, M. J. Huston, J. Johansson, C. D. Kilpatrick, A. G. Kim, R. A. Knop, M. P. Kowalski, L. A. Kwok, N. LeBaron, K. W. Lin, C. Liu, J. R. Lu, W. Lu, R. Lunnan, K. Maguire, L. Makrygianni, R. Margutti, D. Maoz, P. M. Veres, T. Moore, A. J. Nayana, M. Nicholl, J. Nordin, S. R. Oates, G. Pignata, A. Polin, D. Poznanski, J. L. Prieto, D. L. Rabinowitz, N. Rehemtulla, M. Rigault, D. Ryczanowski, N. Sarin, S. Schulze, V. G. Shah, X. Sheng, S. P. R. Shilling, B. D. Simmons, A. Singh, G. P. Smith, M. Smith, J. Sollerman, M. T. Soumagnac, C. W. Stubbs, M. Sullivan, A. Suresh, B. Trakhtenbrot, C. Ward, E. Wiston, H. Xiong, Y. Yao, and P. E. Nugent. The La Silla Schmidt Southern Survey. *PASP*, 137(9):094204, Sept. 2025. doi: 10.1088/1538-3873/ae02c5.

S. Miyaji, K. Nomoto, K. Yokoi, and D. Sugimoto. Supernova triggered by electron captures. *PASJ*, 32:303–329, Jan. 1980.

M. Modjaz, K. Z. Stanek, P. M. Garnavich, P. Berlind, S. Blondin, W. Brown, M. Calkins, P. Challis, A. M. Diamond-Stanic, H. Hao, M. Hicken, R. P. Kirshner, and J. L. Prieto. Early-Time Photometry and Spectroscopy of the Fast Evolving SN 2006aj Associated with GRB 060218. *ApJ*, 645(1):L21–L24, July 2006. doi: 10.1086/505906.

M. Moe and R. Di Stefano. Mind Your Ps and Qs: The Interrelation between Period (P) and Mass-ratio (Q) Distributions of Binary Stars. *ApJS*, 230(2):15, June 2017. doi: 10.3847/1538-4365/aa6fb6.

I. G. Momcheva, J. C. Lee, C. Ly, S. Salim, D. A. Dale, M. Ouchi, R. Finn, and Y. Ono. Nebular Attenuation in Hα-selected Star-forming Galaxies at z = 0.8 from the NewHα Survey. *AJ*, 145(2):47, Feb. 2013. doi: 10.1088/0004-6256/145/2/47.

T. Moore, J. Gillanders, M. Nicholl, M. Huber, S. Smartt, S. Srivastav, H. Stevance, T.-W. Chen, K. Chambers, J. Anderson, M. Fulton, S. Oates, C. Angus, G. Pignata, N. Erasmus, H. Gao, J. Bulger, C.-C. Lin, T. Lowe, E. Magnier, P. Minguez, C.-C. Ngeow, X. Sheng, S. A. Sim, K. Smith, R. Wainscoat, S. Yang, D. Young, and K.-J. Zeng. SN 2023zaw: the low-energy explosion of an ultra-stripped star, with non-radioactive heating. *arXiv e-prints*, art. arXiv:2405.13596, May 2024. doi: 10.48550/arXiv.2405.13596.

J. Morag, N. Sapir, and E. Waxman. Shock cooling emission from explosions of red super-giants: I. A numerically calibrated analytic model. *MNRAS*, Mar. 2023. doi: 10.1093/mnras/stad899.

T. Moriya, N. Tominaga, M. Tanaka, K. Nomoto, D. N. Sauer, P. A. Mazzali, K. Maeda, and T. Suzuki. Fallback Supernovae: A Possible Origin of Peculiar Supernovae with Extremely Low Explosion Energies. *ApJ*, 719(2):1445–1453, Aug. 2010. doi: 10.1088/0004-637X/719/2/1445.

T. J. Moriya and J. J. Eldridge. Rapidly evolving faint transients from stripped-envelope electron-capture supernovae. *MNRAS*, 461(2):2155–2161, Sept. 2016. doi: 10.1093/mnras/stw1471.

T. J. Moriya, P. A. Mazzali, N. Tominaga, S. Hachinger, S. I. Blinnikov, T. M. Tauris, K. Takahashi, M. Tanaka, N. Langer, and P. Podsiadlowski. Light-curve and spectral properties of ultrastripped core-collapse supernovae leading to binary neutron stars. *MNRAS*, 466(2):2085–2098, Apr. 2017. doi: 10.1093/mnras/stw3225.

T. J. Moriya, B. M. Subrayan, D. Milisavljevic, and S. I. Blinnikov. Synthetic red supergiant explosion model grid for systematic characterization of Type II supernovae. *PASJ*, 75(3):634–645, June 2023. doi: 10.1093/pasj/psad024.

T. J. Moriya, B. Müller, S. I. Blinnikov, M. Ushakova, E. I. Sorokina, T. M. Tauris, and A. Heger. Type Ibn supernovae from ultra-stripped supernova progenitors. *PASJ*, 77(6):1385–1392, Dec. 2025. doi: 10.1093/pasj/psaf119.

T. J. Moriya, C. Wu, D. Liu, Z.-W. Liu, and B. Wang. Supernovae interacting with Si and S-rich circumstellar matter from double white dwarf mergers. *arXiv e-prints*, art. arXiv:2603.07064, Mar. 2026. doi: 10.48550/arXiv.2603.07064.

V. Morozova, A. L. Piro, M. Renzo, C. D. Ott, D. Clausen, S. M. Couch, J. Ellis, and L. F. Roberts. Light Curves of Core-collapse Supernovae with Substantial Mass Loss Using the New Open-source SuperNova Explosion Code (SNEC). *ApJ*, 814 (1):63, Nov. 2015. doi: 10.1088/0004-637X/814/1/63.

V. Morozova, A. L. Piro, and S. Valenti. Measuring the Progenitor Masses and Dense Circumstellar Material of Type II Supernovae. *ApJ*, 858(1):15, May 2018. doi: 10.3847/1538-4357/aab9a6.

P. Morrissey, M. Matuszewski, D. C. Martin, J. D. Neill, H. Epps, J. Fucik, B. Weber, B. Darvish, S. Adkins, S. Allen, R. Bartos, J. Belicki, J. Cabak, S. Callahan, D. Cowley, M. Crabill, W. Deich, A. Delecroix, G. Doppman, D. Hilyard, E. James, S. Kaye, M. Kokorowski, S. Kwok, K. Lanclos, S. Milner, A. Moore, D. O'Sullivan, P. Parihar, S. Park, A. Phillips, L. Rizzi, C. Rockosi, H. Rodriguez, Y. Salaun, K. Seaman, D. Sheikh, J. Weiss, and R. Zarzaca. The Keck Cosmic Web Imager Integral Field Spectrograph. *ApJ*, 864(1):93, Sept. 2018a. doi: 10.3847/1538-4357/aad597.

P. Morrissey, M. Matuszewski, D. C. Martin, J. D. Neill, H. Epps, J. Fucik, B. Weber, B. Darvish, S. Adkins, S. Allen, R. Bartos, J. Belicki, J. Cabak, S. Callahan, D. Cowley, M. Crabill, W. Deich, A. Delecroix, G. Doppman, D. Hilyard, E. James, S. Kaye, M. Kokorowski, S. Kwok, K. Lanclos, S. Milner, A. Moore, D. O'Sullivan, P. Parihar, S. Park, A. Phillips, L. Rizzi, C. Rockosi, H. Rodriguez, Y. Salaun, K. Seaman, D. Sheikh, J. Weiss, and R. Zarzaca. The Keck Cosmic Web Imager Integral Field Spectrograph. *ApJ*, 864(1):93, Sept. 2018b. doi: 10.3847/1538-4357/aad597.

J. R. Mould, J. P. Huchra, W. L. Freedman, J. Kennicutt, Robert C., L. Ferrarese, H. C. Ford, B. K. Gibson, J. A. Graham, S. M. G. Hughes, G. D. Illingworth, D. D. Kelson, L. M. Macri, B. F. Madore, S. Sakai, K. M. Sebo, N. A. Silbermann, and P. B. Stetson. The Hubble Space Telescope Key Project on the Extragalactic Distance Scale. XXVIII. Combining the Constraints on the Hubble Constant. *ApJ*, 529(2):786–794, Feb. 2000. doi: 10.1086/308304.

B. Müller. The Status of Multi-Dimensional Core-Collapse Supernova Models. *PASA*, 33:e048, Sept. 2016. doi: 10.1017/pasa.2016.40.

B. Müller, D. W. Gay, A. Heger, T. M. Tauris, and S. A. Sim. Multidimensional simulations of ultrastripped supernovae to shock breakout. *MNRAS*, 479(3): 3675–3689, Sept. 2018. doi: 10.1093/mnras/sty1683.

T. Müller, J. L. Prieto, O. Pejcha, and A. Clocchiatti. The Nickel Mass Distribution of Normal Type II Supernovae. *ApJ*, 841(2):127, June 2017. doi: 10.3847/1538-4357/aa72f1.

T. E. Müller-Bravo, C. P. Gutiérrez, M. Sullivan, A. Jerkstrand, J. P. Anderson, S. González-Gaitán, J. Sollerman, I. Arcavi, J. Burke, L. Galbany, A. Gal-Yam, M. Gromadzki, D. Hiramatsu, G. Hosseinzadeh, D. A. Howell, C. Inserra,

E. Kankare, A. Kozyreva, C. McCully, M. Nicholl, S. Smartt, S. Valenti, and D. R. Young. The low-luminosity Type II SN 2016aqf: a well-monitored spectral evolution of the Ni/Fe abundance ratio. *MNRAS*, 497(1):361–377, Sept. 2020. doi: 10.1093/mnras/staa1932.

Y. Murai, M. Tanaka, M. Kawabata, K. Taguchi, R. S. Teja, T. Nakaoka, K. Maeda, K. S. Kawabata, T. Nagao, T. J. Moriya, D. K. Sahu, G. C. Anupama, N. Tominaga, T. Morokuma, R. Imazawa, S. Inutsuka, K. Isogai, T. Kasuga, N. Kobayashi, S. Kondo, H. Maehara, Y. Mori, Y. Niino, M. Ogawa, R. Ohsawa, S.-i. Okumura, S. Saito, S. Sako, H. Takahashi, K. Uno, and M. Yamanaka. Intermediate-luminosity Type IIP SN 2021gmj: a low-energy explosion with signatures of circumstellar material. *MNRAS*, 528(3):4209–4227, Mar. 2024. doi: 10.1093/mnras/stae170.

T. Nagao, H. Kuncarayakti, K. Maeda, T. Moore, A. Pastorello, S. Mattila, K. Uno, S. J. Smartt, S. A. Sim, L. Ferrari, L. Tomasella, J. P. Anderson, T. W. Chen, L. Galbany, H. Gao, M. Gromadzki, C. P. Gutiérrez, C. Inserra, E. Kankare, E. A. Magnier, T. E. Müller-Bravo, A. Reguitti, and D. R. Young. Photometry and spectroscopy of the Type Icn supernova 2021ckj. The diverse properties of the ejecta and circumstellar matter of Type Icn supernovae. *A&A*, 673:A27, May 2023. doi: 10.1051/0004-6361/202346084.

A. P. Nagy and J. Vinkó. A two-component model for fitting light curves of core-collapse supernovae. *A&A*, 589:A53, May 2016. doi: 10.1051/0004-6361/201527931.

T. Nakaoka, K. S. Kawabata, K. Maeda, M. Tanaka, M. Yamanaka, T. J. Moriya, N. Tominaga, T. Morokuma, K. Takaki, M. Kawabata, N. Kawahara, R. Itoh, K. Shiki, H. Mori, J. Hirochi, T. Abe, M. Uemura, M. Yoshida, H. Akitaya, Y. Moritani, I. Ueno, T. Urano, M. Isogai, H. Hanayama, and T. Nagayama. The Low-luminosity Type IIP Supernova 2016bkv with Early-phase Circumstellar Interaction. *ApJ*, 859(2):78, June 2018. doi: 10.3847/1538-4357/aabee7.

T. Nakaoka, K. Maeda, M. Yamanaka, M. Tanaka, M. Kawabata, T. J. Moriya, K. S. Kawabata, N. Tominaga, K. Takagi, F. Imazato, T. Morokuma, S. Sako, R. Ohsawa, T. Nagao, J.-a. Jiang, U. Burgaz, K. Taguchi, M. Uemura, H. Akitaya, M. Sasada, K. Isogai, M. Otsuka, and H. Maehara. Calcium-rich Transient SN 2019ehk in a Star-forming Environment: Yet Another Candidate for a Precursor of a Double Neutron-star Binary. *ApJ*, 912(1):30, May 2021. doi: 10.3847/1538-4357/abe765.

E. Nakar and A. L. Piro. Supernovae with Two Peaks in the Optical Light Curve and the Signature of Progenitors with Low-mass Extended Envelopes. *ApJ*, 788 (2):193, June 2014. doi: 10.1088/0004-637X/788/2/193.

E. Nakar, D. Poznanski, and B. Katz. The Importance of ^{56}Ni in Shaping the Light Curves of Type II Supernovae. *ApJ*, 823(2):127, June 2016. doi: 10.3847/0004-637X/823/2/127.

J. Neumann, D. Thomas, C. Maraston, L. Hill, L. Nanni, O. Wenman, J. Lian, J. Comparat, V. Gonzalez-Perez, K. B. Westfall, R. Yan, Y. Chen, G. S. Stringfellow, M. A. Bershady, J. R. Brownstein, N. Drory, and D. P. Schneider. The MaNGA FIREFLY value added catalogue: resolved stellar populations of 10 010 nearby galaxies. *MNRAS*, 513(4):5988–6012, July 2022. doi: 10.1093/mnras/stac1260.

M. Nicholl and S. J. Smartt. Seeing double: the frequency and detectability of double-peaked superluminous supernova light curves. *MNRAS*, 457(1):L79–L83, Mar. 2016. doi: 10.1093/mnrasl/slv210.

M. Nicholl, S. J. Smartt, A. Jerkstrand, S. A. Sim, C. Inserra, J. P. Anderson, C. Baltay, S. Benetti, K. Chambers, T. W. Chen, N. Elias-Rosa, U. Feindt, H. A. Flewelling, M. Fraser, A. Gal-Yam, L. Galbany, M. E. Huber, T. Kangas, E. Kankare, R. Kotak, T. Krühler, K. Maguire, R. McKinnon, D. Rabinowitz, S. Rostami, S. Schulze, K. W. Smith, M. Sullivan, J. L. Tonry, S. Valenti, and D. R. Young. LSQ14bdq: A Type Ic Super-luminous Supernova with a Double-peaked Light Curve. *ApJ*, 807(1):L18, July 2015. doi: 10.1088/2041-8205/807/1/L18.

S. Noll, D. Burgarella, E. Giovannoli, V. Buat, D. Marcillac, and J. C. Muñoz-Mateos. Analysis of galaxy spectral energy distributions from far-UV to far-IR with CIGALE: studying a SINGS test sample. *A&A*, 507(3):1793–1813, Dec. 2009. doi: 10.1051/0004-6361/200912497.

K. Nomoto. Evolution of 8-10 solar mass stars toward electron capture supernovae. I - Formation of electron-degenerate O + NE + MG cores. *ApJ*, 277:791–805, Feb. 1984. doi: 10.1086/161749.

K. Nomoto. Evolution of 8–10 M_{sun} Stars toward Electron Capture Supernovae. II. Collapse of an O + NE + MG Core. *ApJ*, 322:206, Nov. 1987. doi: 10.1086/165716.

K. Nomoto, W. M. Sparks, R. A. Fesen, T. R. Gull, S. Miyaji, and D. Sugimoto. The Crab Nebula's progenitor. *Nature*, 299(5886):803–805, Oct. 1982. doi: 10.1038/299803a0.

K. Nomoto, M. Hashimoto, T. Tsujimoto, F. K. Thielemann, N. Kishimoto, Y. Kubo, and N. Nakasato. Nucleosynthesis in type II supernovae. *Nucl. Phys. A*, 616:79–90, Feb. 1997. doi: 10.1016/S0375-9474(97)00076-6.

K. Nomoto, C. Kobayashi, and N. Tominaga. Nucleosynthesis in Stars and the Chemical Enrichment of Galaxies. *ARA&A*, 51(1):457–509, Aug. 2013. doi: 10.1146/annurev-astro-082812-140956.

E. O. Ofek, I. Rabinak, J. D. Neill, I. Arcavi, S. B. Cenko, E. Waxman, S. R. Kulkarni, A. Gal-Yam, P. E. Nugent, L. Bildsten, J. S. Bloom, A. V. Filippenko, K. Forster, D. A. Howell, J. Jacobsen, M. M. Kasliwal, N. Law, C. Martin, D. Poznanski, R. M. Quimby, K. J. Shen, M. Sullivan, R. Dekany, G. Rahmer, D. Hale, R. Smith, J. Zolkower, V. Velur, R. Walters, J. Henning, K. Bui, and D. McKenna. Supernova

PTF 09UJ: A Possible Shock Breakout from a Dense Circumstellar Wind. *ApJ*, 724(2):1396–1401, Dec. 2010. doi: 10.1088/0004-637X/724/2/1396.

J. B. Oke and J. E. Gunn. An Efficient Low Resolution and Moderate Resolution Spectrograph for the Hale Telescope. *PASP*, 94:586, June 1982. doi: 10.1086/131027.

J. B. Oke, J. G. Cohen, M. Carr, J. Cromer, A. Dingizian, F. H. Harris, S. Labrecque, R. Lucinio, W. Schaal, H. Epps, and J. Miller. The Keck Low-Resolution Imaging Spectrometer. *PASP*, 107:375, Apr. 1995. doi: 10.1086/133562.

D. O'Neill, R. Kotak, M. Fraser, S. A. Sim, S. Benetti, S. J. Smartt, S. Mattila, C. Ashall, E. Callis, N. Elias-Rosa, M. Gromadzki, and S. J. Prentice. A progenitor candidate for the type II-P supernova SN 2018aoq in NGC 4151. *A&A*, 622:L1, Feb. 2019. doi: 10.1051/0004-6361/201834566.

D. O'Neill, R. Kotak, M. Fraser, S. Mattila, G. Pietrzyński, and J. L. Prieto. Revisiting the progenitor of the low-luminosity type II-plateau supernova, SN 2008bk. *A&A*, 645:L7, Jan. 2021. doi: 10.1051/0004-6361/202039546.

O. Papish and N. Soker. Exploding core collapse supernovae with jittering jets. *MNRAS*, 416(3):1697–1702, Sept. 2011. doi: 10.1111/j.1365-2966.2011.18671.x.

A. Pastorello, L. Zampieri, M. Turatto, E. Cappellaro, W. P. S. Meikle, S. Benetti, D. Branch, E. Baron, F. Patat, M. Armstrong, G. Altavilla, M. Salvo, and M. Riello. Low-luminosity Type II supernovae: spectroscopic and photometric evolution. *MNRAS*, 347(1):74–94, Jan. 2004. doi: 10.1111/j.1365-2966.2004.07173.x.

A. Pastorello, D. Sauer, S. Taubenberger, P. A. Mazzali, K. Nomoto, K. S. Kawabata, S. Benetti, N. Elias-Rosa, A. Harutyunyan, H. Navasardyan, L. Zampieri, T. Iijima, M. T. Botticella, G. di Rico, M. Del Principe, M. Dolci, S. Gagliardi, M. Ragni, and G. Valentini. SN 2005cs in M51 - I. The first month of evolution of a subluminous SN II plateau. *MNRAS*, 370(4):1752–1762, Aug. 2006a. doi: 10.1111/j.1365-2966.2006.10587.x.

A. Pastorello, D. Sauer, S. Taubenberger, P. A. Mazzali, K. Nomoto, K. S. Kawabata, S. Benetti, N. Elias-Rosa, A. Harutyunyan, H. Navasardyan, L. Zampieri, T. Iijima, M. T. Botticella, G. di Rico, M. Del Principe, M. Dolci, S. Gagliardi, M. Ragni, and G. Valentini. SN 2005cs in M51 - I. The first month of evolution of a subluminous SN II plateau. *MNRAS*, 370(4):1752–1762, Aug. 2006b. doi: 10.1111/j.1365-2966.2006.10587.x.

A. Pastorello, S. J. Smartt, S. Mattila, J. J. Eldridge, D. Young, K. Itagaki, H. Yamaoka, H. Navasardyan, S. Valenti, F. Patat, I. Agnoletto, T. Augusteijn, S. Benetti, E. Cappellaro, T. Boles, J. Bonnet-Bidaud, M. T. Botticella, F. Bufano, C. Cao, J. Deng, M. Dennefeld, N. Elias-Rosa, A. Harutyunyan, F. P. Keenan,

T. Iijima, V. Lorenzi, P. A. Mazzali, X. Meng, S. Nakano, T. B. Nielsen, J. V. Smoker, V. Stanishev, M. Turatto, D. Xu, and L. Zampieri. A giant outburst two years before the core-collapse of a massive star. *Nature*, 447:829–832, June 2007. doi: 10.1038/nature05825.

A. Pastorello, S. Mattila, L. Zampieri, M. Della Valle, S. J. Smartt, S. Valenti, I. Agnoletto, S. Benetti, C. R. Benn, D. Branch, E. Cappellaro, M. Dennefeld, J. J. Eldridge, A. Gal-Yam, A. Harutyunyan, I. Hunter, H. Kjeldsen, Y. Lipkin, P. A. Mazzali, P. Milne, H. Navasardyan, E. O. Ofek, E. Pian, O. Shemmer, S. Spiro, R. A. Stathakis, S. Taubenberger, M. Turatto, and H. Yamaoka. Massive stars exploding in a He-rich circumstellar medium - I. Type Ibn (SN 2006jc-like) events. *MNRAS*, 389(1):113–130, Sept. 2008. doi: 10.1111/j.1365-2966.2008.13602.x.

A. Pastorello, S. Valenti, L. Zampieri, H. Navasardyan, S. Taubenberger, S. J. Smartt, A. A. Arkharov, O. Bärnbantner, H. Barwig, S. Benetti, P. Birtwhistle, M. T. Botticella, E. Cappellaro, M. Del Principe, F. di Mille, G. di Rico, M. Dolci, N. Elias-Rosa, N. V. Efimova, M. Fiedler, A. Harutyunyan, P. A. Höflich, W. Kloehr, V. M. Larionov, V. Lorenzi, J. R. Maund, N. Napoleone, M. Ragni, M. Richmond, C. Ries, S. Spiro, S. Temporin, M. Turatto, and J. C. Wheeler. SN 2005cs in M51 - II. Complete evolution in the optical and the near-infrared. *MNRAS*, 394(4): 2266–2282, Apr. 2009a. doi: 10.1111/j.1365-2966.2009.14505.x.

A. Pastorello, S. Valenti, L. Zampieri, H. Navasardyan, S. Taubenberger, S. J. Smartt, A. A. Arkharov, O. Bärnbantner, H. Barwig, S. Benetti, P. Birtwhistle, M. T. Botticella, E. Cappellaro, M. Del Principe, F. di Mille, G. di Rico, M. Dolci, N. Elias-Rosa, N. V. Efimova, M. Fiedler, A. Harutyunyan, P. A. Höflich, W. Kloehr, V. M. Larionov, V. Lorenzi, J. R. Maund, N. Napoleone, M. Ragni, M. Richmond, C. Ries, S. Spiro, S. Temporin, M. Turatto, and J. C. Wheeler. SN 2005cs in M51 - II. Complete evolution in the optical and the near-infrared. *MNRAS*, 394(4): 2266–2282, Apr. 2009b. doi: 10.1111/j.1365-2966.2009.14505.x.

A. Pastorello, S. Benetti, P. J. Brown, D. Y. Tsvetkov, C. Inserra, S. Taubenberger, L. Tomasella, M. Fraser, D. J. Rich, M. T. Botticella, F. Bufano, E. Cappellaro, M. Ergon, E. S. Gorbovskoy, A. Harutyunyan, F. Huang, R. Kotak, V. M. Lipunov, L. Magill, M. Miluzio, N. Morrell, P. Ochner, S. J. Smartt, J. Sollerman, S. Spiro, M. D. Stritzinger, M. Turatto, S. Valenti, X. Wang, D. E. Wright, V. V. Yurkov, L. Zampieri, and T. Zhang. Massive stars exploding in a He-rich circumstellar medium - IV. Transitional Type Ibn supernovae. *MNRAS*, 449(2):1921–1940, May 2015. doi: 10.1093/mnras/stu2745.

B. Paxton, L. Bildsten, A. Dotter, F. Herwig, P. Lesaffre, and F. Timmes. MESA: Modules for Experiments in Stellar Astrophysics. Astrophysics Source Code Library, Oct. 2010.

O. Pejcha and J. L. Prieto. A Global Model of The Light Curves and Expansion Velocities of Type II-plateau Supernovae. *ApJ*, 799(2):215, Feb. 2015. doi: 10.1088/0004-637X/799/2/215.

O. Pejcha, B. D. Metzger, and K. Tomida. Binary stellar mergers with marginally bound ejecta: excretion discs, inflated envelopes, outflows, and their luminous transients. *MNRAS*, 461(3):2527–2539, Sept. 2016. doi: 10.1093/mnras/stw1481.

C. Pellegrino, D. A. Howell, G. Terreran, I. Arcavi, K. A. Bostroem, P. J. Brown, J. Burke, Y. Dong, A. Gilkis, D. Hiramatsu, G. Hosseinzadeh, C. McCully, M. Modjaz, M. Newsome, E. Padilla Gonzalez, T. A. Pritchard, D. J. Sand, S. Valenti, and M. Williamson. The Diverse Properties of Type Icn Supernovae Point to Multiple Progenitor Channels. *arXiv e-prints*, art. arXiv:2205.07894, May 2022a.

C. Pellegrino, D. A. Howell, G. Terreran, I. Arcavi, K. A. Bostroem, P. J. Brown, J. Burke, Y. Dong, A. Gilkis, D. Hiramatsu, G. Hosseinzadeh, C. McCully, M. Modjaz, M. Newsome, E. Padilla Gonzalez, T. A. Pritchard, D. J. Sand, S. Valenti, and M. Williamson. The Diverse Properties of Type Icn Supernovae Point to Multiple Progenitor Channels. *arXiv e-prints*, art. arXiv:2205.07894, May 2022b.

H. B. Perets, A. Gal-yam, R. M. Crockett, J. P. Anderson, P. A. James, M. Sullivan, J. D. Neill, and D. C. Leonard. The Old Environment of the Faint Calcium-rich Supernova SN 2005cz. *ApJ*, 728(2):L36, Feb. 2011. doi: 10.1088/2041-8205/728/2/L36.

D. A. Perley. Fully Automated Reduction of Longslit Spectroscopy with the Low Resolution Imaging Spectrometer at the Keck Observatory. *PASP*, 131(8):084503, Aug. 2019. doi: 10.1088/1538-3873/ab215d.

D. A. Perley, P. A. Mazzali, L. Yan, S. B. Cenko, S. Gezari, K. Taggart, N. Blagorodnova, C. Fremling, B. Mockler, A. Singh, N. Tominaga, M. Tanaka, A. M. Watson, T. Ahumada, G. C. Anupama, C. Ashall, R. L. Becerra, D. Bersier, V. Bhalerao, J. S. Bloom, N. R. Butler, C. Copperwheat, M. W. Coughlin, K. De, A. J. Drake, D. A. Duev, S. Frederick, J. J. González, A. Goobar, M. Heida, A. Y. Q. Ho, J. Horst, T. Hung, R. Itoh, J. E. Jencson, M. M. Kasliwal, N. Kawai, T. Khanam, S. R. Kulkarni, B. Kumar, H. Kumar, A. S. Kutyrev, W. H. Lee, K. Maeda, A. Mahabal, K. L. Murata, J. D. Neill, C.-C. Ngeow, B. Penprase, E. Pian, R. Quimby, E. Ramirez-Ruiz, M. G. Richer, C. G. Román-Zúñiga, D. K. Sahu, S. Srivastav, Q. Socia, J. Sollerman, Y. Tachibana, F. Taddia, S. Tinyanont, E. Troja, C. Ward, J. Wee, and P.-C. Yu. The fast, luminous ultraviolet transient AT2018cow: extreme supernova, or disruption of a star by an intermediate-mass black hole? *MNRAS*, 484:1031–1049, Mar. 2019. doi: 10.1093/mnras/sty3420.

D. A. Perley, C. Fremling, J. Sollerman, A. A. Miller, A. S. Dahiwale, Y. Sharma, E. C. Bellm, R. Biswas, T. G. Brink, R. J. Bruch, K. De, R. Dekany, A. J. Drake, D. A. Duev, A. V. Filippenko, A. Gal-Yam, A. Goobar, M. J. Graham, M. L. Graham, A. Y. Q. Ho, I. Irani, M. M. Kasliwal, Y.-L. Kim, S. R. Kulkarni, A. Mahabal, F. J. Masci, S. Modak, J. D. Neill, J. Nordin, R. L. Riddle, M. T. Soumagnac, N. L. Strotjohann, S. Schulze, K. Taggart, A. Tzanidakis, R. S.

Walters, and L. Yan. The Zwicky Transient Facility Bright Transient Survey. II. A Public Statistical Sample for Exploring Supernova Demographics. *ApJ*, 904 (1):35, Nov. 2020. doi: 10.3847/1538-4357/abbd98.

D. A. Perley, J. Sollerman, S. Schulze, Y. Yao, C. Fremling, A. Gal-Yam, A. Y. Q. Ho, Y. Yang, E. C. Kool, I. Irani, L. Yan, I. Andreoni, D. Baade, E. C. Bellm, T. G. Brink, T.-W. Chen, A. Cikota, M. W. Coughlin, A. Dahiwale, R. Dekany, D. A. Duev, A. V. Filippenko, P. Hoeflich, M. M. Kasliwal, S. R. Kulkarni, R. Lunnan, F. J. Masci, J. R. Maund, M. S. Medford, R. Riddle, P. Rosnet, D. L. Shupe, N. L. Strotjohann, A. Tzanidakis, and W. Zheng. The Type Icn SN 2021csp: Implications for the Origins of the Fastest Supernovae and the Fates of Wolf-Rayet Stars. *ApJ*, 927(2):180, Mar. 2022a. doi: 10.3847/1538-4357/ac478e.

D. A. Perley, J. Sollerman, S. Schulze, Y. Yao, C. Fremling, A. Gal-Yam, A. Y. Q. Ho, Y. Yang, E. C. Kool, I. Irani, L. Yan, I. Andreoni, D. Baade, E. C. Bellm, T. G. Brink, T.-W. Chen, A. Cikota, M. W. Coughlin, A. Dahiwale, R. Dekany, D. A. Duev, A. V. Filippenko, P. Hoeflich, M. M. Kasliwal, S. R. Kulkarni, R. Lunnan, F. J. Masci, J. R. Maund, M. S. Medford, R. Riddle, P. Rosnet, D. L. Shupe, N. L. Strotjohann, A. Tzanidakis, and W. Zheng. The Type Icn SN 2021csp: Implications for the Origins of the Fastest Supernovae and the Fates of Wolf-Rayet Stars. *ApJ*, 927(2):180, Mar. 2022b. doi: 10.3847/1538-4357/ac478e.

M. M. Phillips, J. D. Simon, N. Morrell, C. R. Burns, N. L. J. Cox, R. J. Foley, A. I. Karakas, F. Patat, A. Sternberg, R. E. Williams, A. Gal-Yam, E. Y. Hsiao, D. C. Leonard, S. E. Persson, M. Stritzinger, I. B. Thompson, A. Campillay, C. Contreras, G. Folatelli, W. L. Freedman, M. Hamuy, M. Roth, G. A. Shields, N. B. Suntzeff, L. Chomiuk, I. I. Ivans, B. F. Madore, B. E. Penprase, D. Perley, G. Pignata, G. Preston, and A. M. Soderberg. On the Source of the Dust Extinction in Type Ia Supernovae and the Discovery of Anomalously Strong Na I Absorption. *ApJ*, 779(1):38, Dec. 2013. doi: 10.1088/0004-637X/779/1/38.

A. S. Piascik, I. A. Steele, S. D. Bates, C. J. Mottram, R. J. Smith, R. M. Barnsley, and B. Bolton. SPRAT: Spectrograph for the Rapid Acquisition of Transients. In S. K. Ramsay, I. S. McLean, and H. Takami, editors, *Ground-based and Airborne Instrumentation for Astronomy V*, volume 9147 of *Society of Photo-Optical Instrumentation Engineers (SPIE) Conference Series*, page 91478H, July 2014. doi: 10.1117/12.2055117.

A. L. Piro. Using Double-peaked Supernova Light Curves to Study Extended Material. *ApJ*, 808(2):L51, Aug. 2015. doi: 10.1088/2041-8205/808/2/L51.

A. L. Piro and V. S. Morozova. Exploring the Potential Diversity of Early Type Ia Supernova Light Curves. *ApJ*, 826(1):96, July 2016. doi: 10.3847/0004-637X/826/1/96.

A. L. Piro, A. Haynie, and Y. Yao. Shock Cooling Emission from Extended Material Revisited. *ApJ*, 909(2):209, Mar. 2021. doi: 10.3847/1538-4357/abe2b1.

Planck Collaboration, N. Aghanim, Y. Akrami, M. Ashdown, J. Aumont, C. Baccigalupi, M. Ballardini, A. J. Banday, R. B. Barreiro, N. Bartolo, S. Basak, R. Battye, K. Benabed, J.-P. Bernard, M. Bersanelli, P. Bielewicz, J. J. Bock, J. R. Bond, J. Borrill, F. R. Bouchet, F. Boulanger, M. Bucher, C. Burigana, R. C. Butler, E. Calabrese, J.-F. Cardoso, J. Carron, A. Challinor, H. C. Chiang, J. Chluba, L. P. L. Colombo, C. Combet, D. Contreras, B. P. Crill, F. Cuttaia, P. de Bernardis, G. de Zotti, J. Delabrouille, J.-M. Delouis, E. Di Valentino, J. M. Diego, O. Doré, M. Douspis, A. Ducout, X. Dupac, S. Dusini, G. Efstathiou, F. Elsner, T. A. Enßlin, H. K. Eriksen, Y. Fantaye, M. Farhang, J. Fergusson, R. Fernandez-Cobos, F. Finelli, F. Forastieri, M. Frailis, A. A. Fraisse, E. Franceschi, A. Frolov, S. Galeotta, S. Galli, K. Ganga, R. T. Génova-Santos, M. Gerbino, T. Ghosh, J. González-Nuevo, K. M. Górski, S. Gratton, A. Gruppuso, J. E. Gudmundsson, J. Hamann, W. Handley, F. K. Hansen, D. Herranz, S. R. Hildebrandt, E. Hivon, Z. Huang, A. H. Jaffe, W. C. Jones, A. Karakci, E. Keihänen, R. Keskitalo, K. Kiiveri, J. Kim, T. S. Kisner, L. Knox, N. Krachmalnicoff, M. Kunz, H. Kurki-Suonio, G. Lagache, J.-M. Lamarre, A. Lasenby, M. Lattanzi, C. R. Lawrence, M. Le Jeune, P. Lemos, J. Lesgourgues, F. Levrier, A. Lewis, M. Liguori, P. B. Lilje, M. Lilley, V. Lindholm, M. López-Caniego, P. M. Lubin, Y.-Z. Ma, J. F. Macías-Pérez, G. Maggio, D. Maino, N. Mandolesi, A. Mangilli, A. Marcos-Caballero, M. Maris, P. G. Martin, M. Martinelli, E. Martínez-González, S. Matarrese, N. Mauri, J. D. McEwen, P. R. Meinhold, A. Melchiorri, A. Mennella, M. Migliaccio, M. Millea, S. Mitra, M.-A. Miville-Deschênes, D. Molinari, L. Montier, G. Morgante, A. Moss, P. Natoli, H. U. Nørgaard-Nielsen, L. Pagano, D. Paoletti, B. Partridge, G. Patanchon, H. V. Peiris, F. Perrotta, V. Pettorino, F. Piacentini, L. Polastri, G. Polenta, J.-L. Puget, J. P. Rachen, M. Reinecke, M. Remazeilles, A. Renzi, G. Rocha, C. Rosset, G. Roudier, J. A. Rubiño-Martín, B. Ruiz-Granados, L. Salvati, M. Sandri, M. Savelainen, D. Scott, E. P. S. Shellard, C. Sirignano, G. Sirri, L. D. Spencer, R. Sunyaev, A.-S. Suur-Uski, J. A. Tauber, D. Tavagnacco, M. Tenti, L. Toffolatti, M. Tomasi, T. Trombetti, L. Valenziano, J. Valiviita, B. Van Tent, L. Vibert, P. Vielva, F. Villa, N. Vittorio, B. D. Wandelt, I. K. Wehus, M. White, S. D. M. White, A. Zacchei, and A. Zonca. Planck 2018 results. VI. Cosmological parameters. *A&A*, 641:A6, Sept. 2020. doi: 10.1051/0004-6361/201833910.

E. Pllumbi, I. Tamborra, S. Wanajo, H.-T. Janka, and L. Hüdepohl. Impact of Neutrino Flavor Oscillations on the Neutrino-driven Wind Nucleosynthesis of an Electron-capture Supernova. *ApJ*, 808(2):188, Aug. 2015. doi: 10.1088/0004-637X/808/2/188.

P. Podsiadlowski, P. C. Joss, and J. J. L. Hsu. Presupernova Evolution in Massive Interacting Binaries. *ApJ*, 391:246, May 1992. doi: 10.1086/171341.

P. Podsiadlowski, Z. Han, and S. Rappaport. Cataclysmic variables with evolved secondaries and the progenitors of AM CVn stars. *MNRAS*, 340(4):1214–1228, Apr. 2003. doi: 10.1046/j.1365-8711.2003.06380.x.

P. Podsiadlowski, N. Langer, A. J. T. Poelarends, S. Rappaport, A. Heger, and E. Pfahl. The Effects of Binary Evolution on the Dynamics of Core Collapse and Neutron Star Kicks. *ApJ*, 612(2):1044–1051, Sept. 2004. doi: 10.1086/421713.

A. J. T. Poelarends, F. Herwig, N. Langer, and A. Heger. The Supernova Channel of Super-AGB Stars. *ApJ*, 675(1):614–625, Mar. 2008. doi: 10.1086/520872.

A. J. T. Poelarends, S. Wurtz, J. Tarka, L. Cole Adams, and S. T. Hills. Electron Capture Supernovae from Close Binary Systems. *ApJ*, 850(2):197, Dec. 2017. doi: 10.3847/1538-4357/aa988a.

A. Polin, P. Nugent, and D. Kasen. Nebular Models of Sub-Chandrasekhar Mass Type Ia Supernovae: Clues to the Origin of Ca-rich Transients. *ApJ*, 906(1):65, Jan. 2021. doi: 10.3847/1538-4357/abcccc.

D. V. Popov. An Analytical Model for the Plateau Stage of Type II Supernovae. *ApJ*, 414:712, Sept. 1993. doi: 10.1086/173117.

D. Poznanski. An emerging coherent picture of red supergiant supernova explosions. *MNRAS*, 436:3224–3230, Dec. 2013. doi: 10.1093/mnras/stt1800.

D. Poznanski, R. Chornock, P. E. Nugent, J. S. Bloom, A. V. Filippenko, M. Ganeshalingam, D. C. Leonard, W. Li, and R. C. Thomas. An Unusually Fast-Evolving Supernova. *Science*, 327(5961):58, Jan. 2010. doi: 10.1126/science.1181709.

D. Poznanski, M. Ganeshalingam, J. M. Silverman, and A. V. Filippenko. Low-resolution sodium D absorption is a bad proxy for extinction. *MNRAS*, 415(1): L81–L84, July 2011. doi: 10.1111/j.1745-3933.2011.01084.x.

D. Poznanski, J. X. Prochaska, and J. S. Bloom. An empirical relation between sodium absorption and dust extinction. *MNRAS*, 426(2):1465–1474, Oct. 2012. doi: 10.1111/j.1365-2966.2012.21796.x.

M. Pozzo, W. P. S. Meikle, A. Fassia, T. Geballe, P. Lundqvist, N. N. Chugai, and J. Sollerman. On the source of the late-time infrared luminosity of SN 1998S and other Type II supernovae. *MNRAS*, 352(2):457–477, Aug. 2004. doi: 10.1111/j.1365-2966.2004.07951.x.

M. Pozzo, W. P. S. Meikle, J. T. Rayner, R. D. Joseph, A. V. Filippenko, R. J. Foley, W. Li, S. Mattila, and J. Sollerman. Optical and infrared observations of the TypeIIP SN2002hh from days 3 to 397. *MNRAS*, 368(3):1169–1195, May 2006. doi: 10.1111/j.1365-2966.2006.10204.x.

S. J. Prentice, C. Ashall, P. A. James, L. Short, P. A. Mazzali, D. Bersier, P. A. Crowther, C. Barbarino, T.-W. Chen, C. M. Copperwheat, M. J. Darnley, L. Denneau, N. Elias-Rosa, M. Fraser, L. Galbany, A. Gal-Yam, J. Harmanen, D. A. Howell, G. Hosseinzadeh, C. Inserra, E. Kankare, E. Karamehmetoglu, G. P. Lamb, M. Limongi, K. Maguire, C. McCully, F. Olivares E, A. S. Piascik, G. Pignata, D. E. Reichart, A. Rest, T. Reynolds, Ó. Rodríguez, J. L. O. Saario, S. Schulze, S. J.

Smartt, K. W. Smith, J. Sollerman, B. Stalder, M. Sullivan, F. Taddia, S. Valenti, S. D. Vergani, S. C. Williams, and D. R. Young. Investigating the properties of stripped-envelope supernovae; what are the implications for their progenitors? *MNRAS*, 485(2):1559–1578, May 2019. doi: 10.1093/mnras/sty3399.

S. J. Prentice, K. Maguire, A. Flörs, S. Taubenberger, C. Inserra, C. Frohmaier, T. W. Chen, J. P. Anderson, C. Ashall, P. Clark, M. Fraser, L. Galbany, A. Gal-Yam, M. Gromadzki, C. P. Gutiérrez, P. A. James, P. G. Jonker, E. Kankare, G. Leloudas, M. R. Magee, P. A. Mazzali, M. Nicholl, M. Pursiainen, K. Skillen, S. J. Smartt, K. W. Smith, C. Vogl, and D. R. Young. The rise and fall of an extraordinary Ca-rich transient. The discovery of ATLAS19dqr/SN 2019bkc. *A&A*, 635:A186, Mar. 2020. doi: 10.1051/0004-6361/201936515.

S. J. Prentice, K. Maguire, L. Siebenaler, and A. Jerkstrand. Oxygen and calcium nebular emission line relationships in core-collapse supernovae and Ca-rich transients. *MNRAS*, 514(4):5686–5705, Aug. 2022. doi: 10.1093/mnras/stac1657.

J. Prochaska, J. Hennawi, K. Westfall, R. Cooke, F. Wang, T. Hsyu, F. Davies, E. Farina, and D. Pelliccia. PypeIt: The Python Spectroscopic Data Reduction Pipeline. *The Journal of Open Source Software*, 5(56):2308, Dec. 2020a. doi: 10.21105/joss.02308.

J. X. Prochaska, J. Hennawi, R. Cooke, K. Westfall, F. Wang, EmAstro, Tiffanyhsyu, A. Wasserman, A. Villaume, Marijana777, J. Schindler, D. Young, S. Simha, M. Wilde, N. Tejos, J. Isbell, A. Flörs, N. Sandford, Z. Vasović, E. Betts, and B. Holden. pypeit/PypeIt: Release 1.0.0, Apr. 2020b.

J. X. Prochaska, J. F. Hennawi, K. B. Westfall, R. J. Cooke, F. Wang, T. Hsyu, F. B. Davies, E. P. Farina, and D. Pelliccia. Pypeit: The python spectroscopic data reduction pipeline. *Journal of Open Source Software*, 5(56):2308, 2020. doi: 10.21105/joss.02308. URL `https://doi.org/10.21105/joss.02308`.

M. L. Pumo, M. Turatto, M. T. Botticella, A. Pastorello, S. Valenti, L. Zampieri, S. Benetti, E. Cappellaro, and F. Patat. EC-SNe from Super-Asymptotic Giant Branch Progenitors: Theoretical Models Versus Observations. *ApJ*, 705(2): L138–L142, Nov. 2009. doi: 10.1088/0004-637X/705/2/L138.

M. L. Pumo, L. Zampieri, S. Spiro, A. Pastorello, S. Benetti, E. Cappellaro, G. Manicò, and M. Turatto. Radiation-hydrodynamical modelling of underluminous Type II plateau supernovae. *MNRAS*, 464(3):3013–3020, Jan. 2017. doi: 10.1093/mnras/stw2625.

M. Pursiainen, G. Leloudas, S. Schulze, P. Charalampopoulos, C. R. Angus, J. P. Anderson, F. Bauer, T. W. Chen, L. Galbany, M. Gromadzki, C. P. Gutiérrez, C. Inserra, J. Lyman, T. E. Müller-Bravo, M. Nicholl, S. J. Smartt, L. Tartaglia, P. Wiseman, and D. R. Young. SN 2023emq: A Flash-ionized Ibn Supernova with Possible C III Emission. *ApJ*, 959(1):L10, Dec. 2023. doi: 10.3847/2041-8213/ad103d.

E. Quataert and J. Shiode. Wave-driven mass loss in the last year of stellar evolution: setting the stage for the most luminous core-collapse supernovae. *MNRAS*, 423 (1):L92–L96, June 2012a. doi: 10.1111/j.1745-3933.2012.01264.x.

E. Quataert and J. Shiode. Wave-driven mass loss in the last year of stellar evolution: setting the stage for the most luminous core-collapse supernovae. *MNRAS*, 423 (1):L92–L96, June 2012b. doi: 10.1111/j.1745-3933.2012.01264.x.

I. Rabinak and E. Waxman. The Early UV/Optical Emission from Core-collapse Supernovae. *ApJ*, 728:63, Feb. 2011a. doi: 10.1088/0004-637X/728/1/63.

I. Rabinak and E. Waxman. The Early UV/Optical Emission from Core-collapse Supernovae. *ApJ*, 728(1):63, Feb. 2011b. doi: 10.1088/0004-637X/728/1/63.

T. Rauscher, A. Heger, R. D. Hoffman, and S. E. Woosley. Nucleosynthesis in Massive Stars with Improved Nuclear and Stellar Physics. *ApJ*, 576(1):323–348, Sept. 2002. doi: 10.1086/341728.

A. Reguitti, M. L. Pumo, P. A. Mazzali, A. Pastorello, G. Pignata, N. Elias-Rosa, S. J. Prentice, T. Reynolds, S. Benetti, O. Rodrìguez, S. Mattila, and H. Kuncarayakti. Low-luminosity Type II supernovae - III. SN 2018hwm, a faint event with an unusually long plateau. *MNRAS*, 501(1):1059–1071, Feb. 2021. doi: 10.1093/mnras/staa3730.

N. Rehemtulla, W. V. Jacobson-Galán, A. Singh, A. A. Miller, C. D. Kilpatrick, K. R. Hinds, C. Liu, S. Schulze, J. Sollerman, T. Jegou du Laz, T. Ahumada, K. Auchettl, S. J. Brennan, M. W. Coughlin, C. Fremling, A. Gangopadhyay, D. A. Perley, N. Z. Prusinski, J. Purdum, Y.-J. Qin, S. Romagnoli, J. Shi, J. L. Wise, T. X. Chen, S. L. Groom, D. O. Jones, M. M. Kasliwal, R. Smith, N. Sravan, and S. R. Kulkarni. The BTSbot-nearby Discovery of SN 2024jlf: Rapid, Autonomous Follow-up Probes Interaction in an 18.5 Mpc Type IIP Supernova. *ApJ*, 985(2):241, June 2025. doi: 10.3847/1538-4357/adcf1e.

M. Renzo, R. Farmer, S. Justham, Y. Götberg, S. E. de Mink, E. Zapartas, P. Marchant, and N. Smith. Predictions for the hydrogen-free ejecta of pulsational pair-instability supernovae. *A&A*, 640:A56, Aug. 2020. doi: 10.1051/0004-6361/202037710.

M. W. Richmond, S. D. van Dyk, W. Ho, C. Y. Peng, Y. Paik, R. R. Treffers, A. V. Filippenko, J. Bustamante-Donas, M. Moeller, C. Pawellek, H. Tartara, and M. Spence. UBVRI Photometry of the Type IC SN 1994I in M51. *AJ*, 111:327, Jan. 1996. doi: 10.1086/117785.

M. Rigault, J. D. Neill, N. Blagorodnova, A. Dugas, M. Feeney, R. Walters, V. Brinnel, Y. Copin, C. Fremling, J. Nordin, and J. Sollerman. Fully automated integral field spectrograph pipeline for the SEDMachine: pysedm. *A&A*, 627:A115, July 2019. doi: 10.1051/0004-6361/201935344.

C. Ritossa, E. Garcia-Berro, and I. Iben, Jr. On the Evolution of Stars That Form Electron-degenerate Cores Processed by Carbon Burning. II. Isotope Abundances and Thermal Pulses in a 10 M_{sun} Model with an ONe Core and Applications to Long-Period Variables, Classical Novae, and Accretion-induced Collapse. *ApJ*, 460:489, Mar. 1996. doi: 10.1086/176987.

C. Ritossa, E. García-Berro, and I. Iben, Jr. On the Evolution of Stars that Form Electron-degenerate Cores Processed by Carbon Burning. V. Shell Convection Sustained by Helium Burning, Transient Neon Burning, Dredge-out, Urca Cooling, and Other Properties of an 11 M_{solar} Population I Model Star. *ApJ*, 515(1): 381–397, Apr. 1999. doi: 10.1086/307017.

M. Roberson, C. Fremling, and M. Kasliwal. DBSP_DRP: A Python package for automated spectroscopic data reduction of DBSP data. *The Journal of Open Source Software*, 7(70):3612, Feb. 2022. doi: 10.21105/joss.03612.

Ó. Rodríguez. Luminosity distribution of Type II supernova progenitors. *MNRAS*, 515(1):897–913, Sept. 2022. doi: 10.1093/mnras/stac1831.

Ó. Rodríguez, N. Meza, J. Pineda-García, and M. Ramirez. The iron yield of normal Type II supernovae. *MNRAS*, 505(2):1742–1774, Aug. 2021. doi: 10.1093/mnras/stab1335.

P. W. A. Roming, T. E. Kennedy, K. O. Mason, J. A. Nousek, L. Ahr, R. E. Bingham, P. S. Broos, M. J. Carter, B. K. Hancock, H. E. Huckle, S. D. Hunsberger, H. Kawakami, R. Killough, T. S. Koch, M. K. McLelland, K. Smith, P. J. Smith, J. C. Soto, P. T. Boyd, A. A. Breeveld, S. T. Holland, M. Ivanushkina, M. S. Pryzby, M. D. Still, and J. Stock. The Swift Ultra-Violet/Optical Telescope. *Space Sci. Rev.*, 120(3-4):95–142, Oct. 2005. doi: 10.1007/s11214-005-5095-4.

S. Rose, R. M. Lau, J. E. Jencson, M. M. Kasliwal, K. De, M. E. Ressler, O. D. Fox, and M. J. Hankins. Investigating the Electron Capture Supernova Candidate AT 2019abn with JWST Spectroscopy. *arXiv e-prints*, art. arXiv:2407.20430, July 2024. doi: 10.48550/arXiv.2407.20430.

R. Ruiz-Carmona, I. Sfaradi, and A. Horesh. Type IIP supernova SN2016X in radio frequencies. *A&A*, 666:A82, Oct. 2022. doi: 10.1051/0004-6361/202142024.

I. Sagiv, A. Gal-Yam, E. O. Ofek, E. Waxman, O. Aharonson, S. R. Kulkarni, E. Nakar, D. Maoz, B. Trakhtenbrot, E. S. Phinney, J. Topaz, C. Beichman, J. Murthy, and S. P. Worden. Science with a Wide-field UV Transient Explorer. *AJ*, 147(4):79, Apr. 2014. doi: 10.1088/0004-6256/147/4/79.

D. K. Sahu, G. C. Anupama, S. Srividya, and S. Muneer. Photometric and spectroscopic evolution of the Type IIP supernova SN 2004et. *MNRAS*, 372(3): 1315–1324, Nov. 2006. doi: 10.1111/j.1365-2966.2006.10937.x.

E. E. Salpeter. The Luminosity Function and Stellar Evolution. *ApJ*, 121:161, Jan. 1955. doi: 10.1086/145971.

H. Sana, S. E. de Mink, A. de Koter, N. Langer, C. J. Evans, M. Gieles, E. Gosset, R. G. Izzard, J. B. Le Bouquin, and F. R. N. Schneider. Binary Interaction Dominates the Evolution of Massive Stars. *Science*, 337(6093):444, July 2012. doi: 10.1126/science.1223344.

H. Sana, J.-B. Le Bouquin, S. Lacour, J.-P. Berger, G. Duvert, L. Gauchet, B. Norris, J. Olofsson, D. Pickel, G. Zins, O. Absil, A. de Koter, K. Kratter, O. Schnurr, and H. Zinnecker. Southern Massive Stars at High Angular Resolution: Observational Campaign and Companion Detection. *ApJS*, 215(1):15, Nov. 2014. doi: 10.1088/0067-0049/215/1/15.

N. E. Sanders, A. M. Soderberg, S. Gezari, M. Betancourt, R. Chornock, E. Berger, R. J. Foley, P. Challis, M. Drout, R. P. Kirshner, R. Lunnan, G. H. Marion, R. Margutti, R. McKinnon, D. Milisavljevic, G. Narayan, A. Rest, E. Kankare, S. Mattila, S. J. Smartt, M. E. Huber, W. S. Burgett, P. W. Draper, K. W. Hodapp, N. Kaiser, R. P. Kudritzki, E. A. Magnier, N. Metcalfe, J. S. Morgan, P. A. Price, J. L. Tonry, R. J. Wainscoat, and C. Waters. Toward Characterization of the Type IIP Supernova Progenitor Population: A Statistical Sample of Light Curves from Pan-STARRS1. *ApJ*, 799(2):208, Feb. 2015. doi: 10.1088/0004-637X/799/2/208.

M. A. Sandoval, W. R. Hix, O. E. B. Messer, E. J. Lentz, and J. A. Harris. Three-dimensional Core-collapse Supernova Simulations with 160 Isotopic Species Evolved to Shock Breakout. *ApJ*, 921(2):113, Nov. 2021. doi: 10.3847/1538-4357/ac1d49.

A. Sarangi, M. Matsuura, and E. R. Micelotta. Dust in Supernovae and Supernova Remnants I: Formation Scenarios. *Space Sci. Rev.*, 214(3):63, Apr. 2018. doi: 10.1007/s11214-018-0492-7.

N. Sarin, M. Hübner, C. M. B. Omand, C. N. Setzer, and et al. REDBACK: a Bayesian inference software package for electromagnetic transients. *MNRAS*, 531(1):1203–1227, June 2024. doi: 10.1093/mnras/stae1238.

M. Sasdelli, E. E. O. Ishida, W. Hillebrandt, C. Ashall, P. A. Mazzali, and S. J. Prentice. Breaking the colour-reddening degeneracy in Type Ia supernovae. *MNRAS*, 460(1):373–382, July 2016. doi: 10.1093/mnras/stw900.

M. Sato, N. Tominaga, S. I. Blinnikov, M. S. Potashov, T. J. Moriya, and D. Hiramatsu. A Robust Light-curve Diagnostic for Electron-capture Supernovae and Low-mass Fe-core-collapse Supernovae. *ApJ*, 970(2):163, Aug. 2024. doi: 10.3847/1538-4357/ad50cb.

R. Sawada, K. Kashiyama, and Y. Suwa. On the Energy Source of Ultrastripped Supernovae. *ApJ*, 927(2):223, Mar. 2022. doi: 10.3847/1538-4357/ac53ae.

E. F. Schlafly and D. P. Finkbeiner. Measuring Reddening with Sloan Digital Sky Survey Stellar Spectra and Recalibrating SFD. *ApJ*, 737:103, Aug. 2011. doi: 10.1088/0004-637X/737/2/103.

F. R. N. Schneider, P. Podsiadlowski, and E. Laplace. Bimodal Black Hole Mass Distribution and Chirp Masses of Binary Black Hole Mergers. *ApJ*, 950(2):L9, June 2023. doi: 10.3847/2041-8213/acd77a.

S. Schulze, O. Yaron, J. Sollerman, G. Leloudas, A. Gal, A. H. Wright, R. Lunnan, A. Gal-Yam, E. O. Ofek, D. A. Perley, A. V. Filippenko, M. M. Kasliwal, S. R. Kulkarni, P. E. Nugent, R. M. Quimby, M. Sullivan, N. Linn Strothjohann, I. Arcavi, S. Ben-Ami, F. Bianco, J. S. Bloom, K. De, M. Fraser, C. U. Fremling, A. Horesh, J. Johansson, P. L. Kelly, S. Knezevic, K. Maguire, A. Nyholm, . Semeli Papadogiannakis, T. Petrushevska, A. Rubin, L. Yan, Y. Yang, S. M. Adams, F. Bufano, K. I. Clubb, R. J. Foley, Y. Green, J. Harmanen, A. Y. Q. Ho, I. M. Hook, G. Hosseinzadeh, D. A. Howell, A. K. H. Kong, R. Kotak, T. Matheson, C. McCully, D. Milisavljevic, Y.-C. Pan, D. Poznanski, I. Shivvers, and S. van Velzen. The Palomar Transient Factory Core-Collapse Supernova Host-Galaxy Sample. I. Host-Galaxy Distribution Functions and Environment-Dependence of CCSNe. *arXiv e-prints*, art. arXiv:2008.05988, Aug. 2020.

K. J. Shen, D. Kasen, N. N. Weinberg, L. Bildsten, and E. Scannapieco. Thermonuclear .Ia Supernovae from Helium Shell Detonations: Explosion Models and Observables. *ApJ*, 715(2):767–774, June 2010. doi: 10.1088/0004-637X/715/2/767.

L. Shingles, K. W. Smith, D. R. Young, S. J. Smartt, J. Tonry, L. Denneau, A. Heinze, H. Weiland, H. Flewelling, B. Stalder, A. Clocchiatti, F. Förster, G. Pignata, A. Rest, J. Anderson, C. Stubbs, and N. Erasmus. Release of the ATLAS Forced Photometry server for public use. *Transient Name Server AstroNote*, 7:1–7, Jan. 2021.

J. H. Shiode and E. Quataert. Setting the Stage for Circumstellar Interaction in Core-Collapse Supernovae. II. Wave-driven Mass Loss in Supernova Progenitors. *ApJ*, 780(1):96, Jan. 2014. doi: 10.1088/0004-637X/780/1/96.

H. Shivkumar, A. D. Jaodand, A. Balasubramanian, C. Fremling, A. Corsi, A. Tzanidakis, S. Nissanke, M. Kasliwal, M. Brightman, G. Raaijmakers, K. K. Madsen, F. Harrison, D. Carbone, A. J. Nayana, J.-M. Désert, and I. Andreoni. SN2019wxt: An Ultrastripped Supernova Candidate Discovered in the Electromagnetic Follow-up of a Gravitational Wave Trigger. *ApJ*, 952(1):86, July 2023. doi: 10.3847/1538-4357/acd5d5.

I. Shivvers, M. Modjaz, W. Zheng, Y. Liu, A. V. Filippenko, J. M. Silverman, T. Matheson, A. Pastorello, O. Graur, R. J. Foley, R. Chornock, N. Smith, J. Leaman, and S. Benetti. Revisiting the Lick Observatory Supernova Search Volume-limited Sample: Updated Classifications and Revised Stripped-envelope Supernova Fractions. *PASP*, 129(975):054201, May 2017. doi: 10.1088/1538-3873/aa54a6.

M. Shrestha, J. Pearson, S. Wyatt, D. J. Sand, G. Hosseinzadeh, K. A. Bostroem, J. E. Andrews, Y. Dong, E. Hoang, D. Janzen, J. E. Jencson, M. Lundquist,

D. Mehta, N. M. Retamal, S. Valenti, J. C. Rastinejad, P. Daly, D. Porter, J. Hinz, S. Self, B. Weiner, G. G. Williams, D. Hiramatsu, D. A. Howell, C. McCully, E. P. Gonzalez, C. Pellegrino, G. Terreran, M. Newsome, J. Farah, K. Itagaki, S. W. Jha, L. Kwok, N. Smith, M. Schwab, J. Rho, and Y. Yang. Evidence of Weak Circumstellar Medium Interaction in the Type II SN 2023axu. *ApJ*, 961(2): 247, Feb. 2024. doi: 10.3847/1538-4357/ad11e1.

Y. Shvartzvald, E. Waxman, A. Gal-Yam, E. O. Ofek, S. Ben-Ami, D. Berge, M. Kowalski, R. Bühler, S. Worm, J. E. Rhoads, I. Arcavi, D. Maoz, D. Polishook, N. Stone, B. Trakhtenbrot, M. Ackermann, O. Aharonson, O. Birnholtz, D. Chelouche, D. Guetta, N. Hallakoun, A. Horesh, D. Kushnir, T. Mazeh, J. Nordin, A. Ofir, S. Ohm, D. Parsons, A. Pe'er, H. B. Perets, V. Perdelwitz, D. Poznanski, I. Sadeh, I. Sagiv, S. Shahaf, M. Soumagnac, L. Tal-Or, J. Van Santen, B. Zackay, O. Guttman, P. Rekhi, A. Townsend, A. Weinstein, and I. Wold. ULTRASAT: A wide-field time-domain UV space telescope. *arXiv e-prints*, art. arXiv:2304.14482, Apr. 2023. doi: 10.48550/arXiv.2304.14482.

M. R. Siebert, K. Davis, S. Tinyanont, R. J. Foley, and E. Strasburger. UCSC Transient Classification Report for 2021-07-09. *Transient Name Server Classification Report*, 2021-2383:1–2383, July 2021.

L. Siess. Evolution of massive AGB stars. I. Carbon burning phase. *A&A*, 448(2): 717–729, Mar. 2006. doi: 10.1051/0004-6361:20053043.

L. Siess. Evolution of massive AGB stars. II. model properties at non-solar metallicity and the fate of Super-AGB stars. *A&A*, 476(2):893–909, Dec. 2007. doi: 10.1051/0004-6361:20078132.

L. Siess and U. Lebreuilly. Case A and B evolution towards electron capture supernova. *A&A*, 614:A99, June 2018. doi: 10.1051/0004-6361/201732502.

J. Silva-Farfán, F. Förster, T. J. Moriya, L. Hernández-García, A. M. Muñoz Arancibia, P. Sánchez-Sáez, J. P. Anderson, J. L. Tonry, and A. Clocchiatti. Physical Properties of Type II Supernovae Inferred from ZTF and ATLAS Photometric Data. *ApJ*, 969(1):57, July 2024. doi: 10.3847/1538-4357/ad402a.

J. M. Silverman, R. J. Foley, A. V. Filippenko, M. Ganeshalingam, A. J. Barth, R. Chornock, C. V. Griffith, J. J. Kong, N. Lee, D. C. Leonard, T. Matheson, E. G. Miller, T. N. Steele, B. J. Barris, J. S. Bloom, B. E. Cobb, A. L. Coil, L.-B. Desroches, E. L. Gates, L. C. Ho, S. W. Jha, M. T. Kandrashoff, W. Li, K. S. Mandel, M. Modjaz, M. R. Moore, R. E. Mostardi, M. S. Papenkova, S. Park, D. A. Perley, D. Poznanski, C. A. Reuter, J. Scala, F. J. D. Serduke, J. C. Shields, B. J. Swift, J. L. Tonry, S. D. Van Dyk, X. Wang, and D. S. Wong. Berkeley Supernova Ia Program - I. Observations, data reduction and spectroscopic sample of 582 low-redshift Type Ia supernovae. *MNRAS*, 425(3):1789–1818, Sept. 2012. doi: 10.1111/j.1365-2966.2012.21270.x.

A. Singh, B. Kumar, T. J. Moriya, G. C. Anupama, D. K. Sahu, P. J. Brown, J. E. Andrews, and N. Smith. Observational Signature of Circumstellar Interaction and ^{56}Ni-mixing in the Type II Supernova 2016gfy. *ApJ*, 882(1):68, Sept. 2019. doi: 10.3847/1538-4357/ab3050.

A. Singh, R. S. Teja, T. J. Moriya, K. Maeda, K. S. Kawabata, M. Tanaka, R. Imazawa, T. Nakaoka, A. Gangopadhyay, M. Yamanaka, V. Swain, D. K. Sahu, G. C. Anupama, B. Kumar, R. M. Anche, Y. Sano, A. Raj, V. K. Agnihotri, V. Bhalerao, D. Bisht, M. S. Bisht, K. Belwal, S. K. Chakrabarti, M. Fujii, T. Nagayama, K. Matsumoto, T. Hamada, M. Kawabata, A. Kumar, R. Kumar, B. K. Malkan, P. Smith, Y. Sakagami, K. Taguchi, N. Tominaga, and A. Watanabe. Unravelling the Asphericities in the Explosion and Multifaceted Circumstellar Matter of SN 2023ixf. *ApJ*, 975(1):132, Nov. 2024b. doi: 10.3847/1538-4357/ad7955.

A. Singh, R. S. Teja, T. J. Moriya, K. Maeda, K. S. Kawabata, M. Tanaka, R. Imazawa, T. Nakaoka, A. Gangopadhyay, M. Yamanaka, V. Swain, D. K. Sahu, G. C. Anupama, B. Kumar, R. M. Anche, Y. Sano, A. Raj, V. K. Agnihotri, V. Bhalerao, D. Bisht, M. S. Bisht, K. Belwal, S. K. Chakrabarti, M. Fujii, T. Nagayama, K. Matsumoto, T. Hamada, M. Kawabata, A. Kumar, R. Kumar, B. K. Malkan, P. Smith, Y. Sakagami, K. Taguchi, N. Tominaga, and A. Watanabe. Unravelling the Asphericities in the Explosion and Multifaceted Circumstellar Matter of SN 2023ixf. *ApJ*, 975(1):132, Nov. 2024a. doi: 10.3847/1538-4357/ad7955.

M. F. Skrutskie, R. M. Cutri, R. Stiening, M. D. Weinberg, S. Schneider, J. M. Carpenter, C. Beichman, R. Capps, T. Chester, J. Elias, J. Huchra, J. Liebert, C. Lonsdale, D. G. Monet, S. Price, P. Seitzer, T. Jarrett, J. D. Kirkpatrick, J. E. Gizis, E. Howard, T. Evans, J. Fowler, L. Fullmer, R. Hurt, R. Light, E. L. Kopan, K. A. Marsh, H. L. McCallon, R. Tam, S. Van Dyk, and S. Wheelock. The Two Micron All Sky Survey (2MASS). *AJ*, 131:1163–1183, Feb. 2006. doi: 10.1086/498708.

S. J. Smartt. Observational Constraints on the Progenitors of Core-Collapse Supernovae: The Case for Missing High-Mass Stars. *PASA*, 32:e016, Apr. 2015. doi: 10.1017/pasa.2015.17.

S. J. Smartt, J. J. Eldridge, R. M. Crockett, and J. R. Maund. The death of massive stars - I. Observational constraints on the progenitors of Type II-P supernovae. *MNRAS*, 395:1409–1437, May 2009. doi: 10.1111/j.1365-2966.2009.14506.x.

S. J. Smartt, S. Valenti, M. Fraser, C. Inserra, D. R. Young, M. Sullivan, A. Pastorello, S. Benetti, A. Gal-Yam, C. Knapic, M. Molinaro, R. Smareglia, K. W. Smith, S. Taubenberger, O. Yaron, J. P. Anderson, C. Ashall, C. Balland, C. Baltay, C. Barbarino, F. E. Bauer, S. Baumont, D. Bersier, N. Blagorodnova, S. Bongard, M. T. Botticella, F. Bufano, M. Bulla, E. Cappellaro, H. Campbell, F. Cellier-Holzem, T. W. Chen, M. J. Childress, A. Clocchiatti, C. Contreras, M. Dall'Ora, J. Danziger, T. de Jaeger, A. De Cia, M. Della Valle, M. Dennefeld, N. Elias-Rosa, N. Elman, U. Feindt, M. Fleury, E. Gall, S. Gonzalez-Gaitan, L. Galbany,

A. Morales Garoffolo, L. Greggio, L. L. Guillou, S. Hachinger, E. Hadjiyska, P. E. Hage, W. Hillebrandt, S. Hodgkin, E. Y. Hsiao, P. A. James, A. Jerkstrand, T. Kangas, E. Kankare, R. Kotak, M. Kromer, H. Kuncarayakti, G. Leloudas, P. Lundqvist, J. D. Lyman, I. M. Hook, K. Maguire, I. Manulis, S. J. Margheim, S. Mattila, J. R. Maund, P. A. Mazzali, M. McCrum, R. McKinnon, M. E. Moreno-Raya, M. Nicholl, P. Nugent, R. Pain, G. Pignata, M. M. Phillips, J. Polshaw, M. L. Pumo, D. Rabinowitz, E. Reilly, C. Romero-Cañizales, R. Scalzo, B. Schmidt, S. Schulze, S. Sim, J. Sollerman, F. Taddia, L. Tartaglia, G. Terreran, L. Tomasella, M. Turatto, E. Walker, N. A. Walton, L. Wyrzykowski, F. Yuan, and L. Zampieri. PESSTO: survey description and products from the first data release by the Public ESO Spectroscopic Survey of Transient Objects. *A&A*, 579: A40, Jul 2015. doi: 10.1051/0004-6361/201425237.

K. W. Smith, S. J. Smartt, D. R. Young, J. L. Tonry, L. Denneau, H. Flewelling, A. N. Heinze, H. J. Weiland, B. Stalder, A. Rest, C. W. Stubbs, J. P. Anderson, T. W. Chen, P. Clark, A. Do, F. Förster, M. Fulton, J. Gillanders, O. R. McBrien, D. O'Neill, S. Srivastav, and D. E. Wright. Design and Operation of the ATLAS Transient Science Server. *PASP*, 132(1014):085002, Aug. 2020. doi: 10.1088/1538-3873/ab936e.

M. Smith, M. Sullivan, C. B. D'Andrea, F. J. Castander, R. Casas, S. Prajs, A. Papadopoulos, R. C. Nichol, N. V. Karpenka, S. R. Bernard, P. Brown, R. Cartier, J. Cooke, C. Curtin, T. M. Davis, D. A. Finley, R. J. Foley, A. Gal-Yam, D. A. Goldstein, S. González-Gaitán, R. R. Gupta, D. A. Howell, C. Inserra, R. Kessler, C. Lidman, J. Marriner, P. Nugent, T. A. Pritchard, M. Sako, S. Smartt, R. C. Smith, H. Spinka, R. C. Thomas, R. C. Wolf, A. Zenteno, T. M. C. Abbott, A. Benoit-Lévy, E. Bertin, D. Brooks, E. Buckley-Geer, A. Carnero Rosell, M. Carrasco Kind, J. Carretero, M. Crocce, C. E. Cunha, L. N. da Costa, S. Desai, H. T. Diehl, P. Doel, J. Estrada, A. E. Evrard, B. Flaugher, P. Fosalba, J. Frieman, D. W. Gerdes, D. Gruen, R. A. Gruendl, D. J. James, K. Kuehn, N. Kuropatkin, O. Lahav, T. S. Li, J. L. Marshall, P. Martini, C. J. Miller, R. Miquel, B. Nord, R. Ogando, A. A. Plazas, K. Reil, A. K. Romer, A. Roodman, E. S. Rykoff, E. Sanchez, V. Scarpine, M. Schubnell, I. Sevilla-Noarbe, M. Soares-Santos, F. Sobreira, E. Suchyta, M. E. C. Swanson, G. Tarle, A. R. Walker, W. Wester, and DES Collaboration. DES14X3taz: A Type I Superluminous Supernova Showing a Luminous, Rapidly Cooling Initial Pre-peak Bump. *ApJ*, 818(1):L8, Feb. 2016. doi: 10.3847/2041-8205/818/1/L8.

N. Smith. The Crab nebula and the class of Type IIn-P supernovae caused by sub-energetic electron-capture explosions. *MNRAS*, 434(1):102–113, Sept. 2013. doi: 10.1093/mnras/stt1004.

N. Smith. Mass Loss: Its Effect on the Evolution and Fate of High-Mass Stars. *ARA&A*, 52:487–528, Aug. 2014. doi: 10.1146/annurev-astro-081913-040025.

N. Smith. Interacting Supernovae: Types IIn and Ibn. In A. W. Alsabti and P. Murdin, editors, *Handbook of Supernovae*, page 403. 2017. doi: 10.1007/978-3-319-21846-5_38.

N. Smith, R. J. Foley, and A. V. Filippenko. Dust Formation and He II λ4686 Emission in the Dense Shell of the Peculiar Type Ib Supernova 2006jc. *ApJ*, 680 (1):568–579, June 2008. doi: 10.1086/587860.

J. Sollerman. Optical and infrared observations of radioactive elements in supernovae. *New Astron. Rev.*, 46(8-10):493–498, July 2002. doi: 10.1016/S1387-6473(02)00189-6.

J. Sollerman. ZTF Transient Discovery Report for 2023-12-07. *Transient Name Server Discovery Report*, 2023-3158:1, Dec. 2023.

J. Sollerman, B. Leibundgut, and J. Spyromilio. SN 1996N - A type Ib supernova at late phases. *A&A*, 337:207–215, Sept. 1998.

J. Sollerman, S. Yang, S. Schulze, N. L. Strotjohann, A. Jerkstrand, S. D. Van Dyk, E. C. Kool, C. Barbarino, T. G. Brink, R. Bruch, K. De, A. V. Filippenko, C. Fremling, K. C. Patra, D. Perley, L. Yan, Y. Yang, I. Andreoni, R. Campbell, M. Coughlin, M. Kasliwal, Y.-L. Kim, M. Rigault, K. Shin, A. Tzanidakis, M. C. B. Ashley, A. M. Moore, and T. Travouillon. The Type II supernova SN 2020jfo in M 61, implications for progenitor system, and explosion dynamics. *A&A*, 655:A105, Nov. 2021. doi: 10.1051/0004-6361/202141374.

J. Soon, D. Adams, K. De, A. Galla, M. Hankins, M. M. Kasliwal, A. M. Moore, S. M. Adams, J. Antoszewski, M. Ashley, A.-N. Babul, J. Bland-Hawthorn, J. Cooke, O. De Marco, A. Delacroix, H. Devillepoix, S. C. Ellis, K. C. Freeman, D. Hale, A. Heger, J. E. Jencson, R. M. Lau, D. McKenna, E. Ofek, S. Ryder, R. Simcoe, J. L. Sokoloski, R. Soria, R. M. Smith, and T. D. Travouillon. Wide-field dynamic astronomy in the near-infrared with Palomar Gattini-IR and DREAMS. In S. C. Ellis and C. d'Orgeville, editors, *Advances in Optical Astronomical Instrumentation 2019*, volume 11203 of *Society of Photo-Optical Instrumentation Engineers (SPIE) Conference Series*, page 1120307, Jan. 2020. doi: 10.1117/12.2539594.

J. S. Speagle. DYNESTY: a dynamic nested sampling package for estimating Bayesian posteriors and evidences. *MNRAS*, 493(3):3132–3158, Apr. 2020. doi: 10.1093/mnras/staa278.

S. Spiro, A. Pastorello, M. L. Pumo, L. Zampieri, M. Turatto, S. J. Smartt, S. Benetti, E. Cappellaro, S. Valenti, I. Agnoletto, G. Altavilla, T. Aoki, E. Brocato, E. M. Corsini, A. Di Cianno, N. Elias-Rosa, M. Hamuy, K. Enya, M. Fiaschi, G. Folatelli, S. Desidera, A. Harutyunyan, D. A. Howell, A. Kawka, Y. Kobayashi, B. Leibundgut, T. Minezaki, H. Navasardyan, K. Nomoto, S. Mattila, A. Pietrinferni, G. Pignata, G. Raimondo, M. Salvo, B. P. Schmidt, J. Sollerman, J. Spyromilio, S. Taubenberger, G. Valentini, S. Vennes, and Y. Yoshii. Low luminosity

Type II supernovae - II. Pointing towards moderate mass precursors. *MNRAS*, 439(3):2873–2892, Apr. 2014. doi: 10.1093/mnras/stu156.

C. M. Springob, M. P. Haynes, R. Giovanelli, and B. R. Kent. A Digital Archive of H I 21 Centimeter Line Spectra of Optically Targeted Galaxies. *ApJS*, 160(1): 149–162, Sept. 2005. doi: 10.1086/431550.

N. Sravan, P. Marchant, and V. Kalogera. Progenitors of Type IIb Supernovae. I. Evolutionary Pathways and Rates. *ApJ*, 885(2):130, Nov. 2019. doi: 10.3847/1538-4357/ab4ad7.

N. Sravan, P. Marchant, V. Kalogera, D. Milisavljevic, and R. Margutti. Progenitors of Type IIb Supernovae. II. Observable Properties. *ApJ*, 903(1):70, Nov. 2020. doi: 10.3847/1538-4357/abb8d5.

I. A. Steele, R. J. Smith, P. C. Rees, I. P. Baker, S. D. Bates, M. F. Bode, M. K. Bowman, D. Carter, J. Etherton, M. J. Ford, S. N. Fraser, A. Gomboc, R. D. J. Lett, A. G. Mansfield, J. M. Marchant, G. A. Medrano-Cerda, C. J. Mottram, D. Raback, A. B. Scott, M. D. Tomlinson, and R. Zamanov. The Liverpool Telescope: performance and first results. In J. Oschmann, Jacobus M., editor, *Ground-based Telescopes*, volume 5489 of *Society of Photo-Optical Instrumentation Engineers (SPIE) Conference Series*, pages 679–692, Oct. 2004. doi: 10.1117/12.551456.

G. Stockinger, H. T. Janka, D. Kresse, T. Melson, T. Ertl, M. Gabler, A. Gessner, A. Wongwathanarat, A. Tolstov, S. C. Leung, K. Nomoto, and A. Heger. Three-dimensional models of core-collapse supernovae from low-mass progenitors with implications for Crab. *MNRAS*, 496(2):2039–2084, Aug. 2020. doi: 10.1093/mnras/staa1691.

M. D. Stritzinger, F. Taddia, C. R. Burns, M. M. Phillips, M. Bersten, C. Contreras, G. Folatelli, S. Holmbo, E. Y. Hsiao, P. Hoeflich, G. Leloudas, N. Morrell, J. Sollerman, and N. B. Suntzeff. The Carnegie Supernova Project I. Methods to estimate host-galaxy reddening of stripped-envelope supernovae. *A&A*, 609: A135, Feb. 2018. doi: 10.1051/0004-6361/201730843.

N. L. Strotjohann, E. O. Ofek, A. Gal-Yam, M. Sullivan, S. R. Kulkarni, N. J. Shaviv, C. Fremling, M. M. Kasliwal, P. E. Nugent, Y. Cao, I. Arcavi, J. Sollerman, A. V. Filippenko, O. Yaron, R. Laher, and J. Surace. Search for Precursor Eruptions among Type IIb Supernovae. *ApJ*, 811(2):117, Oct. 2015. doi: 10.1088/0004-637X/811/2/117.

N. L. Strotjohann, E. O. Ofek, A. Gal-Yam, R. Bruch, S. Schulze, N. Shaviv, J. Sollerman, A. V. Filippenko, O. Yaron, C. Fremling, J. Nordin, E. C. Kool, D. A. Perley, A. Y. Q. Ho, Y. Yang, Y. Yao, M. T. Soumagnac, M. L. Graham, C. Barbarino, L. Tartaglia, K. De, D. A. Goldstein, D. O. Cook, T. G. Brink, K. Taggart, L. Yan, R. Lunnan, M. Kasliwal, S. R. Kulkarni, P. E. Nugent, F. J. Masci, P. Rosnet, S. M. Adams, I. Andreoni, A. Bagdasaryan, E. C. Bellm, K. Burdge, D. A. Duev, A. Dugas, S. Frederick, S. Goldwasser, M. Hankins,

I. Irani, V. Karambelkar, T. Kupfer, J. Liang, J. D. Neill, M. Porter, R. L. Riddle, Y. Sharma, P. Short, F. Taddia, A. Tzanidakis, J. van Roestel, R. Walters, and Z. Zhuang. Bright, Months-long Stellar Outbursts Announce the Explosion of Interaction-powered Supernovae. *ApJ*, 907(2):99, Feb. 2021. doi: 10.3847/1538-4357/abd032.

N. L. Strotjohann, E. O. Ofek, A. Gal-Yam, J. Sollerman, P. Chen, O. Yaron, B. Zackay, N. Rehemtulla, P. Gris, F. J. Masci, B. Rusholme, and J. Purdum. Direct detection of supernova progenitor stars with ZTF and LSST. *arXiv e-prints*, art. arXiv:2303.00010, Feb. 2023. doi: 10.48550/arXiv.2303.00010.

B. M. Subrayan, D. Milisavljevic, T. J. Moriya, K. E. Weil, G. Lentner, M. Linvill, J. Banovetz, B. Garretson, J. Reynolds, N. Sravan, R. Chornock, and R. Margutti. Inferencing Progenitor and Explosion Properties of Evolving Core-collapse Supernovae from Zwicky Transient Facility Light Curves. *ApJ*, 945(1):46, Mar. 2023. doi: 10.3847/1538-4357/aca80a.

T. Sukhbold, T. Ertl, S. E. Woosley, J. M. Brown, and H. T. Janka. Core-collapse Supernovae from 9 to 120 Solar Masses Based on Neutrino-powered Explosions. *ApJ*, 821(1):38, Apr. 2016. doi: 10.3847/0004-637X/821/1/38.

Y. Suwa, T. Yoshida, M. Shibata, H. Umeda, and K. Takahashi. Neutrino-driven explosions of ultra-stripped Type Ic supernovae generating binary neutron stars. *MNRAS*, 454(3):3073–3081, Dec. 2015. doi: 10.1093/mnras/stv2195.

T. Szalai, J. Vinkó, R. Könyves-Tóth, A. P. Nagy, K. A. Bostroem, K. Sárneczky, P. J. Brown, O. Pejcha, A. Bódi, B. Cseh, G. Csörnyei, Z. Dencs, O. Hanyecz, B. Ignácz, C. Kalup, L. Kriskovics, A. Ordasi, A. Pál, B. Seli, Á. Sódor, R. Szakáts, K. Vida, G. Zsidi, Konkoly Team, I. Arcavi, C. Ashall, J. Burke, L. Galbany, D. Hiramatsu, G. Hosseinzadeh, E. Y. Hsiao, D. A. Howell, C. McCully, S. Moran, J. Rho, D. J. Sand, M. Shahbandeh, S. Valenti, X. Wang, J. C. Wheeler, and G. Supernova Project. The Type II-P Supernova 2017eaw: From Explosion to the Nebular Phase. *ApJ*, 876(1):19, May 2019. doi: 10.3847/1538-4357/ab12d0.

Y. Tachibana and A. A. Miller. A Morphological Classification Model to Identify Unresolved PanSTARRS1 Sources: Application in the ZTF Real-time Pipeline. *PASP*, 130(12):128001, Dec. 2018. doi: 10.1088/1538-3873/aae3d9.

F. Taddia, J. Sollerman, G. Leloudas, M. D. Stritzinger, S. Valenti, L. Galbany, R. Kessler, D. P. Schneider, and J. C. Wheeler. Early-time light curves of Type Ib/c supernovae from the SDSS-II Supernova Survey. *A&A*, 574:A60, Feb. 2015. doi: 10.1051/0004-6361/201423915.

F. Taddia, C. Fremling, J. Sollerman, A. Corsi, A. Gal-Yam, E. Karamehmetoglu, R. Lunnan, B. Bue, M. Ergon, M. Kasliwal, P. M. Vreeswijk, and P. R. Wozniak. iPTF15dtg: a double-peaked Type Ic supernova from a massive progenitor. *A&A*, 592:A89, Aug. 2016. doi: 10.1051/0004-6361/201628703.

F. Taddia, M. D. Stritzinger, M. Bersten, E. Baron, C. Burns, C. Contreras, S. Holmbo, E. Y. Hsiao, N. Morrell, M. M. Phillips, J. Sollerman, and N. B. Suntzeff. The Carnegie Supernova Project I. Analysis of stripped-envelope supernova light curves. *A&A*, 609:A136, Feb. 2018. doi: 10.1051/0004-6361/201730844.

K. Taggart and D. A. Perley. Core-collapse, superluminous, and gamma-ray burst supernova host galaxy populations at low redshift: the importance of dwarf and starbursting galaxies. *MNRAS*, 503(3):3931–3952, May 2021. doi: 10.1093/mnras/stab174.

K. Takahashi, T. Yoshida, and H. Umeda. Evolution of Progenitors for Electron Capture Supernovae. *ApJ*, 771(1):28, July 2013. doi: 10.1088/0004-637X/771/1/28.

K. Takáts, M. L. Pumo, N. Elias-Rosa, A. Pastorello, G. Pignata, E. Paillas, L. Zampieri, J. P. Anderson, J. Vinkó, S. Benetti, M.-T. Botticella, F. Bufano, A. Campillay, R. Cartier, M. Ergon, G. Folatelli, R. J. Foley, F. Förster, M. Hamuy, V.-P. Hentunen, E. Kankare, G. Leloudas, N. Morrell, M. Nissinen, M. M. Phillips, S. J. Smartt, M. Stritzinger, S. Taubenberger, S. Valenti, S. D. Van Dyk, J. B. Haislip, A. P. LaCluyze, J. P. Moore, and D. Reichart. SN 2009N: linking normal and subluminous Type II-P SNe. *MNRAS*, 438(1):368–387, Feb. 2014. doi: 10.1093/mnras/stt2203.

K. Takáts, G. Pignata, M. L. Pumo, E. Paillas, L. Zampieri, N. Elias-Rosa, S. Benetti, F. Bufano, E. Cappellaro, M. Ergon, M. Fraser, M. Hamuy, C. Inserra, E. Kankare, S. J. Smartt, M. D. Stritzinger, S. D. Van Dyk, J. B. Haislip, A. P. LaCluyze, J. P. Moore, and D. Reichart. SN 2009ib: a Type II-P supernova with an unusually long plateau. *MNRAS*, 450(3):3137–3154, July 2015. doi: 10.1093/mnras/stv857.

T. M. Tauris, N. Langer, T. J. Moriya, P. Podsiadlowski, S.-C. Yoon, and S. I. Blinnikov. Ultra-stripped Type Ic Supernovae from Close Binary Evolution. *ApJ*, 778(2):L23, Dec. 2013. doi: 10.1088/2041-8205/778/2/L23.

T. M. Tauris, N. Langer, and P. Podsiadlowski. Ultra-stripped supernovae: progenitors and fate. *MNRAS*, 451(2):2123–2144, Aug. 2015. doi: 10.1093/mnras/stv990.

T. M. Tauris, M. Kramer, P. C. C. Freire, N. Wex, H.-T. Janka, N. Langer, P. Podsiadlowski, E. Bozzo, S. Chaty, M. U. Kruckow, E. P. J. van den Heuvel, J. Antoniadis, R. P. Breton, and D. J. Champion. Formation of Double Neutron Star Systems. *ApJ*, 846(2):170, Sept. 2017. doi: 10.3847/1538-4357/aa7e89.

M. Taylor, D. Cinabro, B. Dilday, L. Galbany, R. R. Gupta, R. Kessler, J. Marriner, R. C. Nichol, M. Richmond, D. P. Schneider, and J. Sollerman. The Core Collapse Supernova Rate from the SDSS-II Supernova Survey. *ApJ*, 792(2):135, Sept. 2014. doi: 10.1088/0004-637X/792/2/135.

R. S. Teja, A. Singh, D. K. Sahu, G. C. Anupama, B. Kumar, and A. J. Nayana. SN 2020jfo: A Short-plateau Type II Supernova from a Low-mass Progenitor. *ApJ*, 930(1):34, May 2022. doi: 10.3847/1538-4357/ac610b.

R. S. Teja, A. Singh, D. K. Sahu, G. C. Anupama, B. Kumar, T. Nakaoka, K. S. Kawabata, M. Yamanaka, A. Takey, and M. Kawabata. SN 2018gj: A Short Plateau Type II Supernova with Persistent Blueshifted Ha Emission. *ApJ*, 954(2): 155, Sept. 2023. doi: 10.3847/1538-4357/acdf5e.

R. S. Teja, J. A. Goldberg, D. K. Sahu, G. C. Anupama, A. Singh, V. Swain, and V. Bhalerao. SN 2021wvw: A Core-collapse Supernova at the Subluminous, Slower, and Shorter End of Type IIPs. *ApJ*, 974(1):44, Oct. 2024. doi: 10.3847/1538-4357/ad67d9.

G. Terreran, A. Jerkstrand, S. Benetti, S. J. Smartt, P. Ochner, L. Tomasella, D. A. Howell, A. Morales-Garoffolo, A. Harutyunyan, E. Kankare, I. Arcavi, E. Cappellaro, N. Elias-Rosa, G. Hosseinzadeh, T. Kangas, A. Pastorello, L. Tartaglia, M. Turatto, S. Valenti, P. Wiggins, and F. Yuan. The multifaceted Type II-L supernova 2014G from pre-maximum to nebular phase. *MNRAS*, 462(1):137–157, Oct. 2016. doi: 10.1093/mnras/stw1591.

T. A. Thompson, J. L. Prieto, K. Z. Stanek, M. D. Kistler, J. F. Beacom, and C. S. Kochanek. A New Class of Luminous Transients and a First Census of their Massive Stellar Progenitors. *ApJ*, 705(2):1364–1384, Nov. 2009. doi: 10.1088/0004-637X/705/2/1364.

L. Tomasella, E. Cappellaro, M. Fraser, M. L. Pumo, A. Pastorello, G. Pignata, S. Benetti, F. Bufano, M. Dennefeld, A. Harutyunyan, T. Iijima, A. Jerkstrand, E. Kankare, R. Kotak, L. Magill, V. Nascimbeni, P. Ochner, A. Siviero, S. Smartt, J. Sollerman, V. Stanishev, F. Taddia, S. Taubenberger, M. Turatto, S. Valenti, D. E. Wright, and L. Zampieri. Comparison of progenitor mass estimates for the Type IIP SN 2012A. *MNRAS*, 434(2):1636–1657, Sept. 2013a. doi: 10.1093/mnras/stt1130.

L. Tomasella, E. Cappellaro, M. Fraser, M. L. Pumo, A. Pastorello, G. Pignata, S. Benetti, F. Bufano, M. Dennefeld, A. Harutyunyan, T. Iijima, A. Jerkstrand, E. Kankare, R. Kotak, L. Magill, V. Nascimbeni, P. Ochner, A. Siviero, S. Smartt, J. Sollerman, V. Stanishev, F. Taddia, S. Taubenberger, M. Turatto, S. Valenti, D. E. Wright, and L. Zampieri. Comparison of progenitor mass estimates for the Type IIP SN 2012A. *MNRAS*, 434(2):1636–1657, Sept. 2013b. doi: 10.1093/mnras/stt1130.

N. Tominaga, S. I. Blinnikov, and K. Nomoto. Supernova Explosions of Super-asymptotic Giant Branch Stars: Multicolor Light Curves of Electron-capture Supernovae. *ApJ*, 771(1):L12, July 2013. doi: 10.1088/2041-8205/771/1/L12.

J. L. Tonry, L. Denneau, A. N. Heinze, B. Stalder, K. W. Smith, S. J. Smartt, C. W. Stubbs, H. J. Weiland, and A. Rest. ATLAS: A High-cadence All-sky Survey System. *PASP*, 130(6):064505, June 2018. doi: 10.1088/1538-3873/aabadf.

S. Toonen, H. B. Perets, A. P. Igoshev, E. Michaely, and Y. Zenati. The demographics of neutron star - white dwarf mergers. Rates, delay-time distributions, and progenitors. *A&A*, 619:A53, Nov. 2018. doi: 10.1051/0004-6361/201833164.

Transient Name Server. Astronote 2024-340: The first science spectrum with the next generation palomar spectrograph (ngps): Classification of ztf24abrfcqd as a type ia supernova. TNS AstroNote 2024-340, Nov. 2024. URL `https://www.wis-tns.org/astronotes/astronote/2024-340`. Released 2024-11-16.

T. Tsujimoto and T. Shigeyama. New Insights Into the Early Stage of the Galactic Chemical Evolution. *Ap&SS*, 265:49–50, July 1999. doi: 10.1023/A:1002144201050.

D. Tsuna, S. C. Wu, J. Fuller, Y. Dong, and A. L. Piro. Merger Precursor: Year-long Transients Preceding Mergers of Low-mass Stripped Stars with Compact Objects. *The Open Journal of Astrophysics*, 7:82, Sept. 2024. doi: 10.33232/001c.123897.

D. Y. Tsvetkov, A. A. Volnova, A. P. Shulga, S. A. Korotkiy, A. Elmhamdi, I. J. Danziger, and M. V. Ereshko. Observations and analysis of two type IIP supernovae: the intrinsically faint object SN 2005cs and the ambiguous object SN 2005ay. *A&A*, 460(3):769–776, Dec. 2006. doi: 10.1051/0004-6361:20065704.

M. Turatto, P. A. Mazzali, T. R. Young, K. Nomoto, K. Iwamoto, S. Benetti, E. Cappellaro, I. J. Danziger, D. F. de Mello, M. M. Phillips, N. B. Suntzeff, A. Clocchiatti, A. Piemonte, B. Leibundgut, R. Covarrubias, J. Maza, and J. Sollerman. The Peculiar Type II Supernova 1997D: A Case for a Very Low ^{56}Ni Mass. *ApJ*, 498(2):L129–L133, May 1998. doi: 10.1086/311324.

M. Ugliano, H.-T. Janka, A. Marek, and A. Arcones. Progenitor-explosion Connection and Remnant Birth Masses for Neutrino-driven Supernovae of Iron-core Progenitors. *ApJ*, 757(1):69, Sept. 2012. doi: 10.1088/0004-637X/757/1/69.

A. Uomoto. What Stars Become Peculiar Type I Supernovae? *ApJ*, 310:L35, Nov. 1986. doi: 10.1086/184777.

V. P. Utrobin and N. N. Chugai. Progenitor mass of the type IIP supernova 2005cs. *A&A*, 491(2):507–513, Nov. 2008. doi: 10.1051/0004-6361:200810272.

V. P. Utrobin and N. N. Chugai. High mass of the type IIP supernova 2004et inferred from hydrodynamic modeling. *A&A*, 506(2):829–834, Nov. 2009a. doi: 10.1051/0004-6361/200912273.

V. P. Utrobin and N. N. Chugai. High mass of the type IIP supernova 2004et inferred from hydrodynamic modeling. *A&A*, 506(2):829–834, Nov. 2009b. doi: 10.1051/0004-6361/200912273.

V. P. Utrobin and N. N. Chugai. Resolving the puzzle of type IIP SN 2016X. *MNRAS*, 490(2):2042–2049, Dec. 2019. doi: 10.1093/mnras/stz2716.

V. P. Utrobin, A. Wongwathanarat, H. T. Janka, and E. Müller. Light-curve Analysis of Ordinary Type IIP Supernovae Based on Neutrino-driven Explosion Simulations in Three Dimensions. *ApJ*, 846(1):37, Sept. 2017. doi: 10.3847/1538-4357/aa8594.

S. Valenti, S. Benetti, E. Cappellaro, F. Patat, P. Mazzali, M. Turatto, K. Hurley, K. Maeda, A. Gal-Yam, R. J. Foley, A. V. Filippenko, A. Pastorello, P. Challis, F. Frontera, A. Harutyunyan, M. Iye, K. Kawabata, R. P. Kirshner, W. Li, Y. M. Lipkin, T. Matheson, K. Nomoto, E. O. Ofek, Y. Ohyama, E. Pian, D. Poznanski, M. Salvo, D. N. Sauer, B. P. Schmidt, A. Soderberg, and L. Zampieri. The broad-lined Type Ic supernova 2003jd. *MNRAS*, 383(4):1485–1500, Feb. 2008. doi: 10.1111/j.1365-2966.2007.12647.x.

S. Valenti, D. Sand, M. Stritzinger, D. A. Howell, I. Arcavi, C. McCully, M. J. Childress, E. Y. Hsiao, C. Contreras, N. Morrell, M. M. Phillips, M. Gromadzki, R. P. Kirshner, and G. H. Marion. Supernova 2013by: a Type IIL supernova with a IIP-like light-curve drop*. *MNRAS*, 448(3):2608–2616, Apr. 2015. doi: 10.1093/mnras/stv208.

S. Valenti, D. A. Howell, M. D. Stritzinger, M. L. Graham, G. Hosseinzadeh, I. Arcavi, L. Bildsten, A. Jerkstrand, C. McCully, A. Pastorello, A. L. Piro, D. Sand, S. J. Smartt, G. Terreran, C. Baltay, S. Benetti, P. Brown, A. V. Filippenko, M. Fraser, D. Rabinowitz, M. Sullivan, and F. Yuan. The diversity of Type II supernova versus the similarity in their progenitors. *MNRAS*, 459(4):3939–3962, July 2016. doi: 10.1093/mnras/stw870.

G. Valerin, M. L. Pumo, A. Pastorello, A. Reguitti, N. Elias-Rosa, C. P. Gútierrez, E. Kankare, M. Fraser, P. A. Mazzali, D. A. Howell, R. Kotak, L. Galbany, S. C. Williams, Y. Z. Cai, I. Salmaso, V. Pinter, T. E. Müller-Bravo, J. Burke, E. Padilla Gonzalez, D. Hiramatsu, C. McCully, M. Newsome, and C. Pellegrino. Low luminosity Type II supernovae - IV. SN 2020cxd and SN 2021aai, at the edges of the sub-luminous supernovae class. *MNRAS*, 513(4):4983–4999, July 2022. doi: 10.1093/mnras/stac1182.

G. Valerin, A. Pastorello, A. Reguitti, S. Benetti, Y. Z. Cai, T. W. Chen, D. Eappachen, N. Elias-Rosa, M. Fraser, A. Gangopadhyay, E. Y. Hsiao, D. A. Howell, C. Inserra, L. Izzo, J. Jencson, E. Kankare, R. Kotak, P. A. Mazzali, K. Misra, G. Pignata, S. J. Prentice, D. J. Sand, S. J. Smartt, M. D. Stritzinger, L. Tartaglia, S. Valenti, J. P. Anderson, J. E. Andrews, R. C. Amaro, S. Brennan, F. Bufano, E. Callis, E. Cappellaro, R. Dastidar, M. Della Valle, A. Fiore, M. D.

Fulton, L. Galbany, T. Heikkilä, D. Hiramatsu, E. Karamehmetoglu, H. Kuncarayakti, G. Leloudas, M. Lundquist, C. McCully, T. E. Müller-Bravo, M. Nicholl, P. Ochner, E. Padilla Gonzalez, E. Paraskeva, C. Pellegrino, A. Rau, D. E. Reichart, T. M. Reynolds, R. Roy, I. Salmaso, M. Singh, M. Turatto, L. Tomasella, S. Wyatt, and D. R. Young. A study in scarlet: I. Photometric properties of a sample of intermediate-luminosity red transients. *A&A*, 695:A42, Mar. 2025. doi: 10.1051/0004-6361/202451733.

B. F. A. van Baal, A. Jerkstrand, D. Kresse, and H.-T. Janka. Emission line models for the lowest mass core-collapse supernovae – II. Full 3D NLTE radiative transfer modelling of a 9.0 $M_\odot$ neutrino-driven explosion. *arXiv e-prints*, art. arXiv:2511.07540, Nov. 2025. doi: 10.48550/arXiv.2511.07540.

S. van der Walt, A. Crellin-Quick, and J. Bloom. SkyPortal: An Astronomical Data Platform. *The Journal of Open Source Software*, 4(37):1247, May 2019. doi: 10.21105/joss.01247.

S. J. Van der Walt, A. Crellin-Quick, and J. S. Bloom. SkyPortal: An Astronomical Data Platform. *JOSS*, submitted, http://joss.theoj.org/papers/28a83ab43ff3ca23cdd831e82877365a, 2019.

S. J. van der Walt, A. Crellin-Quick, and J. S. Bloom. SkyPortal: An astronomical data platform. *Journal of Open Source Software*, 4(37), may 2019. doi: 10.21105/joss.01247. URL `http://joss.theoj.org/papers/10.21105/joss.01247`.

S. D. Van Dyk. Supernova Progenitors Observed with HST. In A. W. Alsabti and P. Murdin, editors, *Handbook of Supernovae*, page 693. 2017. doi: 10.1007/978-3-319-21846-5_126.

S. D. Van Dyk. Red Supergiants as Supernova Progenitors. *Galaxies*, 13(2):33, Apr. 2025. doi: 10.3390/galaxies13020033.

S. D. van Dyk, R. A. Sramek, K. W. Weiler, M. J. Montes, and N. Panagia. Supernova 1992ad in NGC 4411B. *IAU Circ.*, 6378:2, Apr. 1996.

S. D. Van Dyk, T. J. Davidge, N. Elias-Rosa, S. Taubenberger, W. Li, E. M. Levesque, S. Howerton, G. Pignata, N. Morrell, M. Hamuy, and A. V. Filippenko. Supernova 2008bk and Its Red Supergiant Progenitor. *AJ*, 143(1):19, Jan. 2012a. doi: 10.1088/0004-6256/143/1/19.

S. D. Van Dyk, T. J. Davidge, N. Elias-Rosa, S. Taubenberger, W. Li, E. M. Levesque, S. Howerton, G. Pignata, N. Morrell, M. Hamuy, and A. V. Filippenko. Supernova 2008bk and Its Red Supergiant Progenitor. *AJ*, 143(1):19, Jan. 2012b. doi: 10.1088/0004-6256/143/1/19.

S. D. Van Dyk, K. A. Bostroem, W. Zheng, T. G. Brink, O. D. Fox, J. E. Andrews, A. V. Filippenko, Y. Dong, E. Hoang, G. Hosseinzadeh, D. Janzen, J. E. Jencson,

M. J. Lundquist, N. Meza, D. Milisavljevic, J. Pearson, D. J. Sand, M. Shrestha, S. Valenti, and D. A. Howell. Identifying the SN 2022acko progenitor with JWST. *MNRAS*, 524(2):2186–2194, Sept. 2023a. doi: 10.1093/mnras/stad2001.

S. D. Van Dyk, K. A. Bostroem, W. Zheng, T. G. Brink, O. D. Fox, J. E. Andrews, A. V. Filippenko, Y. Dong, E. Hoang, G. Hosseinzadeh, D. Janzen, J. E. Jencson, M. J. Lundquist, N. Meza, D. Milisavljevic, J. Pearson, D. J. Sand, M. Shrestha, S. Valenti, and D. A. Howell. Identifying the SN 2022acko progenitor with JWST. *MNRAS*, 524(2):2186–2194, Sept. 2023b. doi: 10.1093/mnras/stad2001.

J. T. van Loon, M. R. L. Cioni, A. A. Zijlstra, and C. Loup. An empirical formula for the mass-loss rates of dust-enshrouded red supergiants and oxygen-rich Asymptotic Giant Branch stars. *A&A*, 438(1):273–289, July 2005. doi: 10.1051/0004-6361:20042555.

V. A. Villar, J. Guillochon, E. Berger, B. D. Metzger, P. S. Cowperthwaite, M. Nicholl, K. D. Alexander, P. K. Blanchard, R. Chornock, T. Eftekhari, W. Fong, R. Margutti, and P. K. G. Williams. The Combined Ultraviolet, Optical, and Near-infrared Light Curves of the Kilonova Associated with the Binary Neutron Star Merger GW170817: Unified Data Set, Analytic Models, and Physical Implications. *ApJ*, 851(1):L21, Dec. 2017. doi: 10.3847/2041-8213/aa9c84.

P. M. Vreeswijk, G. Leloudas, A. Gal-Yam, A. De Cia, D. A. Perley, R. M. Quimby, R. Waldman, M. Sullivan, L. Yan, E. O. Ofek, C. Fremling, F. Taddia, J. Sollerman, S. Valenti, I. Arcavi, D. A. Howell, A. V. Filippenko, S. B. Cenko, O. Yaron, M. M. Kasliwal, Y. Cao, S. Ben-Ami, A. Horesh, A. Rubin, R. Lunnan, P. E. Nugent, R. Laher, U. D. Rebbapragada, P. Woźniak, and S. R. Kulkarni. On the Early-time Excess Emission in Hydrogen-poor Superluminous Supernovae. *ApJ*, 835(1):58, Jan. 2017. doi: 10.3847/1538-4357/835/1/58.

S. Wanajo, K. Nomoto, H. T. Janka, F. S. Kitaura, and B. Müller. Nucleosynthesis in Electron Capture Supernovae of Asymptotic Giant Branch Stars. *ApJ*, 695(1): 208–220, Apr. 2009. doi: 10.1088/0004-637X/695/1/208.

S. Wanajo, H.-T. Janka, and B. Müller. Electron-capture Supernovae as The Origin of Elements Beyond Iron. *ApJ*, 726(2):L15, Jan. 2011. doi: 10.1088/2041-8205/726/2/L15.

B. Wang, D. Liu, Y. Guo, and Z. Han. The Formation of Neutron Star Systems through Electron-capture Supernovae: A Review. *arXiv e-prints*, art. arXiv:2509.25915, Sept. 2025. doi: 10.48550/arXiv.2509.25915.

B. Wang, D. Liu, Y. Guo, and Z. Han. The Formation of Electron-capture Supernovae: A Review. *Research in Astronomy and Astrophysics*, 26(3):032001, Mar. 2026. doi: 10.1088/1674-4527/ae2d0e.

E. Waxman and B. Katz. Shock Breakout Theory. In A. W. Alsabti and P. Murdin, editors, *Handbook of Supernovae*, page 967. 2017. doi: 10.1007/978-3-319-21846-5_33.

J. C. Wheeler, V. Johnson, and A. Clocchiatti. Analysis of late-time light curves of Type IIb, Ib and Ic supernovae. *MNRAS*, 450(2):1295–1307, June 2015. doi: 10.1093/mnras/stv650.

D. M. Wilkinson, C. Maraston, D. Goddard, D. Thomas, and T. Parikh. FIREFLY (Fitting IteRativEly For Likelihood analYsis): a full spectral fitting code. *MNRAS*, 472(4):4297–4326, Dec. 2017. doi: 10.1093/mnras/stx2215.

S. E. Woosley. Pulsational Pair-instability Supernovae. *ApJ*, 836(2):244, Feb. 2017. doi: 10.3847/1538-4357/836/2/244.

S. E. Woosley. The Evolution of Massive Helium Stars, Including Mass Loss. *ApJ*, 878(1):49, June 2019. doi: 10.3847/1538-4357/ab1b41.

S. E. Woosley and J. S. Bloom. The Supernova Gamma-Ray Burst Connection. *ARA&A*, 44(1):507–556, Sept. 2006. doi: 10.1146/annurev.astro.43.072103.150558.

S. E. Woosley and A. Heger. The Remarkable Deaths of 9-11 Solar Mass Stars. *ApJ*, 810(1):34, Sept. 2015. doi: 10.1088/0004-637X/810/1/34.

S. E. Woosley and T. A. Weaver. The Evolution and Explosion of Massive Stars. II. Explosive Hydrodynamics and Nucleosynthesis. *ApJS*, 101:181, Nov. 1995. doi: 10.1086/192237.

S. E. Woosley, N. Langer, and T. A. Weaver. The Evolution of Massive Stars Including Mass Loss: Presupernova Models and Explosion. *ApJ*, 411:823, July 1993. doi: 10.1086/172886.

A. H. Wright, A. S. G. Robotham, N. Bourne, S. P. Driver, L. Dunne, S. J. Maddox, M. Alpaslan, S. K. Andrews, A. E. Bauer, J. Bland-Hawthorn, S. Brough, M. J. I. Brown, C. Clarke, M. Cluver, L. J. M. Davies, M. W. Grootes, B. W. Holwerda, A. M. Hopkins, T. H. Jarrett, P. R. Kafle, R. Lange, J. Liske, J. Loveday, A. J. Moffett, P. Norberg, C. C. Popescu, M. Smith, E. N. Taylor, R. J. Tuffs, L. Wang, and S. M. Wilkins. Galaxy And Mass Assembly: accurate panchromatic photometry from optical priors using LAMBDAR. *MNRAS*, 460:765, July 2016. doi: 10.1093/mnras/stw832.

E. L. Wright, P. R. M. Eisenhardt, A. K. Mainzer, M. E. Ressler, R. M. Cutri, T. Jarrett, J. D. Kirkpatrick, D. Padgett, R. S. McMillan, M. Skrutskie, S. A. Stanford, M. Cohen, R. G. Walker, J. C. Mather, D. Leisawitz, T. N. Gautier, III, I. McLean, D. Benford, C. J. Lonsdale, A. Blain, B. Mendez, W. R. Irace, V. Duval, F. Liu, D. Royer, I. Heinrichsen, J. Howard, M. Shannon, M. Kendall, A. L. Walsh, M. Larsen, J. G. Cardon, S. Schick, M. Schwalm, M. Abid, B. Fabinsky, L. Naes, and C.-W. Tsai. The Wide-field Infrared Survey Explorer (WISE): Mission Description and Initial On-orbit Performance. *AJ*, 140:1868, Dec. 2010. doi: 10.1088/0004-6256/140/6/1868.

C. Wu, S. Zha, Y. Cai, Z. Zhang, Y. Yang, D. Xiang, W. Lin, X. Wang, and B. Wang. Light Curves of the Explosion of ONe White Dwarf + CO White Dwarf Merger Remnant and Type Icn Supernovae. *ApJ*, 967(2):L45, June 2024. doi: 10.3847/2041-8213/ad4a7a.

S. Wu and J. Fuller. A Diversity of Wave-driven Presupernova Outbursts. *ApJ*, 906 (1):3, Jan. 2021. doi: 10.3847/1538-4357/abc87c.

S. Wu and J. Fuller. Extreme mass loss in low-mass type Ib/c supernova progenitors. *arXiv e-prints*, art. arXiv:2210.10187, Oct. 2022a.

S. C. Wu and J. Fuller. Wave-driven Outbursts and Variability of Low-mass Supernova Progenitors. *ApJ*, 930(2):119, May 2022b. doi: 10.3847/1538-4357/ac660c.

D. Xiang, X. Wang, J. Mo, L. Wang, S. Smartt, M. Fraser, S. A. Ehgamberdiev, D. Mirzaqulov, J. Zhang, T. Zhang, J. Vinko, J. C. Wheeler, G. Hosseinzadeh, D. A. Howell, C. McCully, J. M. DerKacy, E. Baron, P. Brown, X. Zhang, S. Bi, H. Song, K. Zhang, A. Rest, K. Nomoto, A. Tolstov, and S. Blinnikov. Observations of SN 2017ein Reveal Shock Breakout Emission and a Massive Progenitor Star for a Type Ic Supernova. *ApJ*, 871(2):176, Feb. 2019. doi: 10.3847/1538-4357/aaf8b0.

L. Xiao and J. J. Eldridge. Core-collapse supernova rate synthesis within 11 Mpc. *MNRAS*, 452(3):2597–2605, Sept. 2015. doi: 10.1093/mnras/stv1425.

M. Yamanaka and T. Nagayama. The Near-infrared Echo from SN 2023xgo: Evidence for a Massive Presupernova Eruption in a Type Ibn/Icn Supernova. *ApJ*, 990(2):L44, Sept. 2025. doi: 10.3847/2041-8213/adfe5f.

S. Yan, X. Wang, X. Gao, J. Zhang, A. V. Filippenko, T. G. Brink, J. Mo, W. Lin, D. Xiang, X. Ma, F. Guo, L. Tomasella, S. Benetti, Y. Cai, E. Cappellaro, Z. Chen, Z. Li, A. Pastorello, and T. Zhang. Discovery of the Closest Ultra-stripped Supernova: SN 2021agco in UGC 3855. *ApJ*, 959(2):L32, Dec. 2023. doi: 10.3847/2041-8213/ad0cc3.

S. Yang, J. Sollerman, N. L. Strotjohann, S. Schulze, R. Lunnan, E. Kool, C. Fremling, D. Perley, E. Ofek, T. Schweyer, E. C. Bellm, M. M. Kasliwal, F. J. Masci, M. Rigault, and Y. Yang. A low-energy explosion yields the underluminous Type IIP SN 2020cxd. *A&A*, 655:A90, Nov. 2021. doi: 10.1051/0004-6361/202141244.

Y. Yao, K. De, M. M. Kasliwal, A. Y. Q. Ho, S. Schulze, Z. Li, S. R. Kulkarni, A. Fruchter, D. Rubin, D. A. Perley, J. Fuller, A. L. Piro, C. Fremling, E. C. Bellm, R. Burruss, D. A. Duev, M. Feeney, A. Gal-Yam, V. Z. Golkhou, M. J. Graham, G. Helou, T. Kupfer, R. R. Laher, F. J. Masci, A. A. Miller, B. Rusholme, D. L. Shupe, R. Smith, J. Sollerman, M. T. Soumagnac, and J. Zolkower. SN2019dge: A Helium-rich Ultra-stripped Envelope Supernova. *ApJ*, 900(1):46, Sept. 2020. doi: 10.3847/1538-4357/abaa3d.

O. Yaron and A. Gal-Yam. WISeREP—An Interactive Supernova Data Repository. *PASP*, 124(917):668, July 2012a. doi: 10.1086/666656.

O. Yaron and A. Gal-Yam. WISeREP - An Interactive Supernova Data Repository. *PASP*, 124:668–681, July 2012b. doi: 10.1086/666656.

O. Yaron, D. A. Perley, A. Gal-Yam, J. H. Groh, A. Horesh, E. O. Ofek, S. R. Kulkarni, J. Sollerman, C. Fransson, A. Rubin, P. Szabo, N. Sapir, F. Taddia, S. B. Cenko, S. Valenti, I. Arcavi, D. A. Howell, M. M. Kasliwal, P. M. Vreeswijk, D. Khazov, O. D. Fox, Y. Cao, O. Gnat, P. L. Kelly, P. E. Nugent, A. V. Filippenko, R. R. Laher, P. R. Wozniak, W. H. Lee, U. D. Rebbapragada, K. Maguire, M. Sullivan, and M. T. Soumagnac. Confined dense circumstellar material surrounding a regular type II supernova. *Nature Physics*, 13(5):510–517, Feb. 2017. doi: 10.1038/nphys4025.

S.-C. Yoon. Evolutionary Models for Type Ib/c Supernova Progenitors. *PASA*, 32: e015, Apr. 2015. doi: 10.1017/pasa.2015.16.

S. C. Yoon, S. E. Woosley, and N. Langer. Type Ib/c Supernovae in Binary Systems. I. Evolution and Properties of the Progenitor Stars. *ApJ*, 725(1):940–954, Dec. 2010a. doi: 10.1088/0004-637X/725/1/940.

S.-C. Yoon, S. E. Woosley, and N. Langer. Type Ib/c Supernovae in Binary Systems. I. Evolution and Properties of the Progenitor Stars. *ApJ*, 725:940–954, Dec. 2010b. doi: 10.1088/0004-637X/725/1/940.

T. Yoshida, Y. Suwa, H. Umeda, M. Shibata, and K. Takahashi. Explosive nucleosynthesis of ultra-stripped Type Ic supernovae: application to light trans-iron elements. *MNRAS*, 471(4):4275–4285, Nov. 2017. doi: 10.1093/mnras/stx1738.

F. Yuan, A. Jerkstrand, S. Valenti, J. Sollerman, I. R. Seitenzahl, A. Pastorello, S. Schulze, T.-W. Chen, M. J. Childress, M. Fraser, C. Fremling, R. Kotak, A. J. Ruiter, B. P. Schmidt, S. J. Smartt, F. Taddia, G. Terreran, B. E. Tucker, C. Barbarino, S. Benetti, N. Elias-Rosa, A. Gal-Yam, D. A. Howell, C. Inserra, E. Kankare, M. Y. Lee, K. L. Li, K. Maguire, S. Margheim, A. Mehner, P. Ochner, M. Sullivan, L. Tomasella, and D. R. Young. 450 d of Type II SN 2013ej in optical and near-infrared. *MNRAS*, 461(2):2003–2018, Sept. 2016. doi: 10.1093/mnras/stw1419.

L. Zampieri, A. Pastorello, M. Turatto, E. Cappellaro, S. Benetti, G. Altavilla, P. Mazzali, and M. Hamuy. Peculiar, low-luminosity Type II supernovae: low-energy explosions in massive progenitors? *MNRAS*, 338(3):711–716, Jan. 2003. doi: 10.1046/j.1365-8711.2003.06082.x.

E. Zapartas, S. E. de Mink, R. G. Izzard, S. C. Yoon, C. Badenes, Y. Götberg, A. de Koter, C. J. Neijssel, M. Renzo, A. Schootemeijer, and T. S. Shrotriya. Delay-time distribution of core-collapse supernovae with late events resulting from binary interaction. *A&A*, 601:A29, May 2017. doi: 10.1051/0004-6361/201629685.

E. Zapartas, S. E. de Mink, S. Justham, N. Smith, A. de Koter, M. Renzo, I. Arcavi, R. Farmer, Y. Götberg, and S. Toonen. The diverse lives of progenitors of hydrogen-rich core-collapse supernovae: the role of binary interaction. *A&A*, 631:A5, Nov. 2019. doi: 10.1051/0004-6361/201935854.

E. Zapartas, S. E. de Mink, S. Justham, N. Smith, M. Renzo, and A. de Koter. Effect of binary evolution on the inferred initial and final core masses of hydrogen-rich, Type II supernova progenitors. *A&A*, 645:A6, Jan. 2021. doi: 10.1051/0004-6361/202037744.

Y. Zenati, S. Toonen, and H. B. Perets. Formation and evolution of hybrid He-CO white dwarfs and their properties. *MNRAS*, 482(1):1135–1142, Jan. 2019. doi: 10.1093/mnras/sty2723.

J. Zhang, X. Wang, P. A. Mazzali, J. Bai, T. Zhang, D. Bersier, F. Huang, Y. Fan, J. Mo, J. Wang, W. Yi, C. Wang, Y. Xin, Liangchang, X. Zhang, B. Lun, X. Wang, S. He, and E. S. Walker. Optical and Ultraviolet Observations of a Low-velocity Type II Plateau Supernova 2013am in M65. *ApJ*, 797(1):5, Dec. 2014. doi: 10.1088/0004-637X/797/1/5.

J. Zhang, X. Wang, V. József, Q. Zhai, T. Zhang, A. V. Filippenko, T. G. Brink, W. Zheng, Ł. Wyrzykowski, P. Mikołajczyk, F. Huang, L. Rui, J. Mo, H. Sai, X. Zhang, H. Wang, J. M. DerKacy, E. Baron, K. Sárneczky, A. Bódi, G. Csörnyei, O. Hanyecz, B. Ignácz, C. Kalup, L. Kriskovics, R. Könyves-Tóth, A. Ordasi, A. Pál, Á. Sódor, R. Szakáts, K. Vida, and G. Zsidi. SN 2018zd: an unusual stellar explosion as part of the diverse Type II Supernova landscape. *MNRAS*, 498(1):84–100, Oct. 2020. doi: 10.1093/mnras/staa2273.

W. Zhang, S. E. Woosley, and A. Heger. Fallback and Black Hole Production in Massive Stars. *ApJ*, 679(1):639–654, May 2008. doi: 10.1086/526404.

Z. Zhao, J. Zhang, L. Li, Q. Zhai, Y. Cai, S. Srivastav, X. Wang, H. Lin, Y. Yang, A. V. Filippenko, T. G. Brink, and W. Zheng. SN 2021dbg: A Luminous Type IIP–IIL Supernova Exploding from a Massive Star with a Layered Shell. *ApJ*, 973(2):155, Oct. 2024. doi: 10.3847/1538-4357/ad5fe8.

V. Zubko, E. Dwek, and R. G. Arendt. Interstellar Dust Models Consistent with Extinction, Emission, and Abundance Constraints. *ApJS*, 152(2):211–249, June 2004. doi: 10.1086/382351.